A NEW LOOK AT SILE CLAY DEPOSITS, EASTERN ISTANBUL: DETAILED CHARACTERIZATION AND PROVENANCE

by

HUSEYIN DEMIR

(Under the Direction of Paul A. Schroeder)

ABSTRACT

X-ray diffraction and chemical analyses of lacustrine Oligo-Miocene clay deposits and surrounding rocks in the Sile region northeast of Istanbul, Turkey were conducted to better understand the geologic history of commercially important clay units. Kaolinite is a major constituent, with illite, chlorite, vermiculite, smectite, and mixed-layers also common in the clay deposits that unconformably overlie Paleozoic metasediments, Permian-Triassic Limestones, and Late Cretaceous flysch series and volcanic/volcano-sedimentary rocks. Principal component analysis of elemental concentrations in clays and rocks supports the hypothesis that the lacustrine sediments were derived from highly weathered Paleozoic and Mesozoic sources formed during warm and humid climatic times. Mineral assemblages in the clay deposits were furthered modified by burial diagenetic events and then surface weathering events, initiated with neotectonics in the late Miocene, which continue today in the Earth's critical zone (the complex near surface environment that includes rock, soil, water, air, and living organisms regulating life-sustaining resources).

INDEX WORDS: clays, kaolinite, XRD, QXRD, clay fraction, Principal Component Analysis, geochemistry, Paleoenvironment, clay deposits, provenance, Critical zone

A NEW LOOK AT SILE CLAY DEPOSITS, EASTERN ISTANBUL: DETAILED CHARACTERIZATION AND PROVENANCE

by

HUSEYIN DEMIR
B.A., Ankara University, Turkey, 2014

A Thesis Submitted to the Graduate Faculty of The University of Georgia in Partial Fulfillment of the Requirements for the Degree

MASTER OF SCIENCE

ATHENS, GEORGIA
2021

A NEW LOOK AT SILE CLAY DEPOSITS, EASTERN ISTANBUL: DETAILED CHARACTERIZATION AND PROVENANCE

by

HUSEYIN DEMIR

Major Professor:	Paul A. Schroeder
Committee:	Doug Crowe
	Mattia Pistone

Electronic Version Approved:

Ron Walcott
Vice Provost for Graduate Education and Dean of the Graduate School
The University of Georgia
May 2021

DEDICATION

I dedicate this work to my beautiful and alone country, my family, and Paul Schroeder.

ACKNOWLEDGEMENTS

Thank you to my advisor Paul A. Schroeder for his great advice and collaboration along the way. Great thanks to Ömer Işık Ece, Emin Çiftçi, Yusuf Kağan Kadıoğlu and Halim Mutlu for their references. I would like to thank Istanbul Technical University-Geology and Ankara University-Geology departments for the support. Many thanks to great geologist Orhan Yavuz for guiding me during field studies.

I would like to thank Cumhur Özcan Kılıç, Zeynep Ergun Kılıç, Enes Zengin, Ömer Kamacı, Işıl Nur Güraslan, Işık Su Yazıcı and Bear Jordan for their support along the journey.

This master education is funded by the Republic of Turkey. Great thanks to people who are paying my education with their taxes, to people whom I do not really know, to people who selected and trusted me. I will always try working hard without getting tired in any minute.

Special thanks to Steven Holland, Doug Crowe and Mattia Pistone for their great help and advice.

I would like to acknowledge the Miriam Watts-Wheeler Fund in the department of Geology and the Clay Mineral Society for funding the current research.

TABLE OF CONTENTS

Page

LIST OF TABLES

Page

LIST OF FIGURES

Page

CHAPTER 1
INTRODUCTION

Kaolinite is one of the most common clay minerals on Earth, produced by chemical alteration of feldspars and Al-rich mineral phases occurring during in situ weathering of rocks (i.e., primary) or related to sedimentary processes (i.e., secondary-hosted) (Schroeder and Erickson, 2014). Kaolinite has comprehensive industrial applications, including ceramics, paints, paper, pharmaceutical products, cement, membrane, geopolymer, wastewater treatment, biochar, catalysis, pesticides, detergents, cosmetics (Murray and Keller, 1993; Zunino et al., 2020; Zhang et al., 2020; Fellah et al.,2020; Olu-Owolabi et al.,2021; Gianni et al.,2020; Mubarak et al., 2021; Rashad et al., 2021; Awwad et al., 2020; Cao et al., 2021; Cai et al., 2021). As well as many industrial applications, kaolinite-rich deposits are also essential mineral markers that record paleo-environmental factors that can be used for interpreting the geologic history of a region. Kaolinite-bearing units can carry significant knowledge in terms of the weathering processes of parent materials and soil development mechanisms in time and space for both Earth and other planets (Fackrell et al., 2020).

The Sile region is an excellent natural laboratory to investigate clay occurrences of kaolinite. Sile kaolinite-rich clay deposits are known as one of Turkey's most significant clay resources and are economically important (Ece et al, 2003). These clay-rich units mainly consist of mixed-layer clays, illite, and quartz in addition to kaolinite. Mineral abundances in the deposits vary both vertically and horizontally. Surrounding rocks in the region are comprised of Istanbul Paleozoic meta-sedimentary units[1], Permo-Triassic sedimentary rocks, Late Cretaceous volcanic/volcano-sedimentary[2] rocks and flysch series[3]. These clay deposits are found on top of different aged basement rocks. Previously, volcanic rock hosted clays have been studied (Ece et al, 2003) and they were interpreted to

[1] The Istanbul Paleozoic Units: Continuous sedimentary sequence from Ordovician to Carboniferous, known as the Istanbul Paleozoic Units.
[2] Volcano-sedimentary rocks: Rocks formed from volcanic and sedimentary events
[3] Flysch series: Sequence of sedimentary rock layers that consists of sandstone interbedded with shale, mudstone, and calcareous mudstone.

originate from related volcanism, following post-depositional alteration by humic acid in a lacustrine basin.

The current study is the first attempt to evaluate these clays from a broader perspective. The geological, mineralogical, and geochemical characteristics and genesis of this economically important clay deposit have been examined previously, but not in the context of a multiple working hypothesis that explores different provenances (sediment sources) and different stages of post-depositional alterations. The present study has attempted to fill this gap. The study aims to characterize clay minerals and chemistry in detail and investigate clay-rich units' provenance by applying mineralogical and geochemical methods. This new data will provide a critical conclusion about the genetic relationship of clay rich sediments and their primary host units. Additionally, this research will guide future exploration and utilization of these deposits.

Hypotheses

One of the hypotheses of the study is that clay deposits should be independent of unconformably underlying basements and should be similar regarding mineralogy and geochemistry. The other hypothesis is that the source of sediments for clay deposits should include multiple provenances found in the region. In order to test both hypotheses, clay deposits situated unconformably on top of different basements (i.e., “hosted” by different rocks) and potential source rocks are sampled and compared using mineral and chemical signatures. The sampling plan also included collecting host rocks altered by exposure to modern day weathering to further understand the potential source rocks weathering mineral assemblages that might proxy for paleo-weathering conditions.

CHAPTER 2
GENERAL GEOLOGIC SETTINGS

It is said that "Rocks and soil are gold in Istanbul"[4]. This expression might reflect its popularity throughout history. Istanbul has always been the center of attraction, thanks to its transcontinental location between Europe and Asia. Recent studies have revealed that Istanbul's history goes as far back as to the Neolithic era with first settlements and probably to the Paleolithic era with human traces around the region. In the common era, the city had served as the capital of the Roman Empire, Eastern Roman (Byzantine) Empire, and Ottoman Empire for ages before The Republic of Turkey formed. Today, the city is the economic center of Turkey, with almost 20% of the population of Turkey. Although it has relatively small aerial extent as a city, Istanbul has a very complex geologic history, including both paleotectonic and neotectonic stages[5] of the geologic development. The city is situated on the Thracia (Çatalca) and Kocaeli Plateaus with an average elevation of 150 m. The western and eastern parts are known as Catalca Peninsula and Kocaeli Peninsula, respectively. The study area is in the vicinity of Sile region, which is situated in the northern part of the Kocaeli Peninsula.

Turkey consists of multiple continental fragments, resulting from the development of the Tethys oceanic system and subdivided into six major tectonic fragments, which are the Strandja Massif, Istanbul zone, Sakarya zone, Anatolide-Tauride Block, Kırşehir Massif, and Arabian Platform (Şengör and Yılmaz, 1981). The Pontides to the North is comprised of three regions bearing diverse geological history: including the Rhodope-Strandja, Sakarya, and Istanbul zones. The Istanbul zone is interpreted as a rifted fragment from the Odesa shelf that was translated to the south with the opening of the western Black Sea basin (Okay et al., 1994). According to Tüysüz et al. (2016), the İstanbul Zone was

[4] "Rocks and soil are gold in Istanbul"- This expression that "Istanbul`un taşı toprağı altındır" in Turkish was being used by Ottoman Turks due to attraction of Istanbul, which was the capital of the empire. English translation of this Anatolian expression first appeared in Sen, 2016 published in Geoversitas, where he discussed the meaning of the expression in the introduction.

[5] According to Şengör and Yılmaz (1981), the collision between Arabian and Anatolia indicates the end of the paleotectonic period and the beginning of the neotectonic regime for Anatolia and surrounding areas. This paper is one of the most cited paper in the geology community of Turkey.

emplaced into its present position during Cenomanian time while the three Pontic terranes (mentioned above) were juxtaposed into a single plate (Fig 1 A,B).

The region is part of the Istanbul Zone, which is referred to as the Pontides together with the Strandja and Sakarya Zone. The Pontides are the region north of the Izmir-Ankara-Erzincan suture, which is a remnant of the Tethys ocean. The Istanbul Zone is separated from the Sakarya Zone and the Strandja Massif by the Intra Pontide Suture and Western Black Sea Fault, respectively (Okay and Tüysüz, 1999). It extends from Istanbul to farther east near Zonguldak.

The geology in the Istanbul consists of Paleozoic, Mesozoic and Cenozoic rocks. Much older metamorphic basement units crop out farther east in the Bolu Massif (Ustaömer et al. 2005). The Paleozoic consists of sedimentary sequences ranging in age from the Ordovician to the Carboniferous (Özgül,2012). Paleozoic and Permo-Triassic units are overlain by Late Cretaceous sediments. These units are overlain by reefal carbonates and terrestrial clastics that were deposited in the Eocene and in the Oligocene, respectively. The geology of the region has entered a new stage and experienced entirely different influence since Late Miocene as a result of the North Anatolian Shear System (Şengör and Kindap, 2019). All units in the region are overlain with Plio-Quaternary and Quaternary sediments.

The Istanbul Paleozoic sequence in the study area is represented by different regressivr and transgressive basin units, which are intensely faulted. The sequence starts with early Ordovician clastics that comprises marine turbidites, deltaic deposits and passes upwards into terrestrial fluvial units composed of purple arkosic conglomerate, sandstone, siltstone and shale intercalations. These are overlain by early Ordovician shore-shallow-sea quartz sandstones, and lagoonal-shelf facies middle Ordovician to early Silurian conglomerates and shale and sandstone-shale. These formations are overlain by late Silurian to early Devonian limestone, nodular limestone (shelf-deep shelf transition) and then limestone interlayered with micaceous shale and sandstone that are early to middle Devonian in age, deposited in a deep shelf facies. These were followed by middle to late Devonian-early Carboniferous cherty limestone (deep shelf slope) and early to middle Carboniferous turbiditic sandstone and shale alternation in the uppermost of the Palaezoic succession (Gedik et al., 2005). Different formation names have been used in different

review studies for these Palaezoic units. As such, formation are herein avoided since they are ambiguous. Recently, Ozgul (2012) distinguished members of the Istanbul Paleozoic in more detail. The Istanbul Paleozoic sedimentary sequence is also summarised by Lom et al., (2016).

The Permian-early Triassic (Permo-Triassic, early to middle Triassic?) terrestial succession unconformably covers the Paleozoic units in the study area. This successions are divided into three partly different units (Gedik, 2005). These start at the bottom with red-colored fluvial deposits and passes into shallow water sandstone and carbonate. Sandy and clayey limestone and dolomitic limestone and dolomites characterizing shallow shelf overlie these units (Yurtsever,1982). These series were found only around thrust zone within the study area but more common in the further east. Late Triassic and Jurassic rocks were absent in the study area.

There is a volcanic and volcano-sedimentary rocks sequence found to the northern part of the study area related to arc magmatism resulting from the north-dipping subduction of the Neo-Tethys Ocean along the İzmir-Ankara-Erzincan suture (Şengör and Yılmaz, 1981). Using isotopic data from the Central Pontides, Okay et al. (2006) concluded that the Neo-Tethys was already subducting under the Pontides in the Early Cretaceous (105 Ma.), with the magmatic arc beginning to develop in the Late Cretaceous. U-Pb zircon ages obtained from calc-alkaline andesitic to dacitic dikes within the Istanbul Paleozoic unit in the south yield ages ranging from 72.49 ± 0.79 to 65.44 ± 0.93 Ma (Aysal et al, 2015). The volcanism ceased by the end of the late Cretaceous (Şengör and Kindap, 2019) and these volcanic and volcano-sedimentary rocks are overlain by late Cretaceous-Paleocene pelagic limestone and marl (Ketin and Gümüş 1963). During the Eocene, multiple collisions of small continental fragments resulted in compressional movements, giving rise to pre-Lutetian folding and faulting in the study area (Şengör and Yılmaz, 1981; Gedik et al. (2005). During this event Paleozoic, and Mesozoic units were thrusted over the Upper Cretaceous- early Eocene sequence (Ozgul, 2012), known as the east-west striking Şile Thrust. The Sile Thrust is a back thrust associated with the closing of the northern branch of the Neo-Tethys Ocean, known as the Intra-Pontide Ocean. The Lutetian shelf and shallow marine succession composed of interbedded shale-limestone and sandstone was deposited in the Sile region. Because of the movement of the Sile thrust, the study area

experienced rapid, post collisional uplift and there was no deposition until Pliocene in the region (Lom et al., 2016). However, Gedik et al. (2005) suggested that deposition started in Oligo-Miocene based on the palynological from the coal layer within the terrestrial clastic sediments.

All tectonic events leading up to the Miocene are collectively considered as the Paleotectonic period. The new tectonic era, the Neotectonic, characterized the region since at least the late Miocene. The elimination of the last portion of ocean between Arabian and the Anatolian plates developed the North Anatolian Shear System, and gave rise to the North Anatolian Fault[6], which initiated its' dextral strike-slip motion around late-medial Miocene (Şengör et al. 1985; Yılmaz, 1993; Le Pichon et al.,2001; Okay, 2008). Although the fault was initiated across the full region in the Pliocene (Bozkurt, 2001), the shear system has been extant since late Miocene (Şengör and Kindap, 2019). This new phase reveals itself by extensional features in the study area (Fig 1 C).

Annotated review of key geologic studies in the Sile region

Yeniyol, (1984) studied the kaolin and sedimentary clay deposits located at the north of Istanbul (including the Sile region), which are related to the alteration of Upper Cretaceous volcanic rocks.

Esenli et al., (1997) identified zeolitic alteration on volcanic rocks in Sile region. They identified mordenite mineralization in volcanic rocks that show silicification and a low degree of clay alteration.

Coban et al., (2002) worked on the geochemistry of volcanic rocks and clay minerals in the Sile region, and concluded that clay deposits are derived from volcanic rocks and post depositional alteration.

Okay et al., (1994) studied the tectonics of the Black Sea, unraveling the kinematic history of the sea and its effect on the surrounding regions by providing a tectonic model.

The study of Ece et al., (2003) focused on the genesis of kaolin deposits related to the alteration of volcanic rocks in Sile region. Using their knowledge of the stratigraphy of the region combined with the XRD and SEM results, they concluded that the genesis of kaolin deposits took place in two stages: in situ weathering of the oldest andesitic

[6] This young strike-slip fault zone was first identified by Ketin (1966) upon repeated severe earthquakes.

pyroclastic rocks at the base of a lacustrine basin, followed by surface weathering enhanced transport of altered rocks into the basin.

Ece and Nakagawa, (2003) studied the genesis of kaolin deposits in the Şile region, and considered the differential mobility of elements. The mobility of major and trace elements during the progressive kaolinization gave insights into the geochemical characteristics of the volcanic rocks, and the mineralogical processes that form a kaolin deposit. They studied the geochemical characteristics of andesitic rocks in the area, revealing that these were products of multi-stage island arc magmatism. They also proposed that the Şile kaolins were mainly derived from the alteration of feldspar and muscovite, and that the alteration was initiated by with *in situ* hydrothermal alteration, and secondary alteration continued with surface weathering of these rocks.

Gedik et al., (2005) reported the general geology of the Istanbul and surrounding area describing the geologic history of the region.

Özdamar et al., (2007) studied the mineralogical and technological properties of underclay deposits in the region. The determined the mineralogical, chemical and technological characteristics of the underclays and their potential for use in the ceramic industry for the production of tiles.

Ozgul (2012) reviewed the stratigraphy and structural features of the Paleozoic units of Istanbul, detailing early evolution of the region.

Lom et al., (2016) summarized the general geological and tectonic features of different terranes in the Istanbul region, gathering the previous studies in the region and combining them with their own field observations.

Tüysüz, (2018) explained the Cretaceous geological evolution of the Pontides in the Black Sea Region, including the geodynamic evolution of the volcanic rocks. They concluded that the Black Sea Basin possibly opened in two stages: first a wide-rift style which caused thinning of the continental crust coeval with the opening of Zonguldak-Ulus basin, followed by the Pontide Magmatic Belt, which started to develop as an extensional arc and caused break-up of the already thinned crust causing oceanic spreading in the Western Black Sea basin during the Turonian-Santonian.

Aysal et al., (2018) studied the geochronology, geochemistry and isotope systematics of a mafic-intermediate dike complex in the Istanbul zone. They present new

U-Pb zircon ages ranging from Upper Cretaceous-Campanian to Lower Paleocene-Danian for the intermediate dykes, and Upper Paleocene-Thanetian for a granodiorite stock. They also present major-trace element, mineral chemistry and Sr-Nd isotope data. They concluded that the dike complexes of the Istanbul zone were emplaced in a rifted volcanic arc margin related to the opening of the Black Sea during the Late Cretaceous-Paleocene.

Keskin and Tüysüz, (2018) worked on the stratigraphy, petrogenesis and geodynamic setting of Late Cretaceous volcanism on the SW margin of the Black Sea, Turkey. They made stratigraphic correlations based on their field studies, later combining these with petrography and major-trace element data and petrological models. They argued that during the second stage of magmatism during the Campanian, magmas were derived from two contrasting magma sources: a depleted lithospheric mantle enriched by a subduction component and an enriched lithospheric mantle similar to ocean island basalts. Geodynamically, they proposed that the rifting and temporal change in magma generation was caused by the steepening and rollback of the northward subducting slab of the Tethys ocean.

Boehm et al., (2019) provided biostratigraphic ages from nano/microfossils of Upper Cretaceous volcano-sedimentary units. They also studied the major and trace element characteristics of the volcanic rocks within the units. They concluded that the units were deposited in a pelagic to hemipelagic environment including deep water mass-flow turbidite systems. The biostratigraphic correlations made it possible to specify a date for the main volcanic activity: Turonian-Santonian for the Dereköy Formation and early to middle Campanian for the Cambu Formation. The major and trace element data indicated a volcanic arc setting with calc-alkaline to shoshonitic character for the volcanic rocks.

Şengör and Kindap, (2019) focused on the geologic and geomorphologic settings of the Istanbul, characterizing the current features of its geography. They concluded that the North Anatolian Shear Zone is mostly responsible from current landscapes of Istanbul.

CHAPTER 3
SAMPLING AND ANALYTICAL METHODS

Field Sampling

Samples were collected in three different sampling campaigns in 2017, 2019, and 2020 in the Sile region, northeast of Istanbul (Fig. 2). Sample collecting was limited by mine access and to outcrops along roadsides because much of the region is either forested or urbanized. Representative samples were gathered within the stratigraphic sequence from actively operated private mines in different parts of the region. Three mines were accessed where basement included one of three rock types, including volcanic/volcano-sedimentary rocks, sandstone, and limestone. The contacts between Neogene clay deposits and the underlying basement were gradational and exact boundaries were not observed. However, with each different host rock, clays deposits transitioned into different colored layers that were readily visible (see in Fig 3, 6, 12, 18). In one case, the mining company (Eryilmazlar) drilled into the basement of the quarry located over a sandstone. Sampling of that sandstone was permitted and is included in this study. The Neogene lacustrine deposits clay rich sections were sampled, including those at the bottom and top of coal layers. Rock samples were also collected from potential source rocks to the Neogene lacustrine deposits, including Paleozoic and Mesozoic units. Therefore, when possible, a fresh (i.e., less weathered) sample was collected and then additional samples were collected considering the weathering degree in a vertical succession toward the soil surface. It was assumed that the weathered samples represented recent surficial processes that operate with the critical zone (Schroeder, 2018). In total, 110 samples were collected, photographed, and labeled using an identification scheme that included an “S” for Sile, the campaign year, and sequential number in the order of sample collection (e.g., S17_01) in the field. A table of sample global positioning system (GPS) coordinates and photographs are in appendix I. Approximately 0.5 kg of material was collected, from which 100 g was split and sealed in a plastic bag and transported from Istanbul Technical University (ITU) to the University of Georgia (UGA) for laboratory analyses. Excess material was archived into storage at ITU. In all campaigns, Dr. Orhan Yavuz of the ITU Department of Geological Engineering assisted with sampling and facilitated access to the private mines.

Analytical Methods

X-ray Powder Diffraction (XRD)

XRD was implemented to characterize both bulk and clay fraction (<2 microns) in mineral assemblages of the collected samples. For bulk mineralogy, approximately 10 g of each sample was taken and dried in an oven at 65°C overnight. Approximately 5 g of dried sample was hand-ground with a corundum mortar. The powder was then further ground in a McCrone micronizing mill for 10 minutes with 10 ml ethyl alcohol to reduce the particle size to an average of 5 to 10 microns. This step was performed two times. The first one was with 10% ZnO added as an internal standard (IS) and second one was without the standard. Samples were dried to remove alcohol in an oven at 65°C overnight and then backfilled against a plate glass into a 2.5 x 2.5 cm aluminum holder. The powder was pressed at 400 psi to make a flat self-supporting mount that was even to the holder surface. The purpose is to minimize sample transparency and keep sample geometry tangential to the instrument-focusing circle once placed in the instrument. A Bruker D8 Advance X-ray Diffractometer Instrument (see https://geology.uga.edu/research/lab/x-ray-diffraction-lab) was set up that included a 250 cm goniometer radius, a 0.6mm divergent slit, and Bragg-Bentano geometry. A knife-edge blade was placed 2mm over the samples surface to minimize low angle scatter into the Lynx-Eye® position sensitive detector. A cobalt radiation source operated at 35 kV and 40 mA, was used ($K\alpha_1$ = 1.7890Å and $K\alpha_2$ = 1.7928Å) with an iron filter to minimize Kα radiation. An external NIST Reference standard SRM1976b corundum (α-Al_2O_3) was run to confirm alignment and calibration within 0.05 ° 2Θ tolerance of the certificate value for the strongest reflection peak position. Scan range extended from 2 to 80° 2Θ, using locked-coupled continuous scan mode with a step size of 0.01° 2 Θ and count rate of 0.1 seconds per step. Raw data and plots are presented with patterns and peak positions determined by Bruker Eva® software. Raw data was $K\alpha_2$ stripped. The IS was used to correct for sample displacement error, which is usually less than 0.05° 2Θ. Peak positions were matched with data from the International Centre for Diffraction Data (ICDD) powder diffraction file (PDF) data base. Eva software was used with the 2019-PDF database to find best-fit phases for mineral identification. Structure files for each phase identified were exported, which contained unit cell lattice

parameters, atom types, and atomic coordinates. Many of the sample mineral assemblages included mixed-layer clay minerals. The ICDD-PDF does not contain structure files for mixed-layer clays, therefore only discrete minerals could be assigned to bulk XRD patterns.

Bruker TOPAS® software was used for semi-quantitative models of samples. This program is based on the Rietveld refinement method (Rietveld, 1967). In brief, this method calculates the theoretical diffraction pattern for each phase using kinematic diffraction theory (Schroeder, 2018). It then uses optimization schemes to minimization the difference between observed XRD data and calculated patterns. Included in the TOPAS software are options to optimize structure file data and other parameters such as preferred orientation crystal planes and mean coherent scattering domain size. The routine also optimizes total XRD intensity, which is related to abundance. In all cases, ZnO IS abundance was allowed to be optimize as a check for agreement between model results and the known weight fraction addition of IS. In most cases, the agreement was within $^{+}$/- 10% of the known amount added. Each refinement's goodness-of-fit was evaluated using the weighted profile R-factor (R_{wp}), which is fully explained by Tobi (2006). Generally, model solutions with R_{wp} <15 are considered acceptable for semi-quantitative analysis. It is important to note that the TOPAS software does not allow for mixed-layer structures to be included in the calculations, therefore regardless of other optimization efforts, in some cases, satisfactory R_{wp} values were not achieved. Despite this limitation, consistent practices were used to keep model parameters with similar ranges of values to allow inter-sample comparison of relative abundances.

For fine clay fraction, approximately 10 g of each sample were taken and dried in an oven at 65°C overnight. Dried sample was placed in a centrifuge tube with a solution of 38 g Na-hexametaphosphate and 8 g of Na-carbonate per liter of de-ionized water and dispersed using a Branson Sonifier Cell Disrupter 350 for around 1 minute. The sample was then sieved to remove the sand fraction (>63 micron) with a 230 mesh. The <2 micron clay fraction was separated from <63 micron fraction by using standard centrifugation techniques (Schroeder, 2018). The resultant slurry was considered Na-saturated after this treatment. This step was repeated for different cation treatments. Ca-saturated, Mg-saturated, and K-saturated sample was prepared by exchanging in 0.1 M $CaCl_2$, $MgCl_2$ and

1.0 M KCl solutions, respectively. The slurry was centrifuged to settle all particles with sufficient velocity and time. In order to achieve full saturation, solution renewal and centrifugation steps were repeated. De-ionized water was added to slurry and repeated centrifugation was applied again to remove excess salt (Austin et al., 2020). This fine fraction was then dispersed in 25 to 30 ml of de-ionized water and drop cast by pipette onto a glass petrographic slide (25 mm x 40 mm) and dried overnight. This drying process creates oriented particles that enhance the basal reflections of phyllosilicates / clay minerals. Select duplicate slides was prepared on selected fresh samples for formamide test and detailed characterization to distinguish the presence of halloysite in kaolin bearing samples (Churchman 1990). For the formamide test, samples were exposed to formamide for around 30 minutes and then scanned.

To understand the tri- versus di-octahedral nature of clay, samples were spread onto a zero-background plate with acetone and scanned to detect reflections in the 69° to 74° 2Θ region. A separate mass of the fine fractions was spread as a powder mixed with acetone on a zero background plate to achieve random orientation. This sample was scanned using locked-coupled continuous scan mode with a step size of 0.01° 2Θ and count rate of 3 seconds per step for this process. This specific region contains the reflections for the (060) lattice measurement. Generally, dioctahedral clays have dimensions of ~1.50 Å and trioctahedral clays have dimensions of ~1.54 Å.

The oriented slide(s) was scanned from 2 to 40° 2Θ, using locked-coupled continuous scan mode with a step size of 0.01° 2Θ and count rate of 0.1 seconds per step. Data were collected for each sample in states of air-dried (AD) overnight at ambient relative humidity, ethylene glycol (EG) overnight at 65° C in closed ethylene glycol atmosphere and heated in the oven overnight at 110°C, 350°C, 550°C. Based on locations of the peak and their movement, changes in intensity, or disappearance depending upon stage of treatment the types of clay minerals were identified. In this case of the oriented clay fractions, NEWMOD2 software was used to understand nature of mixed layer clay minerals for the EG-Mg saturated state.

Inductively Coupled Plasma (ICP) Optical Emission Spectroscopy (OES), Mass Spectrometry (MS) and Loss-on-ignition (LOI) analyses

Approximately 5 g of selected samples were weighed and all analyses were performed by Activation Laboratories (Actlabs) in Ontario, Canada for their 4-LITHO (with their RX4 sample preparation) geochemical characterization of major oxides and trace elements. This method uses high temperature (molten) lithium metaborate/tetraborate fusion performed by automation at Actlabs and resultant is immediately digested in a weak nitric acid solution. Then analysis is performed by ICP-OES and ICP-MS (for detection limits, see page 14 https://cdn.actlabs.com/wp-content/uploads/2021/01/Actlabs-Schedule-of-Services-Canada-1.pdf). Loss on ignition is independently measured by heating a known sample mass to 950°C in an open atmosphere to volatilize carbonate, sulfates, hydroxide-bearing, and organic matter components. Mass loss is measured after the heating treatment. Mass gain is possible if reduced iron is present which reacts to form iron oxide.

CHAPTER 4
RESULTS

The hypothesis for this study considers the test of finding multiple sources contributing to the Sile clay deposits based on mineral and chemical properties. Results below are therefore presented by description of the clay minerals in the quarries/mines and then a description of the elemental compositions for the same sample suite. The three clay quarry profiles with different basements include those hosted on: 1) Cretaceous volcanogenic rocks and flysch series, 2) Paleozoic metasediments i.e., shales and sandstones, and 3) Permo-Triassic Limestone. Also presented below are the mineral and chemical properties of the basement and nearby outcroppings from the similarly lithological and aged rock types. When possible, weathering profiles in the basement rocks were sampled to include both relatively fresh outcropping and weathered material with the intent of documenting the effects of modern surficial weathering on mineral and chemical properties.

Mineralogy and elemental composition of clay deposits

Volcanic and volcano-sedimentary rocks hosted clay mine: Clay-rich sediments in this section were observed in the northern part of the study area and unconformably overlie Upper Cretaceous units (Fig. 1). Even though these deposits were found throughout the area and most commonly are hosted on volcanogenic basement much of the area was covered either by dense urbanization or forests. Field observations were therefore limited to select clay quarries and road cuts that allowed good exposure (Fig. 3a, b). A stratigraphic section of the quarry was supplied by mining company personnel and shows that these deposits consist of clay-rich, sand-rich, and gravel-rich interbeds of different thicknesses (Fig. 4). Coal seams and organic-rich sections were also found throughout the section. Gray, yellowish gray, greenish-gray, white, cream, pinkish and reddish-brown, brown, blackish colors of interlayers were identified during the field study (Fig. 5a,b). Different colors of layers within the section were mainly defined by the amount of organic material and iron-rich minerals. Sand-gravel rich lenses and thick-cyclic coal seams were also observed sporadically. In the upper part of the section, there were vertical reddish brown

clay dikes within the relatively unconsolidated horizontal cream sandy layers (Fig. 6a, b). Both field observations and drill core data indicate that these deposits are associated with fluvial-lacustrine environments, as evidenced by channel lag gravels, coal seams, and the textures in the sand layers.

Quartz, kaolinite, illite, and mixed-layer clays were the most abundant phases along the clay-rich section, with feldspars and anatase as minor phases. Gibbsite, goethite, hematite, siderite and pyrite were found at various levels in variable proportions. Semi-quantitative proportions based on Reitveld analysis are shown in Fig. 7. Quartz and phyllosilicates are clearly seen in representative XRD whole-rock patterns (Fig 8.). Anatase is identified with 3.51 Å d-spacing. Gibbsite and goethite are identified by the presence of d-spacing of 4.82 Å and 4.18 Å, respectively. Siderite is identified on the basis of 2.79 Å d-spacing. The d-spacing values of hematite and pyrite are 2.69 Å and 2.71 Å, respectively.

Elemental analysis of select splits of the same whole rocks show good agreement with the QXRD results (Fig. 7). SiO_2 concentrations correlate with quartz and other silicate concentrations. Alumina, alkali element concentrations correlate with feldspar and phyllosilicate concentrations. Increased Fe_2O_3 concentrations correspond with increased concentrations of pyrite, siderite, hematite, and goethite. LOI values correspond with the abundances of phyllosilicates, hydroxides, and carbonates, acknowledging that CO_2 was not measured in the elemental analysis. Some increase in LOI may be attributed to the presence of coal, which was not quantified by the QXRD method and it is assumed that in most samples that the LOI is attributed to dehydroxylation of phyllosilicates and hydroxides, combustion of organic matter, and decarboxylation of carbonates.

Oriented clay fractions (<2μm) were used for identification of clay minerals. Different cations (K, Ca, Mg) were used for saturation, however Mg-saturated samples were used for interpretations and determination of relative abundances of clay minerals that are given in Table 1. The air-dried state diffractogram contains an ~14.2 Å reflection in almost every sample. This peak might indicate the presence of mixed-layers of different hydrated smectite from 12.5 Å to 15 Å or the presence of variable mixed-layer clays with a different Reichwiete (R) order schemes (Reynolds, 1980). Upon ethylene glycol solvation, a part of the ~14.2 Å reflection expanded to ~16.5 Å. The same region also still contained an ~14.2 Å peak. The proportion of expandable layers are subject to change

resulting in a slight variation of ~16.5 Å reflections. This structure is dehydrated to ~14.2 Å region after heating to 110 °C, indicating chlorite/smectite mixed-layer clay. If this reflection would have collapsed to near ~12 Å region at 110 °C, then it could have interpreted as illite/smectite mixed-layers. Upon heating to 350 °C, this expandable structure is collapsed entirely. While a reflection was still observable near the ~12 Å d-spacing at 350 °C, this suggests the presence of hydroxy-interlayered vermiculite. The presence of ~14 Å reflection at 350 ° C and 550 ° C was assigned to chlorite. The persistent 10 Å peak was assigned to mica-like structure (i.e., illite), which was present in all patterns. Kaolinite was identified by the disappearance of the 7 Å peak at 550 °C. A separate formamide (fm) test was performed to determine if there is a halloysite. The lack of change (i.e., expansion to 10Å) suggests halloysite was not present.

Some variations were found between organic-rich zones and following so-called underclay layers (Fig. 10a,b). The difference between these layers was the presence of pyrite in the organic-rich zone. The underclay tends to be grayish because of the disseminated organic material and was often found by the miners to be the best quality clay in terms of economic value. The economic value of different layers is most likely related to impurities of geochemical phases, rather than the amount of kaolinite, which is beyond the current study's scope. Using the term "quality clay" is avoided here but mentioned because this term was used during the field study by mine operators. The coal seam shown in Fig. 10b is one of the cyclic coal layers. These structures are common in this specific region along with the continuous coal layers, which might indicate relatively small but different paleo-lakes in possibly paleo deltaic environment between the main river channels.

The uppermost section on top of the clay deposits had clay-rich dikes zones that were distinguished by their cross-cutting relation with sands (Fig. 11). The dikes' walls are very rich in quartz, while the dikes’ cores were rich in clay. Clay types still seem to be similar to those below in the clay deposits. This section contains Fe-rich minerals (goethite, hematite), which gives the dikes a deep red-brown color.

Paleozoic metasediment silicic-clastic hosted clay mine: This section was observed in the southern part of the study area and unconformably overlies units known as the Istanbul

Paleozoic Units. Yellowish, yellowish-brown, yellowish-white, reddish-brown, and gray sandy and clay-rich layers were recognized during the field study (Fig. 12a,b,c,d). The stratigraphic section of the quarry supplied by the mining company shows that clay-rich layers increase with depth (Fig. 13). Observations from the section's limited area were also consistent with these descriptions, meaning that sand-rich layers tend to increase in the upper levels. No cyclic coal seams were encounter during the field study but continuous thin coal layer intercalations were seen. Field observations and descriptions obtained from drill core suggests more fluvial input in terms of the paleoenvironment, when compared to the volcanogenically hosted clay deposits.

Quartz and phyllosilicates were the major phases identified. Minor phases include feldspars and anatase. Goethite and hematite were identified at minor and trace levels. Semi-quantitative XRD and relative proportions of mineral phases identified are shown in Fig. 14. Compared to the volcanogenically hosted clay quarry mentioned above; there was a greater quartz content and less clay content along the section observed (Fig. 15 and Fig. 16). No siderite, gibbsite, or pyrite were recognized. XRD patterns of oriented clay fractions show the presence of more smectite co-occurring with the kaolinite and illite (Table 2). Greater abundances of smectite-rich layers were recognized in the mixed-layer clays, which were with increasing depth (Fig. 17). Iron-rich lateritic zones are found within these layers. Formamide (fm) test suggested a lack of halloysite.

Elemental analysis of select splits of the same whole rocks show good agreement with the QXRD results (Fig. 14). SiO_2 concentrations correlate with quartz and other silicate concentrations. Alumina and alkali element concentrations correlate with feldspar and phyllosilicate concentrations. Increased Fe_2O_3 concentrations correspond with increased concentrations of hematite and goethite. LOI values correspond with the abundances of phyllosilicates and hydroxides. Some increase in LOI may be attributed to the presence of coal, which as mentioned above is assumed to be LOI attributed to dehydroxylation of phyllosilicates and hydroxides.

Limestone hosted clay mine: This quarry is located in the middle part of the study area and unconformably overlies Permo-Triassic dolomitic limestone. This section is relatively small in size compared to other deposits. The contact of the clay section is visible on top

of the limestone (Fig. 18). In fact, limestone and clay sections are operated by different companies. Alternation of reddish, yellowish-brown, grayish, and cream color layers with continuous coal seams were recognized during the field observation. Coal seams were more visible and thicker compare to the previous one. Field observations showed that the deeper level is clay rich, whereas the uppermost parts was sand-rich. Quartz grains were identified in the lowermost part of the clay section, which is also calcite rich.

Semi-quantitative abundances of minerals are shown in Fig. 19. Quartz and phyllosilicates are the most common phases with the feldspars and anatase occurring as minor phases. The clay content tends to increase with depth (Fig. 20 and Fig. 21). Clay fraction XRD data showed the presence of chlorite/smectite mixed layers long with the kaolinite and illite (Fig. 22). Smectite-rich zones are also identified in some of the layers. No halloysite is found upon fm treatment (Table 3).

Elemental analysis of select splits of the same whole rocks show good agreement with the QXRD results (Fig. 19). SiO_2 concentrations correlate with quartz and other silicate concentrations. Alumina and alkali element concentrations correlate with feldspar and phyllosilicate concentrations. CaO and LOI concentrations correlate with calcite concentrations. Increased Fe_2O_3 concentrations correspond with increased concentrations hematite and goethite. LOI values further correspond with the abundances of coal, phyllosilicates and hydroxides.

Crystal characteristics of clays in clay quarries: Crystal characteristics of illite and kaolinite and (*060*) reflections are given in Table 4. Illite and kaolinite crystallinity were determined by measuring the full width at half maximum (FWHM) of the (*001*) reflections of 10 Å and 7 Å in EG-state, respectively. The 10Å value is similar to the Kübler Index (KI) for illite (Kübler, 1968) and can indicate diagenetic conditions. Based on the averaged values illite FWHM from all quarries (0.479, 0.435, and 0.439 2Θ for volcanic/ volcano-sedimentary rocks, Paleozoic rocks, and limestone clay respectively), the illite appears to have only experienced late stage diagenetic conditions (i.e., not low-grade metamorphic conditions). The illite ratio of samples were determined by measuring the intensity ratio of illite peaks ($(001)/(003)_{\text{air-dried}}$ /$(001)/(003)_{EG}$) in air-dried and EG state (Srodon, 1984). Data obtained (1.25, 1.47, 1.49 2D Θ for volcanic/ volcano-sedimentary rocks, Paleozoic

rocks, and limestone clay respectively) shows the presence of minor amounts (<10%) of expandable layers in illite for all clay mines. The d(*060*) reflections obtained from fine fraction (as a powder dried with acetone to promote more random orientation) indicate the presence of both trioctahedral clays (chlorite and vermiculite) and dioctahedral clays (illite, kaolinite, and montmorillonite).

Mineralogical and elemental composition properties of potential source rocks

Volcanic/volcano-sedimentary rocks: Late Cretaceous volcanic rocks were common in the northern part of the study area. These appear to host/basement rocks for many actively operated clay quarries (Fig. 23). Two different phase assemblages were recognized in terms of the whole and clay mineralogy (Fig. 24 and Table 5). One of which includes quartz and feldspars as major phases. Alteration products were mainly smectite, chlorite/smectite and illite/smectite mixed layer clays with additional minor amounts of mordenite, chlorite and kaolinite. The freshest basement rock obtained from the quarry's drill core is similar to these (SKT-1), meaning the hosted rock for studied clay quarry mainly consists of corrensite, smectite, chlorite, mordenite, and smaller amounts of illite and kaolinite as alteration products. It seems to be that the phases were altered to chlorite/smectite and illite/smectite-rich as weathering products with also a relatively small amount of kaolinite with increased weathering (Fig. 25a, b, c). The other phase assemblage consists primarily of feldspars, which appears to produce smectite as an alteration product (Fig. 26). These outcrops were common in the north along the coast of the Black Sea (Fig. 1).

Elemental analysis of select splits of the same whole rocks show good agreement with the QXRD results (Fig. 24). SiO_2 concentrations correlate with quartz and other silicate concentrations (i.e., plagioclase). Alumina and alkali element concentrations correlate with mordanite, feldspar, and phyllosilicate concentrations. Increased Fe_2O_3 concentrations correspond with increased concentrations of hematite and goethite. LOI values correspond with the abundances of phyllosilicates, hydroxides, and carbonates. As noted above, it is assumed that in most samples that the LOI is attributed to dehydroxylation of phyllosilicates and hydroxides and decarboxylation of carbonates.

Flysch (sandstone and carbonated mudstone): Flysch series are Late Cretaceous in age and transitional with the volcanic and volcano-sedimentary rocks (Fig. 27). Quartz, feldspars,

calcite and phyllosilicates were the major phases (Fig. 28). Illite and vermiculite were the main clay minerals with a small amount of chlorite and kaolinite (Table 6). Vermiculite/chlorite mixed layer clays were also identified (Fig. 29).

Elemental analysis of select splits of the same whole rocks show good agreement with the QXRD results (Fig. 28). SiO_2 concentrations correlate with quartz and other silicate concentrations. Alumina and alkali element concentrations correlate with feldspars and phyllosilicate concentrations. Increased Fe_2O_3 concentrations correspond with increased concentrations of hematite and goethite. LOI values correspond with the abundances of phyllosilicates, hydroxides, and carbonates. As noted above, it is assumed that in most samples that the LOI is attributed to dehydroxylation of phyllosilicates and hydroxides and decarboxylation of carbonates.

Istanbul Paleozoic Units: The Istanbul Paleozoic units consist of a well-developed sedimentary sequence ranging from Early Ordovician to Late Carboniferous. The rock types of this sequence are subject to change throughout the region. In the study area, these units were widespread in the south and the basement rock for one of the clay quarries studied. Both shale and sandstone from the sequence were observed during the field study. Drill cores samples (S20_15 to 19) from the Paleozoic rocks hosted clay quarry were associated with the Ordovician age sandstone) (Fig. 30a). Surface outcrops were also observed (S20_31-32) (Fig. 30b). Whole-rock XRD data shows that major phases are quartz, feldspars, and clay minerals. Anatase, ilmenite, calcite, and hematite are minor phases (Fig. 31). Clay minerals are mostly illite, kaolinite with smectite and chlorite/smectite mixed layers (Fig. 32 and Table 7). The kaolinite content was found to be higher in the surface outcrops, indicating the increase in weathering.

Elemental analysis of select splits of the same whole rocks show good agreement with the QXRD results (Fig. 31). SiO_2 concentrations correlate with quartz and other silicate concentrations. Al_2O_3, alkali, and alkali earth concentrations correlate with feldspar and phyllosilicate concentrations. Increased TiO_2 and Fe_2O_3 concentrations correspond with increased concentrations of ilmenite, anatase, hematite, and goethite. LOI values correspond with the abundances of phyllosilicates, hydroxides, and carbonates. It is

assumed that in most samples that the LOI is attributed to dehydroxylation of phyllosilicates and hydroxides and decarboxylation of carbonates.

Two different shales were identified based on the clay fraction analysis. These were not described separately at the time of sampling since both seemed very similar in hand specimen. These differences might indicate different alteration zones since geochemistry data between these is not different at all. Different shales were mentioned in the literature, as well (Abdusselamoglu, 1963; Kaya 1973). One is Devonian aged shale (Fig. 33a,b,c,d), while the other was Carboniferous (Fig. 34a,b,c,d). Devonian age shale (S20_20-23b) mainly included quartz and clay minerals with small amounts of feldspars. The clay minerals are mainly illite and vermiculite. Limestone intercalations were recognized during the field study (S20_23b). The Carboniferous aged shale (S20_39-42 and S19_24-25) consists of quartz, feldspars, anatase and clay minerals. Clay minerals are mostly kaolinite and vermiculite with illite and chlorite/vermiculite mixed layers (Fig 35, Fig 36, Fig. 37. and Table 7).

Elemental analysis of select splits of the same whole rocks shows agreement with the QXRD results (Fig. 35). SiO_2 concentrations correlate with quartz and other silicate concentrations. Alumina and alkali elements concentrations correlate with feldspar and phyllosilicate concentrations. Fe_2O_3 concentrations do not correspond with concentrations of ilmenite, anatase, hematite, and goethite, which were too low to measure in QXRD, suggesting that these iron forms are poorly ordered. LOI values correspond with the abundances of phyllosilicates and carbonates. It is assumed that in most samples that the LOI is attributed to dehydroxylation of phyllosilicates and decarboxylation of carbonates.

CHAPTER 5
DISCUSSION

The central hypothesis for this study presumes that clay-rich accumulation in the Sile region formed in Neogene lacustrine basins. These kaolinite-rich deposits have been previously studied with the general consensus that these formed from sediments sourced by the alteration products of the volcanic rocks in the surrounding area (Yeniyol, 1984; Çoban et al., 2002; Ece et al., 2003; Ece and Nakagawa, 2003). However, to date, there has been no consensus and/or further evaluation of these clay deposits' regarding genesis from other potential source rocks. A conceptual model is herein proposed that considers multiple sources contributing to the formation of the Sile deposits, with further consideration of post deposition factors including diagenetic changes and subsequent terrestrial weathering within the more recent critical zone. The model recognizes the tectonic regime and climate changes during the geologic timeline from the Paleozoic to today. (Fig. 38).

Timeline: Geologic settings and climate

Geologic and morphotectonic settings: The general geology of the region and related maps are given in the previous sections (Fig. 1). Paleozoic sedimentary rocks are the basement rocks and these are partly and unconformably covered by Triassic limestones and clastic rocks. It is generally accepted that the Istanbul Zone was part of the Odessa shelf (Okay et al., 1994). The study area is located in the Istanbul zone that is part of the Pontide chain (Okay and Tuysuz, 1999). The Pontides extend from west to east along the entire southern coastline of the Black Sea (Ketin, 1966). Widespread arc-magmatism took place during the north-dipping subduction of Neo-Tethys Ocean along the Izmir-Ankara-Erzincan suture (Sengor and Yilmaz 1981). The Late Cretaceous Pontide magmatic arc is comprised of intermediate to basic volcanic and volcano-sedimentary rocks as well as altered calc-alkaline and acidic to intermediate pyroclastics and pelagic micrites (Karacik et al., 2007; Tuysuz et al.,2012). Volcano-sedimentary rocks are intercalated with sub-marine flysch series rocks. These were overlain by Paleocene and Eocene shallow marine limestones (Ketin and Gumus, 1963; Lom et al., 2016), indicating that the region was a marine environment during this time.

The Istanbul zone collided and juxtaposed with the Sakarya zone due to the closing of the northern branch of the Neo-Tethys Ocean (Intra-Pontide Ocean) along the Intra-Pontide suture zone (Okay et al.,1994). These movements resulted in fold and thrust belts parallel to the suture. The east-west striking Sile Thrust resulted from the closing of Intra Pontide Ocean in the early Eocene, with Paleozoic and Mesozoic units thrusted north over younger units, and can be traced for over 50 km (Baykal, 1943; Baykal and Onalan, 1980). Moreover, this tectonic relation has been observed in seismic sections in the eastern Black Sea shelf (Georgiev, 2012). No marine sedimentation has been recognized, and the region has been entirely above sea level since then (Ozcan et al.,2012). The study area experienced post-collisional uplift and peneplanation during this time and widespread erosion occurred. According to Sunal and Tuysuz (2002), this regime continued until the early Miocene. Strike-slip faults propagated perpendicular to this thrust due to ongoing compression and the main river systems developed along these orientations (Gurbuz, 2009).

Pre-Neogene rocks are overlain by clastic deposits consisting of sandstone, mudstone, coal layers and gravel alternations in the region and clay-rich sections studied in the current study are within these deposits. These terrigenous clastic rocks were probably eroded materials transported by rivers during the uplift and peneplanation processes. The palynological studies performed on the pollens obtained from coal and organic rich clay layers in the Kilyos area indicate that deposition started in the late Oligocene (Karlioglu et al., 2009). The environment was surrounded by a mountainous region and pollen was transported to the depositional area. Also found were constituents of lowland freshwater and lakeside freshwater swamp assemblages (Karlioglu et al., 2009). Based on identified fossils in the same area, an independent study concluded that the environment was well-drained upland and lowland with swamp and riparian vegetation under humid, warm temperate to subtropical climate conditions during the early Miocene (Akkemik et al., 2019). Gedik et al., (2005) proposed that these deposits are late Oligocene to early Miocene in age, based on the palynological data. They further report that the deposition occurred with lacustrine, fluvial and fan delta environments, with more fluvial input in the uplifted area in the southern part of the study area. Their study mentioned that these formations are

about 100 m in thickness and vary horizontally and vertically. Our field observations and drill core data are consistent with all of these studies.

The latest closure of the neo-Tethys Ocean along the Bitlis-Zagros suture in the southeast of Anatolia represents the end of the paleotectonic and beginning of the neotectonic period affecting the Anatolia (Sengor et al., 1985). This Middle to early Late Miocene collision between the Arabian and Anatolian plates resulted in both uplift of Anatolia and was a westward escape mechanism along the North Anatolian and East Anatolian fault zones. This mechanism connects the compressional regime to the east and extensional regime to the west of Anatolia (McKenzie, 1970; Sengor and Yilmaz, 1981; McClusky et al., 2000; Okay, 2008; Esat et al., 2021). Due to this mechanism and arrival/onset of the North Anatolian Fault to the region in the Late Pliocene, the tectonic regime changed from compressional to extensional. The morphotectonic features of the peneplain were controlled by this mechanism, and rivers followed new fractures related to the neotectonic period. The region was then covered by Pliocene and Pleistocene gravelly orange-reddish color fluvial deposits (Emre et al.,1998; Sengor, 2011; Sengor and Kindap, 2019). Our field observations as well as mineralogical and geochemistry data agree will with both paleotectonic and neotectonic morphotectonic features. All clay-rich sections studied have thick, relatively unconsolidated fluvial, orange color tops where vertical clay rich dikes reflect the mineralogical properties (kaolinite, illite and Sm/Vm/Ch mixed-layer clay rich) of the clay rich layers below.

Climate timeline: Paleoclimate data are interpreted as a measure of weathering during deposition, in general humid periods correspond to relatively intense weathering. The humid-tropical paleoclimate conditions from Late Triassic to Cretaceous have been reported for Central Europe (Dill, 2020 and references therein). The Cretaceous was characterized by very high atmospheric carbon dioxide levels, which may have been the highest at 20 to 50 times current levels (Berner, 2004). This greenhouse condition is a time that would have promoted intense hydrolysis weathering of both the Paleozoic Istanbul sedimentary rocks and the volcanic/volcano-sedimentary rocks. During the PETM (Paleocene-Eocene Thermal Maximum), global hyperthermal conditions also occurred (Smith et al., 2020), which would have further promoted kaolinite formation. Globally, many of largest sedimentary kaolin-hosted deposits formed at these times (i.e., late

Cretaceous – PETM). Regionally, evidence for this climate is observed in petrified wood from North Central Anatolia, which indicate warm and humid environments in the Middle Eocene (Akkemik et al., 2021), during a period known as the Middle Eocene Climate Optimum globally (Giorgioni et al., 2019). Eocene greenhouse climatic conditions were also reported by Beard et al. (2020) for the same region. Akgun et al., (2013) report a cooling period during the Oligocene compared to Eocene and stated that small-scale temperature and humidity fluctuations took place. However, coal-bearing sediments of Anatolia indicated subtropical and humid conditions based on the palynological data from the late Oligocene. Late Oligocene warming is also supported by oxygen and carbon isotope records from the deep-sea foraminifera (Zachos et al., 2001). Slightly cooler conditions are reported from the Early to late Middle Miocene and then in the late Middle Miocene increased humidity started (Kayseri-Ozel, 2017; Zachos et al., 2001). This temperature and humidity increase corresponded to the Mid-Miocene Climatic Optimum globally (Utescher et al.,2009). Cooling started following the Mid-Miocene Climatic Optimum for both Anatolia and globally (Akgun et al., 2007). Changing climate from humid subtropical in Mid-Miocene to cold temperate climatic conditions in Pliocene for Central Anatolia is also reported by Kayseri-Ozer (2017) and Kayseri Ozer et al. (2017). During the Late Pliocene, glaciations developed in the northern hemisphere (Haug et al., 2005). The prevailing cold and arid conditions also recognized during this time in Anatolia based on the isotope data (Alcicek et al., 2015) and then Quaternary glacial/interglacial fluctuations occurred in the northern hemisphere (Fig. 39).

The tectonic regime, climate and environmental changes during the geologic timeline from the Cretaceous to today are summarized in Figure 39.

Mineralogy and Geochemistry

Mineralogy: QXRD data for both clay-rich sections and surrounding rocks and from quarries are shown Fig. 40 and 41, respectively. Clay-rich formations are composed of quartz, kaolinite, illite and mixed-layer clays. Regardless of host rocks, they have similar mineralogy, with the exception of calcite that is present at the bottom of the limestone-hosted clay section. Pyrite is generally associated with the coal layers, with sulfur presumed to come from organic matter (i.e., a minimal marine sulfate source). There are

siderite occurrences in the volcanic/volcano-sedimentary rocks hosted clay section, which is indicative of fresh water in a reducing environment. There are horizontal and vertical variations in mineralogy, which are related to where in the basin deposition occurred. Elemental analysis and QXRD data show good agreement. Quartz content in QXRD data and Al/Si in geochemistry data are related to sand/clay rich sediment influx to the basins, indicating variable runoff conditions.

According to an A-CN-K (Al_2O_3-CaO, Na_2O-K_2O) ternary plot (Nesbitt et al., 1996) and corresponding CIA (Chemical Index of Alteration) (Nesbitt and Young, 1982), samples from the clay sections cluster in the Al and K rich part. (Fig. 42). CIA values of the clay rich formations are very high, suggesting intense weathering in the source area for the clay-rich formations. Potential source rocks have variable CIA values but have a tendency towards to Al and K rich part with increasing weathering. Volcanic rocks that produce entirely smectite as alteration products plotted near the Al and Ca+Na rich corners. The observation of the clay-rich formations clustering in Al and K rich area of the A-CN-K plot also indicates intense leaching took place in the depositional environment (i.e., loss of alkali and alkali-earth cations). Based on the mineralogical and the A-CN-K plot (combined with CIA), suggests that both Late Cretaceous (volcanic/volcano-sedimentary rocks, flysch series) and the Paleozoic rocks (the Istanbul Paleozoic Units) are the source rocks for the clay-rich formations.

Geochemistry: The available geochemistry data sets obtained by ICP-MS have been evaluated by using principal component analysis (PCA). PCA is a very useful multivariate statistical technique to explore variability, and clusters based on similarities and differences of the samples. This technique handles the data set by reducing dimensionality and retaining most of the variation in the data (Jolliffe, 2002). While doing that, the algorithm identifies principal components responsible for most of the variations in the original data set. Next, it displays these new axes (i.e., principal components) with variation explained in decreasing order, called the scree plot. A scree plot shows as many principal components as there are variables (Holland, 2009). Based on the scree plot, it can be decided which components to use, and samples are then plotted using a few of these meaningful axes representing most of the variation. By plotting, one can easily identify groupings and

similarities/differences among samples and evaluate the variables, known as loadings, controlling them. Scree plot and loadings are generally presented with PCA results. Data were log-transformed and processed in R to fulfill multivariate normality required for PCA and applied to major oxides and rare earth elements (REE) abundances. Iron rich samples and limestones, namely sample S17_8, S20_13, S20_24a, S20_23b, were considered outliers because of their vastly different mineral assemblage and hence were included in the analysis of all data, however they were excluded in subsequent analyses and plots of the different subpopulations.

PCA - clays and host rocks: Principal component analysis (PCA) was implemented for the dataset including potential source rocks and clays to evaluate the entire population of data. Since there are 12 variables in the data set, there were 12 principal components. PCA demonstrates that the first three principal components determined just over 77% of the variation. PC1, PC2 and PC3 explain 45.6%, 21.8% and 9.8% of the variation, respectively. This suggests that PC3 can also be used for interpretations (Fig. 43). The red line in the scree plot is calculated based on one variable's worth of information, meaning that since there are 12 variables, they would contribute 8.3% each to the total variance if they were equally contributed (Holland, 2009).

Loadings indicate the contribution of variables on each principal component. They can have positive or negative loading value, meaning they can be negatively or positively correlated. Whether the loading is large or not is calculated based on the one variable's worth of information (Holland, 2009). In this case, this value is 0.27. According to this value, PC 1 has a strong positive loading for Si and has negative loadings for the rest of the variables with some variations. Mg, Al, Fe, P, K, REE and LOI have strong negative loadings. PC 2 has strong positive loadings for Mn, Ca and Na and has strong negative loadings for Ti, Al, REE. LOI and Ca have strong positive loadings for PC 3, Si and Ti have strong negative loadings (Table 8).

The distribution of samples for the first pair of principal components (PCA1 versus PCA2) is shown in Fig. 44. Samples and vectors corresponding to the loadings show a clear separation between clays and source rocks. It is important to note that all clays are clustered

together regardless of host rocks. Clay samples separated on the right side (highly positive PCA1 loading) are relatively quartz-rich samples.

The PCA1 versus PCA 3 plot suggests some of the source rocks, including volcanic/volcano-sedimentary rocks, Paleozoic rocks and flysch series group with the clays. Again, as in the previous plot, some of the clays are separated with increasing quartz content (Fig. 44). Based on both plots, clays groups are distinguished and mostly loaded with Al, Ti, REE and LOI. Regardless of basement rocks, all clays group together, and there are substantial overlaps, thus supporting the hypothesis that their origins are indistinguishable (i.e., similar). Using this full data set, PCA suggests that the source rocks tend to be grouped together, thus pointing out either of the source groups may be a contributor to the clays.

The overlap of groups in the PCA using all data did not allow for clear understanding of the loadings. Therefore, PCA was applied to subgroups in order to see if elemental trends could be associated with new loadings within each group. Discussed below are PCA results for the clay group and source rock group.

PCA-clays: PCA for clay groups demonstrate that the first two principal components explained 75% of the variation. While PC1 is responsible for 64.7% of the variation, PC2 explains only 10.6% of them (Fig. 45). PC1 has strong positive loading for Si and strong negative loadings for Al, Mg, Ca, Na, K, Ti, REE, LOI, whereas PC2 has strong negative loadings for Fe and Mn (Table 9). The scatter plot verifies that clay groups are clustering together except quartz-rich layers. Organic rich clays and calcite rich clays seem to be differentiated from others with more Fe and Mn loadings. The distribution seen here suggests that clays are mostly loaded with Al, Mg, REE, K, Na, Ti, REE and LOI (Fig. 46). There is no separation between clay groups and these are loaded with Al, Ti, REE, Mg, Na, K, LOI. The question then is which rock types loaded highly for the phases that are found in clays? To answer this question, another PCA was applied only among source rock groups.

PCA-potential source rocks: PCA for potential source rocks shows that the first three principal components explained 74% of the variation. The associated scree plot suggests

that there is also a fourth principal component that might be considered (Fig. 47). Since the difference between the third and fourth is significant, only the first three principal components were used for evaluation.

PC1 is dominated positively by Al, Ti, Fe and REE and has a strong negative loading for Ca. PC2 has strong positive loadings for Mg, LOI and P and has strong negative loadings for Si and Na. PC3 is positively loaded by Mn, Na, K and P (Table 10). The samples' distribution for the first two principal components shows separation among rock groups with some overlaps between them (Fig. 48). Calcite-rich flysch series seem to be distinguished by high Ca loading. Vectors point out that Al, Ti. REE, K , Mg and Fe are rich in Paleozoic rocks. In the other plot below (Fig. 48) separation between rock groups looks similar. Al, Ti, REE Mg, K, Fe are rich in Paleozoic rocks. The fact that phases loaded highly in clays seem to be rich in Paleozoic rocks indicates Paleozoic rocks are the primary source rocks. Contribution from volcanic/volcano-sedimentary rocks and flysch series are less than Paleozoic rocks based on the principal component analyses.

Multiple source hypothesis

Previous studies hypothesize that clay-rich formations are derived from the volcanic rocks in the region (Çoban et al., 2003; Ece et al., 2003). Ece et al. (2003) suggested two stages to explain occurrences of clay deposits. First, weathering of andesitic rocks, tuffs and ashes occurred at the base of the lacustrine basin. Second, andesitic rocks eroded from the surrounding area were transported to the delta-swamp environment and then produced kaolinite-rich formations. At the lowermost levels of these formations, up to 10 m of red and brown color paleosols were reported (Emre et al., 1998). This paleosol was probably the equivalent of highly weathered volcanogenic saprolites that were similarly observed in the modern weathered volcano-sedimentary rocks in this study. These rocks include Illite/Smectite and Chlorite/Smectite mixed layer clays with small amounts of kaolinite as alteration products that represent the alteration product of basement rock obtained from the drill core in the current study. Ece et al., (2003) further suggest that quartz-rich lenses and sandy layers are derived from the granitic pluton located southwest of the study area. This is possible but that hypothesis does not consider the older sedimentary rocks as a possible source.

Bentonites (i.e., Smectite-rich deposits) were reported in the Eastern Pontides, which originated from the same volcanism in the same geologic setting (Kadir et al., 2021; Abdioglu et al., 2005). These are reported as alteration products of Late Cretaceous pyroclastics in shallow marine environment shortly after deposition. Although the same processes are also possible for the study region, there are no such bentonites recognized. Ece et al. (2003) suggested this as a genetic model. They suggested occurrences of smectites as alteration products of pyroclastics which were then transported to the delta environment, where they produced kaolinite-rich layers with post-deposition alteration. There is very long time period for kaolinitization to take place between the Late Cretaceous and Oligo-Miocene, if we assume bentonites occurred shortly after deposition similar to that reported in the Eastern Pontides. Moreover, there are seemingly different host rocks to the clay-rich formations. Since PCA models suggest Paleozoic rocks as the primary source in the current study, it indicates that these two potential sources are probably overlapped in the Oligo-Miocene fluvial-lacustrine environment (Fig. 49) and ended up forming kaolinite, illite and mixed layer-rich, quartz-bearing clay rich sedimentary deposits with intense leaching. Flysch series were also potentially a source rock that gave material to the basin. Ece and Nakagawa (2003) suggested that variable sources based on the geochemistry data, where they indicate “Cr, Ga, Nb and Ta enrichments indicate variable sources”. Mineralogical and geochemistry data in this study are consistent with this multisource theory.

CHAPTER 6
CONCLUSION

(1) Clay and coal-bearing sedimentary deposits formed in fluvial-lacustrine and freshwater delta plain environments during the Oligo-Miocene. These deposits are "hosted", meaning that they occur unconformably on top of various rock types. Volcanic/ Volcano-sedimentary rocks-hosted clay formations occur in the north and limestone-hosted and Paleozoic rocks-hosted clay formations occur in the south were part of the same sedimentary system. While the northern part represents the freshwater delta plain, the southern part has more fluvial input. The distribution and alternation of clay-rich, sand-rich and gravel-rich layers are subject to change depending upon the paleoenvironment. Both continuous and cyclic coal seams were recognized and there were variations in their thicknesses. Sand-rich thick layers with clay dikes were observed in every location. Tectonic influenced morphology and paleoclimate were likely very effective processes operating during the formation of the clay rich sedimentary deposits.

(2) Potential source rocks have distinct mineralogical and chemical signatures and different from clay deposits.

(3) The clay-rich Oligo-Miocene deposits have similar geochemical and mineralogical properties regardless of their underlying host rocks. These were mainly comprised of quartz, kaolinite, illite and mixed-layer clays. Minor phases are siderite, anatase, pyrite, gibbsite, goethite, hematite, feldspar and calcite. The presence of siderite is related to a reducing freshwater environment. Pyrite is associated with organic rich layers. Mixed layer clays are a combination of chlorite, vermiculite and smectite layer types. Discrete chlorite, vermiculite and smectite are also recognized. The d(*060*) reflections obtained from fine fraction indicate the presence of both trioctahedral clays (chlorite and vermiculite) and dioctahedral clays (illite, kaolinite, and montmorillonite). No halloysite is found upon fm treatments.

(4) Based on the mineralogical and CIA data, volcanic/volcano-sedimentary rocks, flysch series and Paleozoic rocks were likely the primary sources for the deposits. The deposits were likely formed as a result of climatically-induced intense leaching during and post-deposition.

(5) Principal component analysis using geochemical data reveals that Paleozoic sedimentary units were also a primary source rock for the clay deposits in addition to the late Cretaceous volcanic/volcano-sedimentary rocks, which was previously suggested to be the main source.

(6) The results obtained in the current study and previous studies indicate that these deposits are multi-source clay deposits.

(7) Future work could extend this type of analysis over a broader section of the region to examine the extent to which modern weathering processes are further modifying the mineral assemblages that are found in these economically important deposits.

REFERENCES

Abdioglu, E. and Arslan, M., 2005. Mineralogy, geochemistry and genesis of bentonites of the Ordu area, NE Turkey. Clay Minerals, 40(1), pp.131-151.

Abdüsselamoğlu, Ş. 1963. İstanbul Boğazı doğusunda mostra veren Paleozoyik arazide stratigrafik ve paleontolojik yeni müşahedeler [New stratigraphic and palaeontologic observations on the Palaeozoic outcrops in the east of İstanbul Strait]. Mineral Research and Exploration Institute (MTA) of Turkey Bulletin 60, 1–7 [in Turkish].

Akgün, F., Akkiraz, M.S., Üçbaş, S.D. and Bozcu, M., 2013. Oligocene vegetation and climate characteristics in north-west Turkey: data from the south-western part of the Thrace Basin. Turkish Journal of Earth Sciences, 22(2), pp.277-303.

Akgün, F., Kayseri, M.S. and Akkiraz, M.S., 2007. Palaeoclimatic evolution and vegetational changes during the Late Oligocene–Miocene period in Western and Central Anatolia (Turkey). Palaeogeography, Palaeoclimatology, Palaeoecology, 253(1-2), pp.56-90.

Akkemik, Ü., Mantzouka, D., Tunç, U. and Koçbulut, F., 2021. The first paleoxylotomical evidence from the Mid-Eocene Climate Optimum from Turkey. Review of Palaeobotany and Palynology, 285, p.104356.

Akkemik, Ü., Akkılıç, H. and Güngör, Y., 2019. Fossil wood from the Neogene of the Kilyos coastal area in Istanbul, Turkey. Palaeontographica Abteilung B Palaeobotany–Palaeophytology, 299(1-6), pp.133-185.

Alçiçek, H., Wesselingh, F.P. and Alçiçek, M.C., 2015. Paleoenvironmental evolution of the late Pliocene–early Pleistocene fluvio-deltaic sequence of the Denizli Basin (SW Turkey). Palaeogeography, Palaeoclimatology, Palaeoecology, 437, pp.98-116.

Austin, J.C., Richter, D.D. and Schroeder, P.A., 2020. Quantification of Mixed-Layer Clays in Multiple Saturation States Using NEWMOD2: Implications for the Potassium Uplift Hypothesis in the SE United States. Clays and Clay Minerals, pp.1-14.

Awwad, A., Amer, M. and Al-aqarbeh, M., 2020. TiO2-kaolinite nanocomposite prepared from the Jordanian Kaolin clay: Adsorption and thermodynamics of Pb (II) and Cd (II) ions in aqueous solution. *Chemistry International*.

Ayda Ustaömer, P., Mundil, R. and Renne, P.R., 2005. U/Pb and Pb/Pb zircon ages for arc-related intrusions of the Bolu Massif (W Pontides, NW Turkey): evidence for Late Precambrian (Cadomian) age. Terra Nova, 17(3), pp.215-223.

Aysal, N., Keskin, M., Peytcheva, I. and Duru, O., 2018. Geochronology, geochemistry and isotope systematics of a mafic–intermediate dyke complex in the İstanbul Zone. New constraints on the evolution of the Black Sea in NW Turkey. Geological Society, London, Special Publications, 464(1), pp.131-168.

Aysal, N., Keskin, M., Peytcheva, I., Duru, O. and Akgündüz, S., 2015. Geochronology, geochemistry and isotope systematics of a mafic-intermediate dyke complex in the İstanbul zone, Northern Turkey. Goldschmidt 2015 Abstracts, 155.

Baykal A. F. & Önalan M. 1979. — Şile Sedimanter Karmaşığı (Şile Olistostromu). Altınlı Sempozyumu Tebliğler Kitabı. İstanbul Üniversitesi Yerbilimleri Fakültesi: 15-25.

Baykal, F., 1943, Şile mıntıkasının jeolojisi: Istanbul Universitesi Fen Fakultesi mecmuası. Seri B, Tabü ilimler, v. (B7/8), p. 166–233.

Beard, K.C., Métais, G., Ocakoğlu, F. and Licht, A., 2020. An omomyid primate from the Pontide microcontinent of north-central Anatolia: Implications for sweepstakes dispersal of terrestrial mammals during the Eocene. Geobios.

Berner, R.A. and Berner, R.A., 2004. The Phanerozoic carbon cycle: CO2 and O2. Oxford University Press on Demand.

Boehm, K., Wagreich, M., Wolfgring, E., Tüysüz, O., Susanne, G.I.E.R. and Yilmaz, İ.Ö., 2019. Upper Cretaceous volcaniclastic complexes and calcareous plankton biostratigraphy in the Western Pontides, NW Turkey. Turkish Journal of Earth Sciences, 28(2), pp.187-206.

Cai, R., Tian, Z., Ye, H., He, Z. and Tang, S., 2021. The role of metakaolin in pore structure evolution of Portland cement pastes revealed by an impedance approach. *Cement and Concrete Composites*, p.103999.

Cao, Z., Wang, Q. and Cheng, H., 2021. Recent advances in kaolinite-based material for photocatalysts. *Chinese Chemical Letters*.

Churchman, G.J., 1990. Relevance of different intercalation tests for distinguishing halloysite from kaolinite in soils. Clays and Clay Minerals, 38(6), pp.591-599.

Çoban, F., Ece, Ö., Yavuz, O. and Özdamar, S., 2003. Petrogenesis of volcanic rocks, and clay mineralogy and genesis of underclays, Sile Region, Istanbul, Turkey. Neues Jahrbuch für Mineralogie-Abhandlungen, pp.1-25.

Dill, H.G., 2020. A geological and mineralogical review of clay mineral deposits and phyllosilicate ore guides in Central Europe–A function of geodynamics and climate change. Ore Geology Reviews, 119, p.103304.

Ece, O.I., Nakagawa, Z.E. and Schroeder, P., 2003. Alteration of volcanic rocks and genesis of kaolin deposits in the Sile Region, northern Istanbul, Turkey. I: Clay mineralogy. Clays and Clay Minerals, 51(6), pp.675-688.

Ece, O.I. and Nakagawa, Z.E., 2003. Alteration of volcanic rocks and genesis of kaolin deposits in the Sile Region, northern Istanbul, Turkey. Part II: differential mobility of elements. Clay Minerals, 38(4), pp.529-550.

Emre, Ö., Erkal, T., Tchepalyga, A., Kazancı, N., Keçer, M., and Ünay, E., 1998, Neogene- Quaternary evolution of the eastern Marmara-Black Sea region, northwest Turkey: Bulletin of Mineral Research and Exploration Institute, v. 120, p. 119–145

Esat, K., Seyitoğlu, G., Aktuğ, B., Kaypak, B. and Ecevitoğlu, B., 2021. The Northwest Central Anatolian Contractional Area: A neotectonic deformation zone bounded by major strike-slip fault zones in the Anatolian Plate. Tectonophysics, p.228776.

Esenli, F., Uz, B. and Kumbasar, I., 1997. Mordenite type zeolite occurrence in the Upper Cretaceous volcanics of Şile region, İstanbul–Turkey. Geological Bulletin of Turkey, 40, pp.43-49.

Fackrell, L.E., Rotz, R.R., Demir, H., and Schroeder, P.A., 2020, A Critical Zone Network Approach to the Study of Mars: White Paper Submitted to the LPI Planetary Science and Astrobiology Decadal Survey July 2020, doi:10.3389/fpsyg.2020.604853.

Fellah, M., Hezil, N., Guerfi, K., Djellabi, R., Montagne, A., Iost, A., Borodin, K. and Obrosov, A., 2020. Mechanistic pathways of cationic and anionic surfactants sorption by kaolinite in water. *Environmental Science and Pollution Research*, pp.1-15.

Gedik İ., Timur E., Duru M. & Pehlivan Ş. 2005b. — 1:50 000 ölçekli Türkiye Jeoloji Haritaları No: 10 İstanbul – F 22d paftası. Maden Tetkik ve Arama Genel Müdürlüğü Jeoloji Etütleri Dairesi: 1-49, 1 foldout map.

Georgiev, G., 2012. Geology and hydrocarbon systems in the Western Black Sea. Turkish Journal of Earth Sciences, 21(5), pp.723-754.

Gianni, E., Avgoustakis, K. and Papoulis, D., 2020. Kaolinite group minerals: Applications in cancer diagnosis and treatment. *European Journal of Pharmaceutics and Biopharmaceutics*, *154*, pp.359-376.

Giorgioni, M., Jovane, L., Rego, E.S., Rodelli, D., Frontalini, F., Coccioni, R., Catanzariti, R. and Özcan, E., 2019. Carbon cycle instability and orbital forcing during the Middle Eocene Climatic Optimum. Scientific reports, 9(1), pp.1-10.

Gürbüz, A., 2009. Orientations of palaeotectonic features as a key to understanding the neotectonic block rotation of the Kocaeli peninsula, NW Turkey. International Geology Review, 51(4), pp.329-344.

Haug, G.H., Ganopolski, A., Sigman, D.M., Rosell-Mele, A., Swann, G.E., Tiedemann, R., Jaccard, S.L., Bollmann, J., Maslin, M.A., Leng, M.J. and Eglinton, G., 2005. North Pacific seasonality and the glaciation of North America 2.7 million years ago. Nature, 433(7028), pp.821-825.

Holland, 2019. Principal Components Analysis (PCA), Department of Geology, University of Geology, Athens, GA 30602-2501

Jolliffe, I.T., 2002. Principal components in regression analysis. Principal component analysis, pp.167-198.

Kadir, S., Külah, T., Erkoyun, H., Uyanık, N.Ö., Eren, M. and Elliott, W.C., 2021. Mineralogy, geochemistry, and genesis of bentonites in Upper Cretaceous pyroclastics of the Bereketli member of the Reşadiye Formation, Reşadiye (Tokat), Turkey. Applied Clay Science, 204, p.106024.

Karacık, Z., Yılmaz, Y., Pearce, J.A. and Ece, Ö.I., 2008. Petrochemistry of the south Marmara granitoids, northwest Anatolia, Turkey. International Journal of Earth Sciences, 97(6), pp.1181-1200.

Kaya, O. 1973. Th e Devonian and Lower Carboniferous stratigraphy of the İstinye, Bostancı and Büyükada subareas. In: Kaya, O. (ed), Paleozoic of İstanbul. Ege Üniversitesi Fen Fakültesi Kitaplar Serisi 40, 1–36

Kayseri-Özer, M.S., 2017. Cenozoic vegetation and climate change in Anatolia—A study based on the IPR-vegetation analysis. Palaeogeography, Palaeoclimatology, Palaeoecology, 467, pp.37-68.

Kayseri-Özer, M.S., Karadenizli, L., Akgün, F., Oyal, N., Saraç, G., Şen, Ş., Tunoğlu, C. and Tuncer, A., 2017. Palaeoclimatic and palaeoenvironmental interpretations of the late Oligocene, late Miocene–early Pliocene in the Çankırı-Çorum Basin. Palaeogeography, Palaeoclimatology, Palaeoecology, 467, pp.16-36.

Karlıoğlu, N., Akkemik, U. and Caner, H., 2009. Detection of some woody plants in Late Oligocene forests of Istanbul. Turkish Journal of Agriculture and Forestry, 33(6), pp.577-584.

Keskin, M. and Tüysüz, O., 2018. Stratigraphy, petrogenesis and geodynamic setting of Late Cretaceous volcanism on the SW margin of the Black Sea, Turkey. Geological Society, London, Special Publications, 464(1), pp.95-130.

Ketin, İ. and Gümüş, Ö., 1963. Sinop-Ayancık arasında III. Bölgeye dahil sahaların jeolojisi, TPAO roporu no: 288.

Ketin, I., 1966, Tectonic units of Anatolia: Bulletin of the Mineral Research and Exploration Institute of Turkey, v. 66, p. 23-34

Kübler, B., 1968. Evaluation quantitative du métamorphisme par la cristallinité de I'illite. Bulletin Centre de Researches de Pau-SNPA, 2, pp.385-397.

Lom, N., Ülgen, S.C., Sakinç, M. and Şengör, A.C., 2016. Geology and stratigraphy of Istanbul region. Geodiversitas, 38(2), pp.175-195.

Le Pichon, X., Şengör, A.M.C., Demirbağ, E., Rangin, C., Imren, C., Armijo, R., Görür, N., Çağatay, N., De Lepinay, B.M., Meyer, B. and Saatçılar, R., 2001. The active main Marmara fault. Earth and Planetary Science Letters, 192(4), pp.595-616.

McClusky, S., Balassanian, S., Barka, A., Demir, C., Ergintav, S., Georgiev, I., Gurkan, O., Hamburger, M., Hurst, K., Kahle, H. and Kastens, K., 2000. Global Positioning System constraints on plate kinematics and dynamics in the eastern Mediterranean and Caucasus. Journal of Geophysical Research: Solid Earth, 105(B3), pp.5695-5719.

McKenzie, D.P., 1970. Plate tectonics of the Mediterranean region. Nature, 226(5242), pp.239-243.

Mubarak, M.F., Zayed, M.A., Nafady, A. and Shahawy, A.E., 2021. Fabrication of Hybrid Materials Based on Waste Polyethylene/Porous Activated Metakaolinite Nanocomposite as an Efficient Membrane for Heavy Metal Desalination Processes. *Adsorption Science & Technology*, *2021*.

Murray, H.H., 1993. Kaolins, kaolins and kaolins. Kaolin genesis and utilization, pp.1-24.

Nesbitt, H.W., Young, G.M., McLennan, S.M. and Keays, R.R., 1996. Effects of chemical weathering and sorting on the petrogenesis of siliciclastic sediments, with implications for provenance studies. The Journal of Geology, 104(5), pp.525-542.

Nesbitt, H. and Young, G.M., 1982. Early Proterozoic climates and plate motions inferred from major element chemistry of lutites. Nature, 299(5885), pp.715-717.

Okay, A.I., 2008. Geology of Turkey: a synopsis. Anschnitt, 21, pp.19-42.

Okay, A.I., Tuysuz, O., Satır, M., Ozkan-Altiner, S., Altiner, D., Sherlock, S. and Eren, R.H., 2006. Cretaceous and Triassic subduction-accretion, high-pressure–low-temperature metamorphism, and continental growth in the Central Pontides, Turkey. Geological Society of America Bulletin, 118(9-10), pp.1247-1269.

Okay, A.I. and Tüysüz, O., 1999. Tethyan sutures of northern Turkey. Geological Society, London, Special Publications, 156(1), pp.475-515.

Okay, A.I., Celal Sengor, A.M. and Görür, N., 1994. Kinematic history of the opening of the Black Sea and its effect on the surrounding regions. Geology, 22(3), pp.267-270.

Olu-Owolabi, B.I., Diagboya, P.N., Mtunzi, F.M. and Düring, R.A., 2021. Utilizing eco-friendly kaolinite-biochar composite adsorbent for removal of ivermectin in aqueous media. *Journal of Environmental Management*, *279*, p.111619.

Özcan, Z., Okay, A., Özcan, E., Hakyemez, A. and ALTINER, S., 2012. Late Cretaceous-Eocene geological evolution of the Pontides based on new stratigraphic and palaeontologic data between the Black Sea coast and Bursa (NW Turkey). Turkish Journal of Earth Sciences, 21(6), pp.933-960.

Özdamar, S., Ece, Ö.I., Kayacı, K. and Küçüker, A.S., 2007. Mineralogical and technological properties of underclays in Sile Region, Istanbul, Turkey.

Özgül, N., 2012. Stratigraphy and some structural features of the İstanbul Paleozoic. Turkish Journal of Earth Sciences, 21(6), pp.817-866.

Rashad, M., Logesh, G., Sabu, U. and Balasubramanian, M., 2021. A novel monolithic mullite microfiltration membrane for oil-in-water emulsion separation. *Journal of Membrane Science*, *620*, p.118857.

Reynolds, R., 1980. Crystal structures of clay minerals and their X-ray identification. Mineralogical Society Monograph (5): 249.

Rietveld, H.M., 1967. Line profiles of neutron powder-diffraction peaks for structure refinement. Acta Crystallographica, 22(1), pp.151-152.

Schroeder, P.A. and Erickson, G., 2014. Kaolin: From ancient porcelains to nanocomposites. Elements, 10(3), pp.177-182.

Schroeder, P.A., 2018. Clays in the critical zone. Cambridge University Press.

Sen, S. 2016. Introduction. Geodiversitas, 38(2), 147-151

Smith, V., Warny, S., Grice, K., Schaefer, B., Whalen, M.T., Vellekoop, J., Chenot, E., Gulick, S.P., Arenillas, I., Arz, J.A. and Bauersachs, T., 2020. Life and death in the Chicxulub impact crater: a record of the Paleocene–Eocene Thermal Maximum. Climate of the Past, 16(5), pp.1889-1899.

Srodon, J., 1984. X-ray powder diffraction identification of illitic materials. . Clays and Clay Miner., 32(5), p.337.

Sunal, G. and Tüysüz, O., 2002. Palaeostress analysis of Tertiary post-collisional structures in the Western Pontides, northern Turkey. Geological Magazine, 139(3), pp.343-359.

Şengör, A.C. and Kindap, T., 2019. The Geology and Geomorphology of Istanbul. In Landscapes and Landforms of Turkey (pp. 249-263). Springer, Cham.

Şengör, A.M.C., 2011. İstanbul Boğazı niçin Boğaziçi'nde açılmıştır. Fiziki Coğrafya Araştırmaları, pp.57-102.

Şengör, A.M.C., Görür, N. and Şaroğlu, F., 1985. Strike-slip faulting and related basin formation in zones of tectonic escape: Turkey as a case study.

Şengör, A.C. and Yilmaz, Y., 1981. Tethyan evolution of Turkey: a plate tectonic approach. Tectonophysics, 75(3-4), pp.181-241.

Toby, B.H., 2006. R factors in Rietveld analysis: How good is good enough?. Powder diffraction, 21(1), pp.67-70.

Tüysüz, O., 2018. Cretaceous geological evolution of the Pontides. Geological Society, London, Special Publications, 464(1), pp.69-94.

Tüysüz, O., Melinte-Dobrinescu, M.C., Yılmaz, İ.Ö., Kirici, S., Švabenická, L. and Skupien, P., 2016. The Kapanboğazı formation: a key unit for understanding Late Cretaceous evolution of the Pontides, N Turkey. Palaeogeography, palaeoclimatology, palaeoecology, 441, pp.565-581.

Tüysüz, O., Yılmaz, İ.Ö., Svabenicka, L. and Kirici, S., 2012. The Unaz formation: a key unit in the Western Black Sea region, N Turkey. Turkish Journal of Earth Sciences, 21(6), pp.1009-1028.

Utescher, T., Mosbrugger, V., Ivanov, D. and Dilcher, D.L., 2009. Present-day climatic equivalents of European Cenozoic climates. Earth and Planetary Science Letters, 284(3-4), pp.544-552.

Yeniyol, M., 1984. Istanbul killerinin olusumu (occurrence of clays of Istanbul). Turkiye Jeoloji Kurumu Bulteni, 5, pp.143-150.

Yılmaz, Y., 1993. New evidence and model on the evolution of the southeast Anatolian orogen. Geological Society of America Bulletin, 105(2), pp.251-271.

Yurtsever A. 1982. — Kocaeli Triyası biyostratigrafi projesi, Gebze-Hereke-Tepecik alanında Mesozoyik-Senozoyik kayalarının jeolojisi. MTA Report no. 7195 (unpublished).

Zachos, J., Pagani, M., Sloan, L., Thomas, E. and Billups, K., 2001. Trends, rhythms, and aberrations in global climate 65 Ma to present. science, 292(5517), pp.686-693.

Zhang, B., Guo, H., Deng, L., Fan, W., Yu, T. and Wang, Q., 2020. Undehydrated kaolinite as materials for the preparation of geopolymer through phosphoric acid-activation. *Applied Clay Science*, *199*, p.105887.

Zunino, F. and Scrivener, K., 2020. Increasing the kaolinite content of raw clays using particle classification techniques for use as supplementary cementitious materials. *Construction and Building Materials*, *244*, p.118335.

Table 1. Relative abundances of clay minerals from volcanic hosted clay section. Ch = chlorite, Sm = smectite, Vm = vermiculite, Kaol = kaolinite, Hly = halloysite, gb = gibbsite, gt = goethite.

Sample #	Ch/Sm	Ch	Vm	il	Kaol	Others	Hly	
S17_1	+	+	+	++++	++++		-	Sequence Bottom
S17_2	+	+	+	++++	++++		-	
S17_3	++	+	+	+++	++++		-	
S17_4	+	+	++	++	++++			
S17_5			+++	++	++++	gb		
S17_6	++		+	++	++++			
S17_7	+++	+	++	+	++++			
S17_8	++	+	+	+	++++	gt		Iron rich crust
S17_9	+++		+	++	++++			
S17_10	++	+	+	++	++++			
S17_11	+	+	+	++++	++++			
S17_12	++	+		+++	++++			
S17_13	+	+	++	+++	++++	gb		Organic rich
S17_14	+	+	+	++++	++++			
S17_15	+++	+	++	++++	++++			
S17_16	+++	+		+++	++++			
S17_17	+++	+		++	++++			
S17_18	++++	+	+++	+	+++	gb		
S17_19	+++	+	+	+++	++++			
S17_20	++	+		+++	++++			
S17_21	++	+	+	++	++++			
S17_22	+++	+		+++	++++		-	
S17_23	+++		+	+	++++			Organic rich
S17_24	++++		++	+	+++	gt		Sequence Top
S17_25	++		+++	+	+++		-	Sequence Top
S19_5	+++	+		+++	++++		-	underclay
S19_6	+++	+	+	+	++++			
S19_7	+++		+	++	++++			Organic rich
S19_26	Sm++++			++	+++			Organic rich
S19_27	++		+	++	++++		-	underclay
S19_29	++	+	+	++++	++++		-	Fluvial channel
S19_30a	+		+	++	++++			sequence bottom
S19_30b	+	+	+	++	++++			
S19_30c	++	+		+++	++++			
S19_30d	++	+	+	++++	++++			
S19_30e	+++	+	+	+++	++++	gt		
S19_30f	+++		+	+	++++			Organic rich,top
S19_31		+	++	++	++++	gb	-	Sequence bottom
S19_1	+		++++		+++	gt		Top, dike
S19_2	+		++++	+	+++	gt		Top, dike
S19_3	+		++	+	++++			Near dike
S19_4a	+			+	++++			Clay sequence
S19_4b	++			+ (I/S ++)	++++			basement

Table 2. Relative abundances of clay minerals from Paleozoic rocks hosted clay section . Ch = chlorite, Sm = smectite, Vm = vermiculite, Kaol = kaolinite, Hly = halloysite, gb = gibbsite, gt = goethite.

Sample #	Sm	Ch/Sm	Vm	il	Kaol	others	Hly	
S20_1			+	++	++++			Sequence top
S20_2			+	++	++++		-	
S20_3				++	++++			
S20_4				+	++++			
S20_5				++	++++	gt		
S20_6	+			+++	++++	gt	-	
S20_7	+			+	++++		-	
S20_8	++++	+	+	++	+++			
S20_9	++	+	+	+	++++		-	
S20_10	+++	+		++	++++			Caol intercalations,
S20_11	++++	++		++	+++			
S20_12	++++	++		+	+++		-	Iron rich zone
S20_13	+				+	gt		
S20_14	++++			+++	++			Sequence bottom

Table 3. Relative abundances of clay minerals from limestone hosted clay section. Ch = chlorite, Sm = smectite, Vm = vermiculite, Kaol = kaolinite, Hly = halloysite, gb = gibbsite, gt = goethite.

Sample #	Sm	Sm/Ch	Ch	Vm	il	Kaol	Others	Hly	
S20_30					+++	++++			Sequence top
S20_29	+	+			++++	++++	gt		
S20_28	+++				+++	++++		-	
S20_27		+++	+	+	++	++++		-	
S20_26		+++	+	+	+	++++			
S20_25		+++	+		++	++++		-	
S20_24b		+++		+	++++	+++	gt	-	Clay basement

Table 4. Crystal characteristics of clay minerals for the quarries. FWHM – full width at half maximum (°2-theta). d(060) in Å. See Appendix F for details.

	Illite ratio (Δ2Θ) (avg)	FWHM (illite) (avg)	FWHM (kaolinite) (avg)	d (060) (avg)	
				~1.50	~ 1.54
1*	1.25	0.479	0.857	+	+
2**	1.47	0.435	0.599	+	+
3***	1.49	0.439	0.785	+	+

**Volcanics and volcano-sedimantary hosted clay mine*

*** Paleozoic hosted clay mine*

**** Limestone hosted clay mine*

Table 5. Relative abundances of clay minerals from volcanic rocks. Ch = chlorite, Sm = smectite, Vm = vermiculite, Kaol = kaolinite, Hly = halloysite, gb = gibbsite, gt = goethite.

Sample #	Sm	Sm/Ch	Sm/illite	Ch	il	kaolinite	mordenite	Hly	
S19_36d	++++								Volcanic
S19_36c	++++								
S19_36b	++++								
S19_36a	++++				+	+			
S19_35	++++								surface
S19_34	++++								
S19_23	++++								
S19_19	++++				++	+	+		
S19_18	++++								
S19_14b				++	++++	++			Volcanosedimanter
S19_14a		++++							
S19_13	++++						++		surface
S19_12	++++						++		
S19_11	++++					+	++		
S19_10	++++						++		
S19_9		++++	+++		++	+			
S19_8a		++++	++++		++	++			
SKT_1	++++			+++	+	++	+++	-	
									drill

Table 6. Relative abundances of clay minerals from flysch series. Ch = chlorite, Sm = smectite, Vm = vermiculite, Kaol = kaolinite, Hly = halloysite, gb = gibbsite, gt = goethite.

Sample #	Vm	Ch	ill	kaol	hly	others
S20_43	+++	++	++++	+		
S20_44	++++	+	+++	++	-	
S20_45	++++	+	+++		-	
S20_46	++++		+++			gt
S20_47	++++	+	++++		-	
S20_48	++++		+++	++		
S19_16	++		++++	+		

Table 7. Relative abundances of clay minerals from Paleozoic sequence . Ch = chlorite, Sm = smectite, Vm = vermiculite, Kaol = kaolinite, Hly = halloysite, gb = gibbsite, gt = goethite.

Sample #	Sm	Sm/Ch	Ch	Ch/Vm	Vm	il	Kaol	others	hly		
S20_15	+	+	+			++++	+		-	sandstone	drill
S20_16	+		+			++++	++				
S20_18	+	+	+			++++	++		-		
S20_19	+		++			++++	++		-		
S20_31	++					++++	++				surface
S20_32	++				+	++++	+++				
S20_20					+++	++++	+			shale	
S20_21					+++	++++					
S20_22					+++	++++					
S20_23a	+				+++	++++					
S19_24		+			+++	++++					
S19_25	+	++			++++	+++	++				
S20_39					+++	++	++++	gt	-		
S20_40				++	+++	+	++++	gt			
S20_41				++	++++	++	++		-		
S20_42				++	+++	++	++++	gt	-		

Table 8. PC-all-loadings.

	PC1	PC2	PC3
Si	**0.31**	0.09	**-0.46**
Al	**-0.30**	**-0.38**	0.01
Fe	**-0.30**	0.08	-0.26
Mn	-0.23	**0.41**	-0.15
Mg	**-0.38**	0.02	-0.10
Ca	-0.21	**0.37**	**0.43**
Na	-0.19	**0.44**	-0.24
K	**-0.33**	0.02	-0.17
P	**-0.34**	0.25	0.01
Ti	-0.22	**-0.39**	**-0.36**
REE	**-0.31**	**-0.28**	-0.17
LOI	**-0.28**	-0.22	**0.50**

Table 9. PC-clay-loadings.

	PC1	PC2
Si	**0.31**	0.25
Al	**-0.33**	0.18
Fe	-0.22	**-0.49**
Mn	-0.14	**-0.66**
Mg	**-0.35**	0.13
Ca	**-0.27**	-0.15
Na	**-0.30**	0.16
K	**-0.30**	0.19
P	-0.20	-0.15
Ti	**-0.28**	0.26
REE	**-0.31**	0.18
LOI	**-0.29**	0.10

Table 10. PC-source-loadings.

	PC1	PC2	PC3
Si	0.18	**-0.47**	0.02
Al	**0.44**	-0.07	-0.15
Fe	**0.42**	0.26	-0.04
Mn	0.03	0.26	**0.44**
Mg	0.22	**0.45**	0.05
Ca	**-0.38**	0.10	0.24
Na	0.03	**-0.39**	**0.43**
K	0.18	-0.08	**0.44**
P	0.01	**0.27**	**0.54**
Ti	**0.45**	0.13	-0.02
REE	**0.34**	0.03	0.01
LOI	-0.25	**0.43**	-0.22

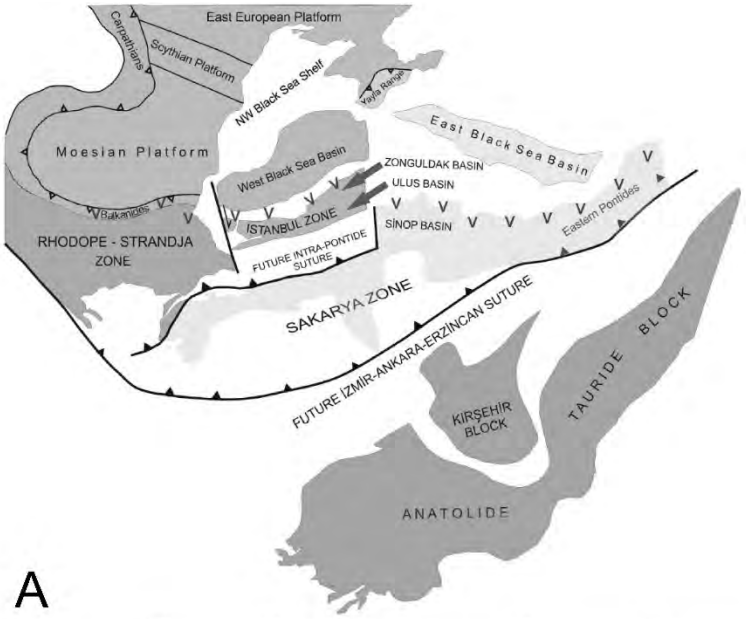
East European Platform
Carpathians
Scythian Platform
NW Black Sea Shelf
Moesian Platform
West Black Sea Basin
East Black Sea Basin
ZONGULDAK BASIN
ULUS BASIN
SİNOP BASIN
ISTANBUL ZONE
FUTURE INTRA-PONTIDE SUTURE
Balkanides
RHODOPE - STRANDJA ZONE
Eastern Pontides
SAKARYA ZONE
FUTURE İZMİR-ANKARA-ERZİNCAN SUTURE
KIRŞEHİR BLOCK
TAURIDE BLOCK
ANATOLIDE
A

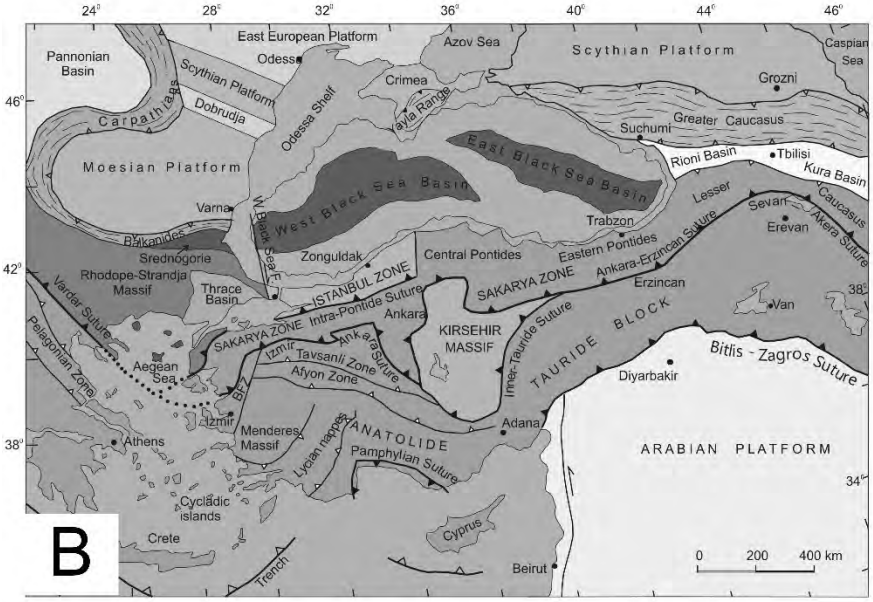
East European Platform
Azov Sea
Scythian Platform
Caspian Sea
Pannonian Basin
Odessa
Crimea
Grozni
Carpathians
Dobrudja
Odessa Shelf
Moesian Platform
Suchumi
Greater Caucasus
Rioni Basin
Tbilisi
Kura Basin
West Black Sea Basin
East Black Sea Basin
Varna
Trabzon
Lesser Caucasus
Sevan
Erevan
Balkanides
Srednogorie
Zonguldak
Central Pontides
Eastern Pontides
Ankara-Erzincan Suture
Akera Suture
Rhodope-Strandja Massif
Thrace Basin
ISTANBUL ZONE
Intra-Pontide Suture
SAKARYA ZONE
Erzincan
Vardar Suture
Ankara
KIRSEHIR MASSIF
Izmir-Tauride Suture
TAURIDE BLOCK
Van
Aegean Sea
Izmir
Tavsanli Zone
Afyon Zone
Ankara Suture
Bitlis - Zagros Suture
Diyarbakir
Pelagonian Zone
BFZ
Menderes Massif
Adana
Athens
ANATOLIDE
Lycian nappes
Pamphylian Suture
ARABIAN PLATFORM
Cycladic islands
Crete
Cyprus
Beirut
Trench
0 200 400 km
B

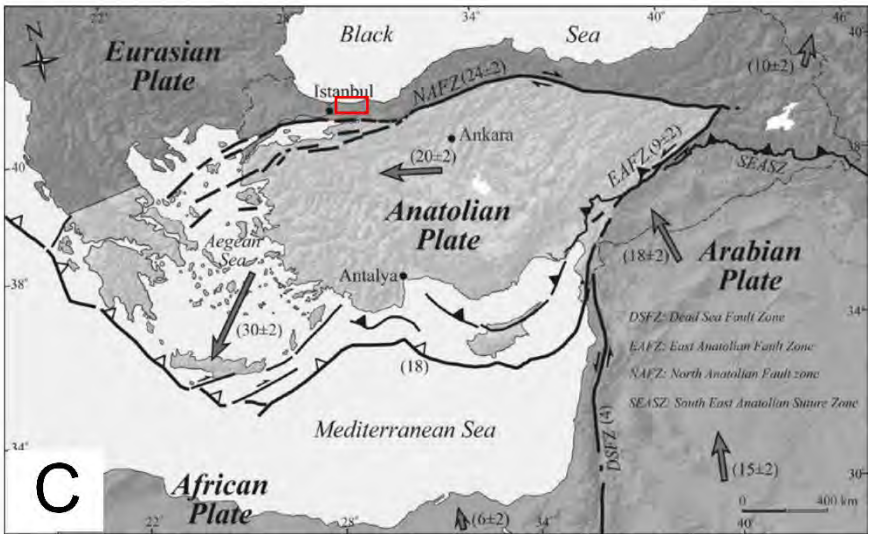
Black Sea
Eurasian Plate
Istanbul
NAFZ(24±2)
(10±2)
Ankara
(20±2)
EAFZ(9±2)
SEASZ
Anatolian Plate
Aegean Sea
Antalya
(18±2)
Arabian Plate
(30±2)
(18)
DSFZ: Dead Sea Fault Zone
EAFZ: East Anatolian Fault Zone
NAFZ: North Anatolian Fault zone
SEASZ: South East Anatolian Suture Zone
Mediterranean Sea
DSFZ (4)
(15±2)
African Plate
(6±2)
0 400 km
C

Figure 1. A- Paleogeography of tectonic units of Turkey (from Tüysüz et al.,2016) B- Tectonic Units of Turkey (modified from Okay and Tüysüz, 2009). C- Boundaries and relative movements of plates and main faults of Turkey (modified from Isik et al., 2014), red color indicates the study area.

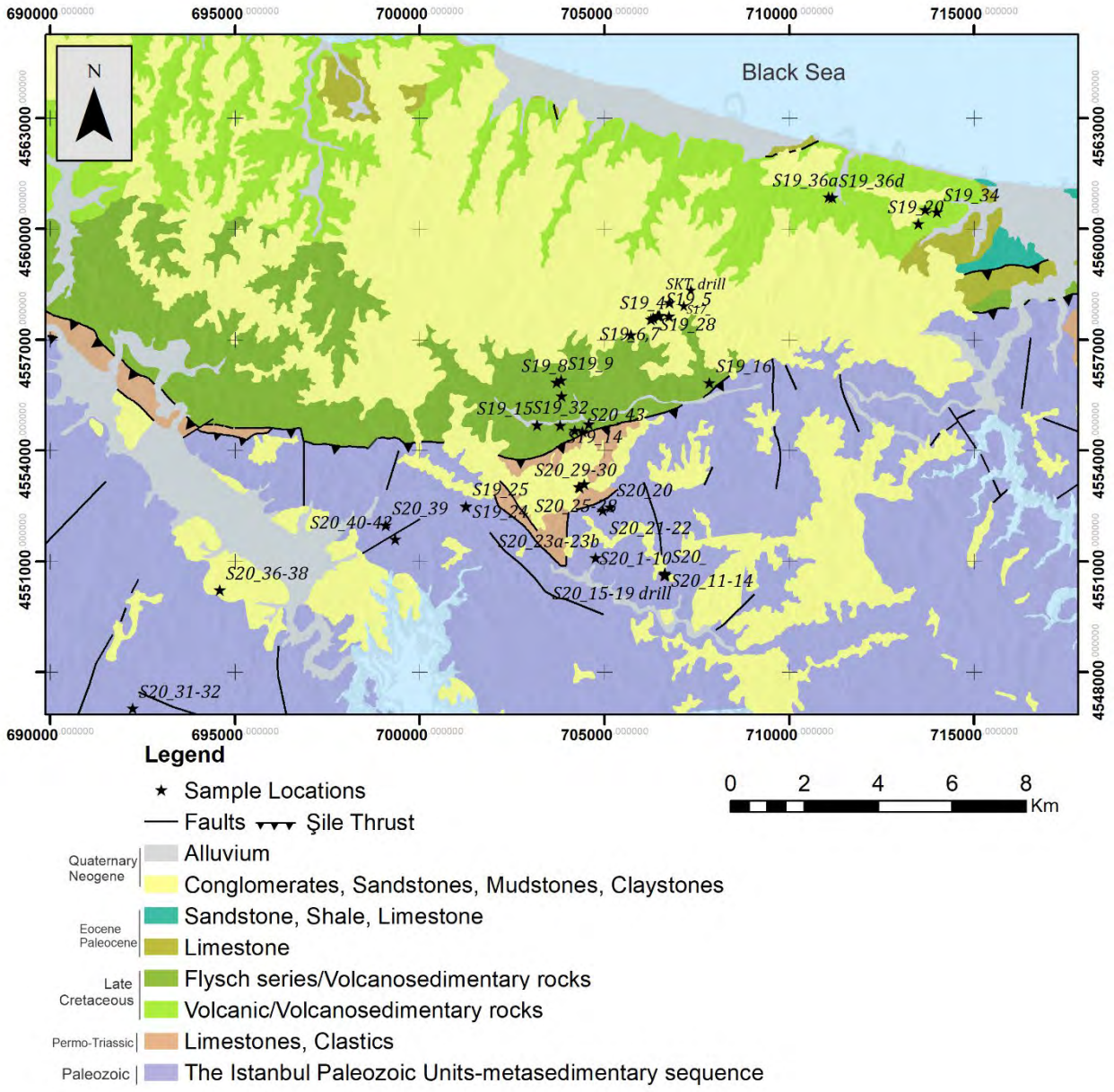

Figure 2. Generalized geology map of the study area (based on the MTA, 2005- 1/50000 scale geological maps of Turkey) and sample locations.

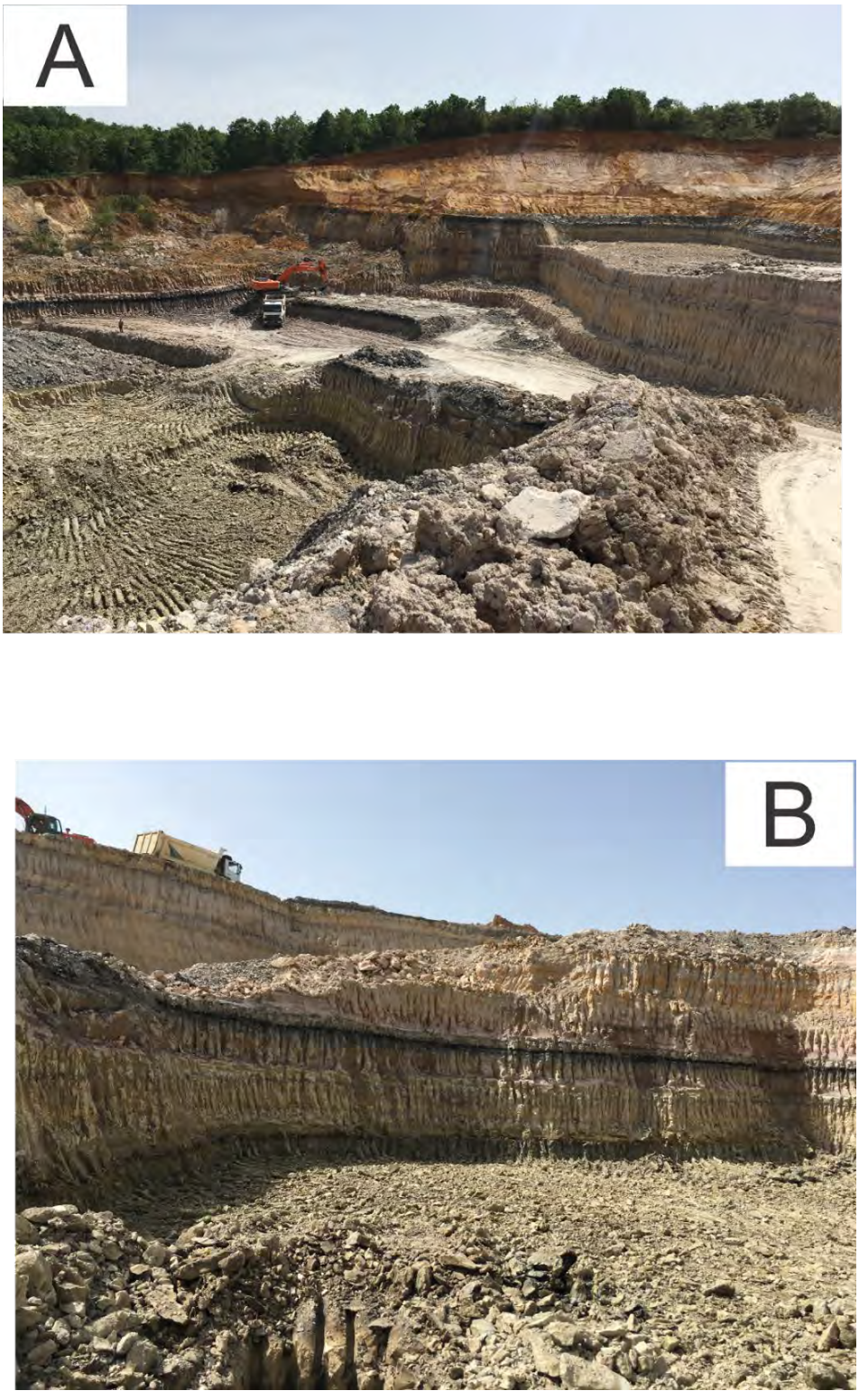

Figure 3. Clay section from the volcanic hosted clay quarry. Trucks used as scale.

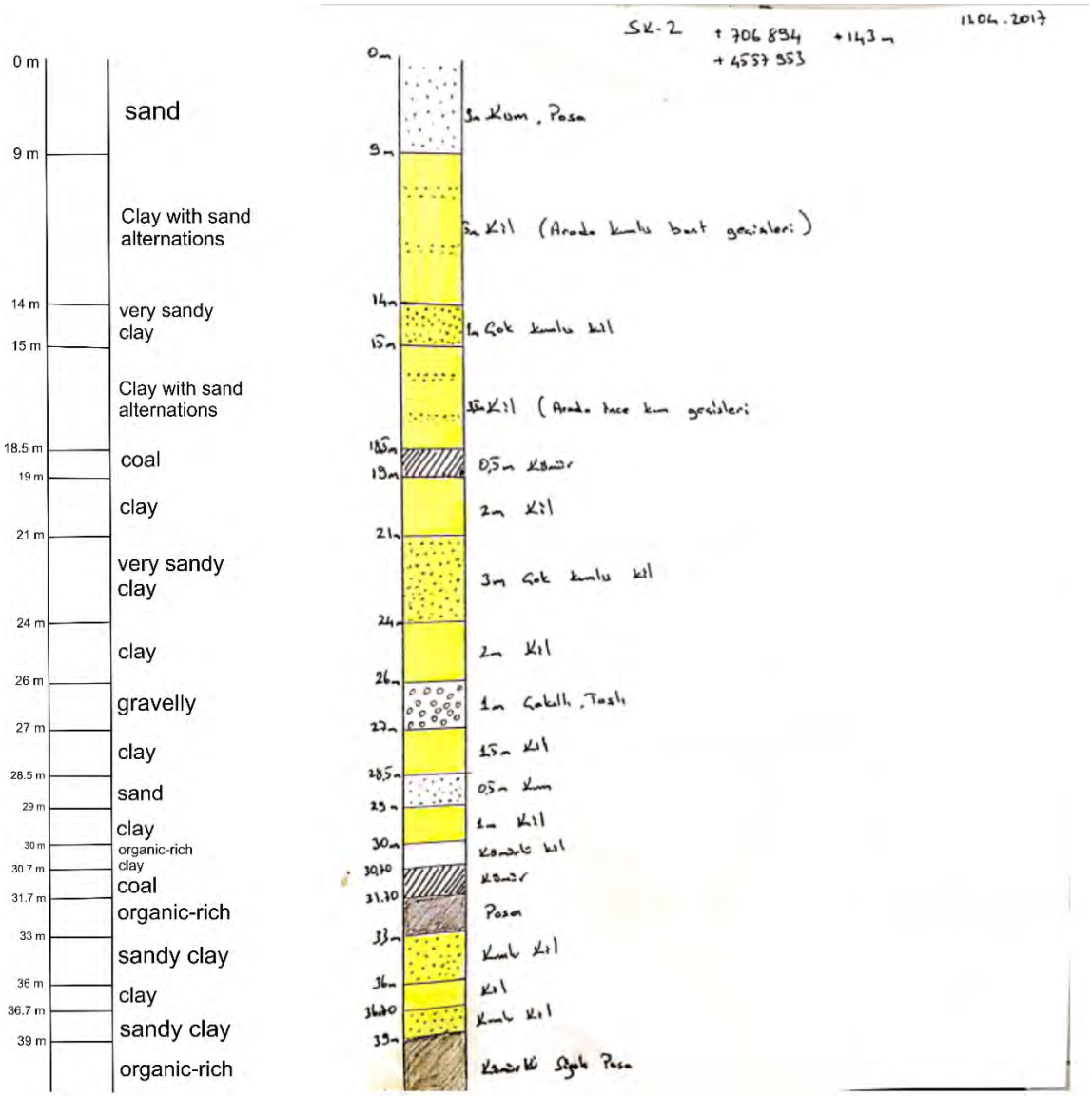

Figure 4. Original drill core data from the mining company (unpublished). (Kil=Clay, Kömür=Coal, Çakıl=Gravel, Kum=Sand)

Figure 5. A-Channel bar between layers and B-Coalified wood

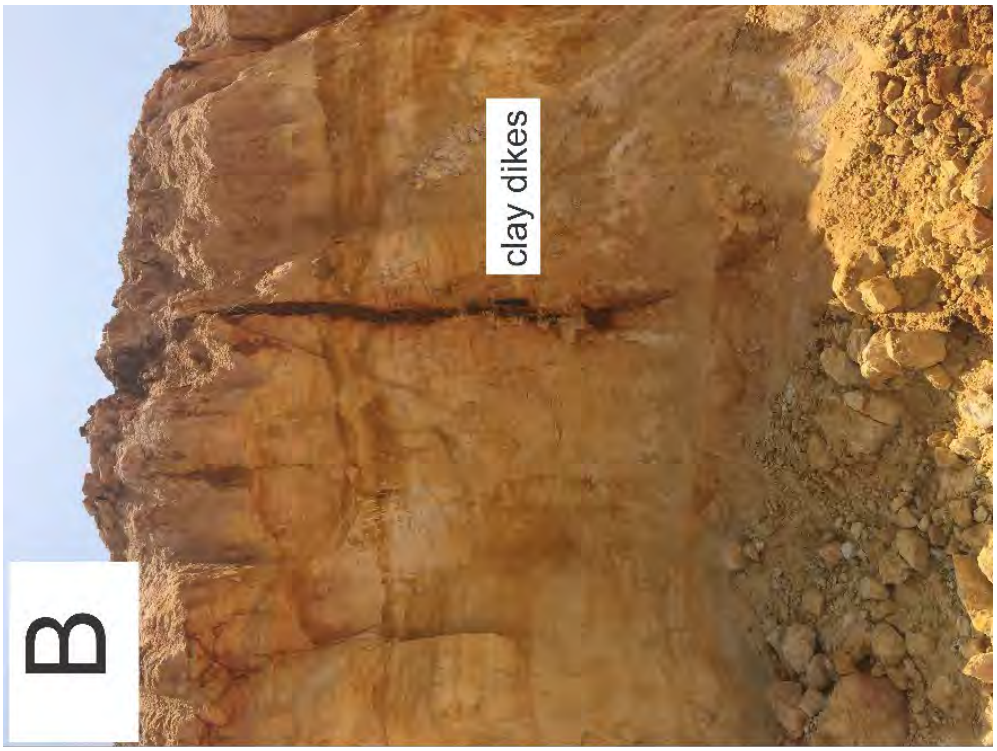

Figure 6. A- Color variations in layers B-clay dikes (geologist and hammer for scale)

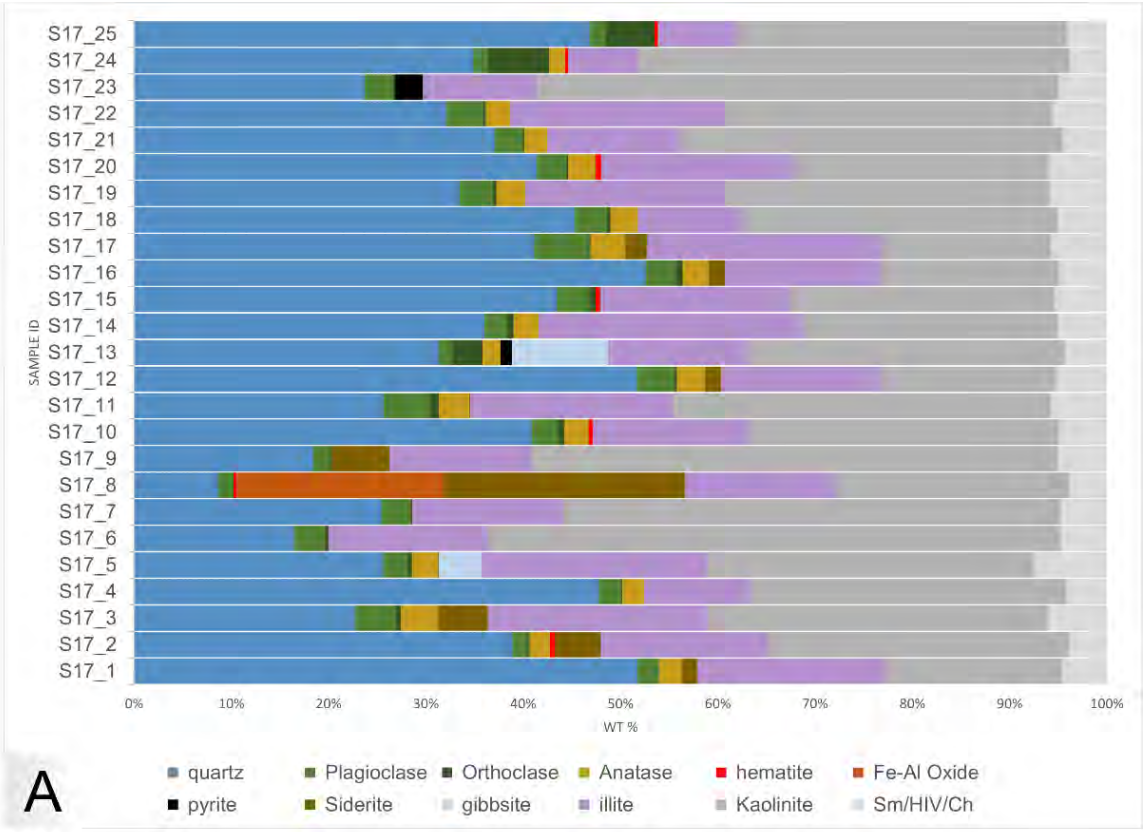
S17_25
S17_24
S17_23
S17_22
S17_21
S17_20
S17_19
S17_18
S17_17
S17_16
S17_15
S17_14
S17_13
S17_12
S17_11
S17_10
S17_9
S17_8
S17_7
S17_6
S17_5
S17_4
S17_3
S17_2
S17_1
SAMPLE ID
0%
10%
20%
30%
40%
50%
60%
70%
80%
90%
100%
WT %
A
quartz
Plagioclase
Orthoclase
Anatase
hematite
Fe-Al Oxide
pyrite
Siderite
gibbsite
illite
Kaolinite
Sm/HIV/Ch

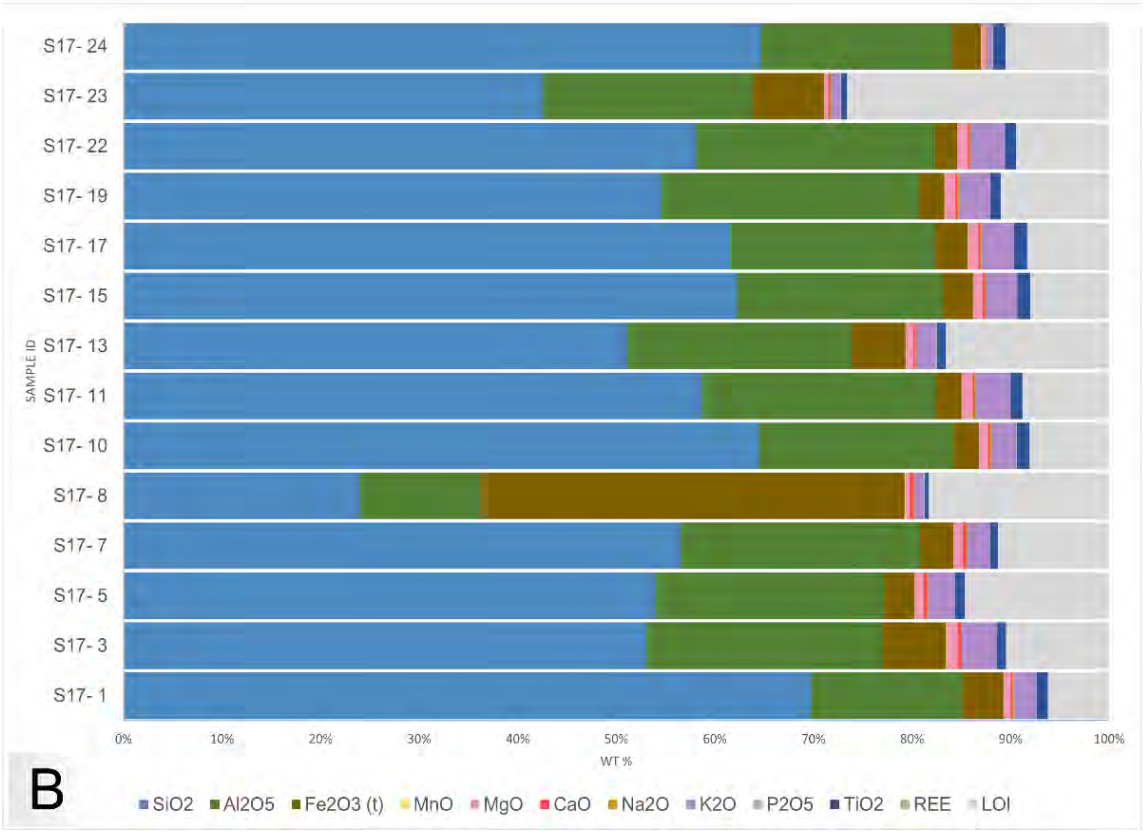
S17- 24
S17- 23
S17- 22
S17- 19
S17- 17
S17- 15
S17- 13
S17- 11
S17- 10
S17- 8
S17- 7
S17- 5
S17- 3
S17- 1
SAMPLE ID
0%
10%
20%
30%
40%
50%
60%
70%
80%
90%
100%
WT %
B
SiO2
Al2O5
Fe2O3 (t)
MnO
MgO
CaO
Na2O
K2O
P2O5
TiO2
REE
LOI

Figure 7. A-Semi-quantitative whole-rock mineralogy from volcanic hosted clay quarry, B-Geochemistry of layers from same section

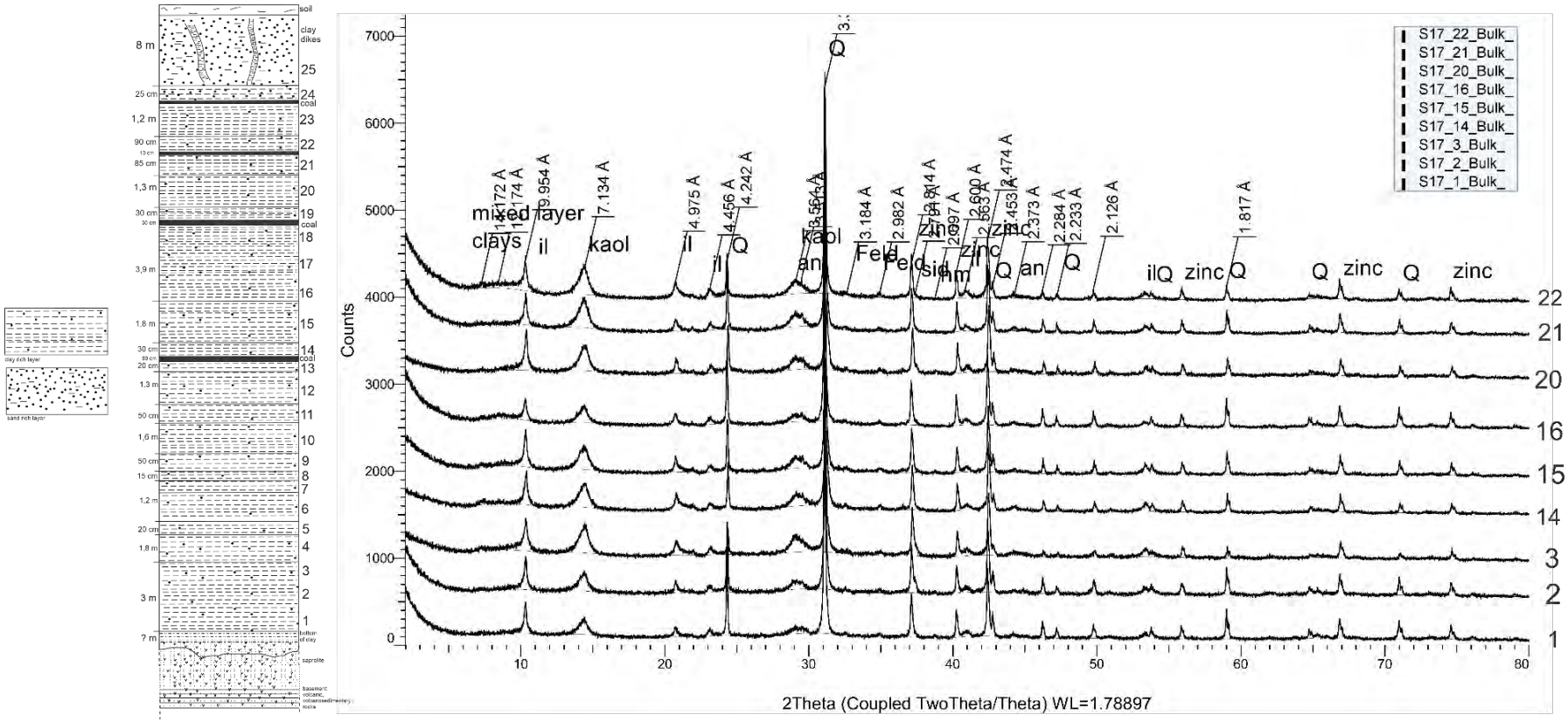
clay rich layer
sand rich layer
soil
clay dikes
coal
bottom of clay
saprolite
basement: volcanic, volcaniclastic-sedimentary rocks
8 m
25 cm
1,2 m
90 cm
85 cm
1,3 m
30 cm
3,9 m
1,8 m
80 cm
20 cm
1,3 m
50 cm
1,6 m
50 cm
15 cm
1,2 m
20 cm
1,8 m
3 m
7 m
Counts
2Theta (Coupled TwoTheta/Theta) WL=1.78897
S17_22_Bulk_
S17_21_Bulk_
S17_20_Bulk_
S17_16_Bulk_
S17_15_Bulk_
S17_14_Bulk_
S17_3_Bulk_
S17_2_Bulk_
S17_1_Bulk_
mixed layer clays
il
kaol
Q
an
Feld
sid
hm
zinc
ilQ
22
21
20
16
15
14
3
2
1

Figure 8. Representative XRD whole-rock pattern from the volcanic hosted clay section observed

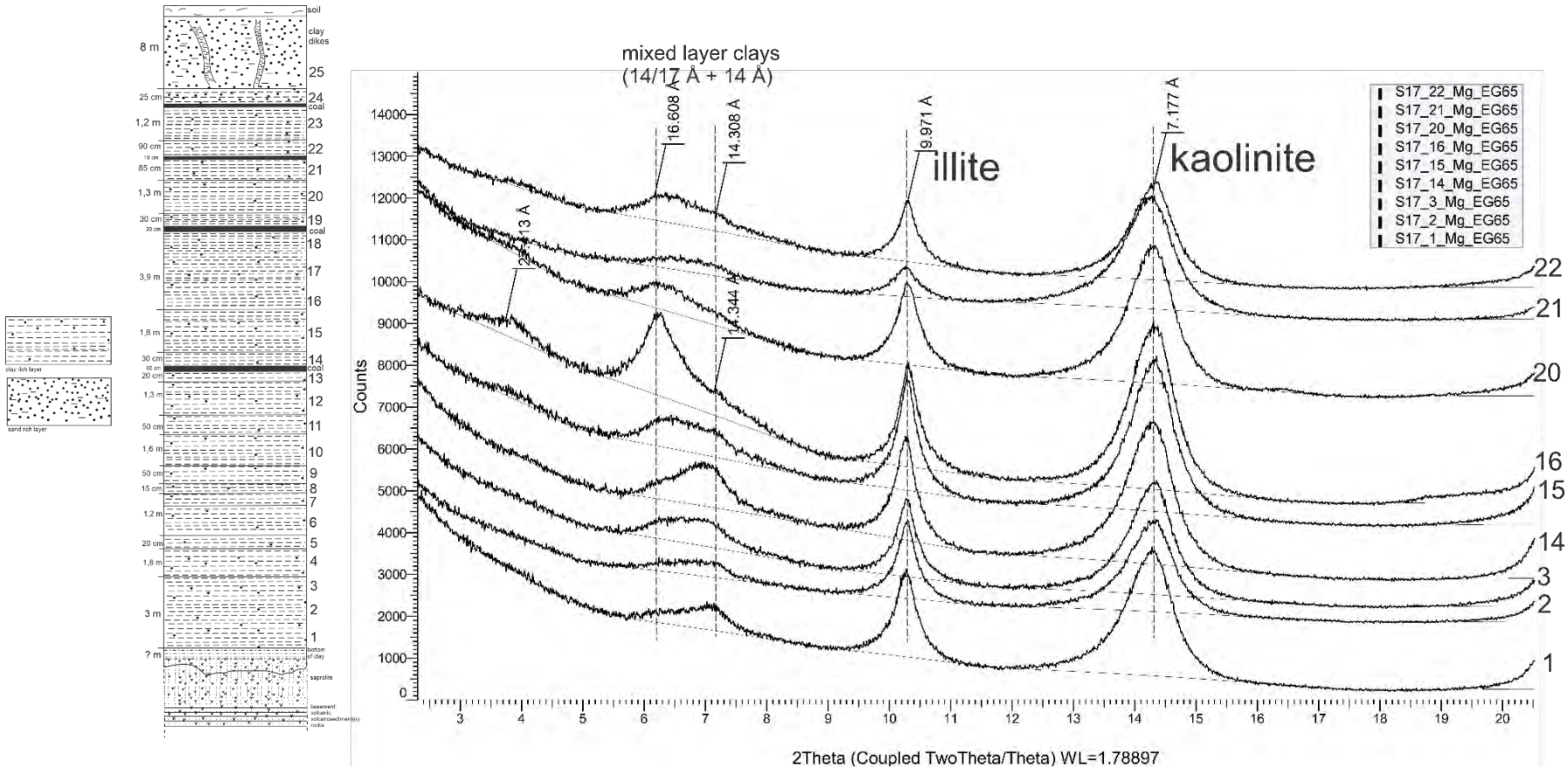
soil
clay dikes
coal
bottom of clay
saprolite
basement: volcanic, volcanosedimentary rocks
clay rich layer
sand rich layer
mixed layer clays
(14/17 Å + 14 Å)
16.608 Å
14.308 Å
9.971 Å
7.177 Å
illite
kaolinite
S17_22_Mg_EG65
S17_21_Mg_EG65
S17_20_Mg_EG65
S17_16_Mg_EG65
S17_15_Mg_EG65
S17_14_Mg_EG65
S17_3_Mg_EG65
S17_2_Mg_EG65
S17_1_Mg_EG65
Counts
2Theta (Coupled TwoTheta/Theta) WL=1.78897

Figure 9. Clay fraction XRD data from volcanic hosted clay section


A
underclay


B
organic rich,
coal zone

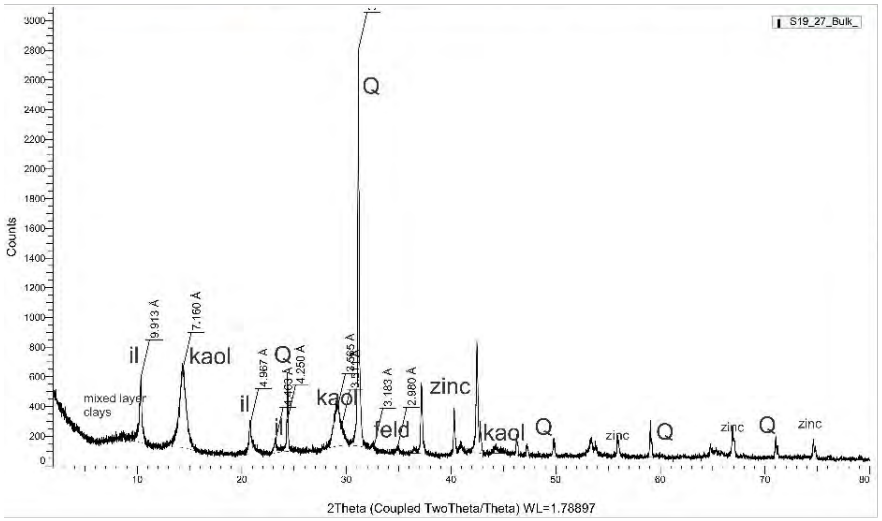
S19_27_Bulk_
Counts
2Theta (Coupled TwoTheta/Theta) WL=1.78897
mixed layer clays
il
kaol
Q
feld
zinc

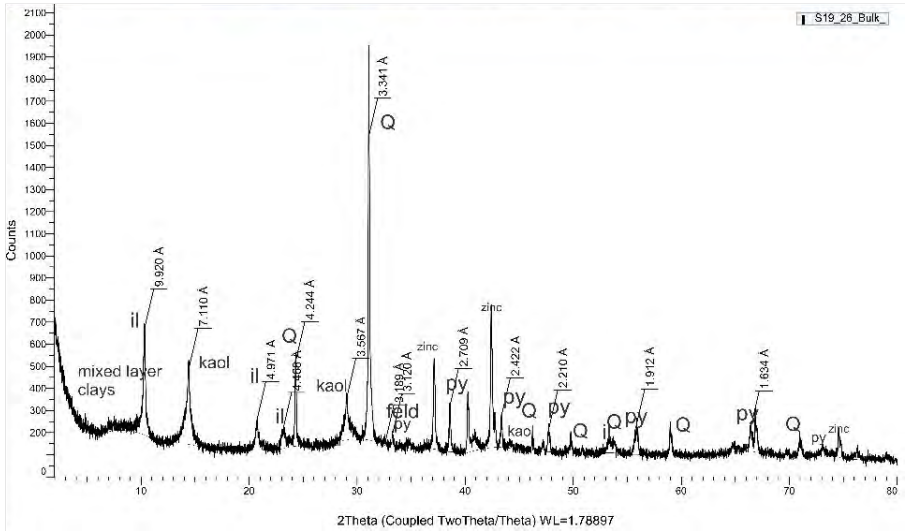
S19_26_Bulk_
Counts
2Theta (Coupled TwoTheta/Theta) WL=1.78897
mixed layer clays
il
kaol
Q
feld
py
zinc

Figure 10. A-Underclay and B-Coal seam

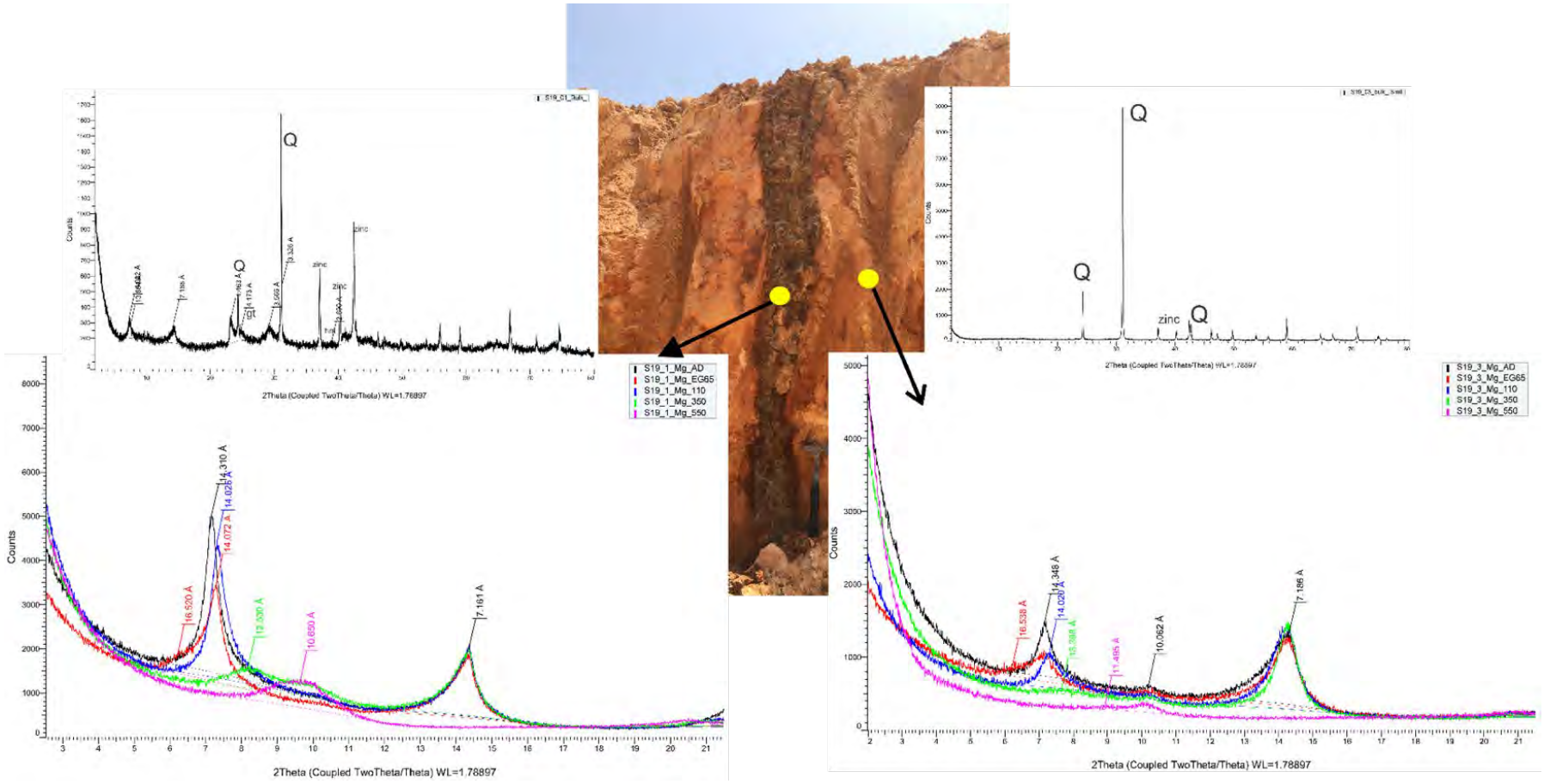
Q
Q
zinc
Q
S19_1_Mg_AD
S19_1_Mg_EG65
S19_1_Mg_110
S19_1_Mg_350
S19_1_Mg_550
Counts
14.310 Å
14.072 Å
14.026 Å
16.520 Å
12.330 Å
10.650 Å
7.161 Å
2Theta (Coupled TwoTheta/Theta) WL=1.78897
Q
Q
zinc
Q
S19_3_Mg_AD
S19_3_Mg_EG65
S19_3_Mg_110
S19_3_Mg_350
S19_3_Mg_550
Counts
16.536 Å
14.348 Å
14.020 Å
13.388 Å
11.495 Å
10.062 Å
7.186 Å
2Theta (Coupled TwoTheta/Theta) WL=1.78897

Figure 11. XRD whole rock and clay fraction patterns from the clay dikes (hammer for scale) (for higher resolution, see page 155 and 157 for whole rock and see page 285 and 287 for the clay fraction XRD pattern)

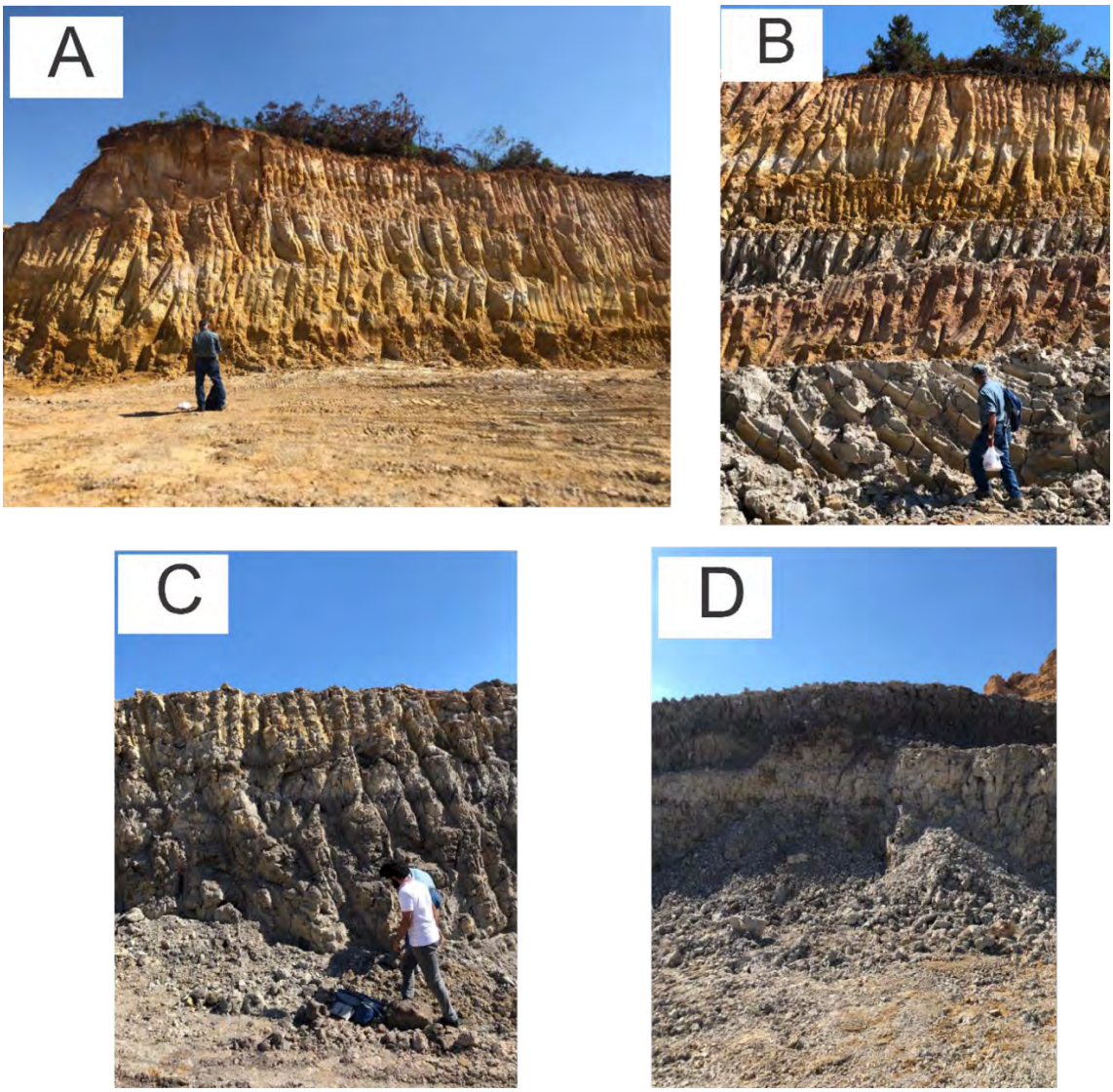

Figure 12. Clay section from the Paleozoic rocks hosted clay quarry. A-The uppermost part, B- Following layers C, D -Deeper part of the section and thin organic rich layers (geologists for scale)

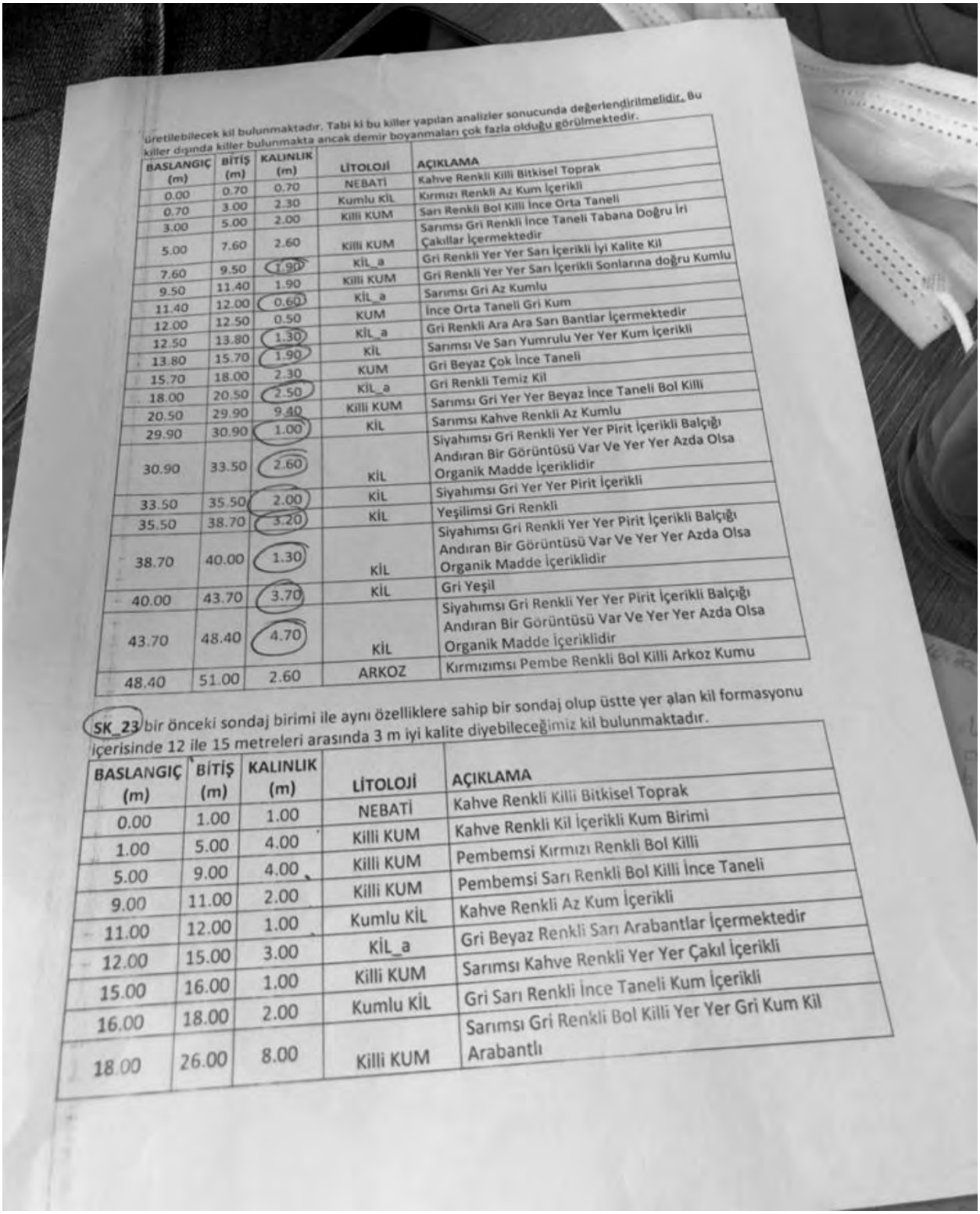

üretilebilecek kil bulunmaktadır. Tabi ki bu killer yapılan analizler sonucunda değerlendirilmelidir. Bu killer dışında killer bulunmakta ancak demir boyanmaları çok fazla olduğu görülmektedir.

BAŞLANGIÇ (m)	BİTİŞ (m)	KALINLIK (m)	LİTOLOJİ	AÇIKLAMA
0.00	0.70	0.70	NEBATİ	Kahve Renkli Killi Bitkisel Toprak
0.70	3.00	2.30	Kumlu KİL	Kırmızı Renkli Az Kum İçerikli
3.00	5.00	2.00	Killi KUM	Sarı Renkli Bol Killi İnce Orta Taneli
5.00	7.60	2.60	Killi KUM	Sarımsı Gri Renkli İnce Taneli Tabana Doğru İri Çakıllar İçermektedir
7.60	9.50	1.90	KİL_a	Gri Renkli Yer Yer Sarı İçerikli İyi Kalite Kil
9.50	11.40	1.90	Killi KUM	Gri Renkli Yer Yer Sarı İçerikli Sonlarına doğru Kumlu
11.40	12.00	0.60	KİL_a	Sarımsı Gri Az Kumlu
12.00	12.50	0.50	KUM	İnce Orta Taneli Gri Kum
12.50	13.80	1.30	KİL_a	Gri Renkli Ara Ara Sarı Bantlar İçermektedir
13.80	15.70	1.90	KİL	Sarımsı Ve Sarı Yumrulu Yer Yer Kum İçerikli
15.70	18.00	2.30	KUM	Gri Beyaz Çok İnce Taneli
18.00	20.50	2.50	KİL_a	Gri Renkli Temiz Kil
20.50	29.90	9.40	Killi KUM	Sarımsı Gri Yer Yer Beyaz İnce Taneli Bol Killi
29.90	30.90	1.00	KİL	Sarımsı Kahve Renkli Az Kumlu
30.90	33.50	2.60	KİL	Siyahımsı Gri Renkli Yer Yer Pirit İçerikli Balçığı Andıran Bir Görüntüsü Var Ve Yer Yer Azda Olsa Organik Madde İçeriklidir
33.50	35.50	2.00	KİL	Siyahımsı Gri Yer Yer Pirit İçerikli
35.50	38.70	3.20	KİL	Yeşilimsi Gri Renkli
38.70	40.00	1.30	KİL	Siyahımsı Gri Renkli Yer Yer Pirit İçerikli Balçığı Andıran Bir Görüntüsü Var Ve Yer Yer Azda Olsa Organik Madde İçeriklidir
40.00	43.70	3.70	KİL	Gri Yeşil
43.70	48.40	4.70	KİL	Siyahımsı Gri Renkli Yer Yer Pirit İçerikli Balçığı Andıran Bir Görüntüsü Var Ve Yer Yer Azda Olsa Organik Madde İçeriklidir
48.40	51.00	2.60	ARKOZ	Kırmızımsı Pembe Renkli Bol Killi Arkoz Kumu

SK_23 bir önceki sondaj birimi ile aynı özelliklere sahip bir sondaj olup üstte yer alan kil formasyonu içerisinde 12 ile 15 metreleri arasında 3 m iyi kalite diyebileceğimiz kil bulunmaktadır.

BAŞLANGIÇ (m)	BİTİŞ (m)	KALINLIK (m)	LİTOLOJİ	AÇIKLAMA
0.00	1.00	1.00	NEBATİ	Kahve Renkli Killi Bitkisel Toprak
1.00	5.00	4.00	Killi KUM	Kahve Renkli Kil İçerikli Kum Birimi
5.00	9.00	4.00	Killi KUM	Pembemsi Kırmızı Renkli Bol Killi
9.00	11.00	2.00	Killi KUM	Pembemsi Sarı Renkli Bol Killi İnce Taneli
11.00	12.00	1.00	Kumlu KİL	Kahve Renkli Az Kum İçerikli
12.00	15.00	3.00	KİL_a	Gri Beyaz Renkli Sarı Arabantlar İçermektedir
15.00	16.00	1.00	Killi KUM	Sarımsı Kahve Renkli Yer Yer Çakıl İçerikli
16.00	18.00	2.00	Kumlu KİL	Gri Sarı Renkli İnce Taneli Kum İçerikli
18.00	26.00	8.00	Killi KUM	Sarımsı Gri Renkli Bol Killi Yer Yer Gri Kum Kil Arabantlı

Figure 13. Original drill core data from the mining company (unpublished).

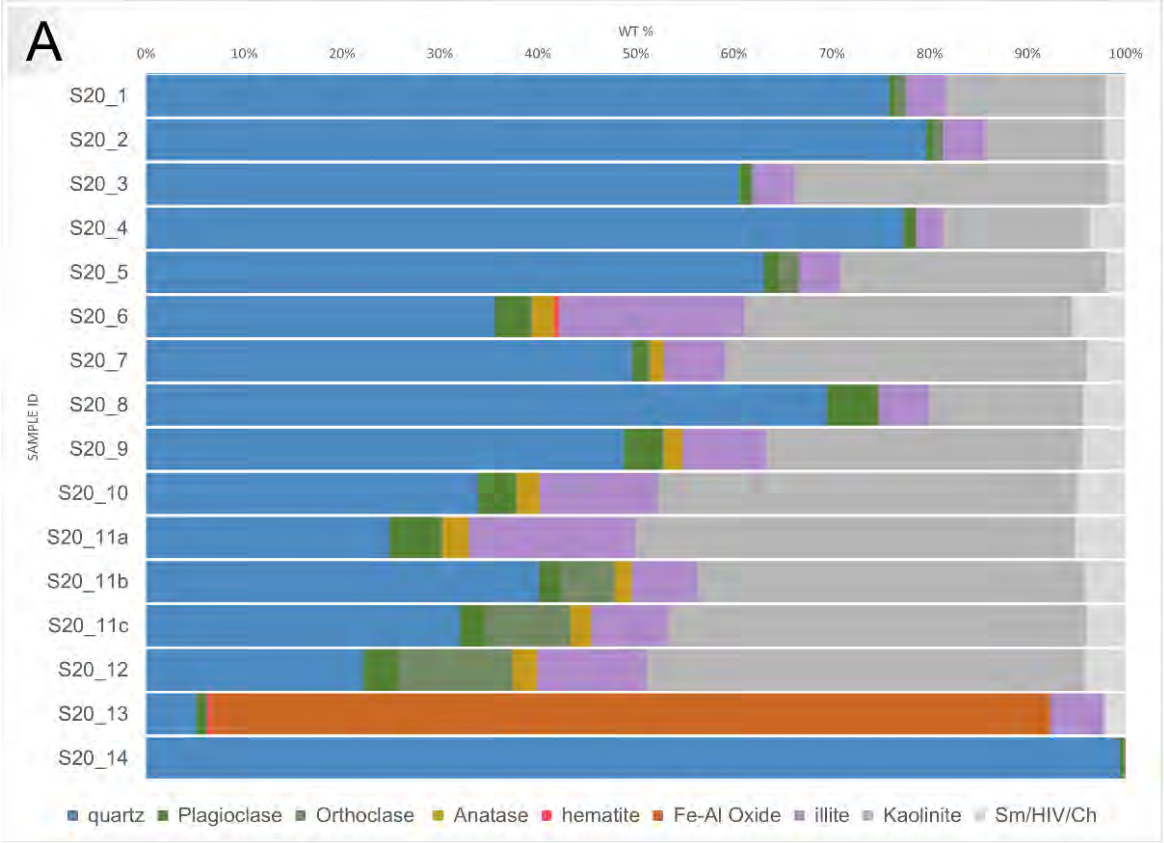
A
WT %
0%
10%
20%
30%
40%
50%
60%
70%
80%
90%
100%
SAMPLE ID
S20_1
S20_2
S20_3
S20_4
S20_5
S20_6
S20_7
S20_8
S20_9
S20_10
S20_11a
S20_11b
S20_11c
S20_12
S20_13
S20_14
quartz
Plagioclase
Orthoclase
Anatase
hematite
Fe-Al Oxide
illite
Kaolinite
Sm/HIV/Ch

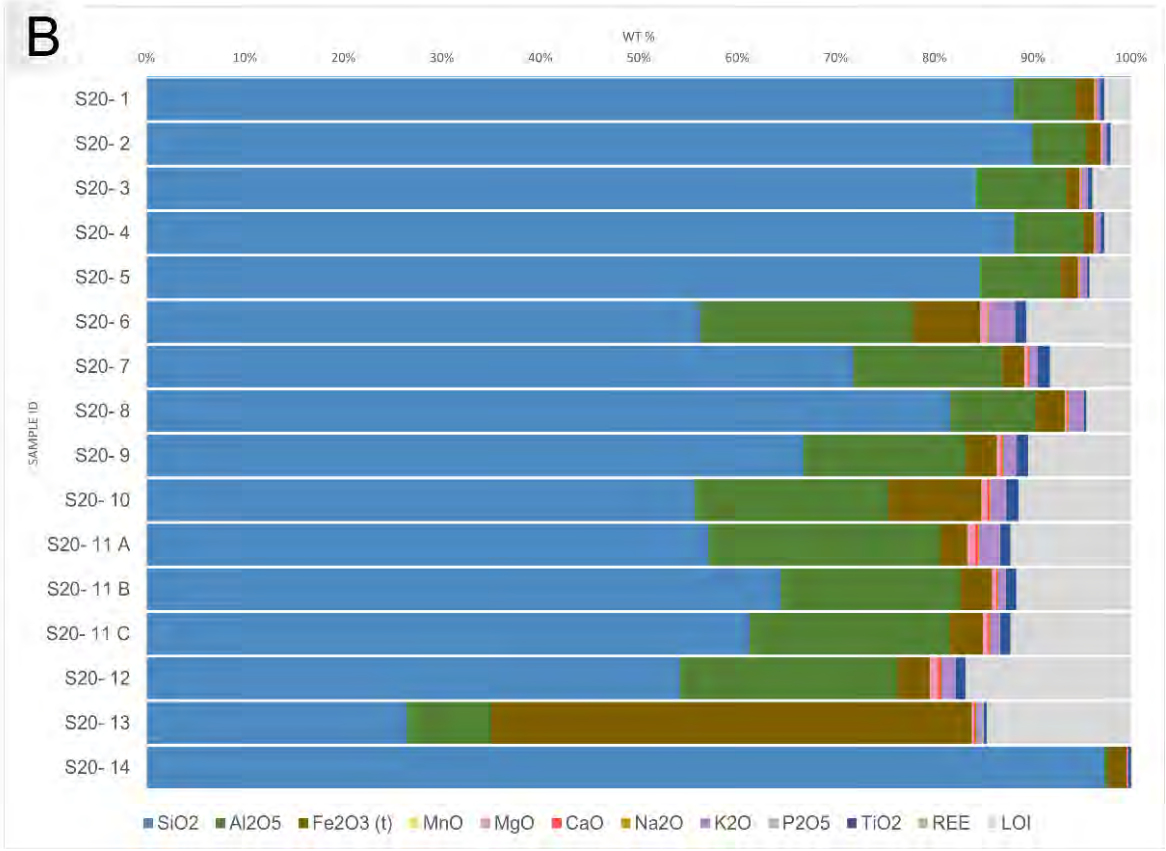
B
WT %
0%
10%
20%
30%
40%
50%
60%
70%
80%
90%
100%
SAMPLE ID
S20- 1
S20- 2
S20- 3
S20- 4
S20- 5
S20- 6
S20- 7
S20- 8
S20- 9
S20- 10
S20- 11 A
S20- 11 B
S20- 11 C
S20- 12
S20- 13
S20- 14
SiO2
Al2O5
Fe2O3 (t)
MnO
MgO
CaO
Na2O
K2O
P2O5
TiO2
REE
LOI

Figure 14. A- Semi-quantitative whole-rock mineralogy from Paleozoic rocks hosted clay quarry, B-Geochemistry of layers from same section

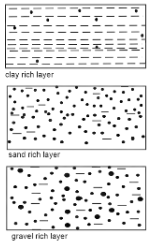
clay rich layer
sand rich layer
gravel rich layer

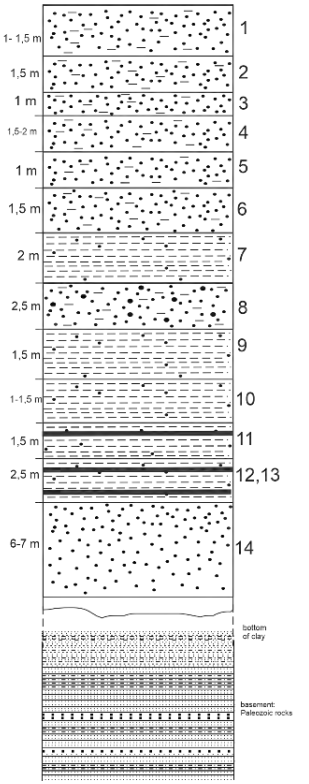
1- 1,5 m
1,5 m
1 m
1,5-2 m
1 m
1,5 m
2 m
2,5 m
1,5 m
1-1,5 m
1,5 m
2,5 m
6-7 m
1
2
3
4
5
6
7
8
9
10
11
12,13
14
bottom of clay
basement: Paleozoic rocks

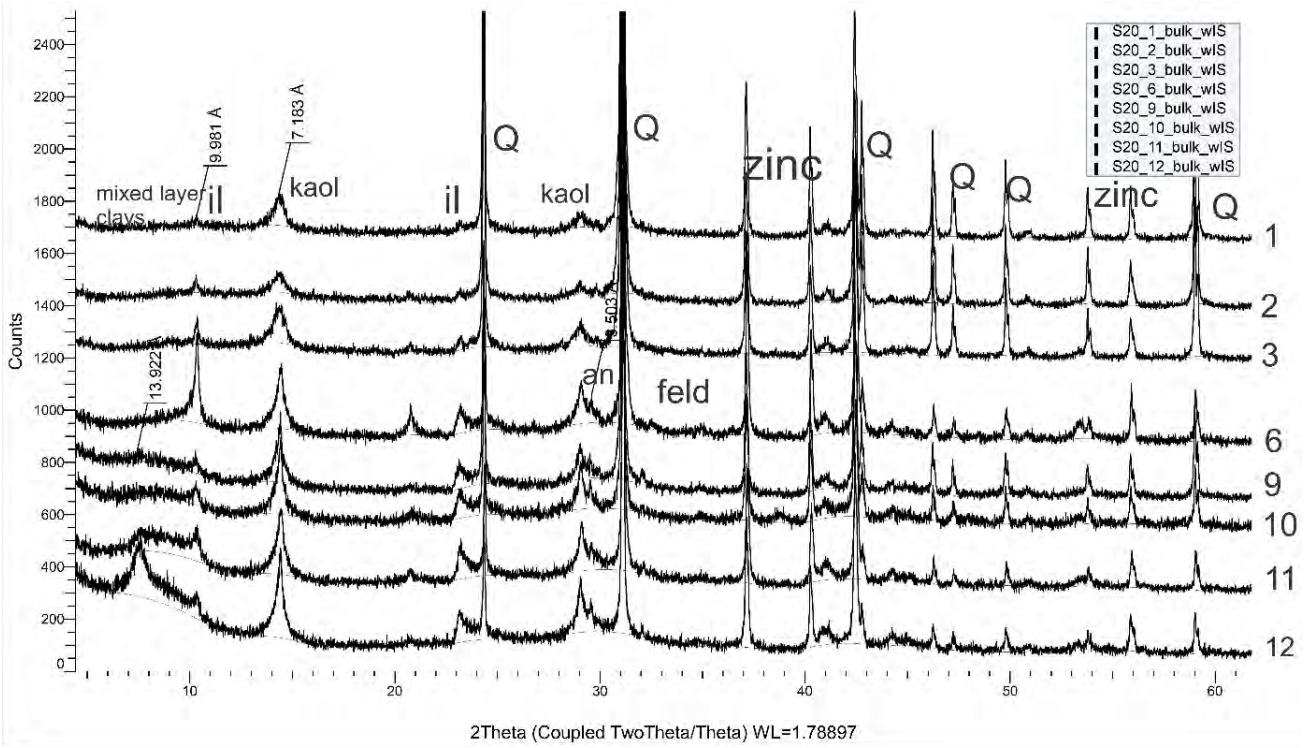
S20_1_bulk_wIS
S20_2_bulk_wIS
S20_3_bulk_wIS
S20_6_bulk_wIS
S20_9_bulk_wIS
S20_10_bulk_wIS
S20_11_bulk_wIS
S20_12_bulk_wIS
Counts
2Theta (Coupled TwoTheta/Theta) WL=1.78897
mixed layer clays
il
kaol
9.981 Å
7.183 Å
13.922 Å
an
feld
zinc
Q

Figure 15. Representative whole rock XRD patterns from the section (for higher resolution, see page 207,208, 209, 212, 213, 216, 217, 220)

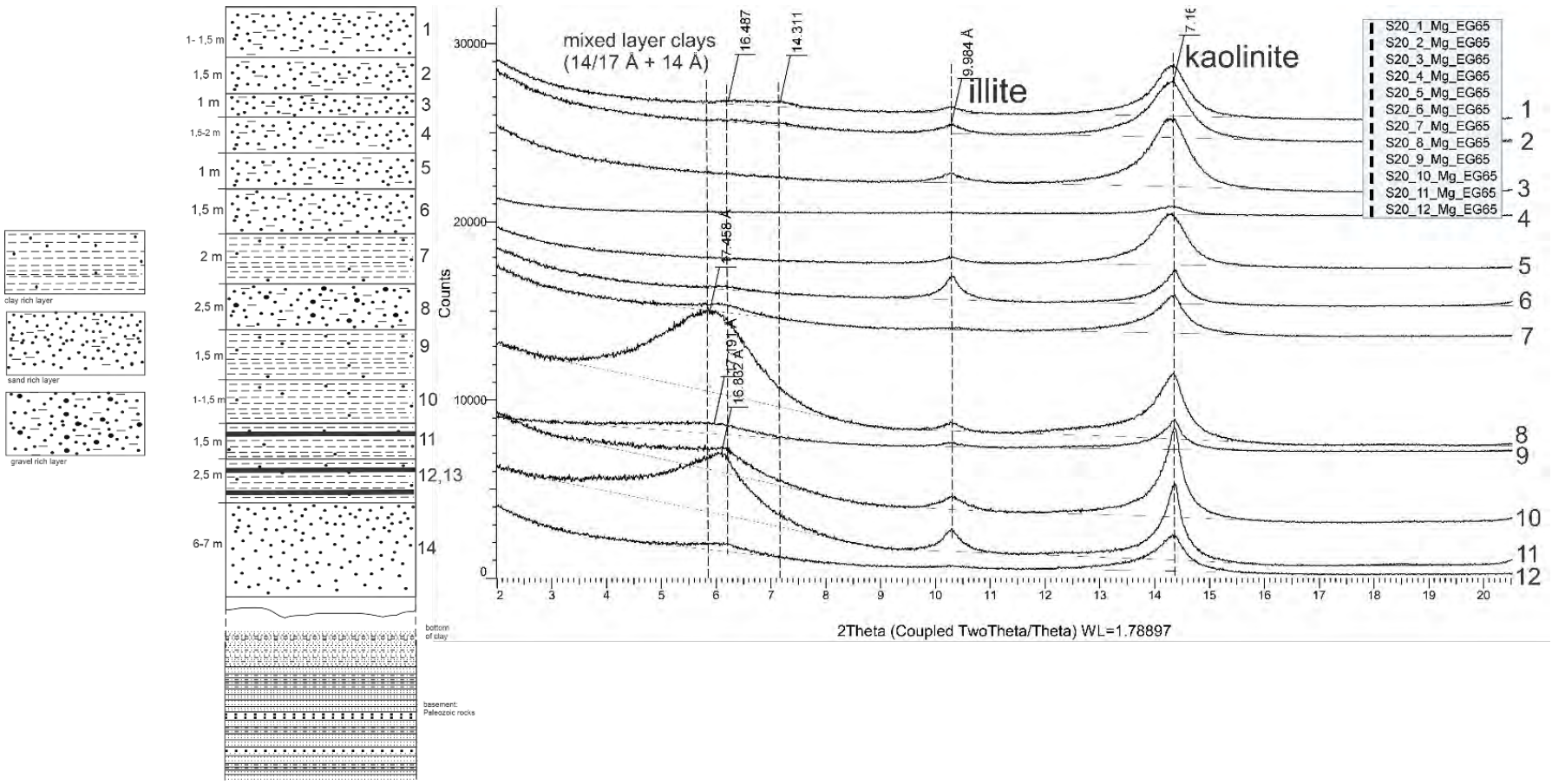
clay rich layer
sand rich layer
gravel rich layer
1- 1,5 m
1,5 m
1 m
1,5-2 m
1 m
1,5 m
2 m
2,5 m
1,5 m
1-1,5 m
1,5 m
2,5 m
6-7 m
1
2
3
4
5
6
7
8
9
10
11
12,13
14
bottom of clay
basement: Paleozoic rocks
mixed layer clays
(14/17 Å + 14 Å)
16.487
14.311
9.984 Å
illite
kaolinite
7.458 Å
16.882 Å
Counts
30000
20000
10000
0
2 3 4 5 6 7 8 9 10 11 12 13 14 15 16 17 18 19 20
2Theta (Coupled TwoTheta/Theta) WL=1.78897
S20_1_Mg_EG65
S20_2_Mg_EG65
S20_3_Mg_EG65
S20_4_Mg_EG65
S20_5_Mg_EG65
S20_6_Mg_EG65
S20_7_Mg_EG65
S20_8_Mg_EG65
S20_9_Mg_EG65
S20_10_Mg_EG65
S20_11_Mg_EG65
S20_12_Mg_EG65
1
2
3
4
5
6
7
8
9
10
11
12

Figure 16. Representative clay fraction XRD patterns from the section.

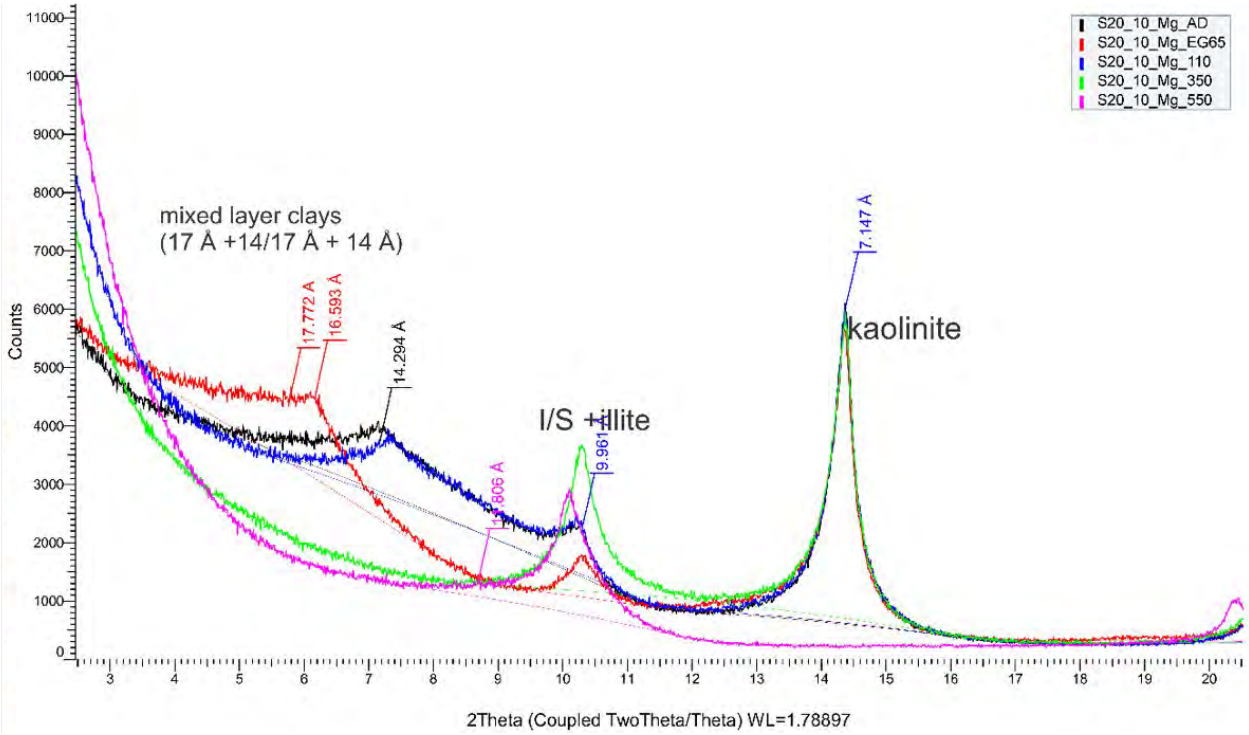
S20_10_Mg_AD
S20_10_Mg_EG65
S20_10_Mg_110
S20_10_Mg_350
S20_10_Mg_550
mixed layer clays
(17 Å +14/17 Å + 14 Å)
17.772 Å
16.593 Å
14.294 Å
I/S +illite
9.961 Å
7.806 Å
7.147 Å
kaolinite
Counts
2Theta (Coupled TwoTheta/Theta) WL=1.78897

Figure 17. XRD clay fraction data from the deeper level of the section. Yellow circle marks sample location in outcrop.

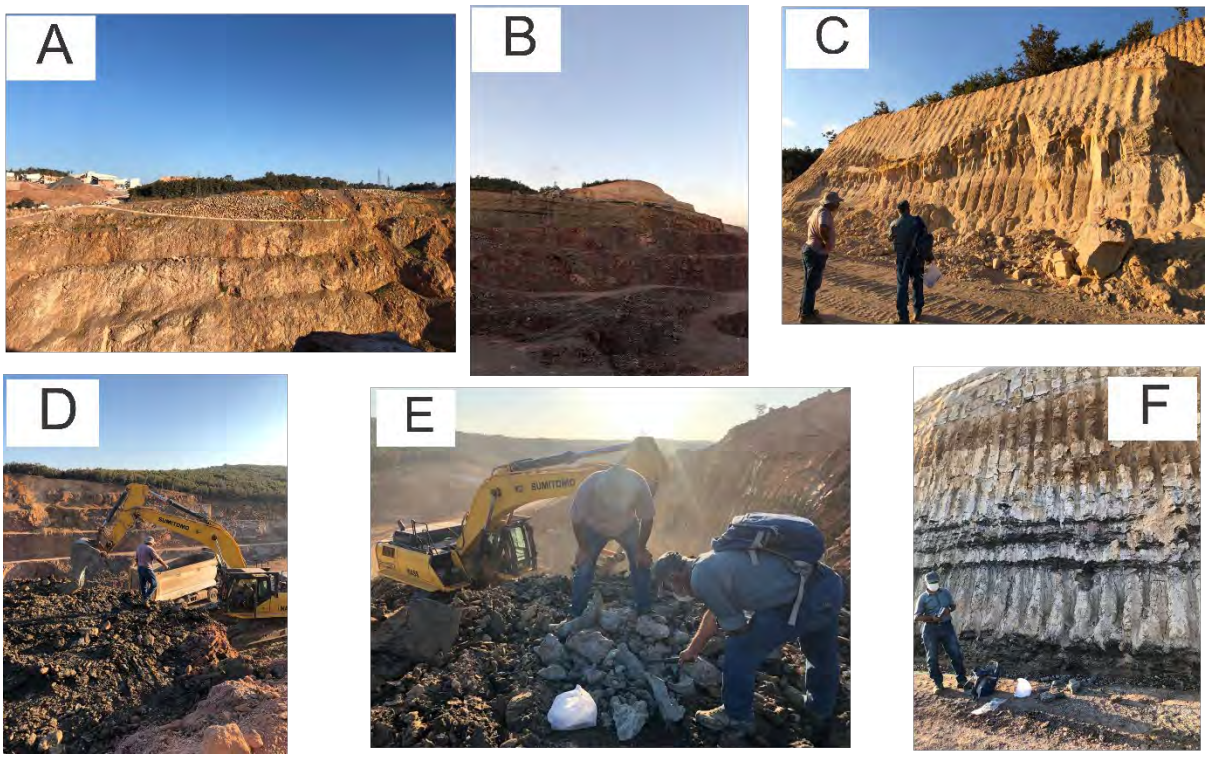

Figure 18. A-General view from the limestone quarry, B-Clay rich section on top of the limestone (cream color), C-The uppermost part of the clay section, D-Coal seam and E-Underclay, F-Clay-coal seam alternations.

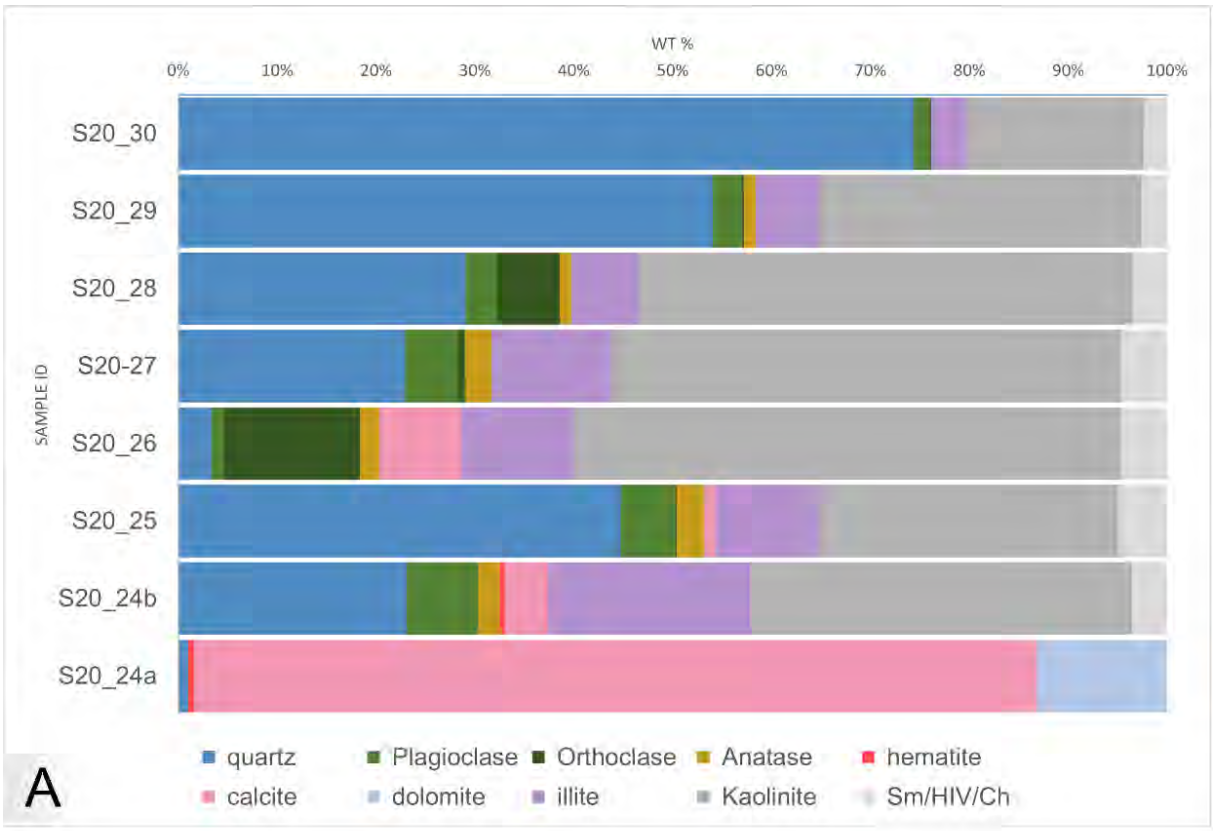
WT %
0%
10%
20%
30%
40%
50%
60%
70%
80%
90%
100%
SAMPLE ID
S20_30
S20_29
S20_28
S20-27
S20_26
S20_25
S20_24b
S20_24a
quartz
Plagioclase
Orthoclase
Anatase
hematite
calcite
dolomite
illite
Kaolinite
Sm/HIV/Ch
A

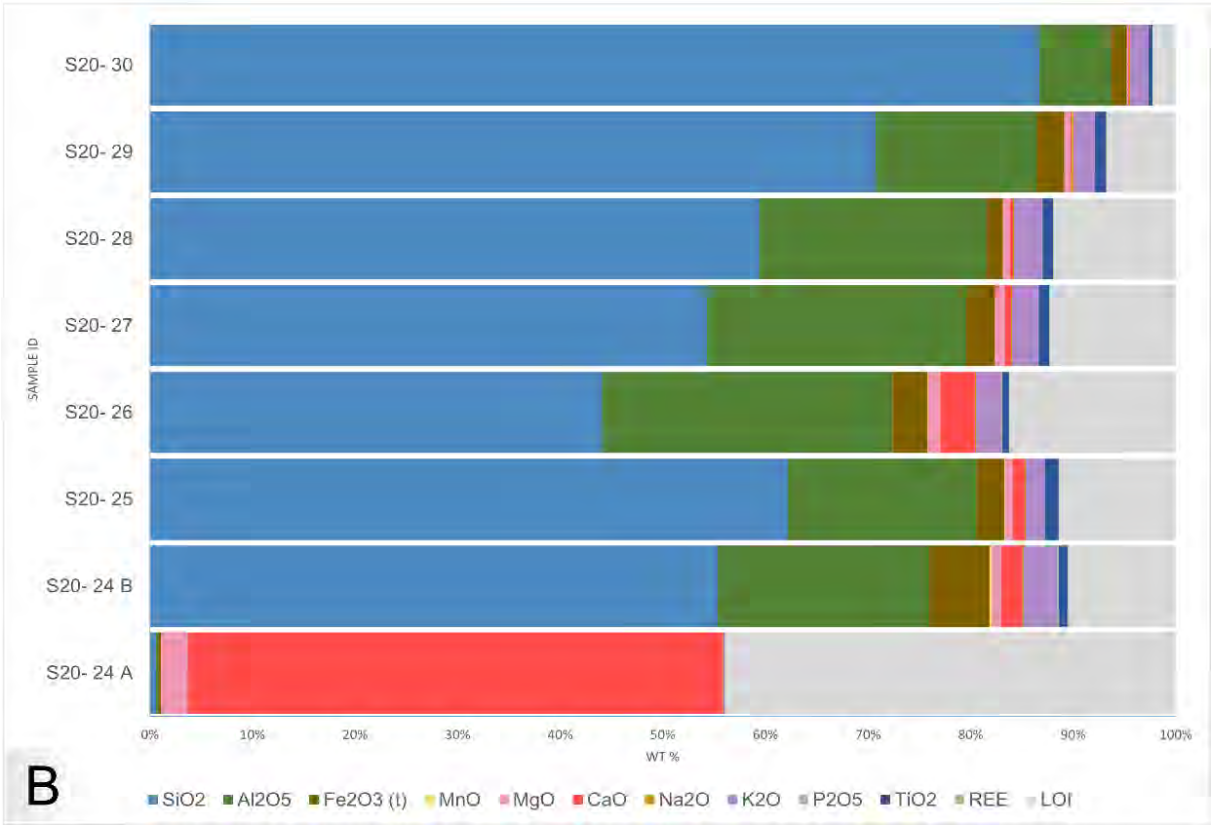
SAMPLE ID
S20- 30
S20- 29
S20- 28
S20- 27
S20- 26
S20- 25
S20- 24 B
S20- 24 A
0%
10%
20%
30%
40%
50%
60%
70%
80%
90%
100%
WT %
SiO2
Al2O5
Fe2O3 (t)
MnO
MgO
CaO
Na2O
K2O
P2O5
TiO2
REE
LOI
B

Figure 19. A- Semi-quantitative XRD whole-rock mineralogy from limestone hosted clay quarry, B-Geochemistry of layers from same section

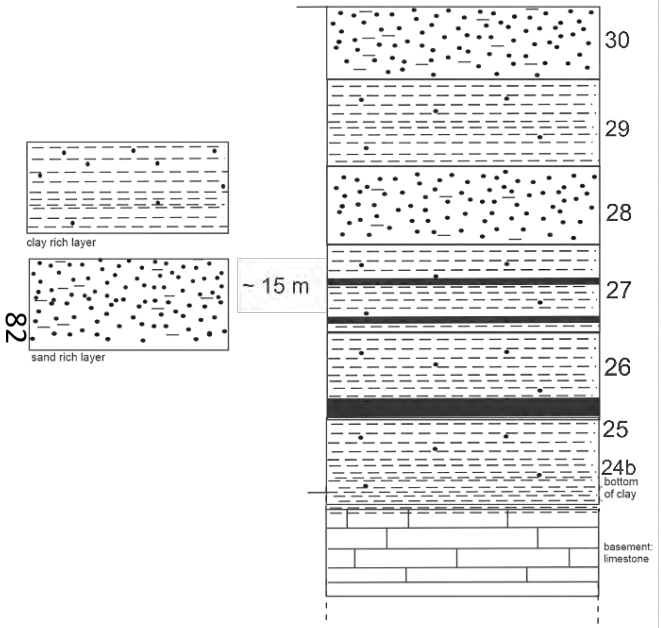
clay rich layer
sand rich layer
~ 15 m
30
29
28
27
26
25
24b
bottom of clay
basement: limestone

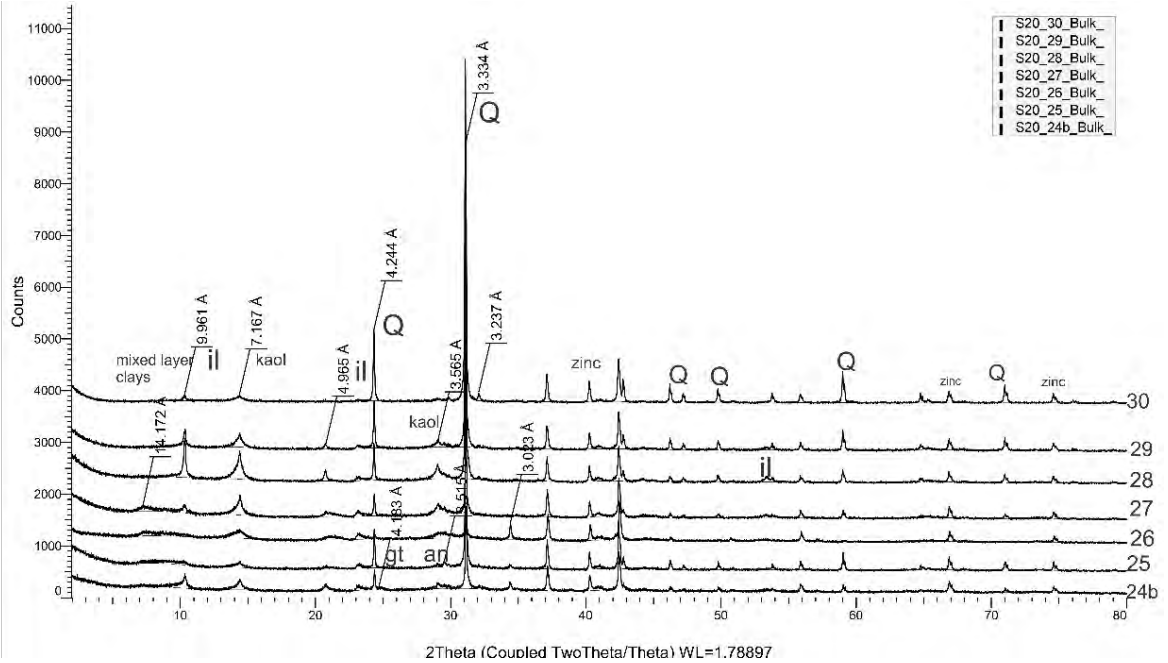
S20_30_Bulk_
S20_29_Bulk_
S20_28_Bulk_
S20_27_Bulk_
S20_26_Bulk_
S20_25_Bulk_
S20_24b_Bulk_
Counts
mixed layer clays
il
kaol
Q
zinc
gt
an
2Theta (Coupled TwoTheta/Theta) WL=1.78897

Figure 20. XRD whole-rock random powder patterns from the section limestone hosted clay deposit.

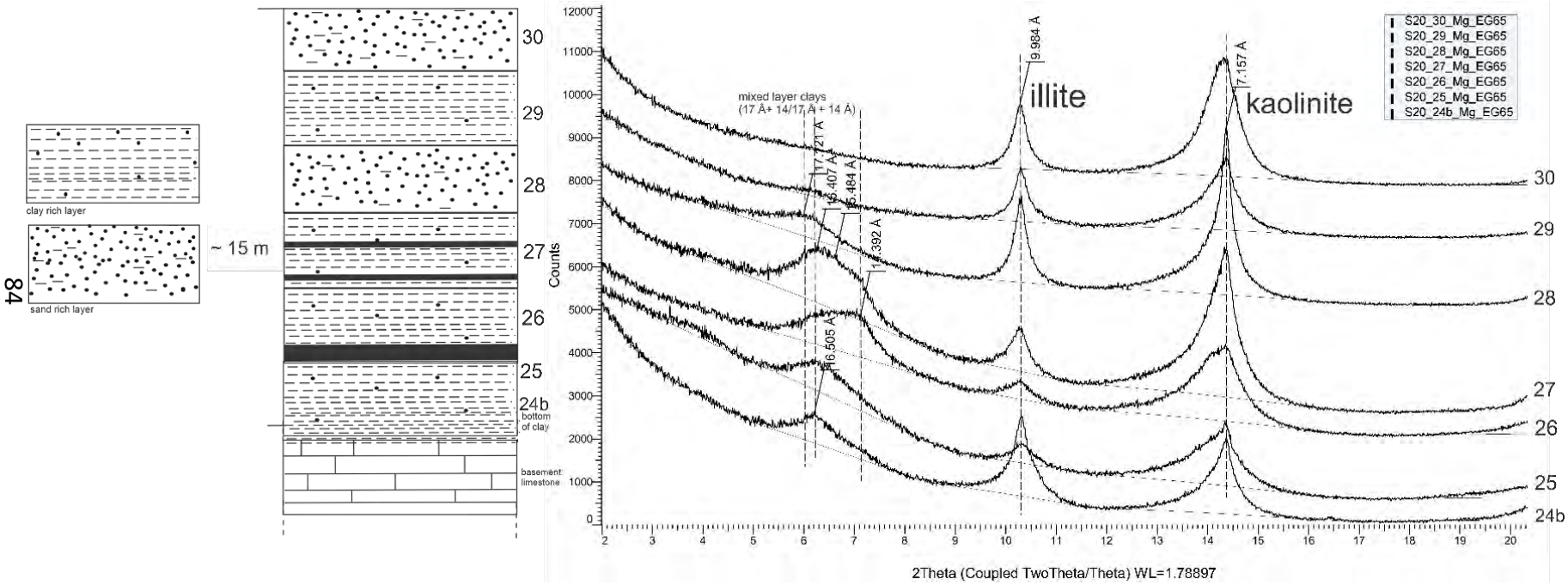
clay rich layer
sand rich layer
~ 15 m
30
29
28
27
26
25
24b
bottom of clay
basement limestone
Counts
mixed layer clays
(17 Å+ 14/17 Å + 14 Å)
17.121 Å
15.407 Å
15.484 Å
14.392 Å
16.505 Å
9.984 Å
illite
7.157 Å
kaolinite
S20_30_Mg_EG65
S20_29_Mg_EG65
S20_28_Mg_EG65
S20_27_Mg_EG65
S20_26_Mg_EG65
S20_25_Mg_EG65
S20_24b_Mg_EG65
2Theta (Coupled TwoTheta/Theta) WL=1.78897

Figure 21. XRD oriented Mg-saturated EG solvated clay fraction patterns of the Limestone hosted section.

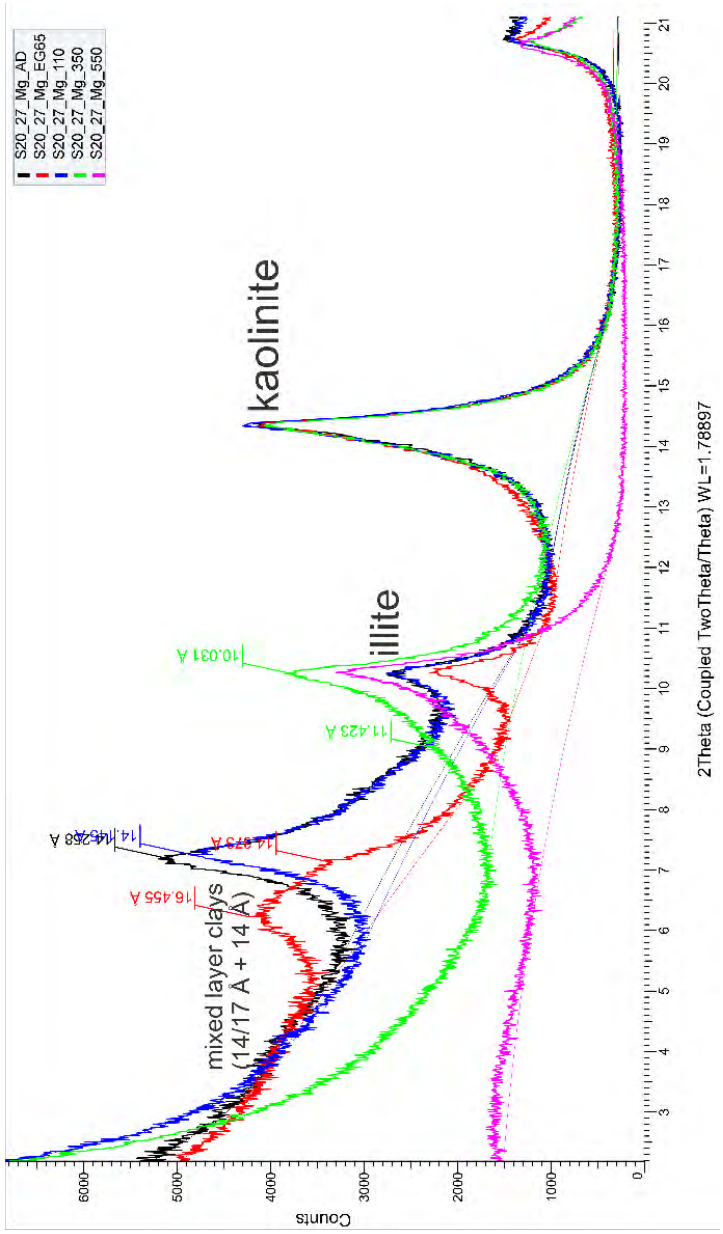
S20_27_Mg_AD
S20_27_Mg_EG65
S20_27_Mg_110
S20_27_Mg_350
S20_27_Mg_550
kaolinite
illite
mixed layer clays
(14/17 Å + 14 Å)
16.455 Å
14.258 Å
14.975 Å
11.423 Å
10.031 Å
Counts
2Theta (Coupled TwoTheta/Theta) WL=1.78897

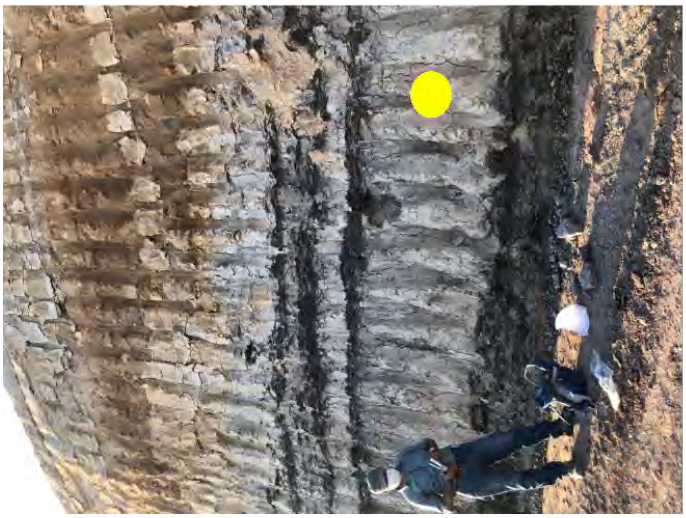

Figure 22. Clay fraction XRD data from the clay layer between the coal seams. Yellow circle marks sample location in outcrop.

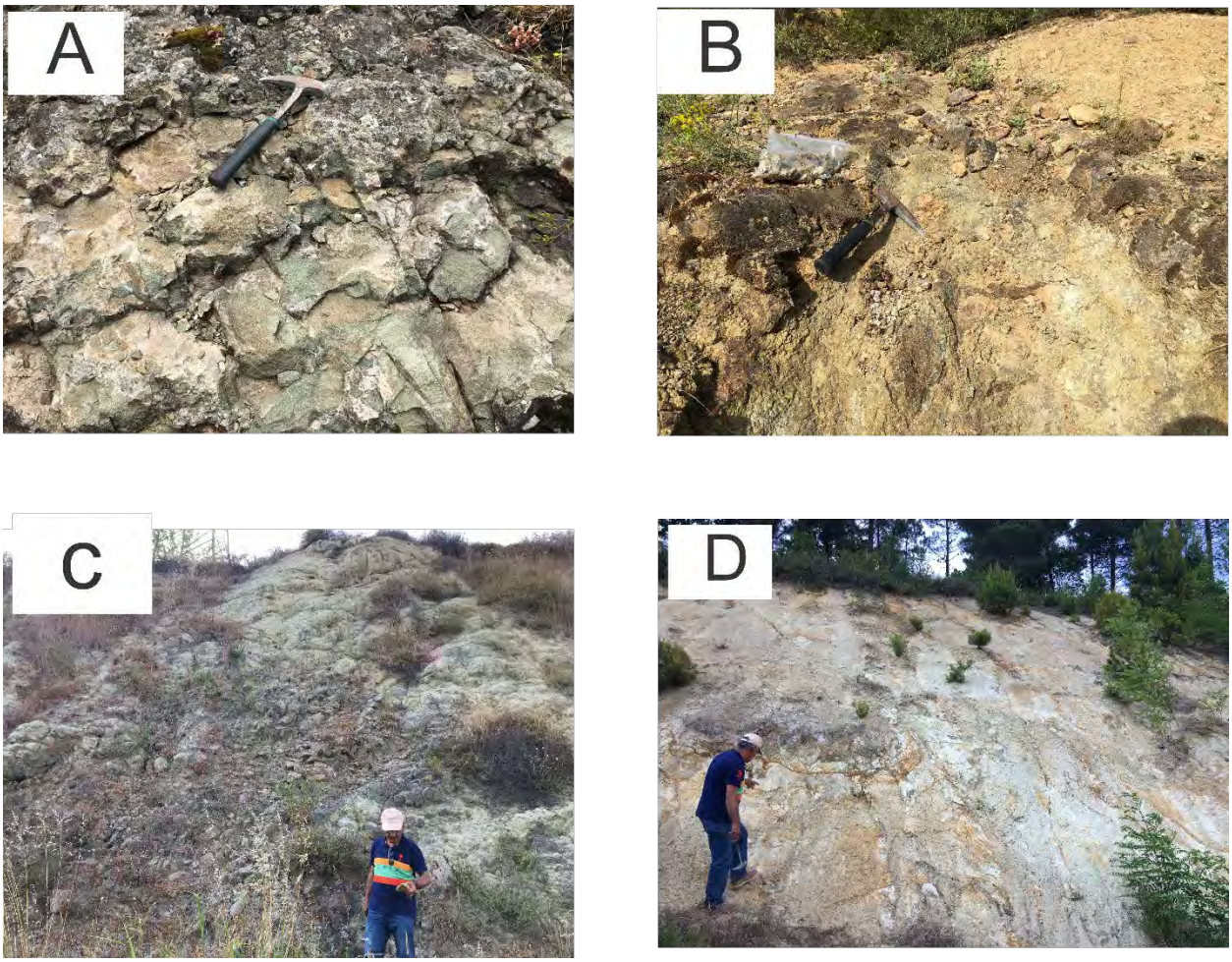

Figure 23. General views regional late Cretaceous volcanic rocks.

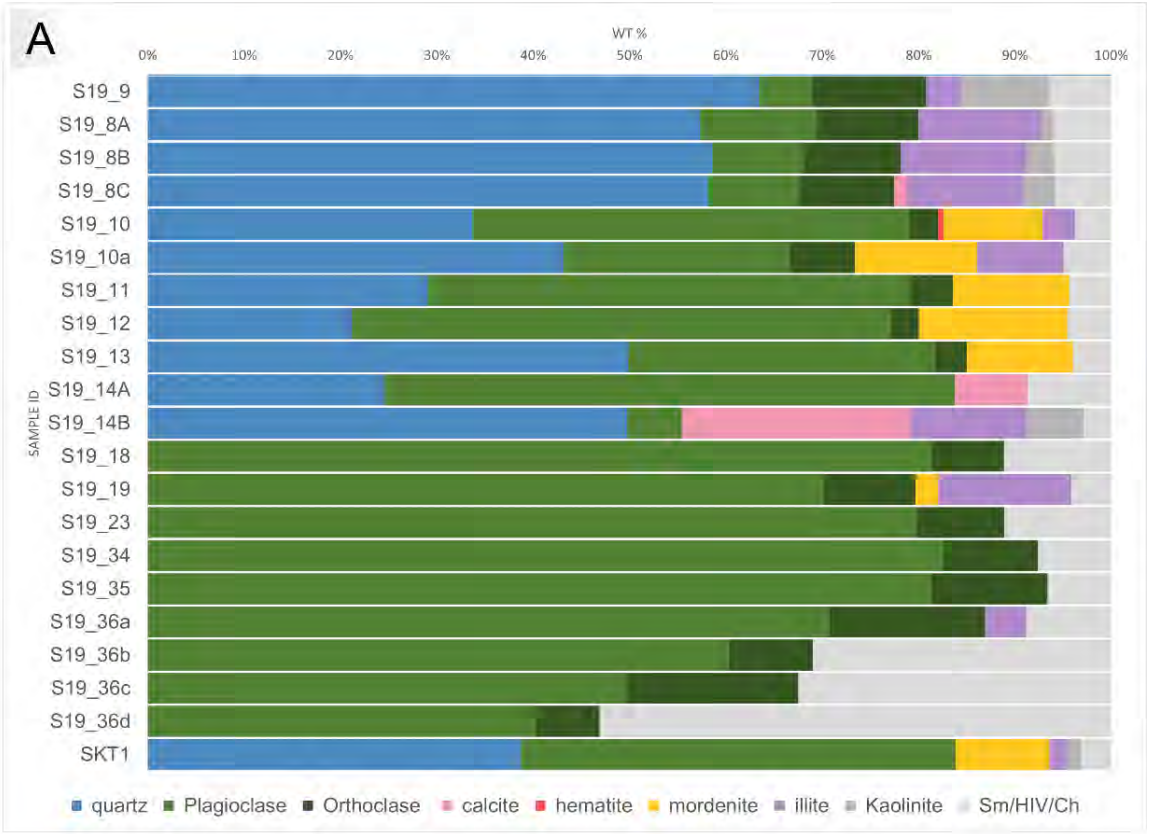
A
WT %
0%
10%
20%
30%
40%
50%
60%
70%
80%
90%
100%
SAMPLE ID
S19_9
S19_8A
S19_8B
S19_8C
S19_10
S19_10a
S19_11
S19_12
S19_13
S19_14A
S19_14B
S19_18
S19_19
S19_23
S19_34
S19_35
S19_36a
S19_36b
S19_36c
S19_36d
SKT1
quartz
Plagioclase
Orthoclase
calcite
hematite
mordenite
illite
Kaolinite
Sm/HIV/Ch

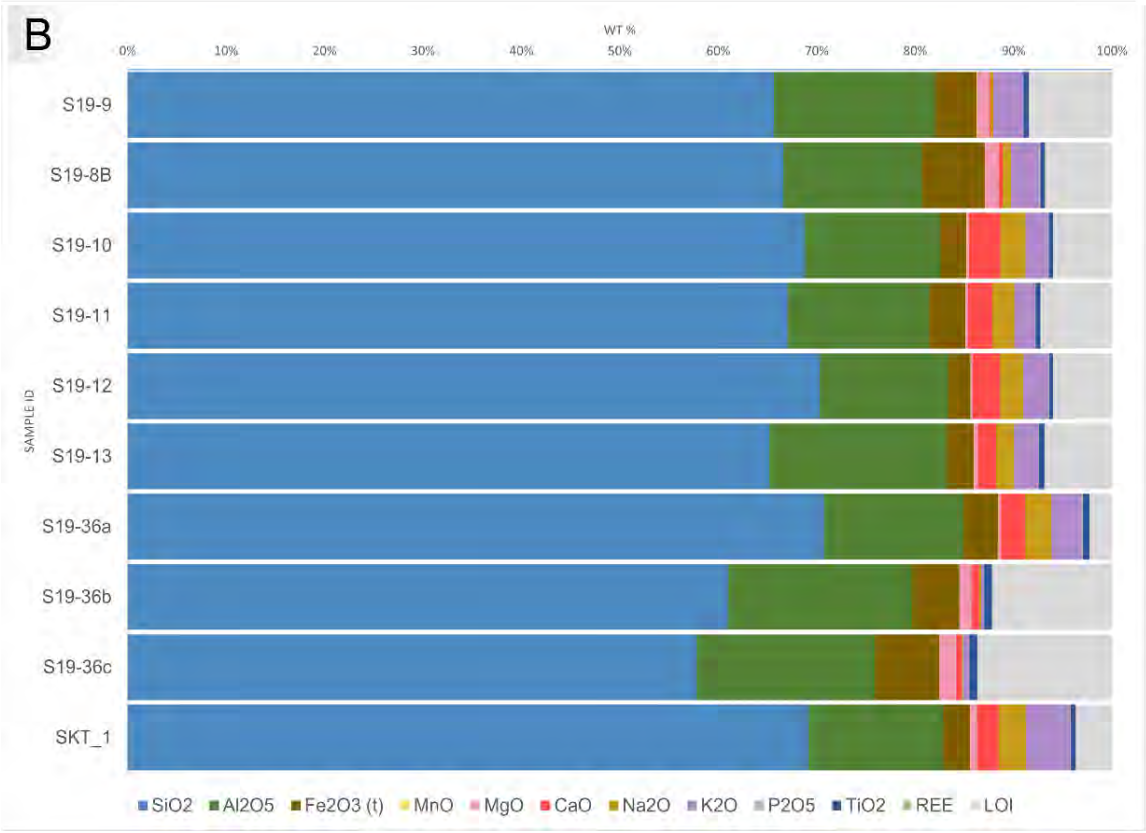
B
WT %
0%
10%
20%
30%
40%
50%
60%
70%
80%
90%
100%
SAMPLE ID
S19-9
S19-8B
S19-10
S19-11
S19-12
S19-13
S19-36a
S19-36b
S19-36c
SKT_1
SiO2
Al2O5
Fe2O3 (t)
MnO
MgO
CaO
Na2O
K2O
P2O5
TiO2
REE
LOI

Figure 24. Semi-quantitative whole-rock mineralogy from volcanics, B-Geochemistry of same rocks

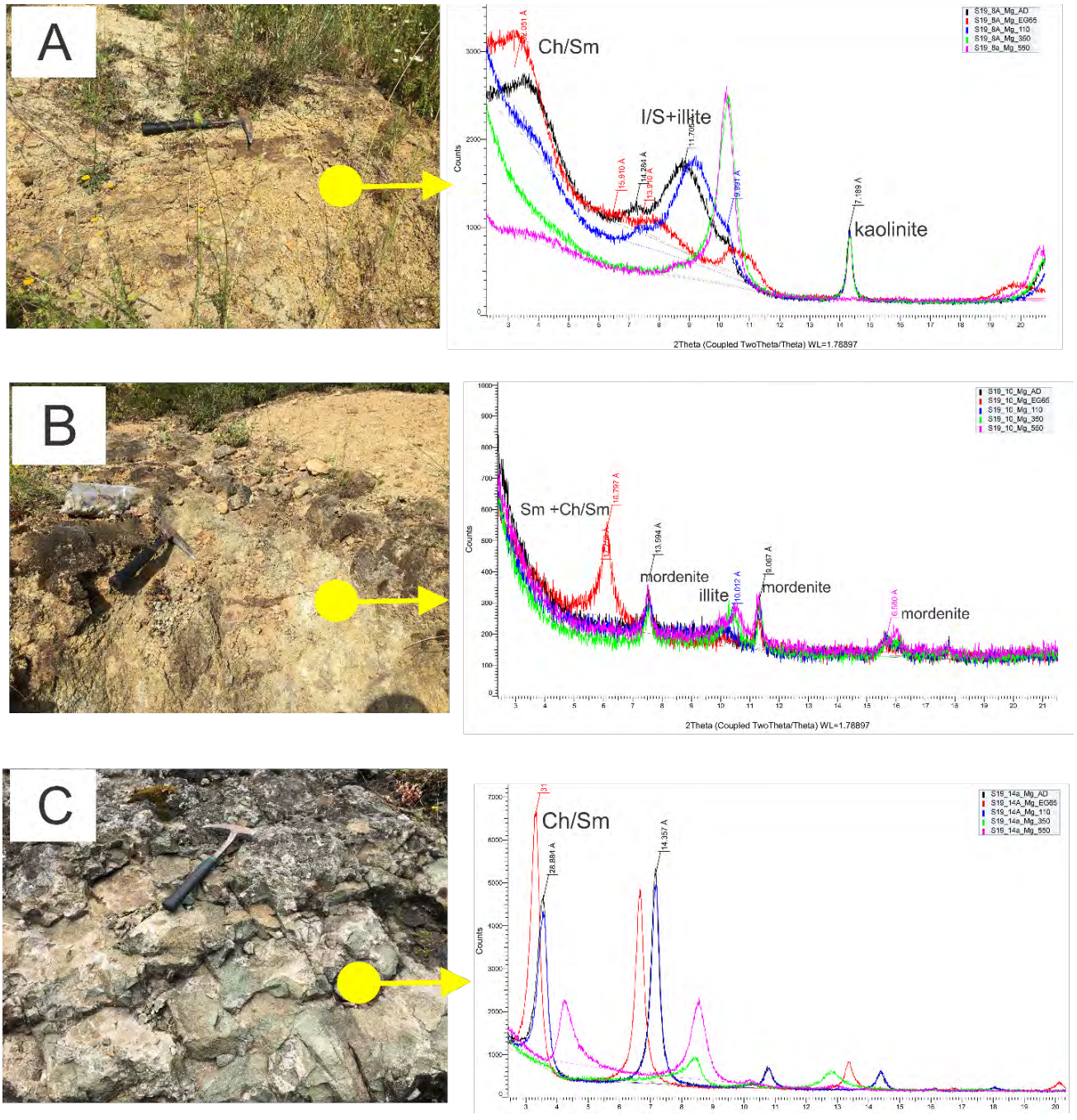

Figure 25. XRD clay fraction patterns from different phases of volcanic/volcano-sedimentary rocks (for higher resolution, see page 323, 325 and 329)


35
34

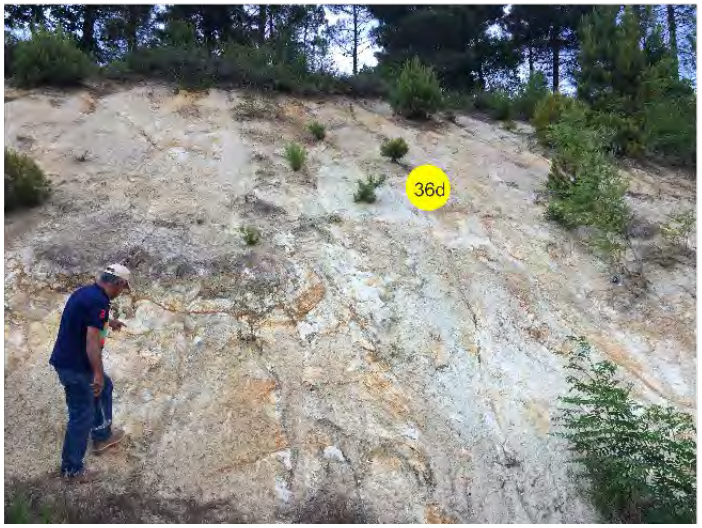
36d

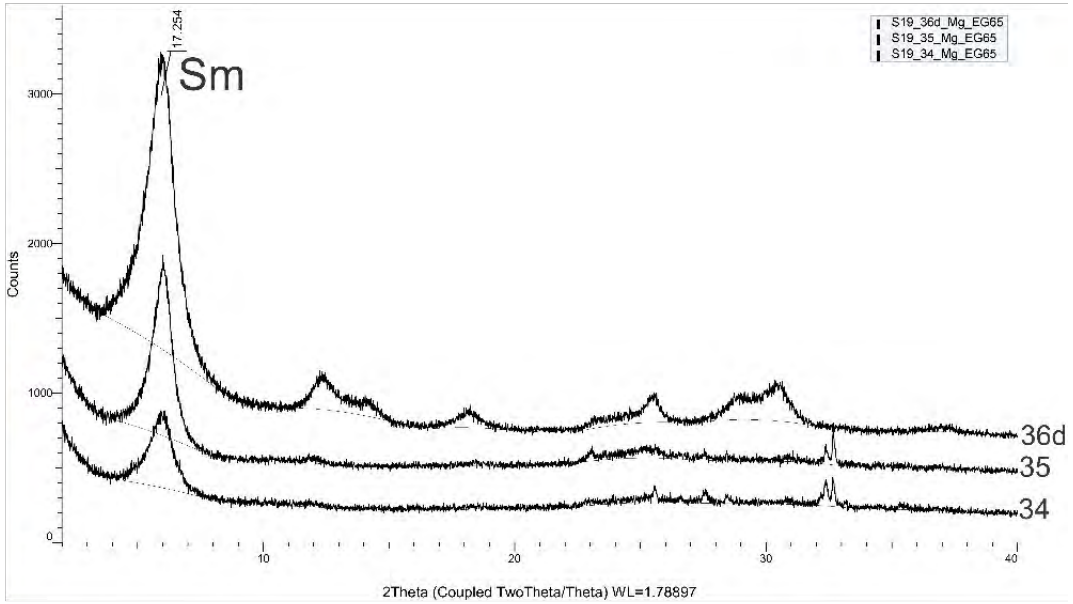
S19_36d_Mg_EG65
S19_35_Mg_EG65
S19_34_Mg_EG65
17.254
Sm
Counts
3000
2000
1000
0
10
20
30
40
36d
35
34
2Theta (Coupled TwoTheta/Theta) WL=1.78897

Figure 26. XRD clay fraction patterns from different phases of volcanics. Yellow circles mark sample location in outcrop.

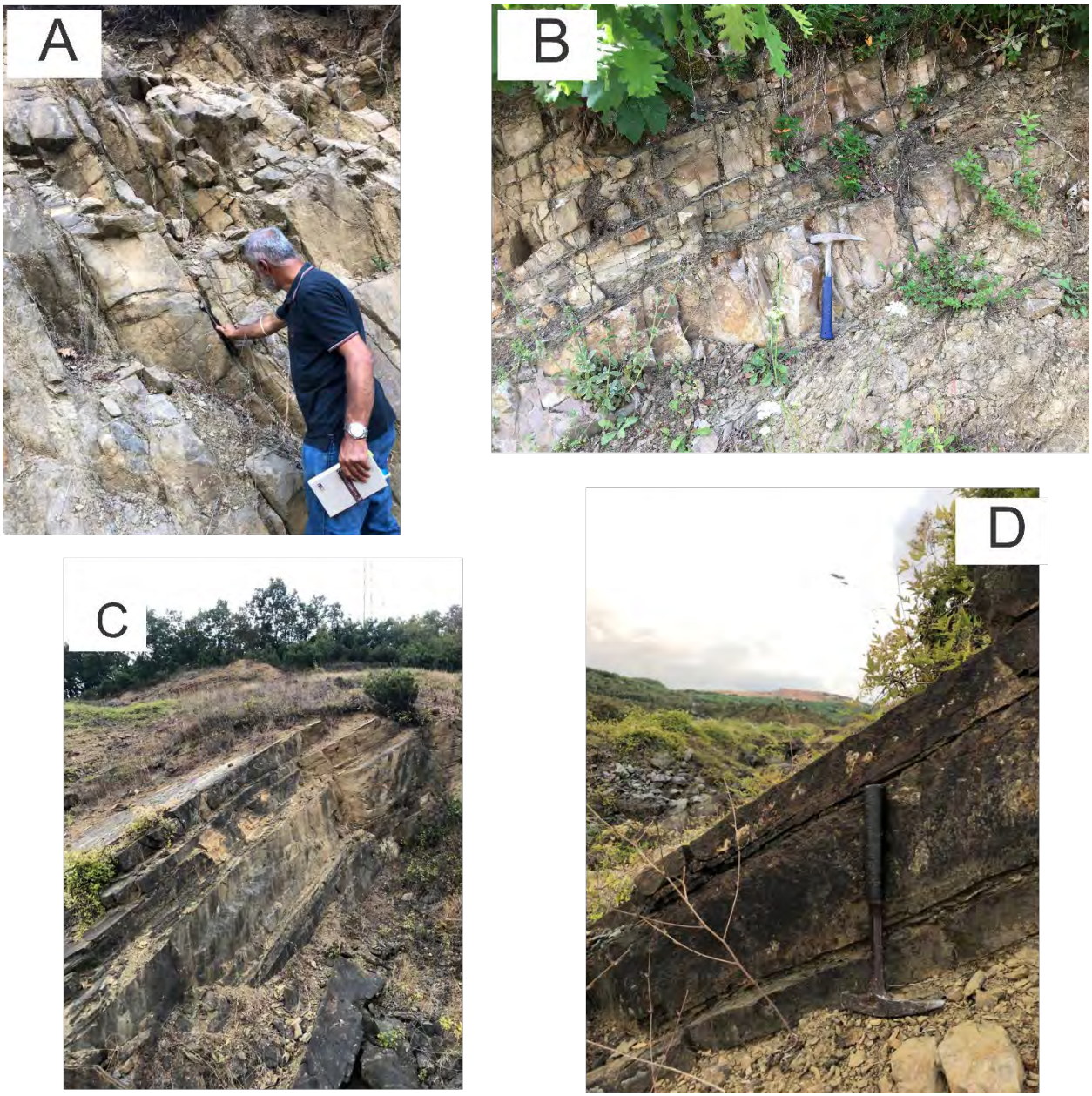

Figure 27. General view of the flysch series outcrops.

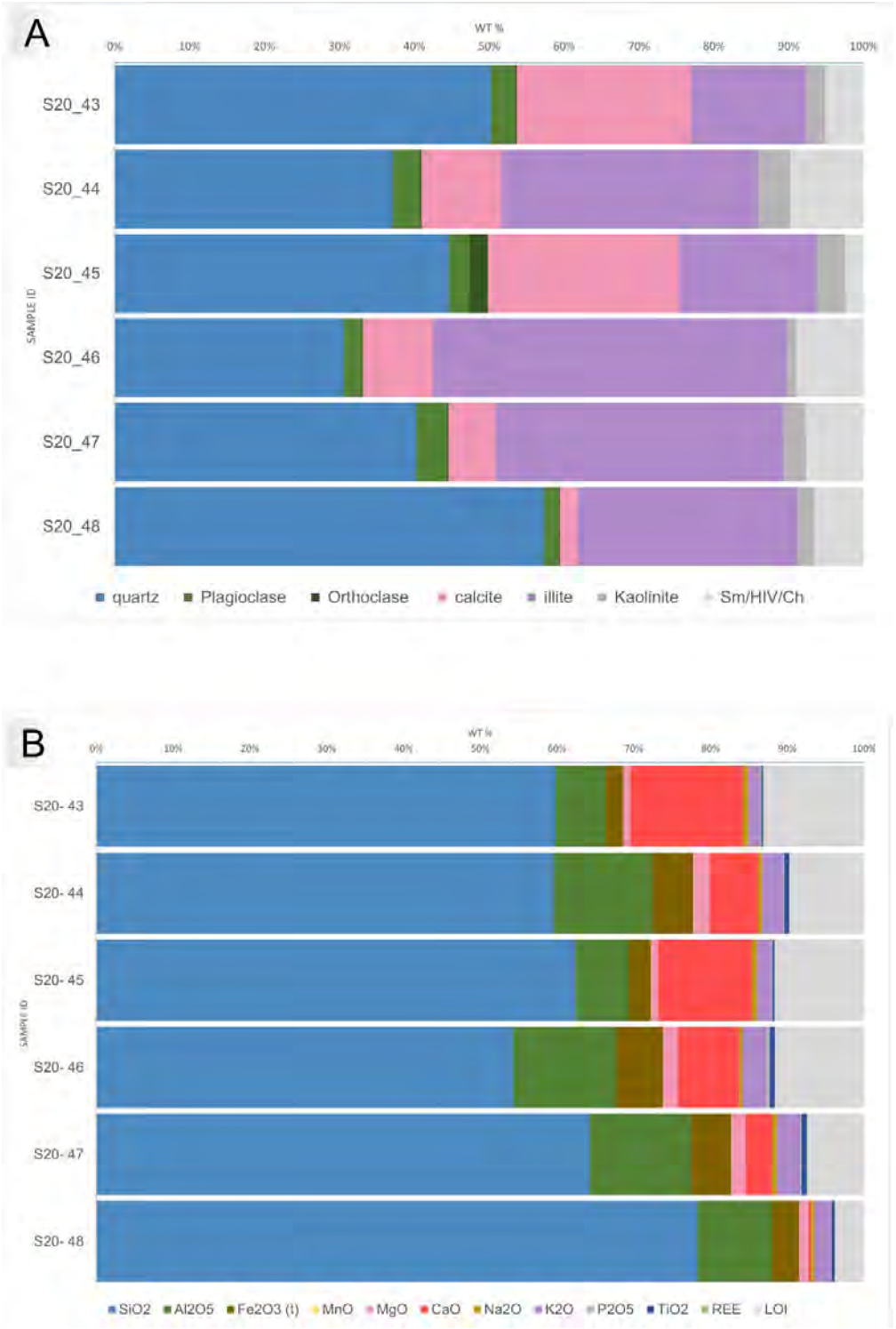

Figure 28. A-Semi-quantitative whole-rock mineralogy from flysch series, B-Geochemistry of same rocks

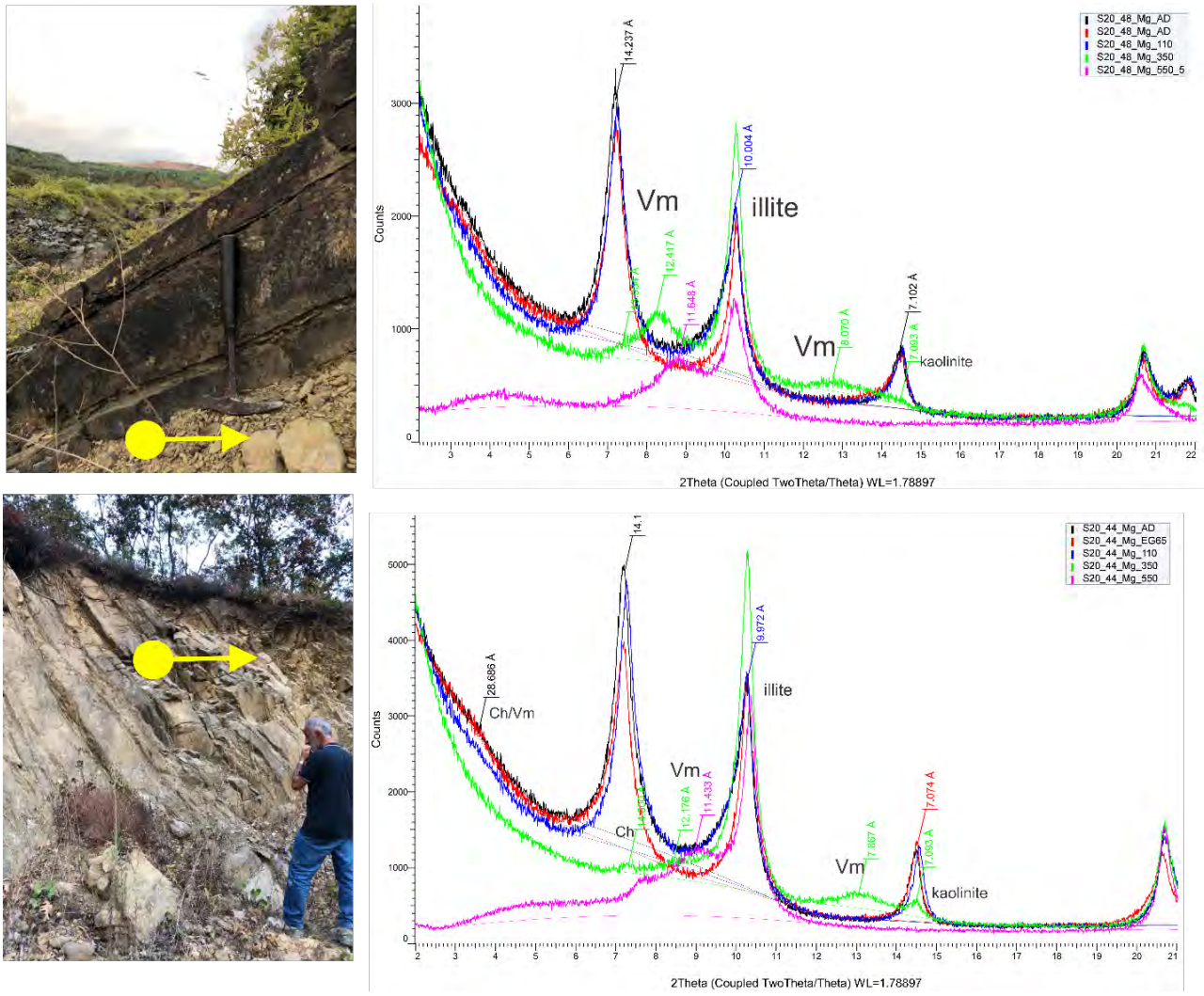

Figure 29. Clay fraction XRD data from flysch series. Yellow circle and arrow marks sample location in outcrop. (For higher resolution, see page 359 and 363)

Figure 30. Paleozoic sandstone from A-Drill core and B-Surface outcrop

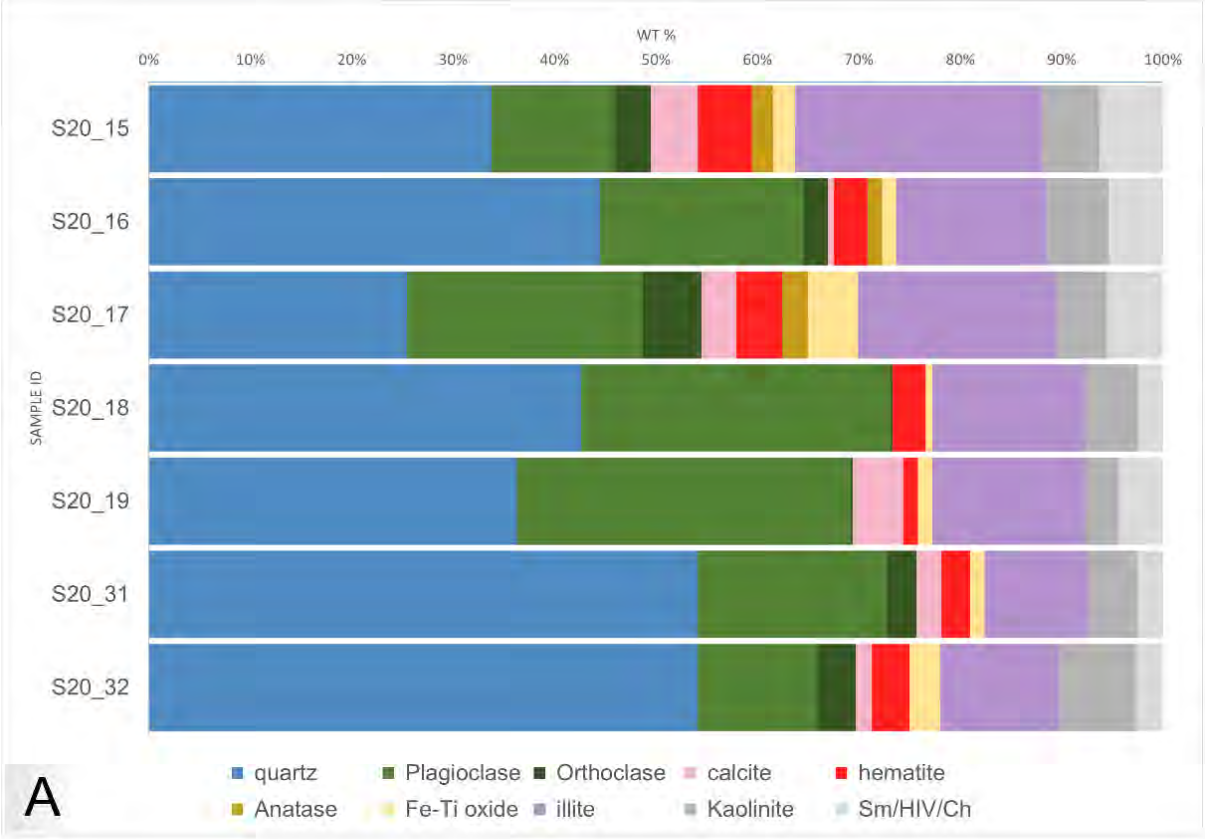
WT %
0%
10%
20%
30%
40%
50%
60%
70%
80%
90%
100%
SAMPLE ID
S20_15
S20_16
S20_17
S20_18
S20_19
S20_31
S20_32
quartz
Plagioclase
Orthoclase
calcite
hematite
Anatase
Fe-Ti oxide
illite
Kaolinite
Sm/HIV/Ch
A

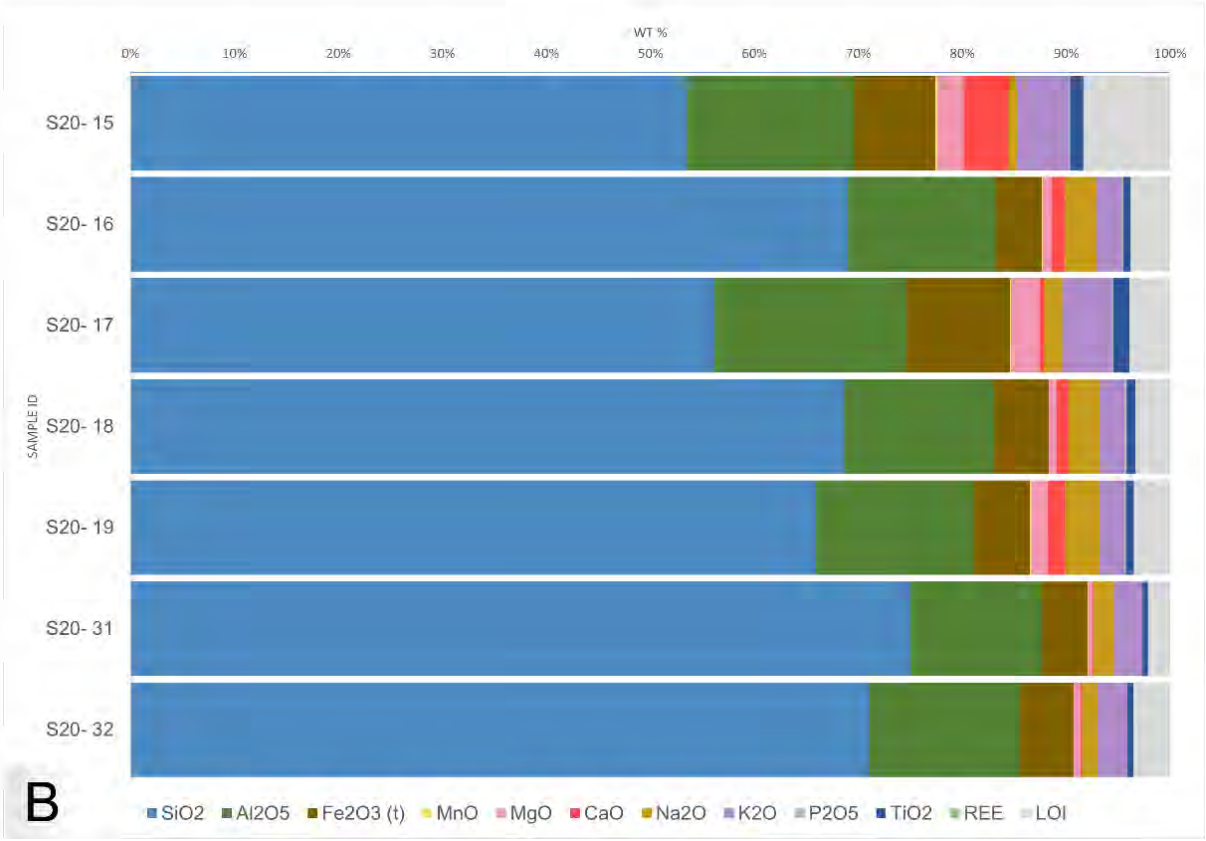
WT %
0%
10%
20%
30%
40%
50%
60%
70%
80%
90%
100%
SAMPLE ID
S20- 15
S20- 16
S20- 17
S20- 18
S20- 19
S20- 31
S20- 32
SiO2
Al2O5
Fe2O3 (t)
MnO
MgO
CaO
Na2O
K2O
P2O5
TiO2
REE
LOI
B

Figure 31. Semi-quantitative whole-rock mineralogy from Paleozoic sandstone, B-Geochemistry of same rocks

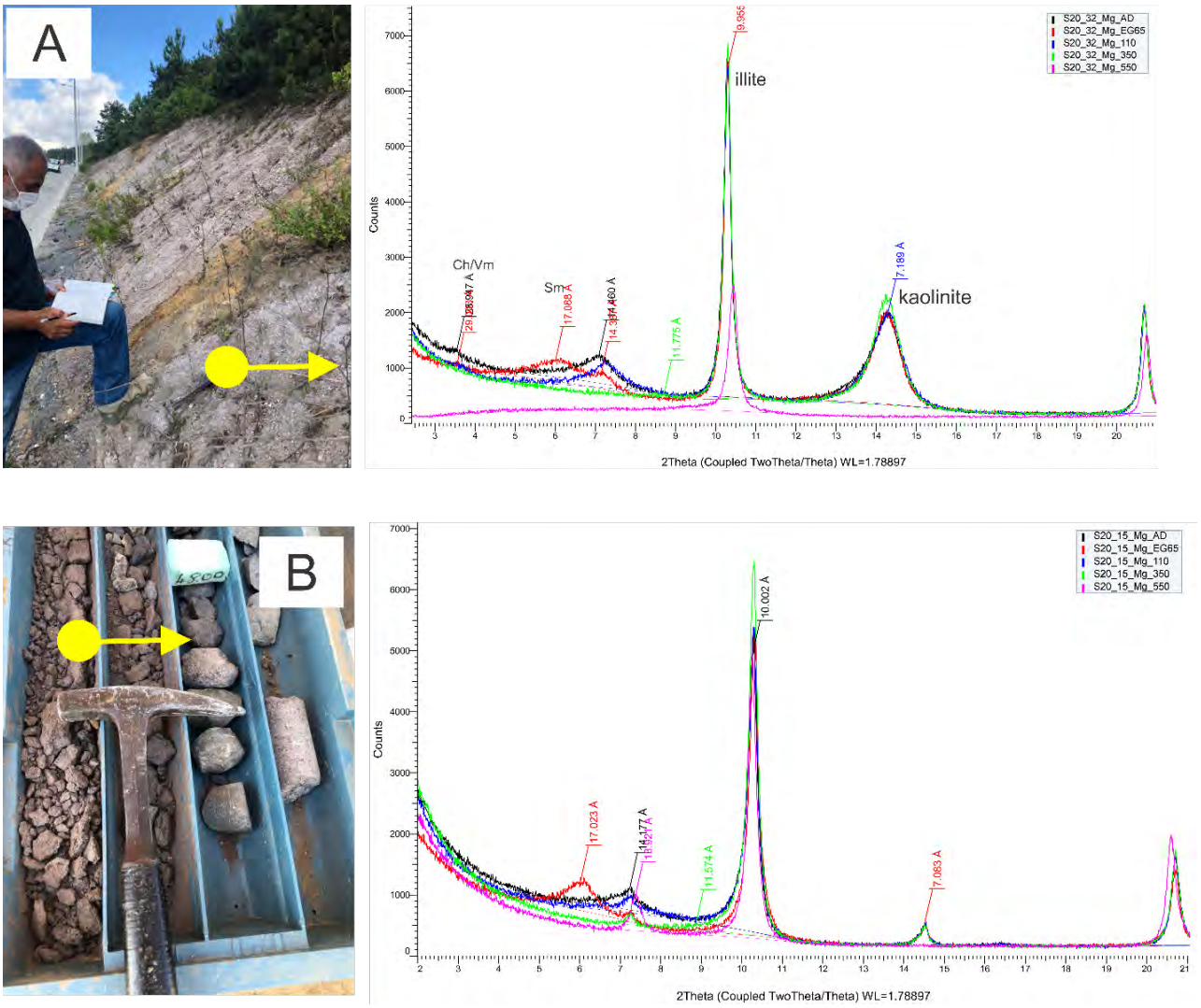

Figure 32. XRD clay fraction data from A-surface outcrop B-Drill core. Yellow circle and arrow marks sample location in outcrop and core (For higher resolution XRD patterns, see pages 343, 352)

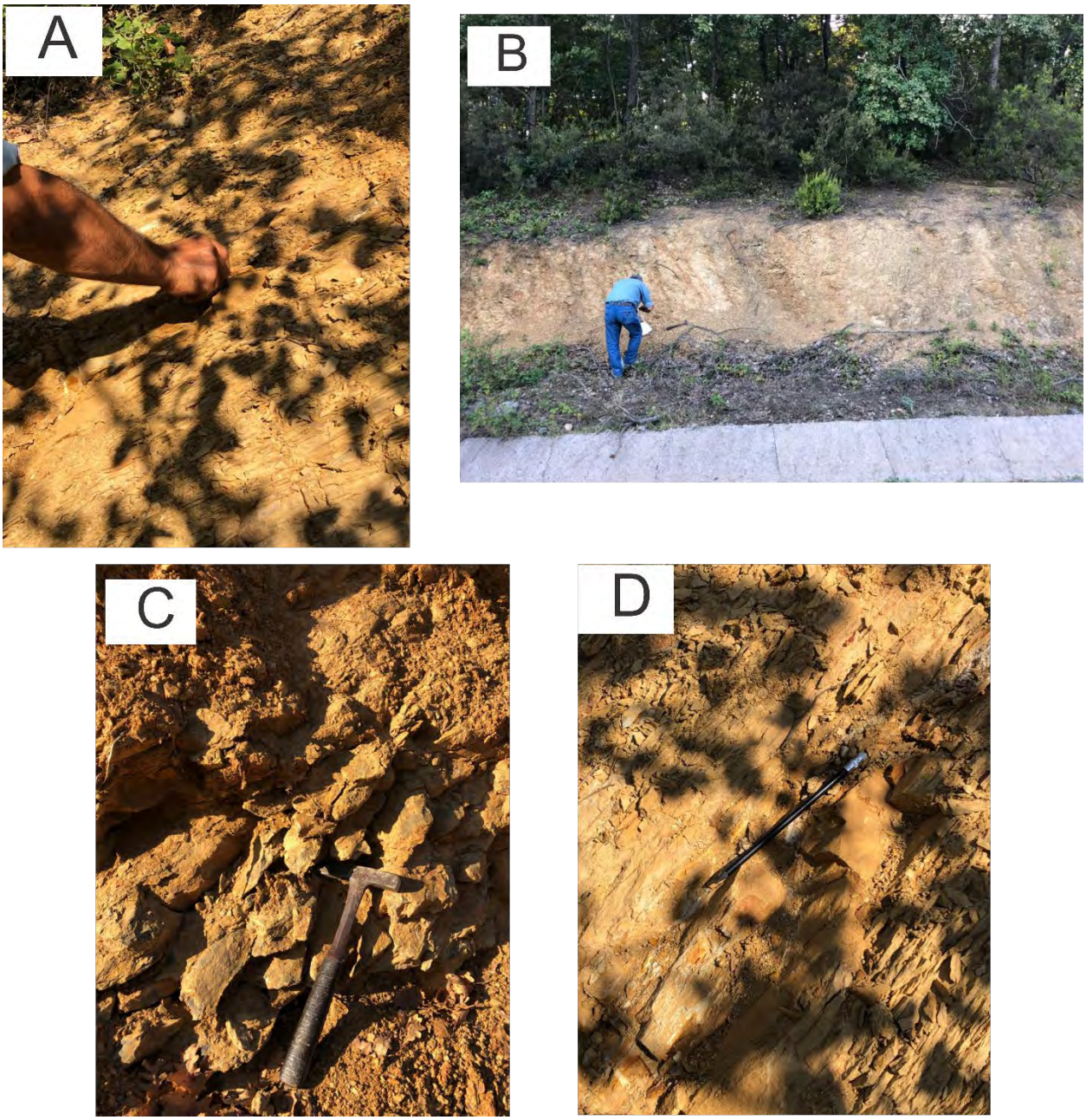

Figure 33. General view of Paleozoic shale (Devonian?) outcrops. A- relatively fresh and B-weathered portions. C-D shale-clayey limestone alternations.

/

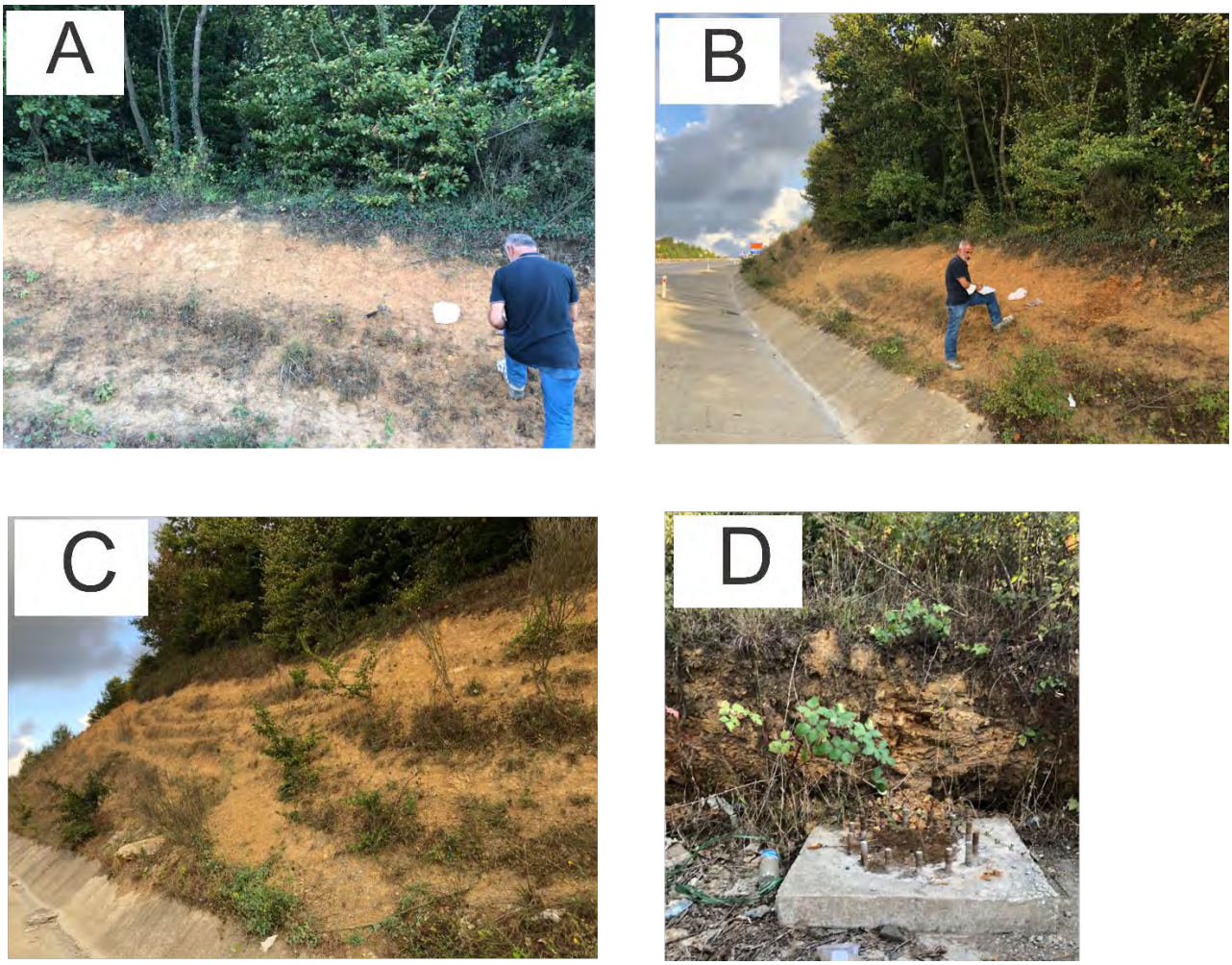

Figure 34. Paleozoic shale rocks (Carboniferous?) A-B relatively weathered and C-D fresh portions

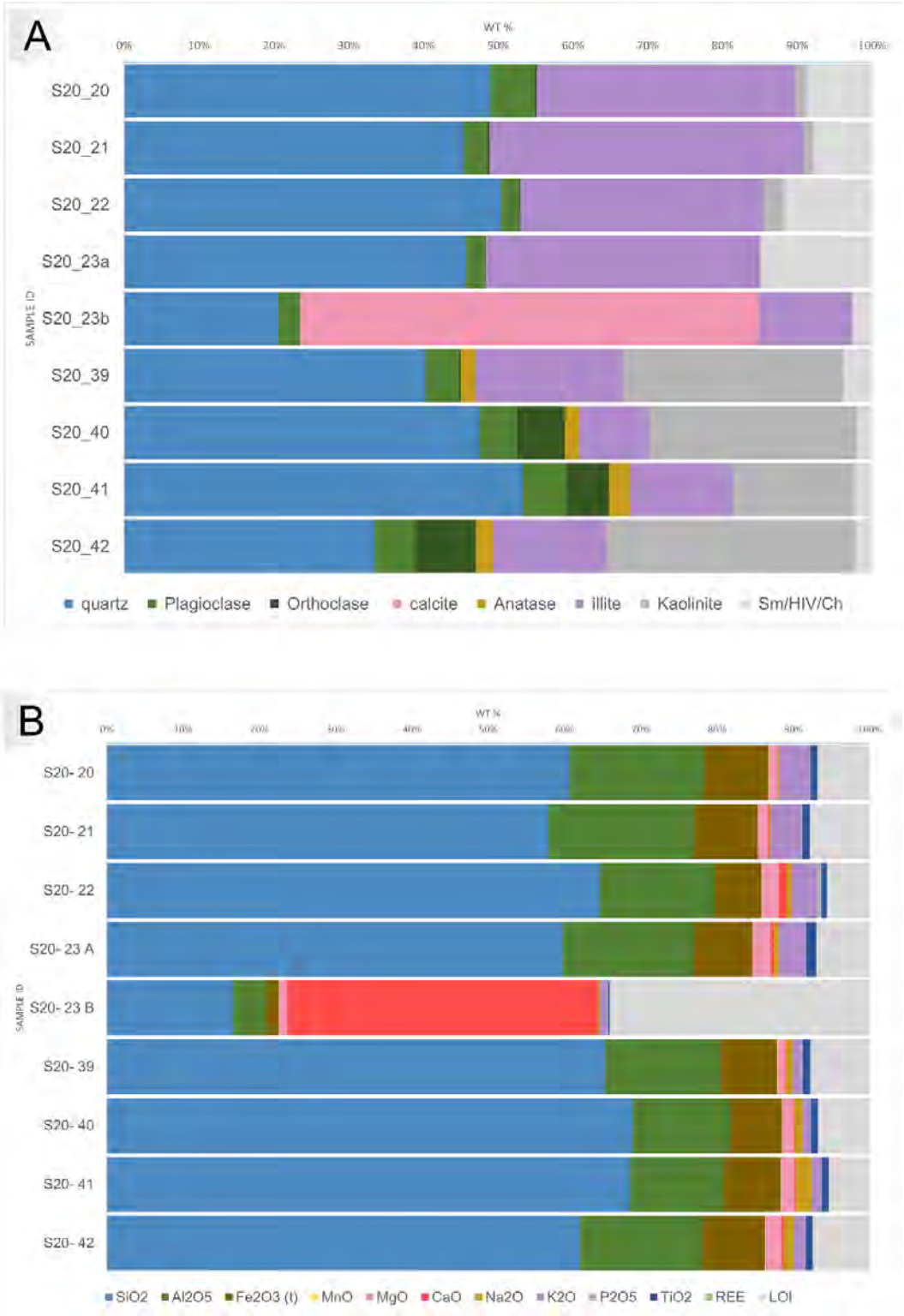

Figure 35. Semi-quantitative whole-rock mineralogy from Paleozoic shales, B-Geochemistry of same rocks

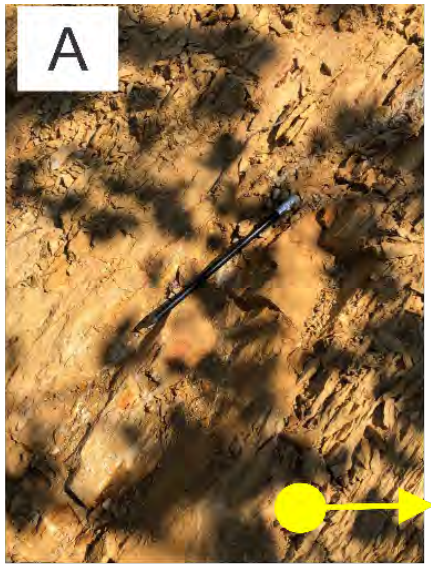
A

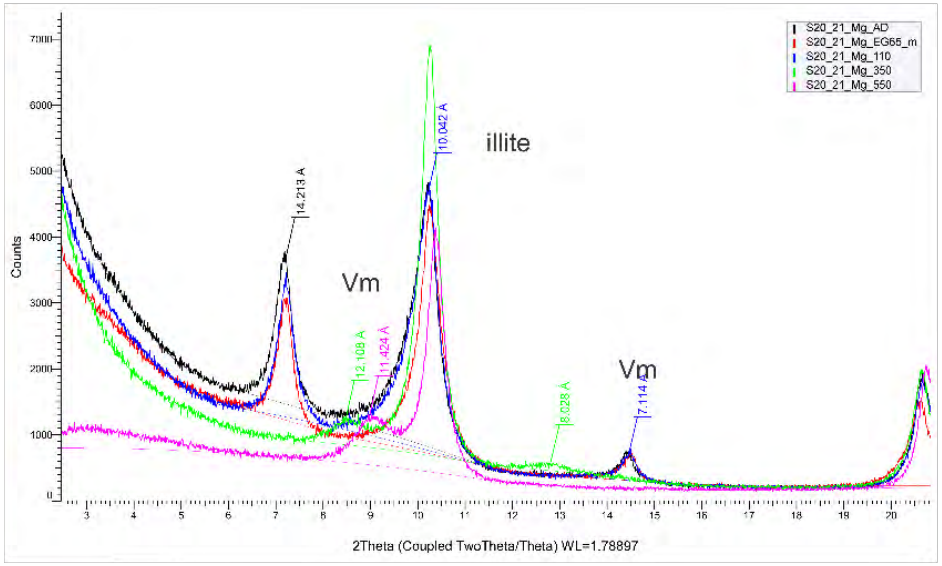
S20_21_Mg_AD
S20_21_Mg_EG65_m
S20_21_Mg_110
S20_21_Mg_350
S20_21_Mg_550
illite
Vm
Vm
14.213 Å
12.108 Å
11.424 Å
10.042 Å
8.028 Å
7.114 Å
Counts
2Theta (Coupled TwoTheta/Theta) WL=1.78897


B

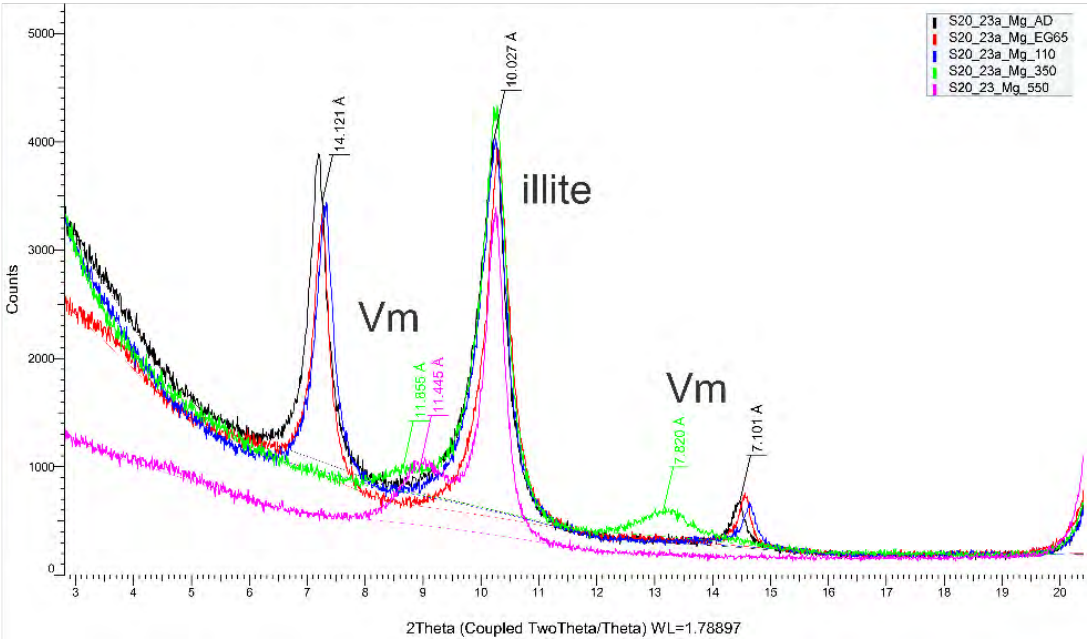
S20_23a_Mg_AD
S20_23a_Mg_EG65
S20_23a_Mg_110
S20_23a_Mg_350
S20_23_Mg_550
illite
Vm
Vm
14.121 Å
11.855 Å
11.445 Å
10.027 Å
7.820 Å
7.101 Å
Counts
2Theta (Coupled TwoTheta/Theta) WL=1.78897

Figure 36. XRD clay fraction data from Devonian shale A-shale layers alternated with limestone B-Relatively weathered zone. Yellow circle and arrow marks sample location in outcrop.

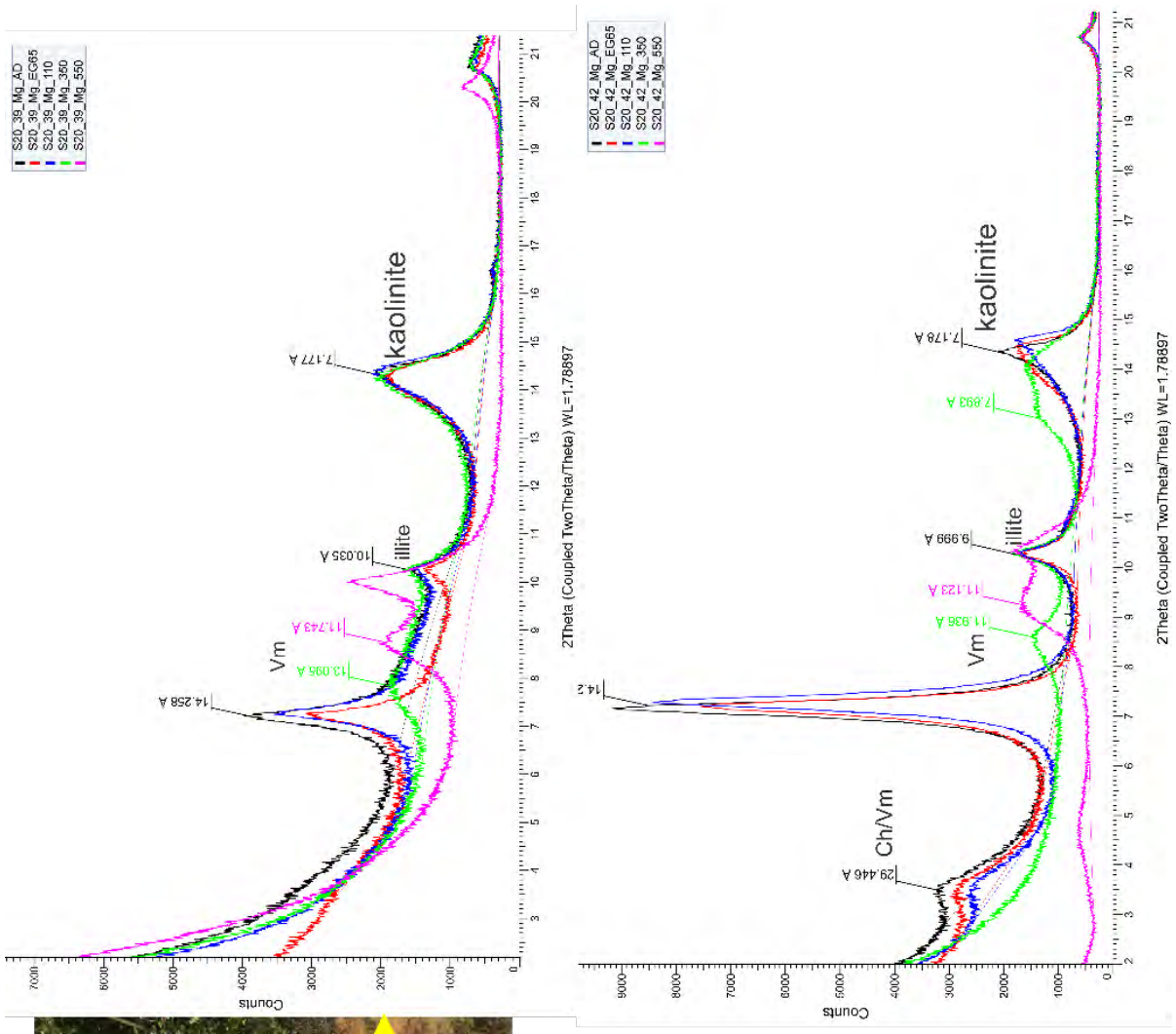
S20_39_Mg_AD
S20_39_Mg_EG65
S20_39_Mg_110
S20_39_Mg_350
S20_39_Mg_550
14.258 Å
13.096 Å
11.743 Å
10.035 Å
7.177 Å
Vm
illite
kaolinite
Counts
2Theta (Coupled TwoTheta/Theta) WL=1.78897
S20_42_Mg_AD
S20_42_Mg_EG65
S20_42_Mg_110
S20_42_Mg_350
S20_42_Mg_550
14.2
29.446 Å
11.836 Å
11.123 Å
9.999 Å
7.893 Å
7.178 Å
Ch/Vm
Vm
illite
kaolinite
Counts
2Theta (Coupled TwoTheta/Theta) WL=1.78897

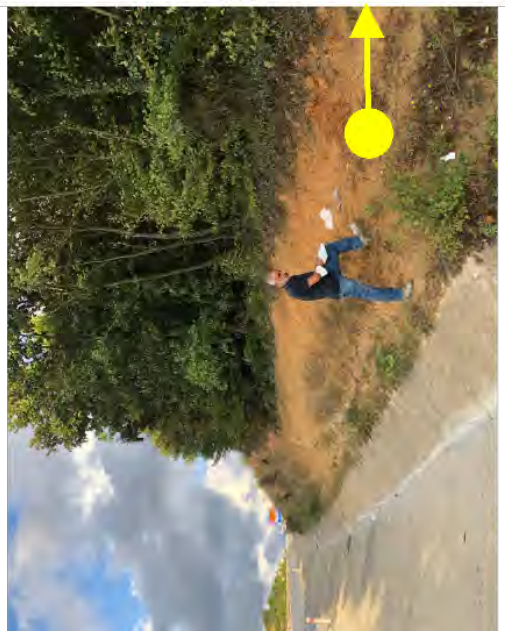

Figure 37. XRD clay fraction data from Carboniferous shale. A-relatively weathered zone B-Relatively fresh zone.

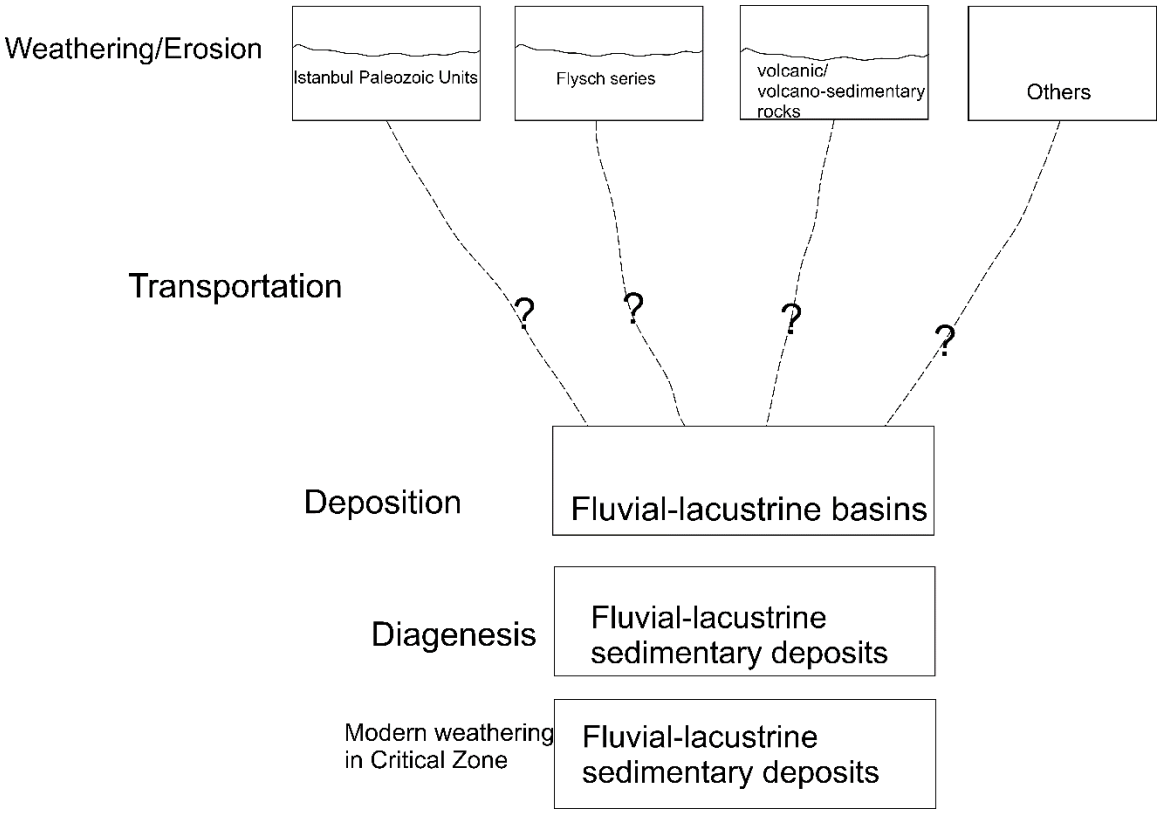

Figure 38. Diagram showing the potential source rocks to the basins. “Others?” stands for the rocks that either behave as outlier in the process of the data (limestone) or couple small outcrops (limestones, clastics) in the study area.

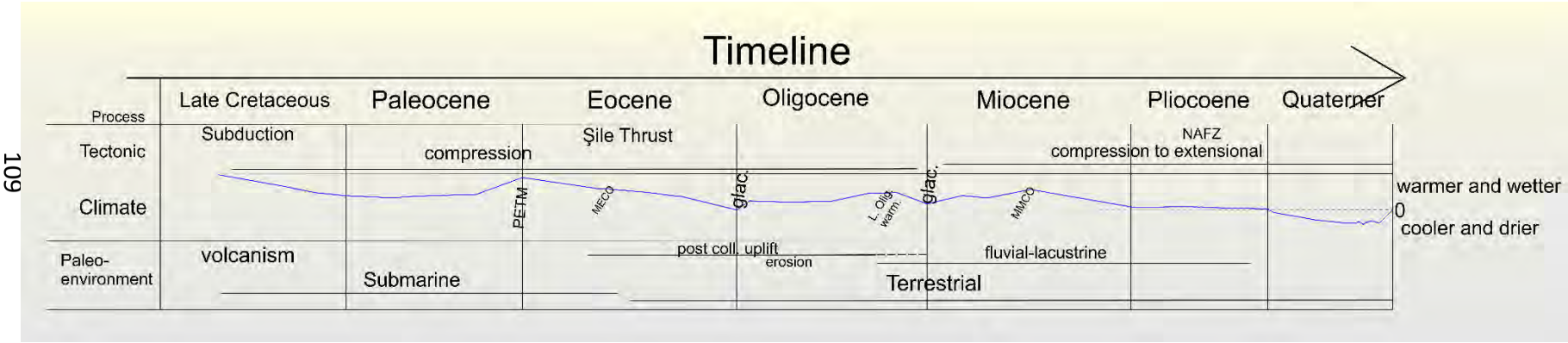
Timeline
Late Cretaceous
Paleocene
Eocene
Oligocene
Miocene
Pliocene
Quaternar
Process
Tectonic
Subduction
compression
Şile Thrust
NAFZ
compression to extensional
Climate
PETM
MECO
glac.
L. Olig. warm.
glac.
MMCO
warmer and wetter
0
cooler and drier
Paleo-environment
volcanism
Submarine
post coll. uplift
erosion
fluvial-lacustrine
Terrestrial

Figure 39. Timeline summarizing the morphotectonic and climate history of the region. Eras are not in scale. Time of deposition is showed in red based on the palynological data. Climate fluctuations throughout the time is drawn based on both Zachos et al.,(2001), Berner (2004) and literature related to Anatolia. It does not show precise values or real data but it can be used as proxy. Detail information and literature is in the text (PETM: Paleocene-Eocene Thermal Maximum; MECO; Middle Eocene Climate Optimum; MMCO:Middle Miocene Climate Optimum; glac:glaciation; L. Olig. Warm.: Late Oligocene Warming; NAFZ: North Anatolian Fault Zone)

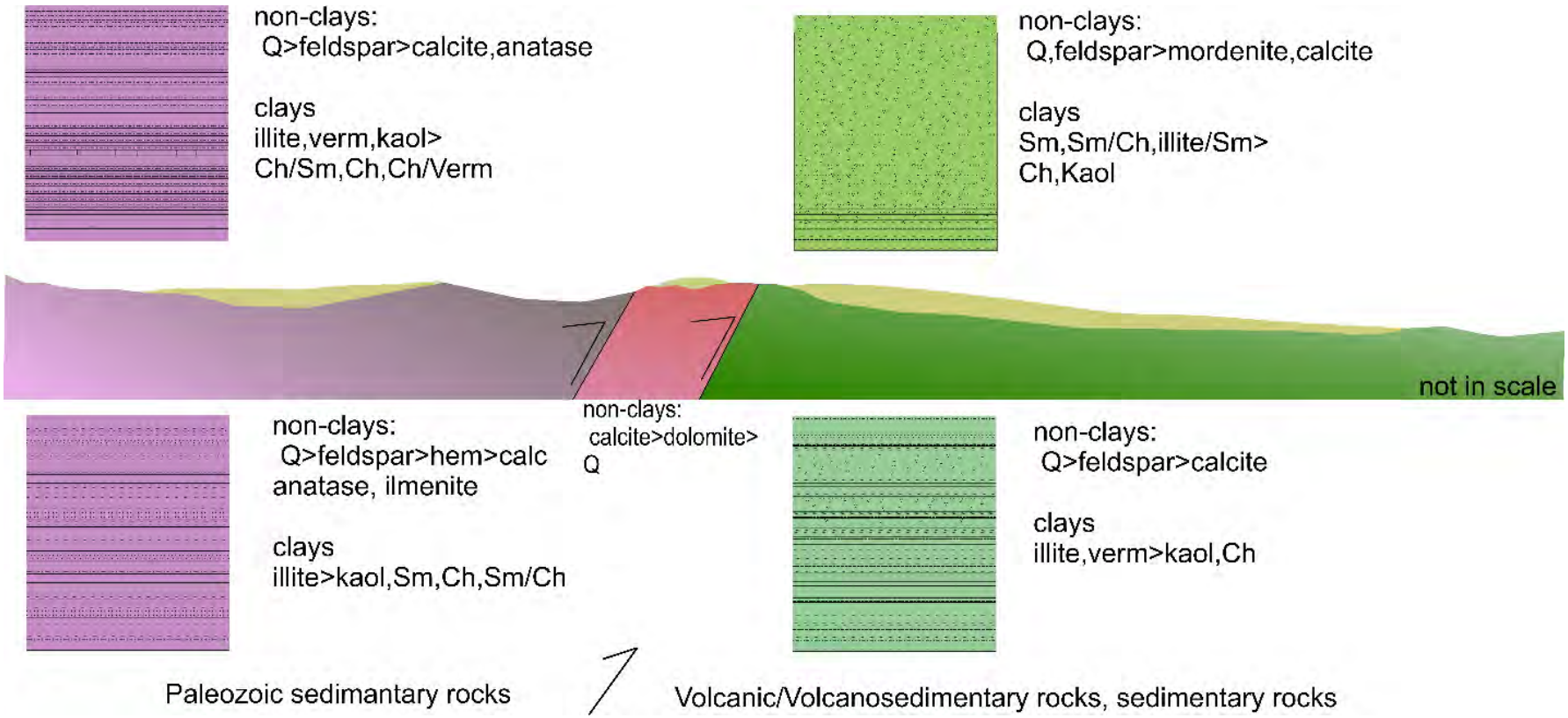
non-clays:
Q>feldspar>calcite,anatase
clays
illite,verm,kaol>
Ch/Sm,Ch,Ch/Verm
non-clays:
Q,feldspar>mordenite,calcite
clays
Sm,Sm/Ch,illite/Sm>
Ch,Kaol
not in scale
non-clays:
Q>feldspar>hem>calc
anatase, ilmenite
clays
illite>kaol,Sm,Ch,Sm/Ch
non-clays:
calcite>dolomite>
Q
non-clays:
Q>feldspar>calcite
clays
illite,verm>kaol,Ch
Paleozoic sedimantary rocks
Volcanic/Volcanosedimentary rocks, sedimentary rocks

Figure 40. Diagram summarizing QXRD data for potential source rocks

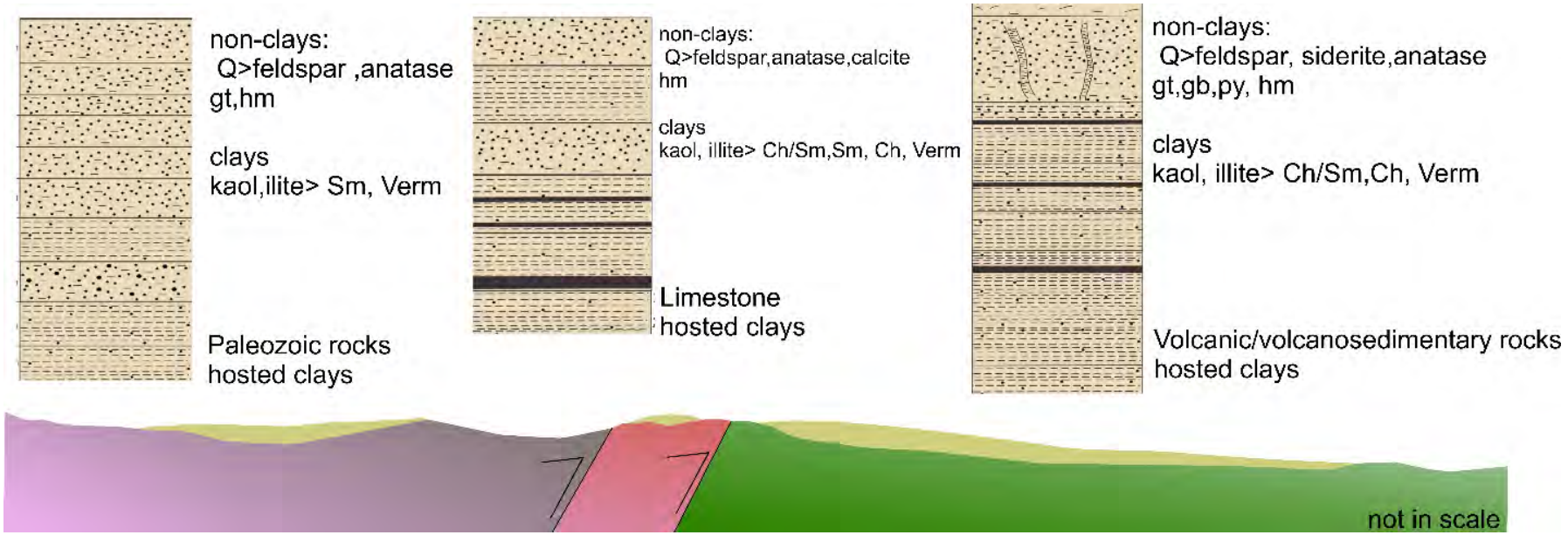
non-clays:
Q>feldspar ,anatase
gt,hm
clays
kaol,ilite> Sm, Verm
Paleozoic rocks
hosted clays
non-clays:
Q>feldspar,anatase,calcite
hm
clays
kaol, illite> Ch/Sm,Sm, Ch, Verm
Limestone
hosted clays
non-clays:
Q>feldspar, siderite,anatase
gt,gb,py, hm
clays
kaol, illite> Ch/Sm,Ch, Verm
Volcanic/volcanosedimentary rocks
hosted clays
not in scale

Figure 41. Diagram summarizing QXRD data for clay sections observed.

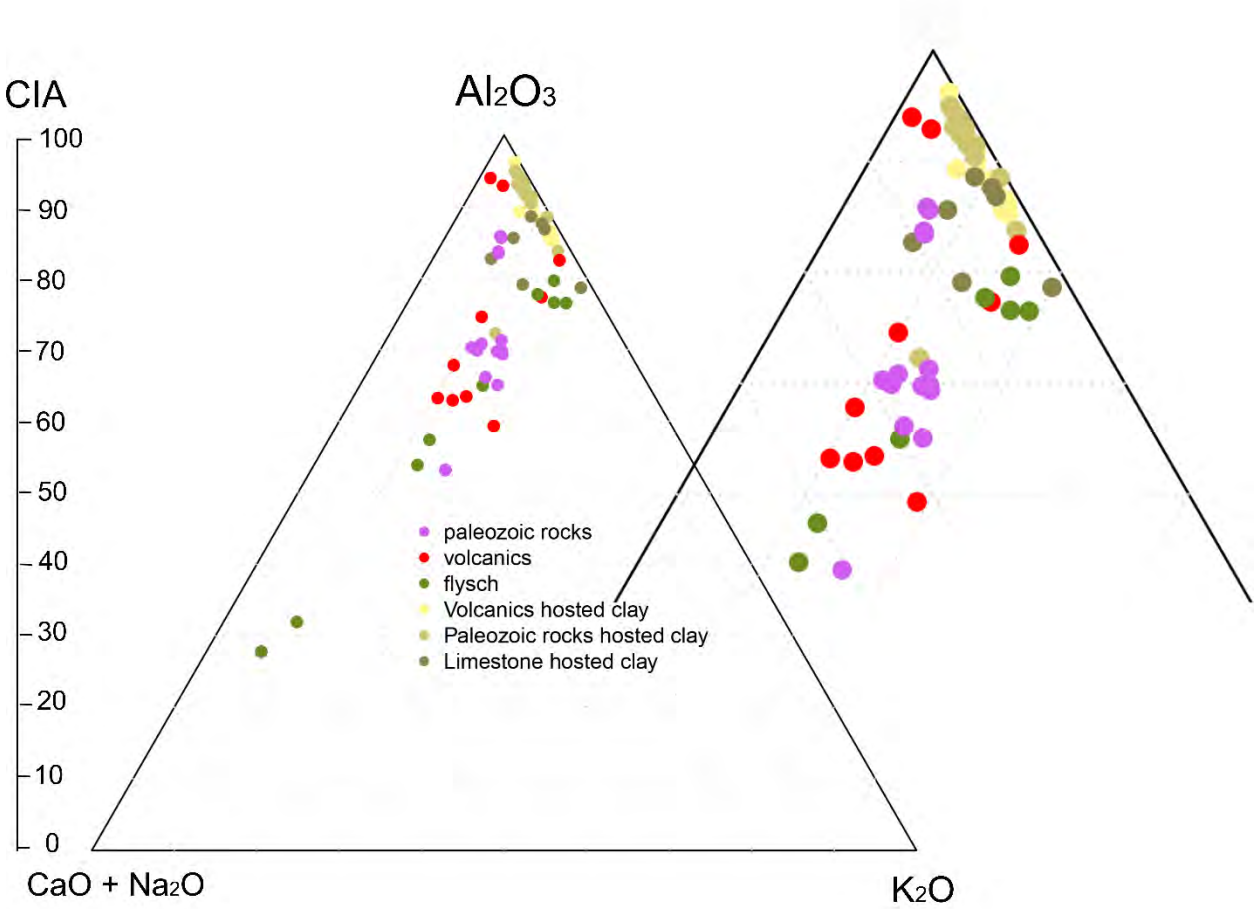

Figure 42. A-CN-K plot and corresponded Chemical Index of Alteration values.

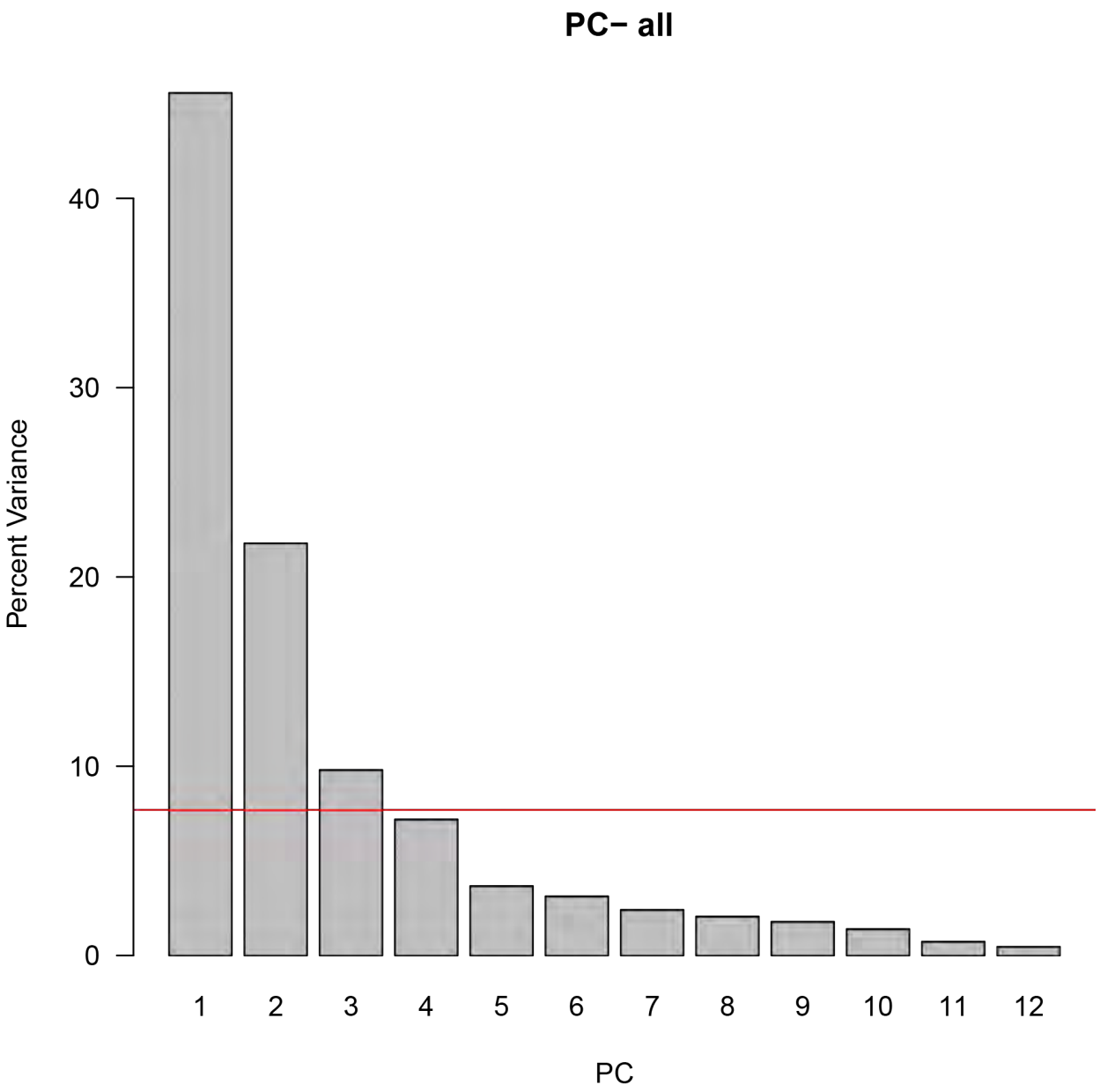

Figure 43. Scree plot for PCA-all data set.

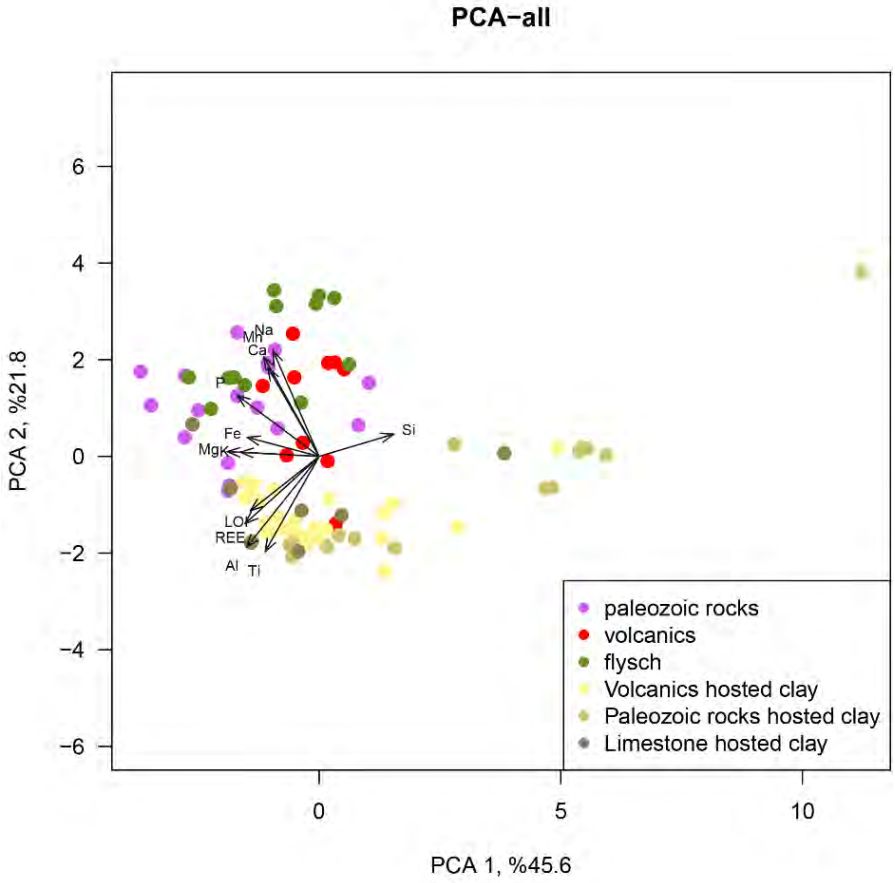
PCA−all
PCA 2, %21.8
PCA 1, %45.6
Na
Mn
Ca
P
Fe
Mgk
Si
LOI
REE
Al
Ti
paleozoic rocks
volcanics
flysch
Volcanics hosted clay
Paleozoic rocks hosted clay
Limestone hosted clay

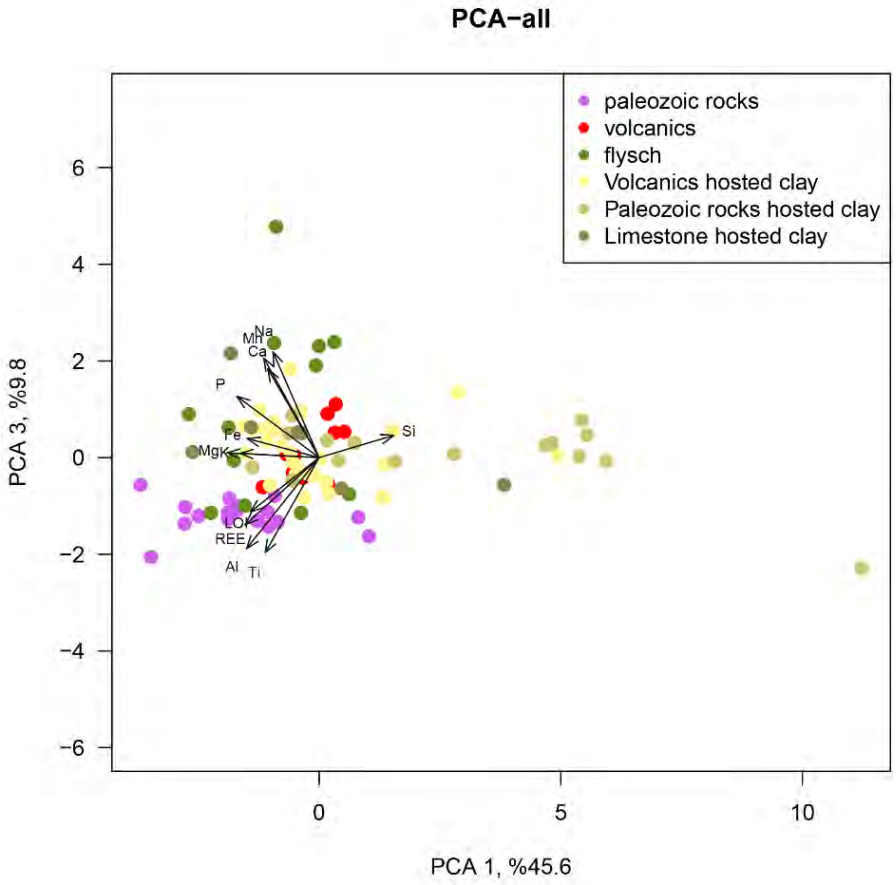
PCA−all
PCA 3, %9.8
PCA 1, %45.6
Na
Mn
Ca
P
Fe
Mgk
Si
LOI
REE
Al
Ti
paleozoic rocks
volcanics
flysch
Volcanics hosted clay
Paleozoic rocks hosted clay
Limestone hosted clay

Figure 44. PCA for all data set.

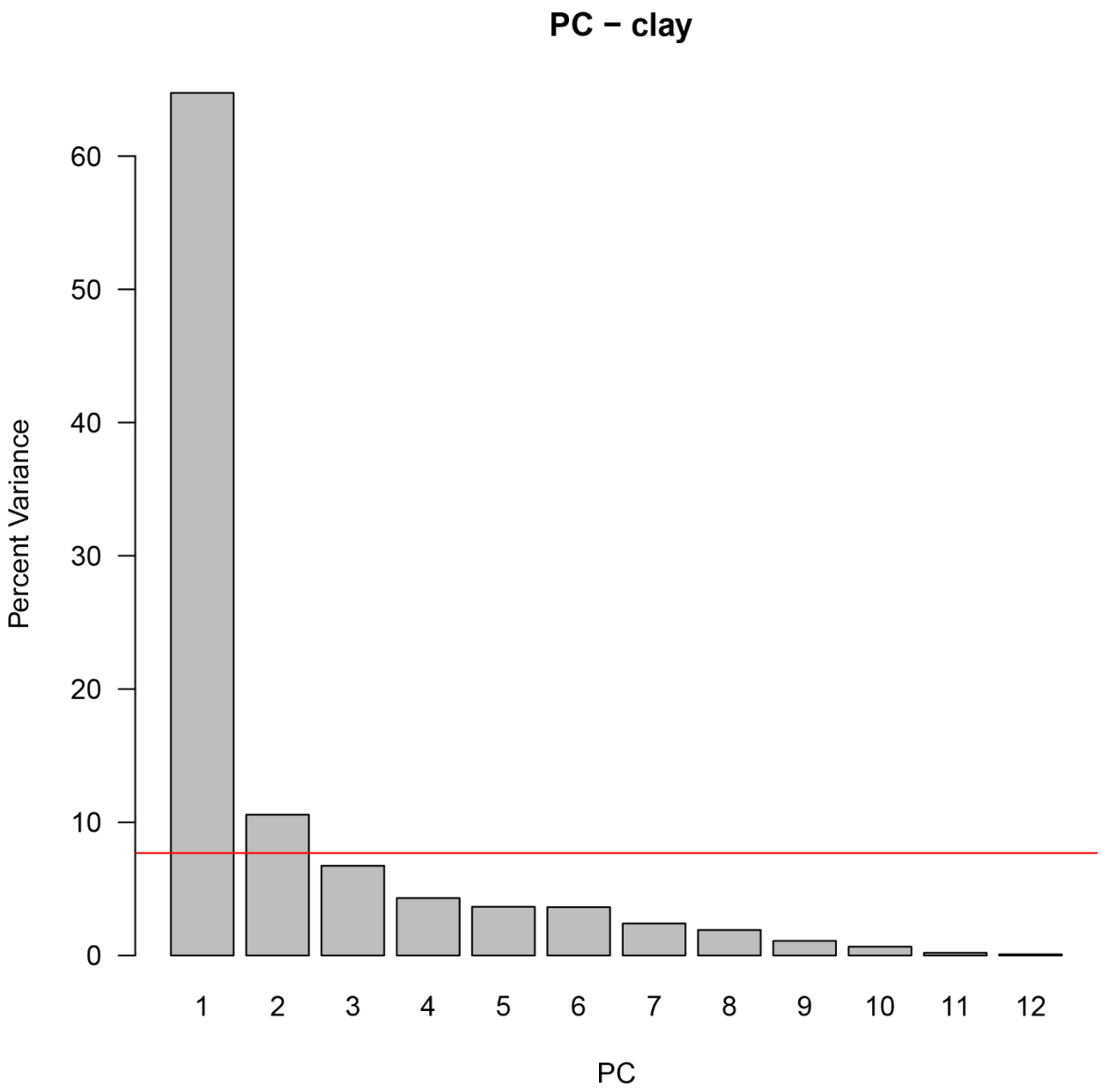

Figure 45. Scree plot for PCA-clays data set.

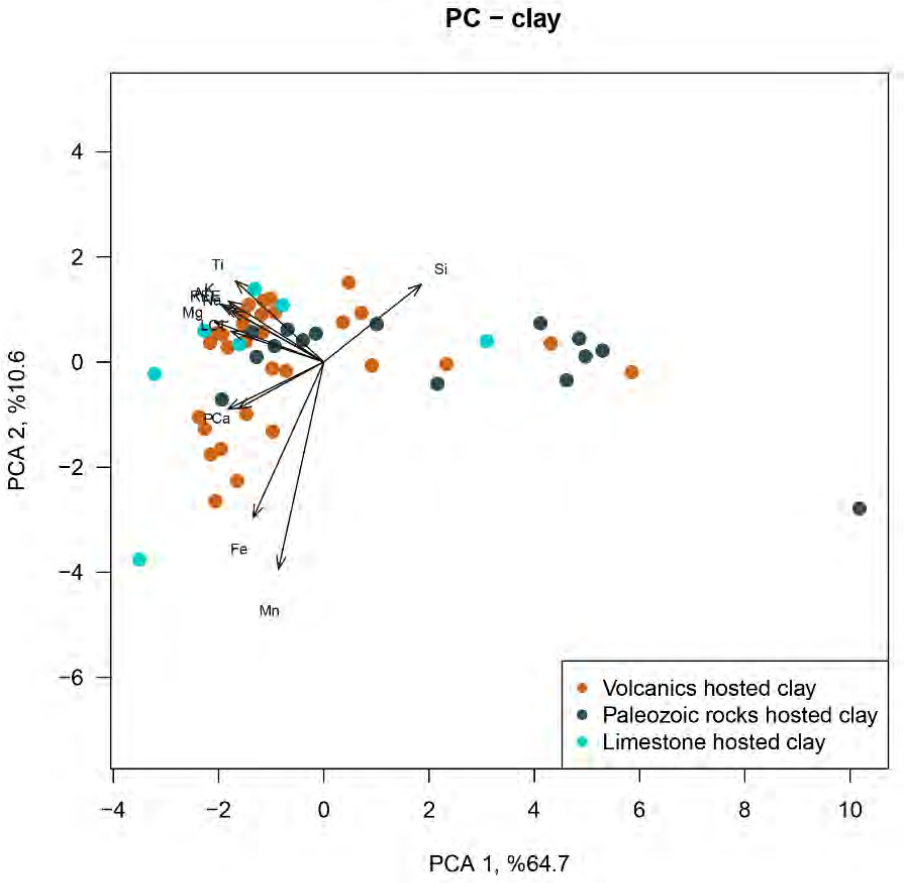
PC – clay
PCA 2, %10.6
PCA 1, %64.7
Ti
Si
Mg
PCa
Fe
Mn
Volcanics hosted clay
Paleozoic rocks hosted clay
Limestone hosted clay

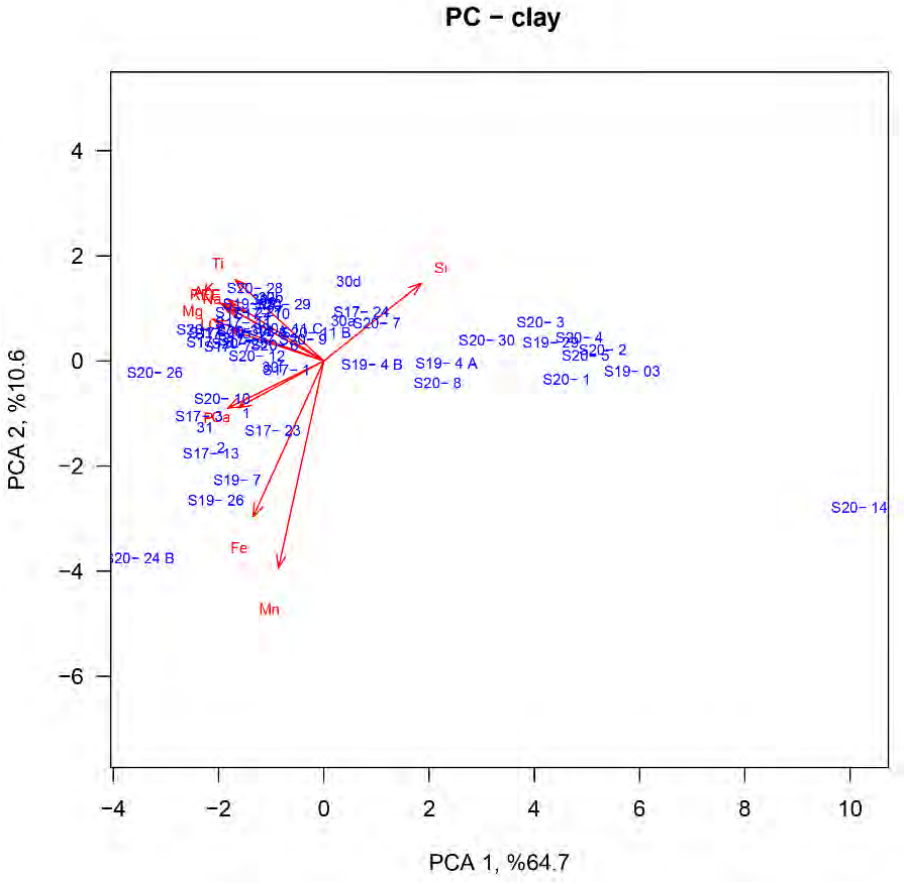
PC – clay
PCA 2, %10.6
PCA 1, %64.7
Ti
Si
Mg
PCa
Fe
Mn
30d
S20– 28
S17– 24
S20– 7
S20– 3
S20– 30
S20– 4
S20– 2
S20– 5
S19– 03
S19– 4 B
S19– 4 A
S20– 8
S20– 1
S20– 12
S20– 26
S20– 10
S17– 23
S17– 13
S19– 7
S19– 26
S20– 14
S20– 24 B

Figure 46. PCA for clay data set. The figure below is the sample positions with the sample codes in the plot.

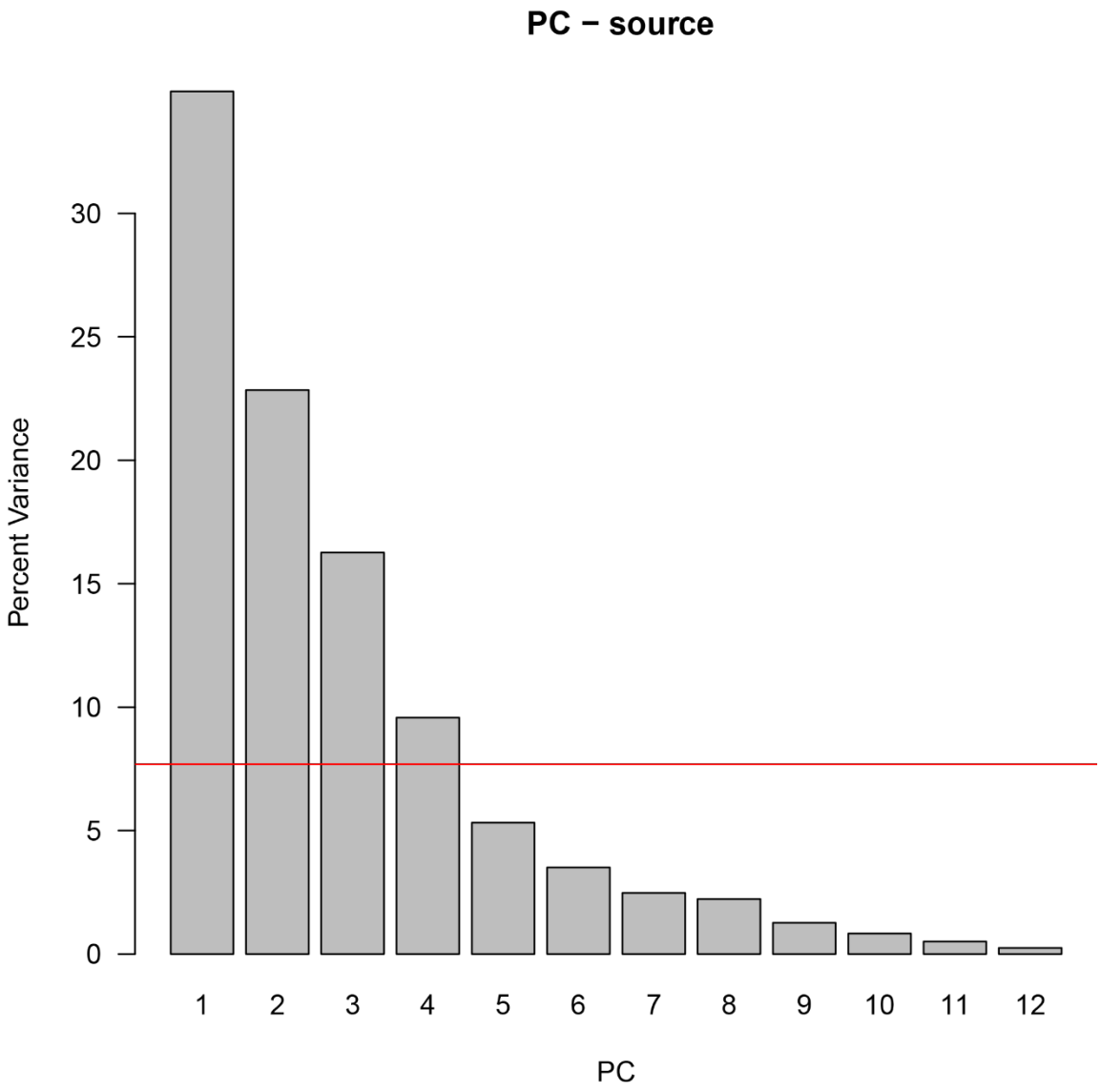

Figure 47. Scree plot for PCA-rocks data set.

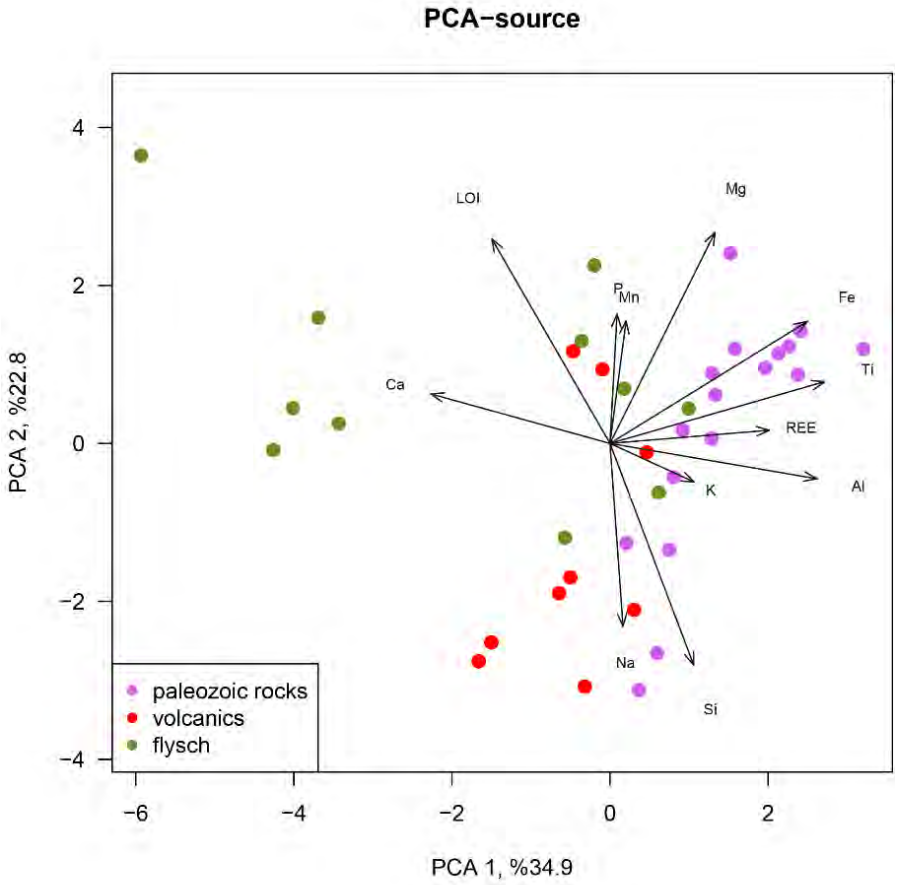
PCA−source
PCA 2, %22.8
PCA 1, %34.9
LOI
Mg
P
Mn
Fe
Ti
Ca
REE
K
Al
Na
Si
paleozoic rocks
volcanics
flysch

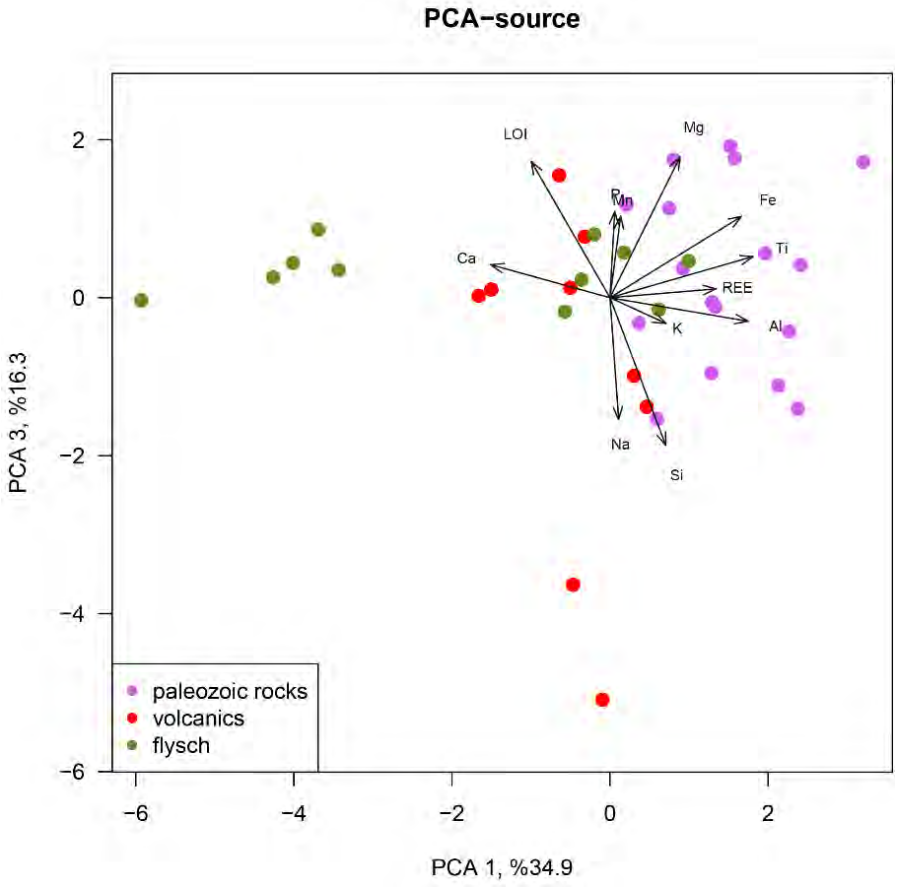
PCA−source
PCA 3, %16.3
PCA 1, %34.9
LOI
Mg
P
Mn
Fe
Ti
Ca
REE
K
Al
Na
Si
paleozoic rocks
volcanics
flysch

Figure 48. PCA for source rocks data set.

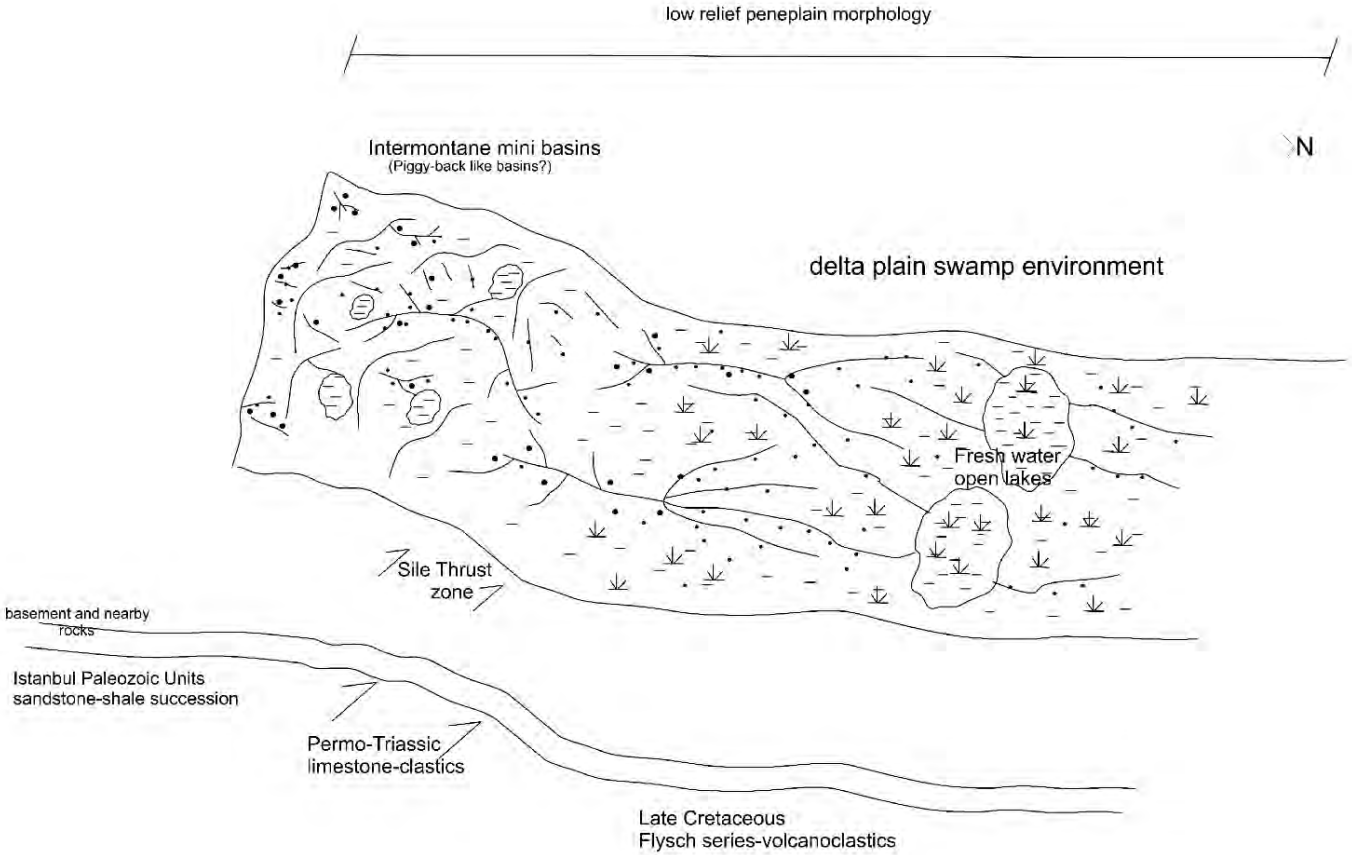
low relief peneplain morphology
N
Intermontane mini basins
(Piggy-back like basins?)
delta plain swamp environment
Fresh water
open lakes
Sile Thrust
zone
basement and nearby
rocks
Istanbul Paleozoic Units
sandstone-shale succession
Permo-Triassic
limestone-clastics
Late Cretaceous
Flysch series-volcanoclastics

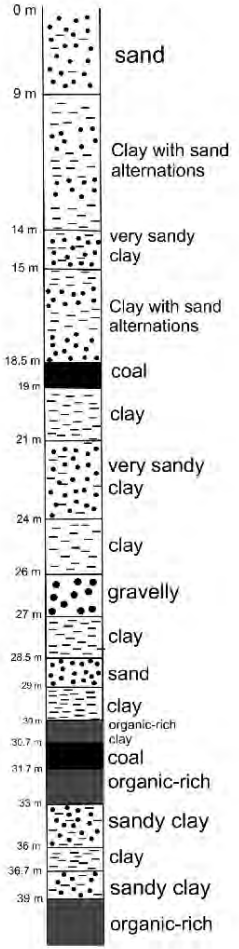
0 m
sand
9 m
Clay with sand
alternations
14 m
very sandy
clay
15 m
Clay with sand
alternations
18.5 m
coal
19 m
clay
21 m
very sandy
clay
24 m
clay
26 m
gravelly
27 m
clay
28.5 m
sand
29 m
clay
30 m
organic-rich
clay
30.7 m
coal
31.7 m
organic-rich
33 m
sandy clay
36 m
clay
36.7 m
sandy clay
39 m
organic-rich

Figure 49. Diagram showing paleo-environmental model with the drill data

APPENDIX A

Sample Locations

Sample	X	Y
S17_1-25	706755	4557629
S19_1-3	706487	4557645
S19_4	706265	4557553
S19_5	706488	4557646
S19_6,7	706498	4557645
S19_8	703704	4555840
S19_9	703831	4555901
S19_10	703846	4555476
S19_14	703805	4554676
S19_15	703178	4554693
S19_16	707938	4555756
S19_18	713680	4560511
S19_20	713541	4560452
S19_24	701259	4552478
S19_25	701256	4552489
S19_26, 27	705720	4557126
S19_28	706325	4557584
S19_29, 30a-30f, 31	706450	4557652
S19_32	704577	4554719
S19_34	714008	4560452
S19_36a	711194	4560861
S19_36d	711168	4560852
SKT_1_drill	706762	4558000
S20_	706558	4550641
S20_1-10	706621	4550623
S20_11-14	706488	4550593
S20_15-19 drill	706600	4550610
S20_20	704759	4552213
S20_21-22	704762	4552227
S20_23a-23b	704769	4551096
S20_24a-24b	704462	4553092
S20_25-28	704330	4552995
S20_29-30	704308	4553019
S20_31-32	692233	4547022
S20_36-38	694587	4550225
S20_39	698525	4551476
S20_40-42	698628	4551454
S20_43	704509	4554287
S20_45-48	704484	4554548

APPENDIX B

XRD whole rock raw data

(Coupled TwoTheta/Theta)

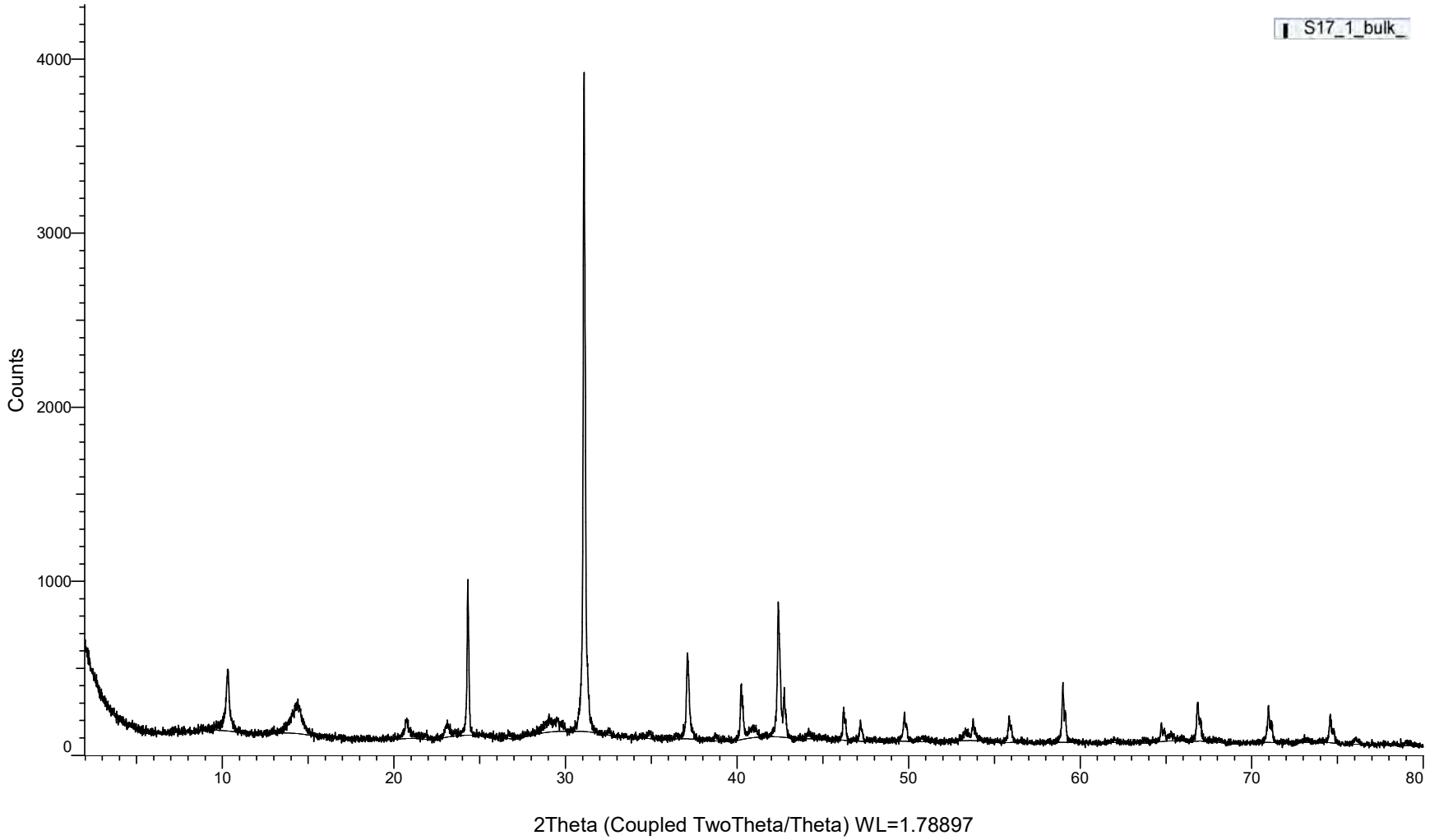

(Coupled TwoTheta/Theta)

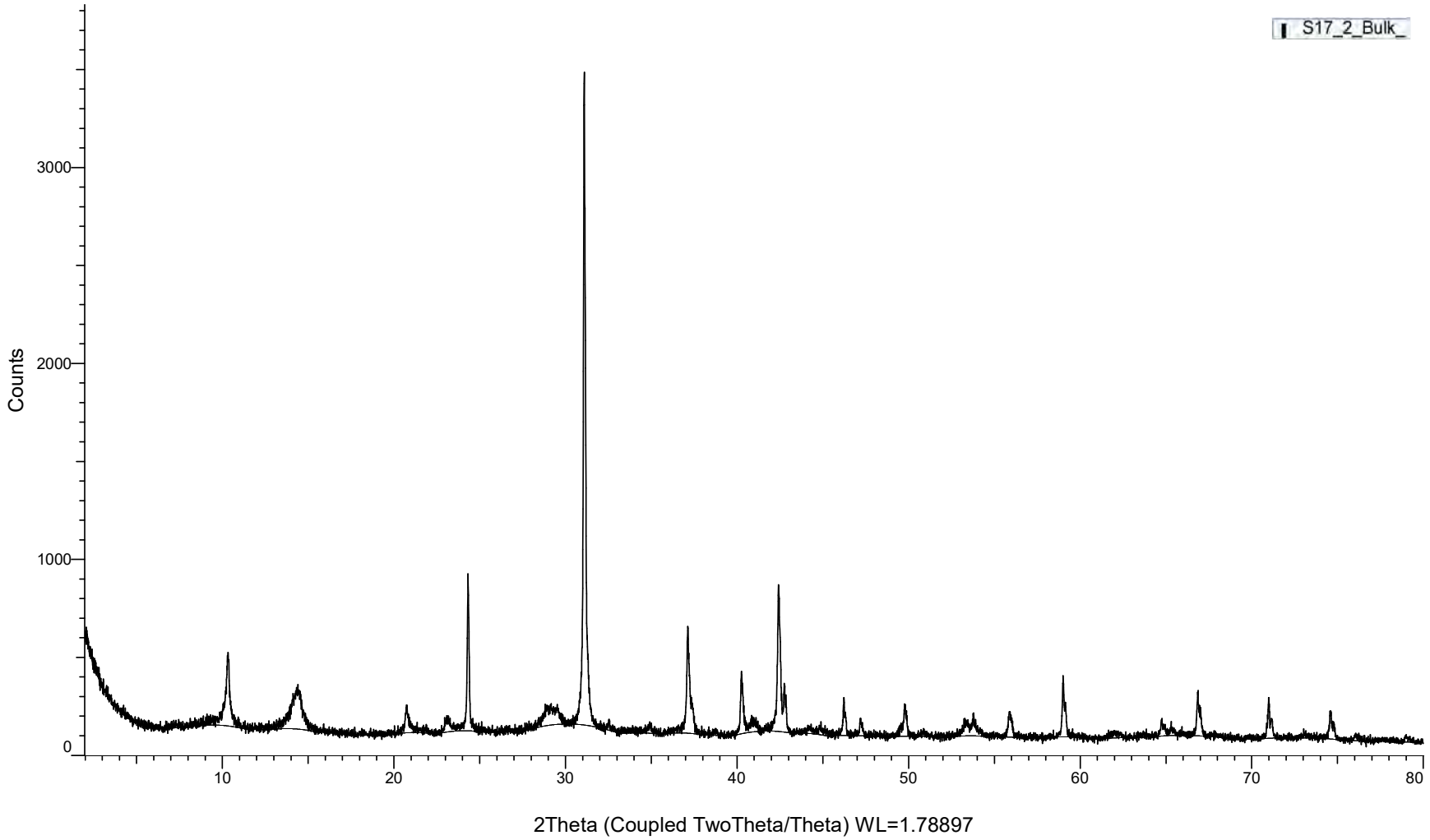

(Coupled TwoTheta/Theta)

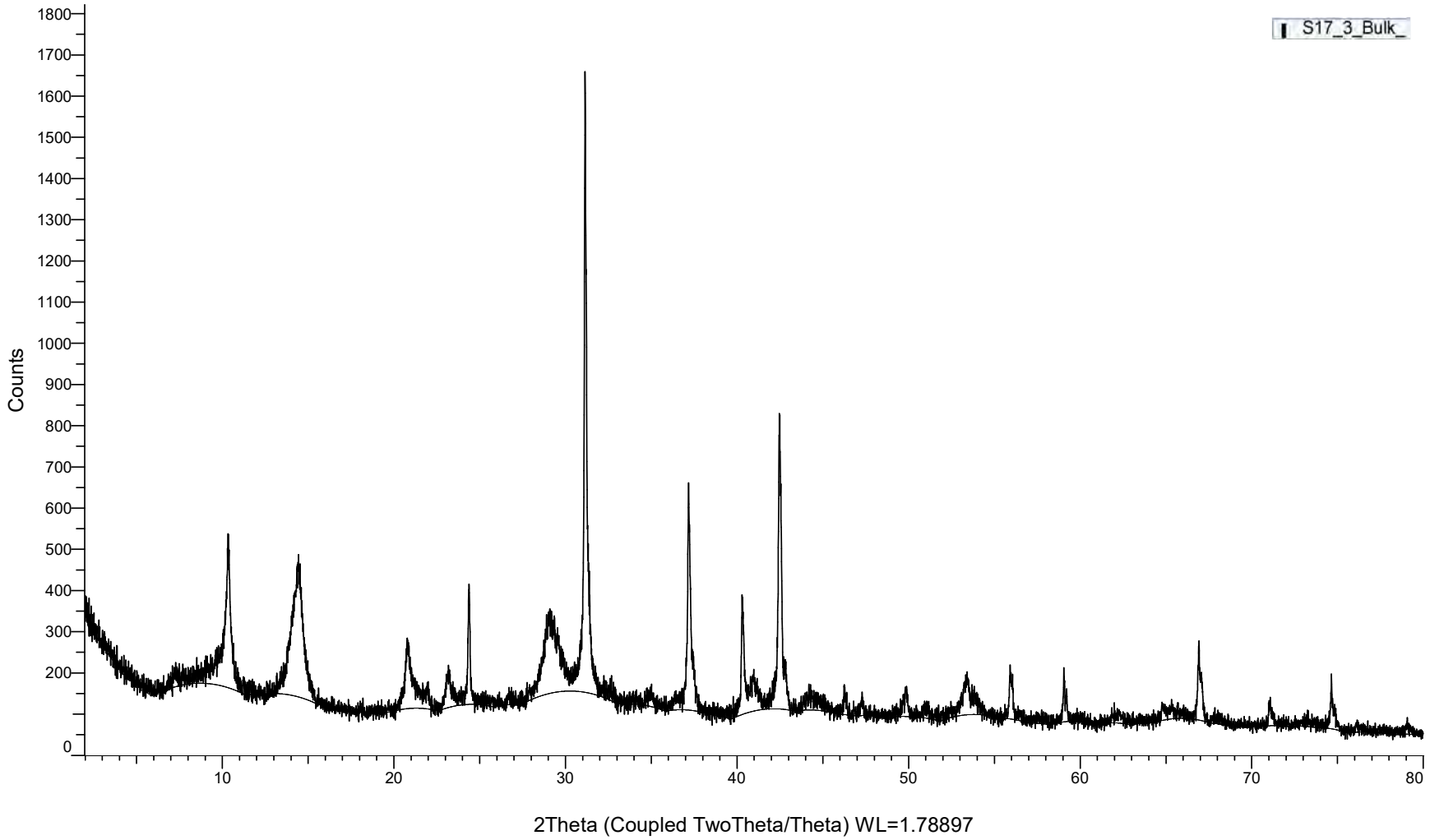

(Coupled TwoTheta/Theta)

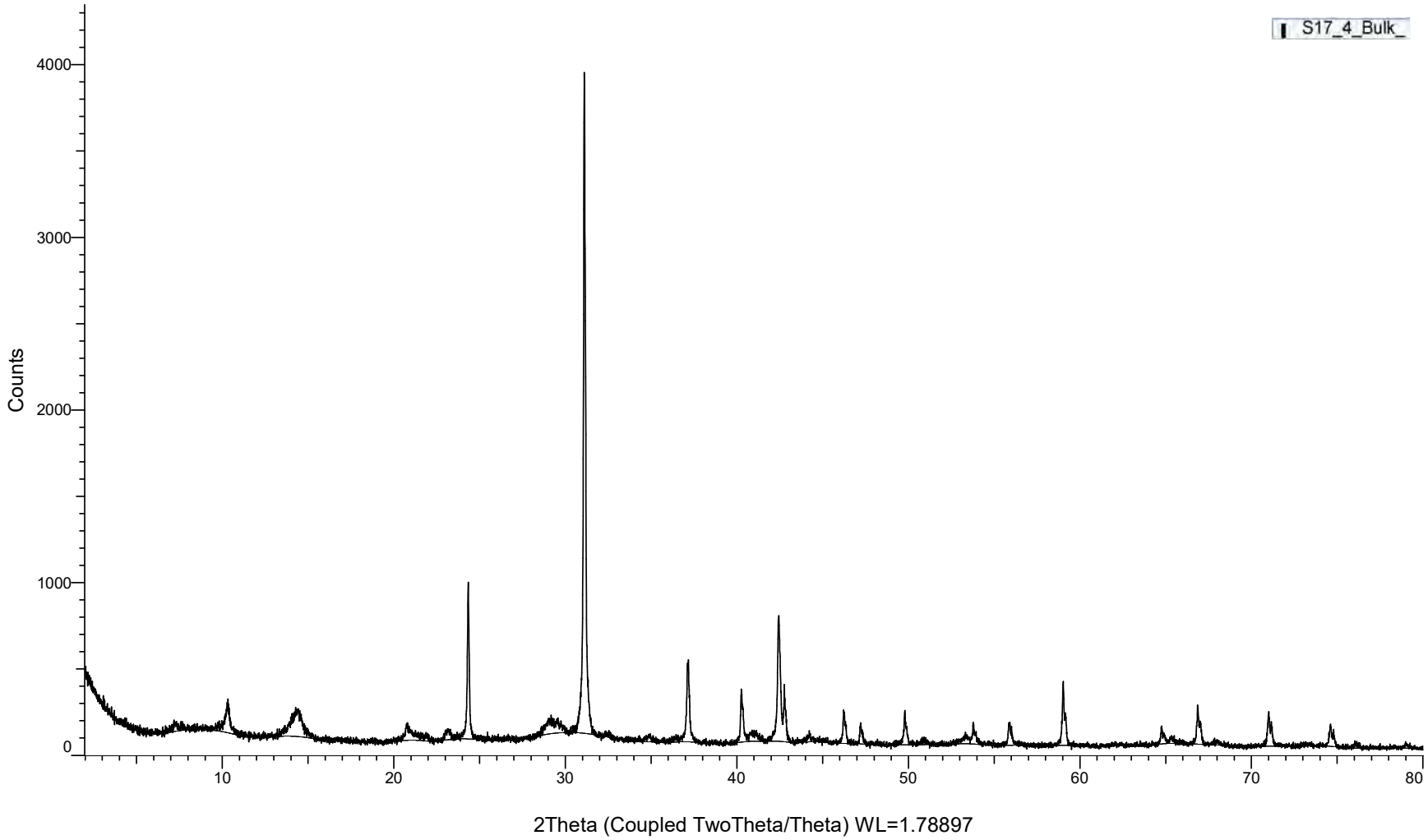

(Coupled TwoTheta/Theta)

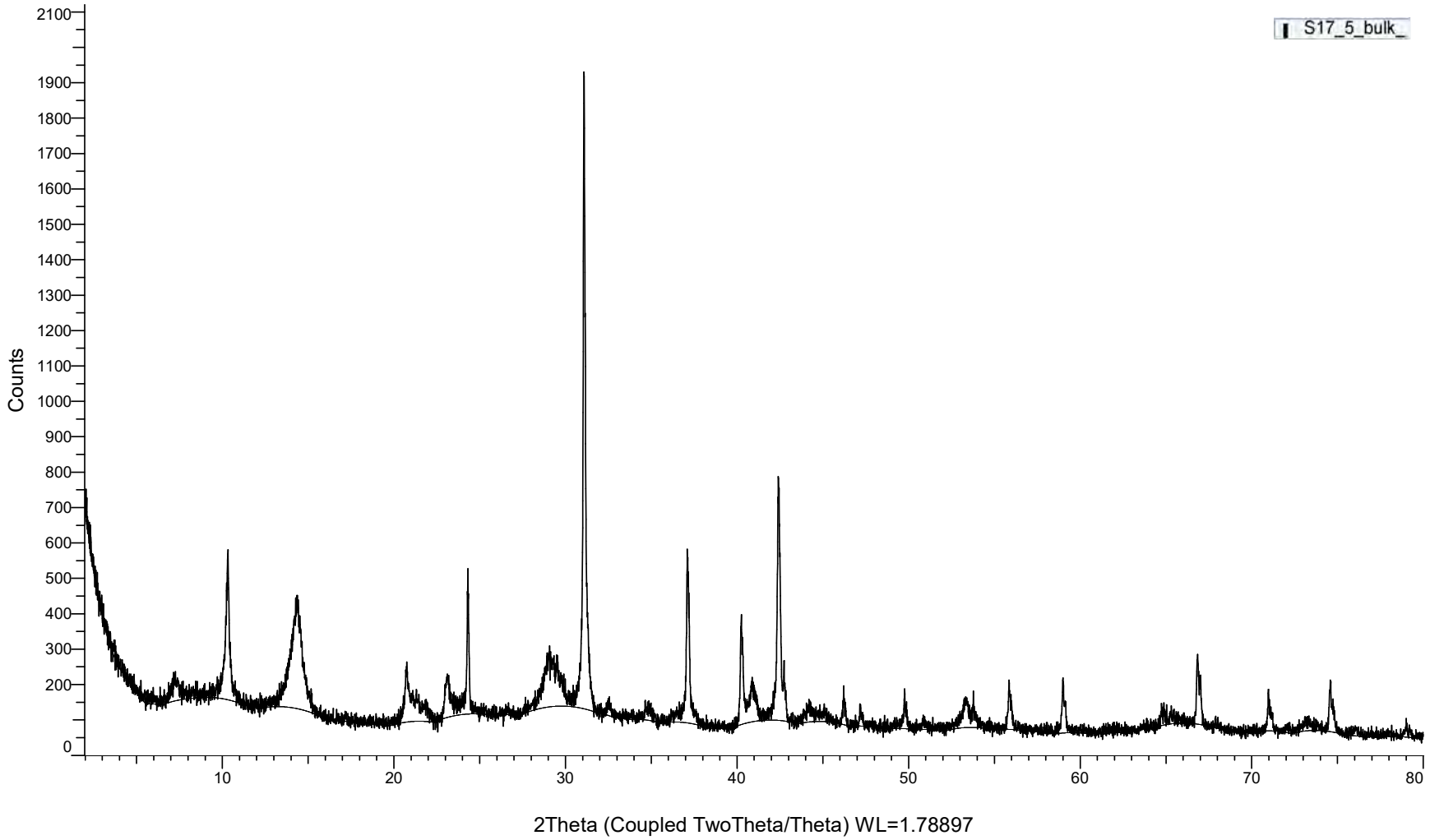

(Coupled TwoTheta/Theta)

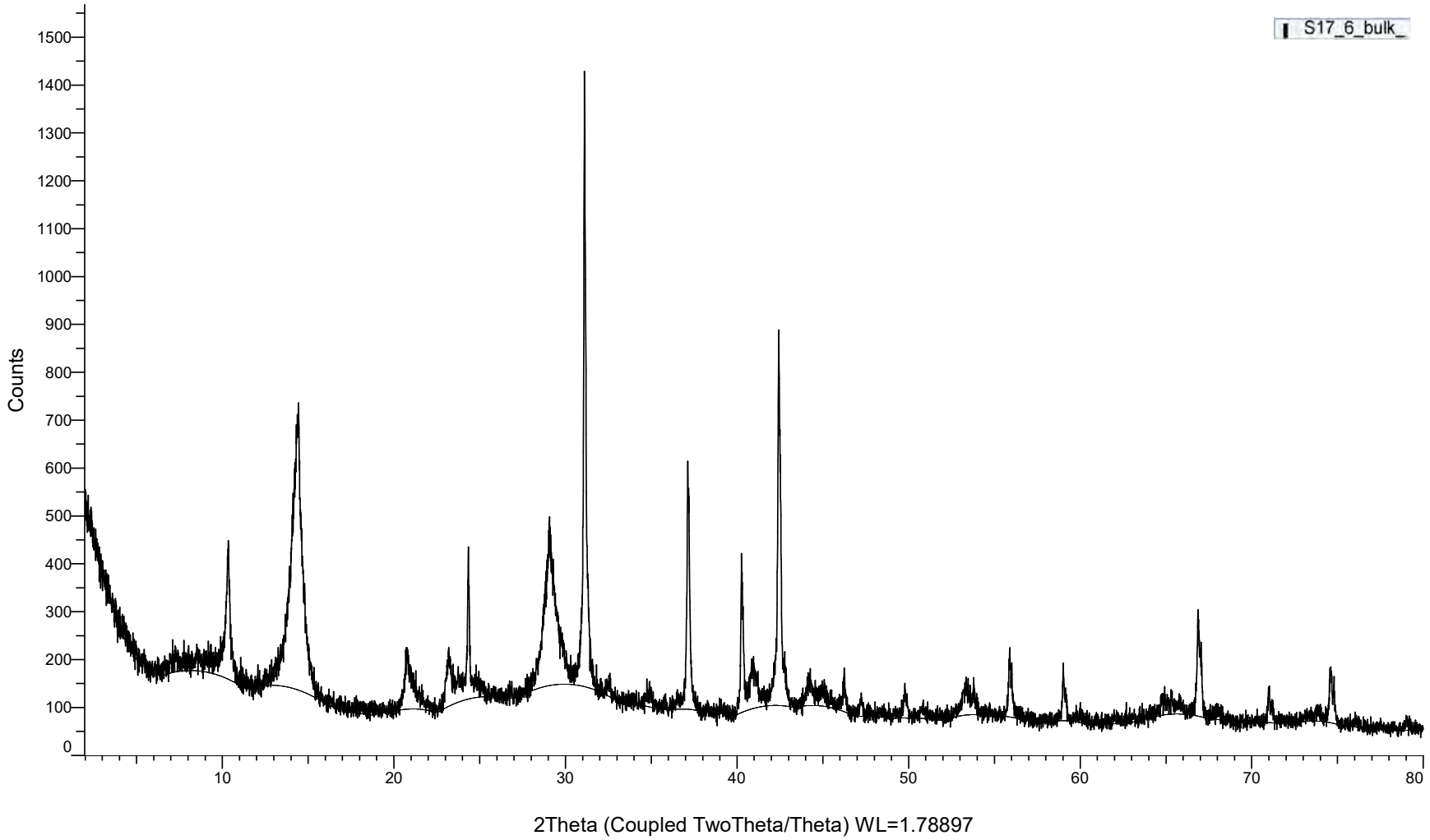

(Coupled TwoTheta/Theta)

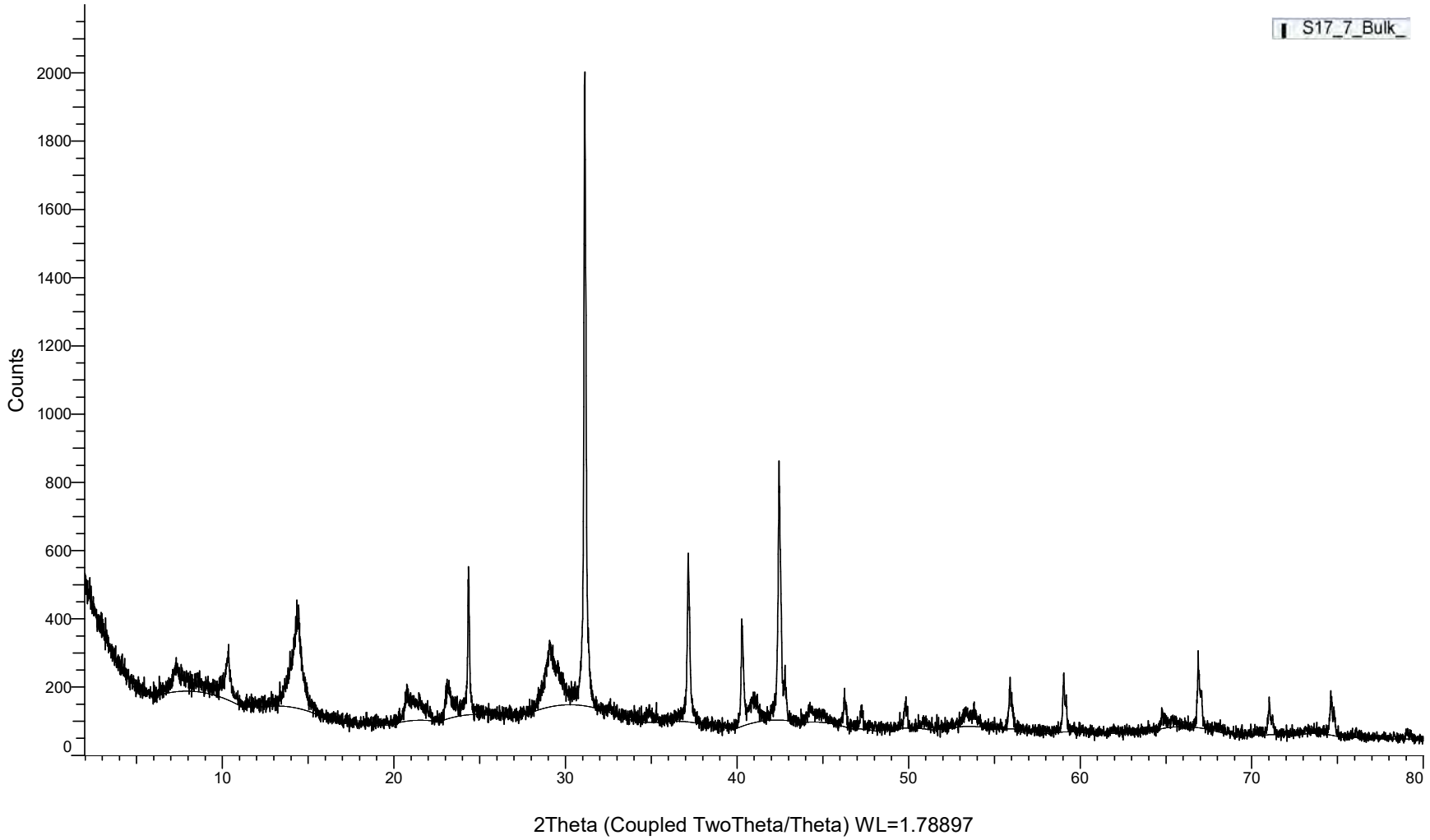

(Coupled TwoTheta/Theta)

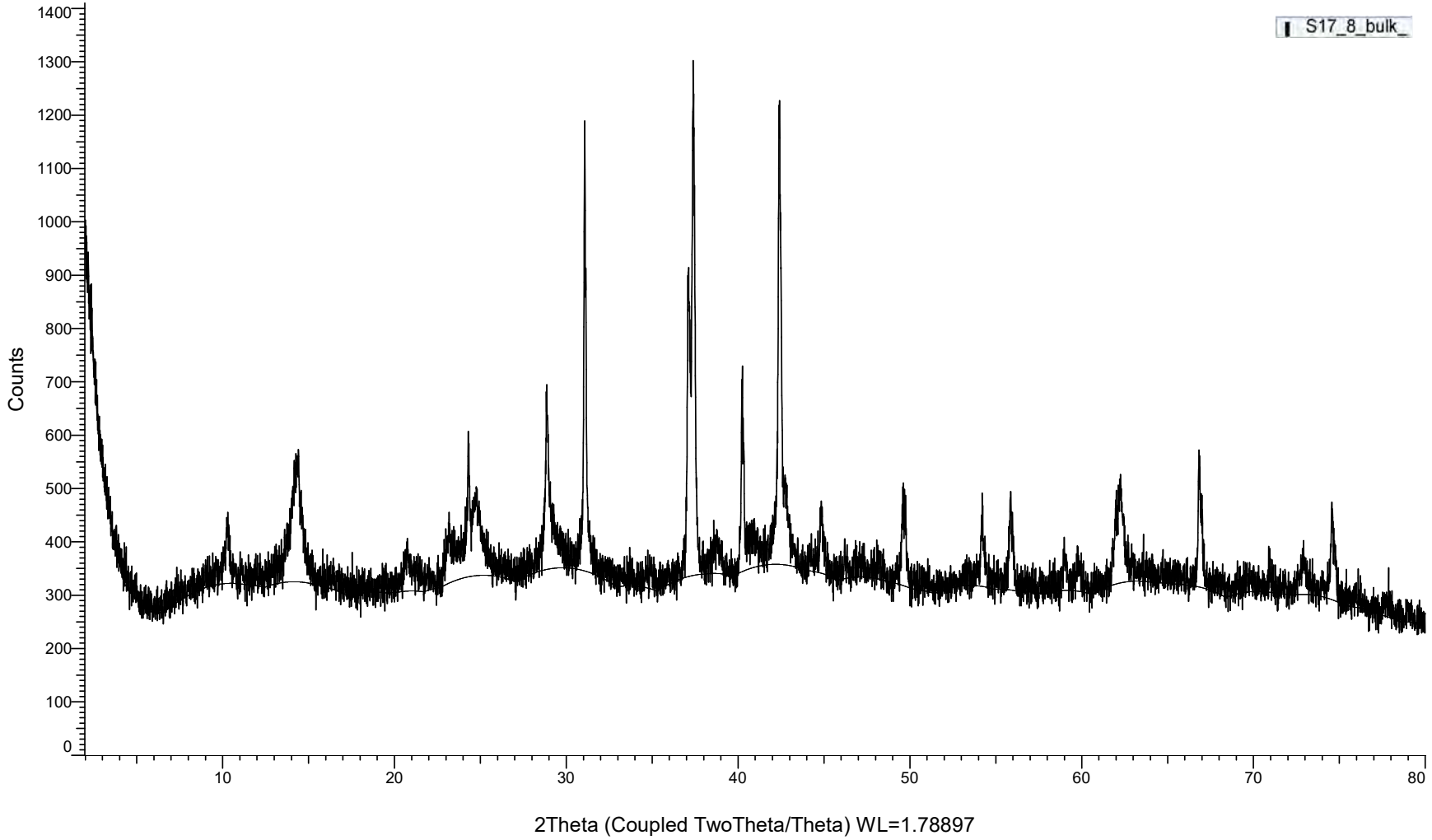

(Coupled TwoTheta/Theta)

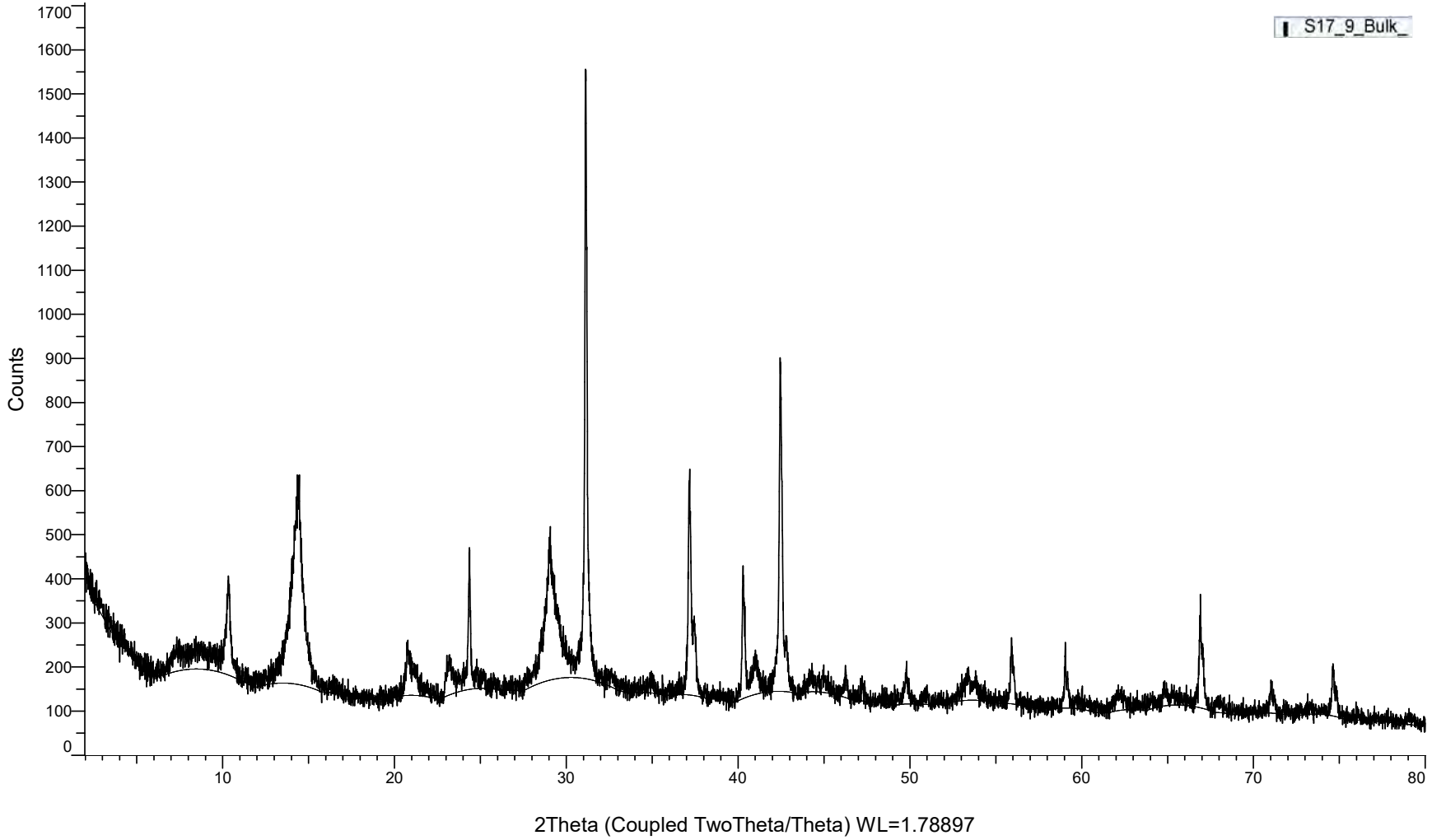

(Coupled TwoTheta/Theta)

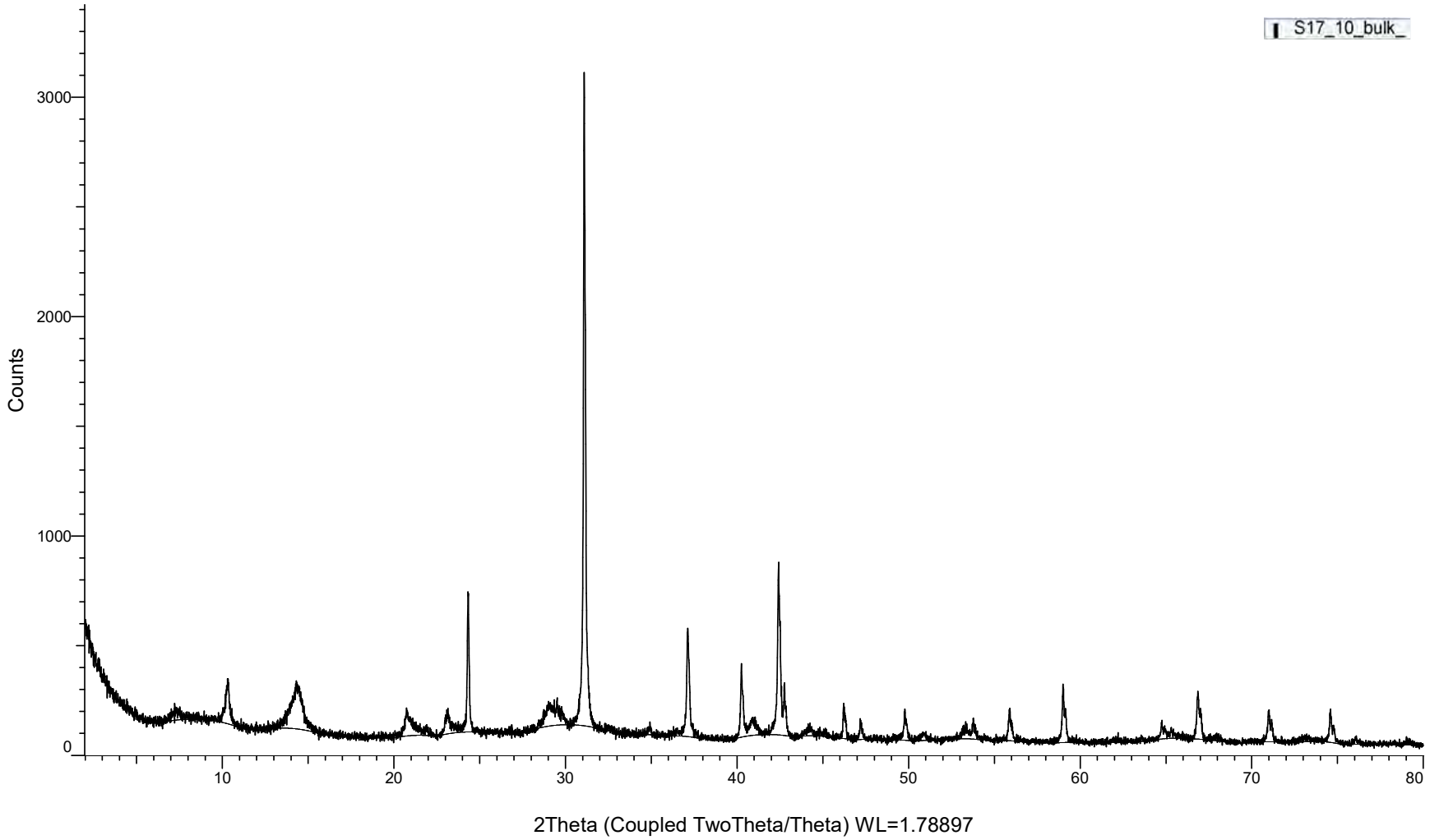

(Coupled TwoTheta/Theta)

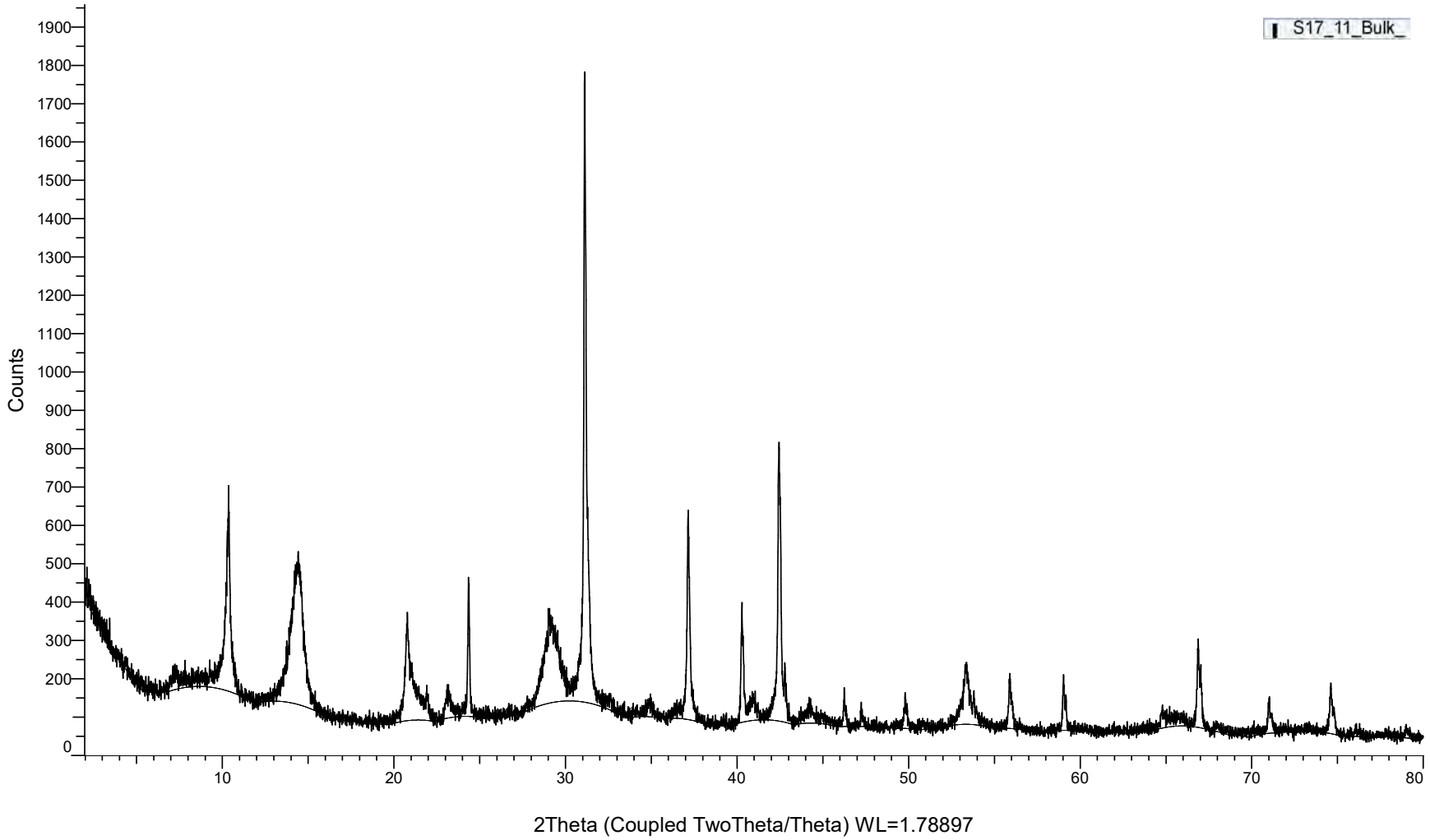

(Coupled TwoTheta/Theta)

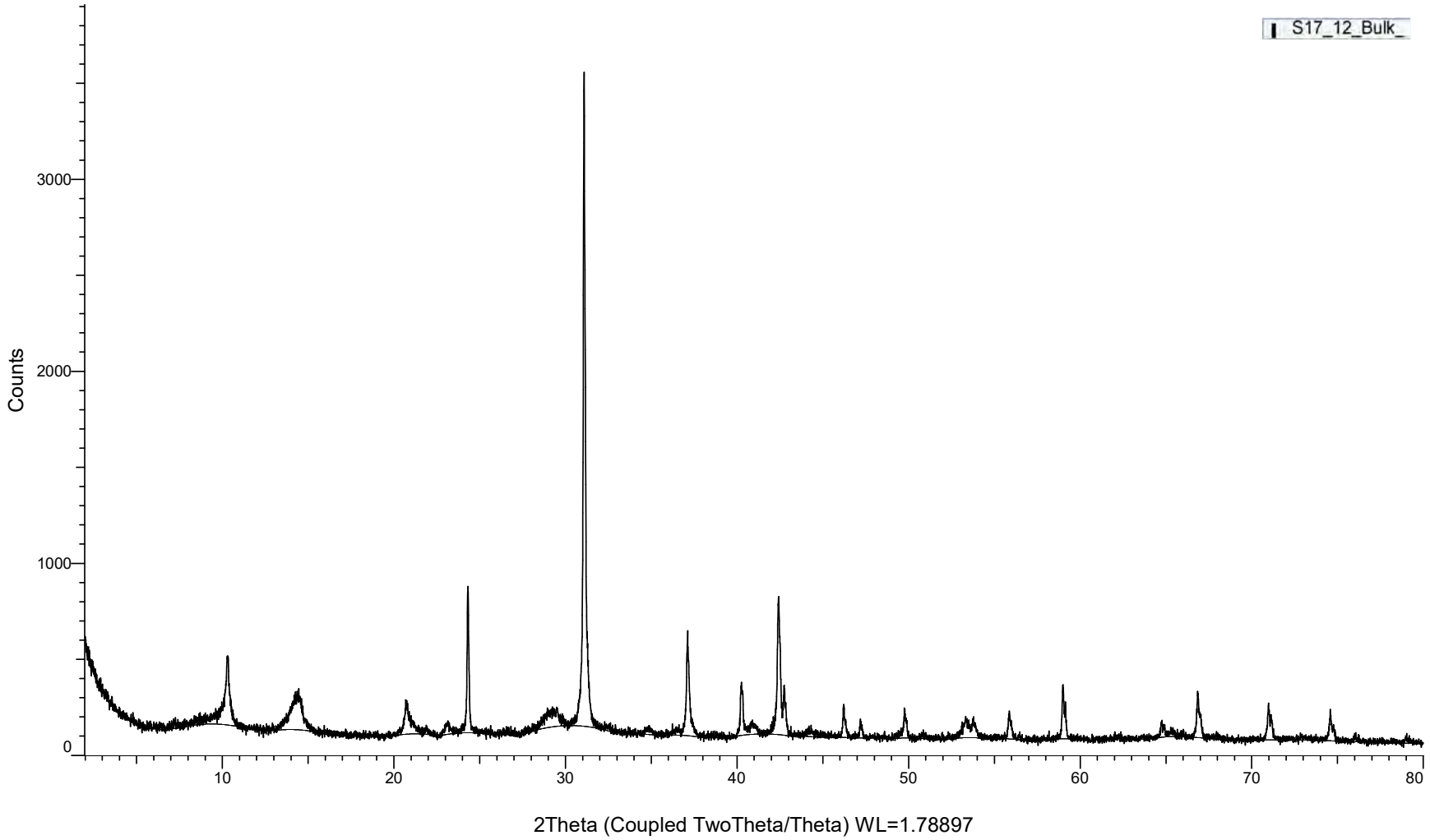

(Coupled TwoTheta/Theta)

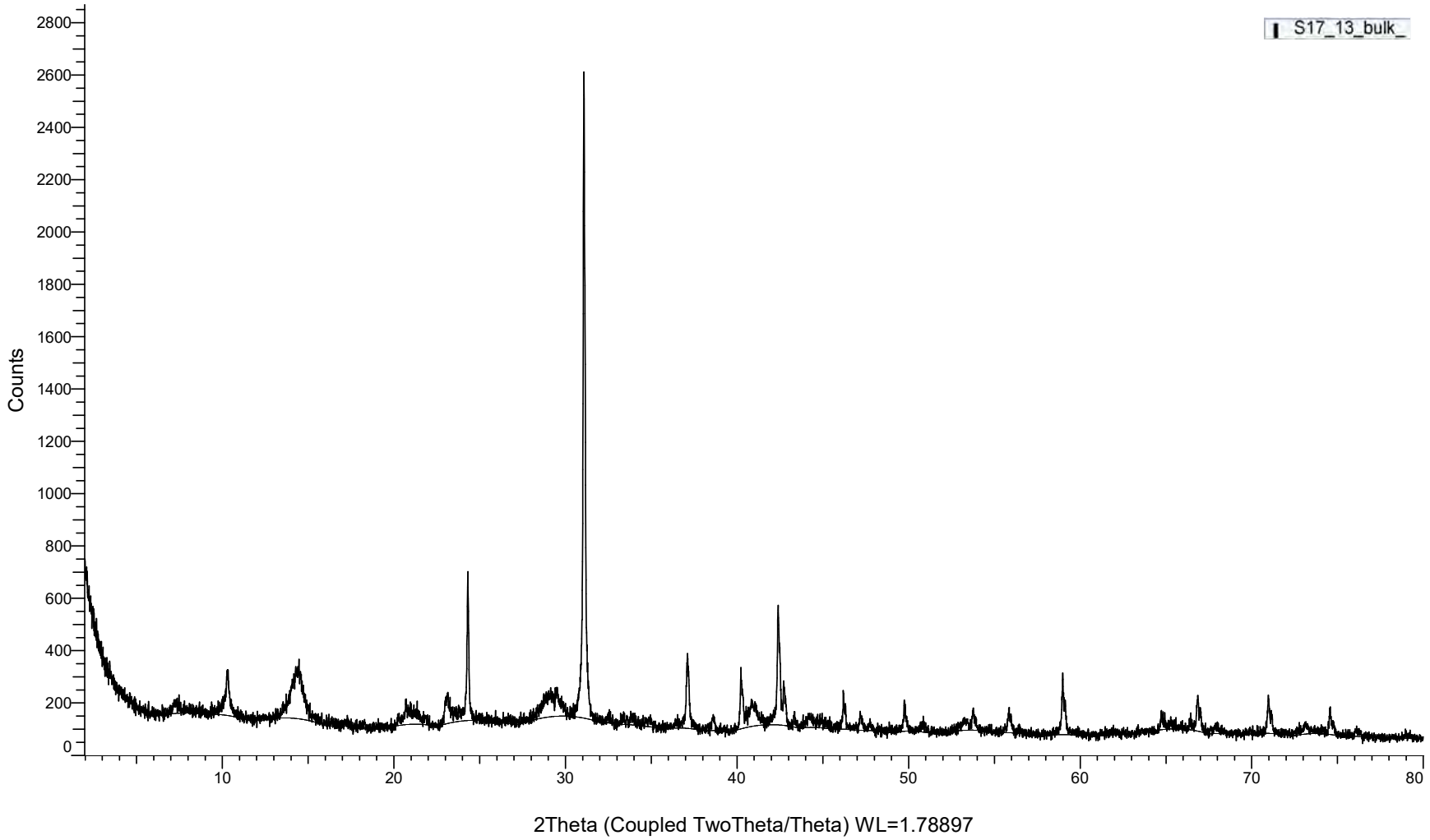

(Coupled TwoTheta/Theta)

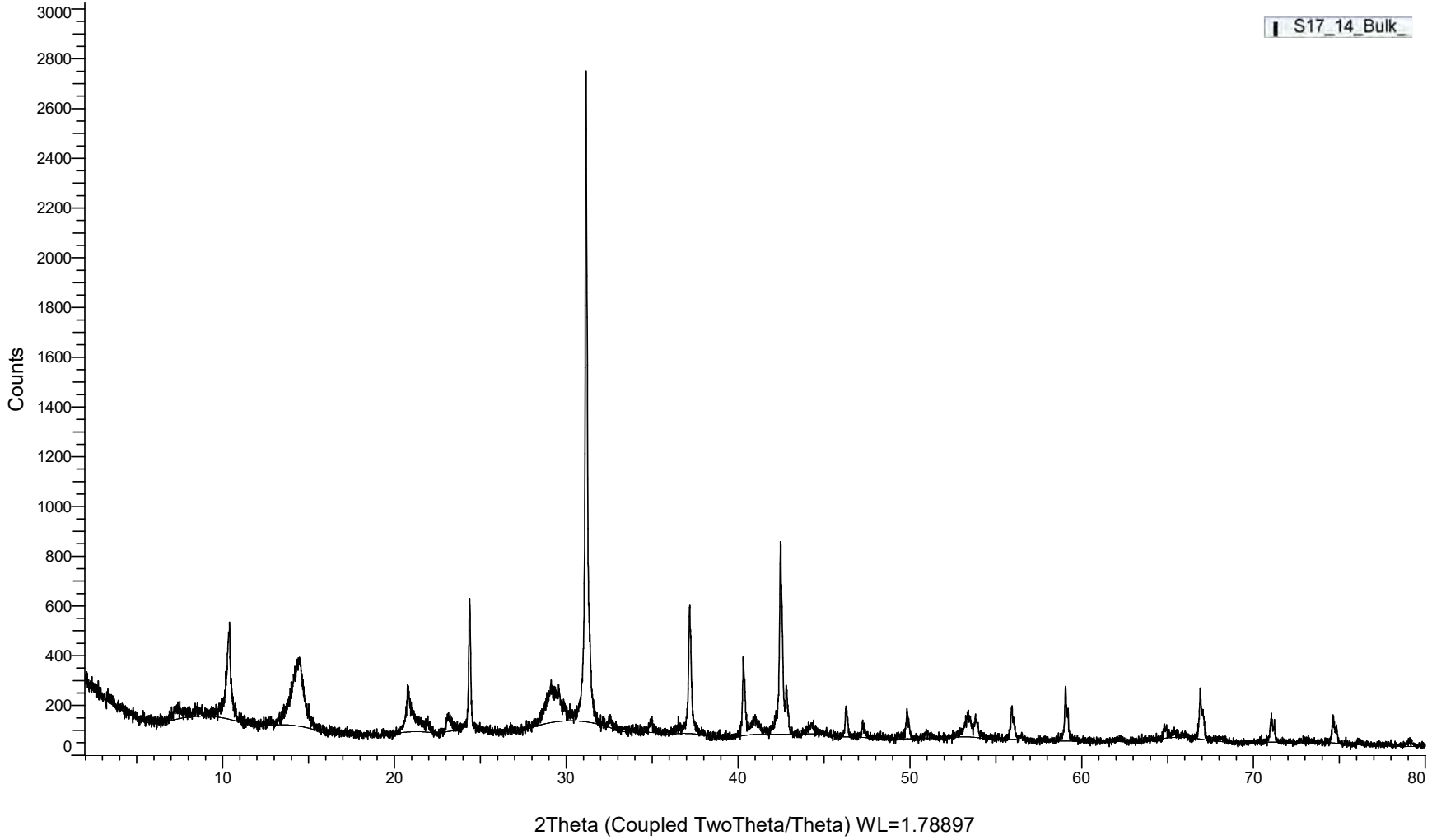

(Coupled TwoTheta/Theta)

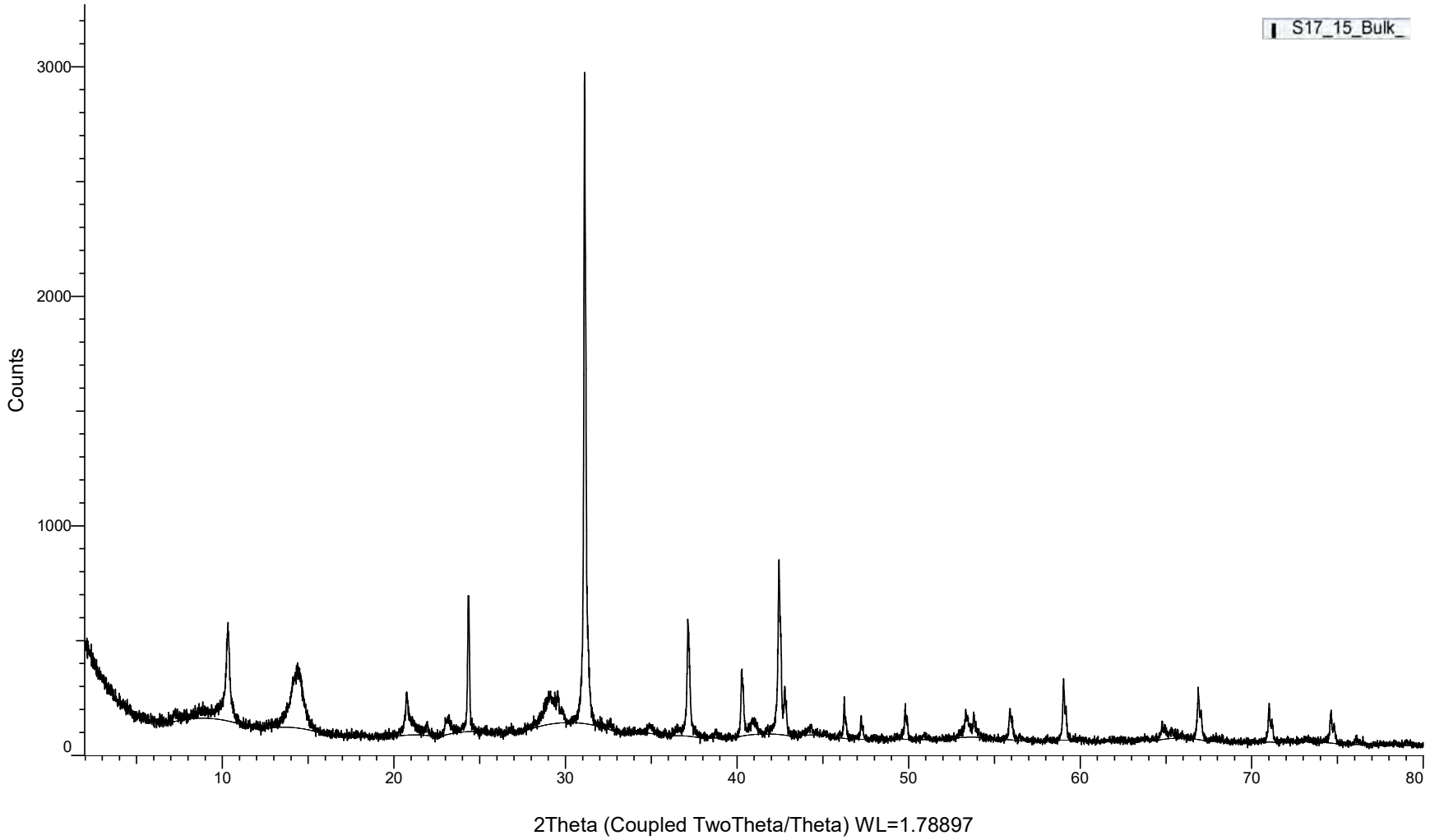

(Coupled TwoTheta/Theta)

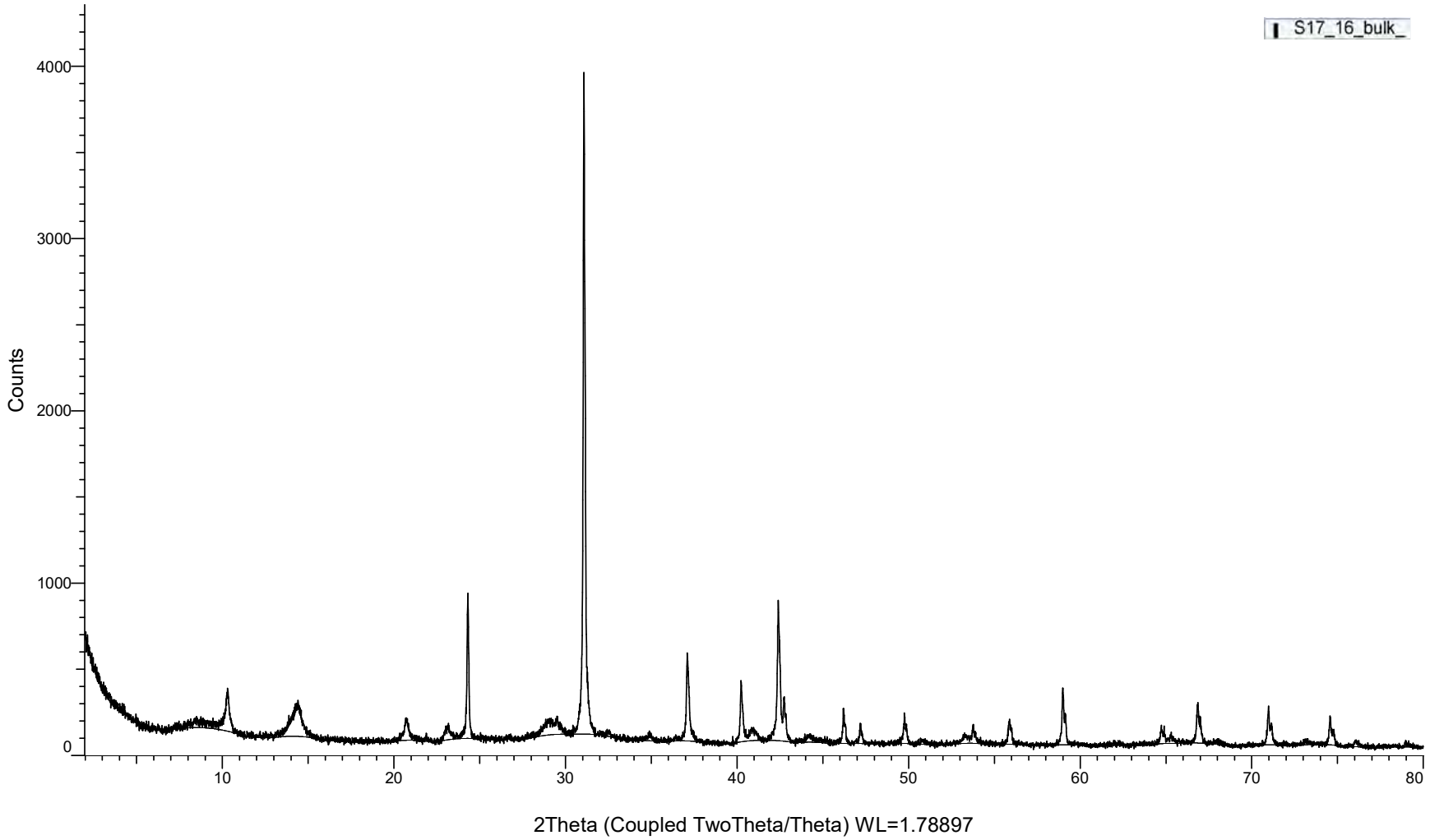

(Coupled TwoTheta/Theta)

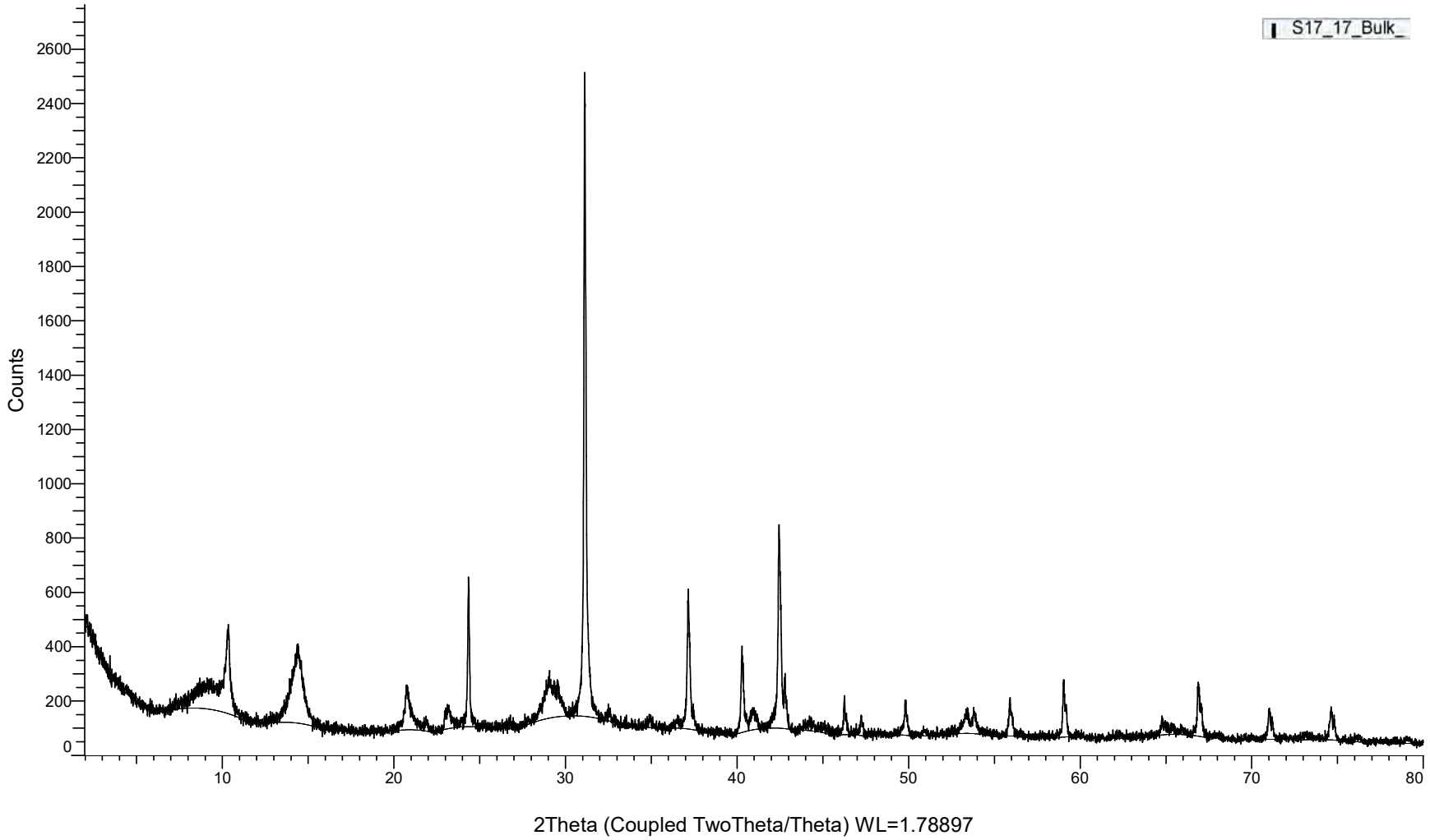

(Coupled TwoTheta/Theta)

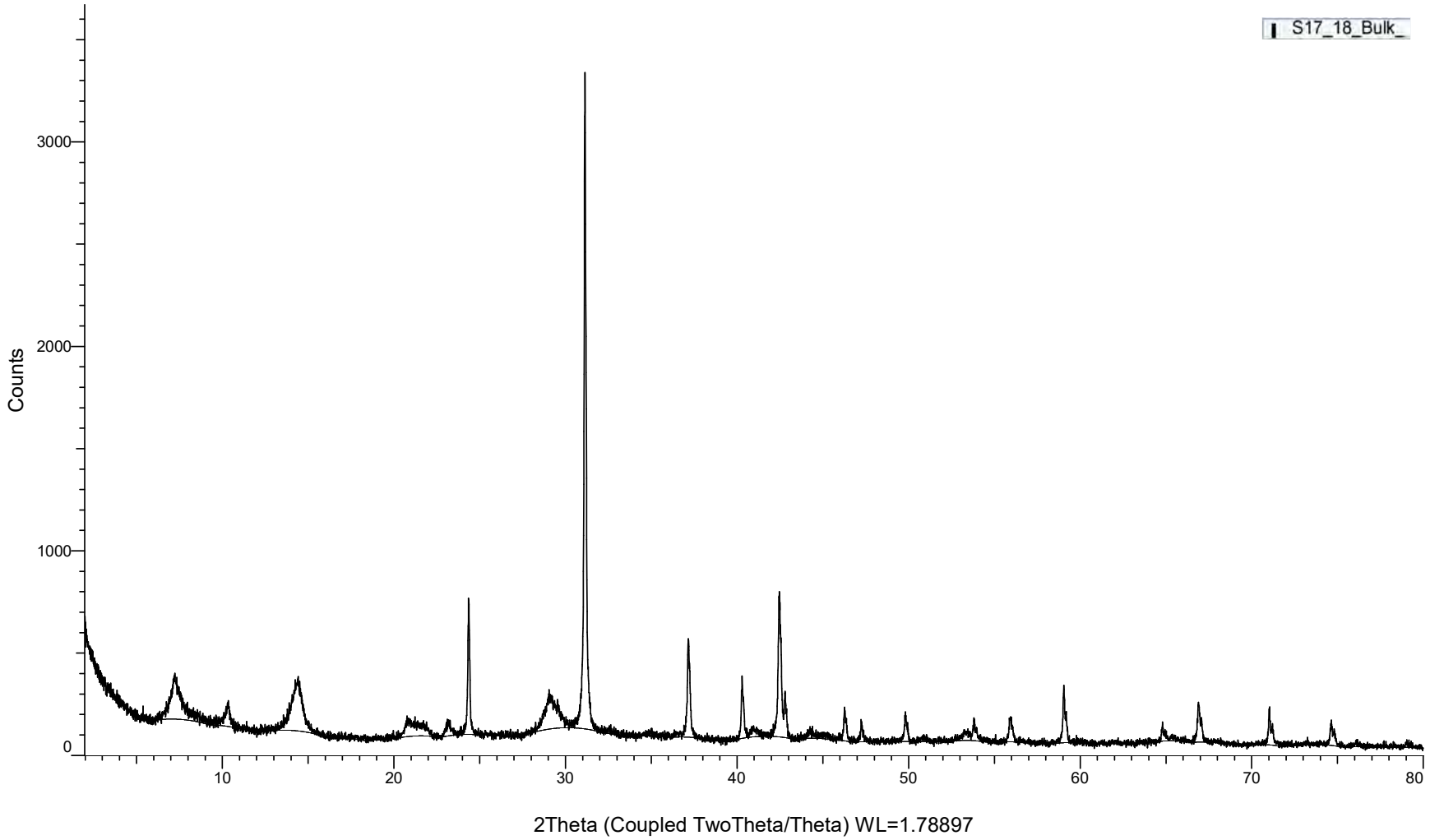

(Coupled TwoTheta/Theta)

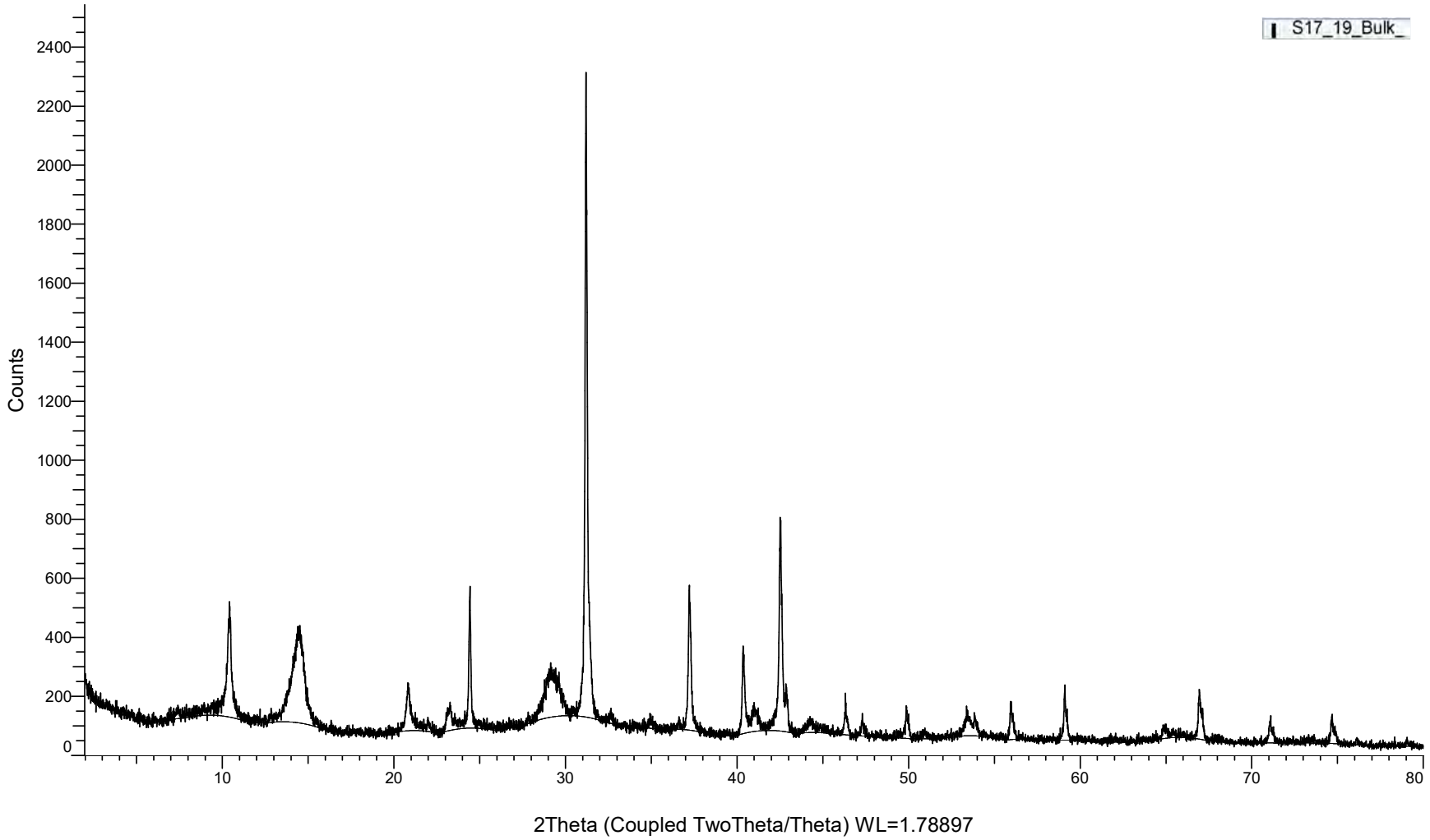

(Coupled TwoTheta/Theta)

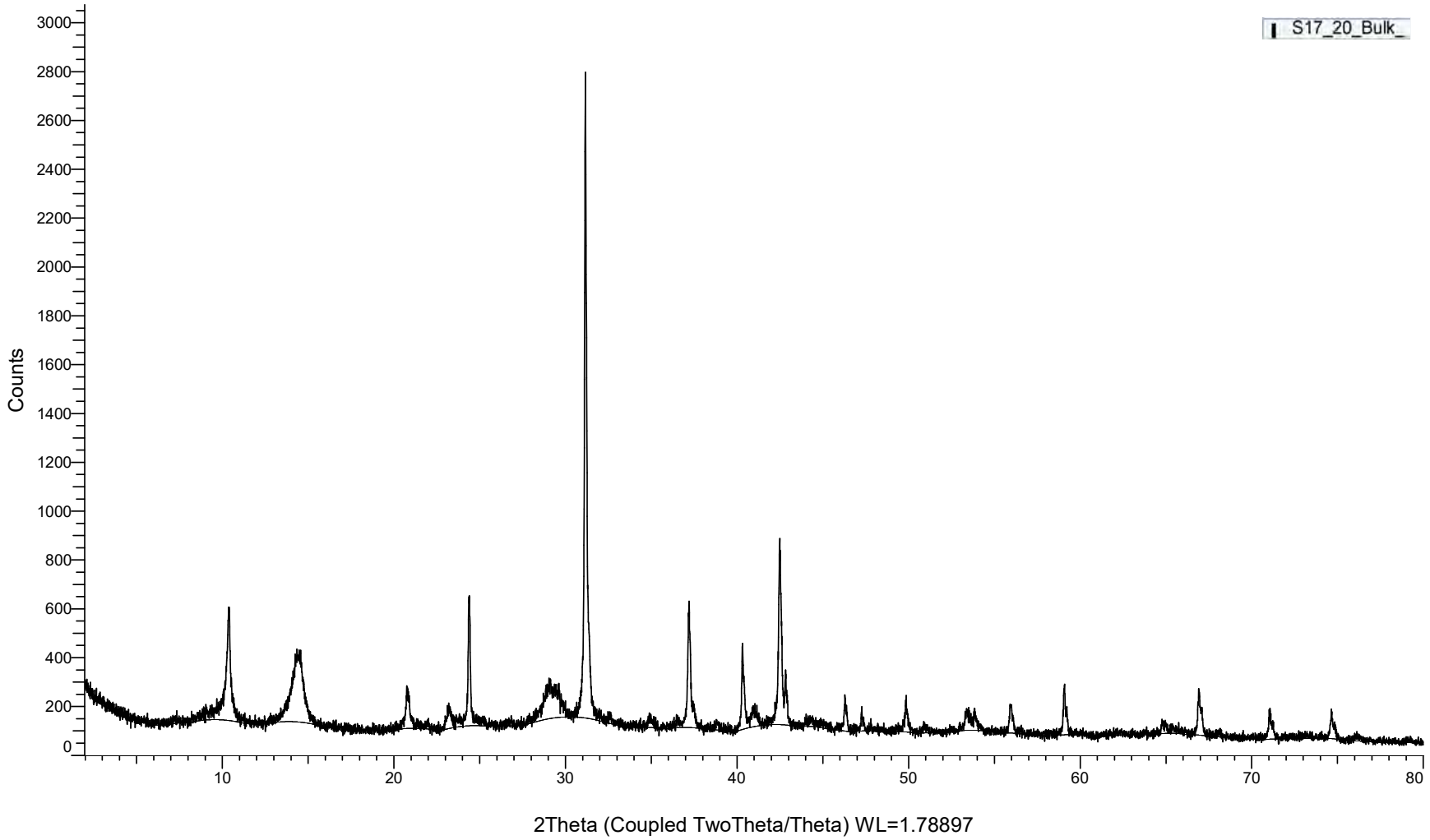

(Coupled TwoTheta/Theta)

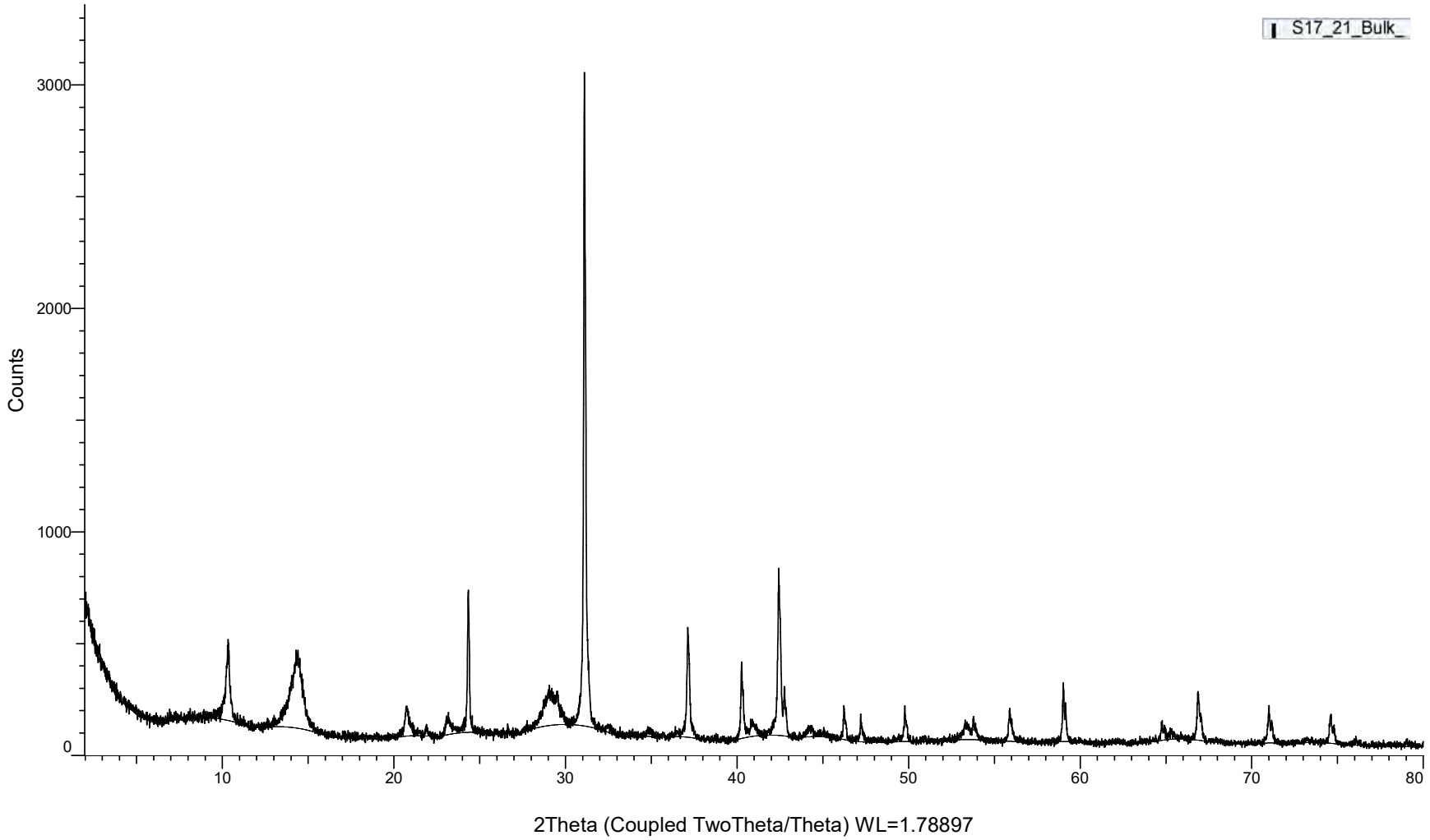

(Coupled TwoTheta/Theta)

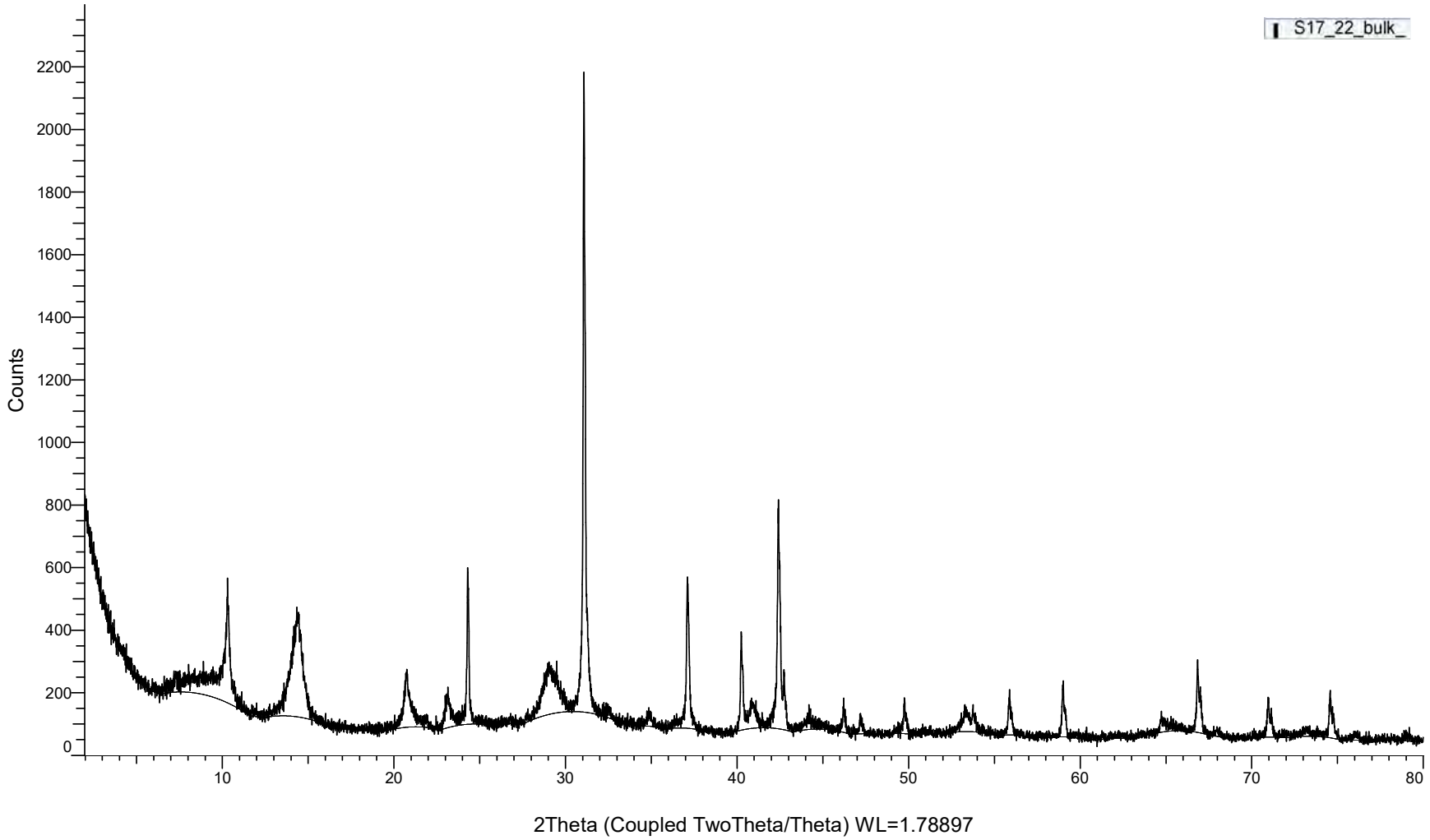

(Coupled TwoTheta/Theta)

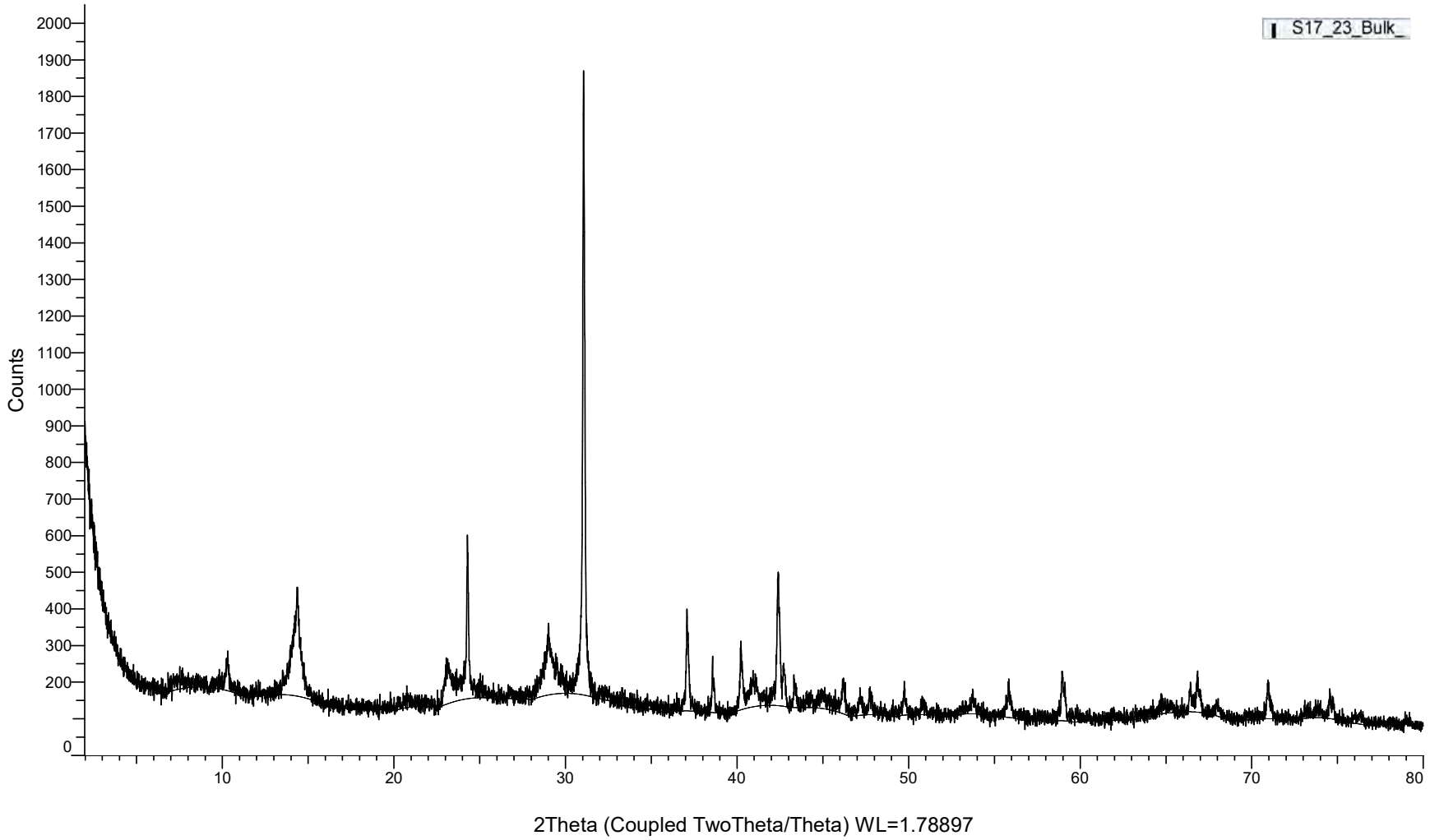

(Coupled TwoTheta/Theta)

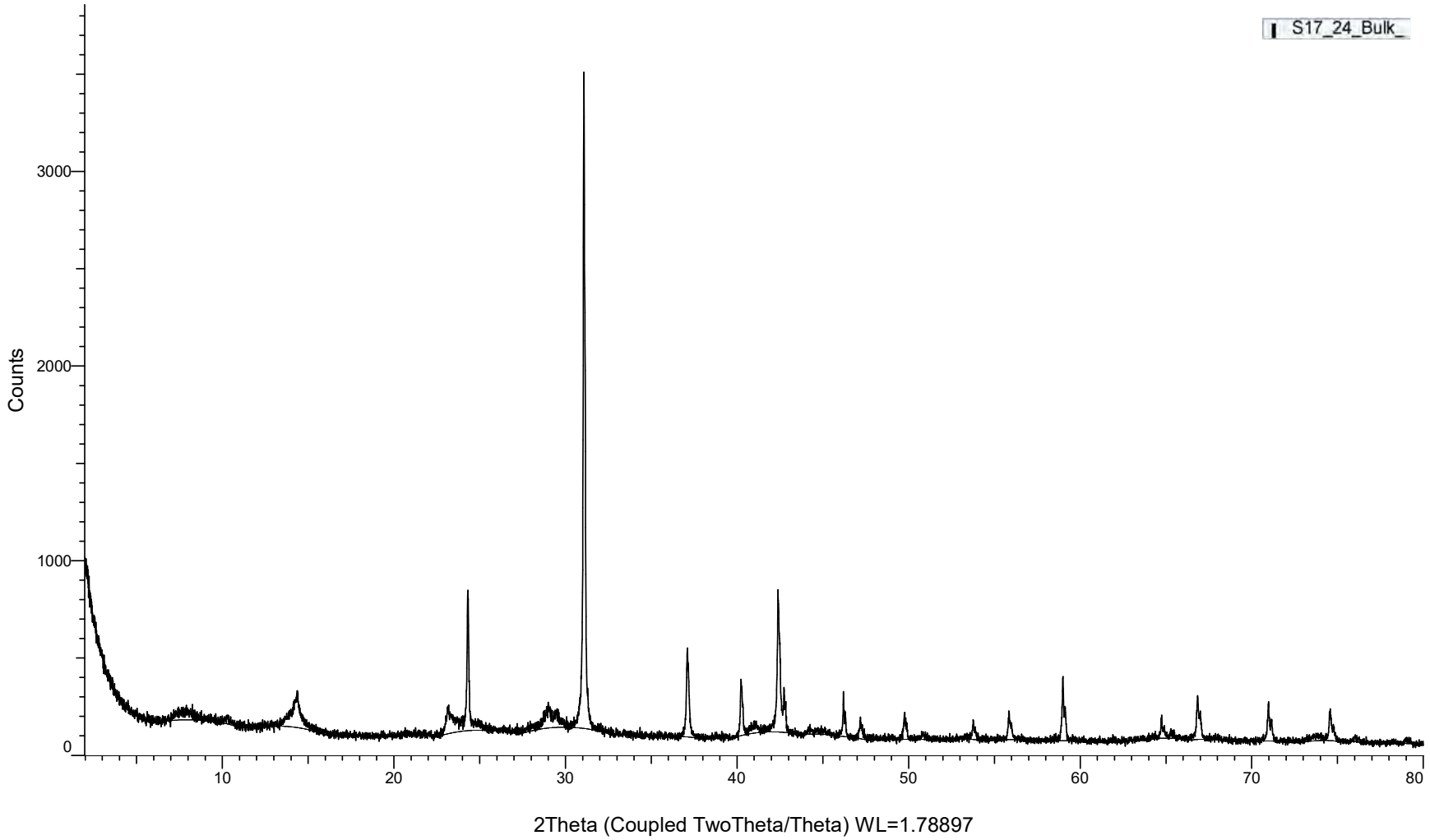

(Coupled TwoTheta/Theta)

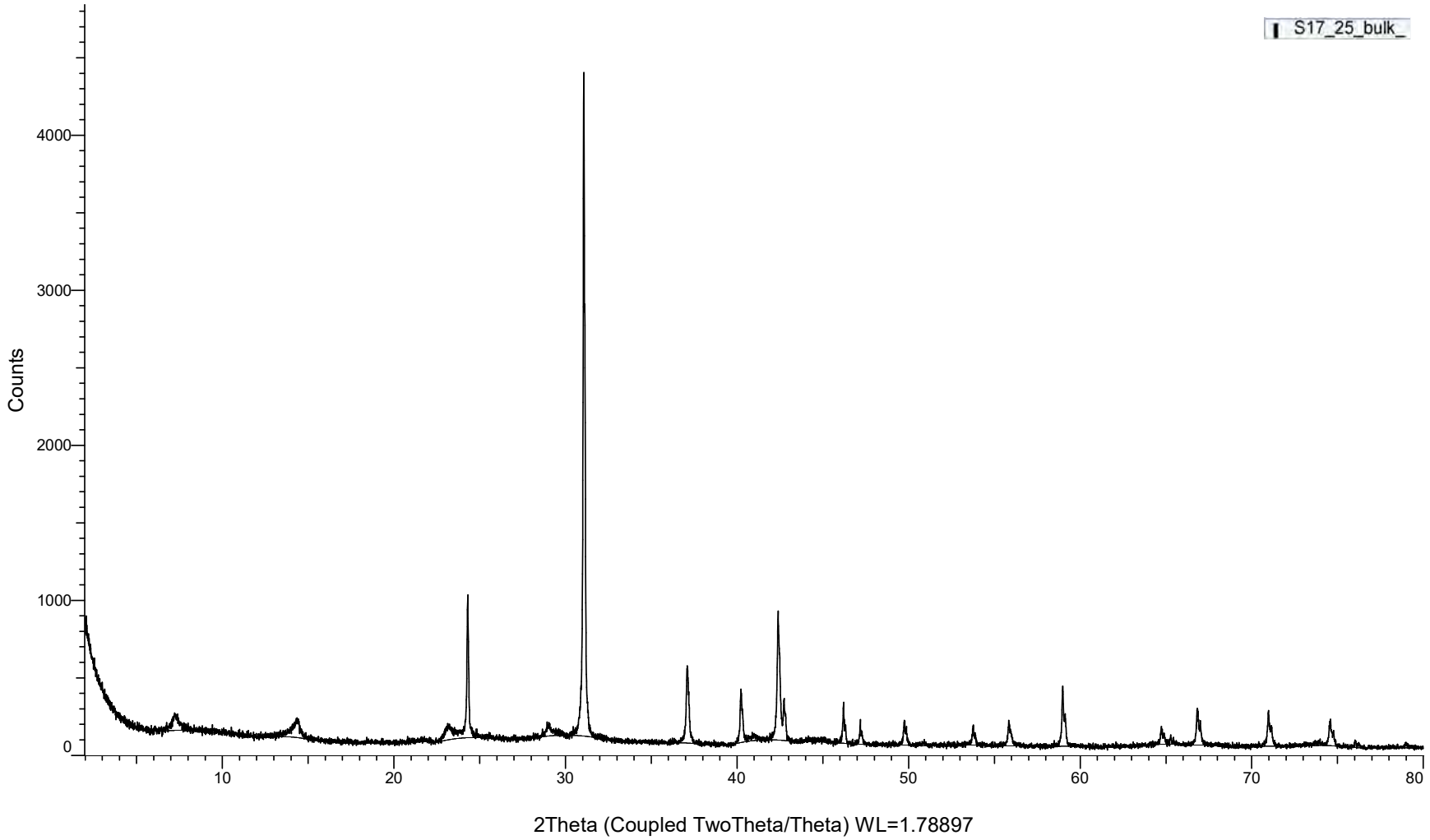

(Coupled TwoTheta/Theta)

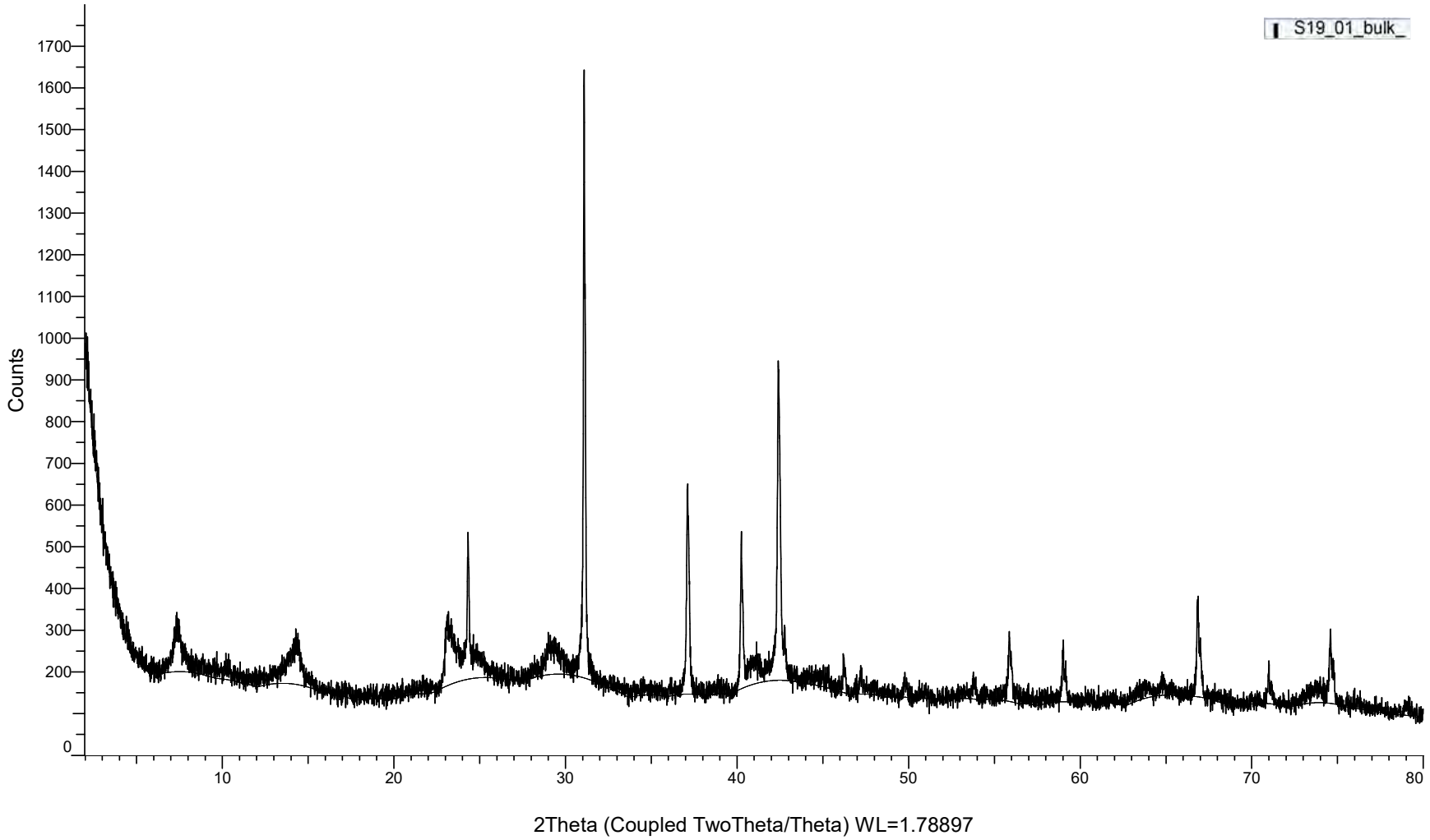

(Coupled TwoTheta/Theta)

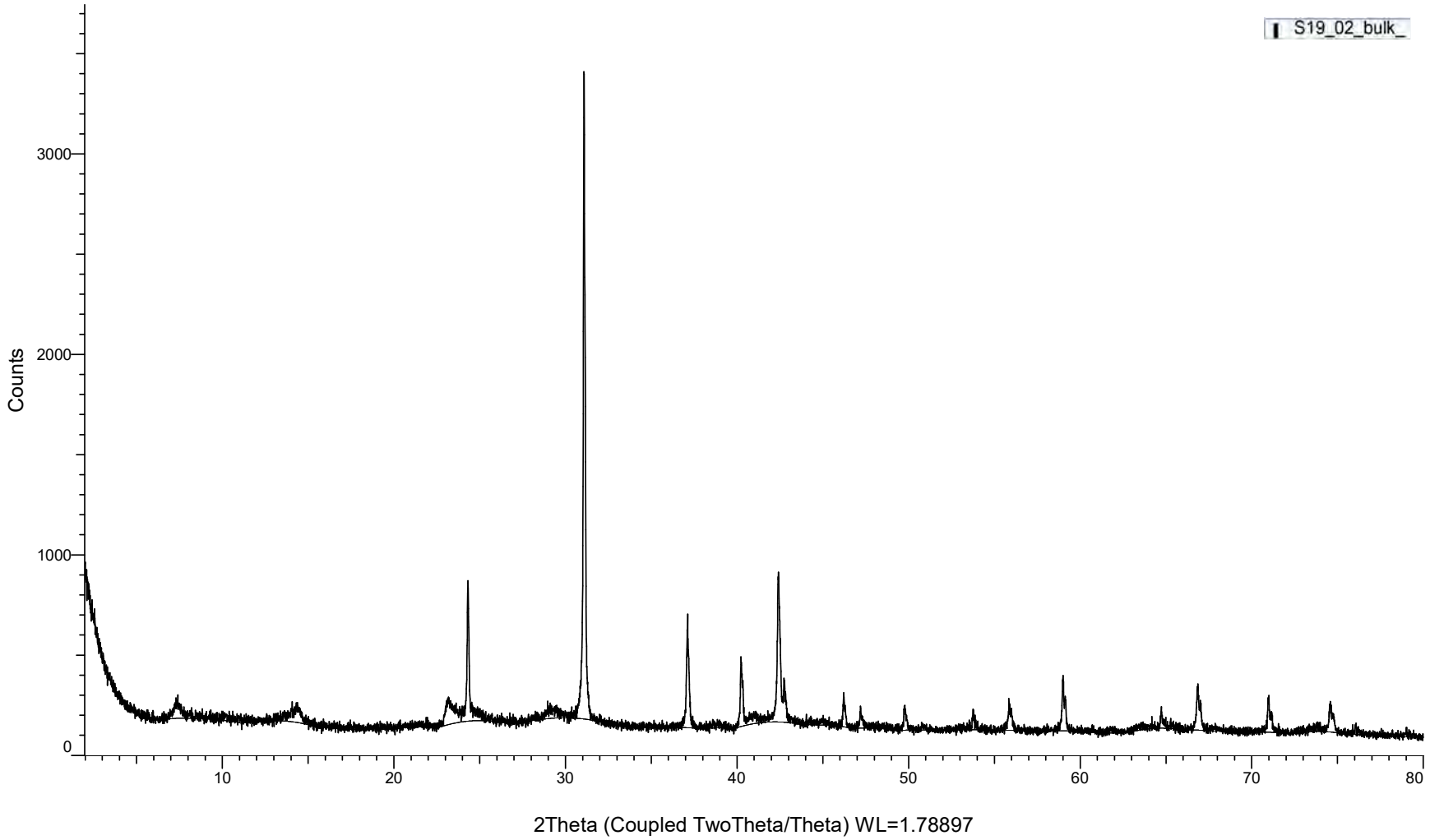

(Coupled TwoTheta/Theta)

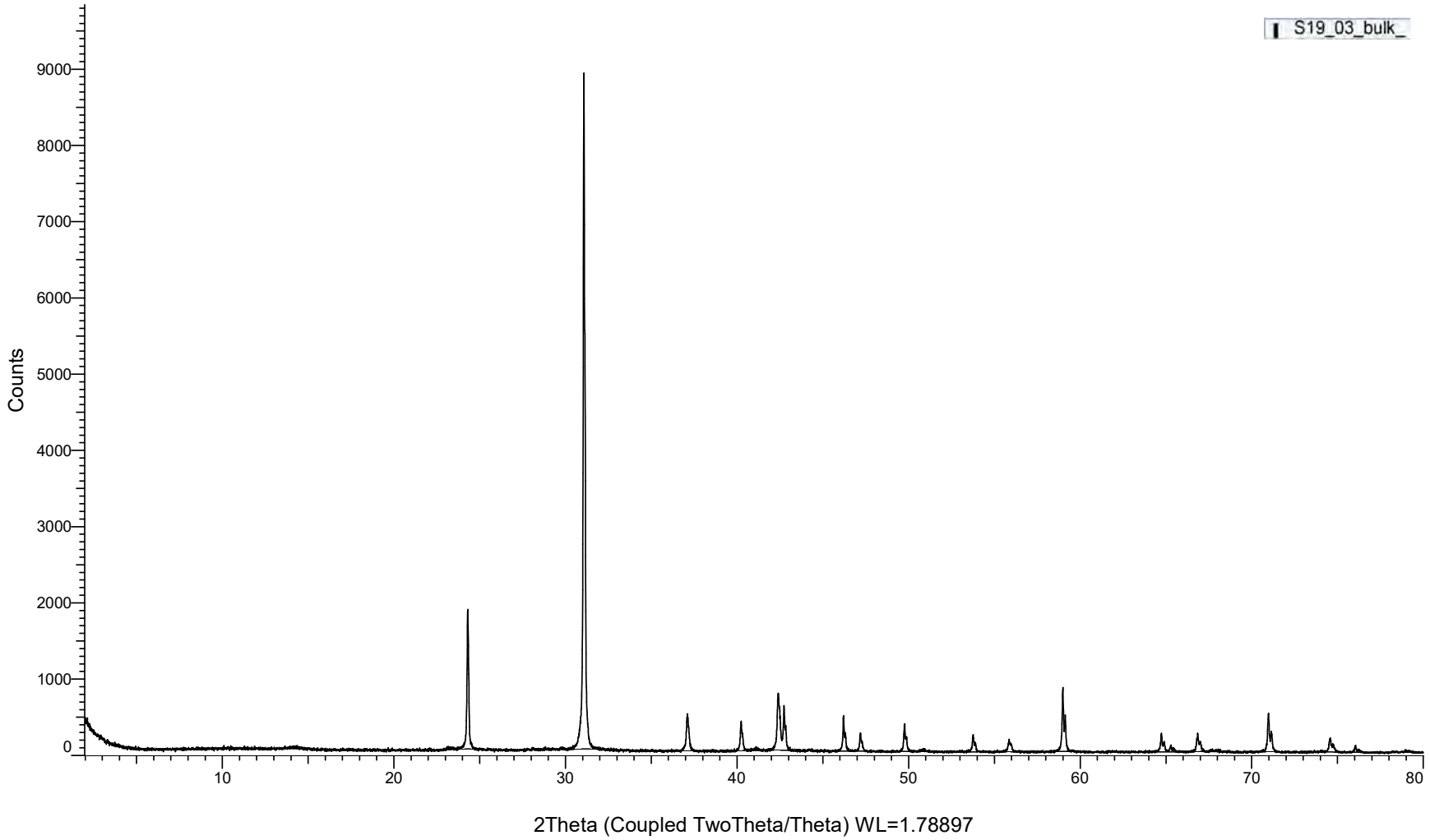

(Coupled TwoTheta/Theta)

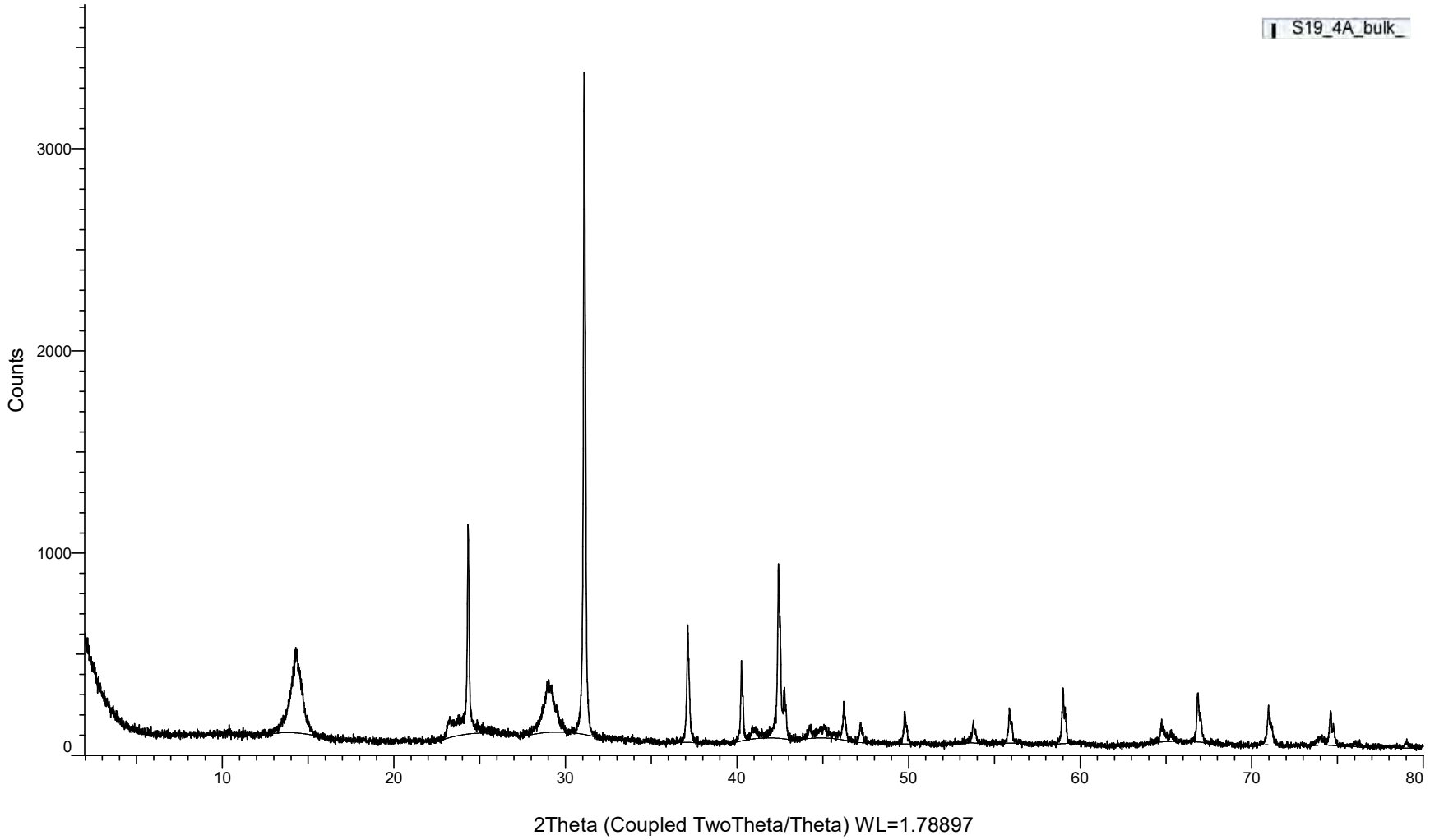

(Coupled TwoTheta/Theta)

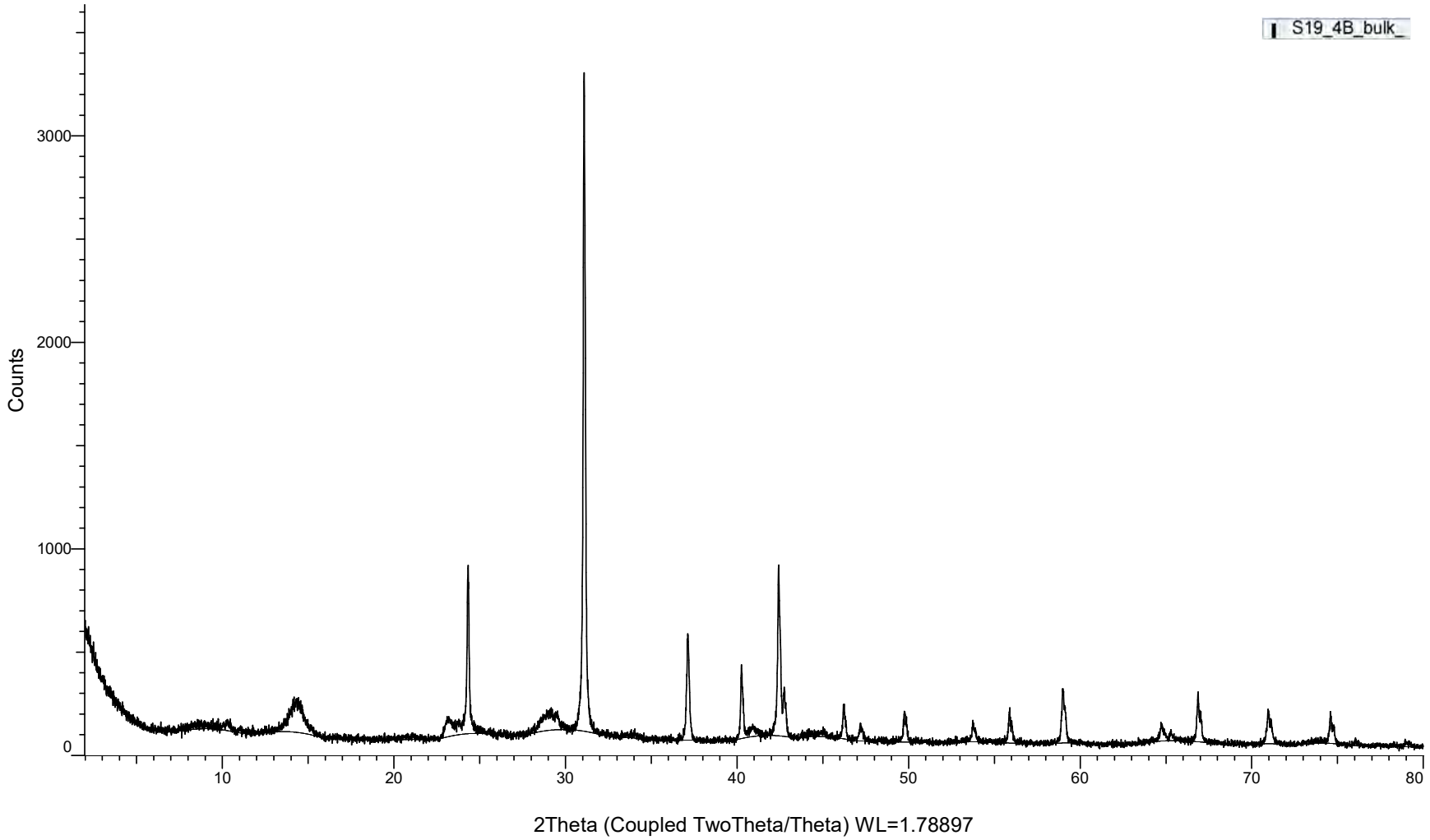

(Coupled TwoTheta/Theta)

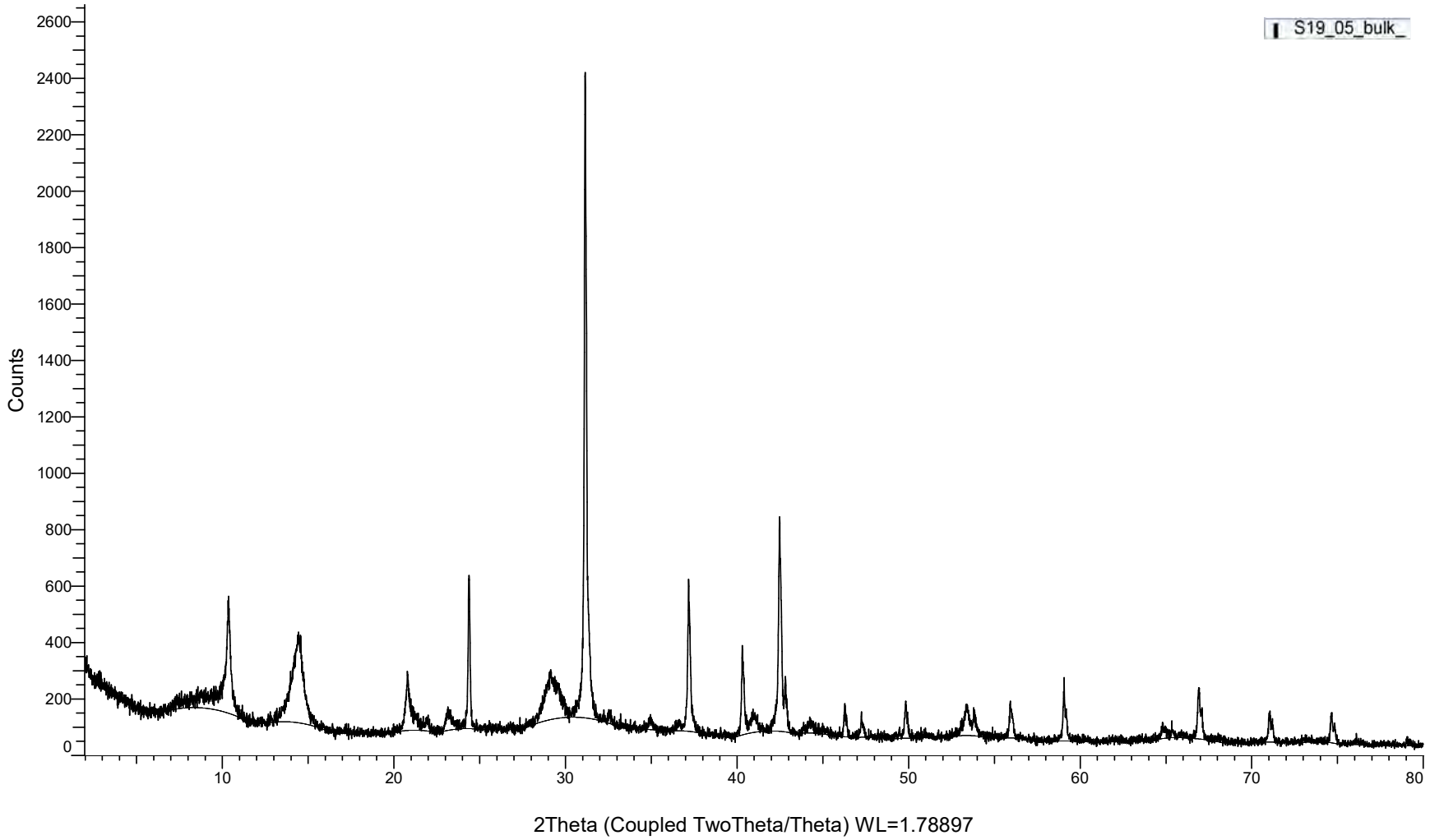

(Coupled TwoTheta/Theta)

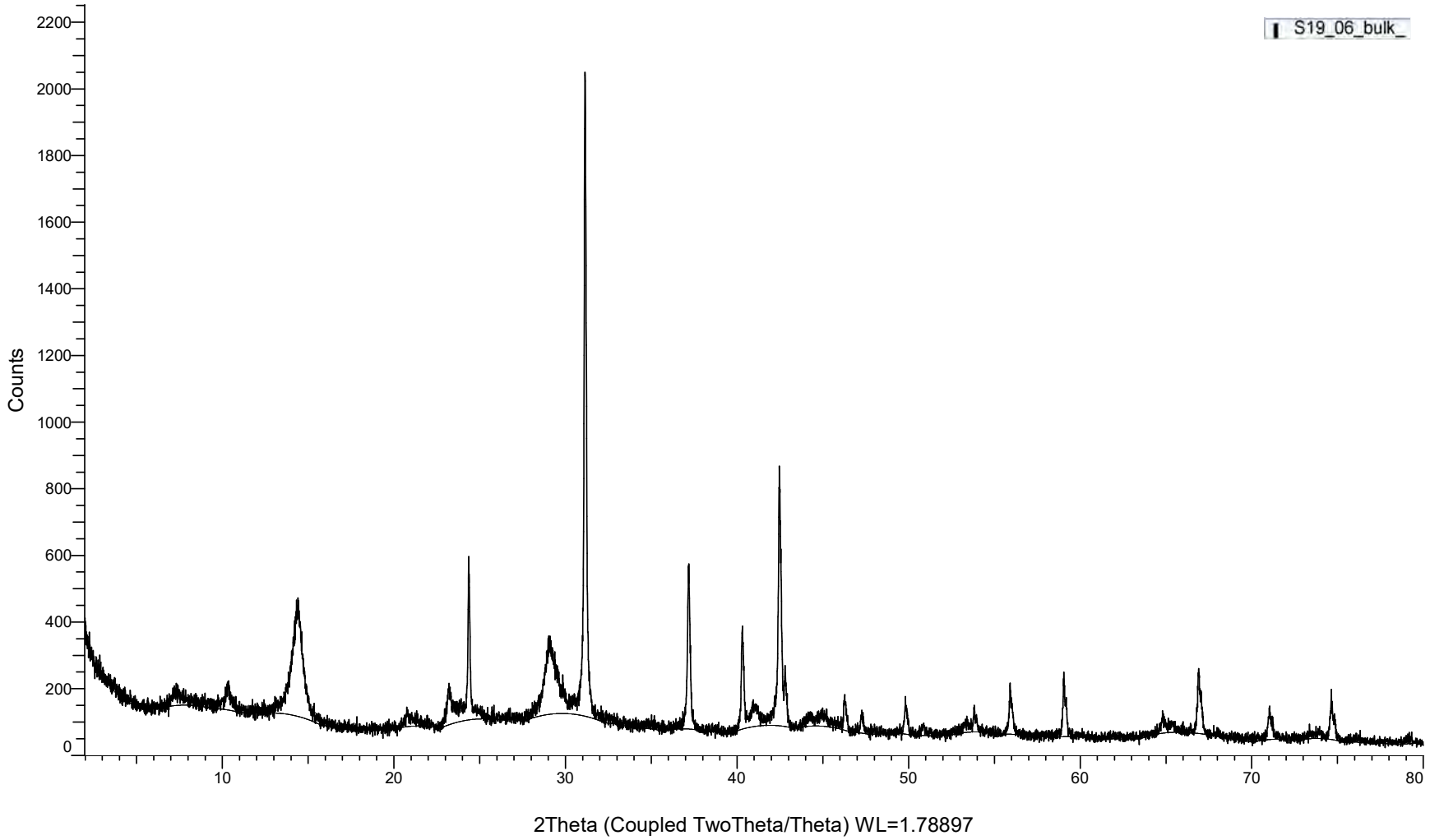

(Coupled TwoTheta/Theta)

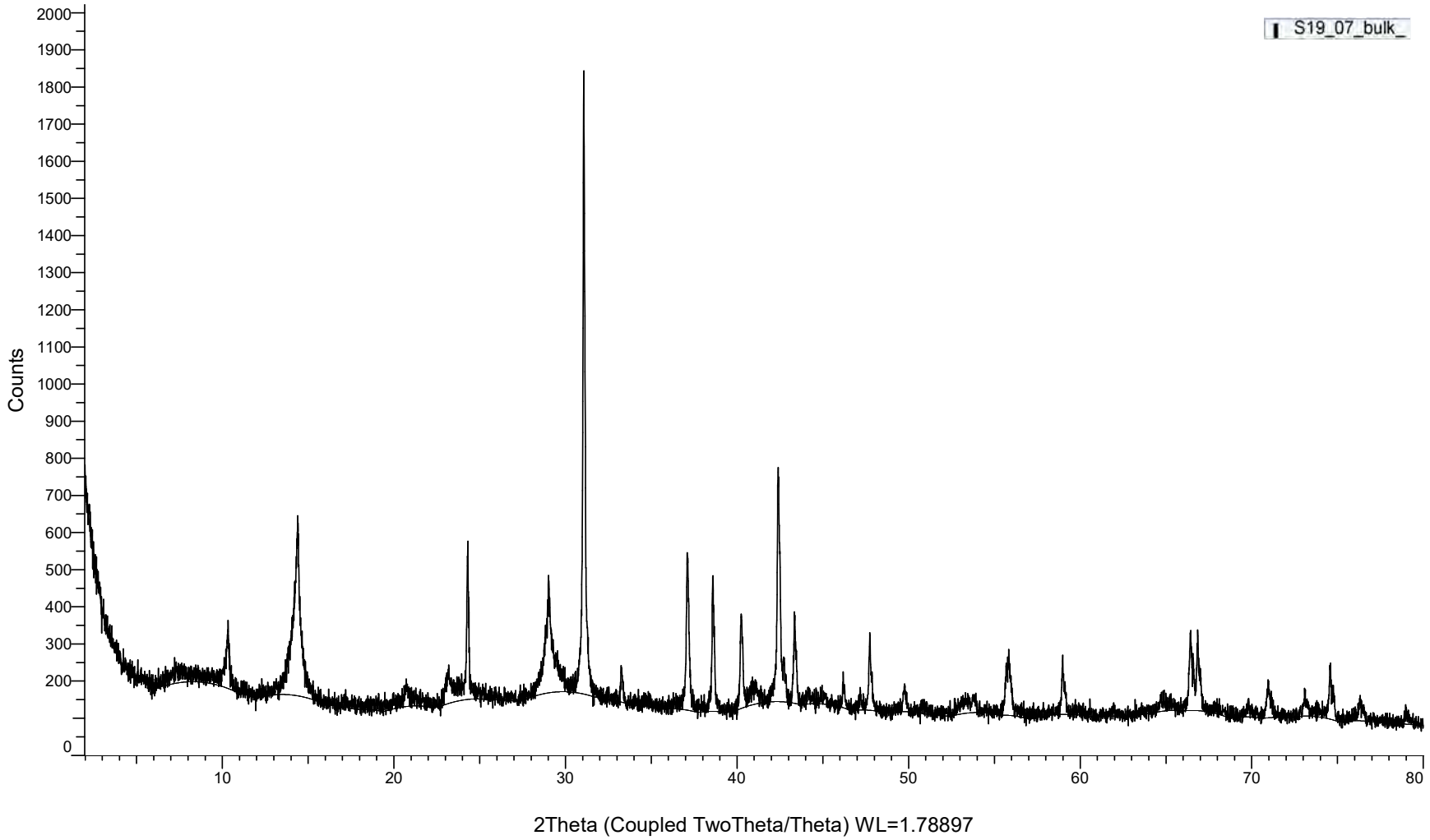

(Coupled TwoTheta/Theta)

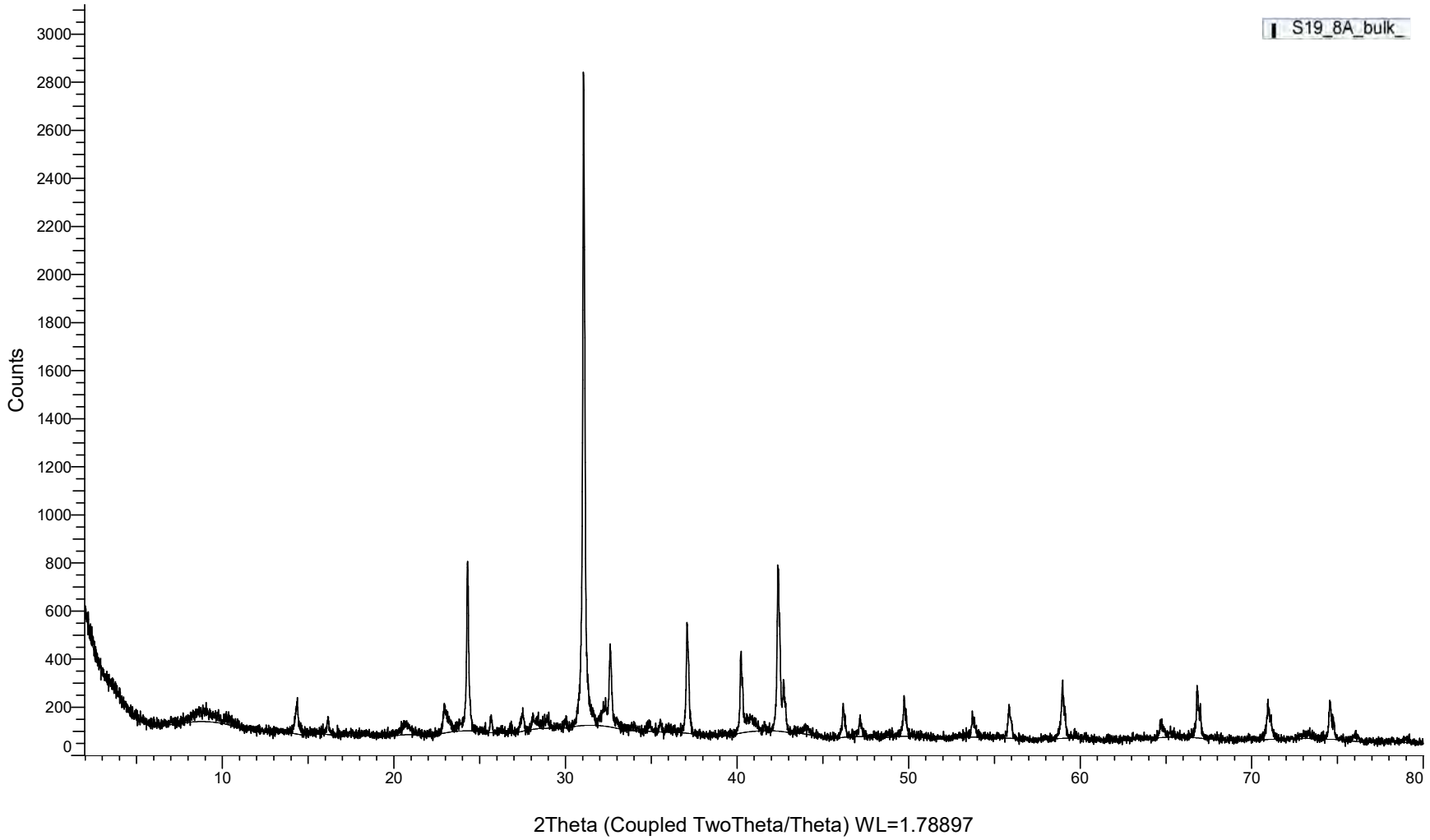

(Coupled TwoTheta/Theta)

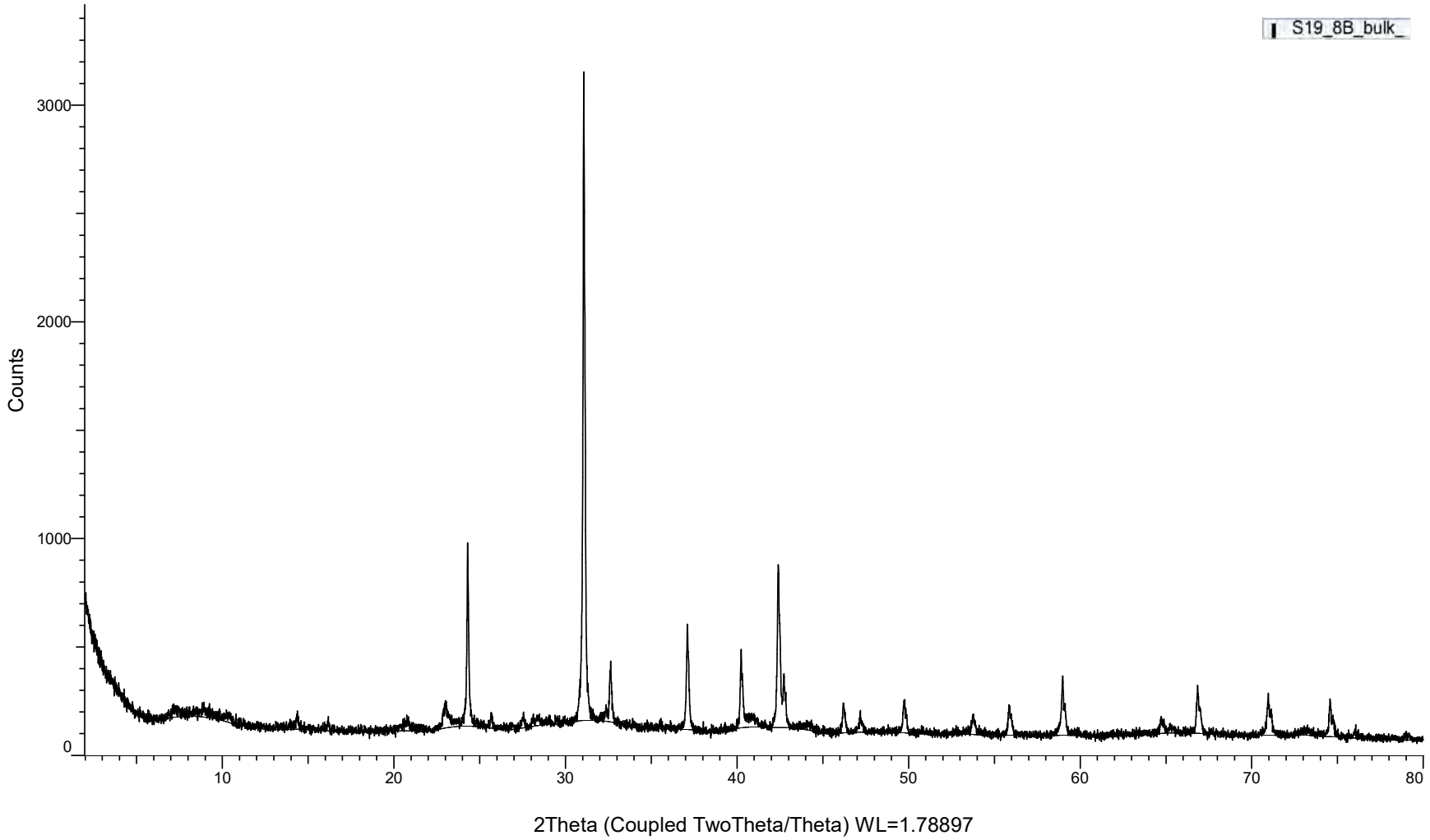

(Coupled TwoTheta/Theta)

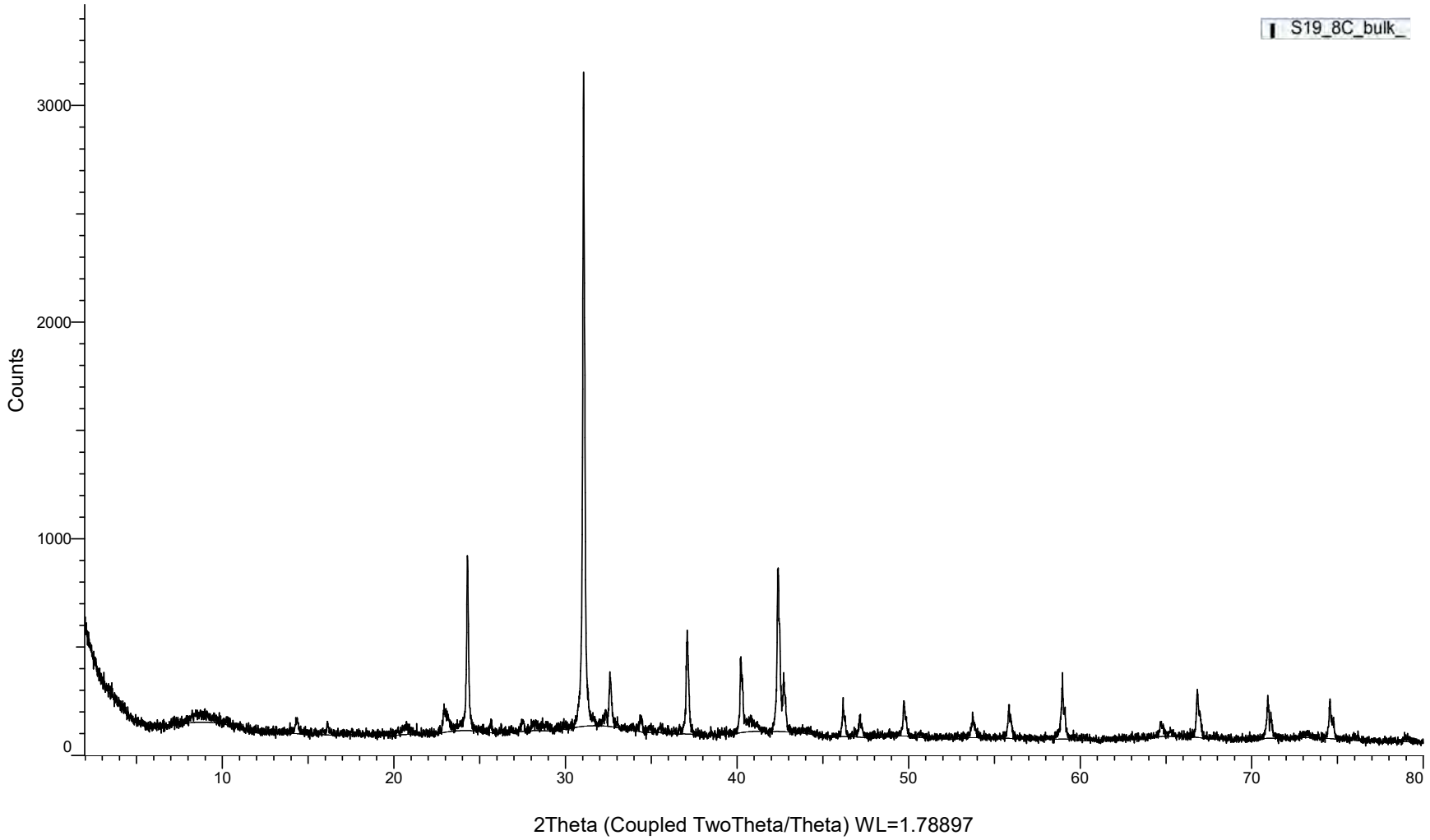

(Coupled TwoTheta/Theta)

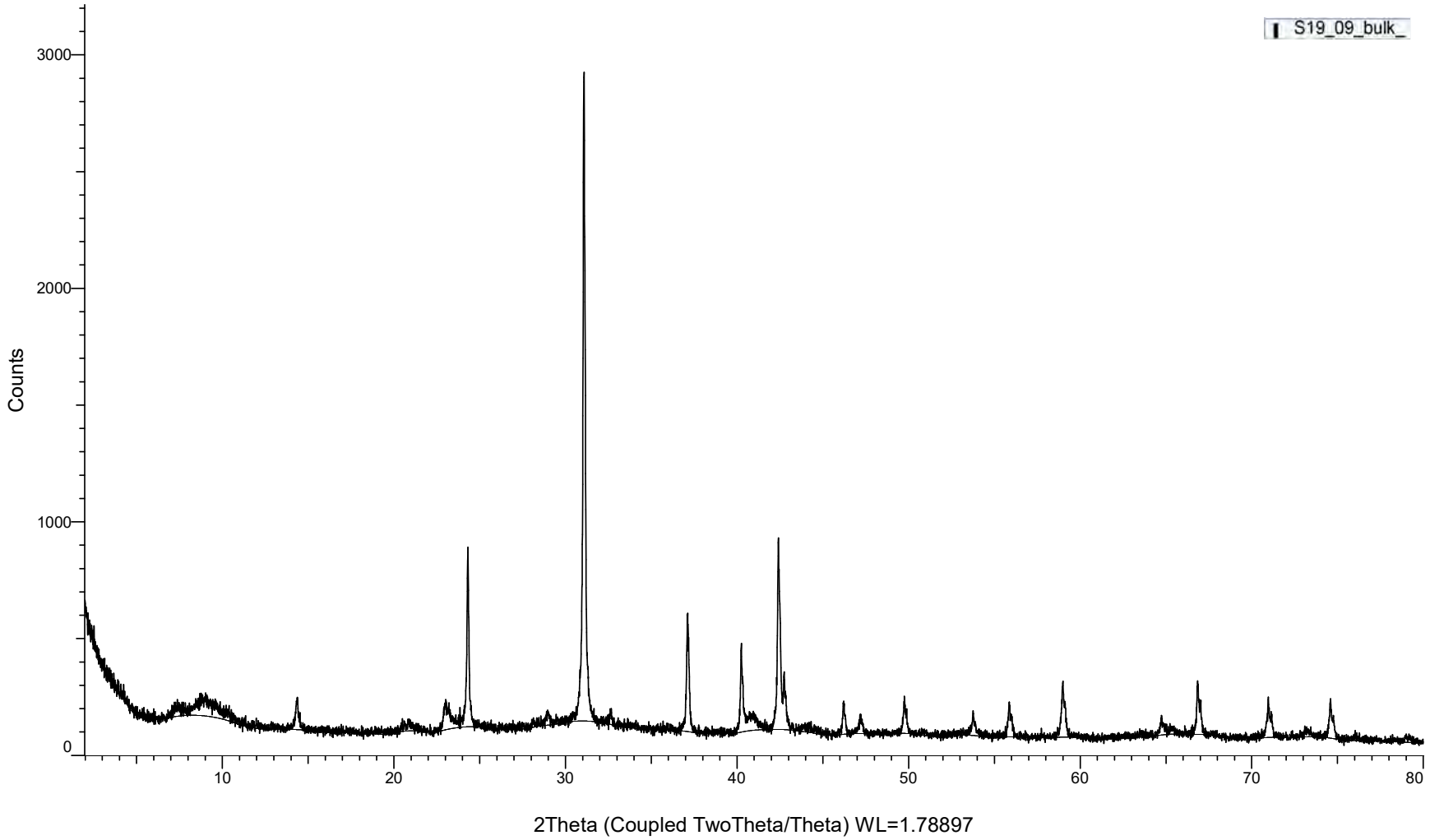

(Coupled TwoTheta/Theta)

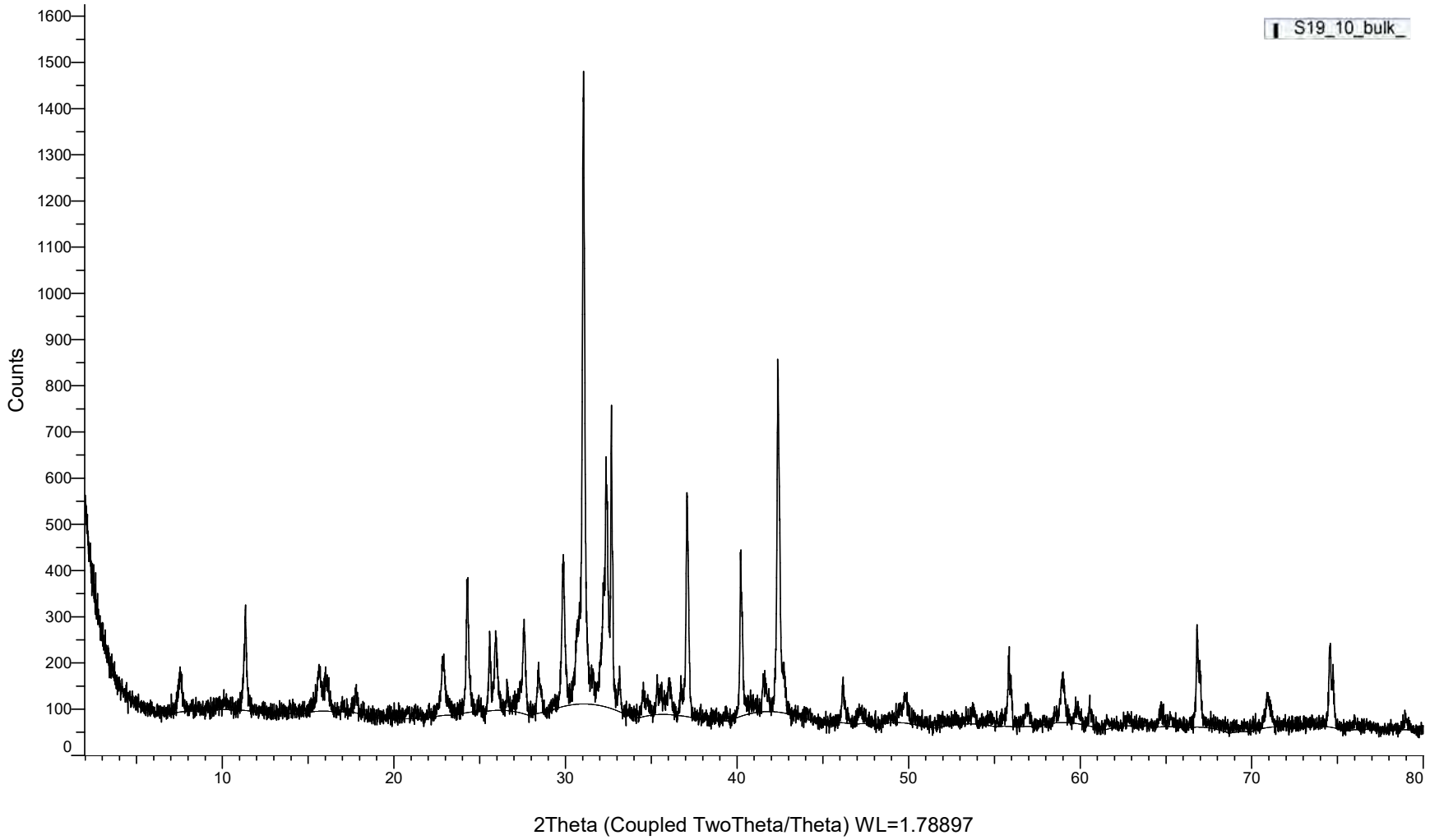

(Coupled TwoTheta/Theta)

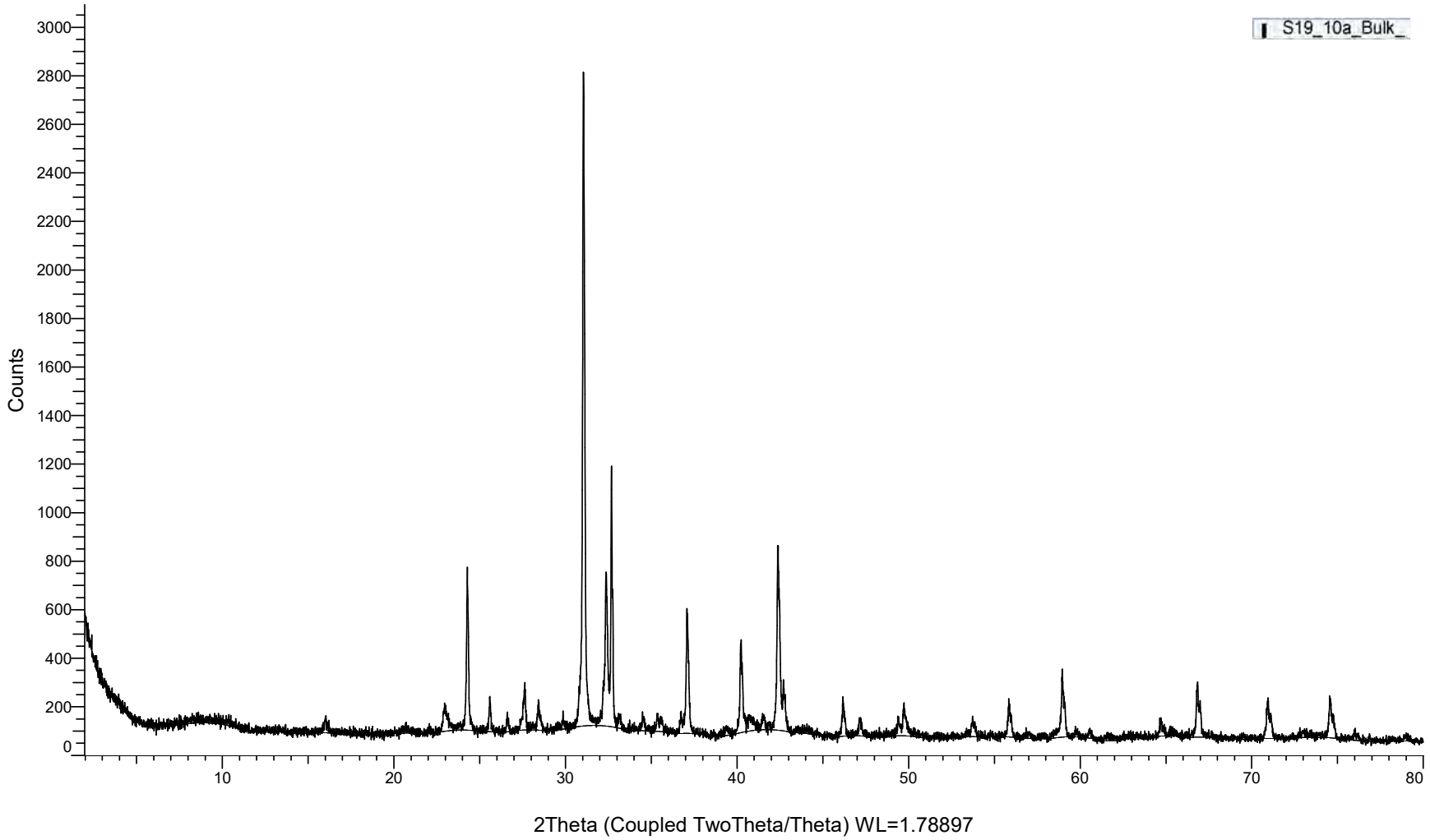

(Coupled TwoTheta/Theta)

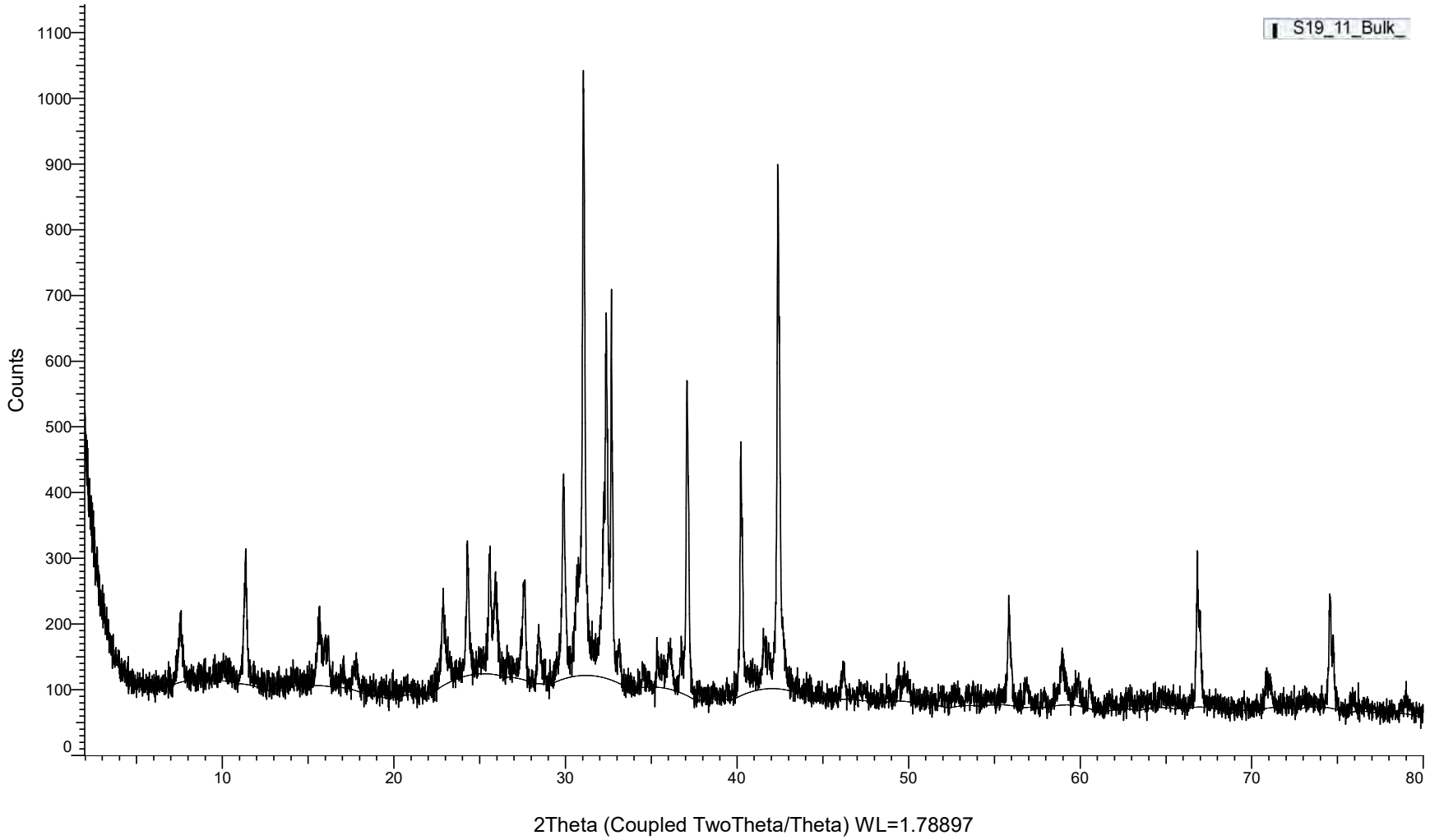

(Coupled TwoTheta/Theta)

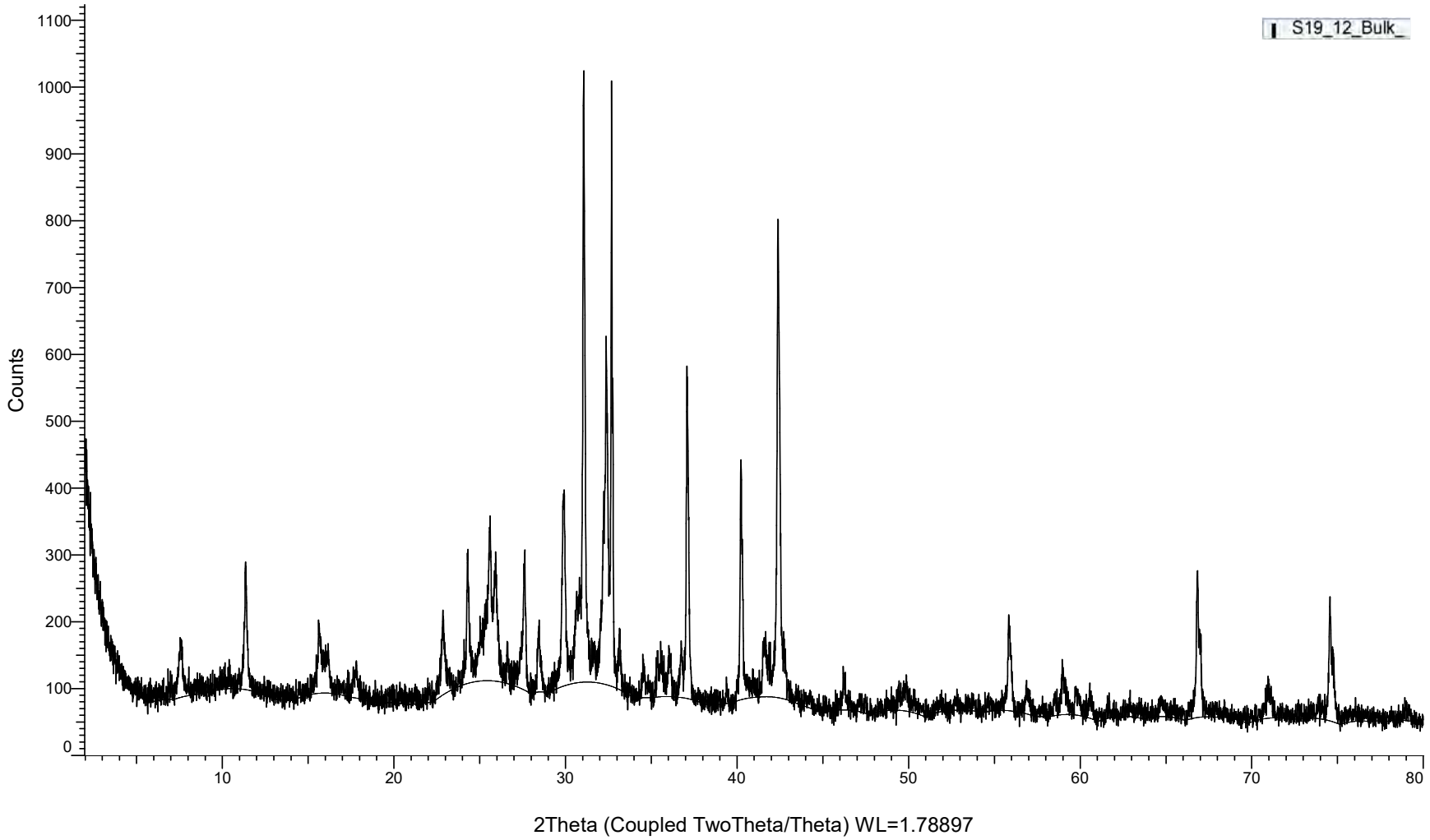

(Coupled TwoTheta/Theta)

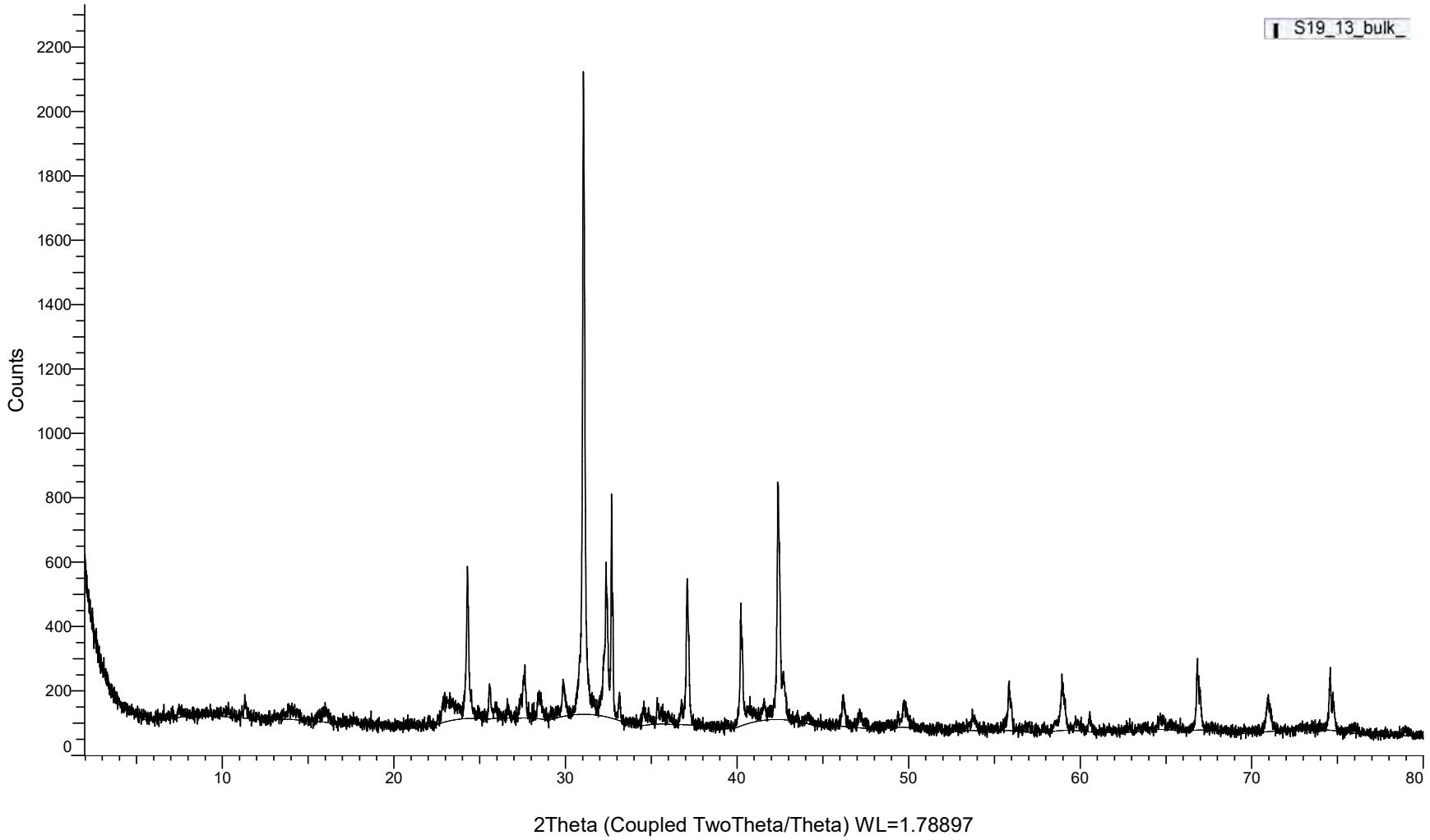

(Coupled TwoTheta/Theta)

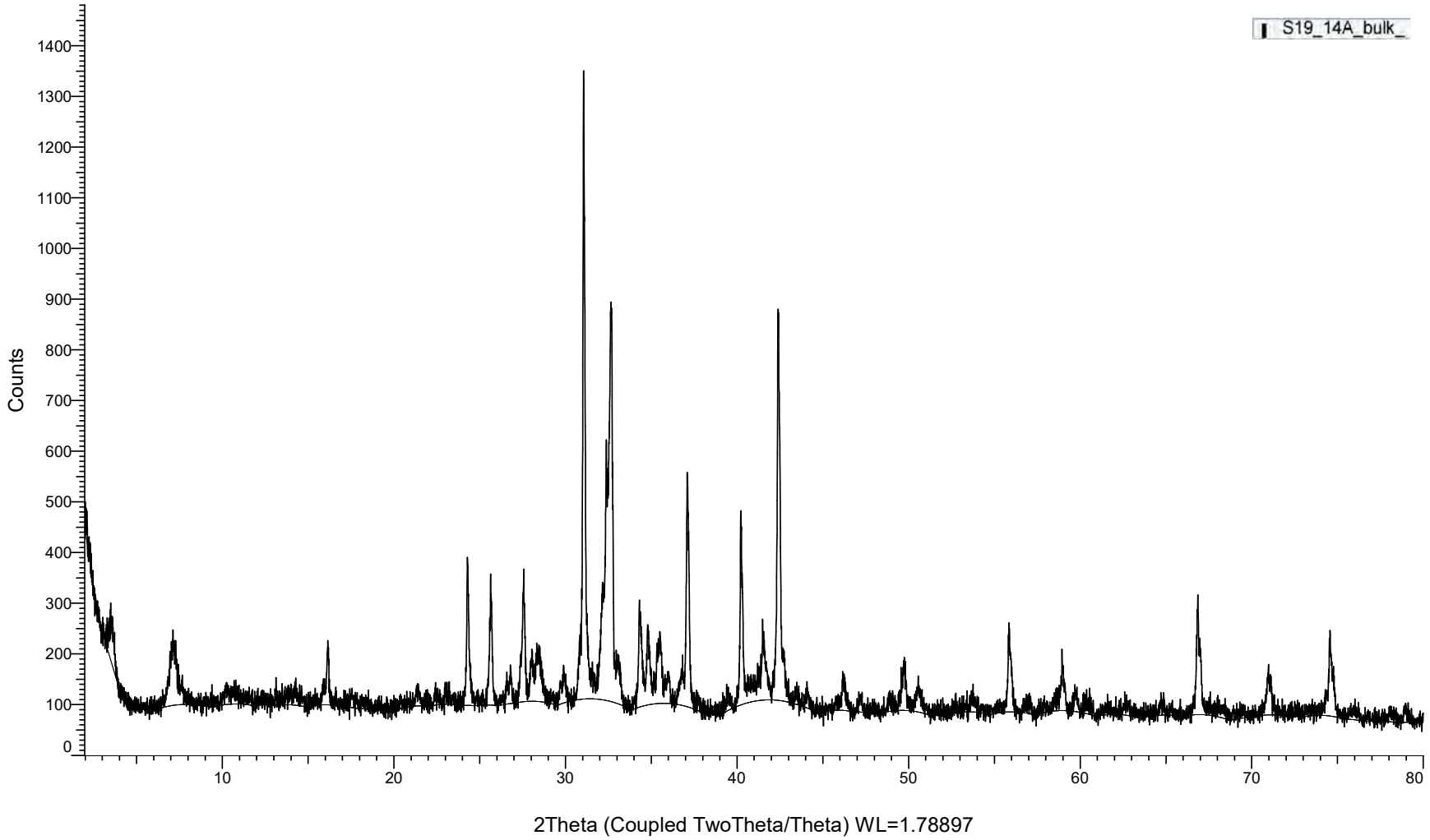

(Coupled TwoTheta/Theta)

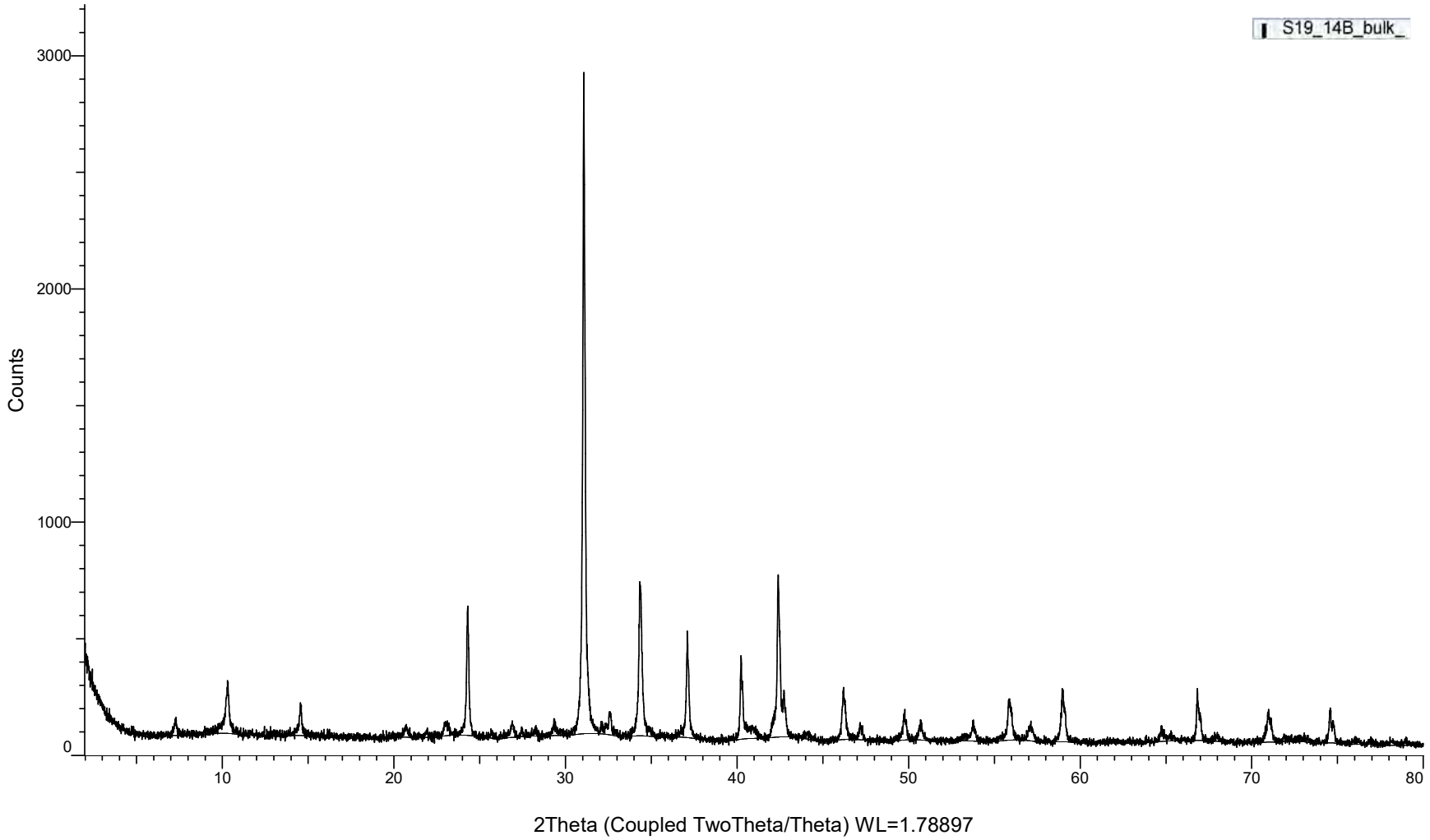

(Coupled TwoTheta/Theta)

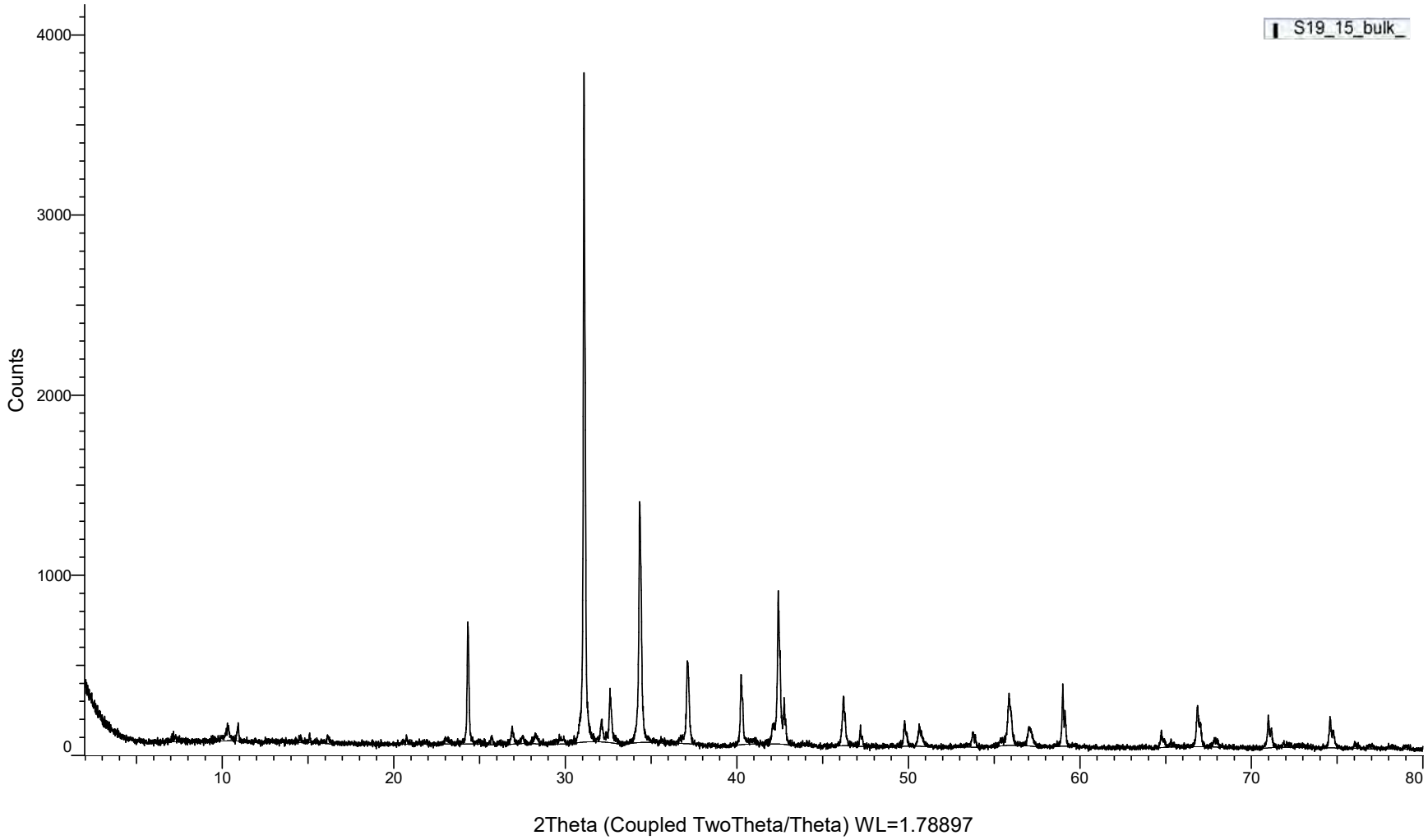

(Coupled TwoTheta/Theta)

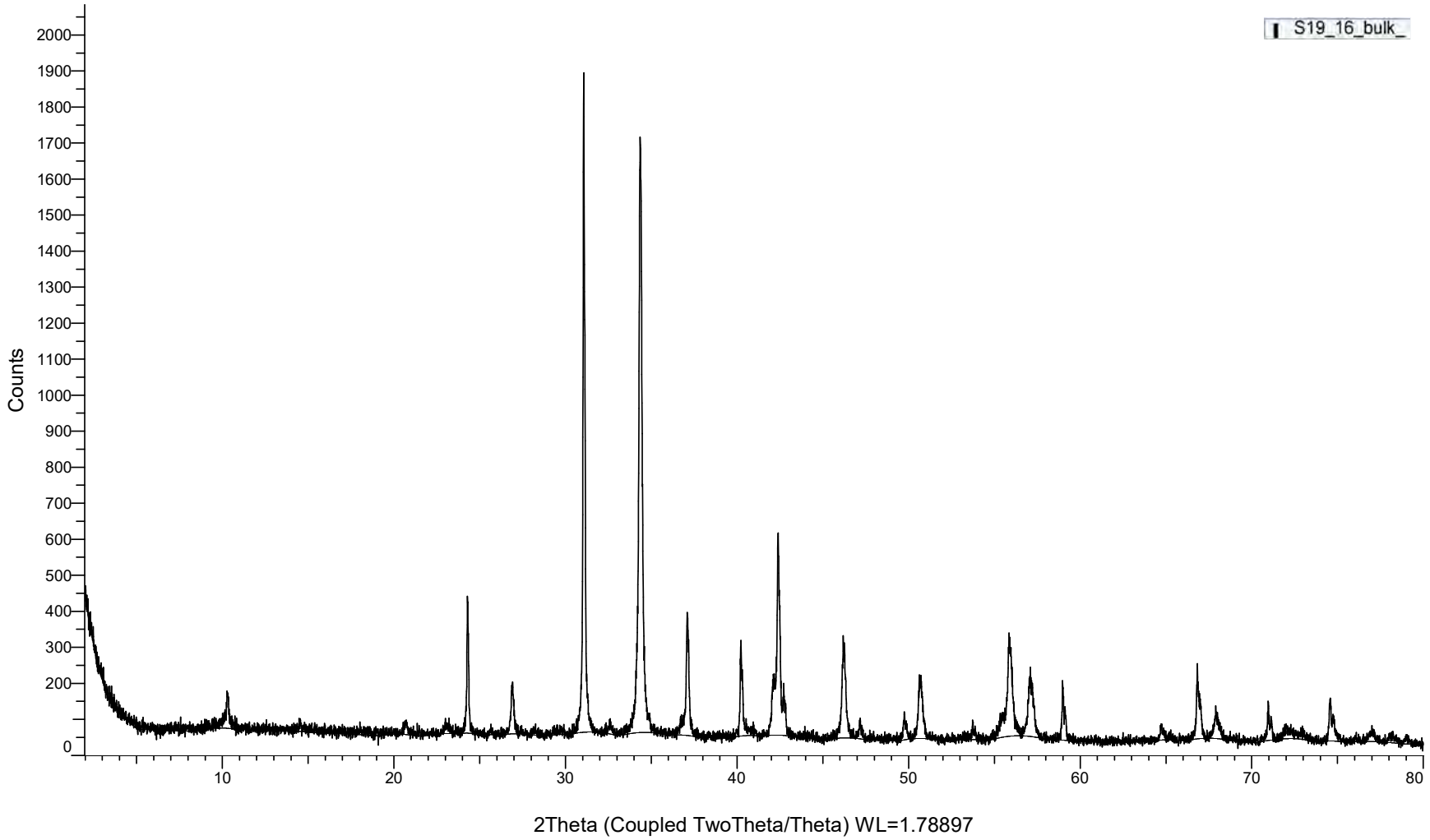

(Coupled TwoTheta/Theta)

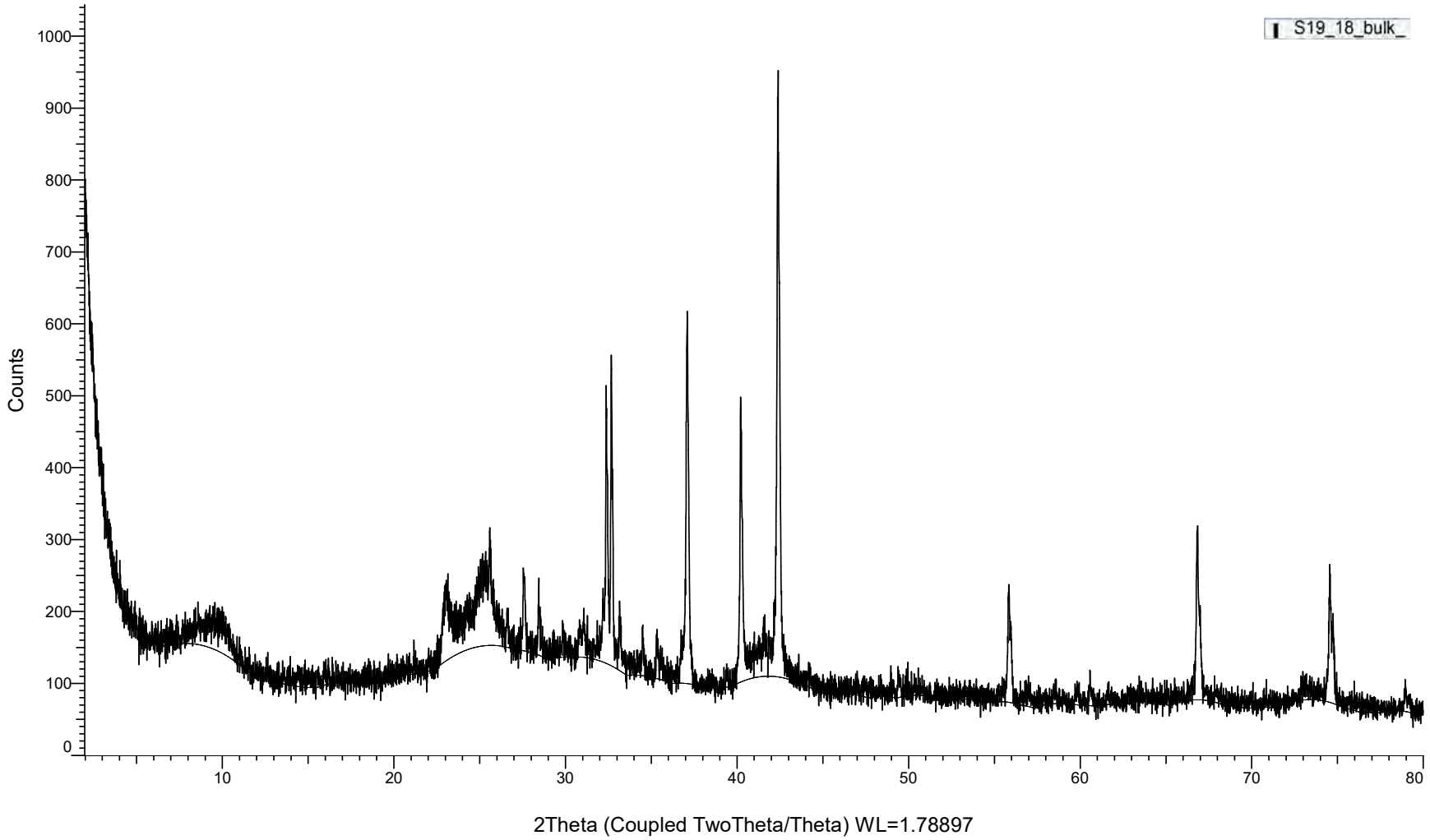

(Coupled TwoTheta/Theta)

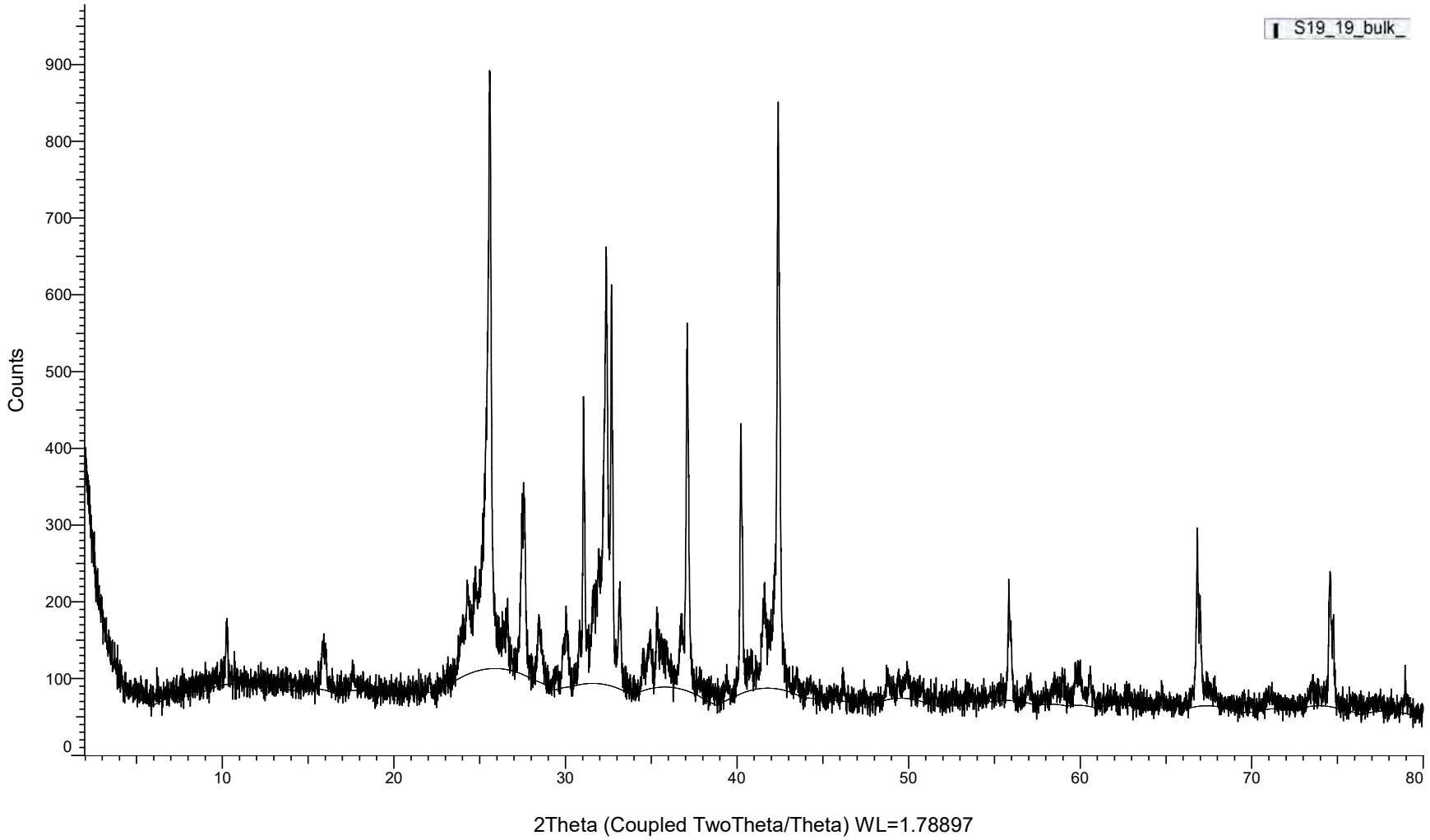

(Coupled TwoTheta/Theta)

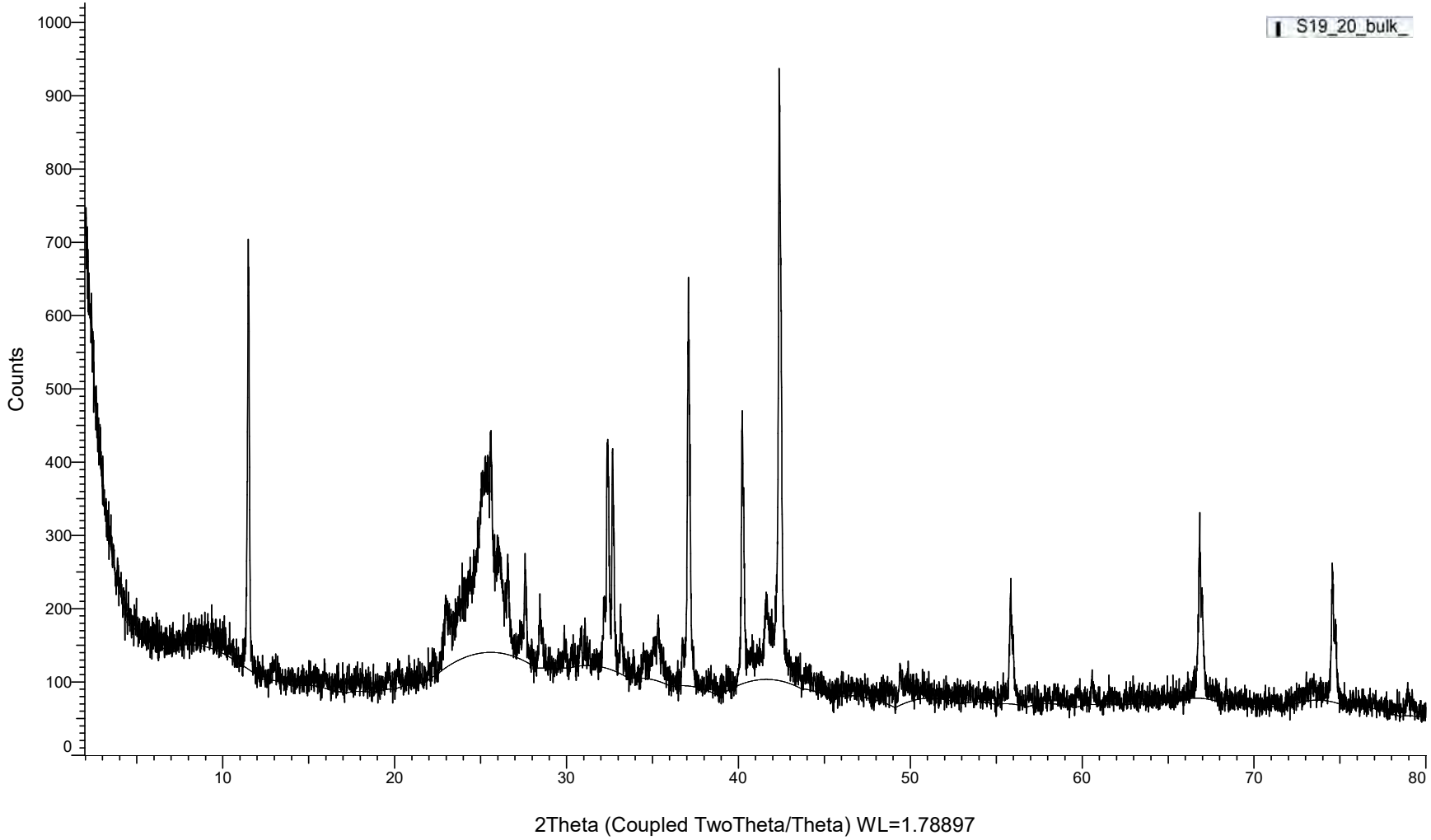

(Coupled TwoTheta/Theta)

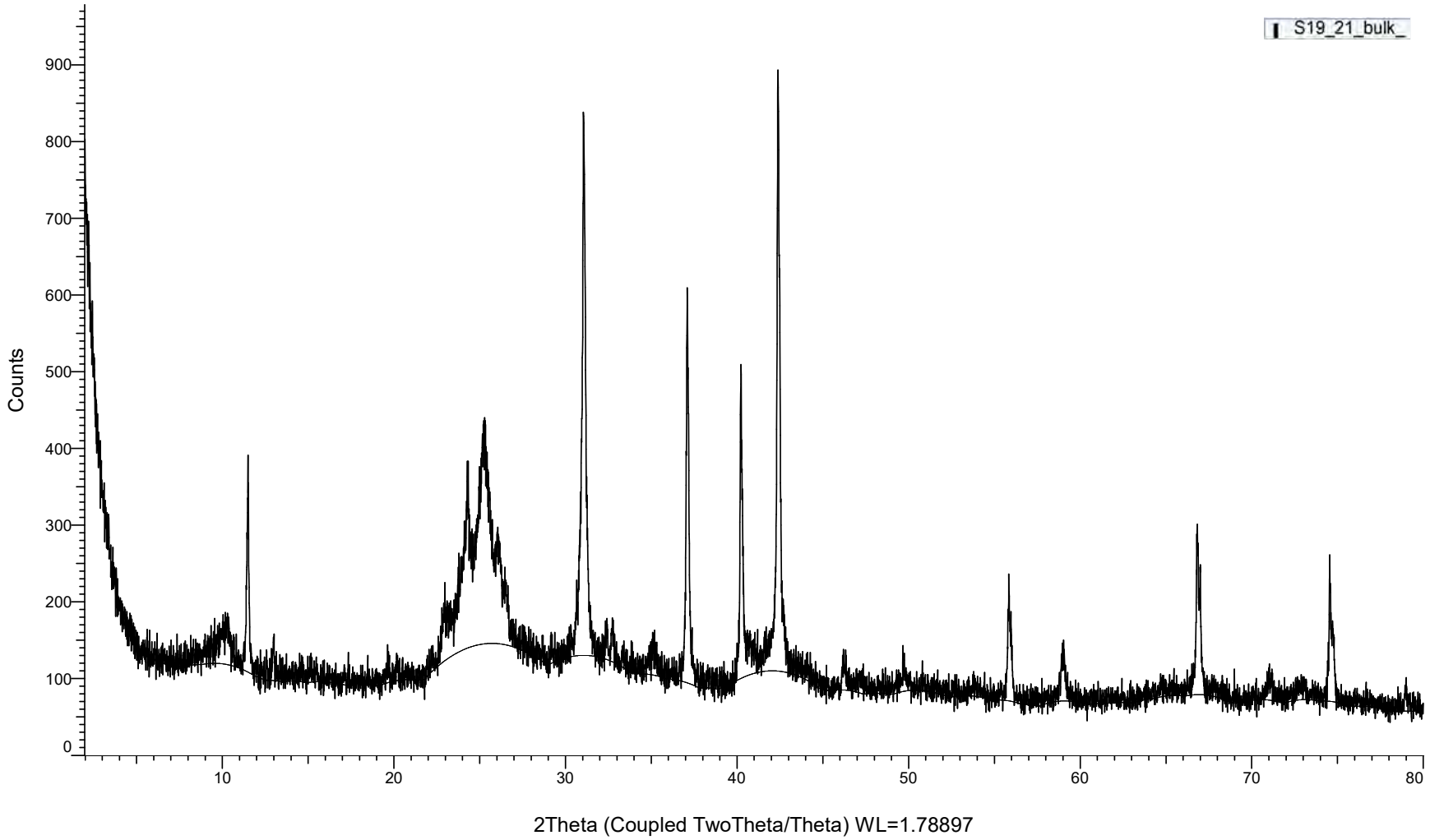

(Coupled TwoTheta/Theta)

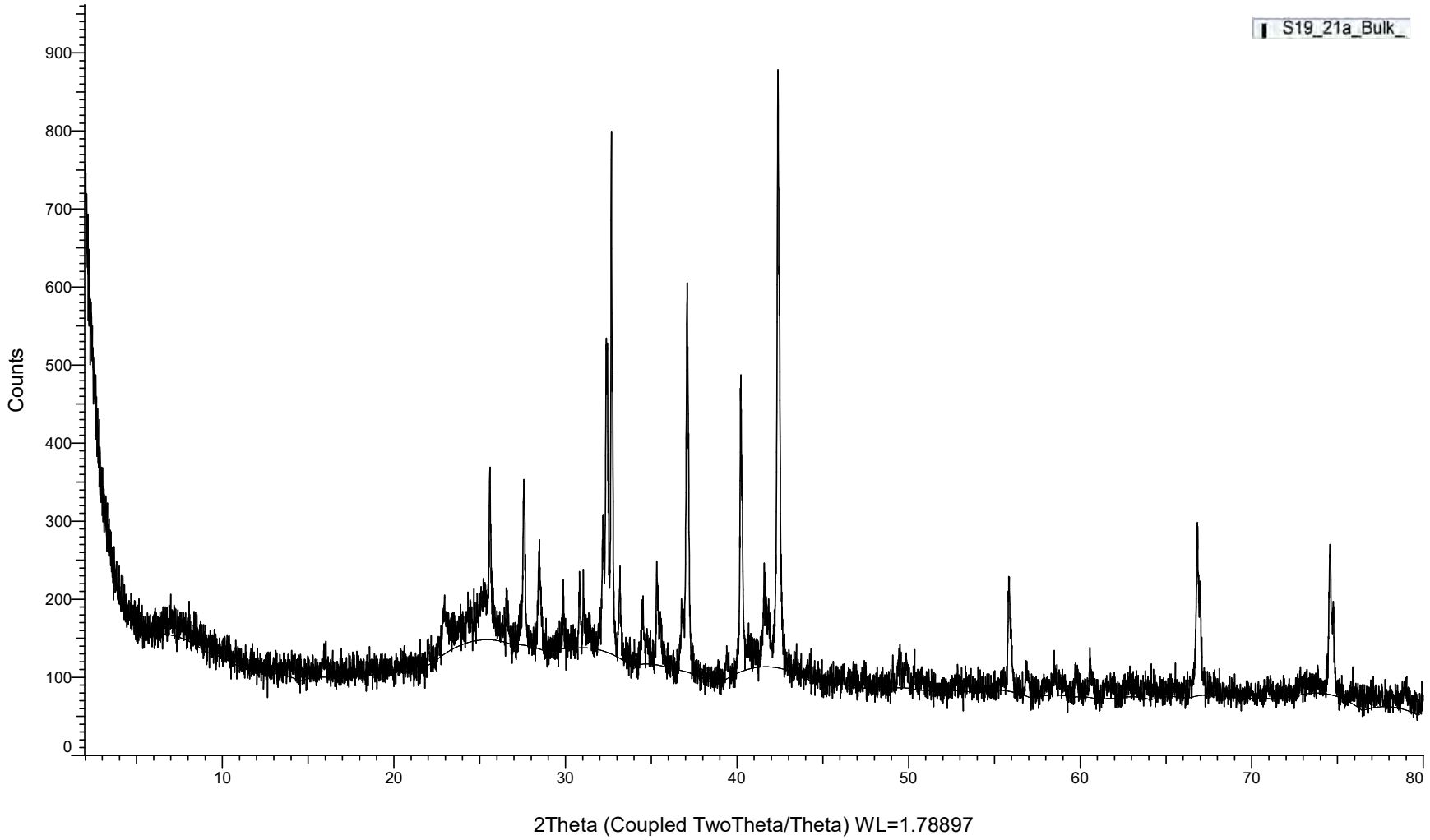

(Coupled TwoTheta/Theta)

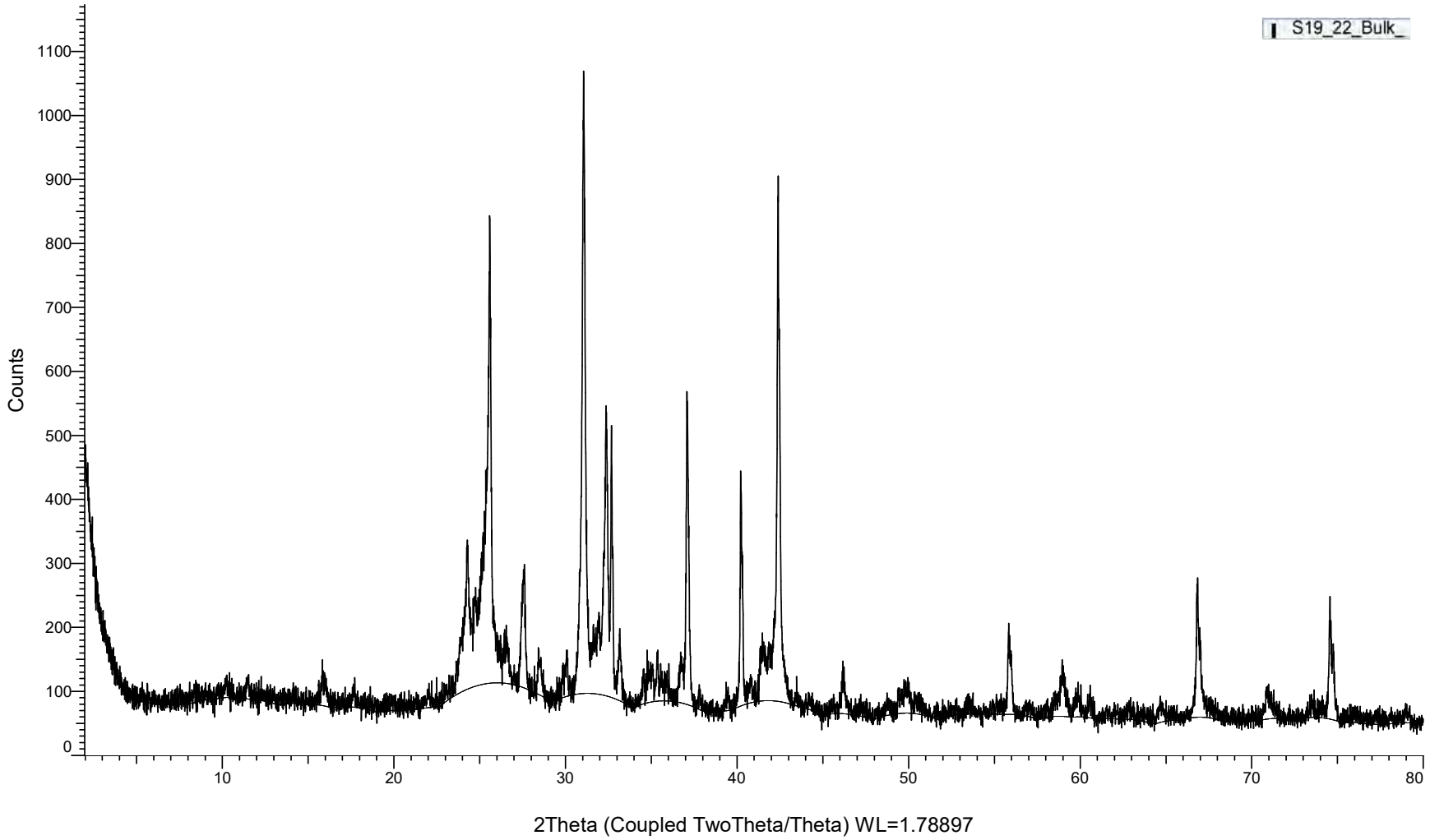

(Coupled TwoTheta/Theta)

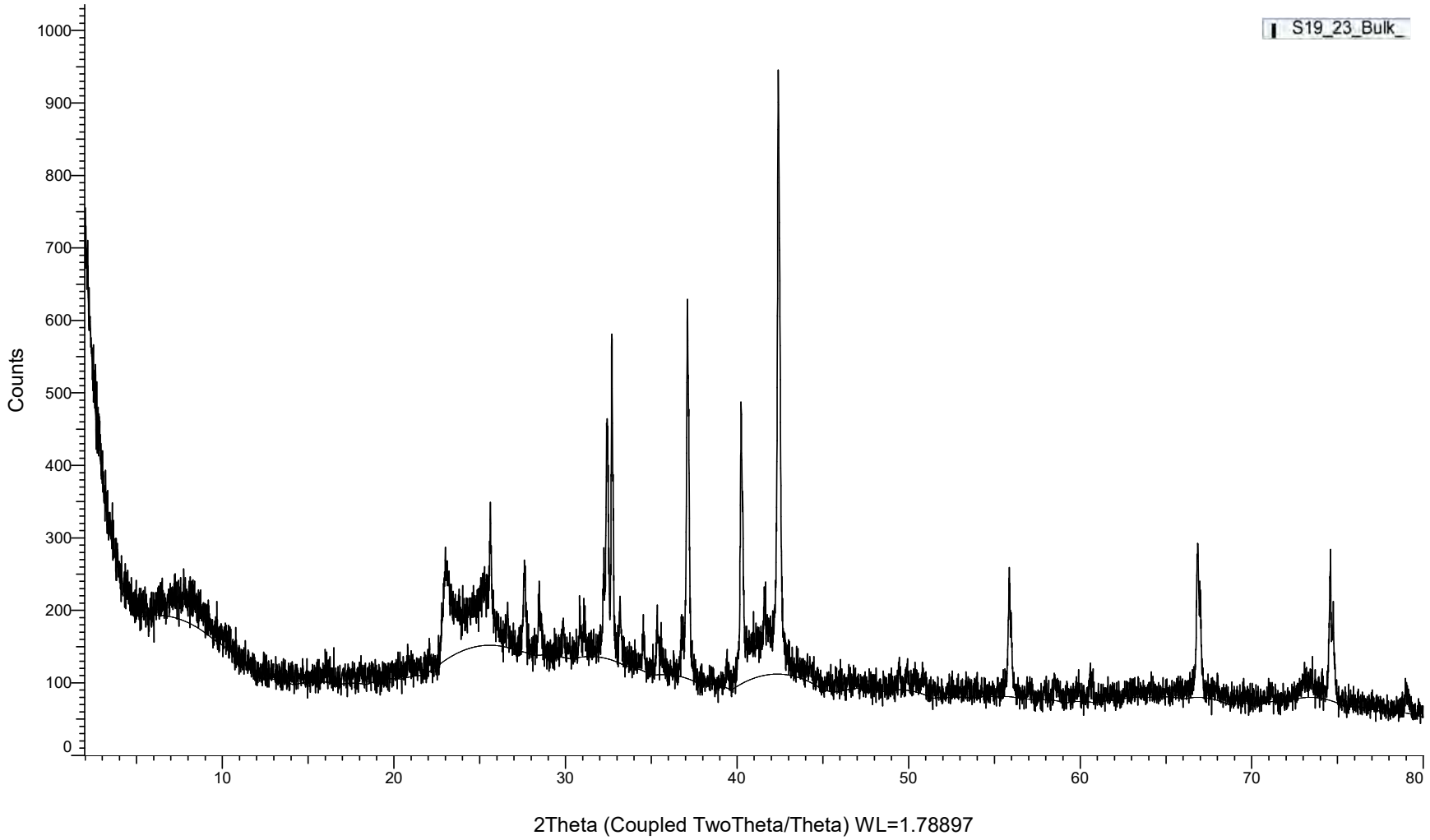

(Coupled TwoTheta/Theta)

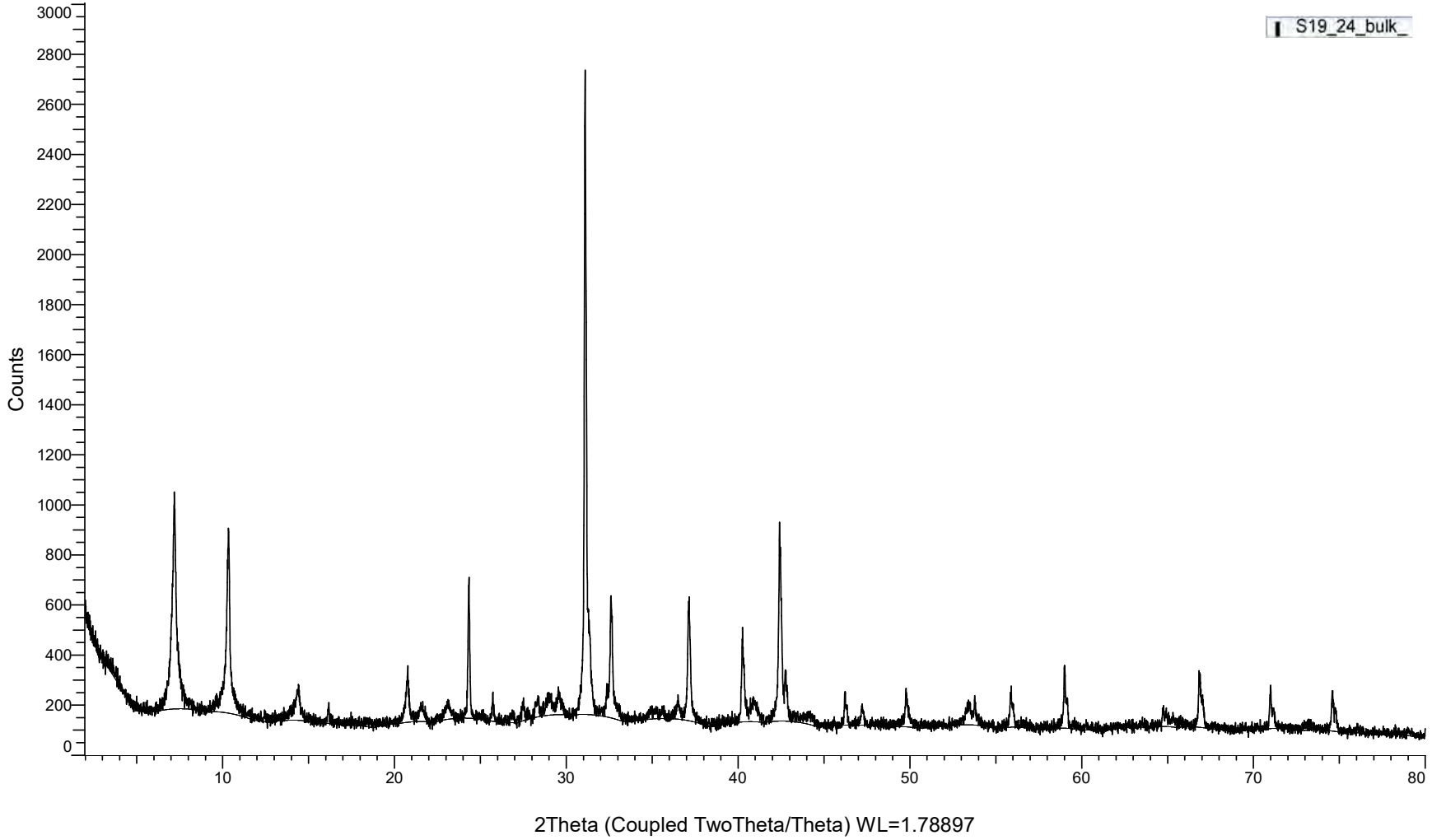

(Coupled TwoTheta/Theta)

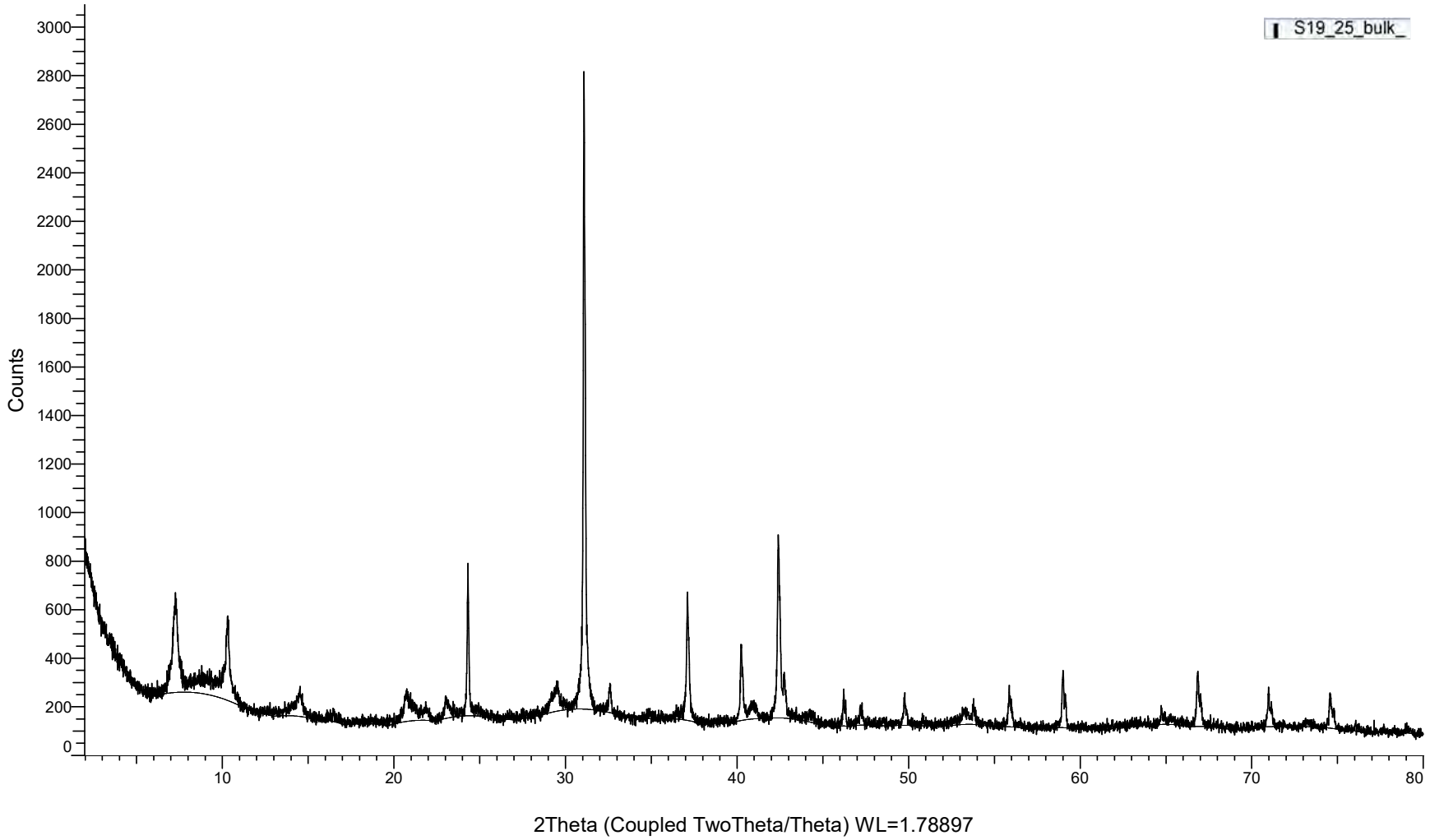

(Coupled TwoTheta/Theta)

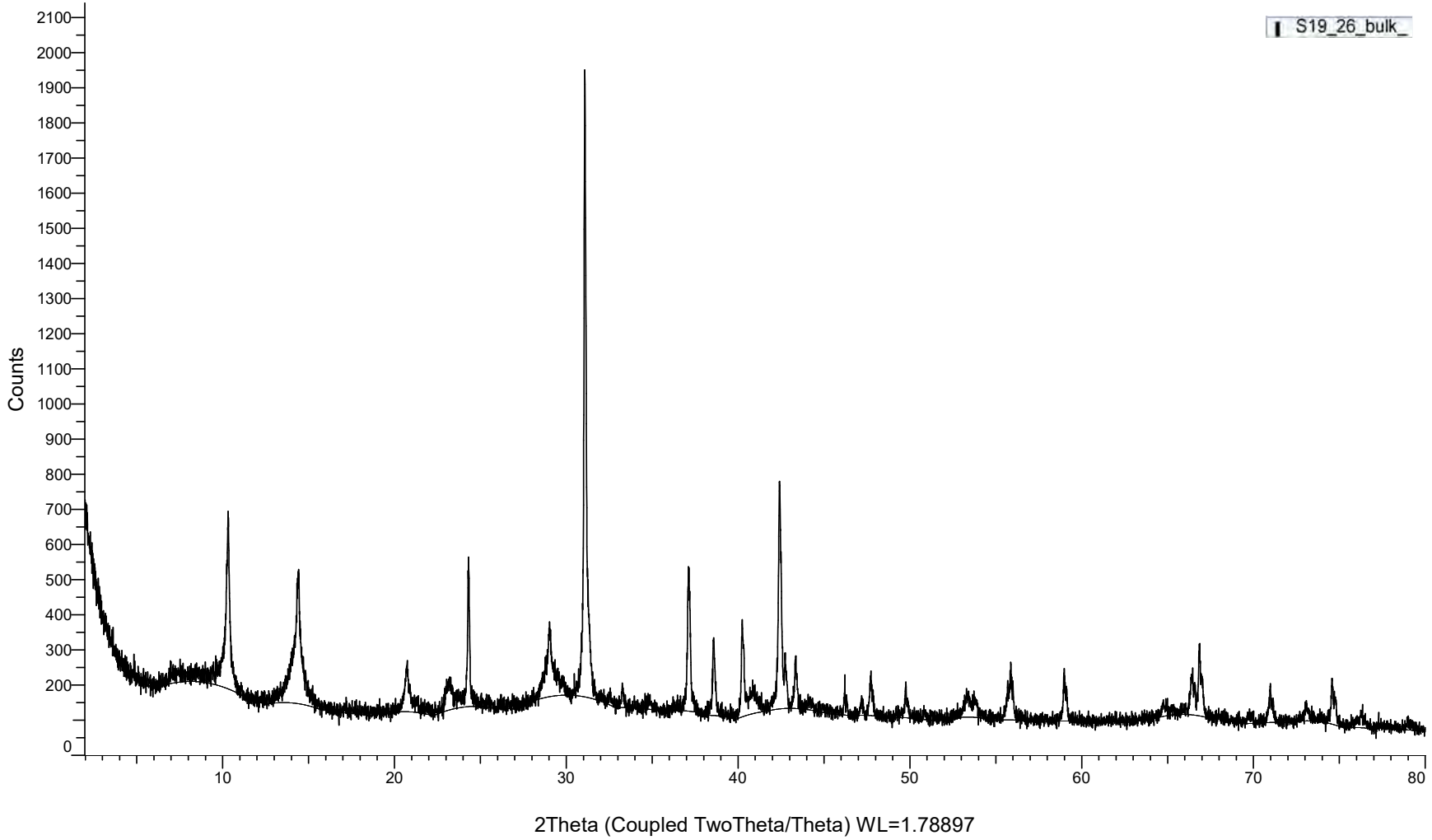

(Coupled TwoTheta/Theta)

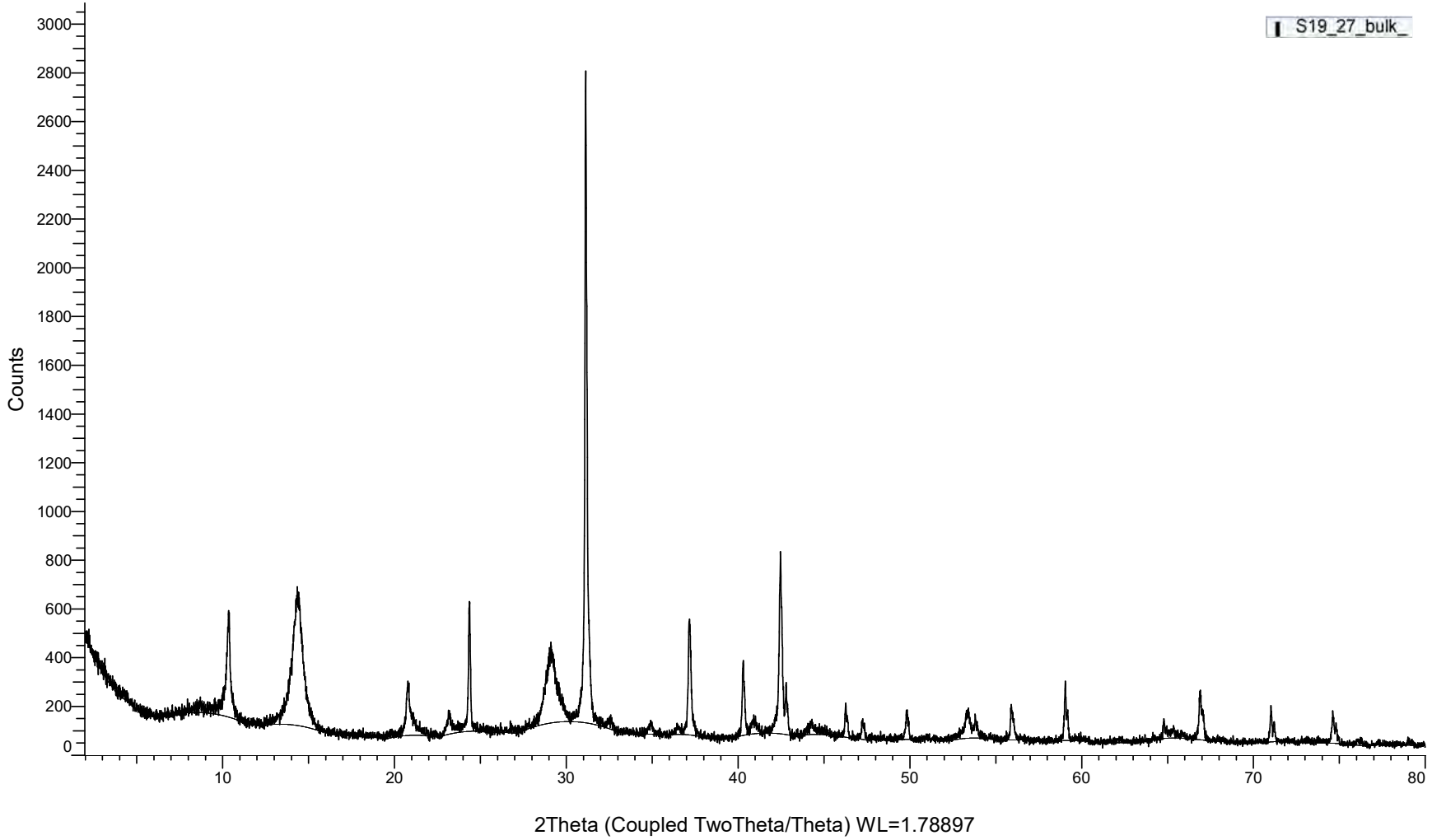

(Coupled TwoTheta/Theta)

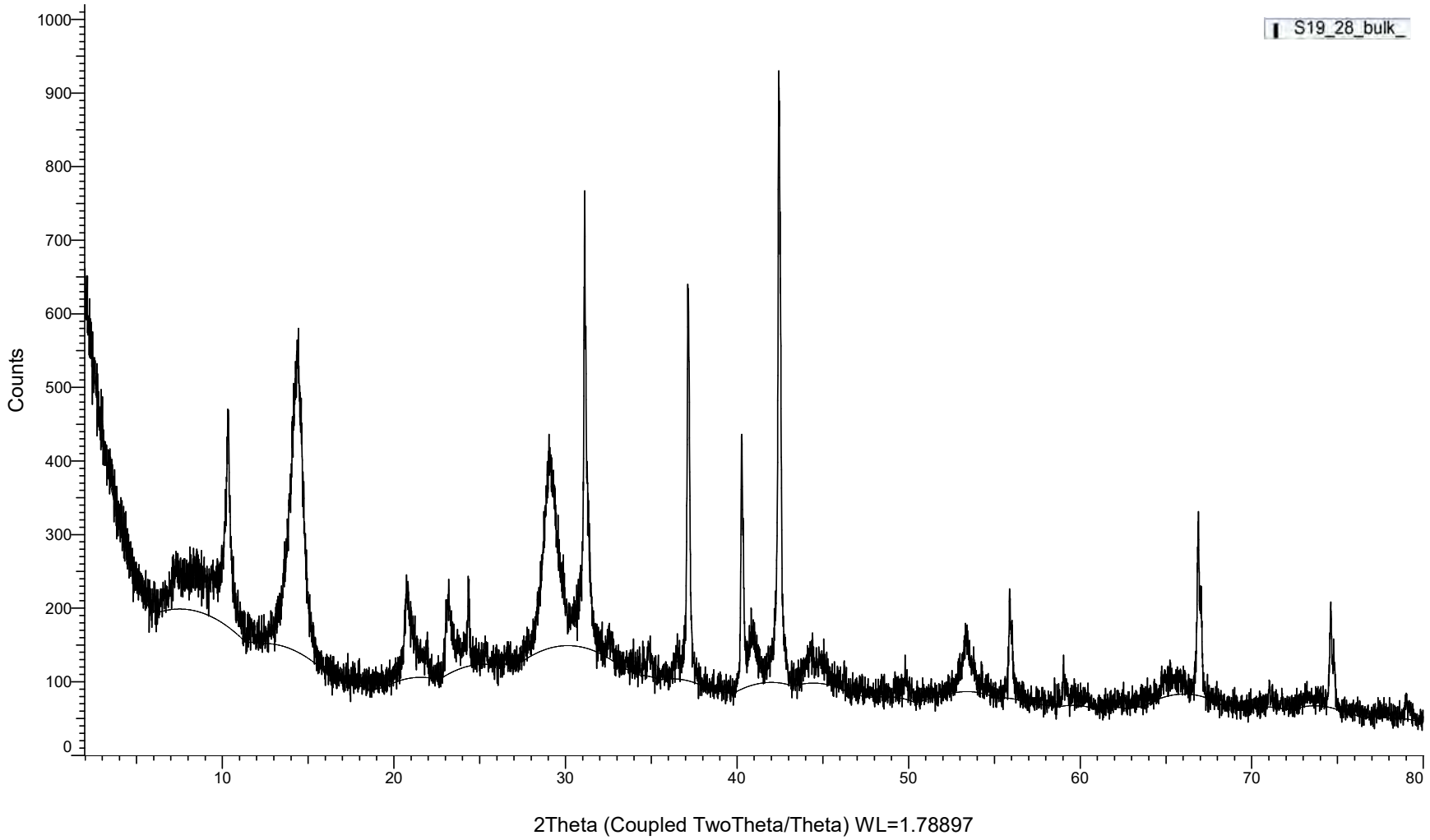

(Coupled TwoTheta/Theta)

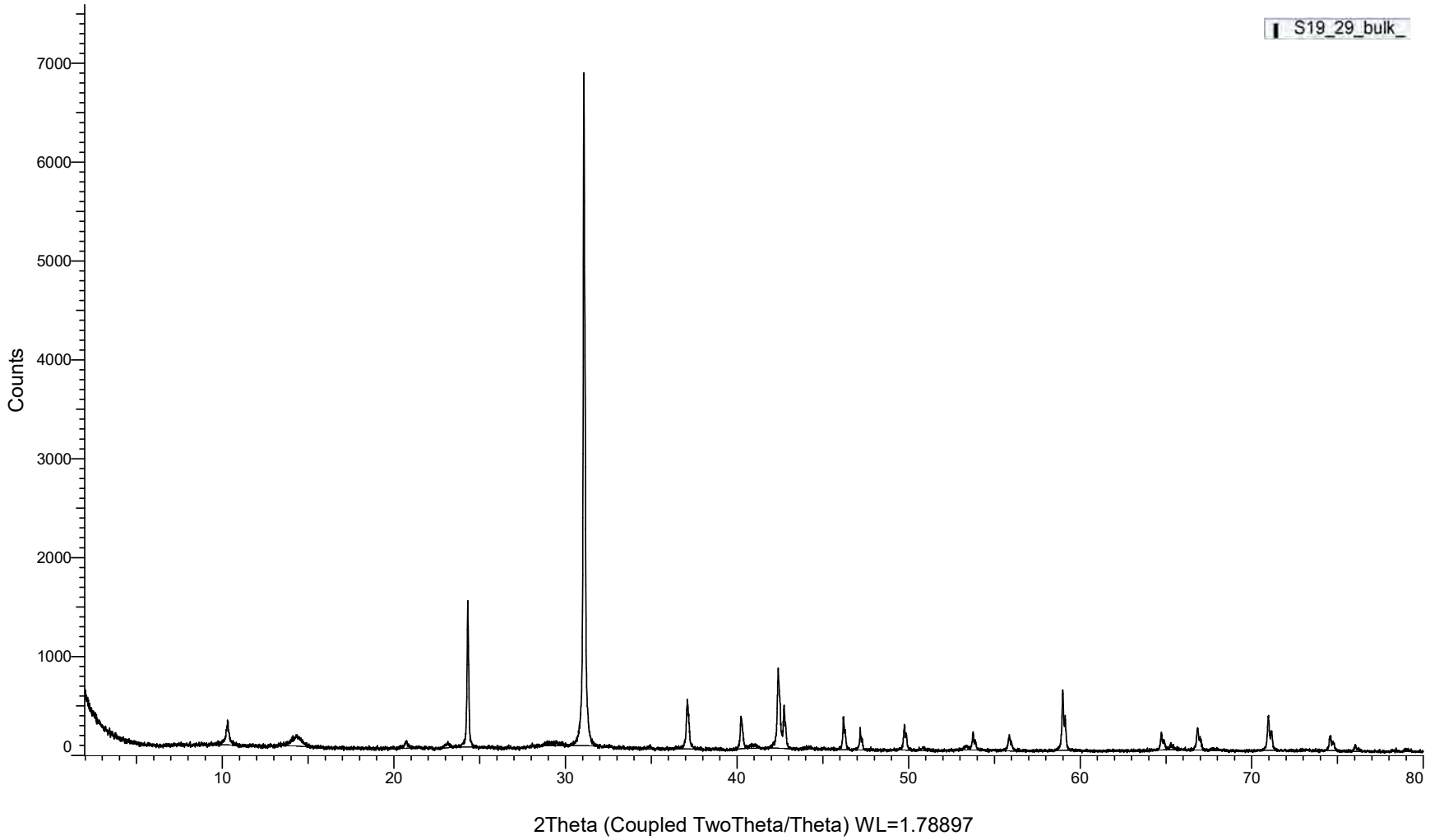

(Coupled TwoTheta/Theta)

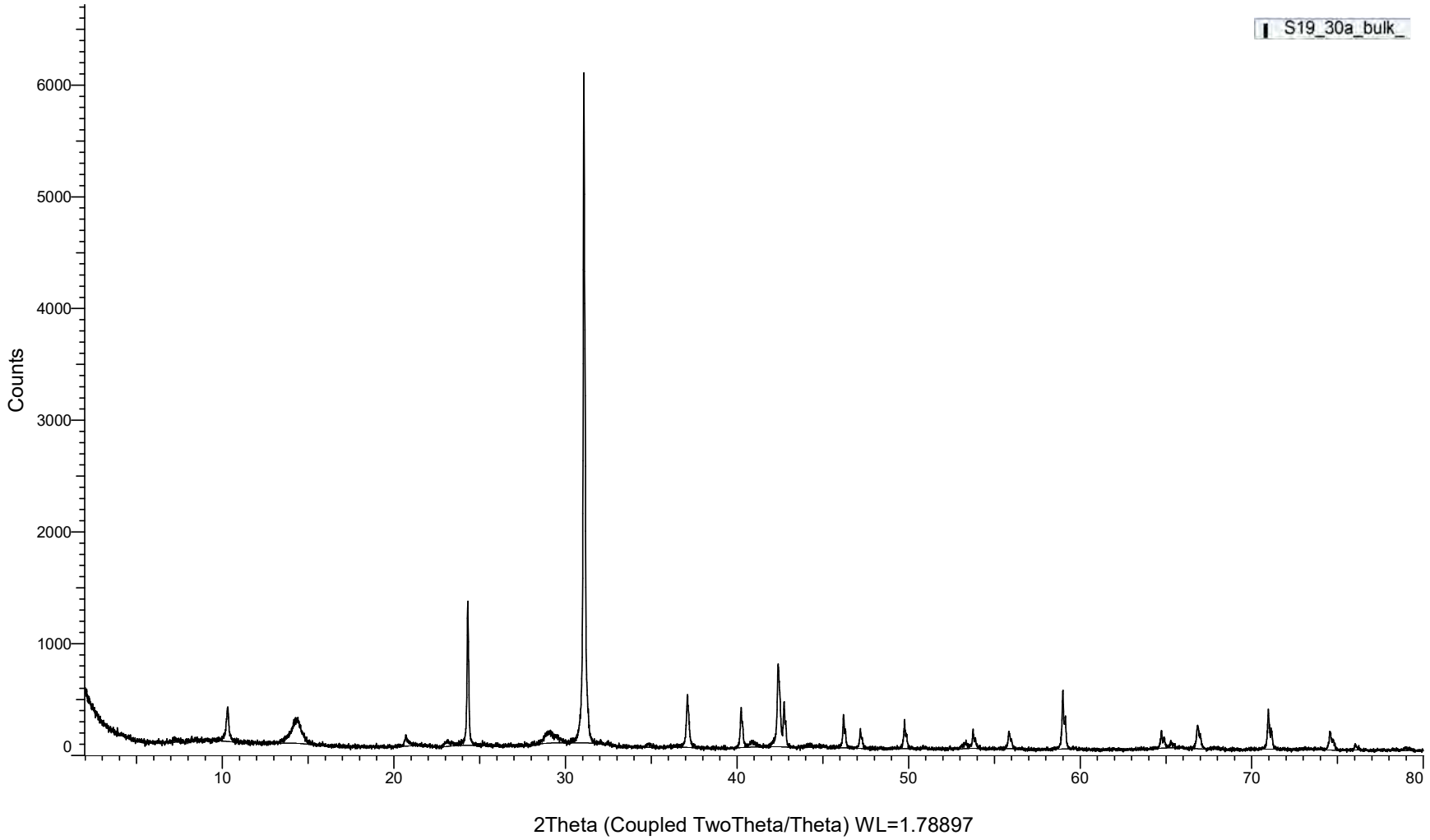

(Coupled TwoTheta/Theta)

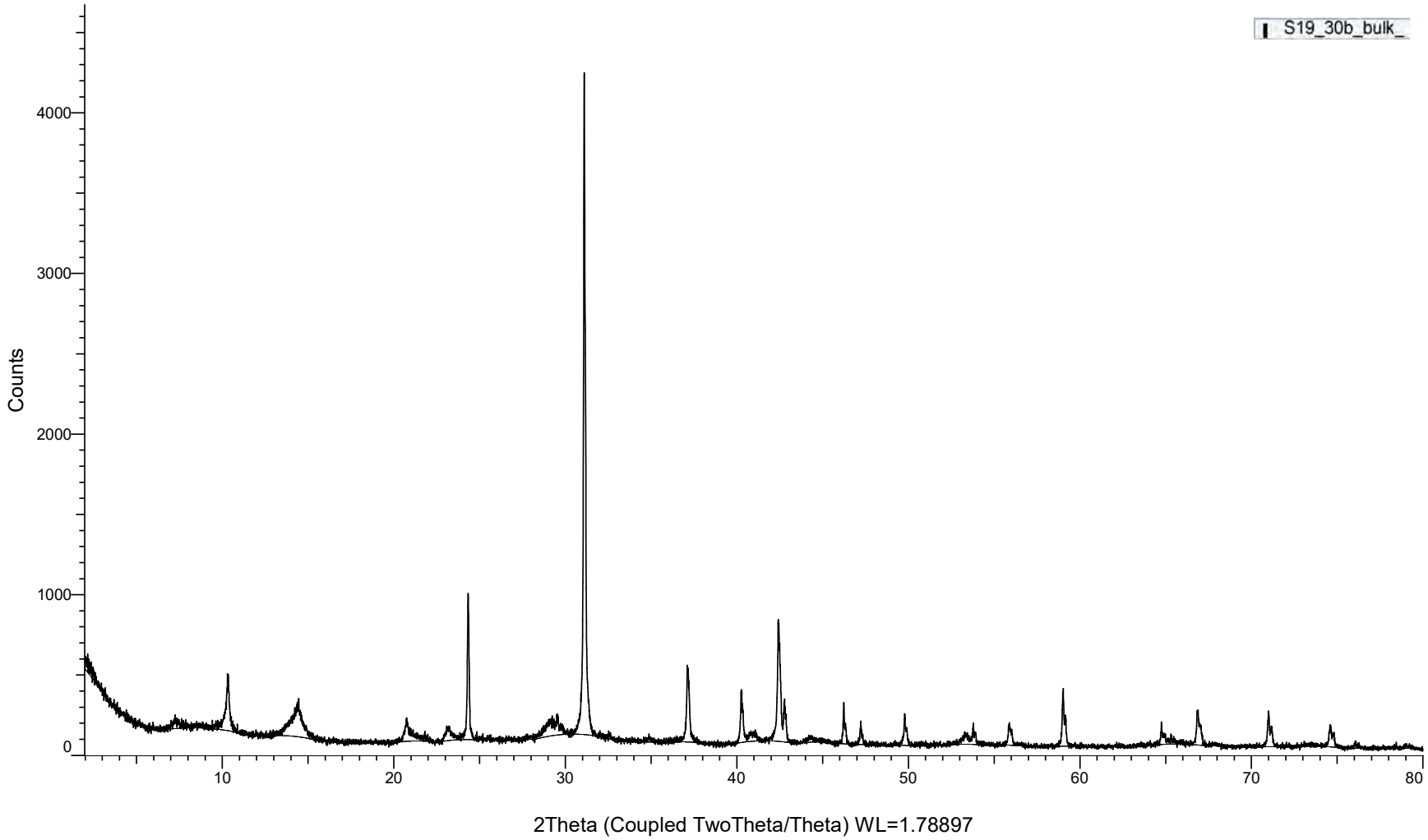

(Coupled TwoTheta/Theta)

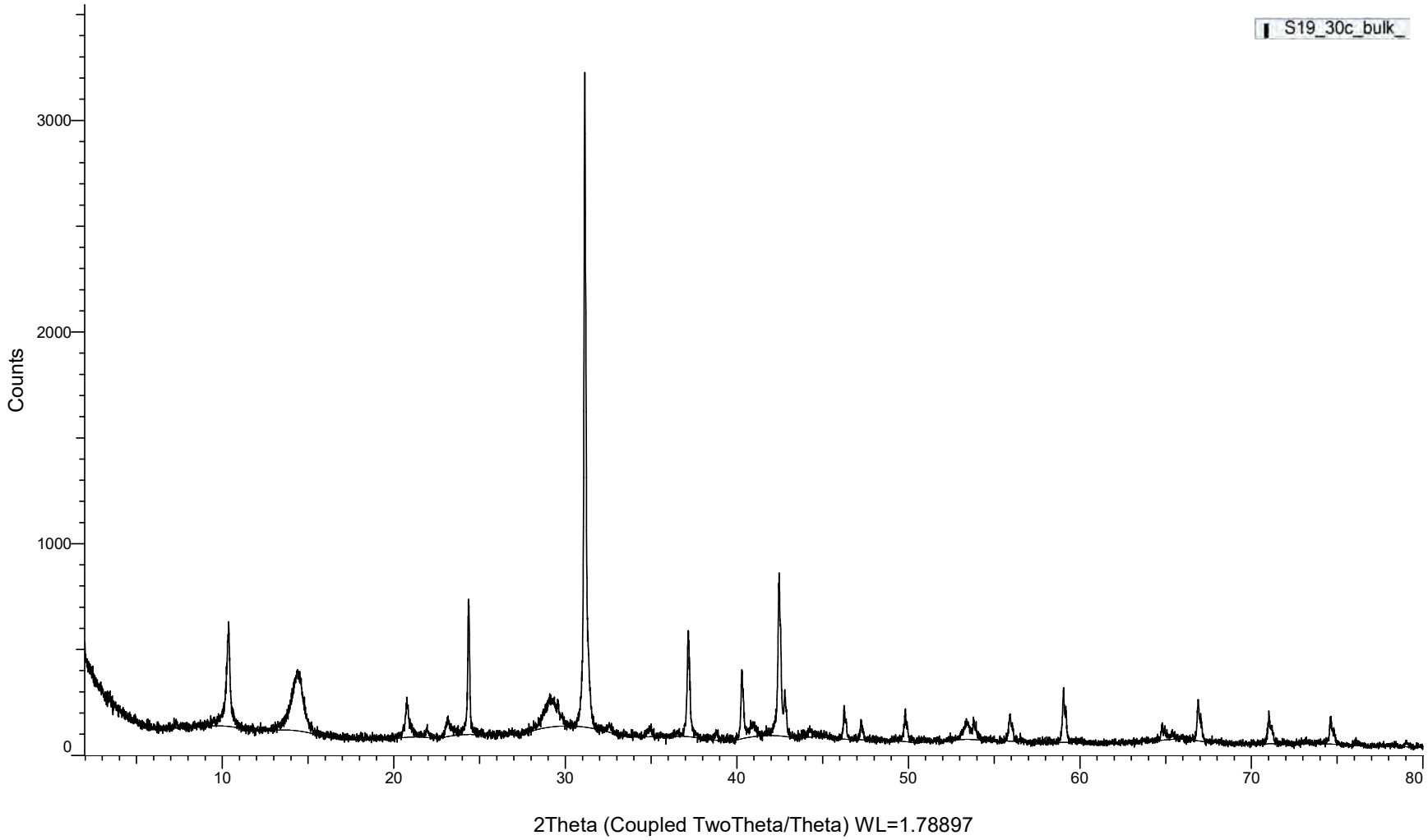

(Coupled TwoTheta/Theta)

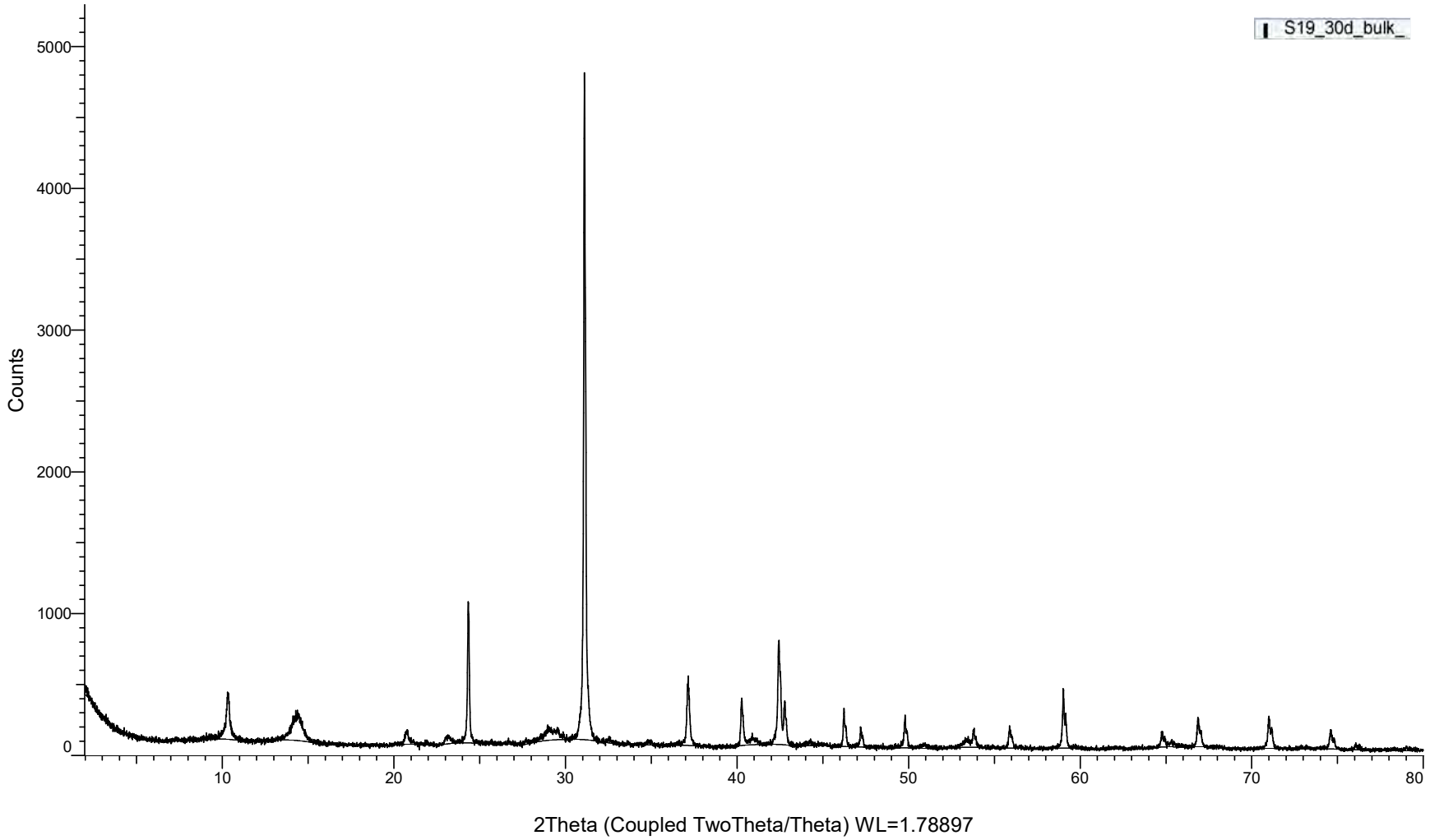

(Coupled TwoTheta/Theta)

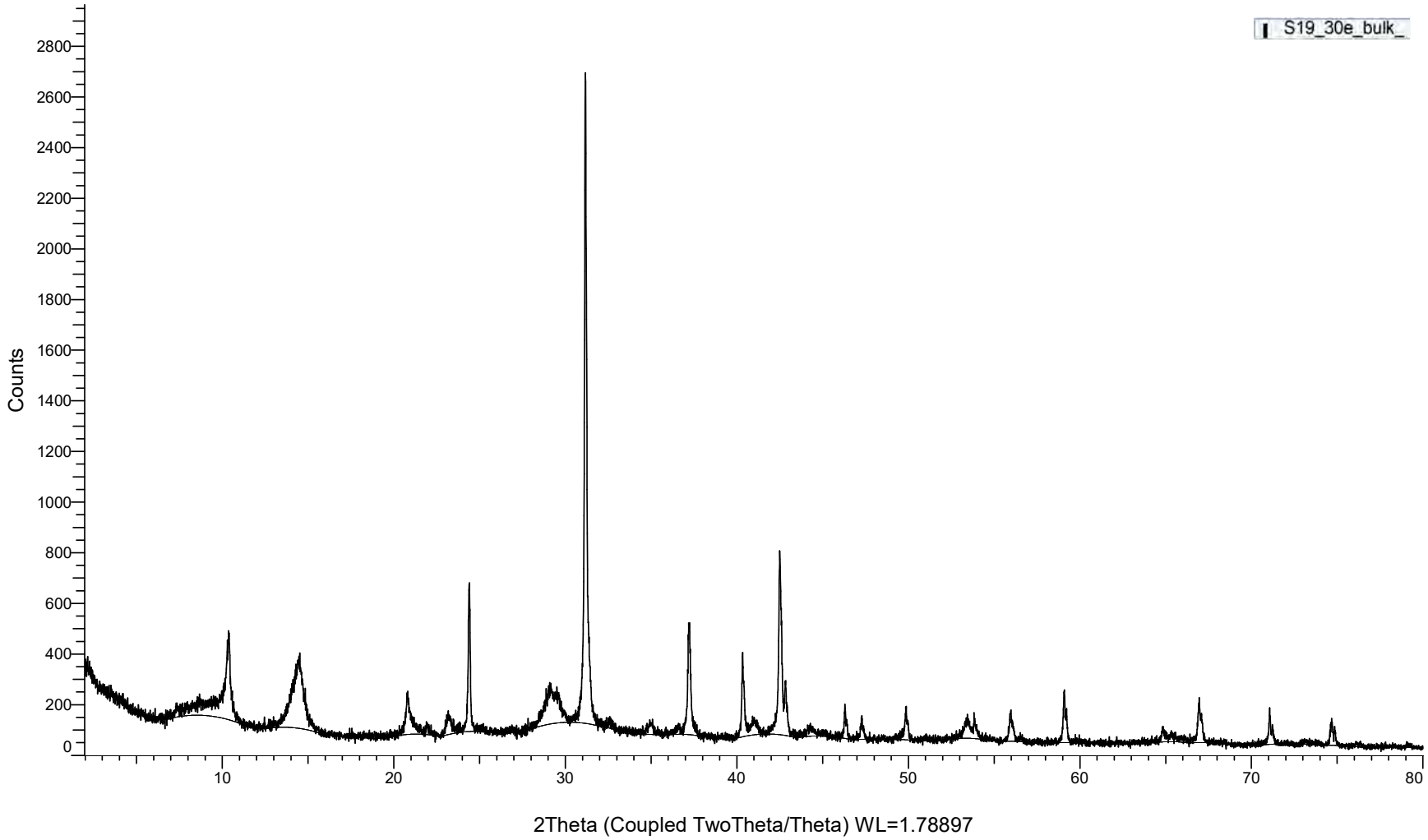

(Coupled TwoTheta/Theta)

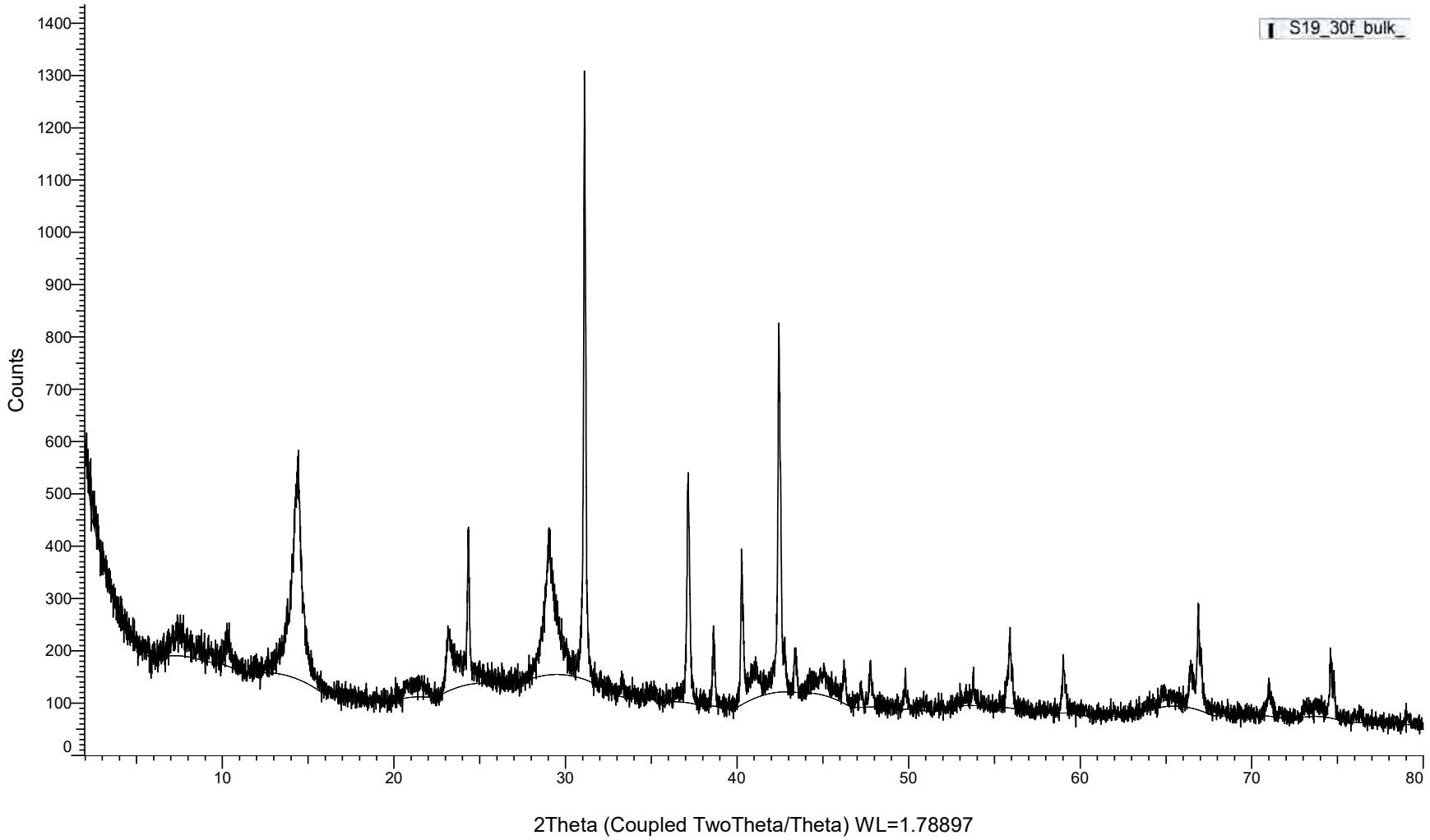

(Coupled TwoTheta/Theta)

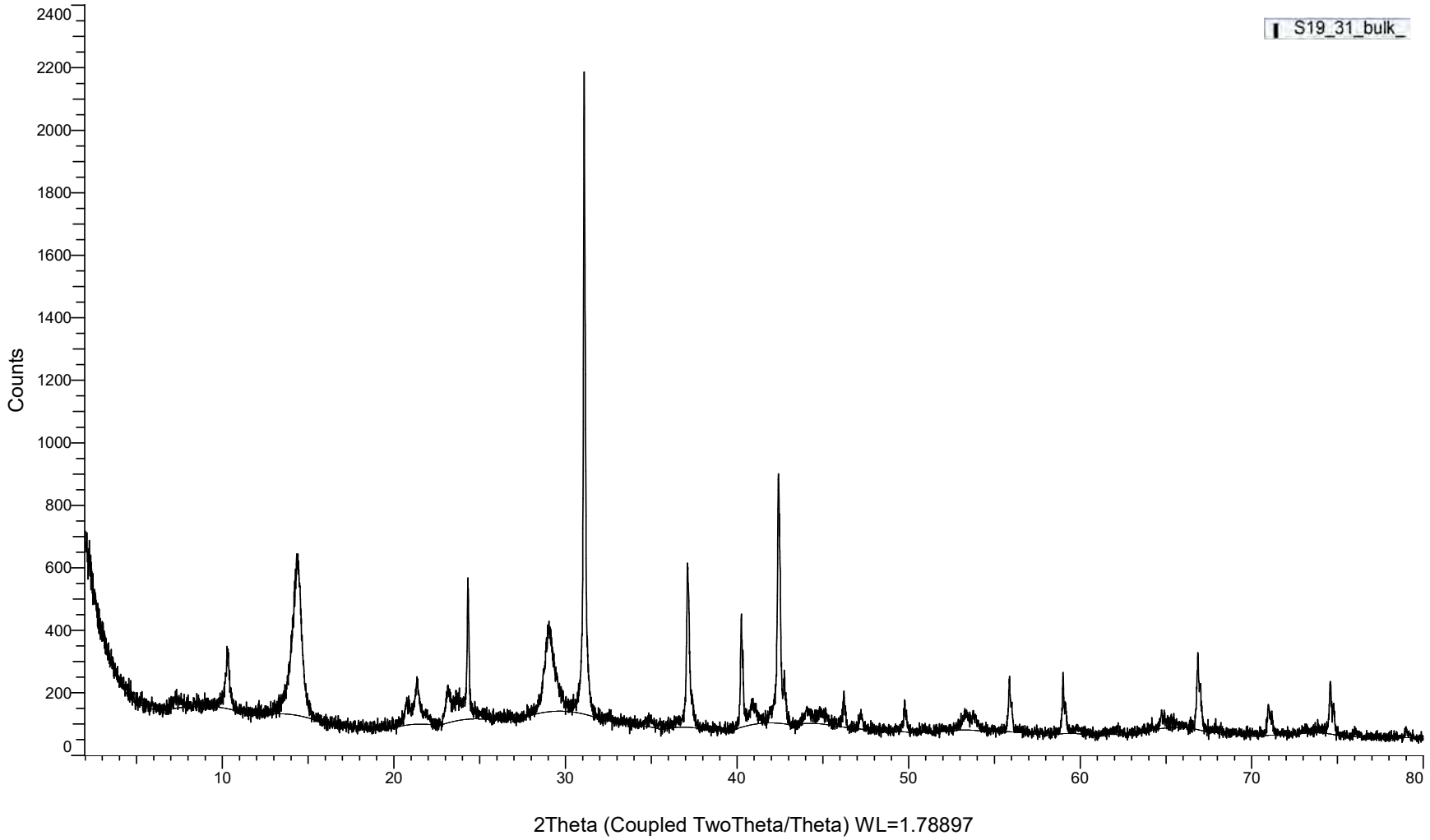

(Coupled TwoTheta/Theta)

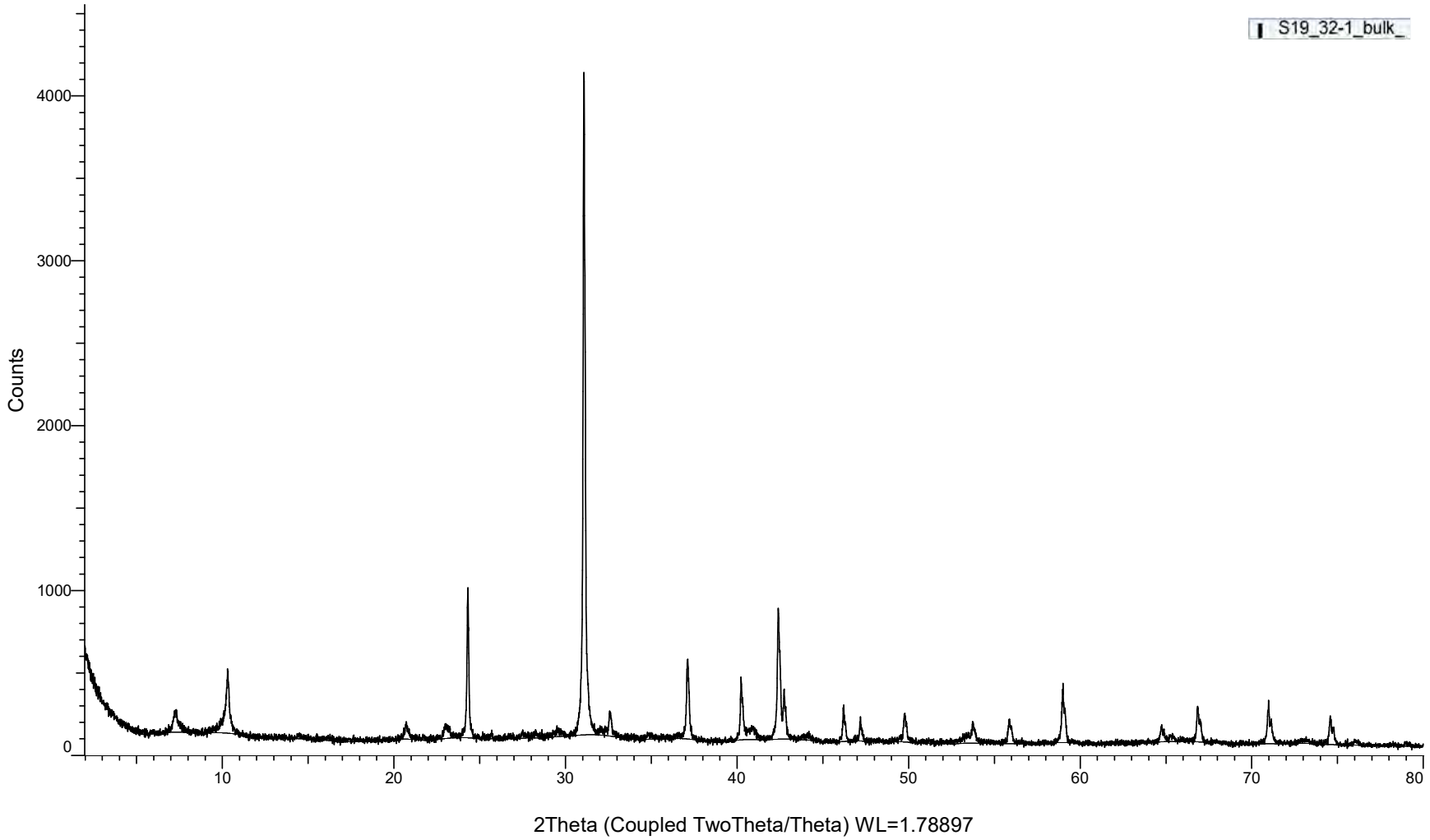

(Coupled TwoTheta/Theta)

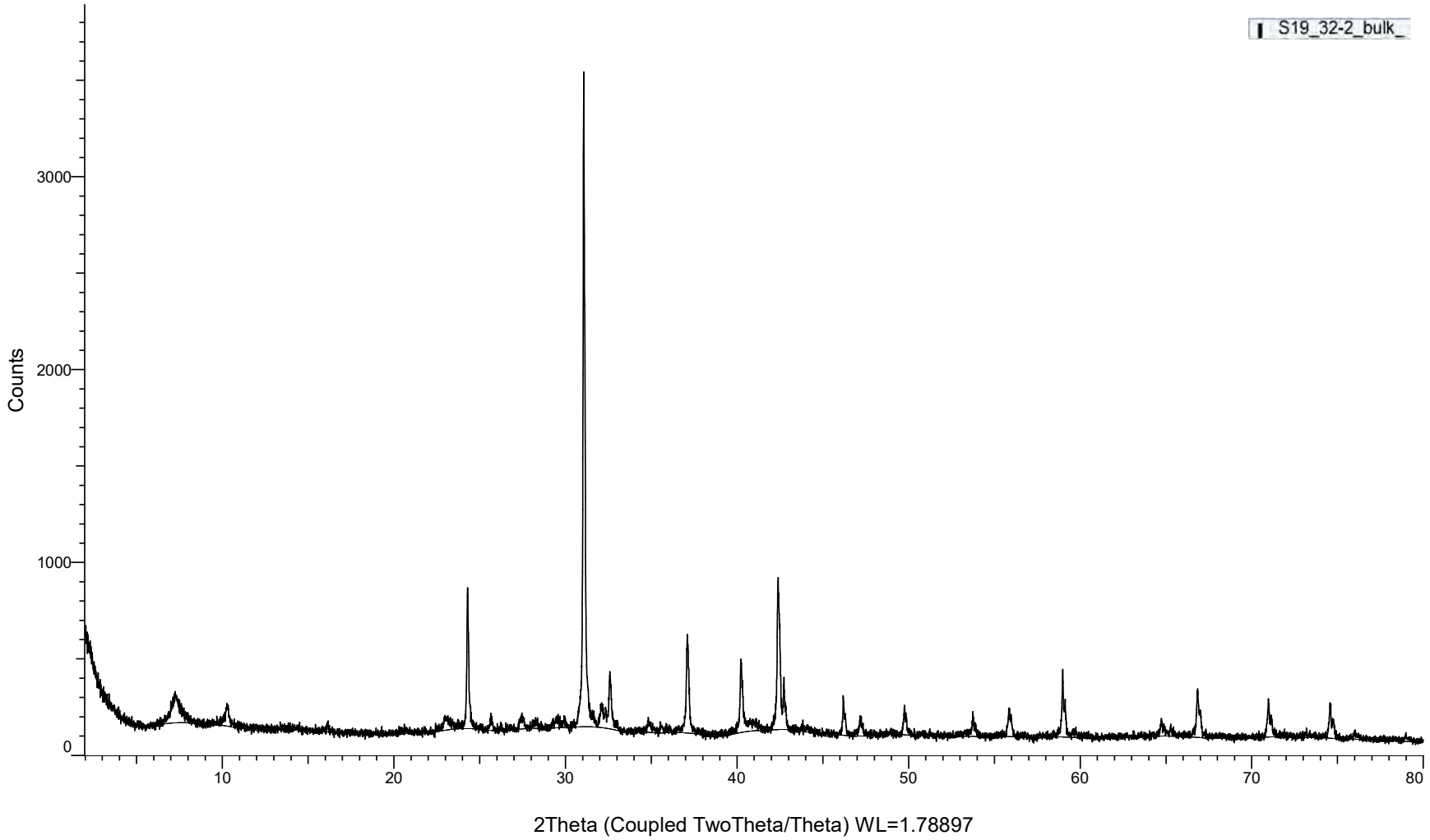

(Coupled TwoTheta/Theta)

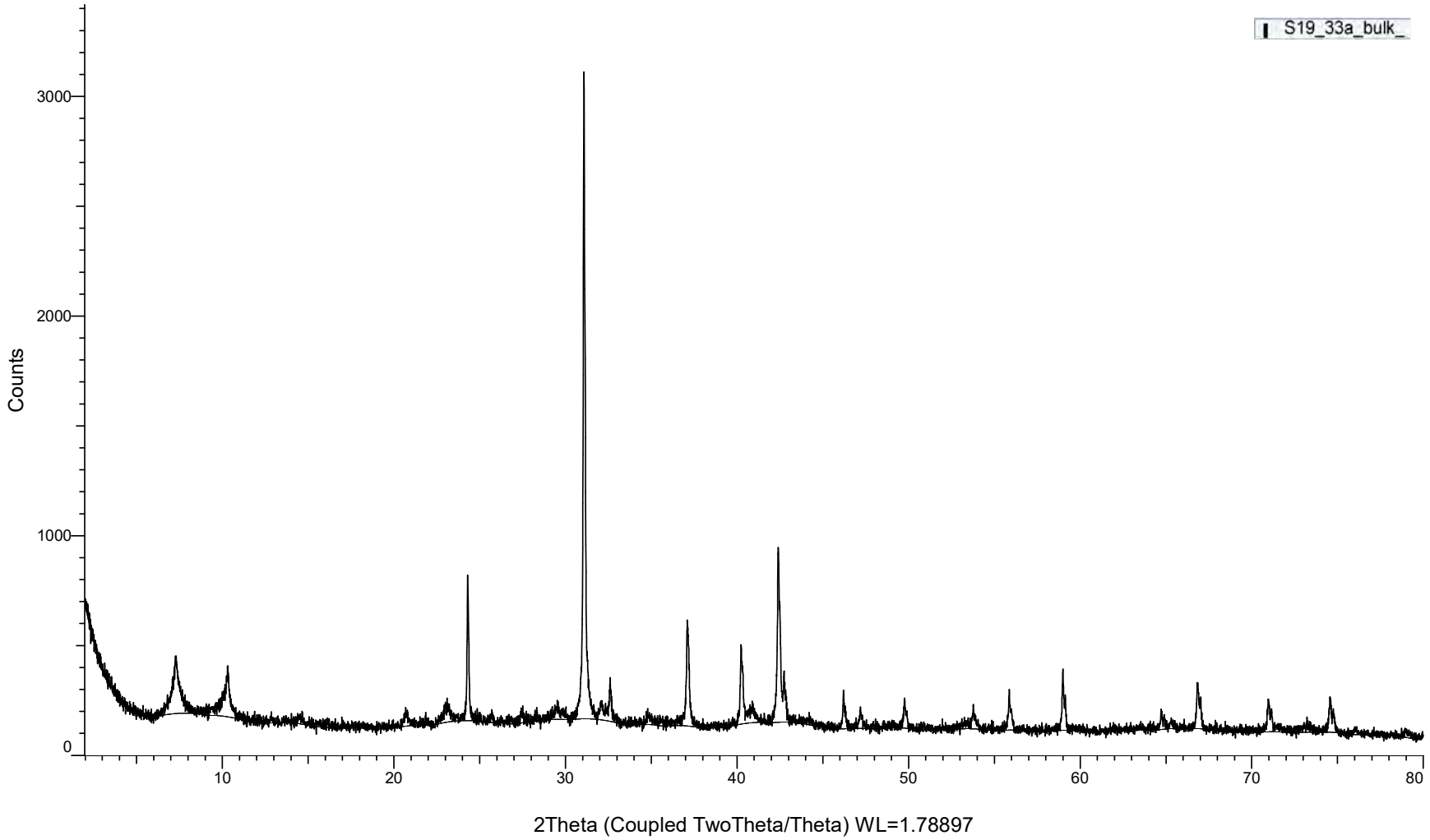

(Coupled TwoTheta/Theta)

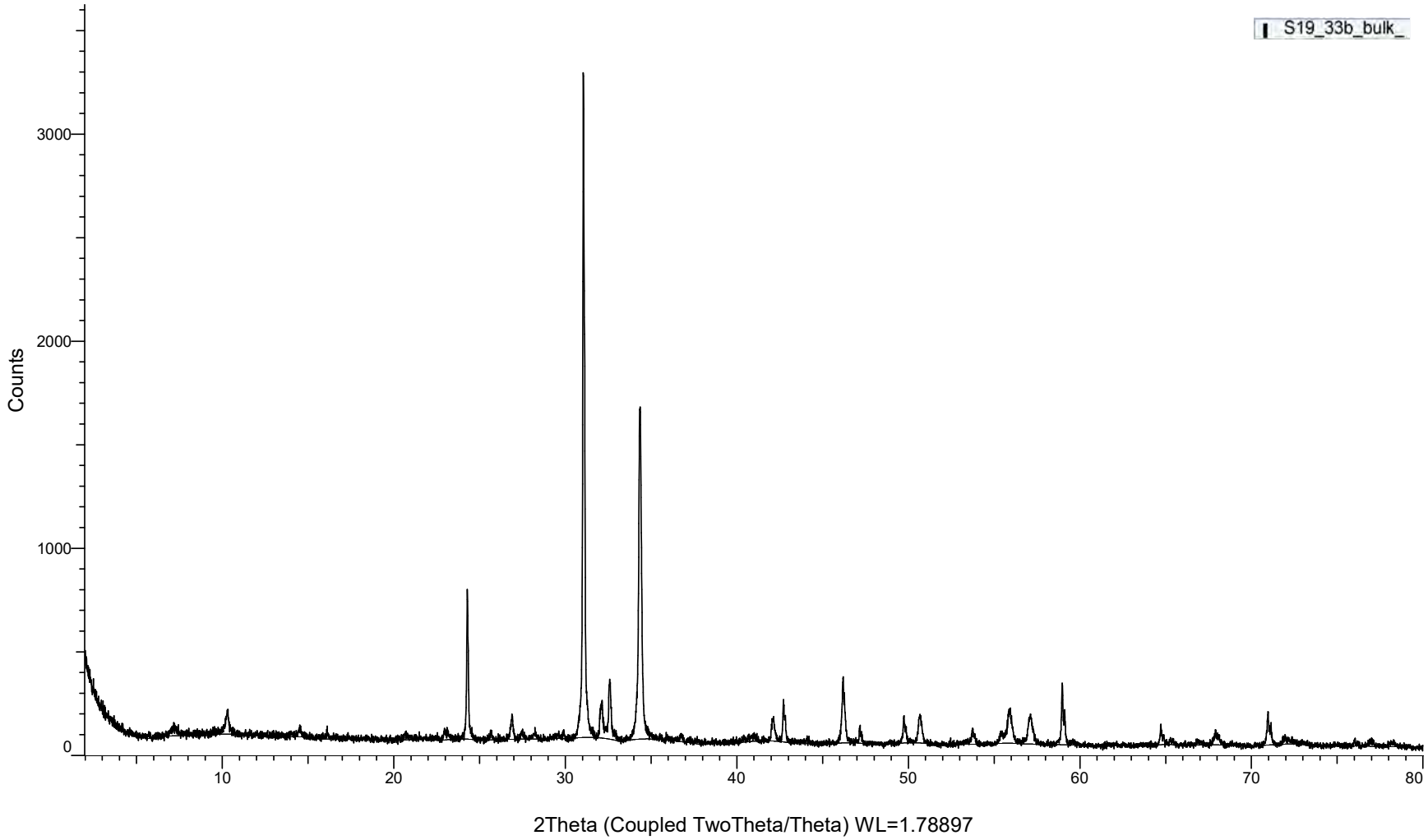

(Coupled TwoTheta/Theta)

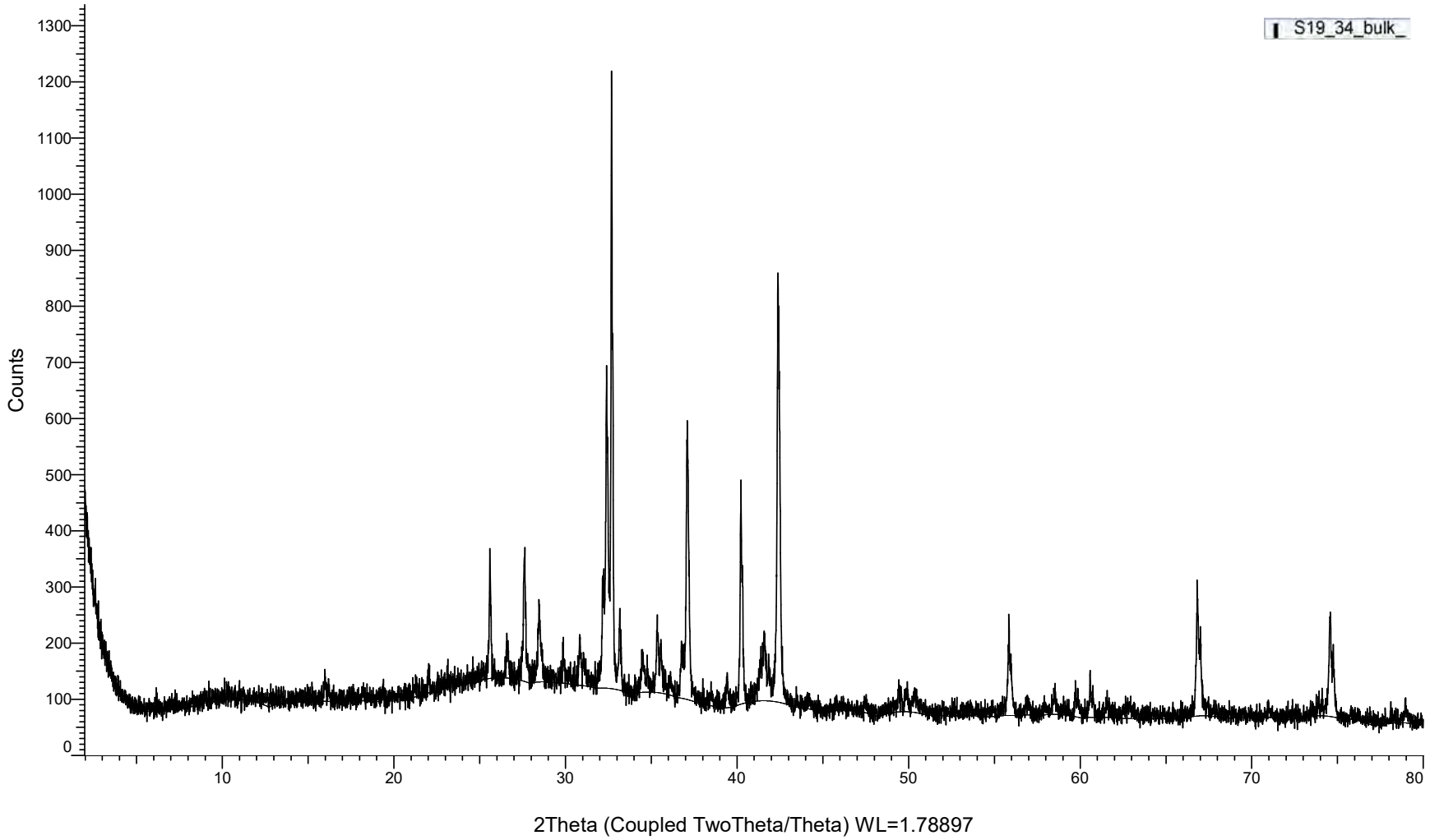

(Coupled TwoTheta/Theta)

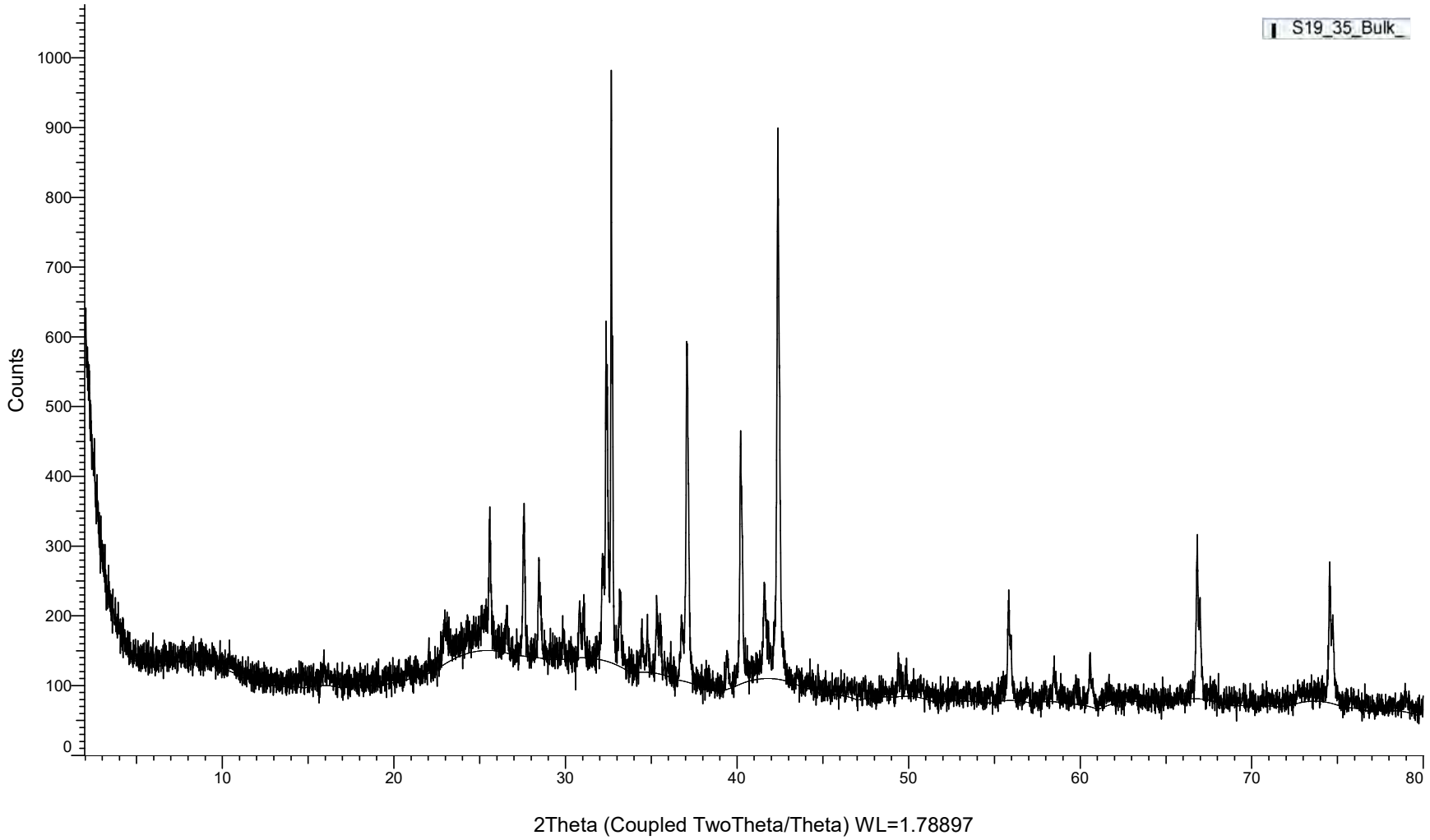

(Coupled TwoTheta/Theta)

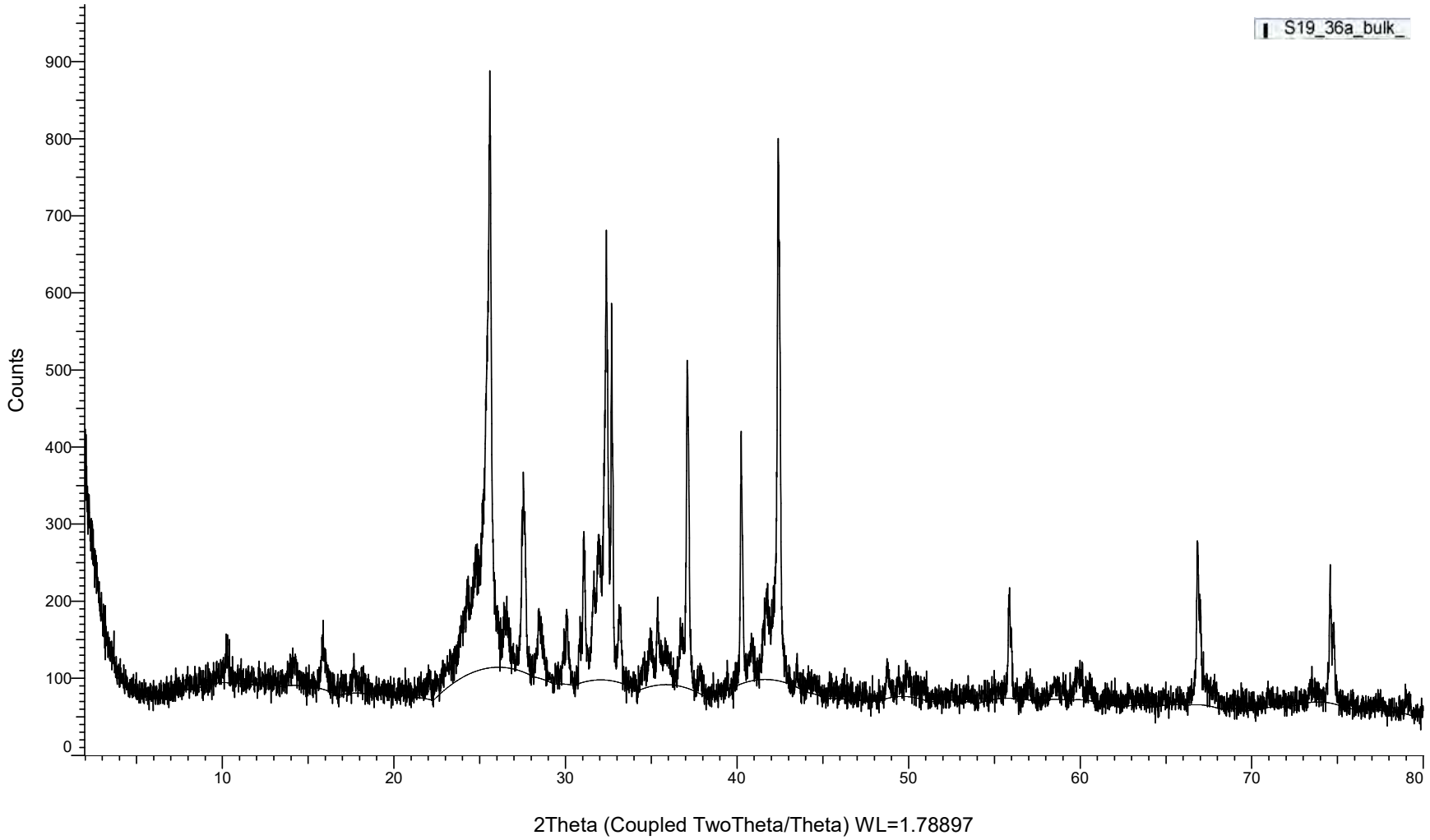

(Coupled TwoTheta/Theta)

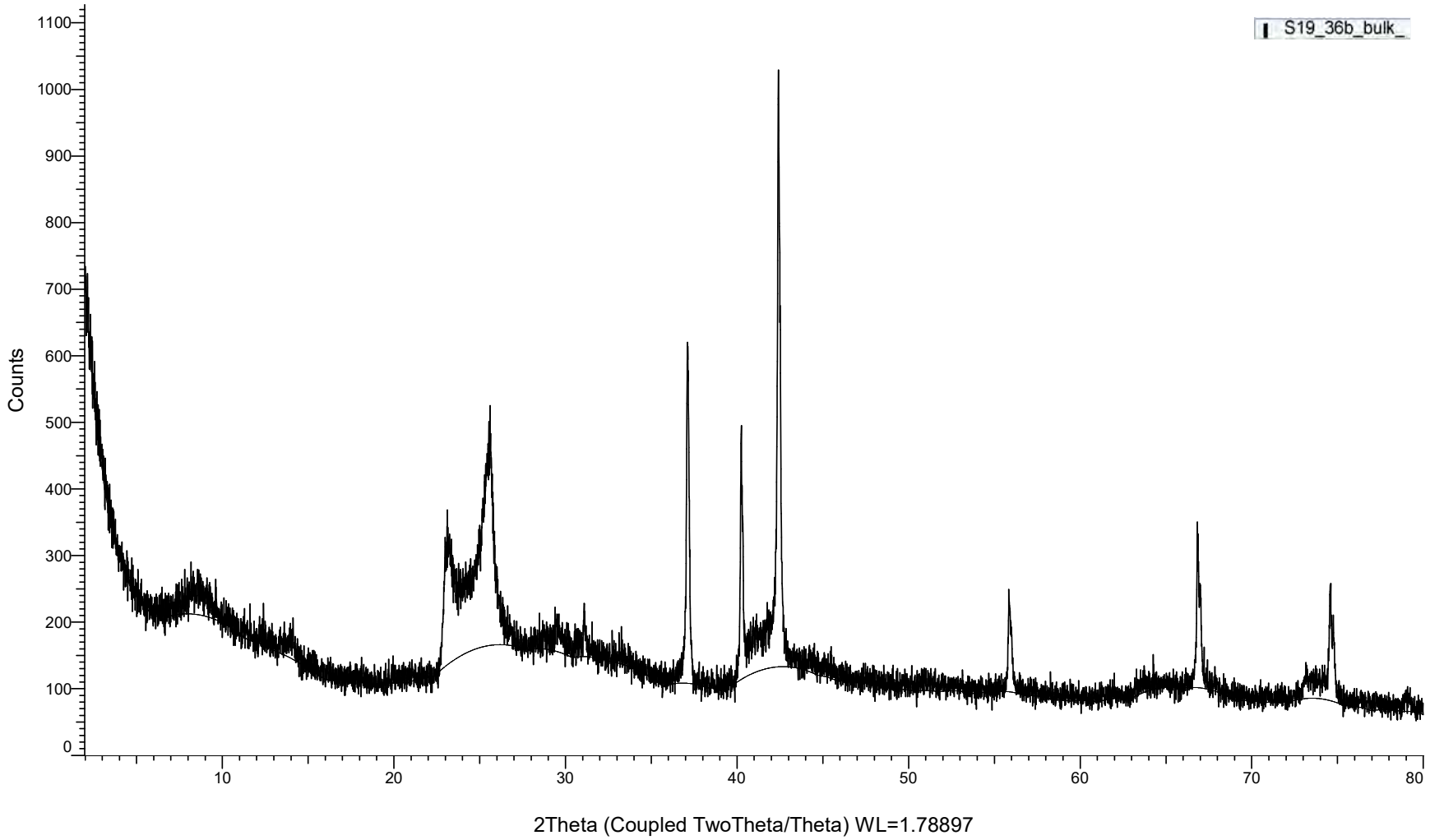

(Coupled TwoTheta/Theta)

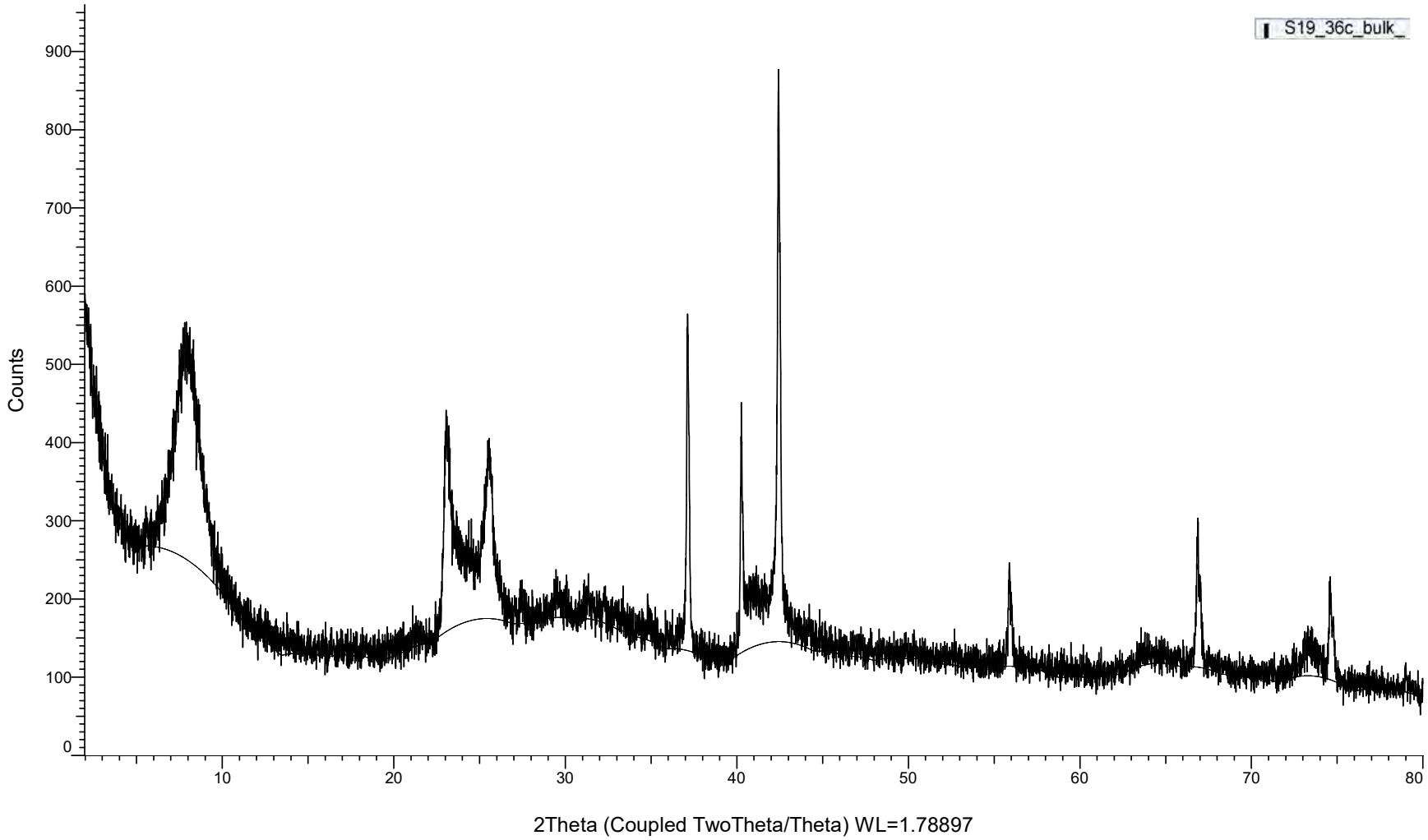

(Coupled TwoTheta/Theta)

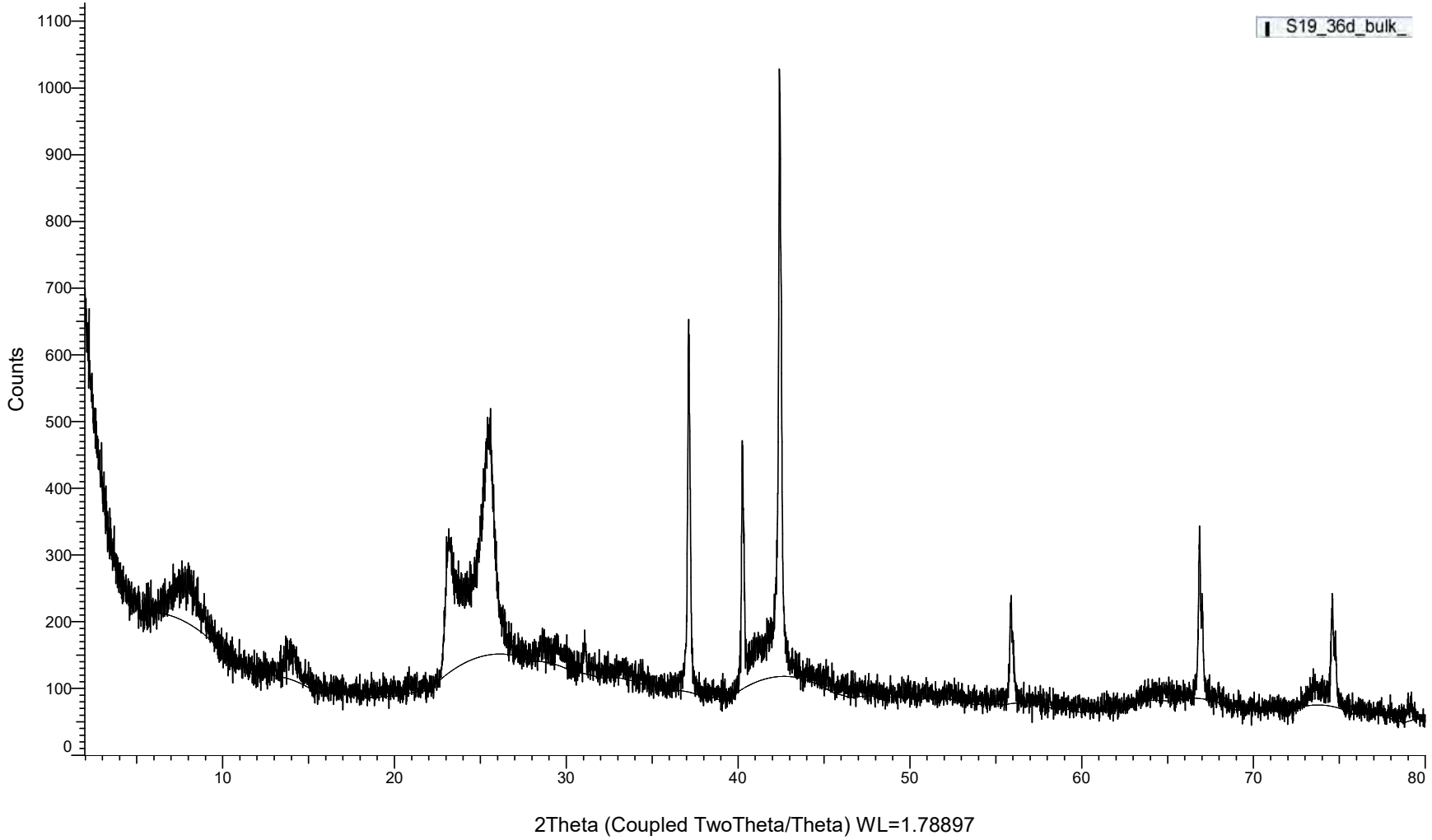

(Coupled TwoTheta/Theta)

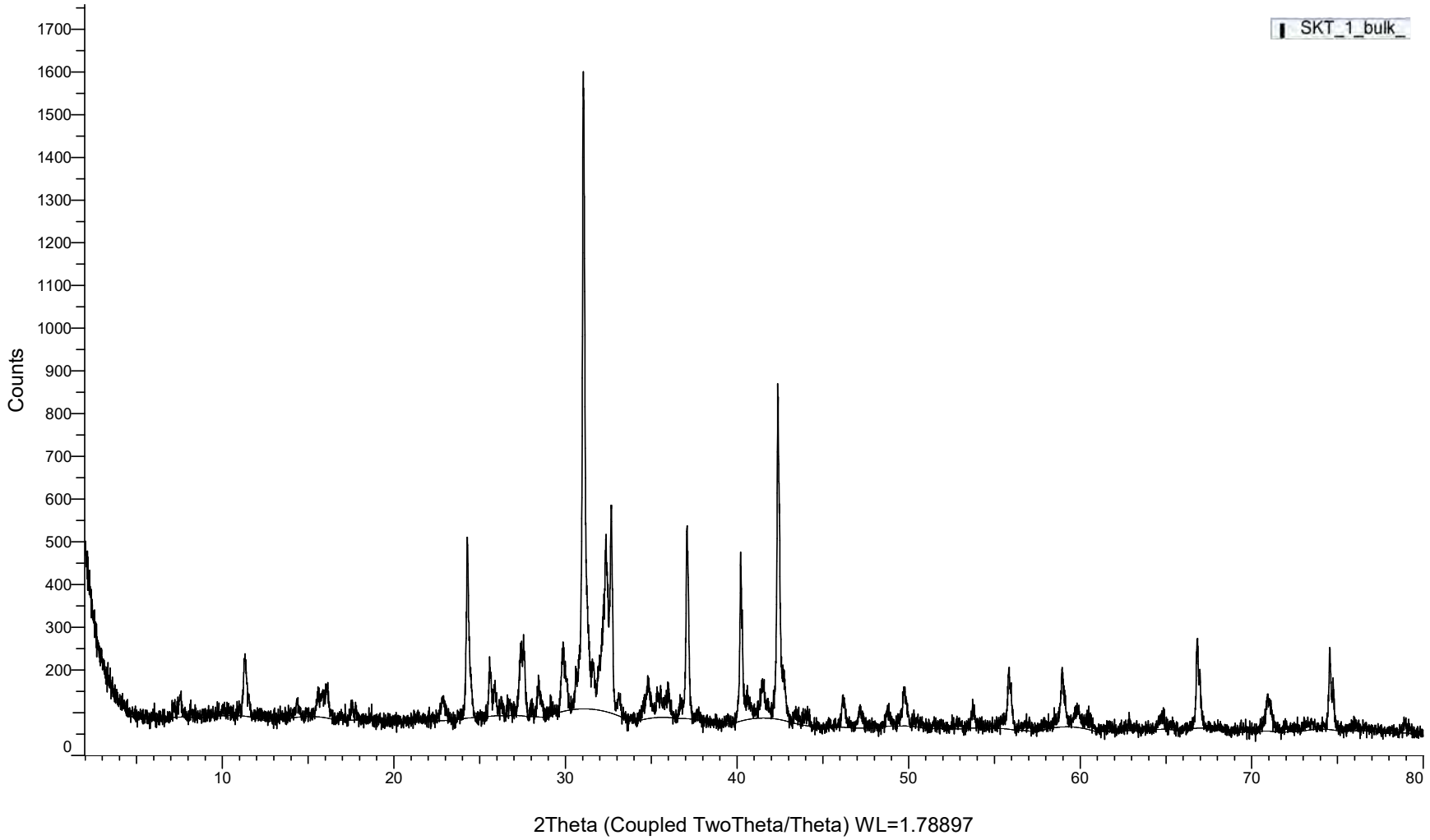

(Coupled TwoTheta/Theta)

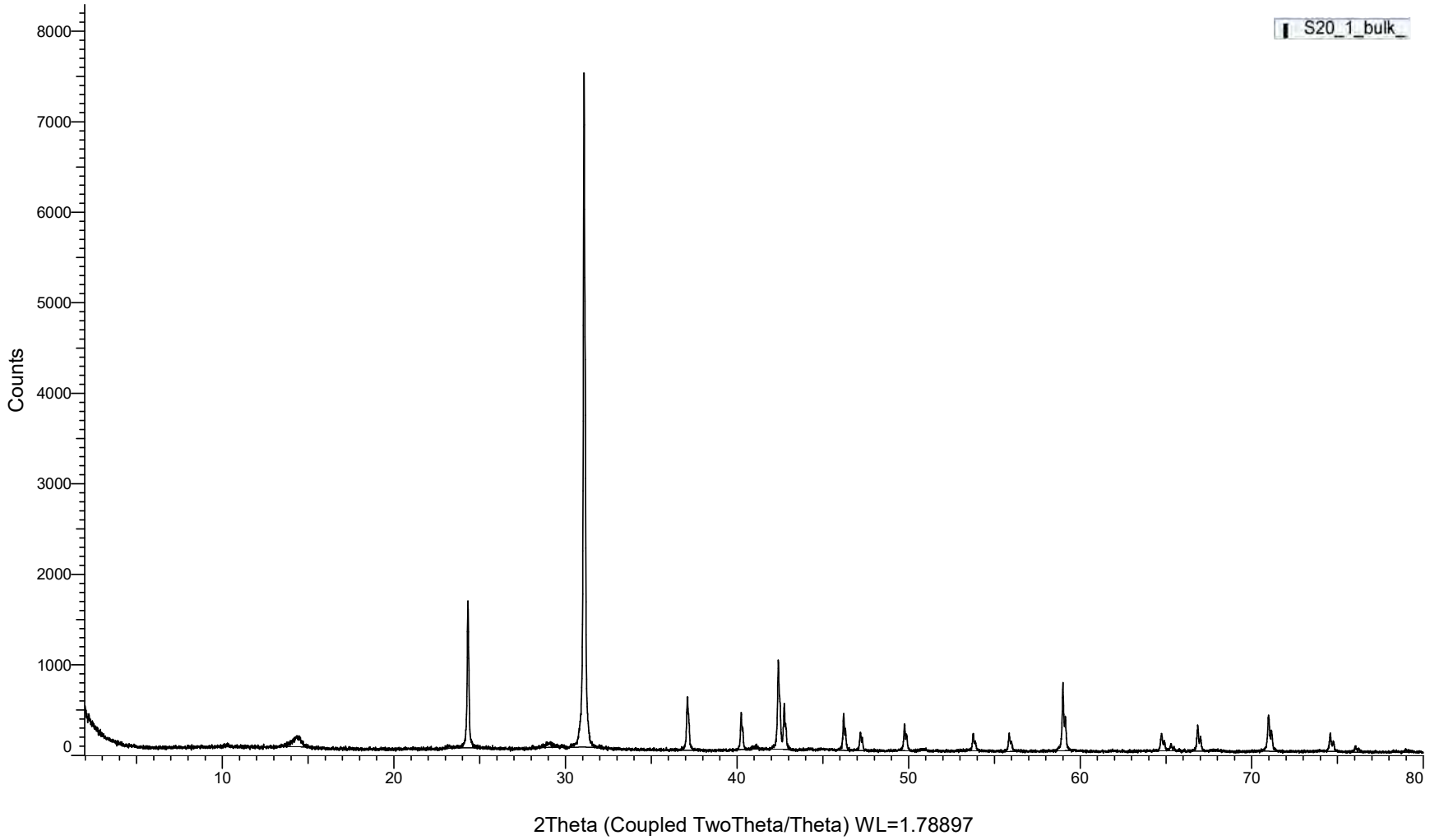

(Coupled TwoTheta/Theta)

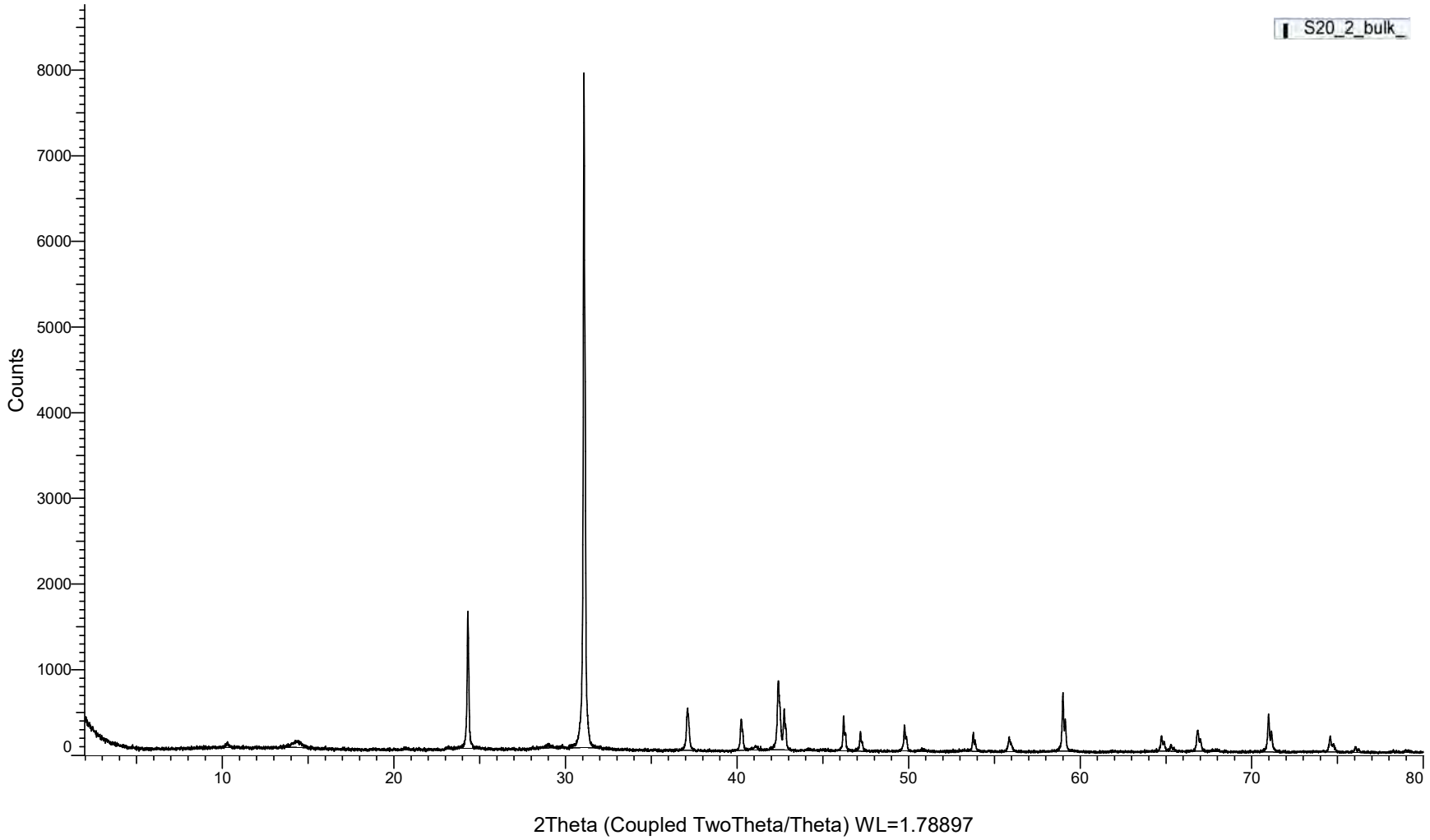

(Coupled TwoTheta/Theta)

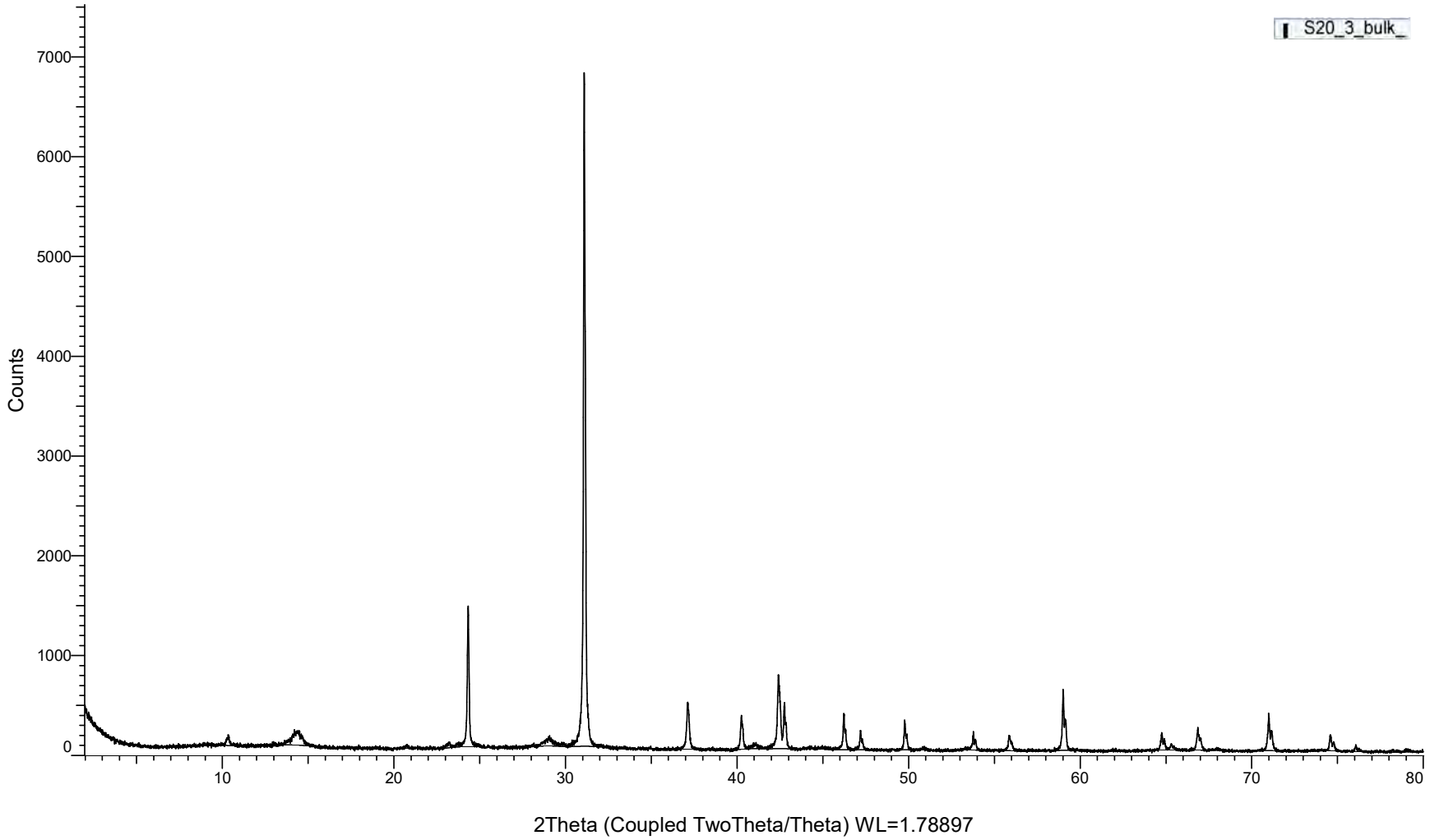

(Coupled TwoTheta/Theta)

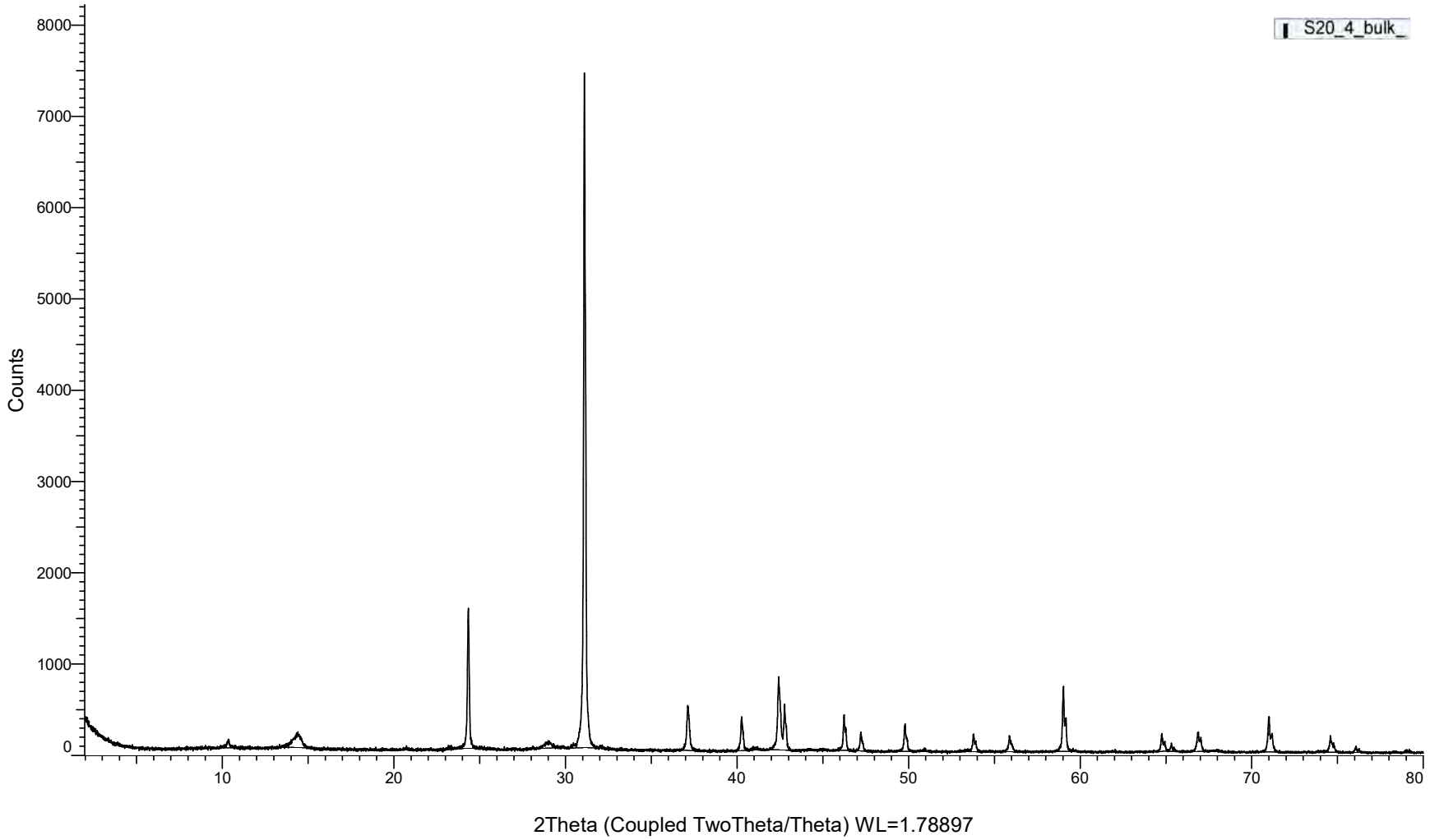

(Coupled TwoTheta/Theta)

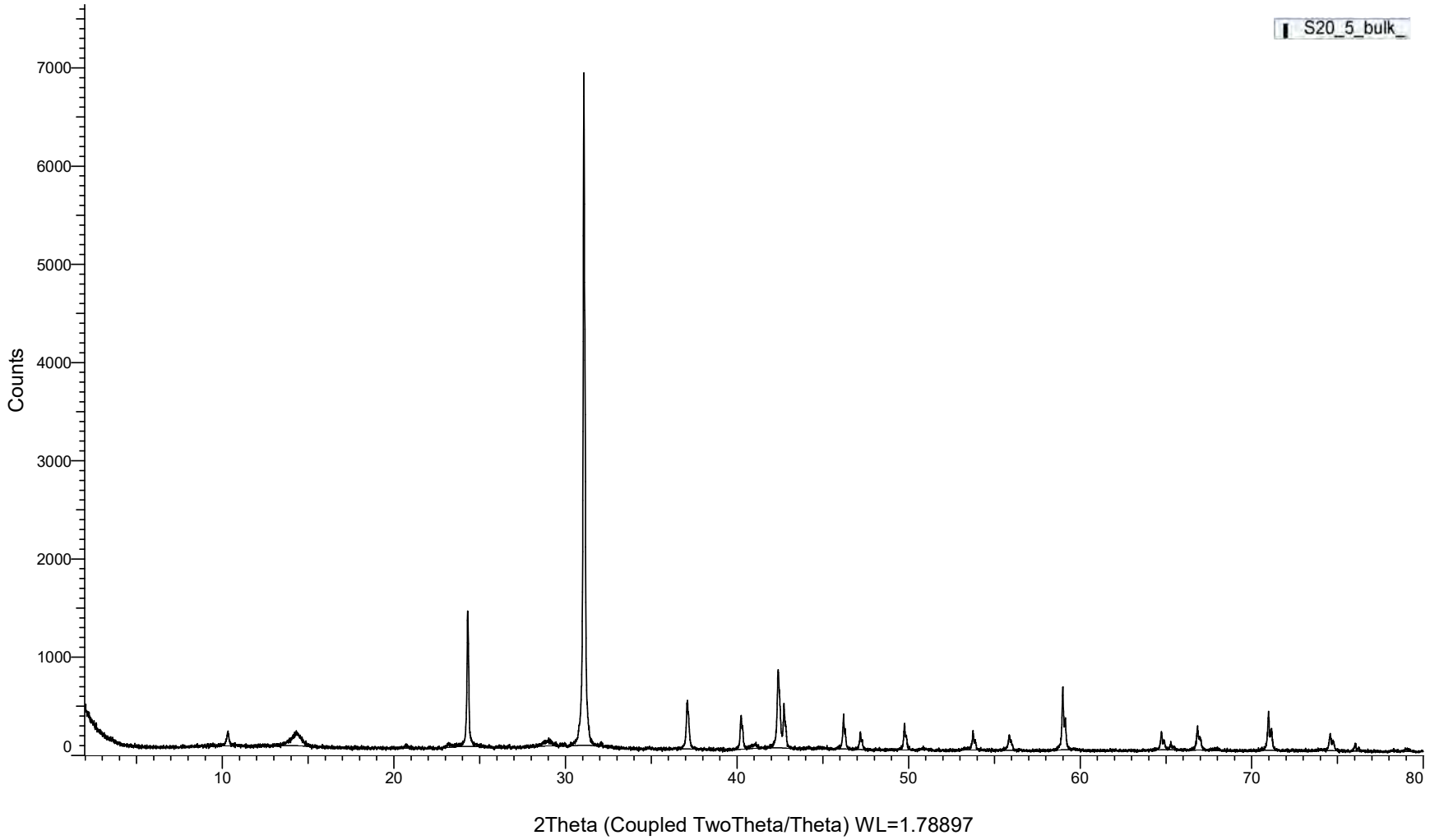

(Coupled TwoTheta/Theta)

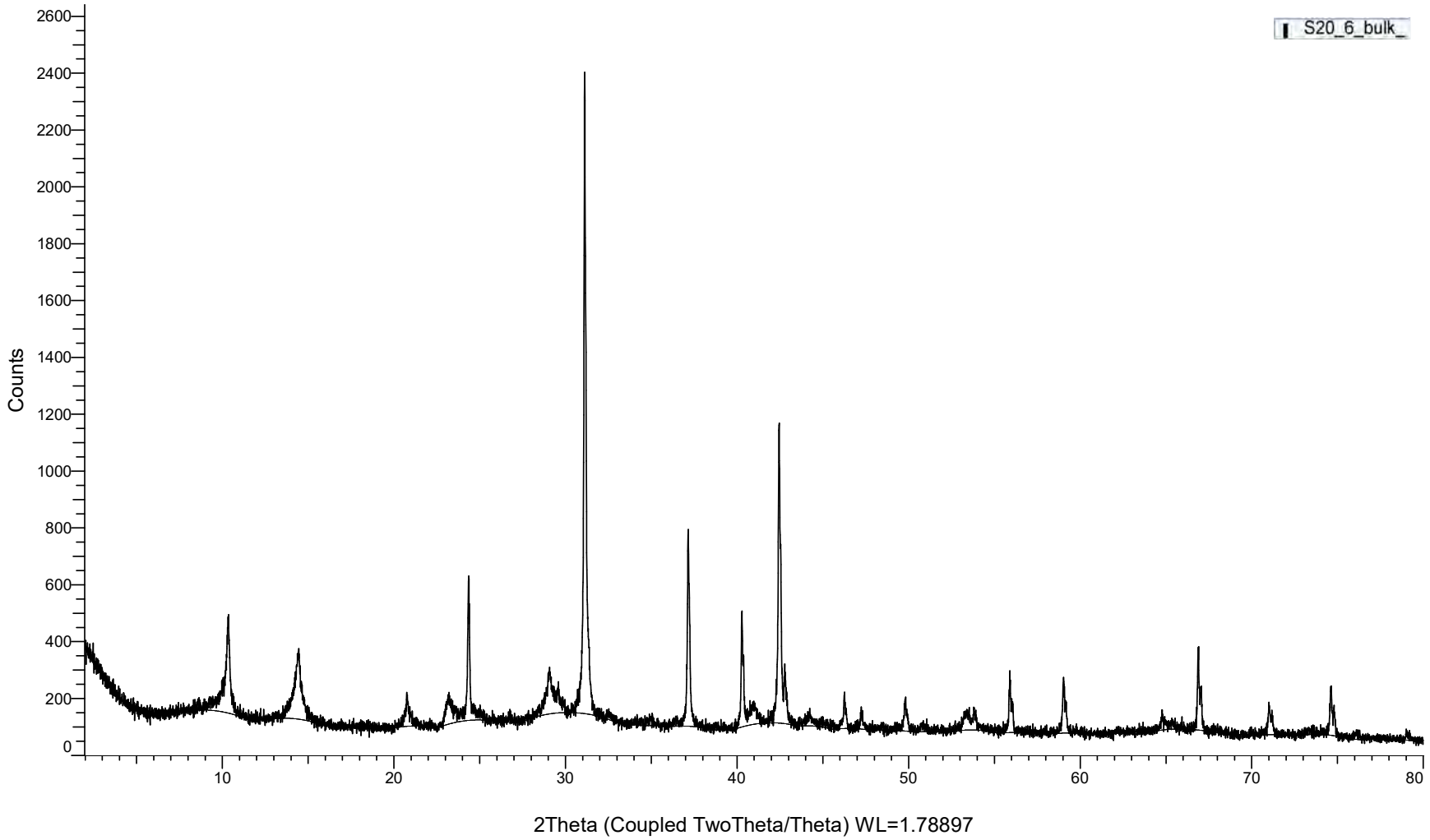

(Coupled TwoTheta/Theta)

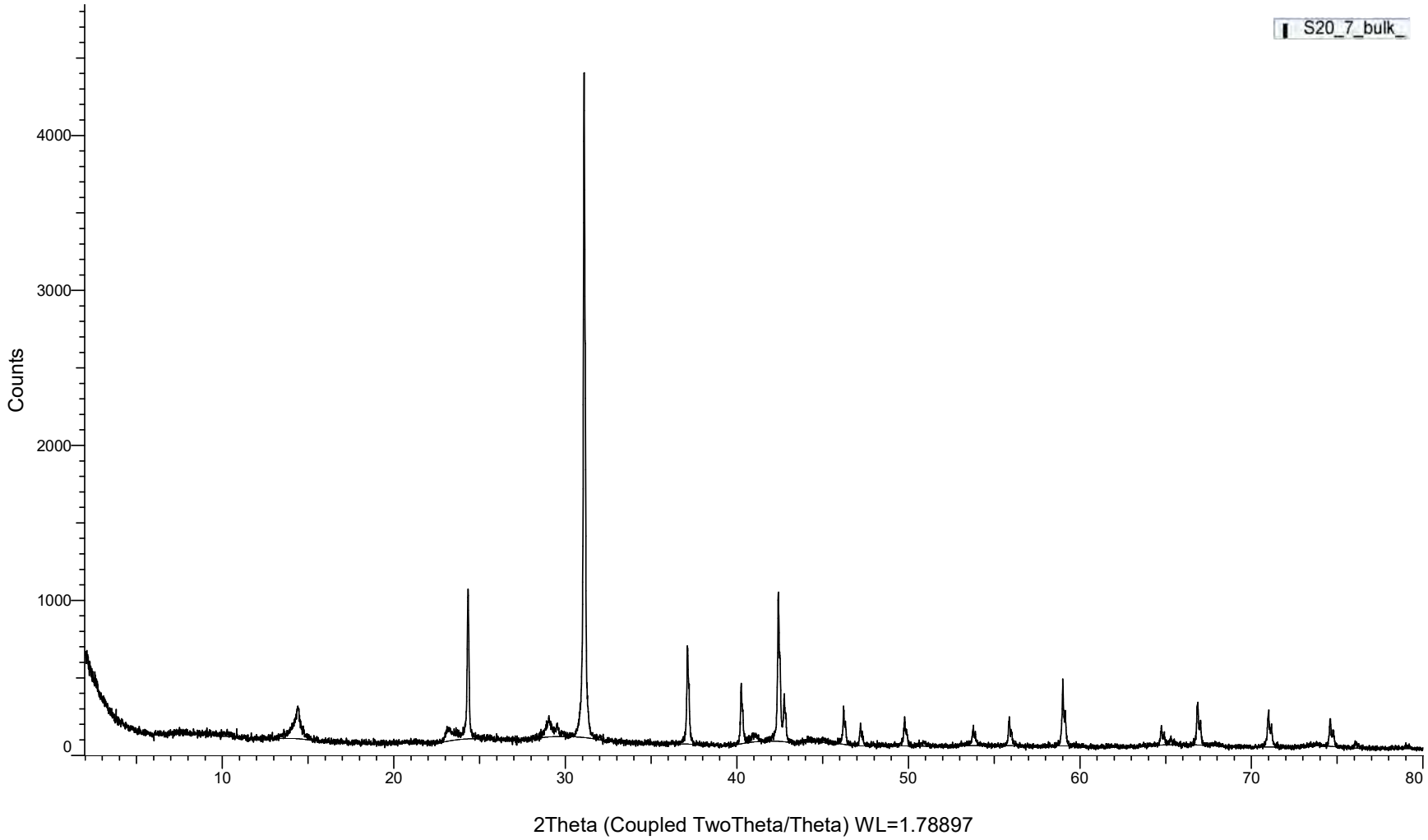

(Coupled TwoTheta/Theta)

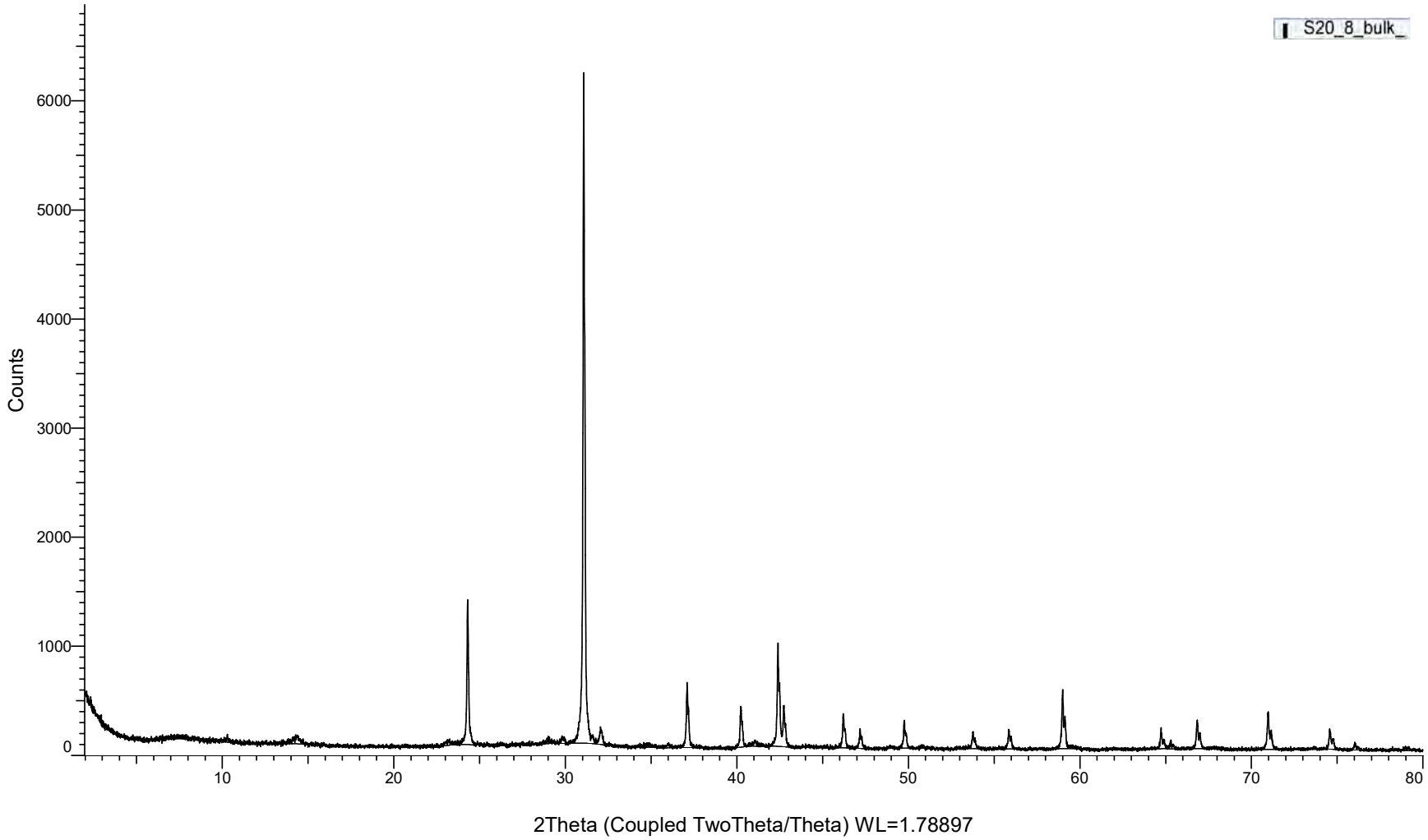

(Coupled TwoTheta/Theta)

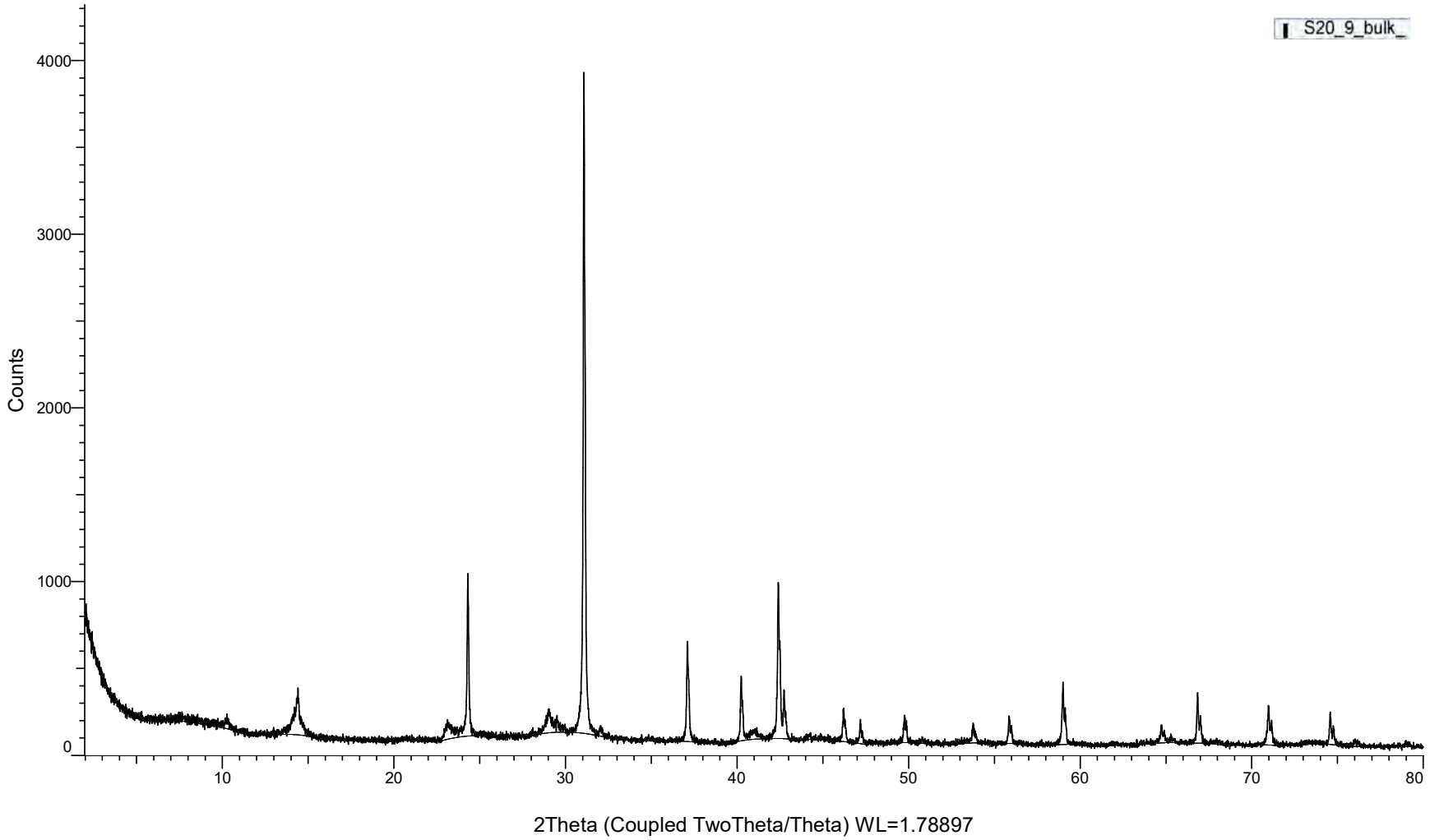

(Coupled TwoTheta/Theta)

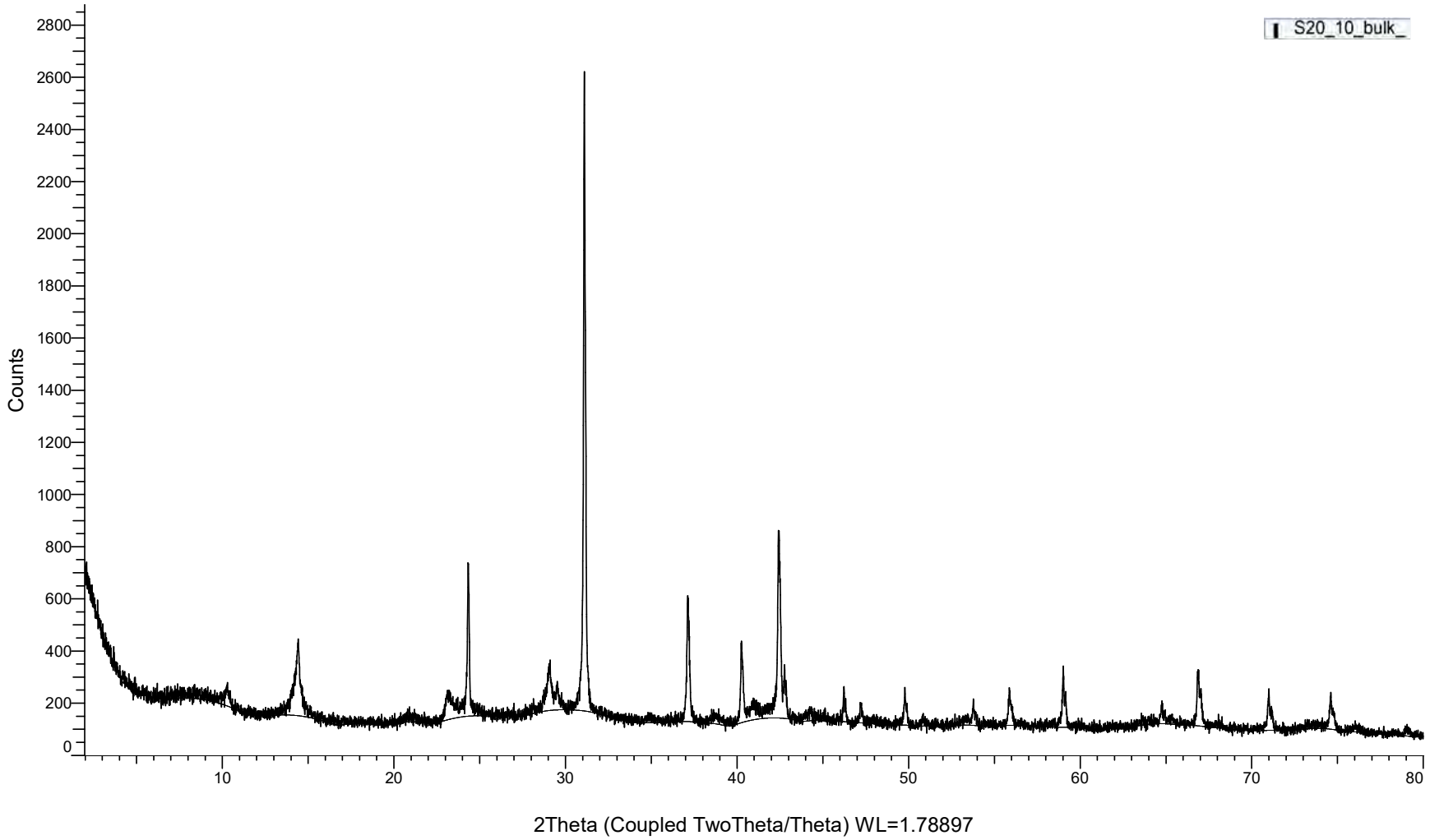

(Coupled TwoTheta/Theta)

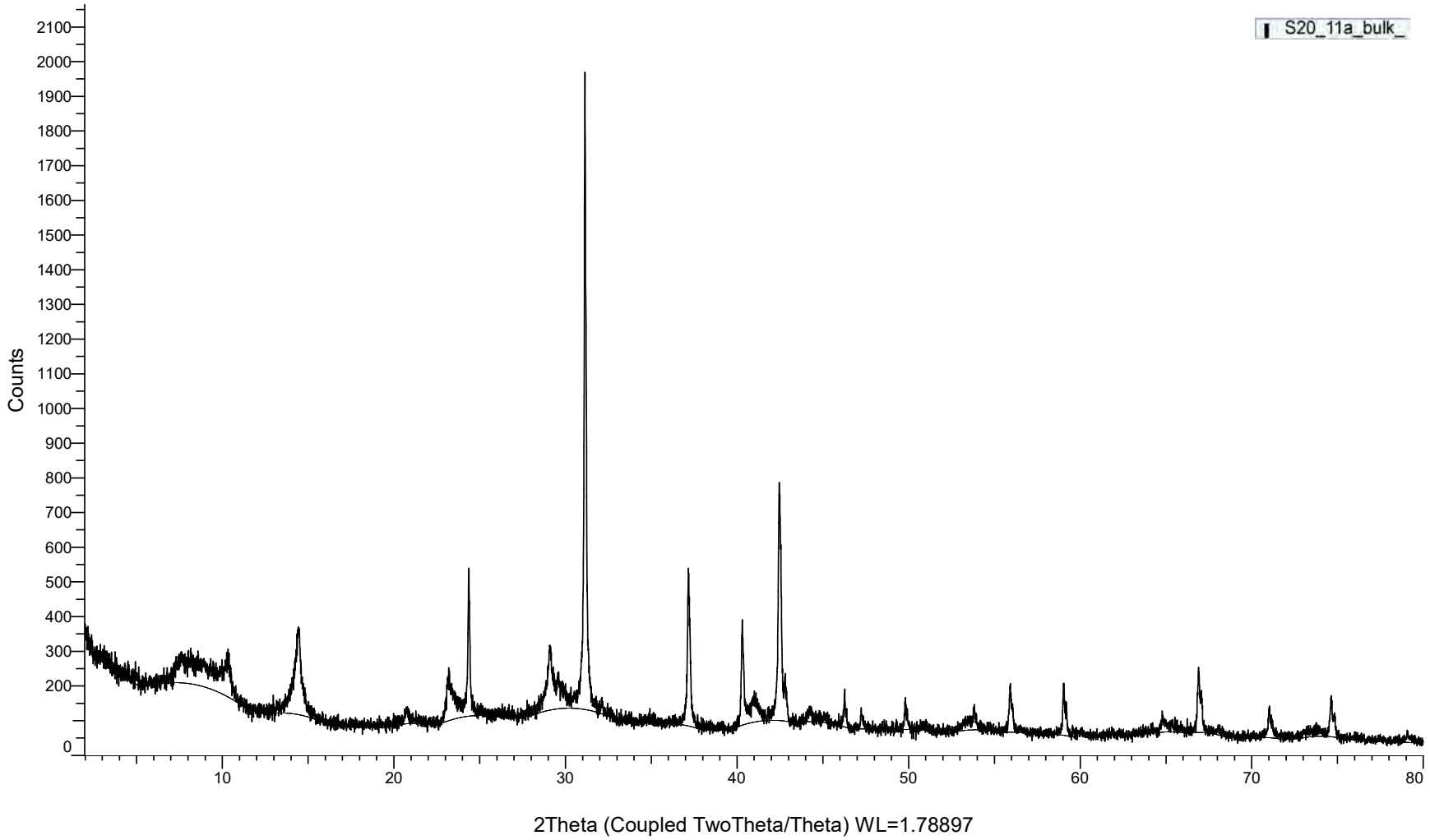

(Coupled TwoTheta/Theta)

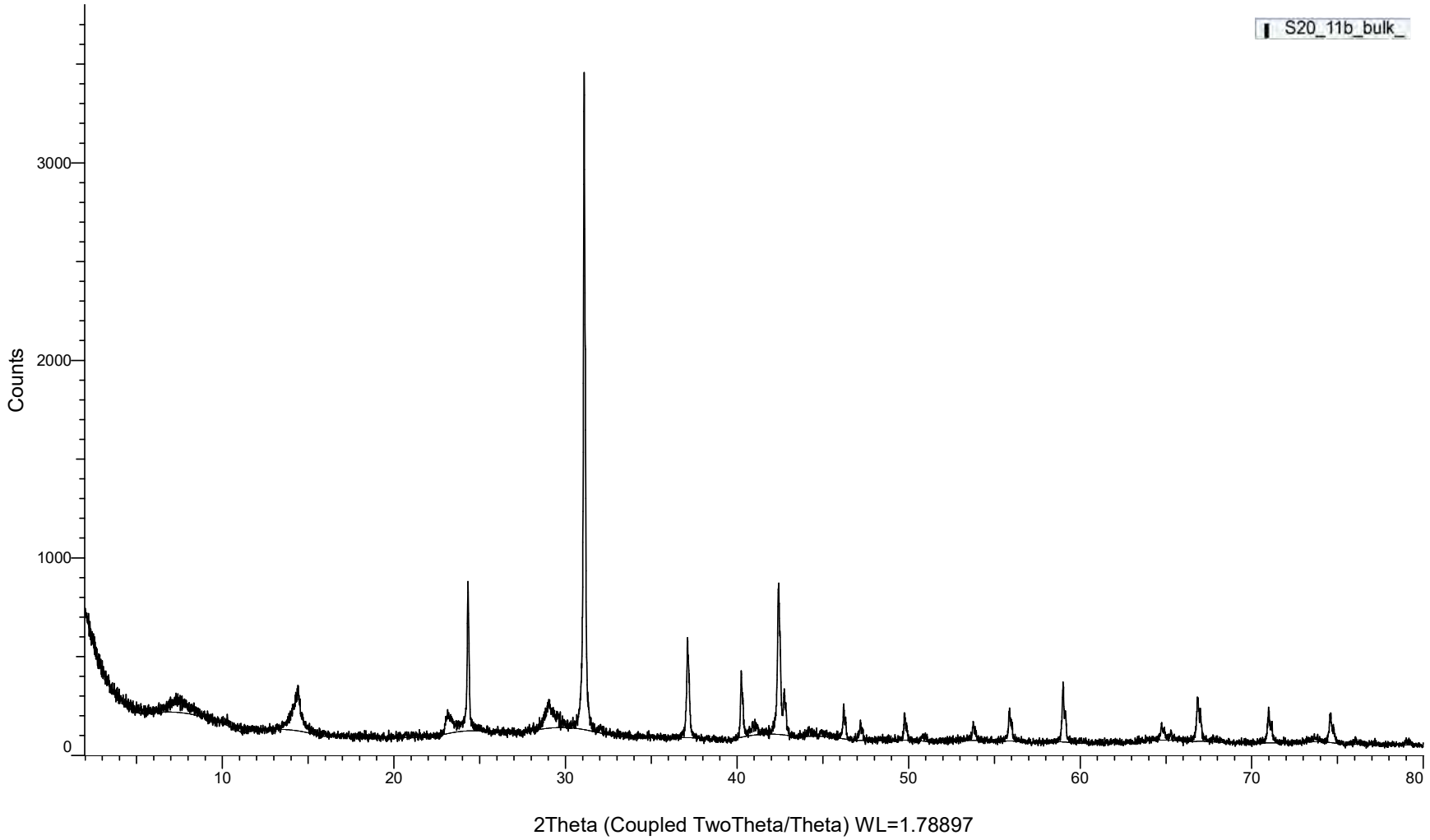

(Coupled TwoTheta/Theta)

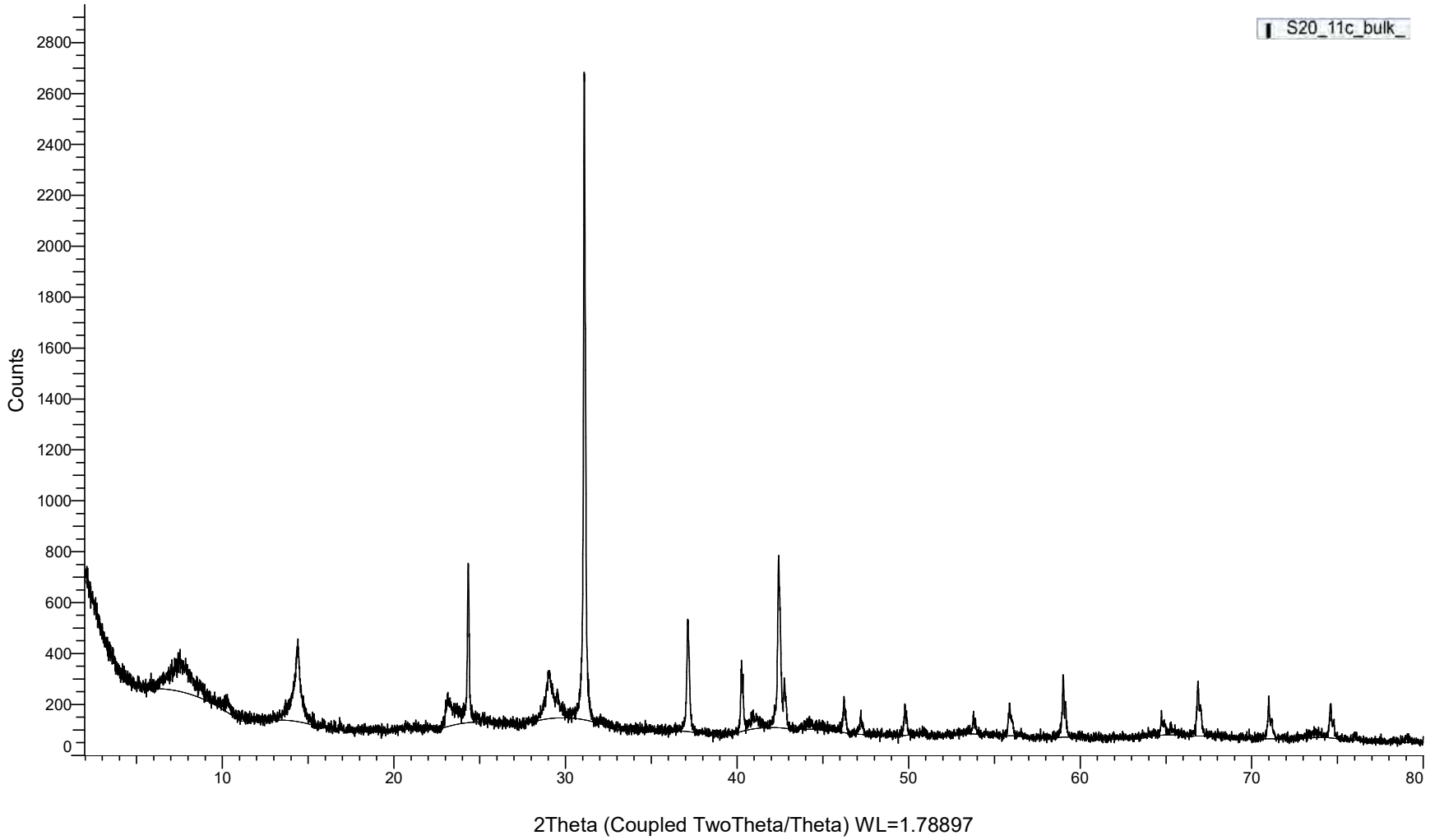

(Coupled TwoTheta/Theta)

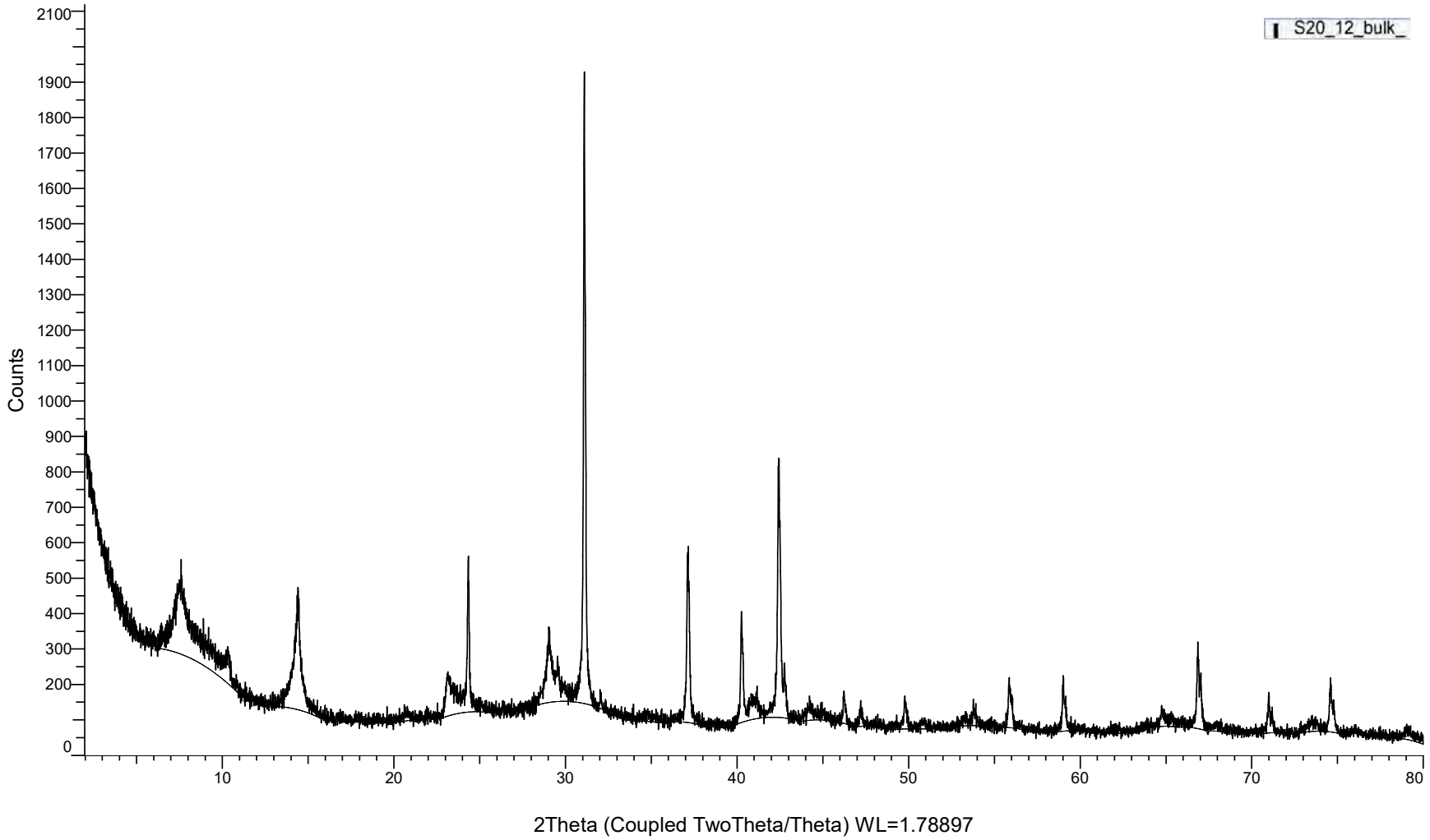

(Coupled TwoTheta/Theta)

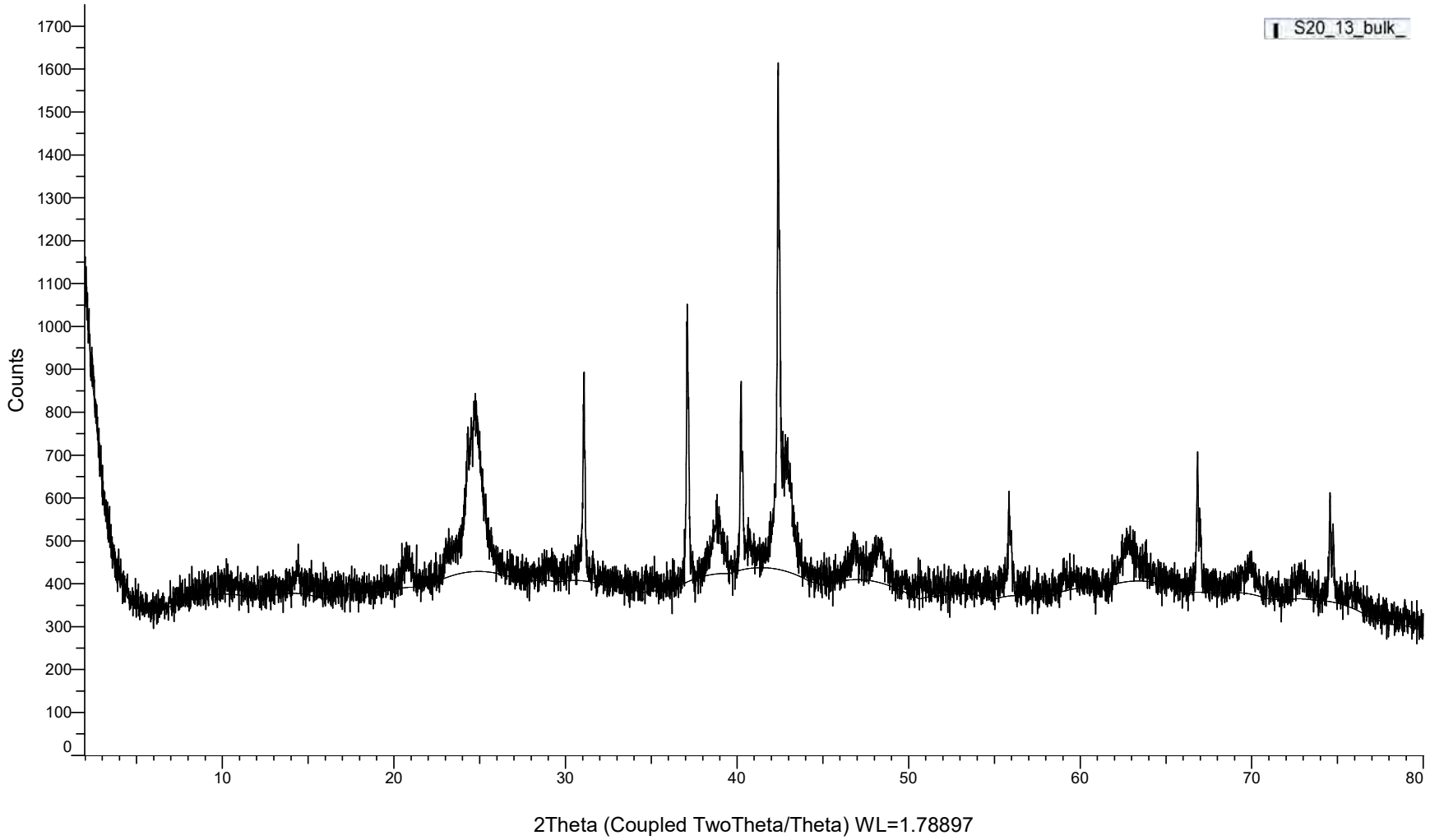

(Coupled TwoTheta/Theta)

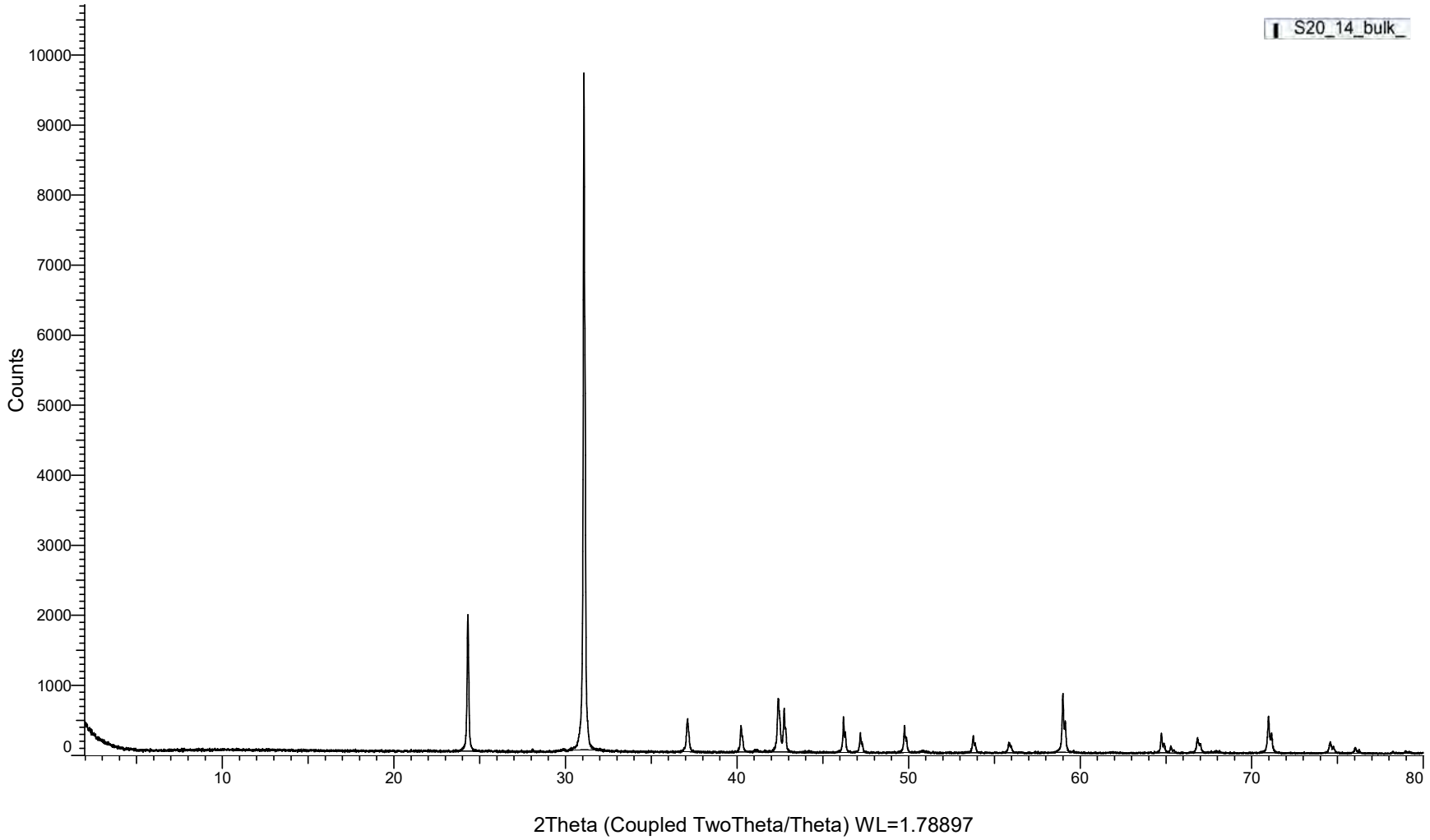

(Coupled TwoTheta/Theta)

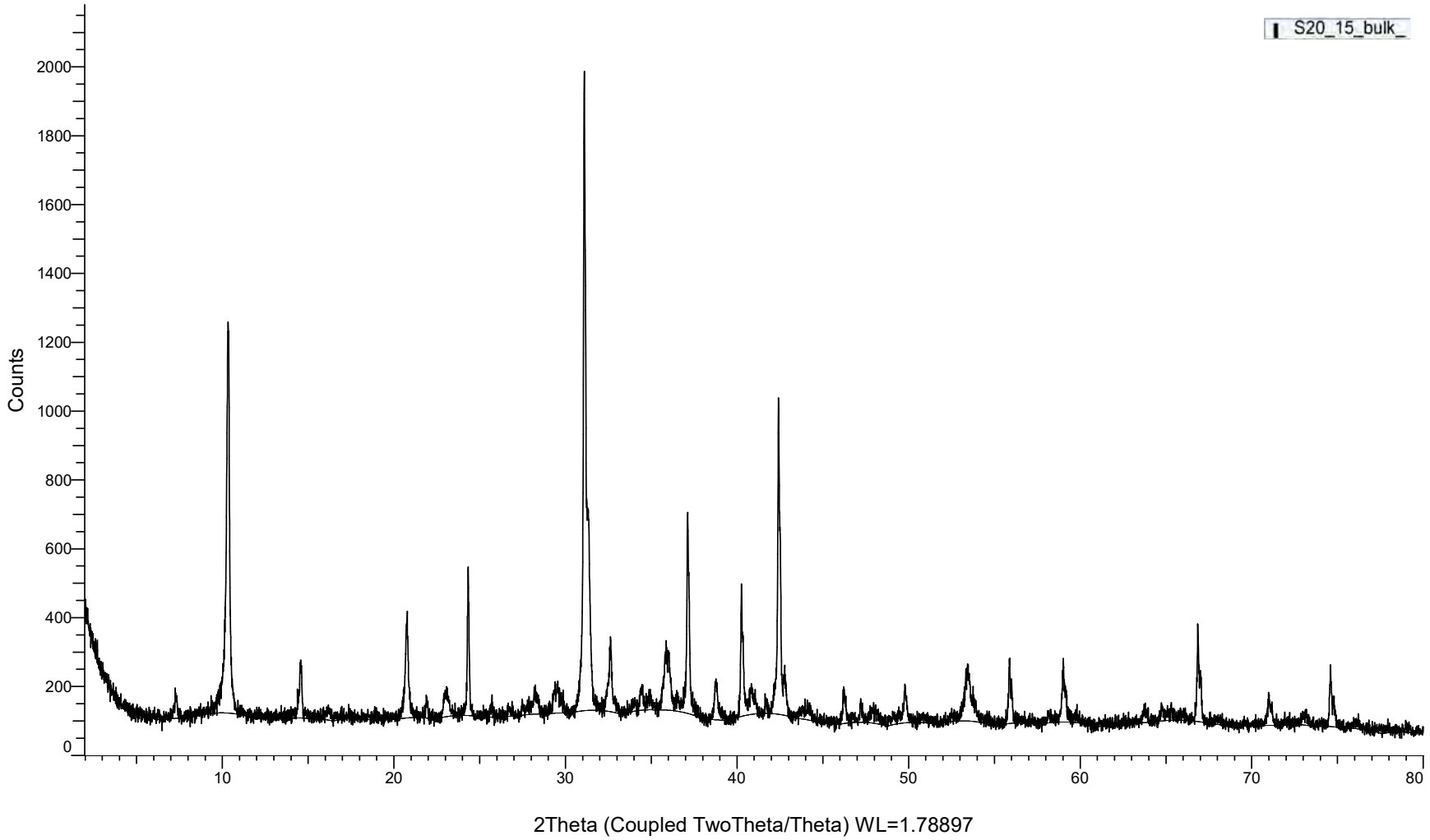

(Coupled TwoTheta/Theta)

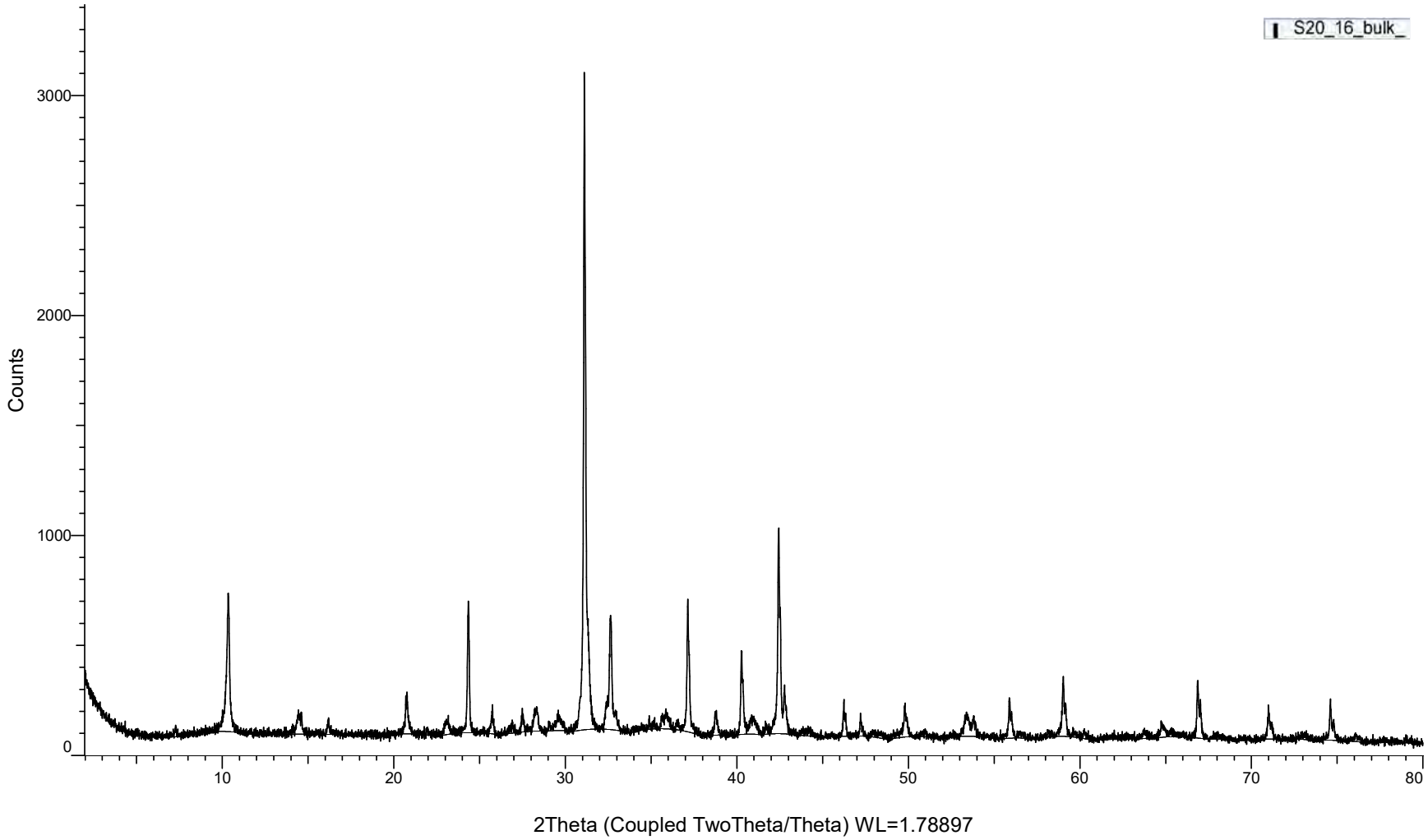

(Coupled TwoTheta/Theta)

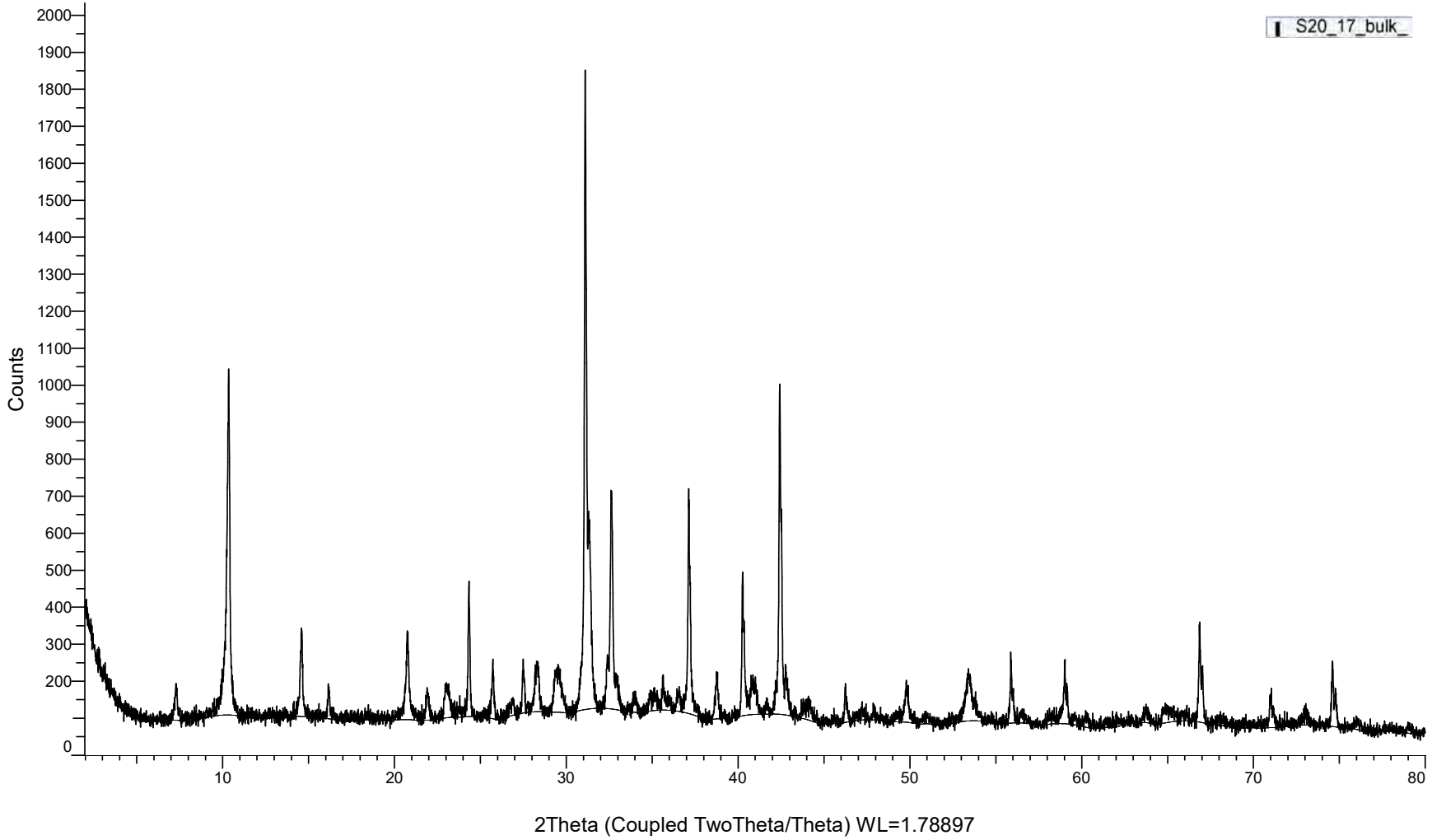

(Coupled TwoTheta/Theta)

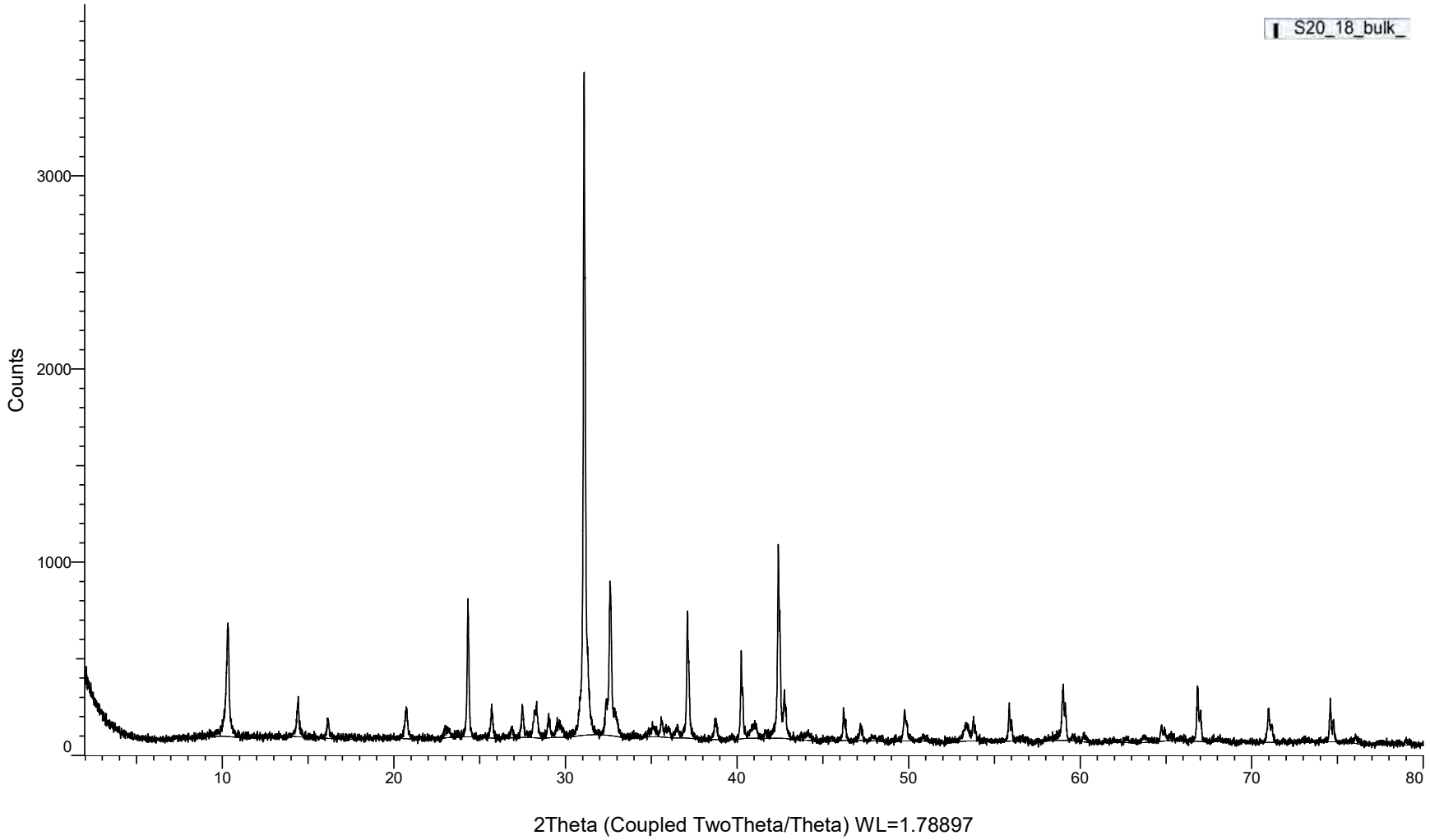

(Coupled TwoTheta/Theta)

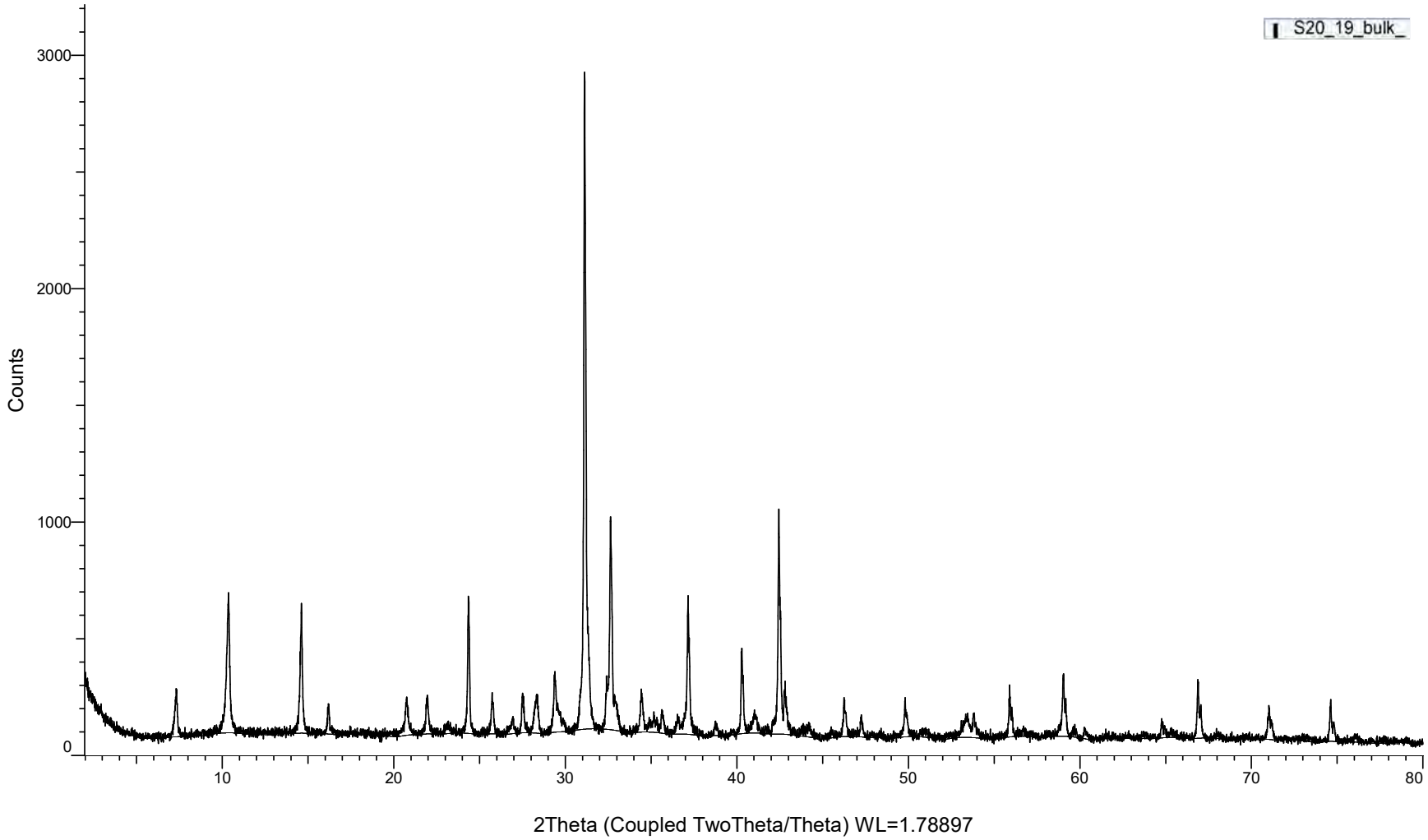

(Coupled TwoTheta/Theta)

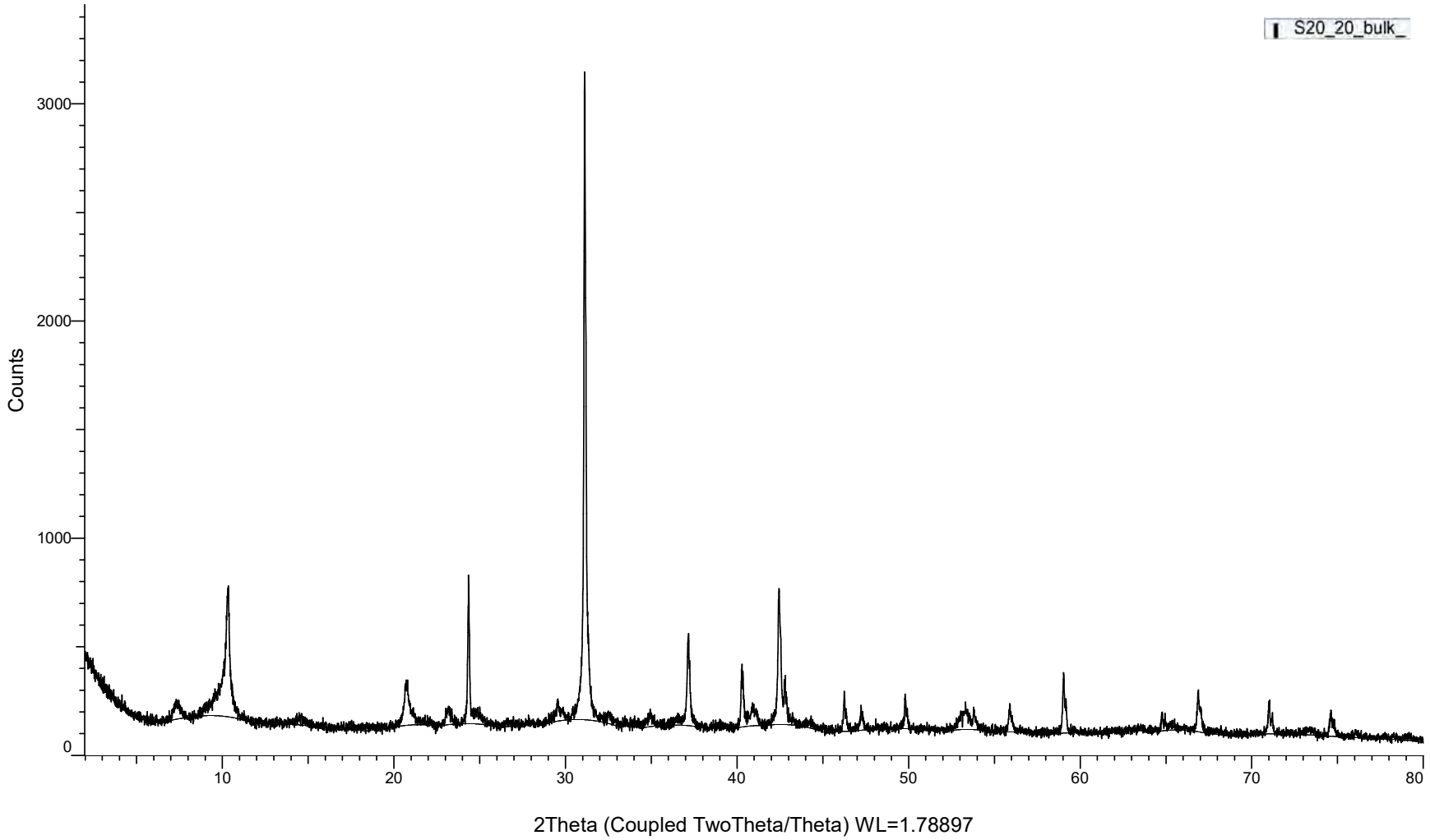

(Coupled TwoTheta/Theta)

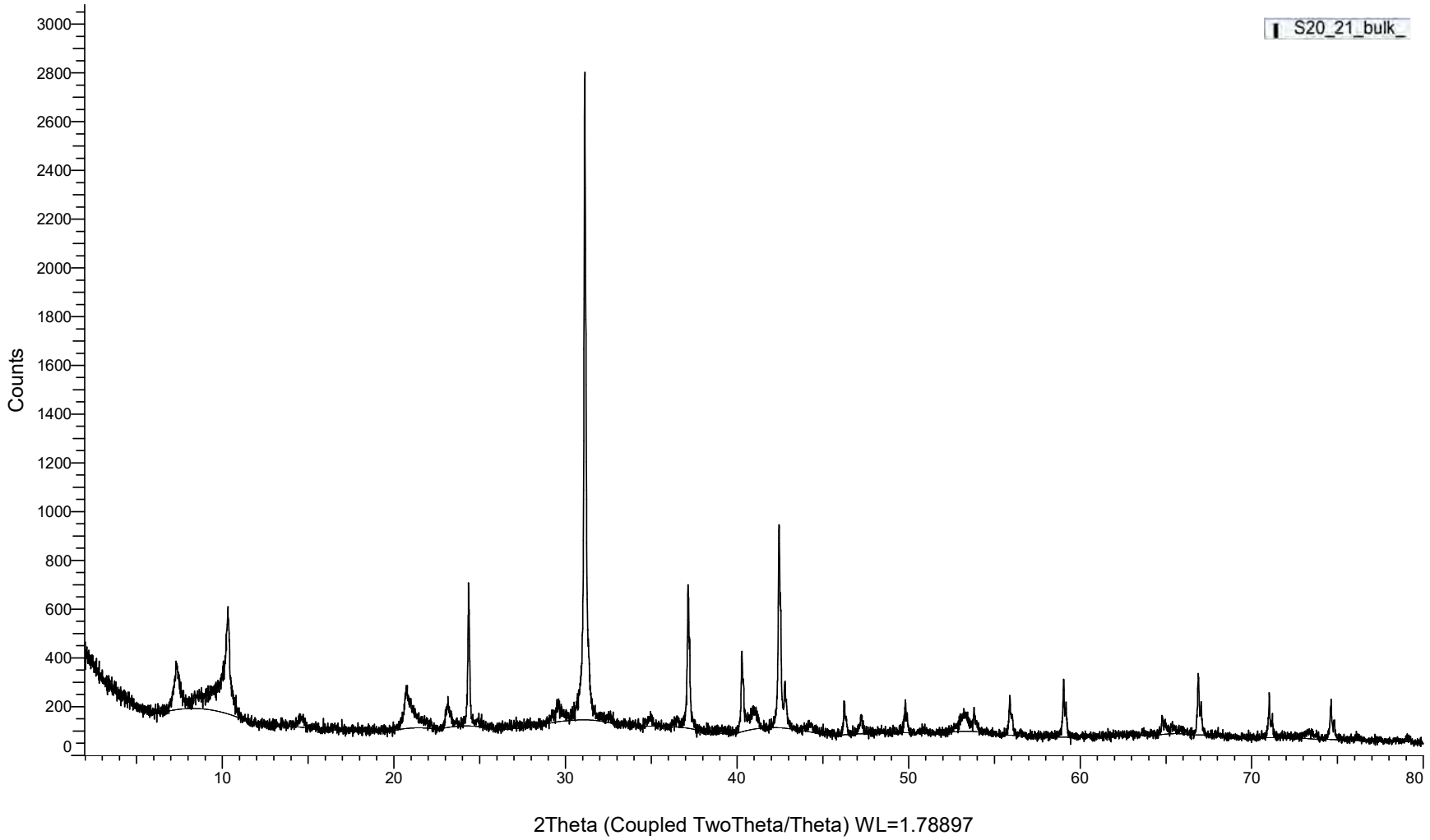

(Coupled TwoTheta/Theta)

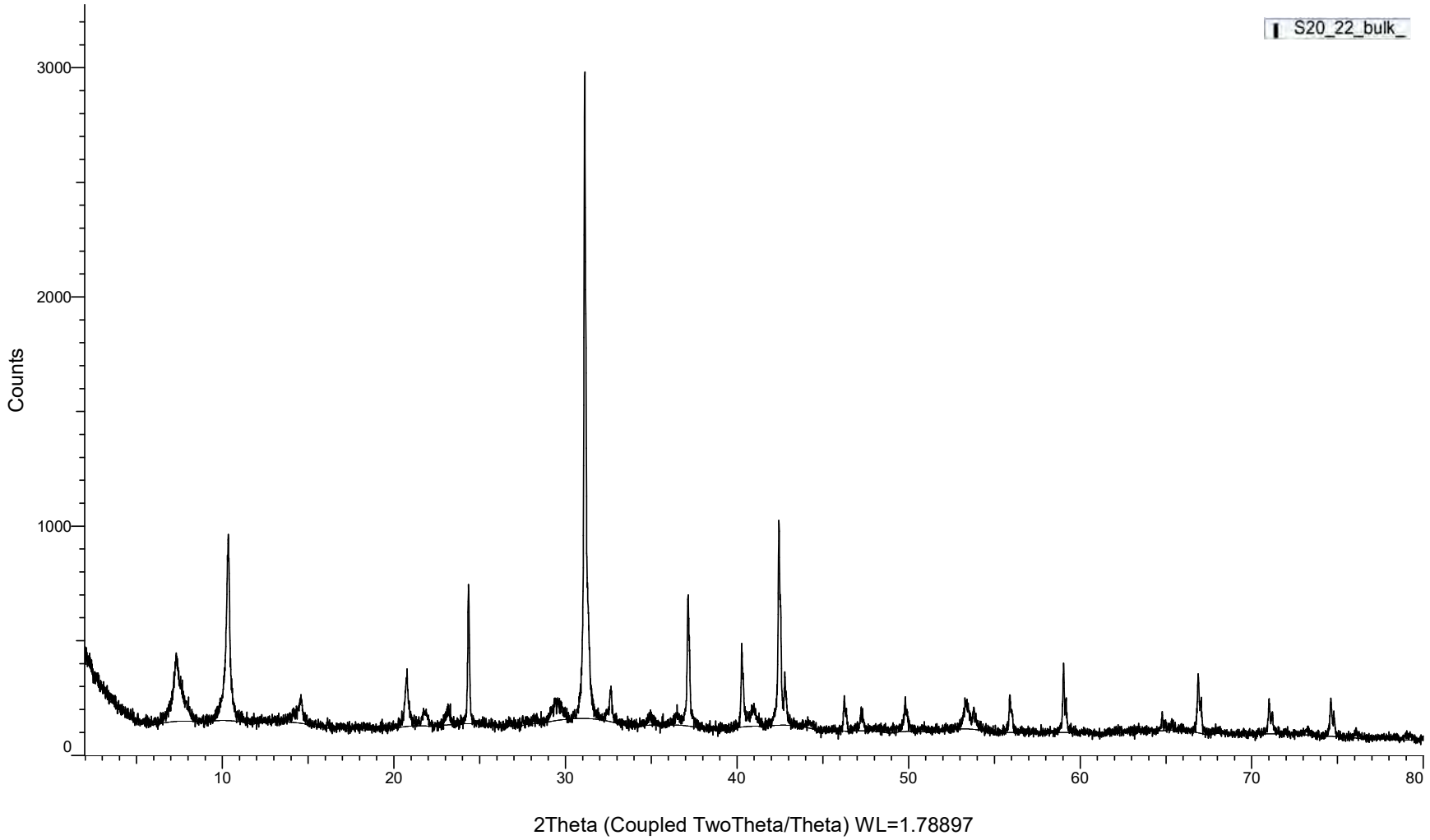

(Coupled TwoTheta/Theta)

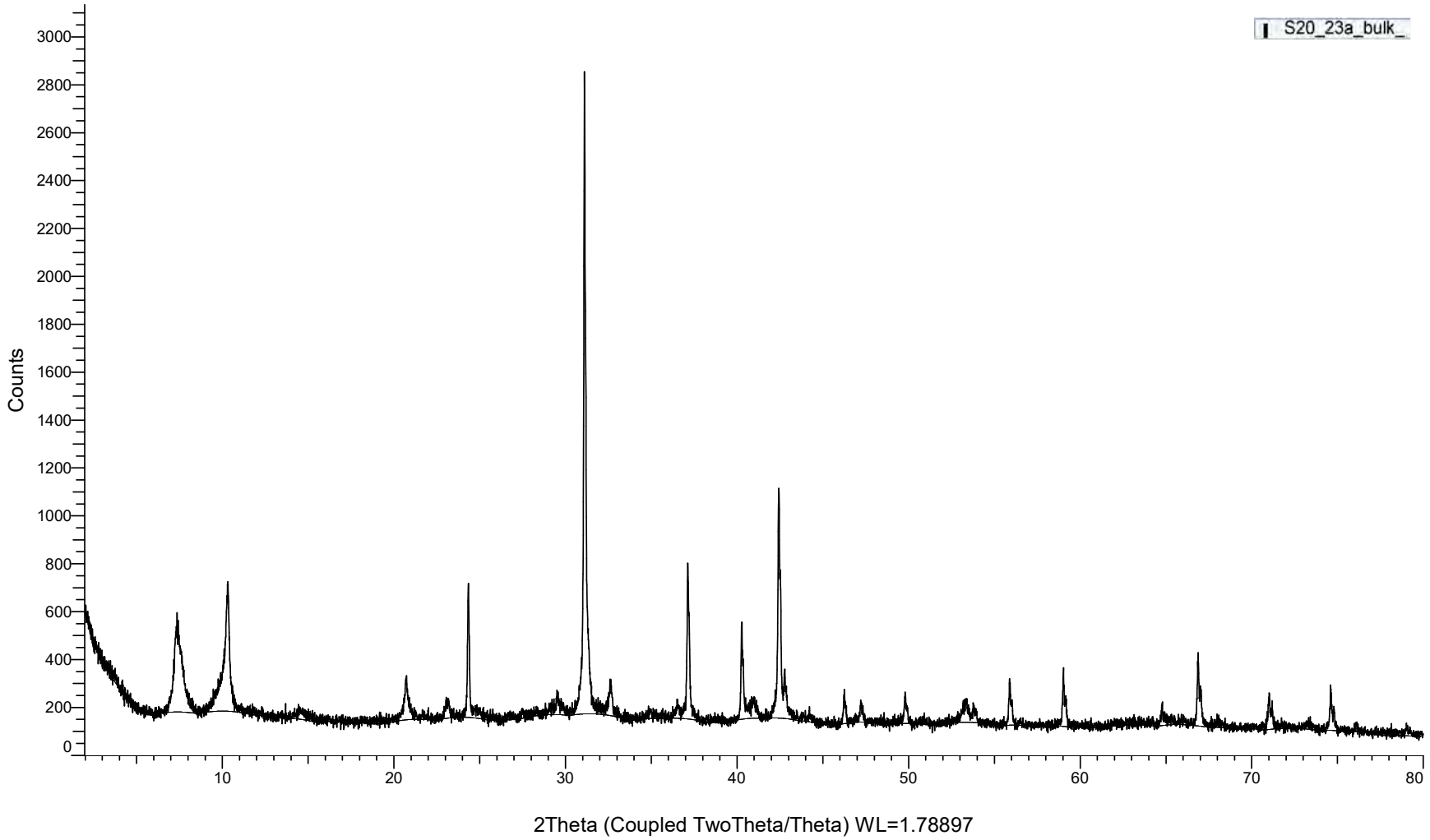

(Coupled TwoTheta/Theta)

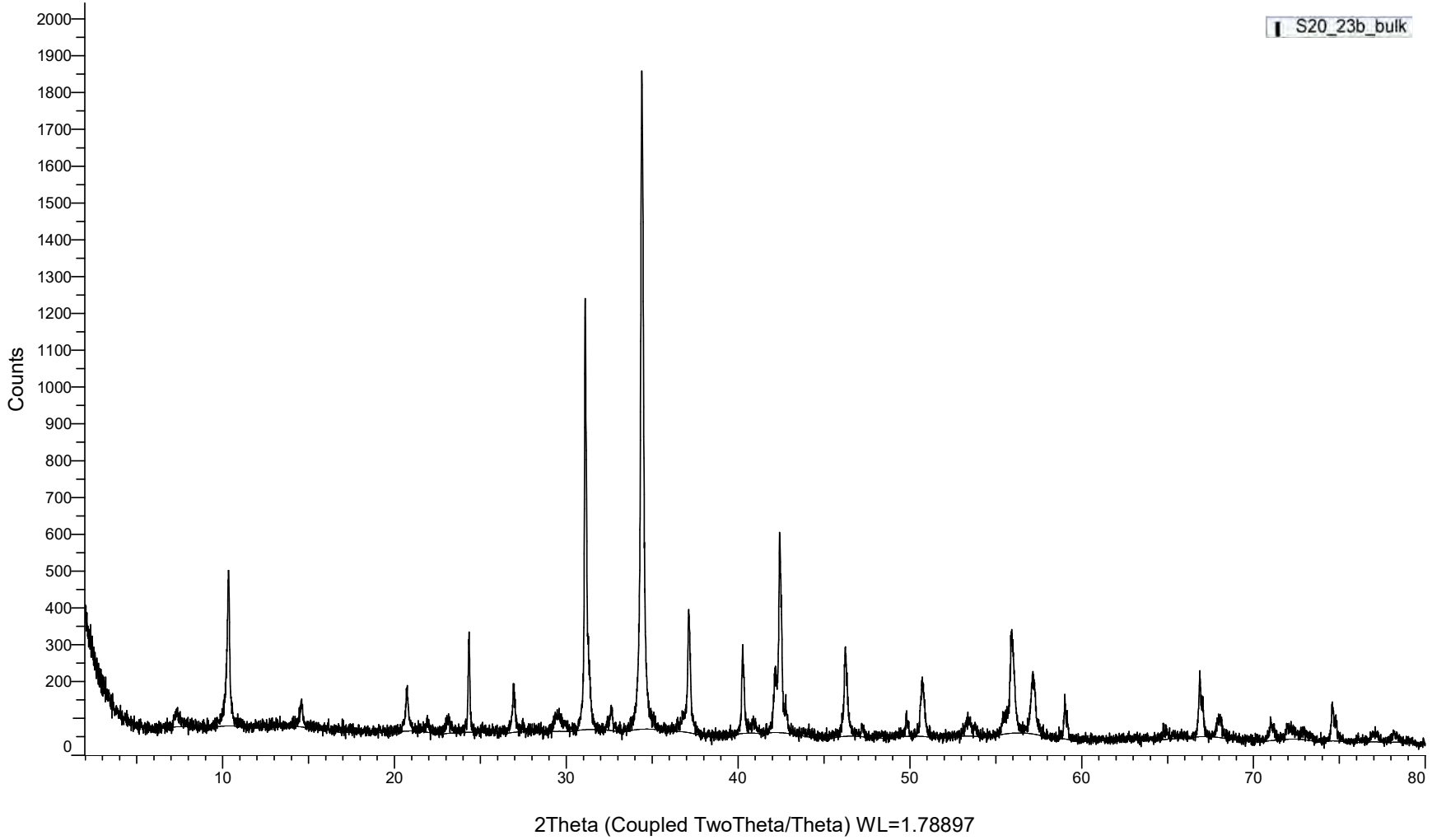

(Coupled TwoTheta/Theta)

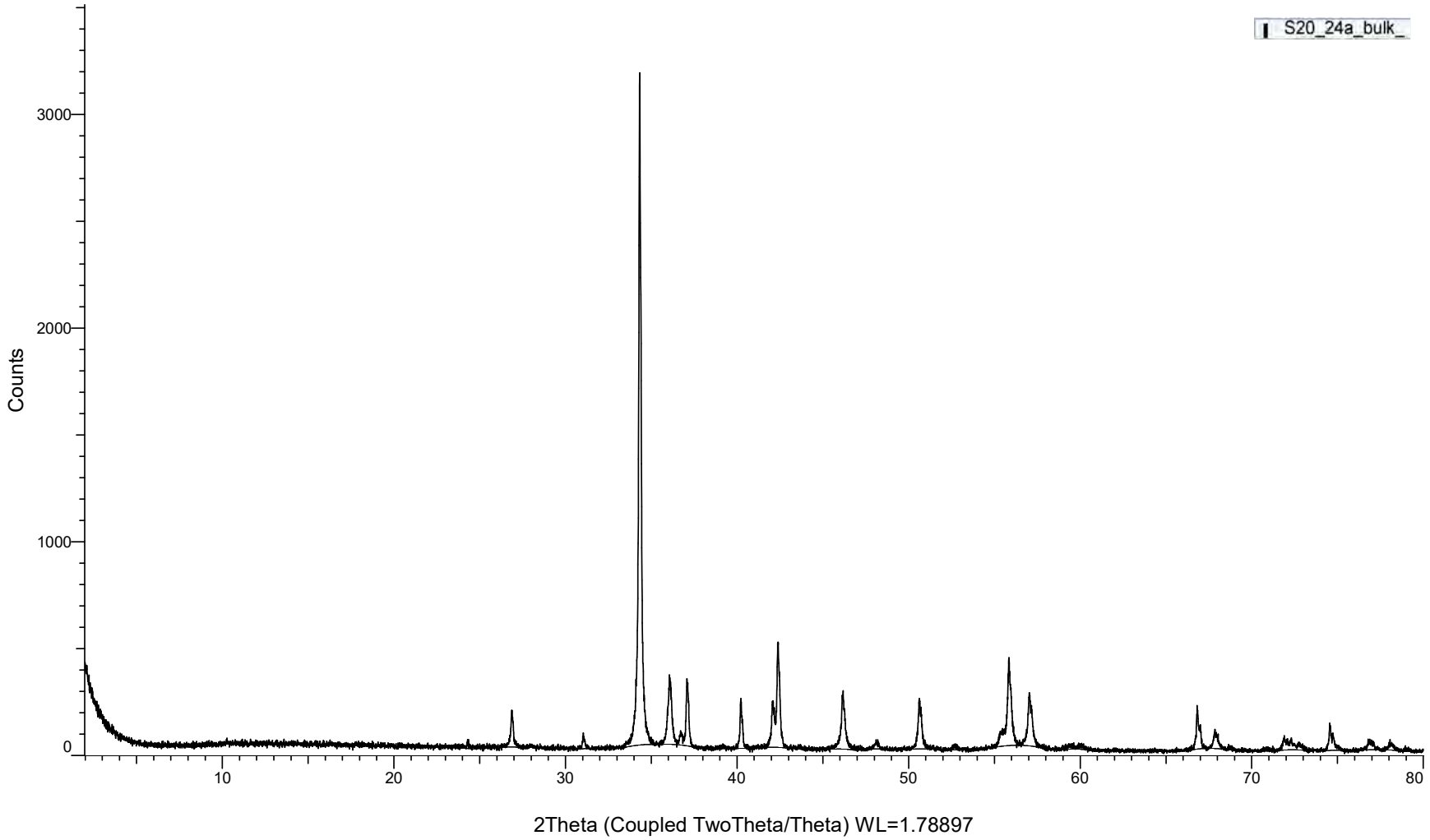

(Coupled TwoTheta/Theta)

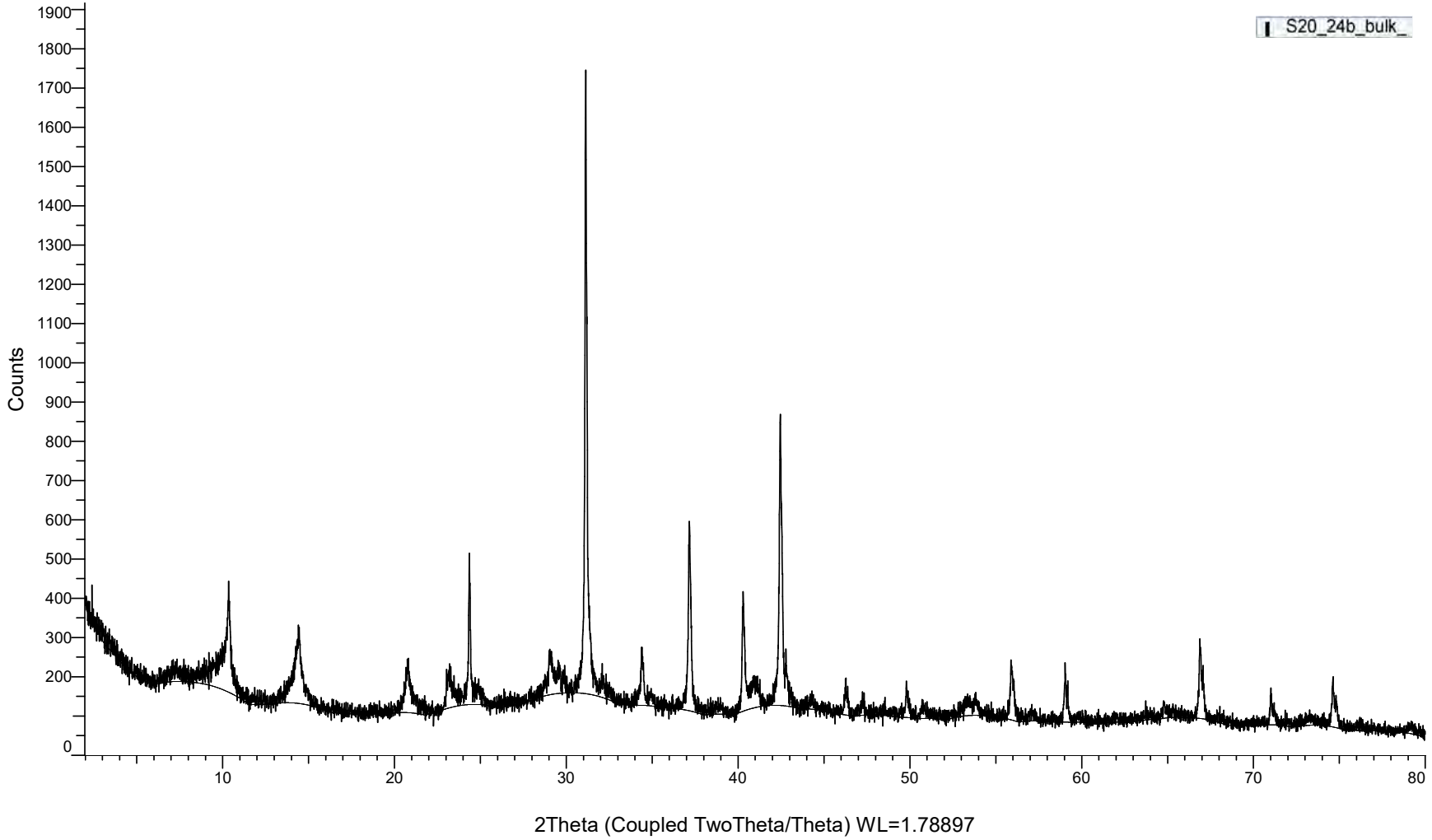

(Coupled TwoTheta/Theta)

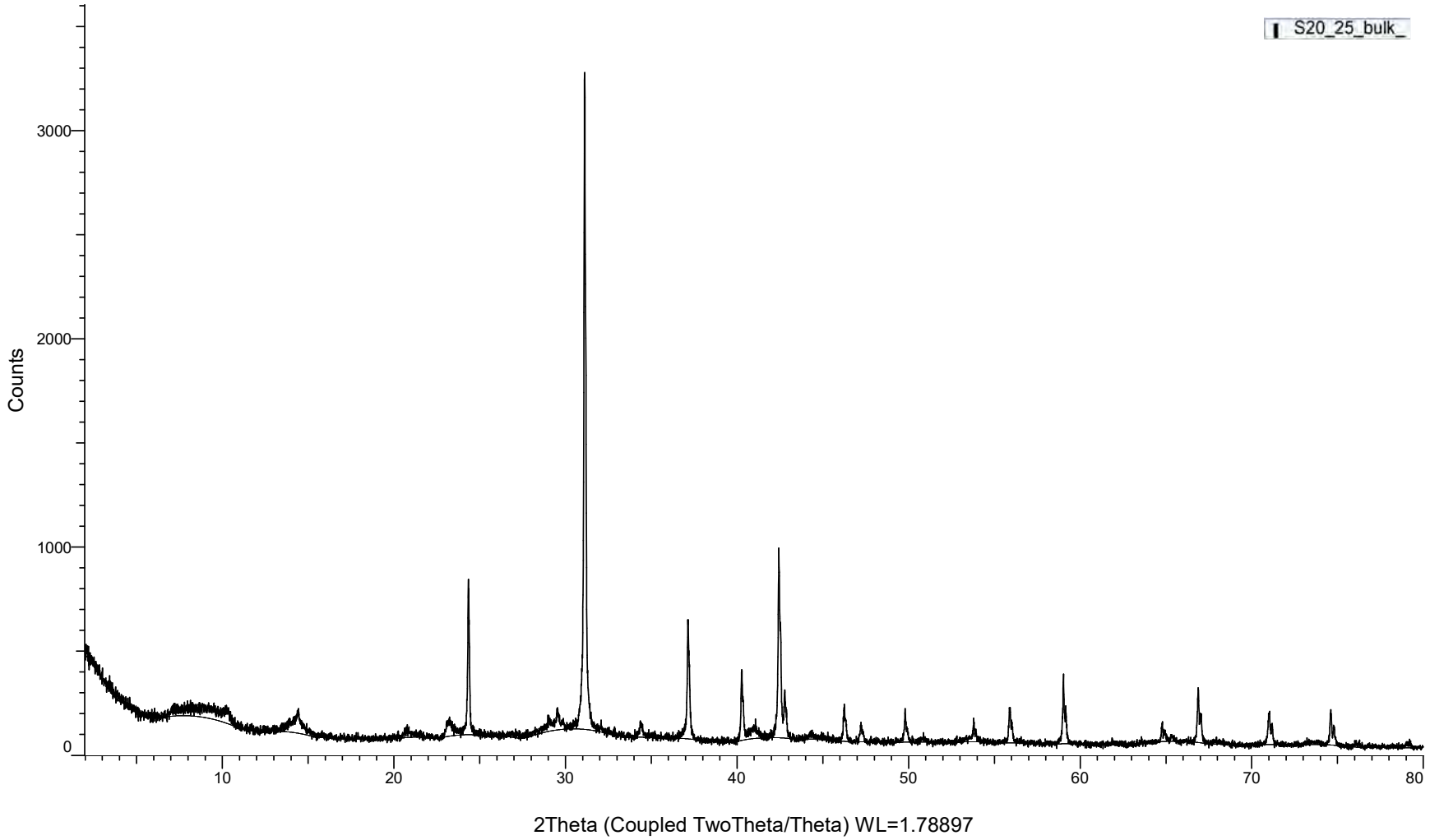

(Coupled TwoTheta/Theta)

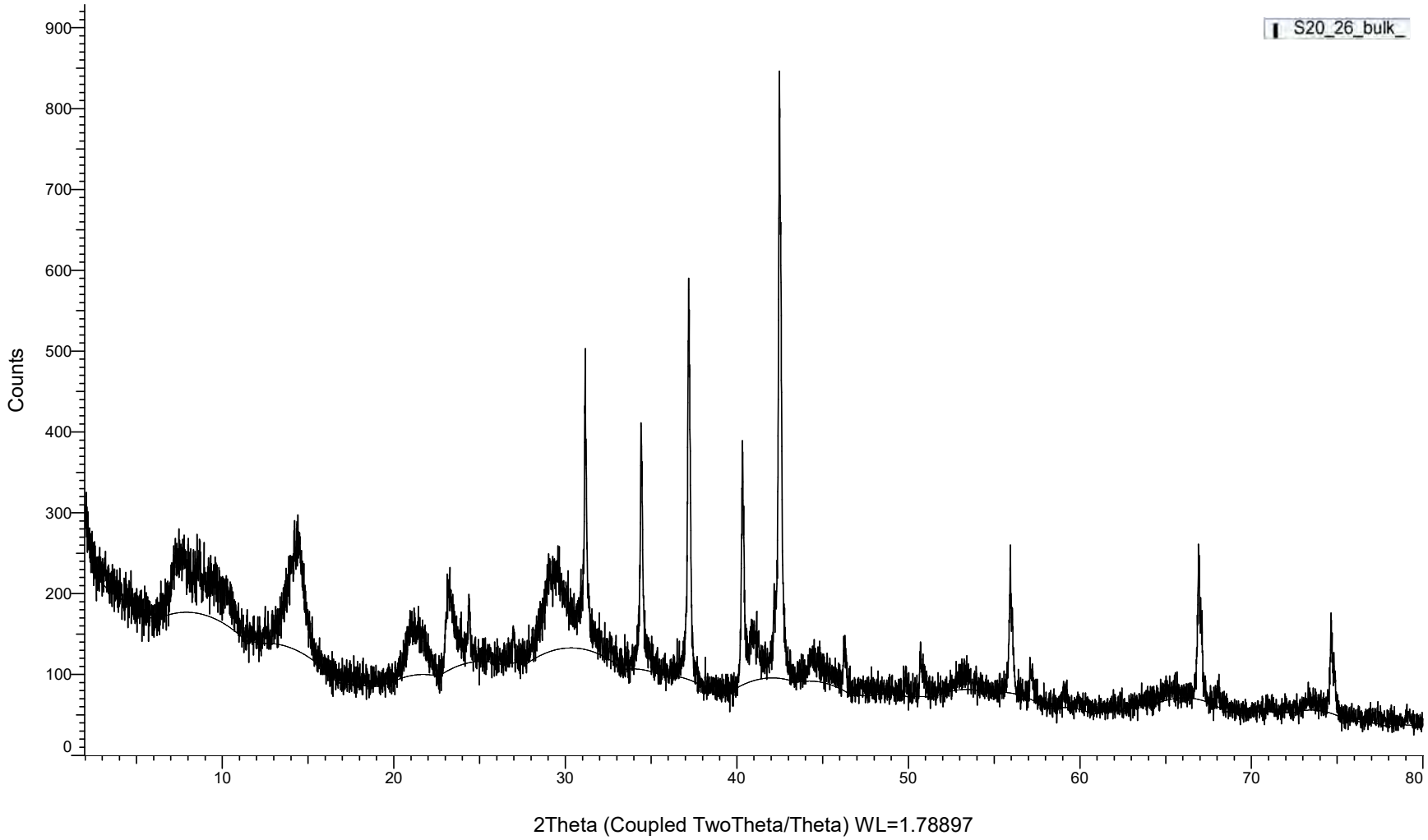

(Coupled TwoTheta/Theta)

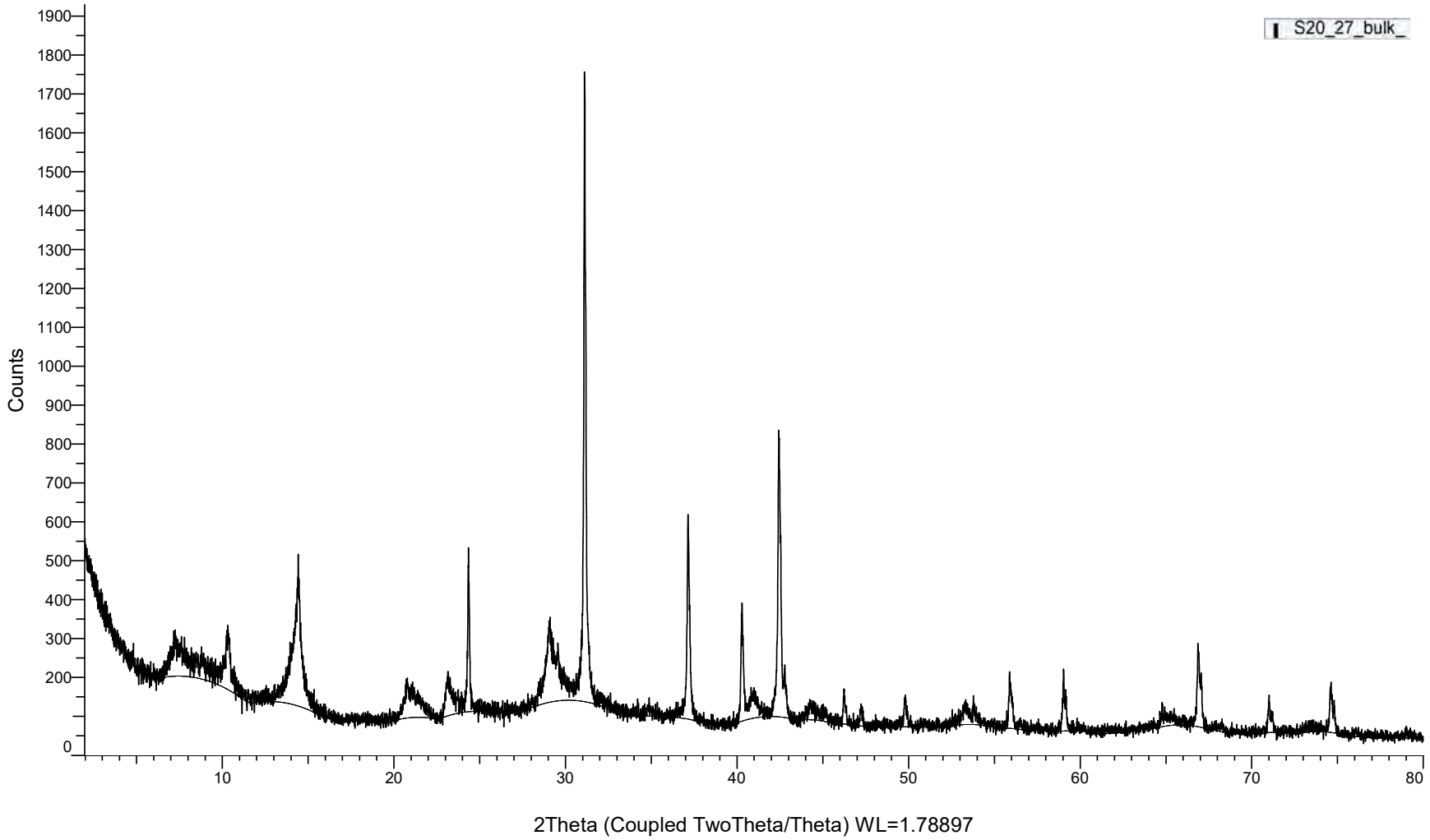

(Coupled TwoTheta/Theta)

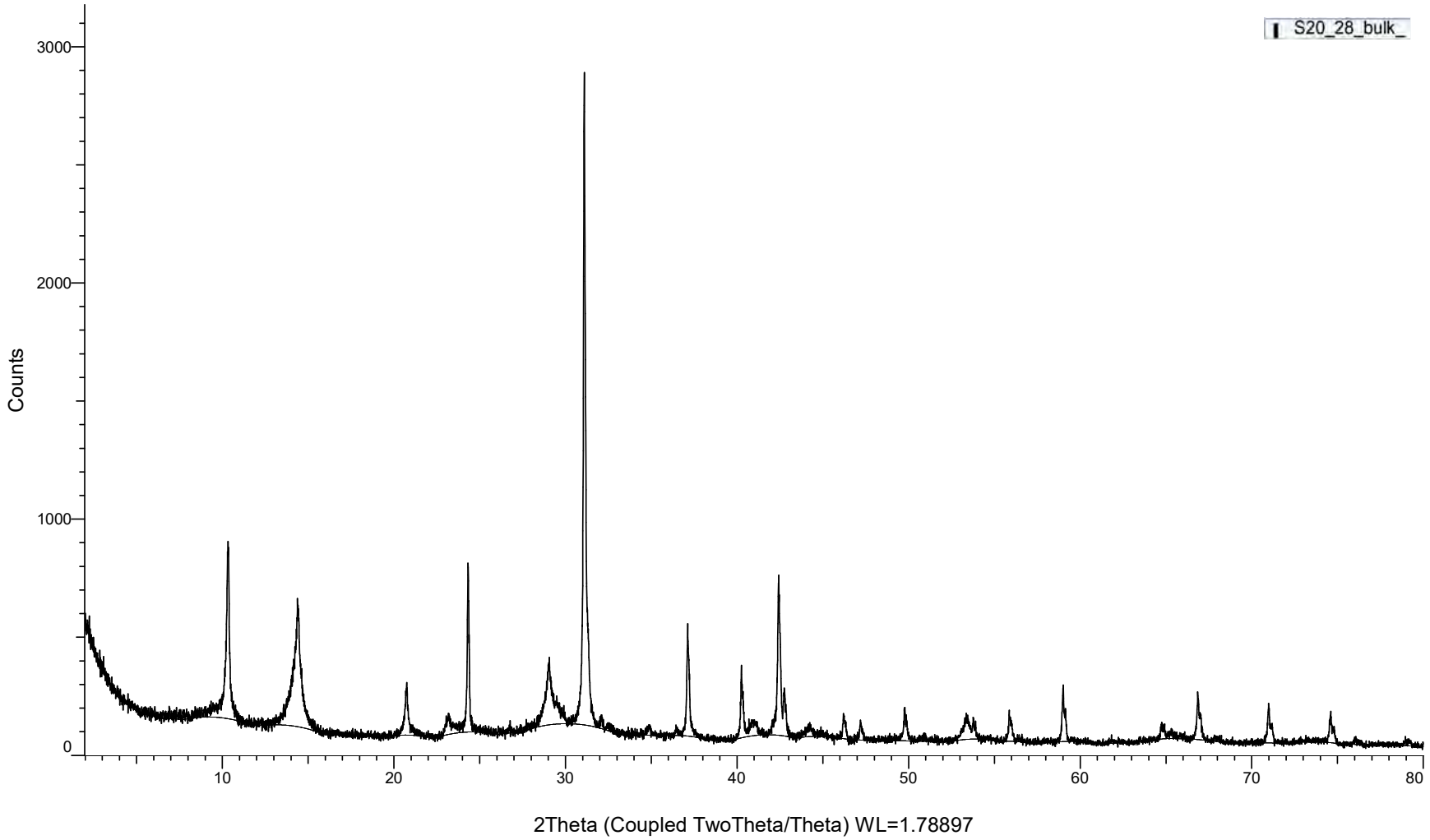

(Coupled TwoTheta/Theta)

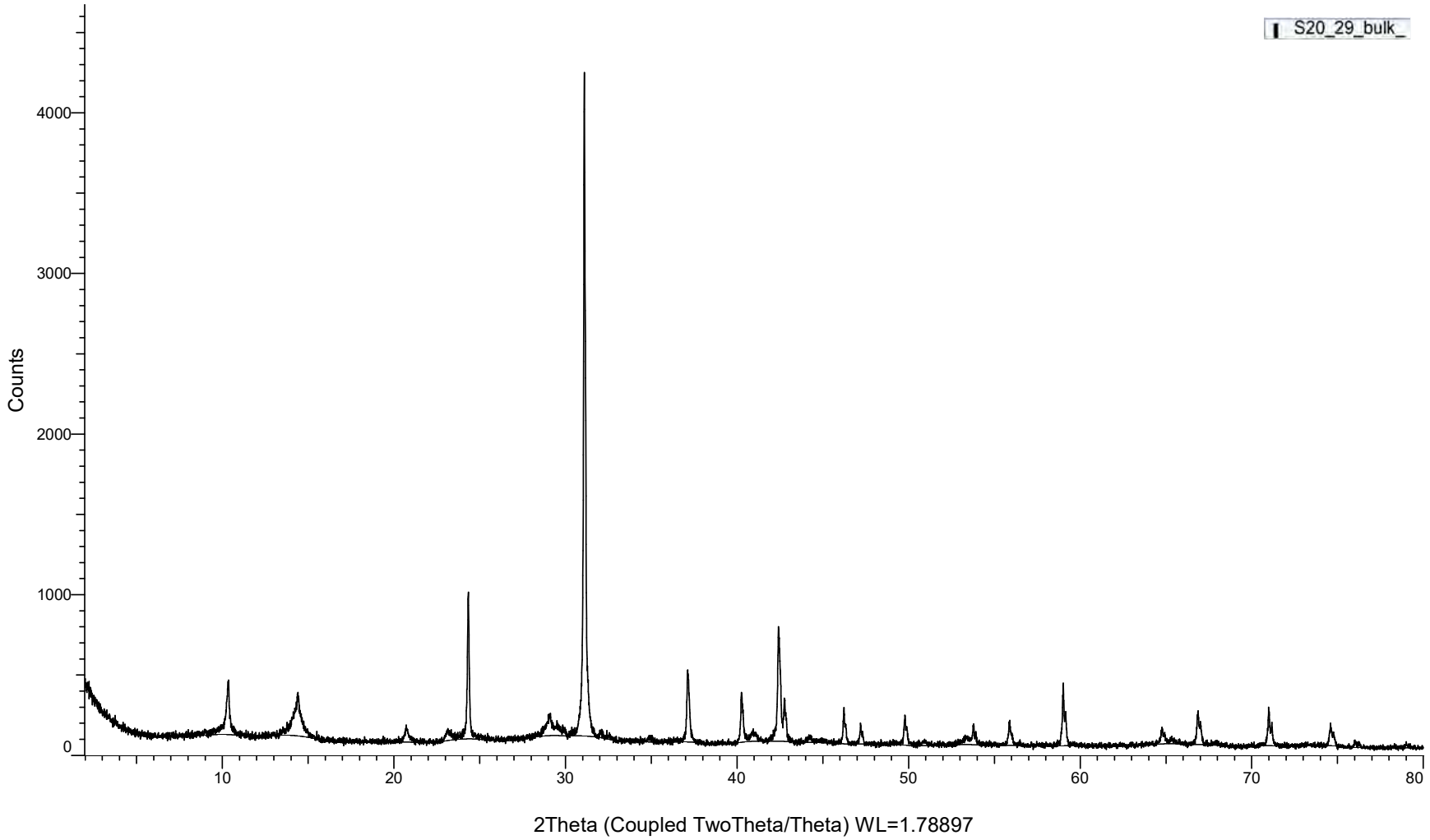

(Coupled TwoTheta/Theta)

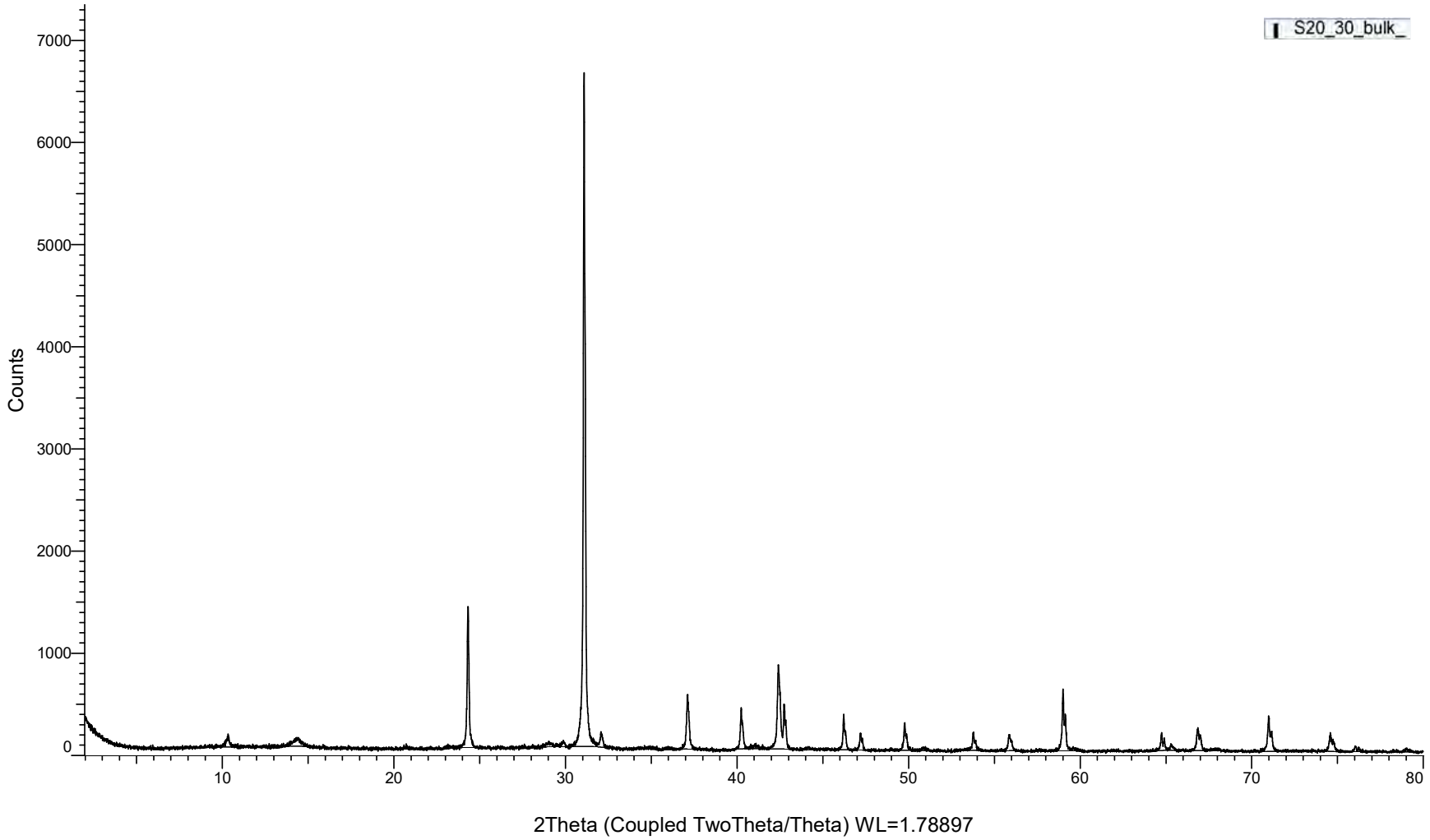

(Coupled TwoTheta/Theta)

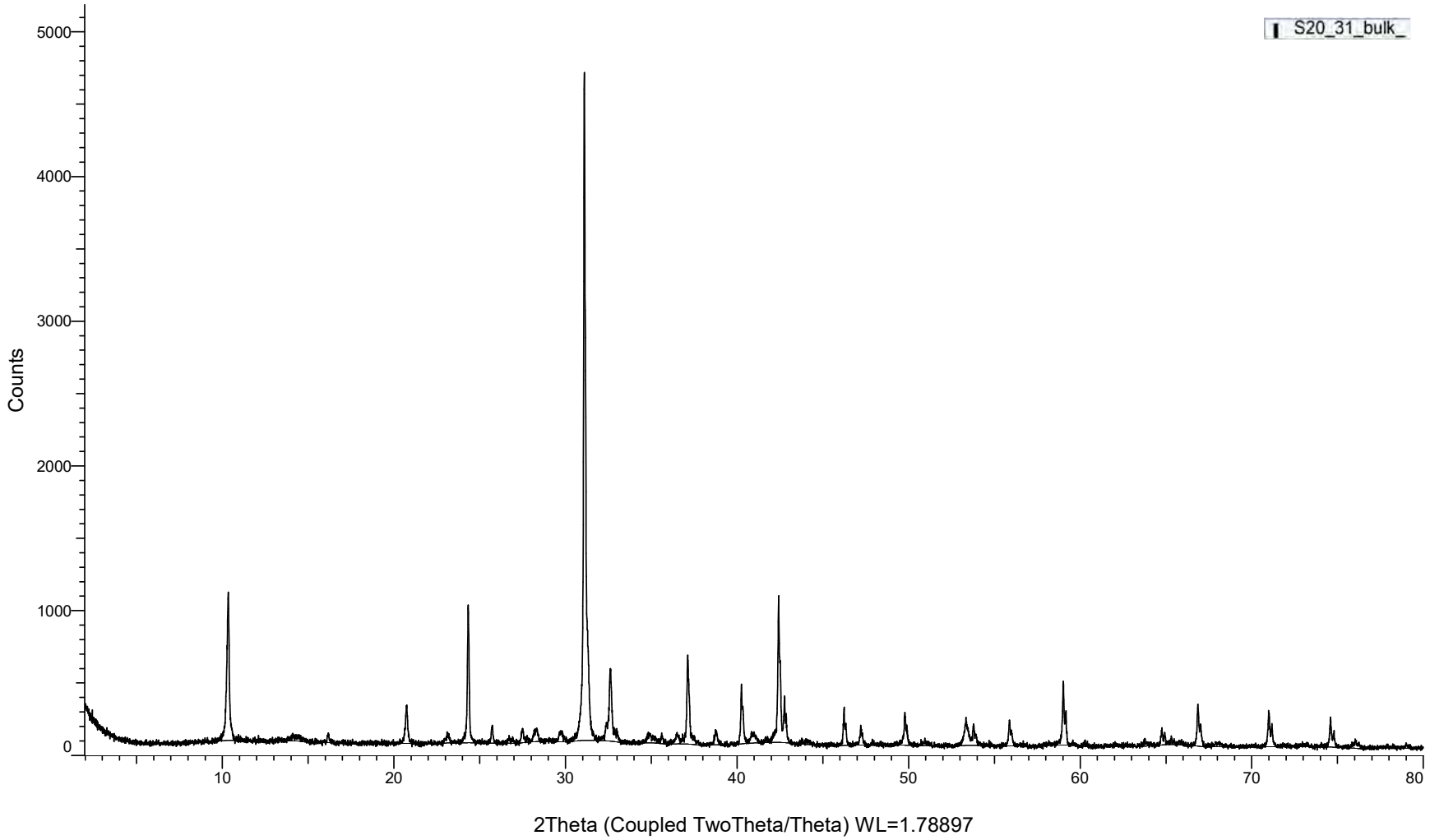

(Coupled TwoTheta/Theta)

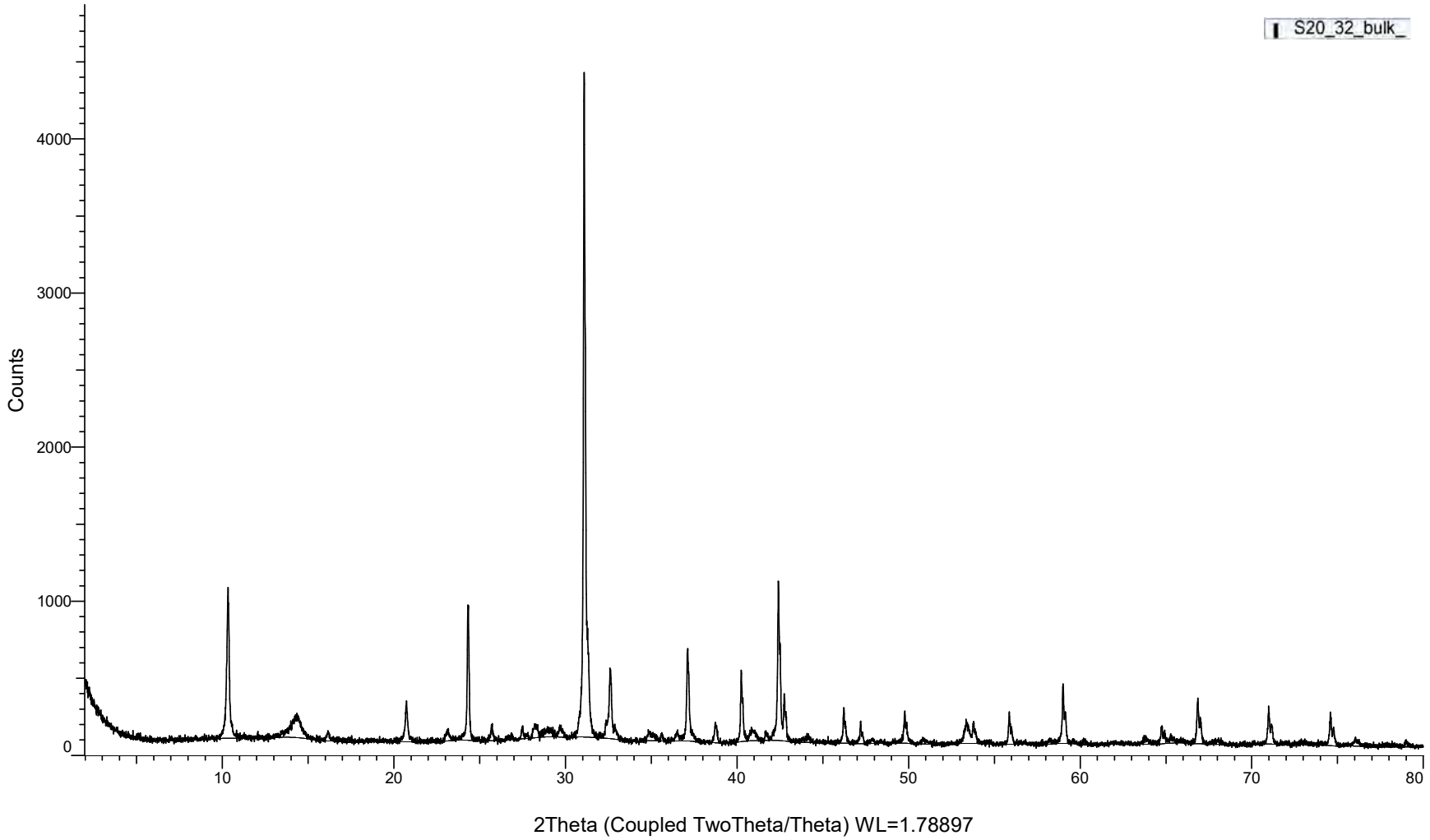

(Coupled TwoTheta/Theta)

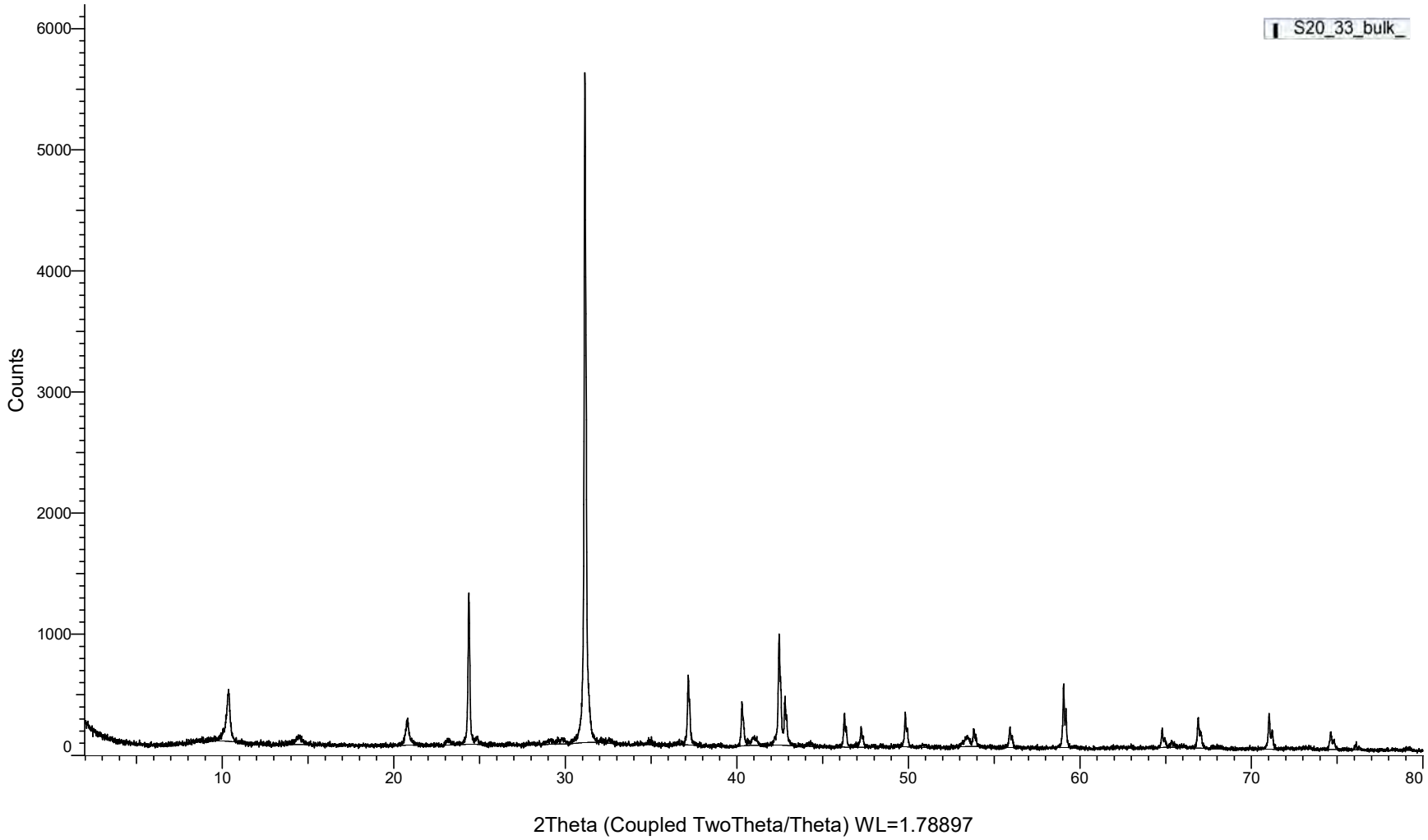

(Coupled TwoTheta/Theta)

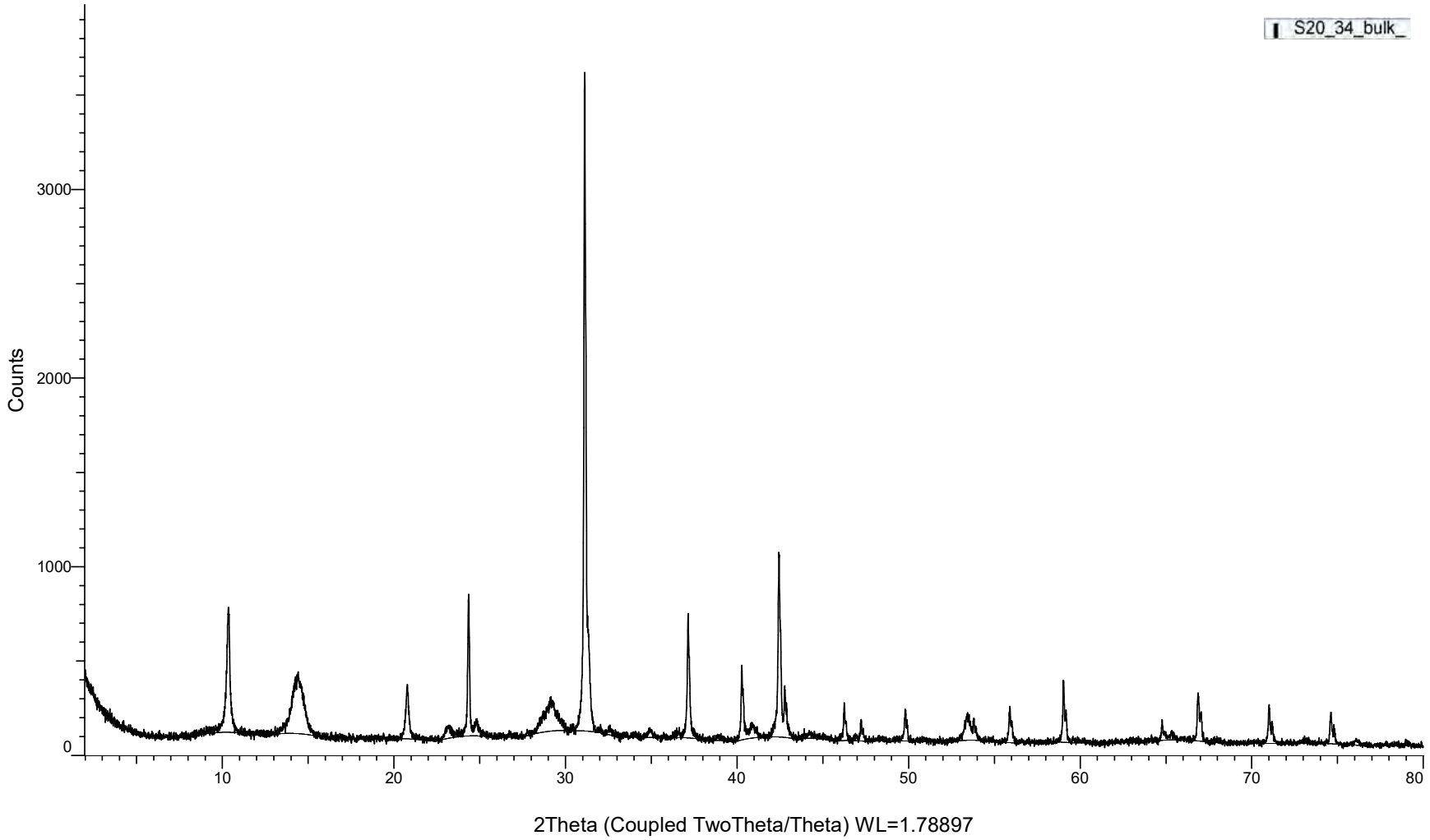

(Coupled TwoTheta/Theta)

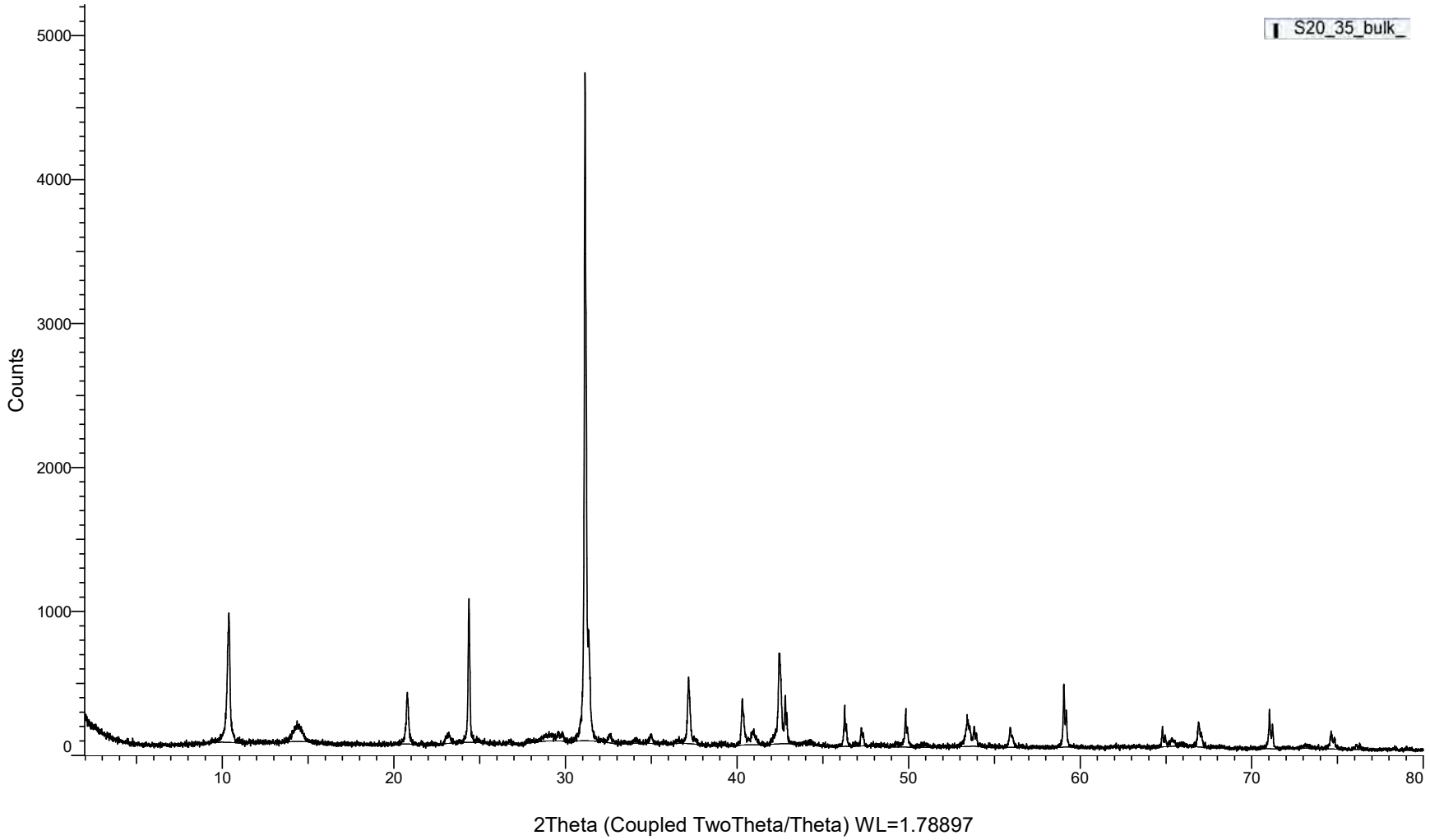

(Coupled TwoTheta/Theta)

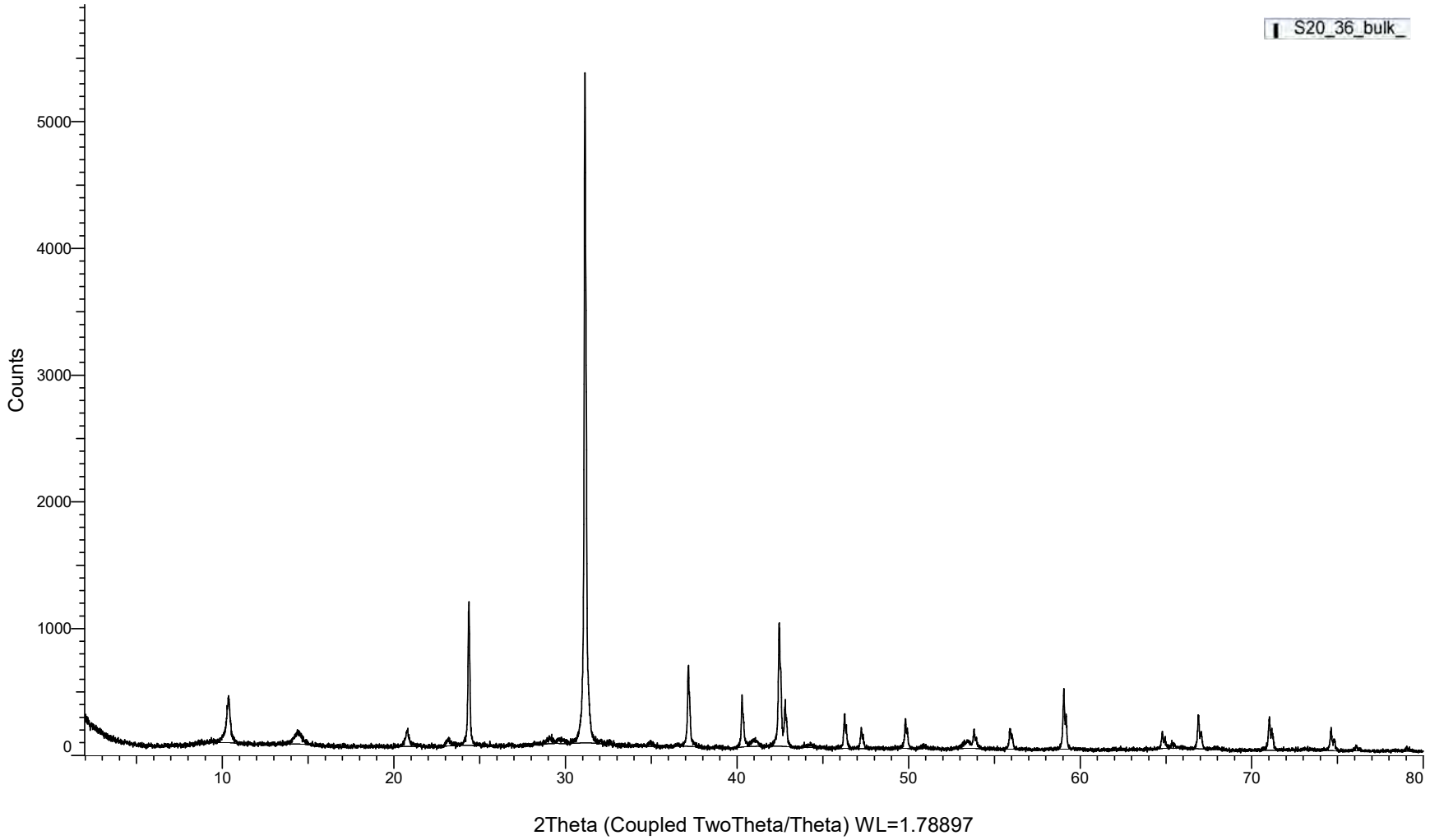

(Coupled TwoTheta/Theta)

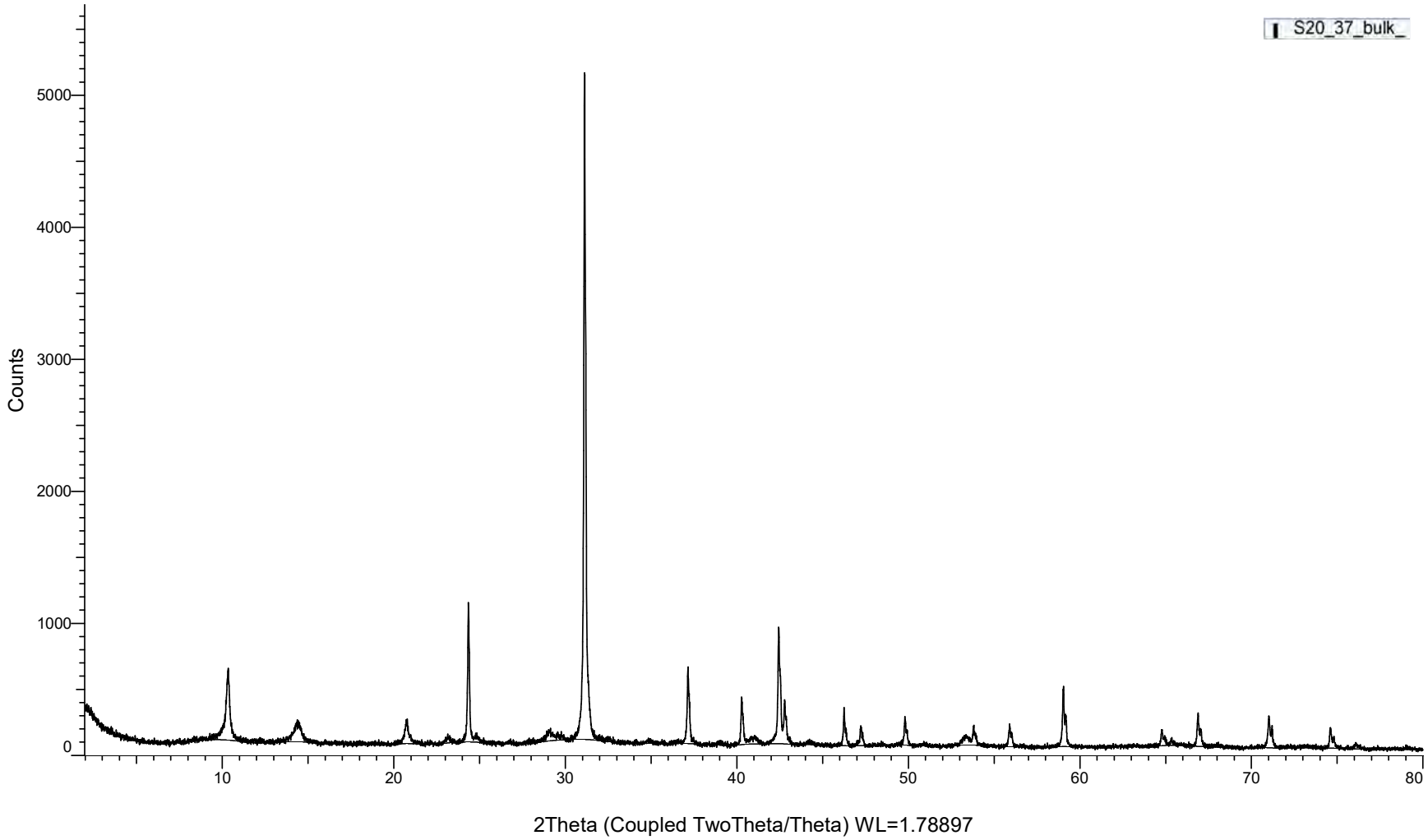

(Coupled TwoTheta/Theta)

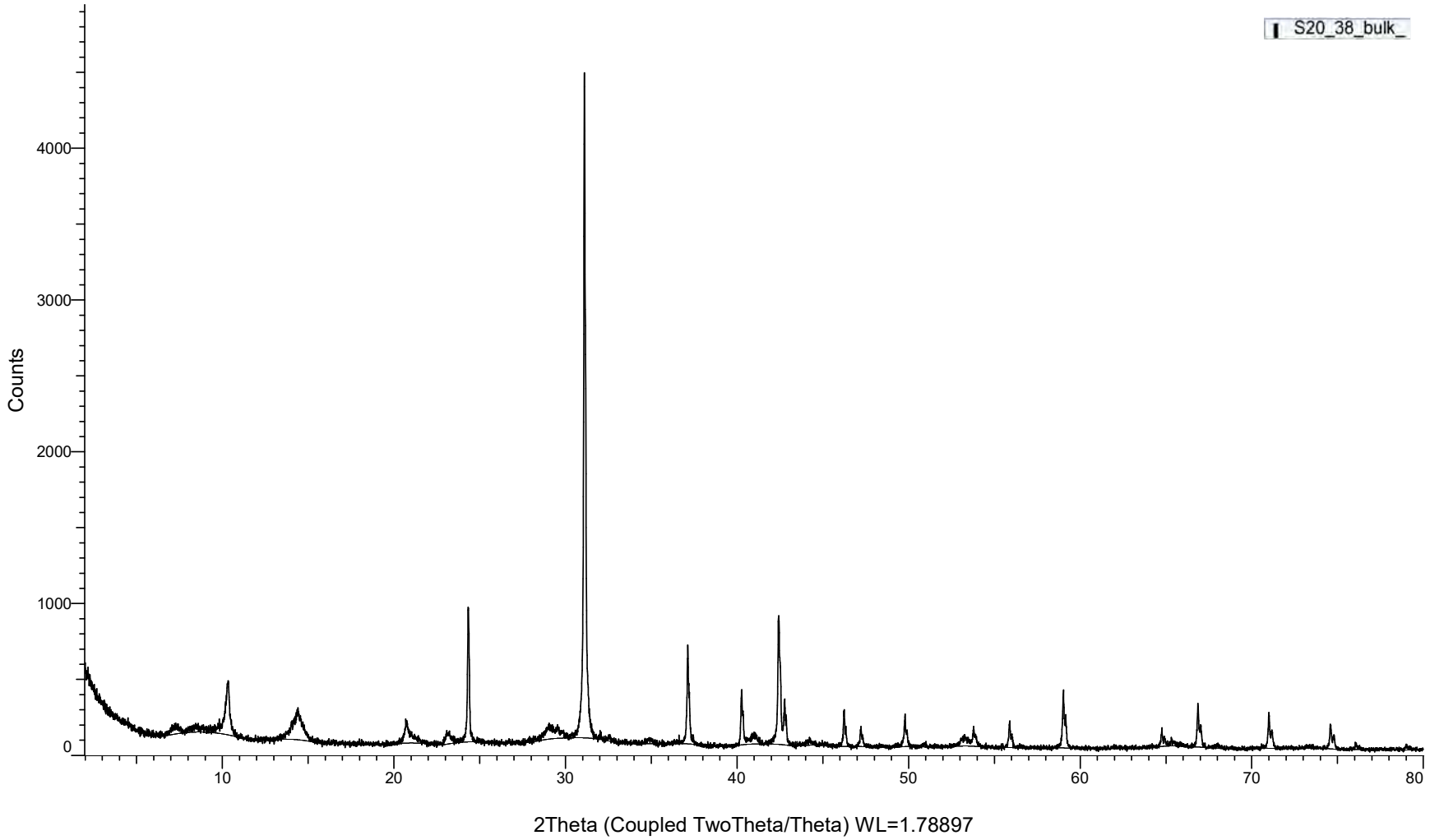

(Coupled TwoTheta/Theta)

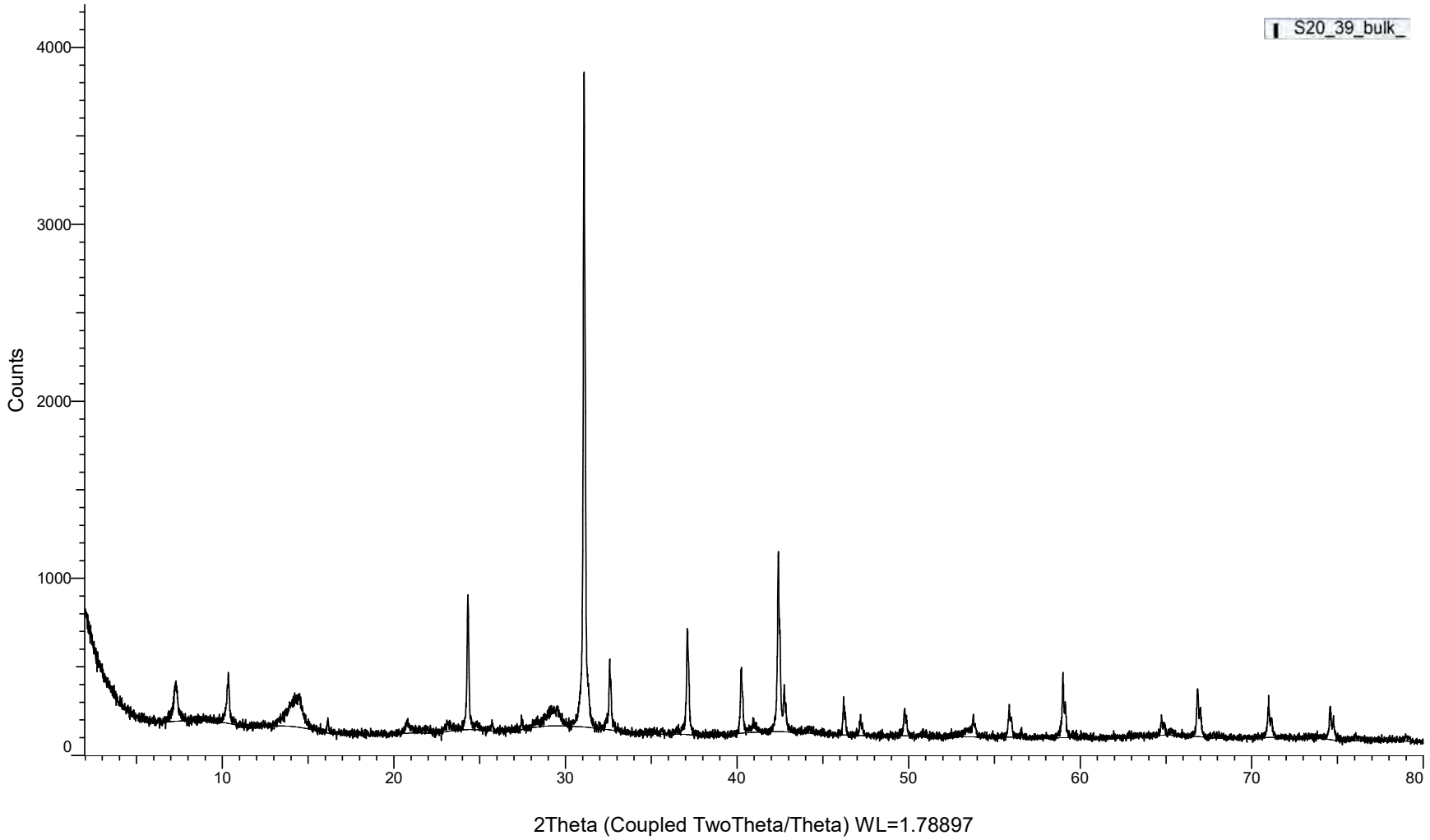

(Coupled TwoTheta/Theta)

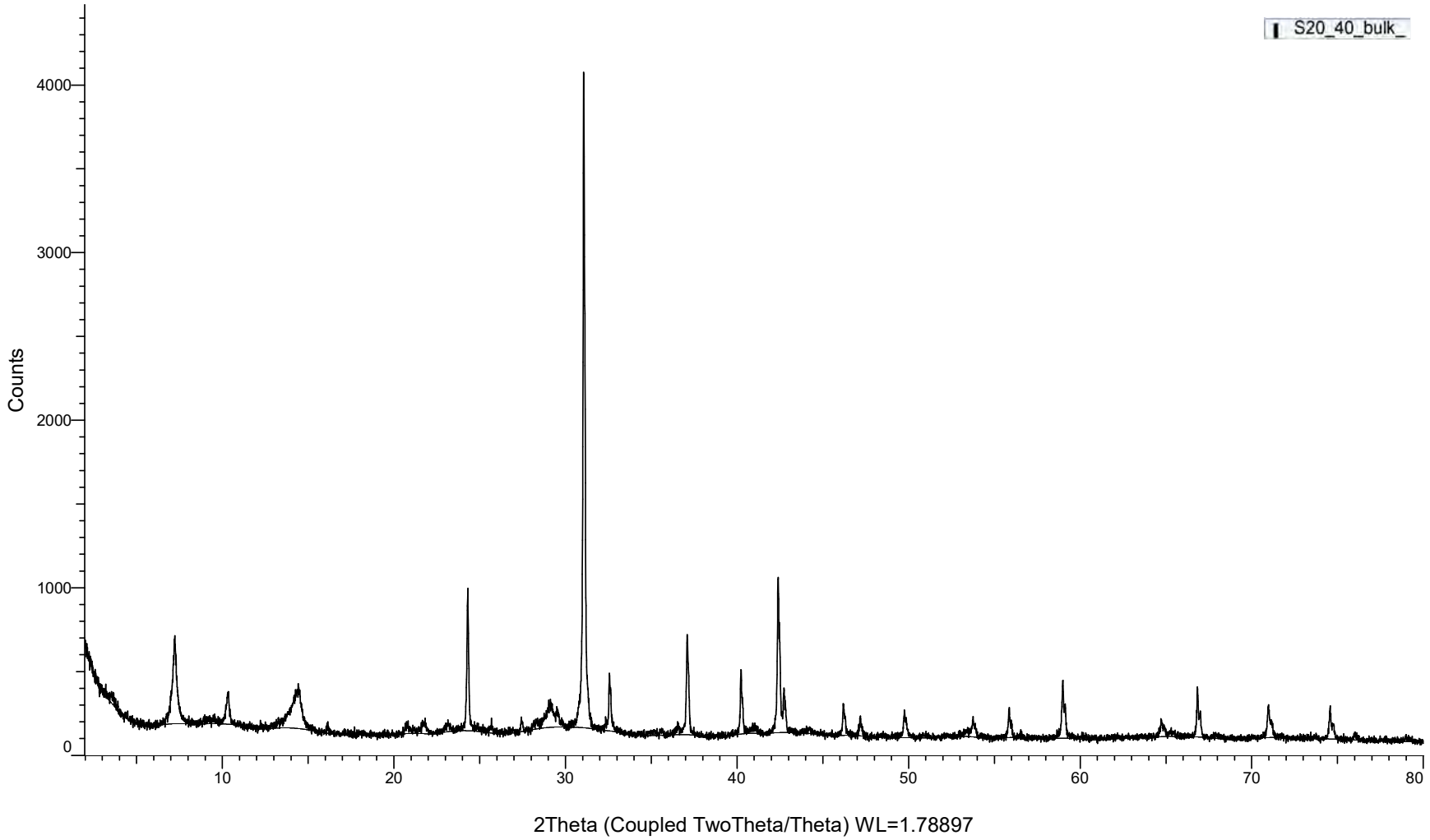

(Coupled TwoTheta/Theta)

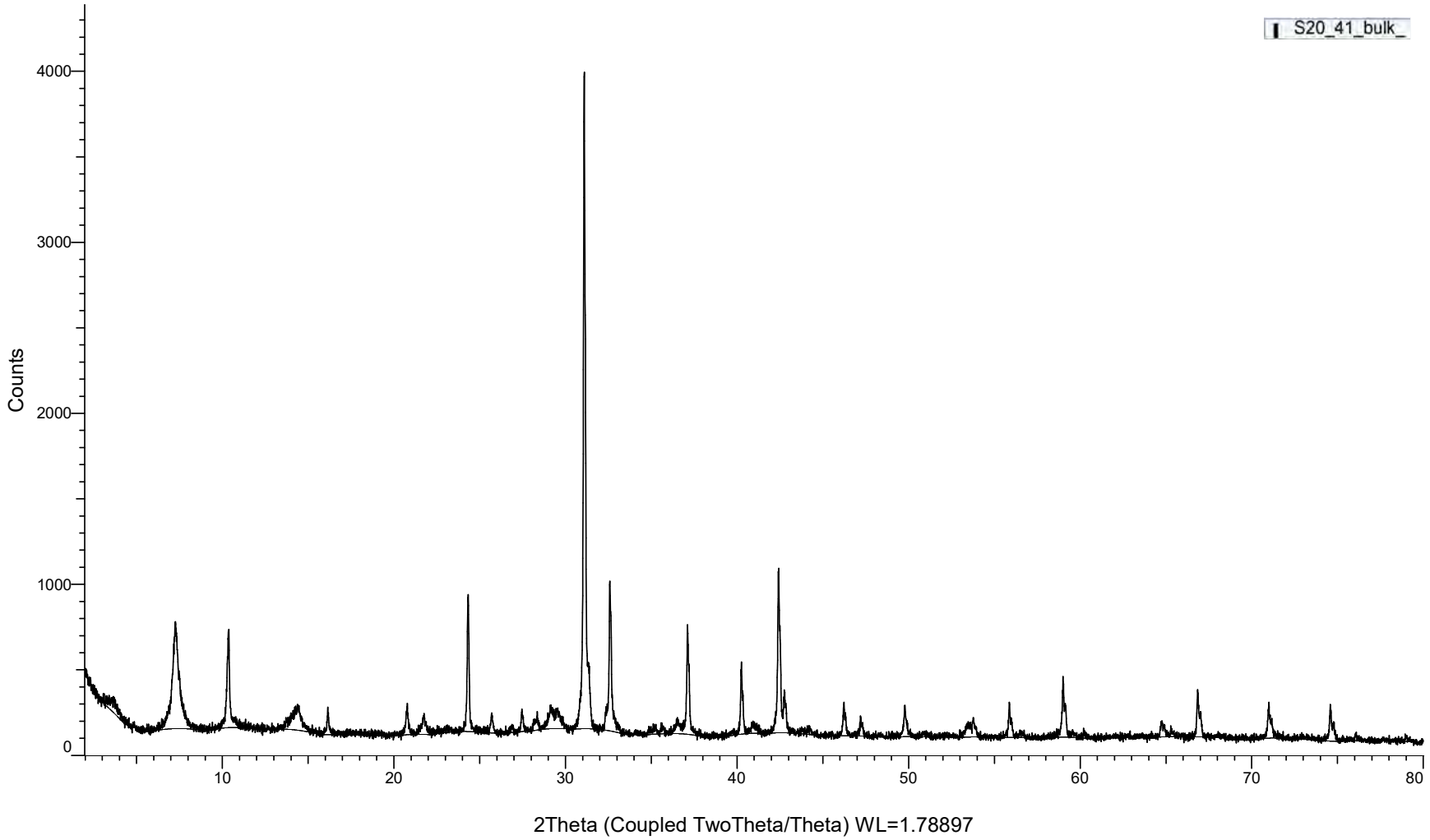

(Coupled TwoTheta/Theta)

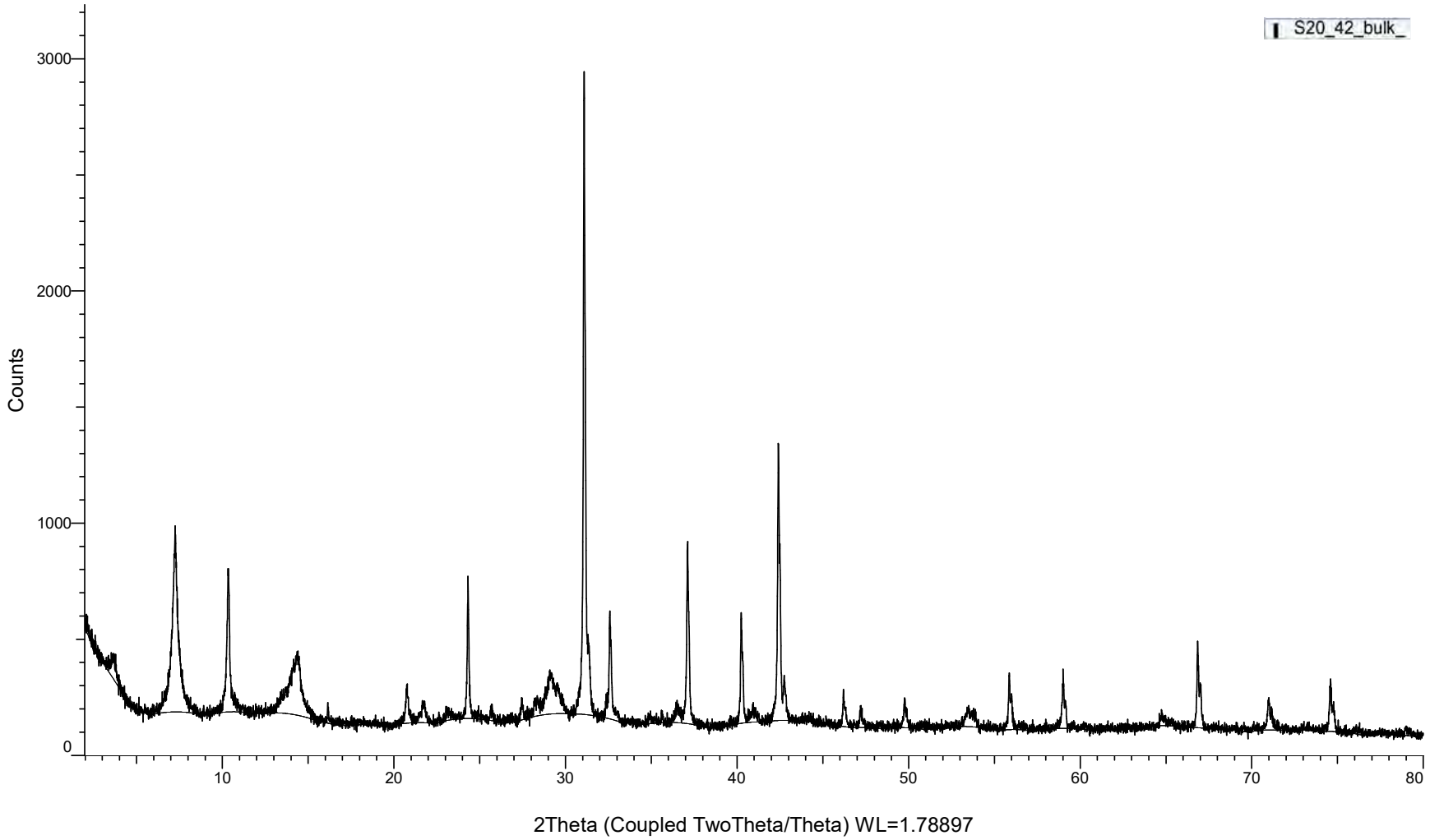

(Coupled TwoTheta/Theta)

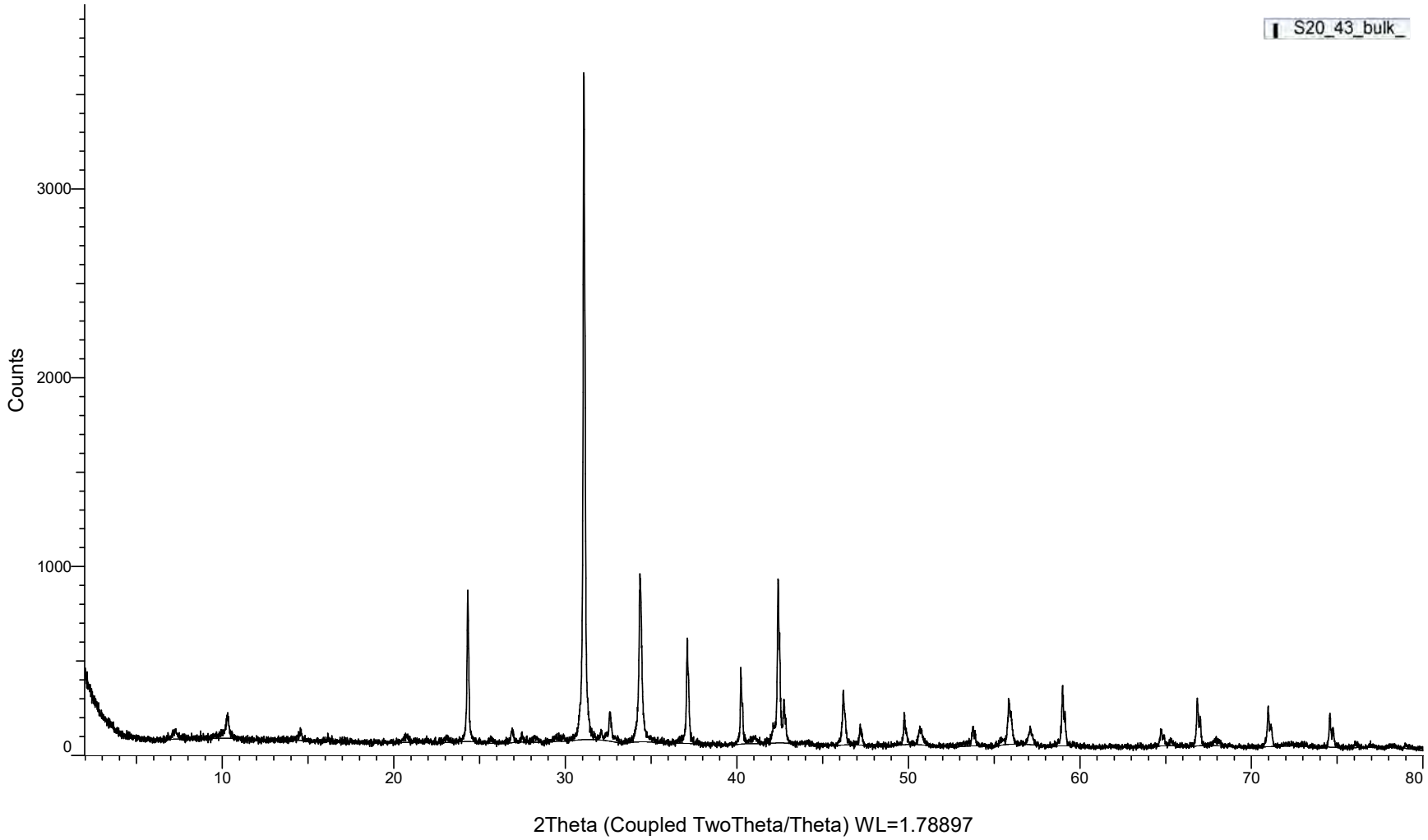

(Coupled TwoTheta/Theta)

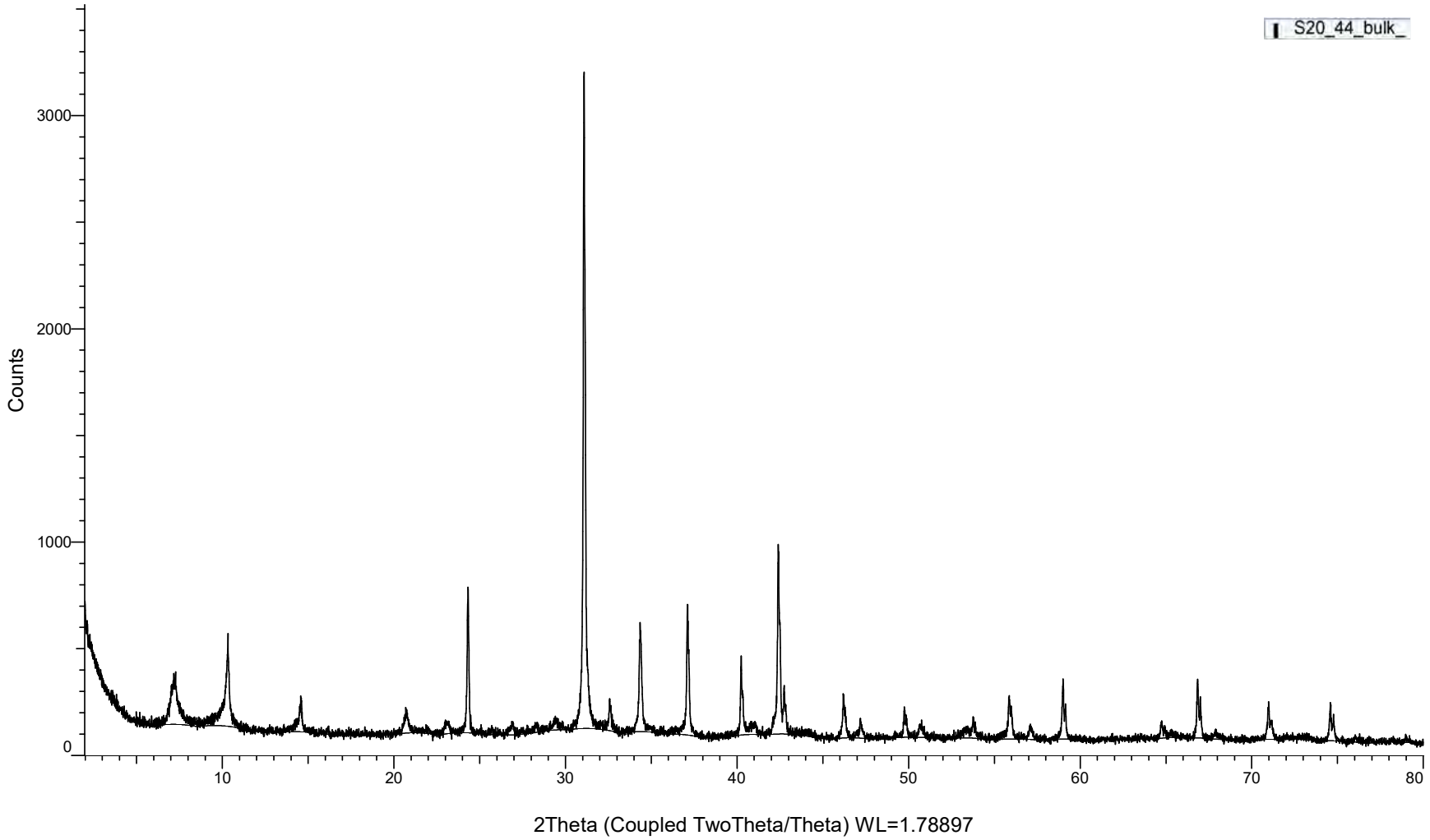

(Coupled TwoTheta/Theta)

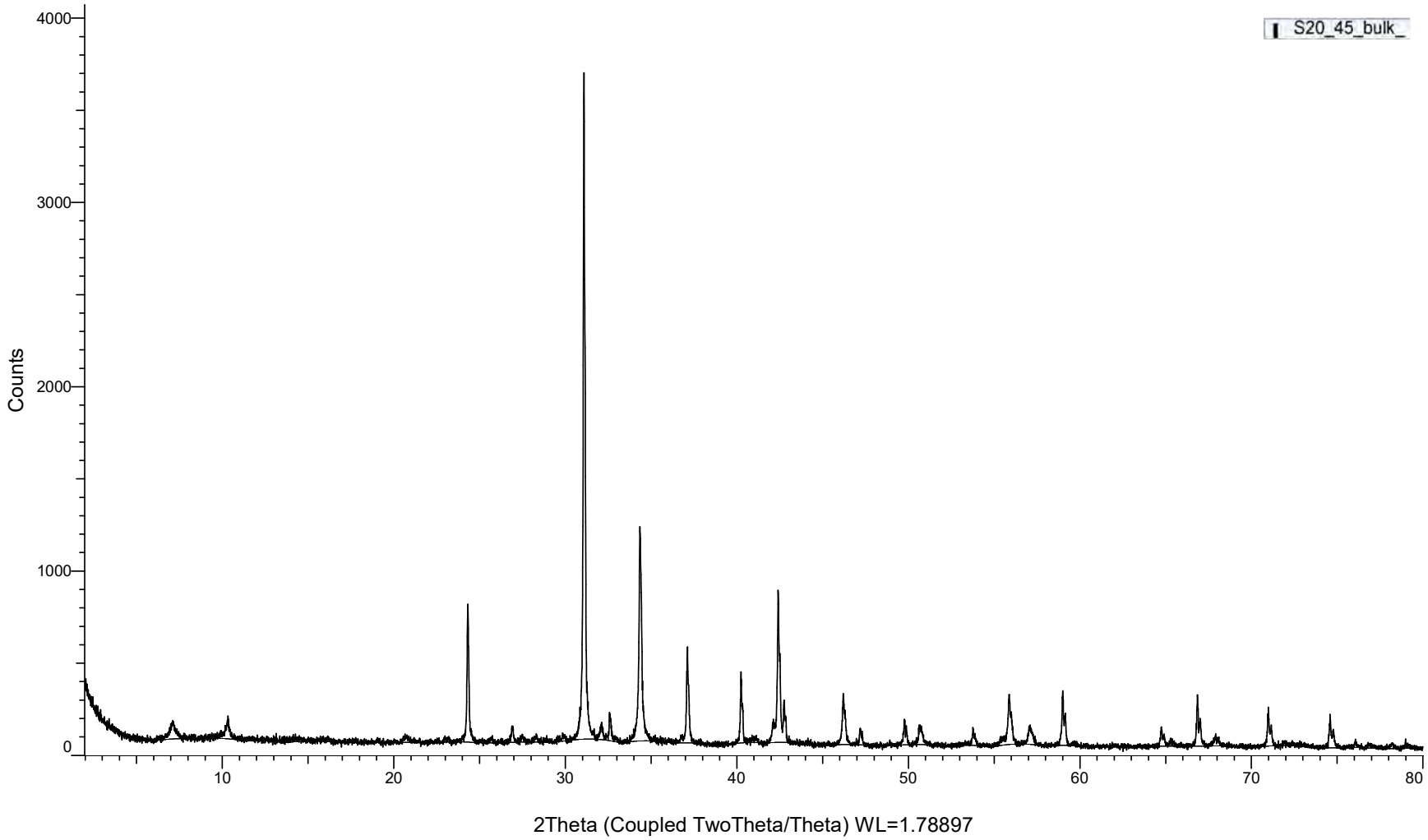

(Coupled TwoTheta/Theta)

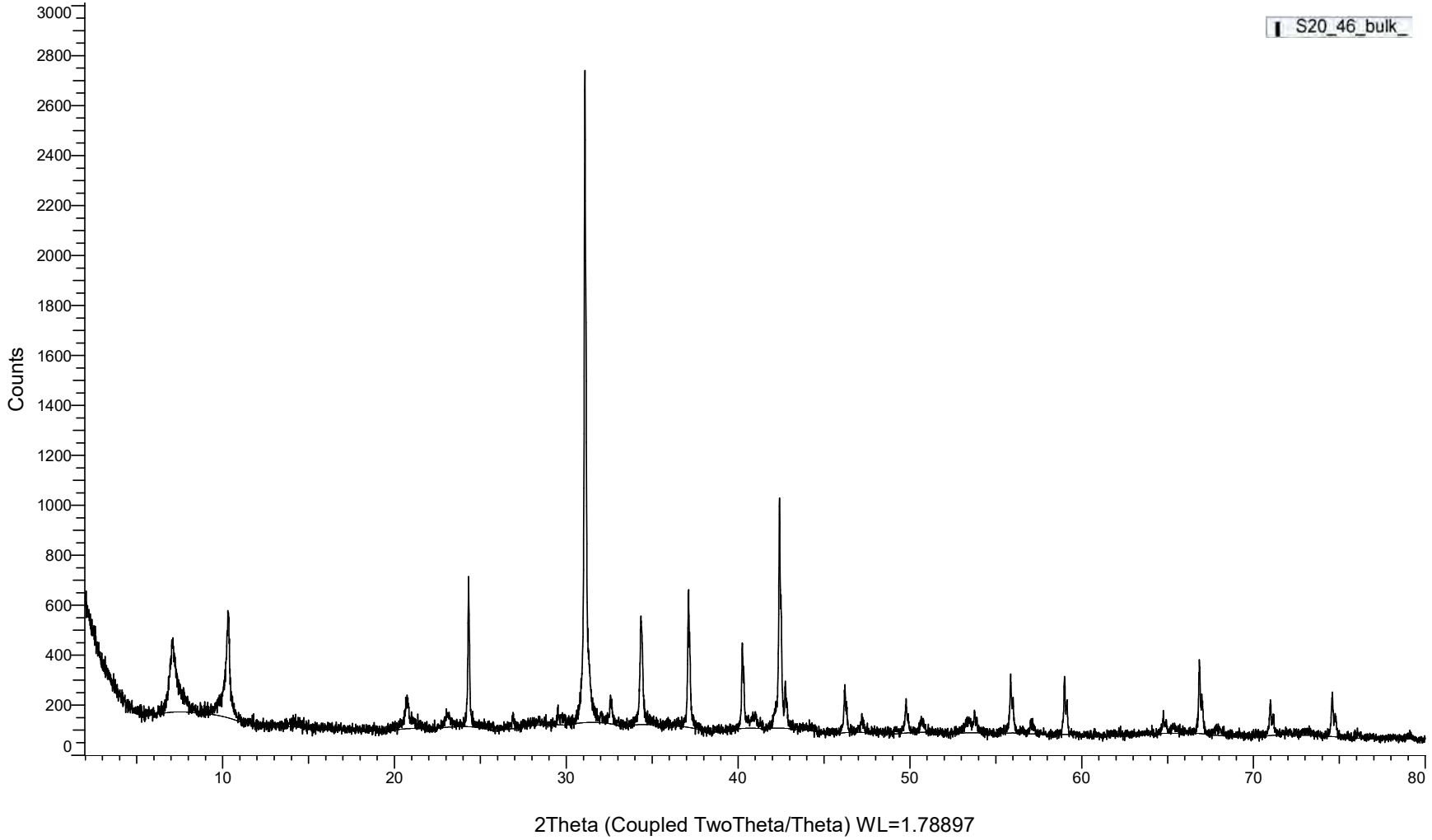

(Coupled TwoTheta/Theta)

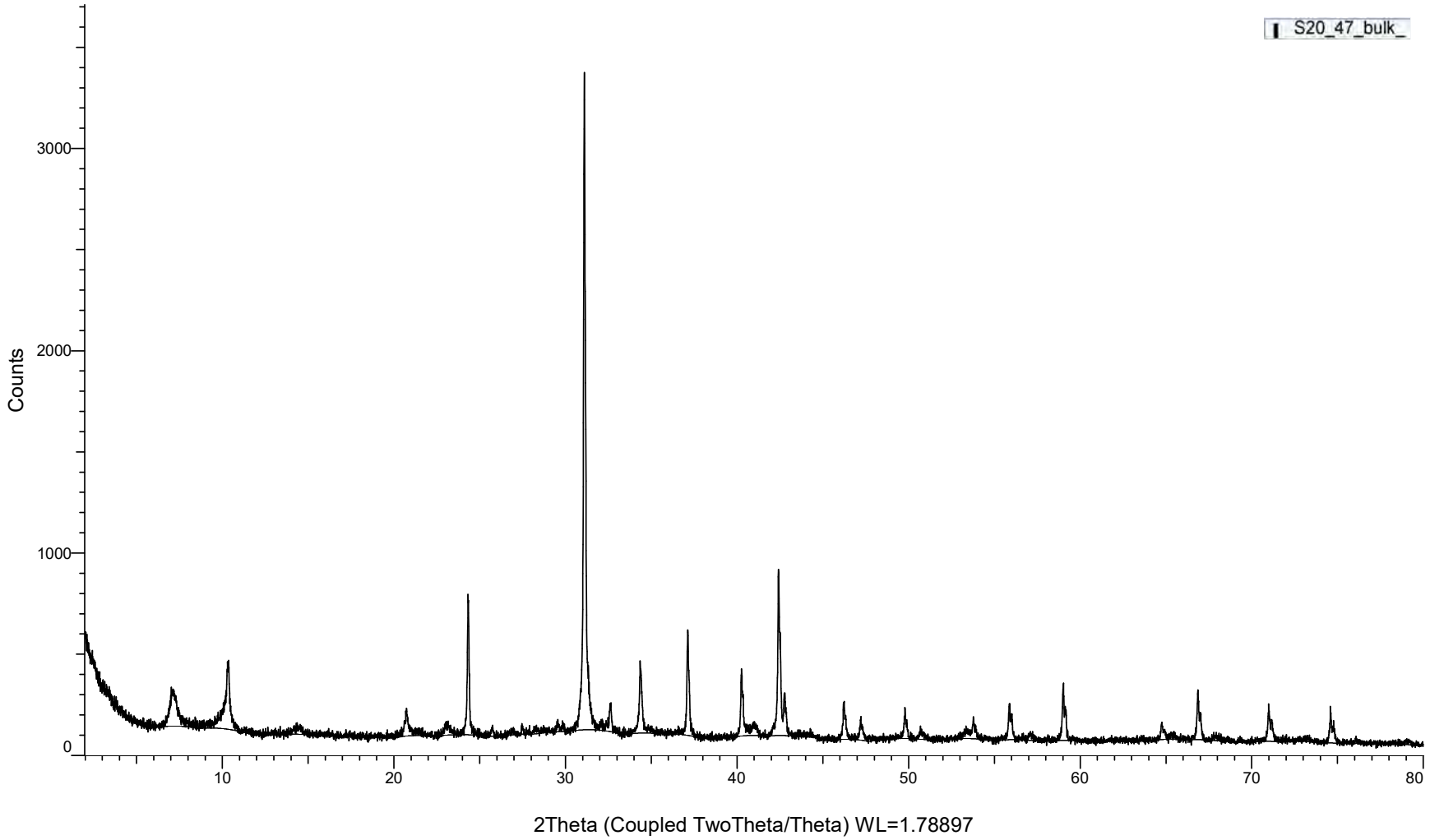

(Coupled TwoTheta/Theta)

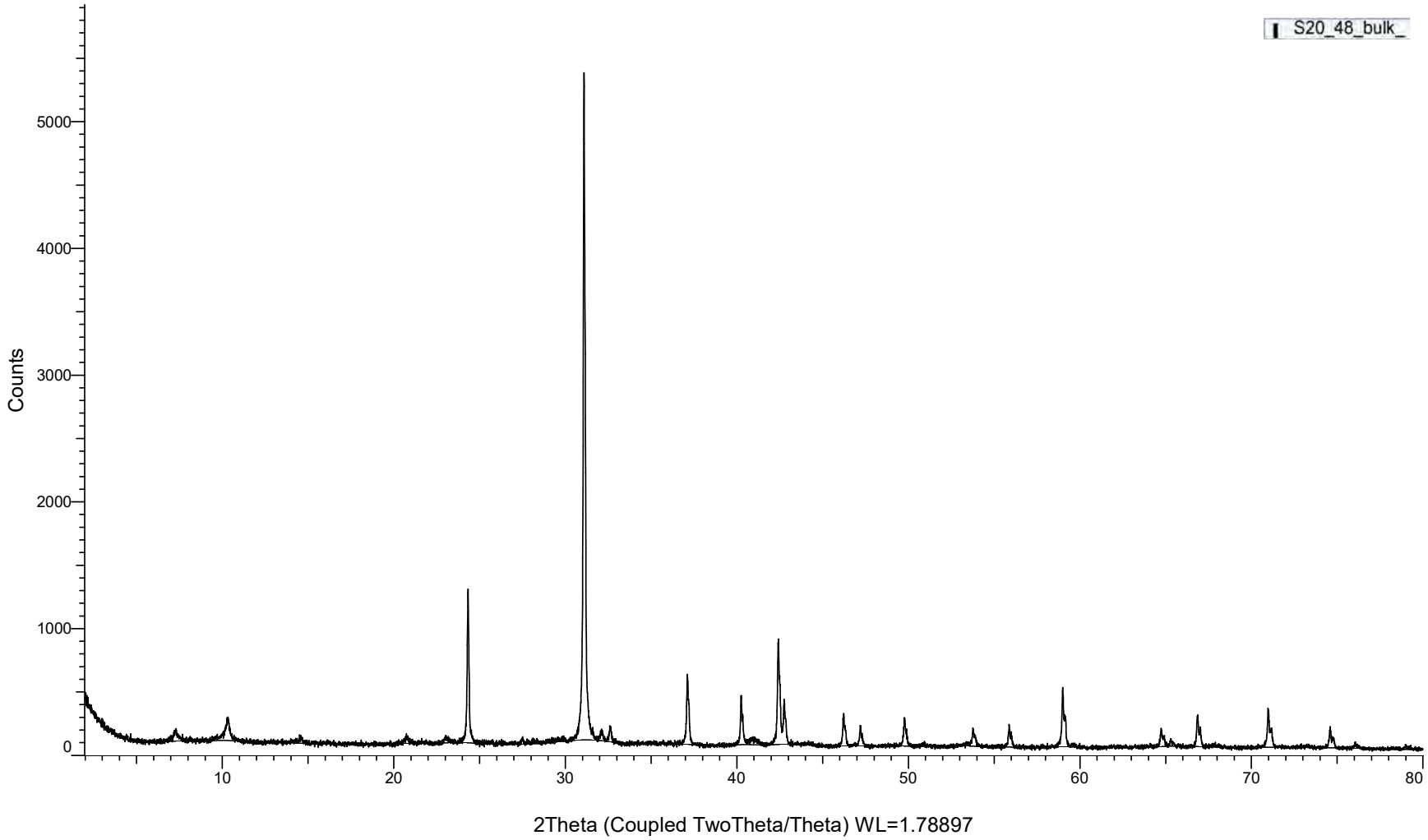

APPENDIX C

XRD clay fraction raw data

(Coupled TwoTheta/Theta)

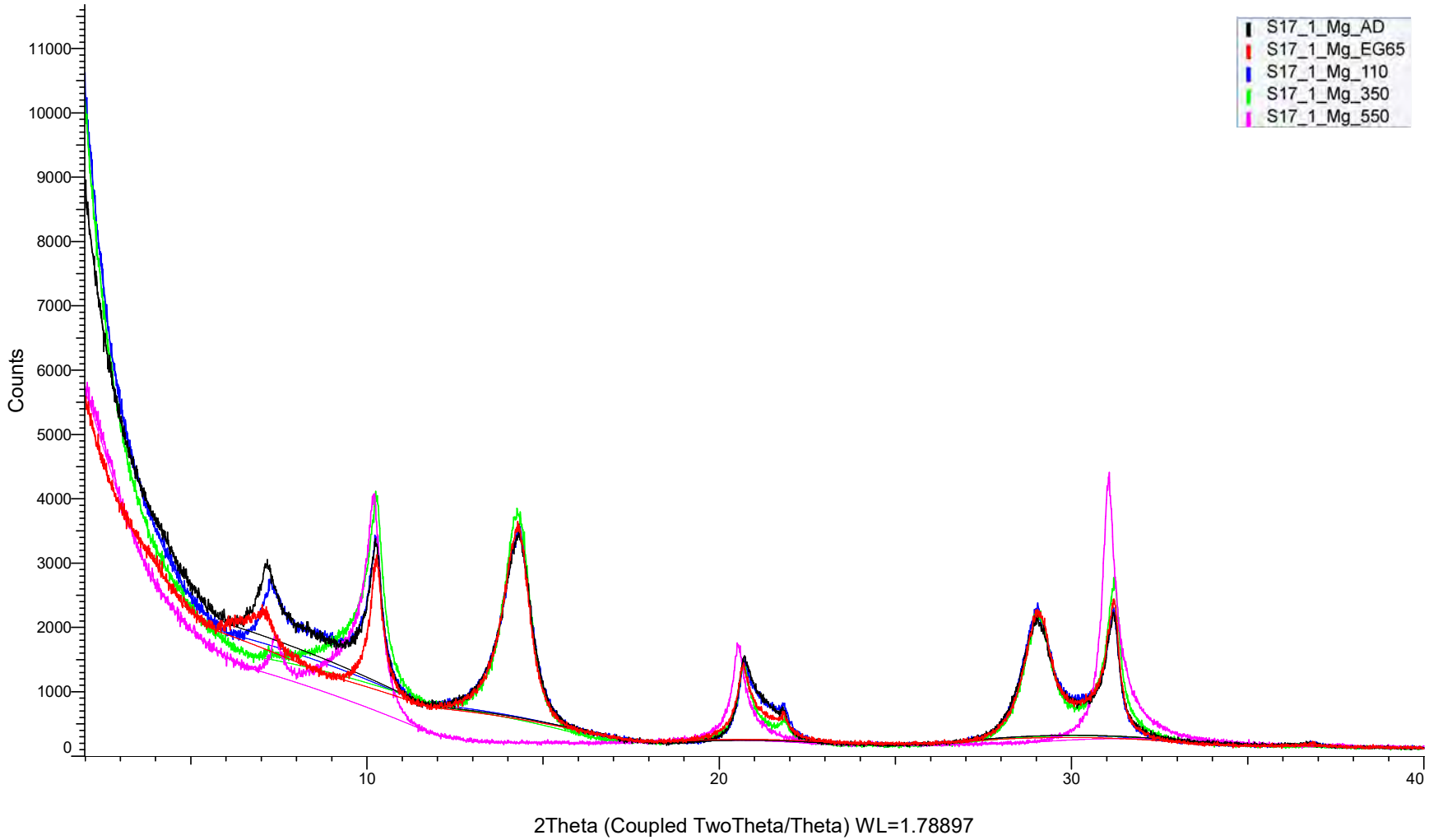

(Coupled TwoTheta/Theta)

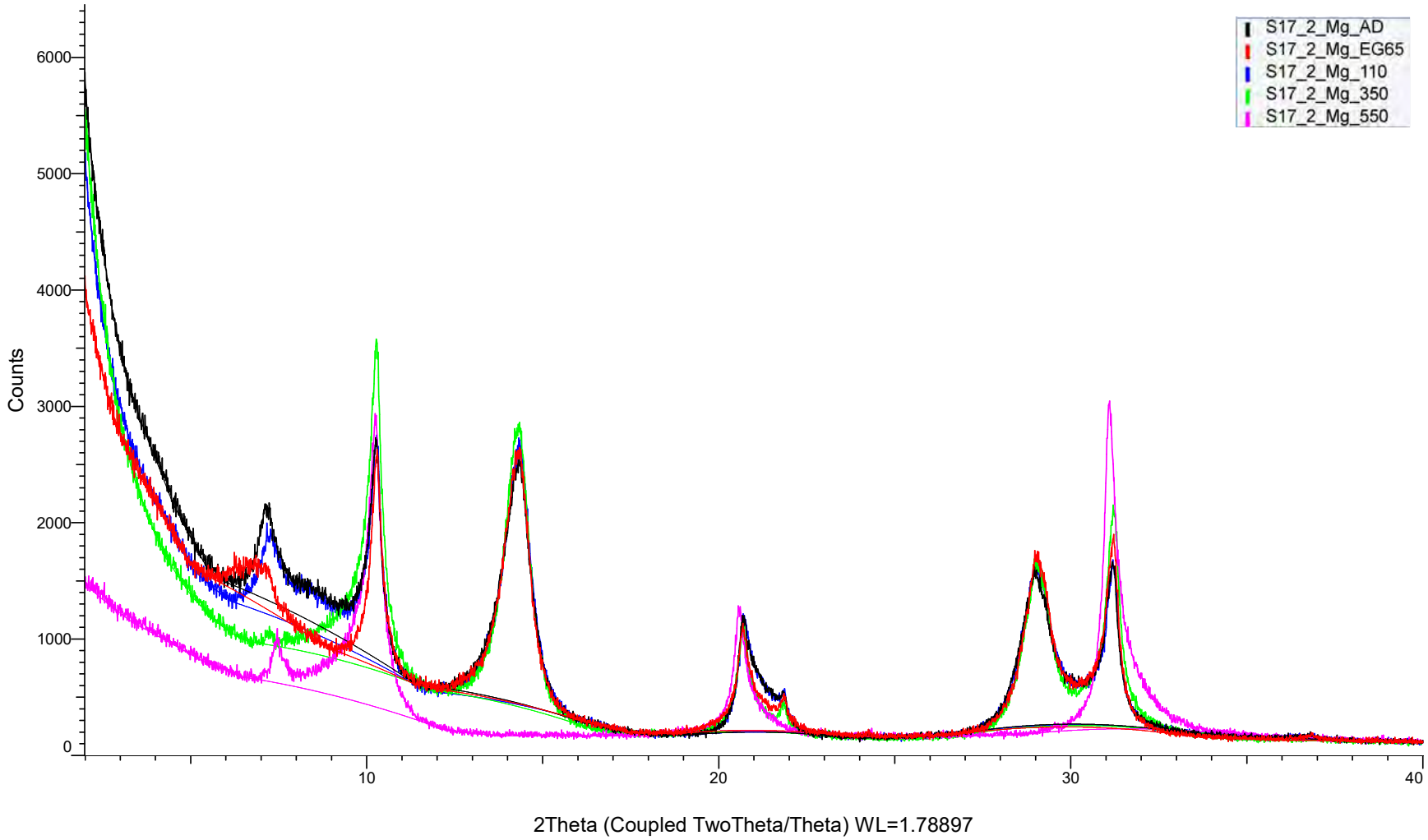

(Coupled TwoTheta/Theta)

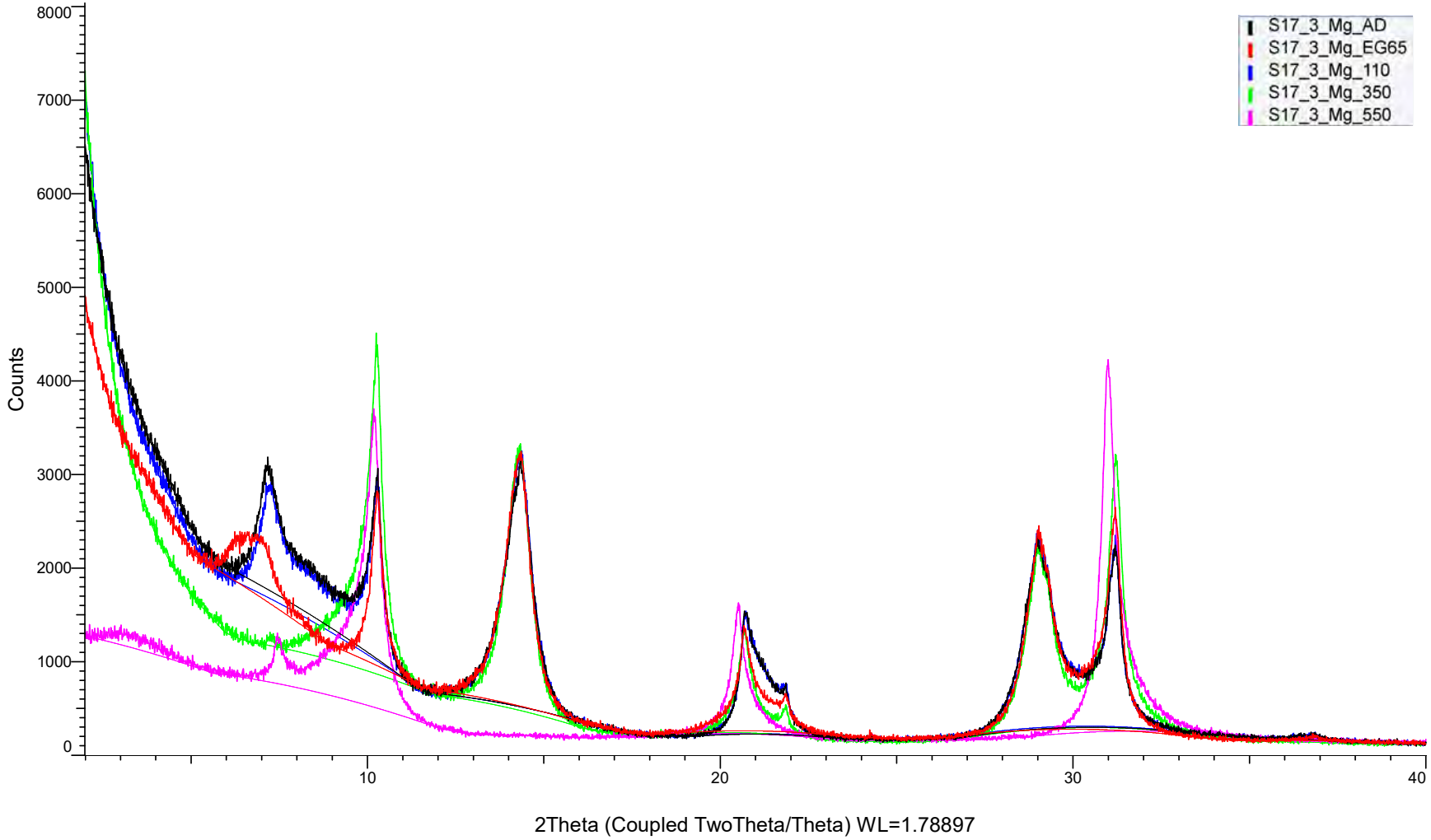

(Coupled TwoTheta/Theta)

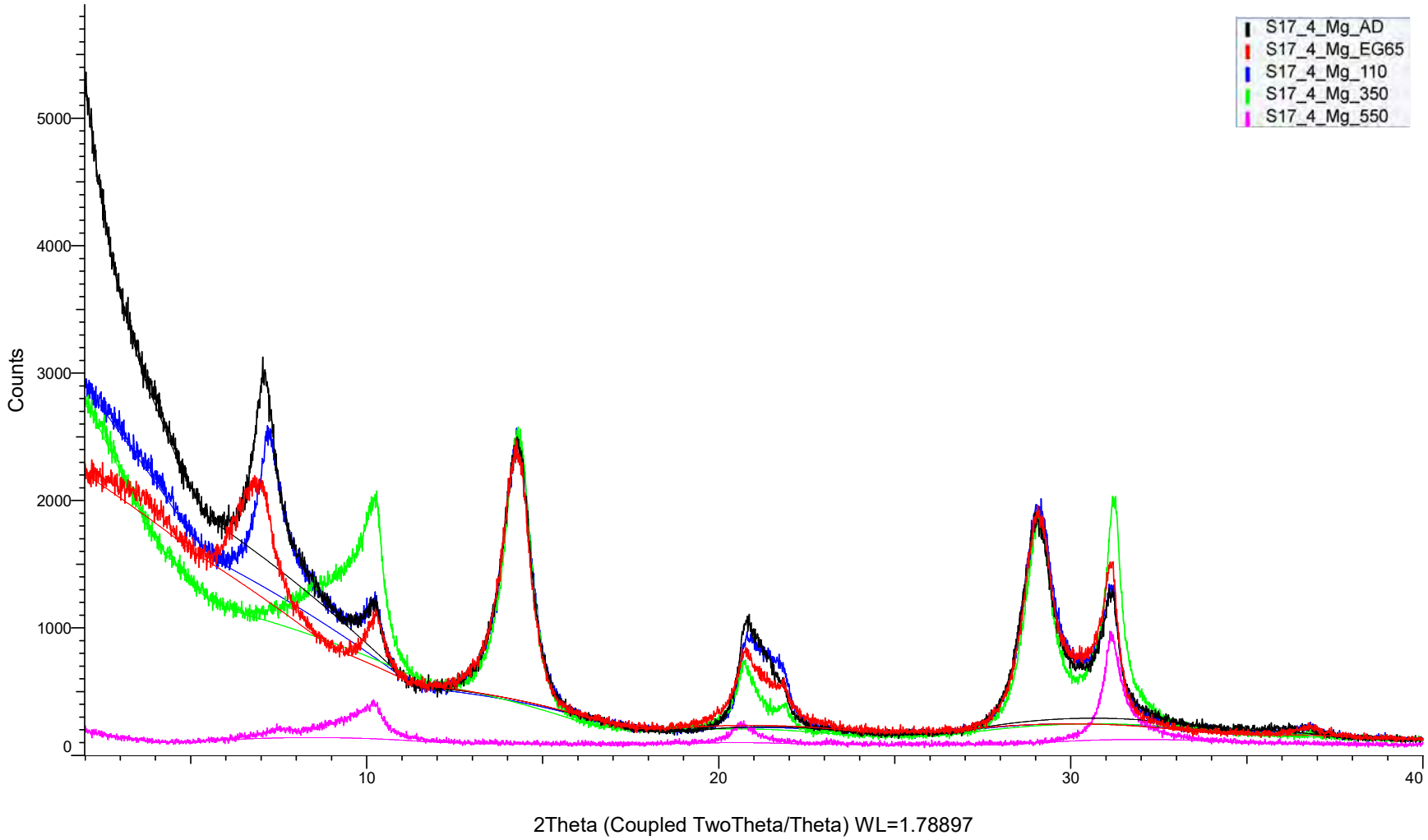

(Coupled TwoTheta/Theta)

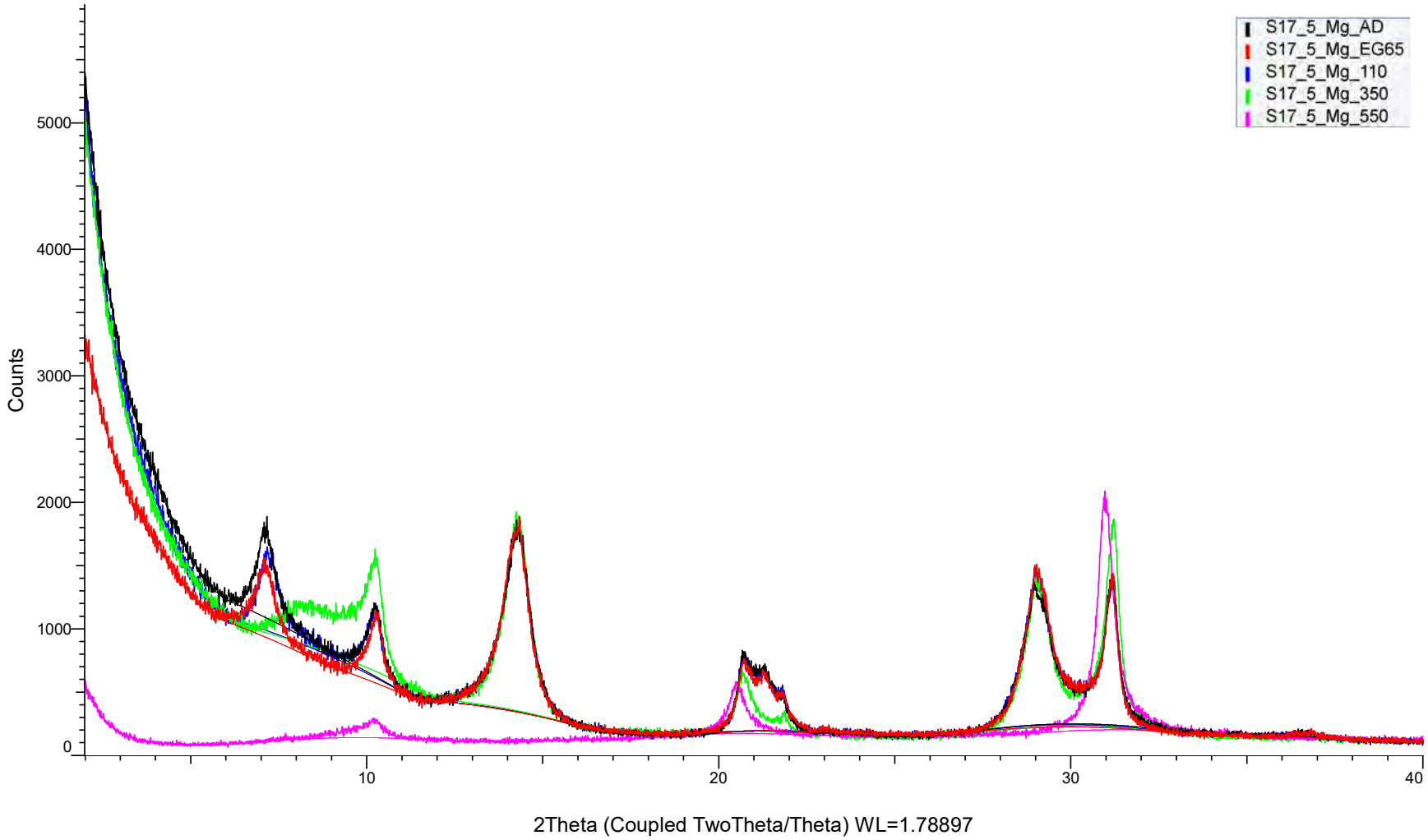

(Coupled TwoTheta/Theta)

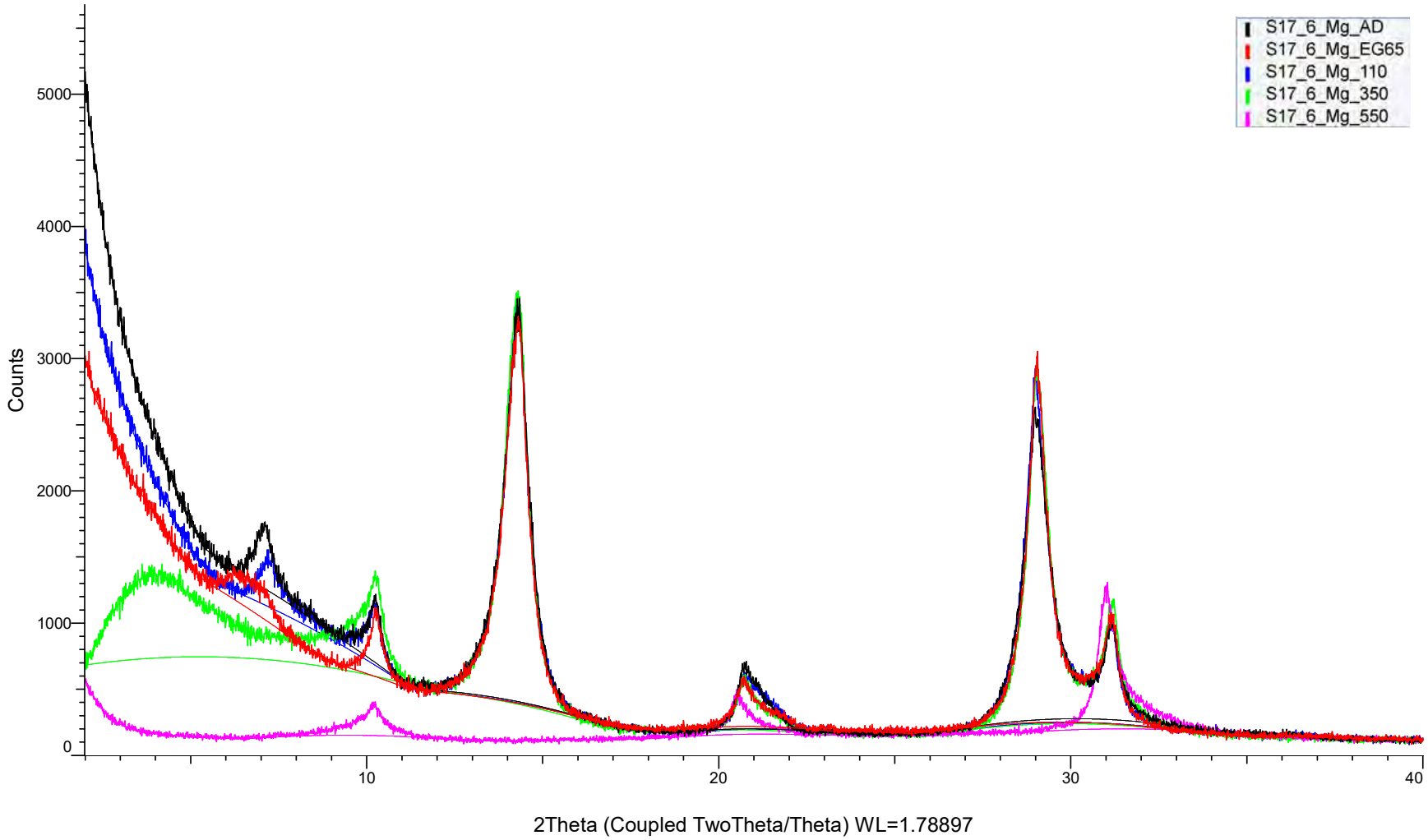

(Coupled TwoTheta/Theta)

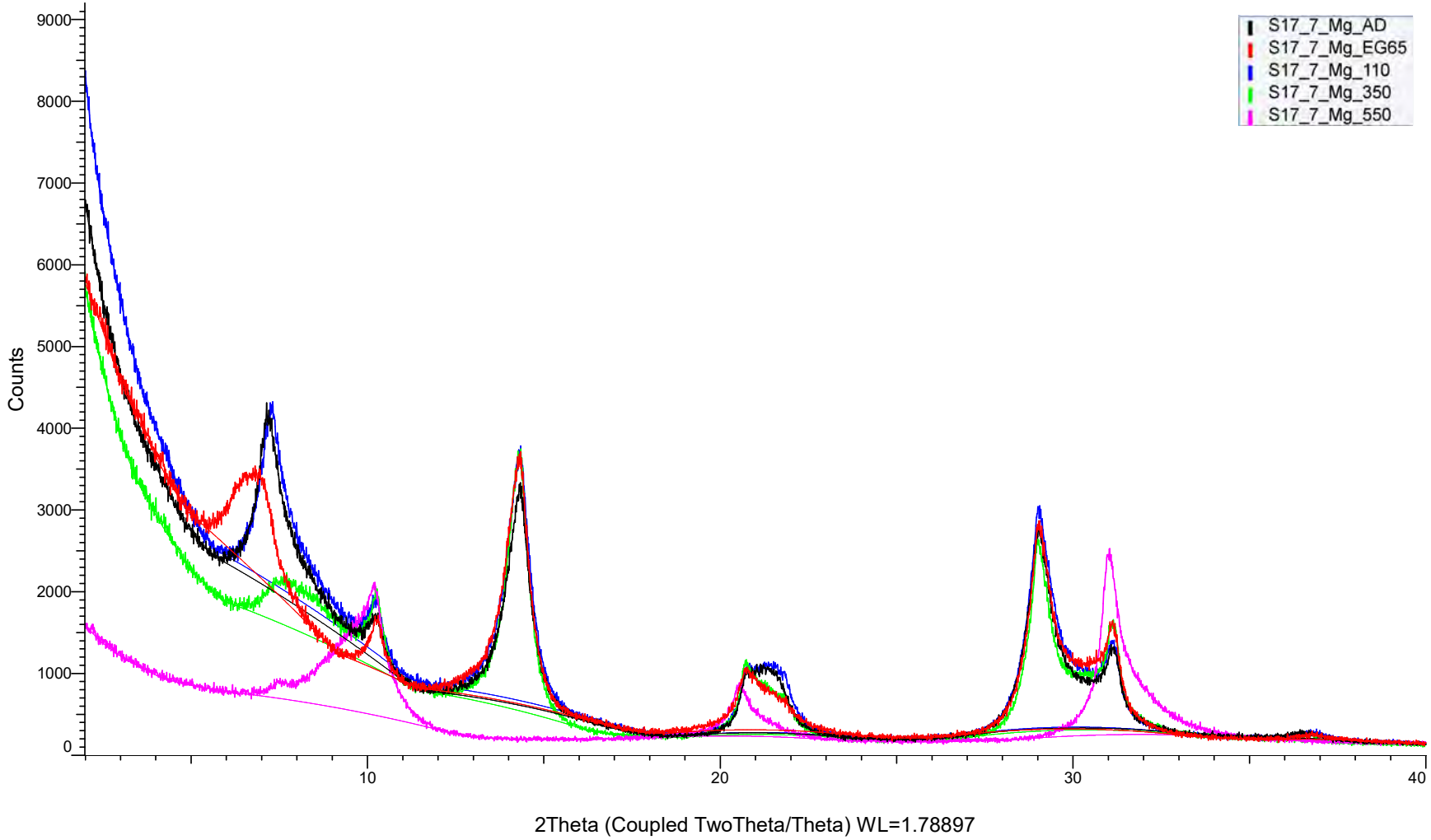

(Coupled TwoTheta/Theta)

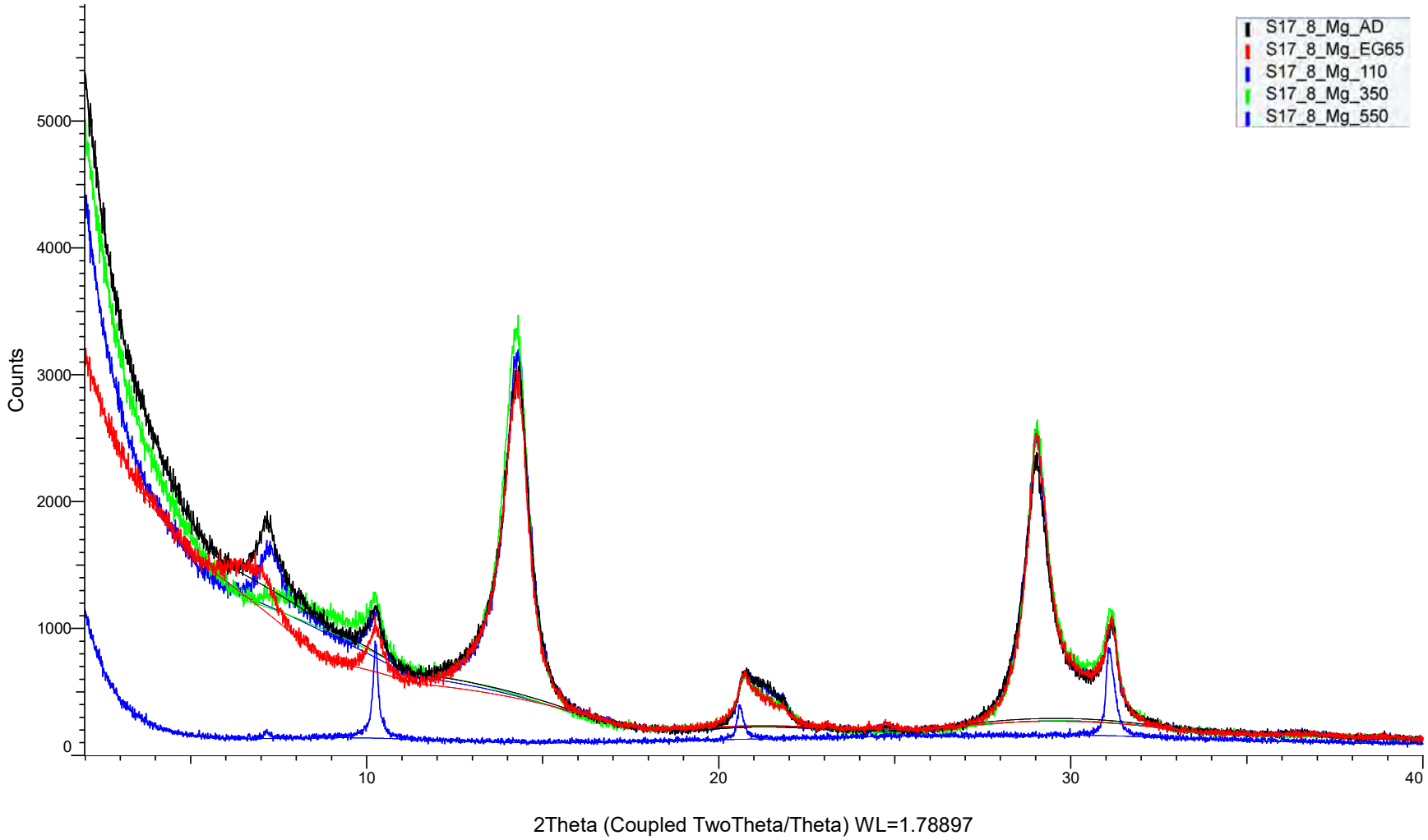

(Coupled TwoTheta/Theta)

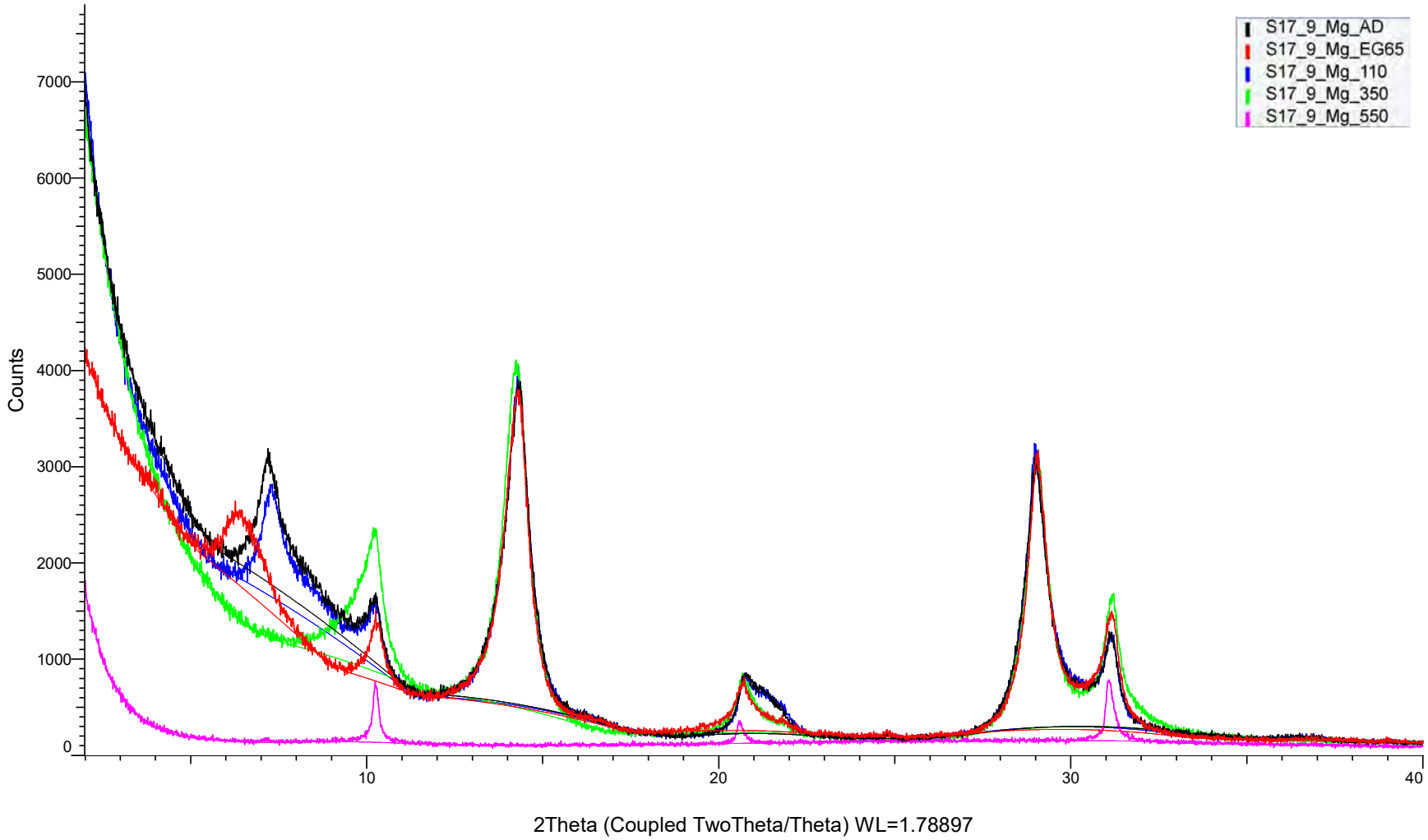

(Coupled TwoTheta/Theta)

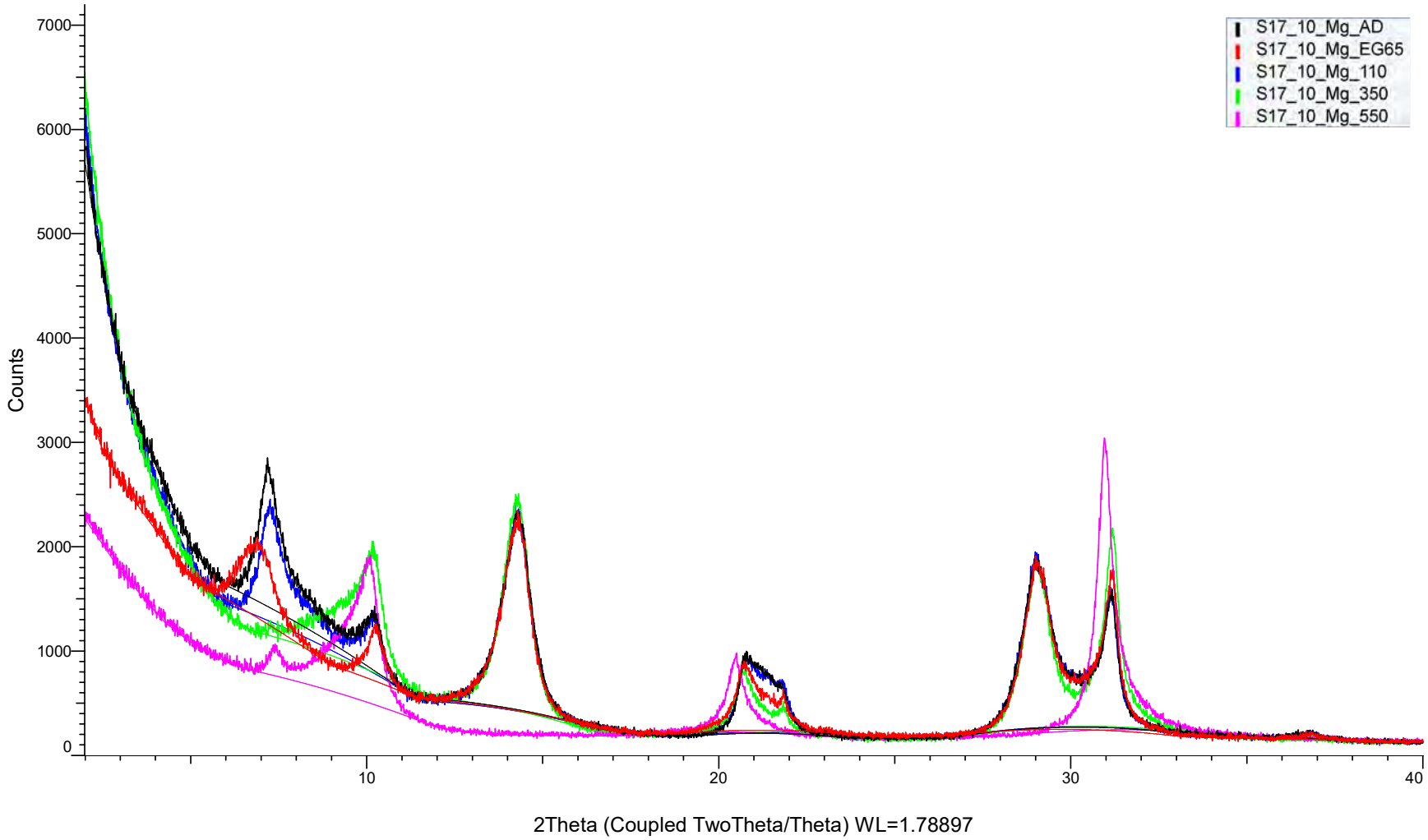

(Coupled TwoTheta/Theta)

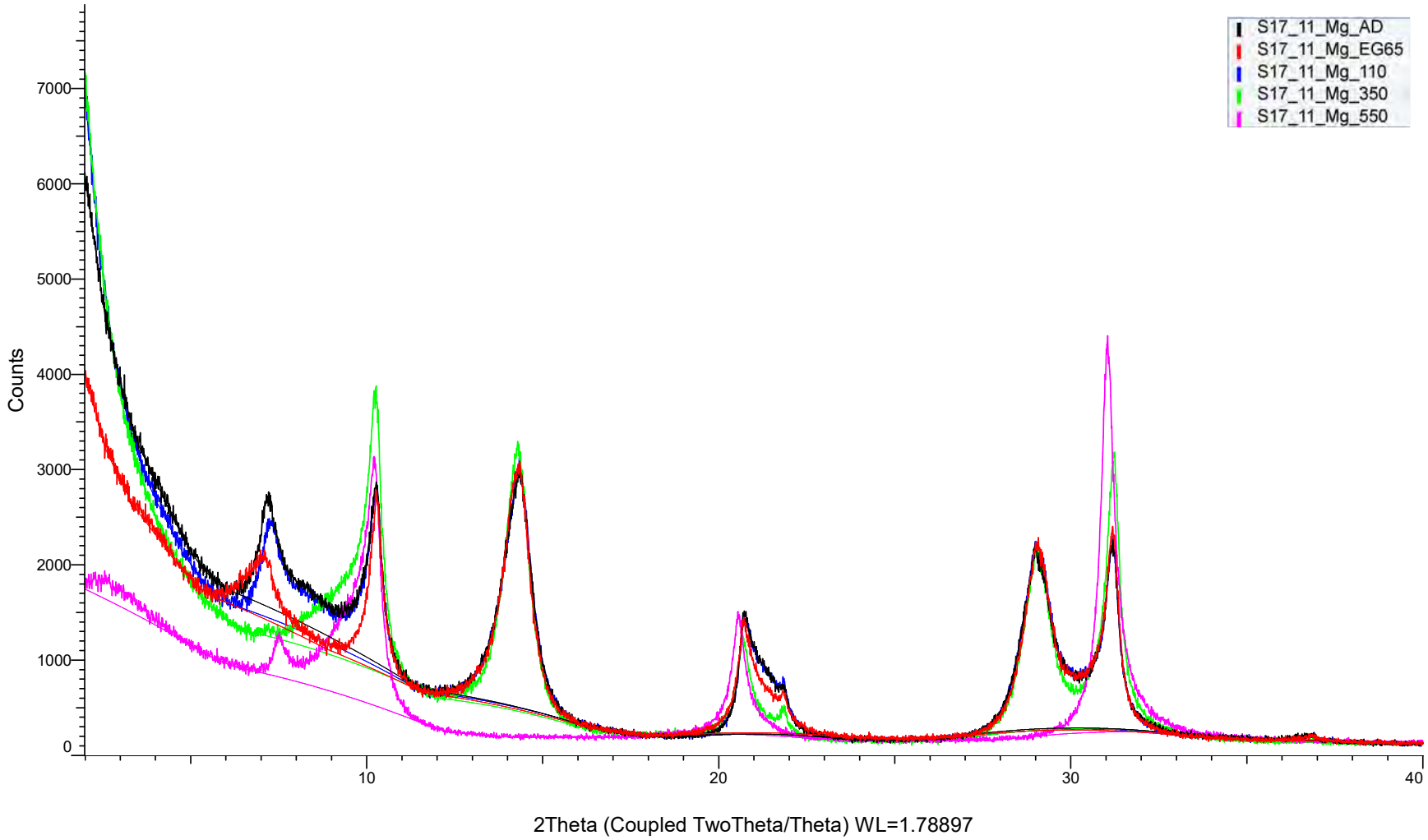

(Coupled TwoTheta/Theta)

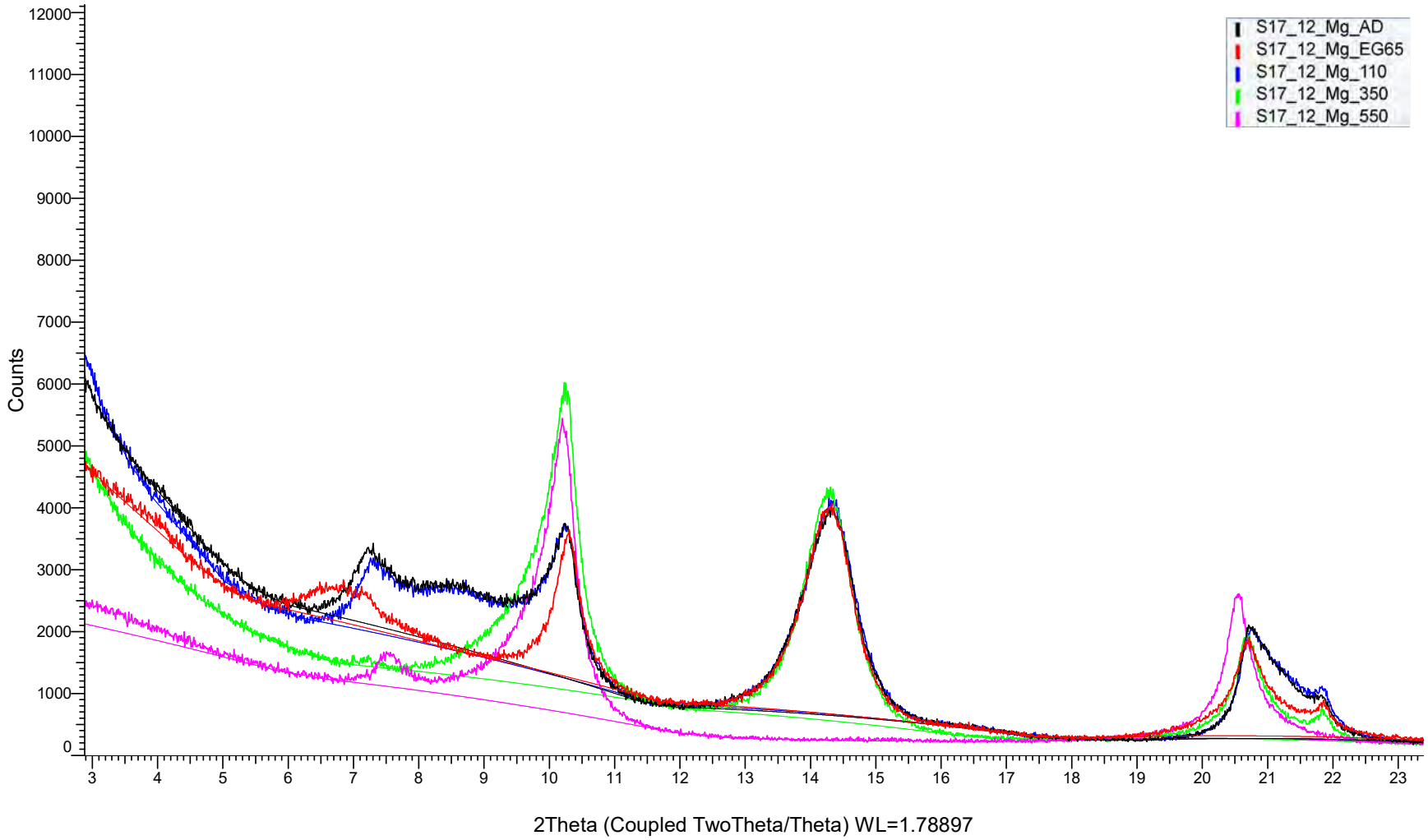

(Coupled TwoTheta/Theta)

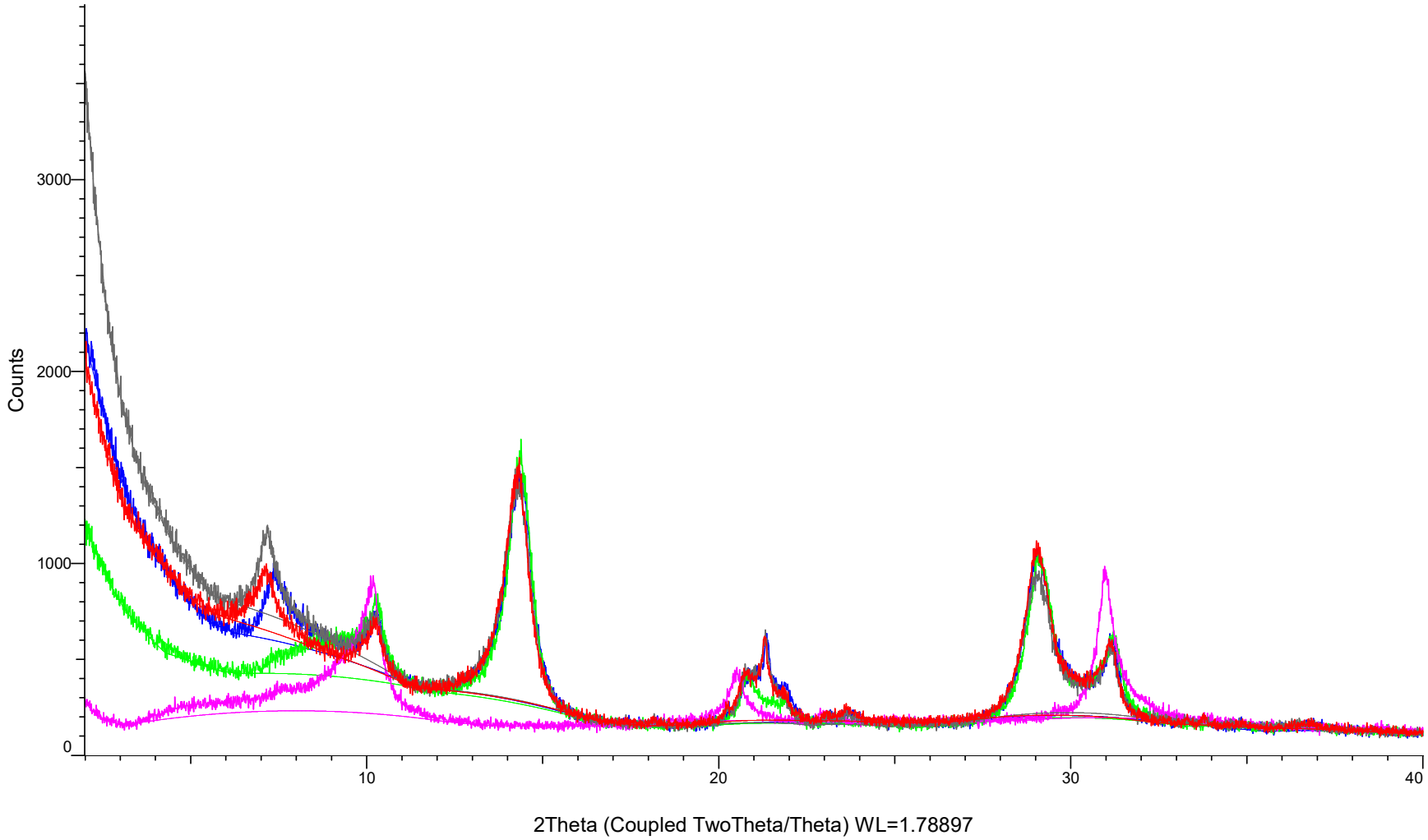

(Coupled TwoTheta/Theta)

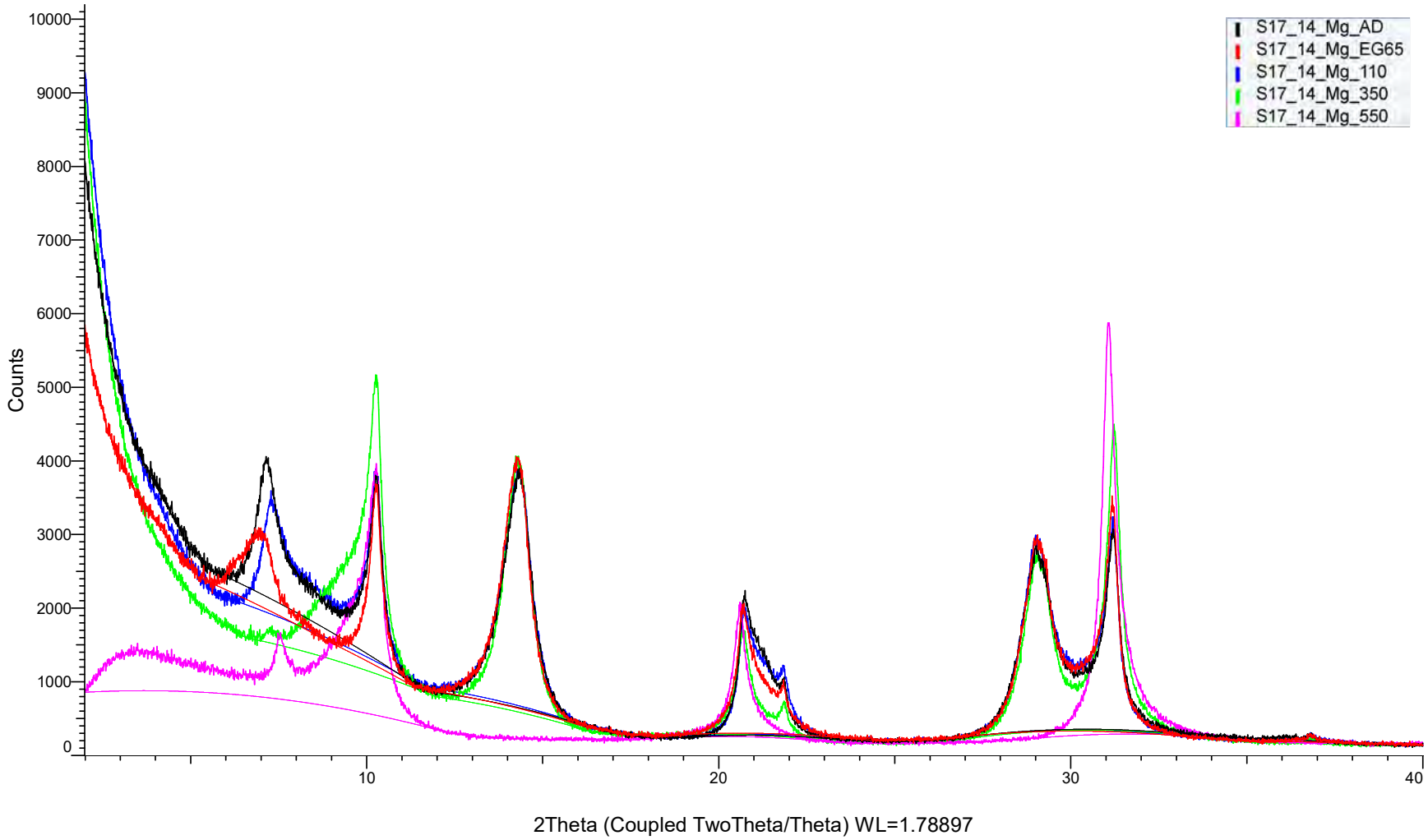

(Coupled TwoTheta/Theta)

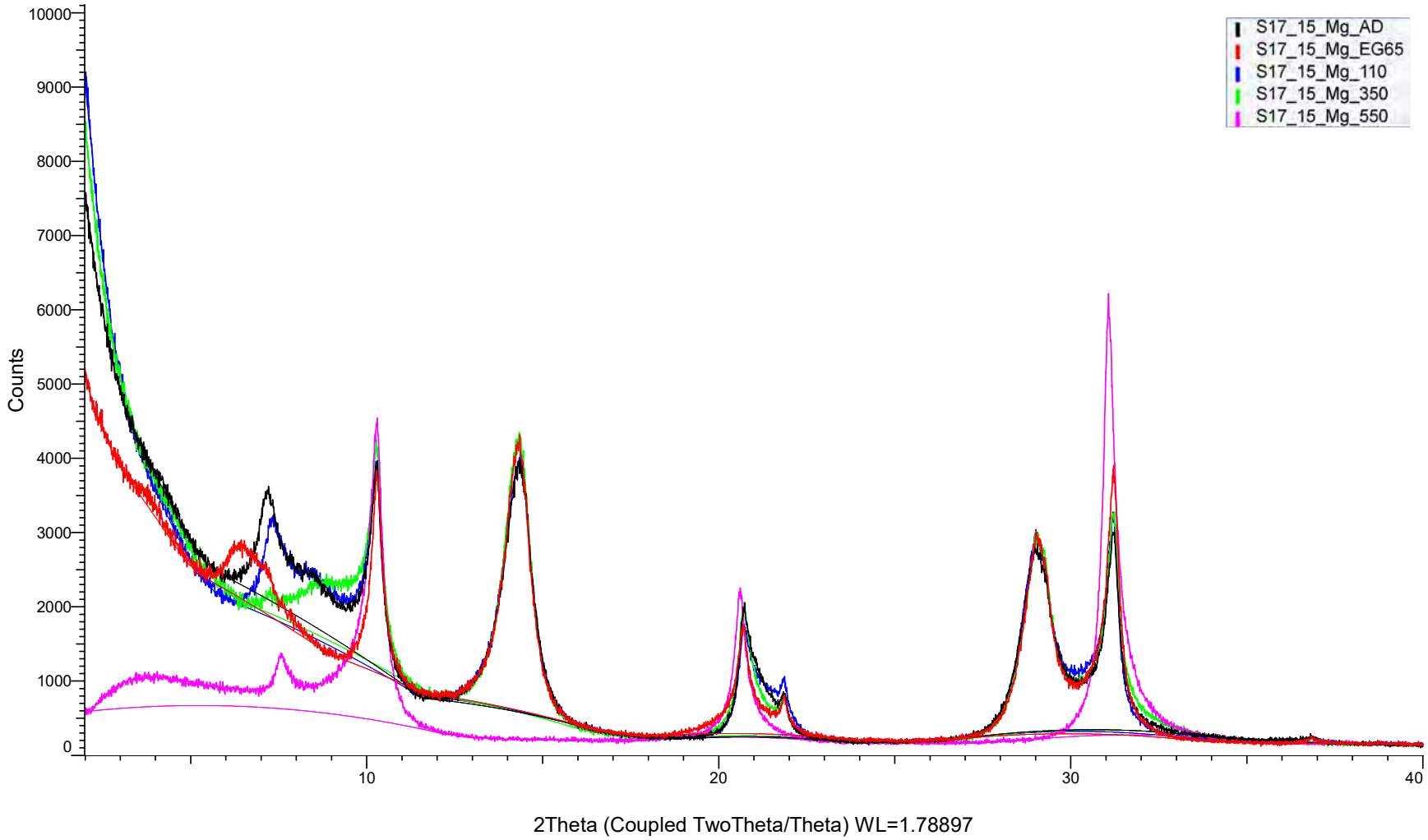

(Coupled TwoTheta/Theta)

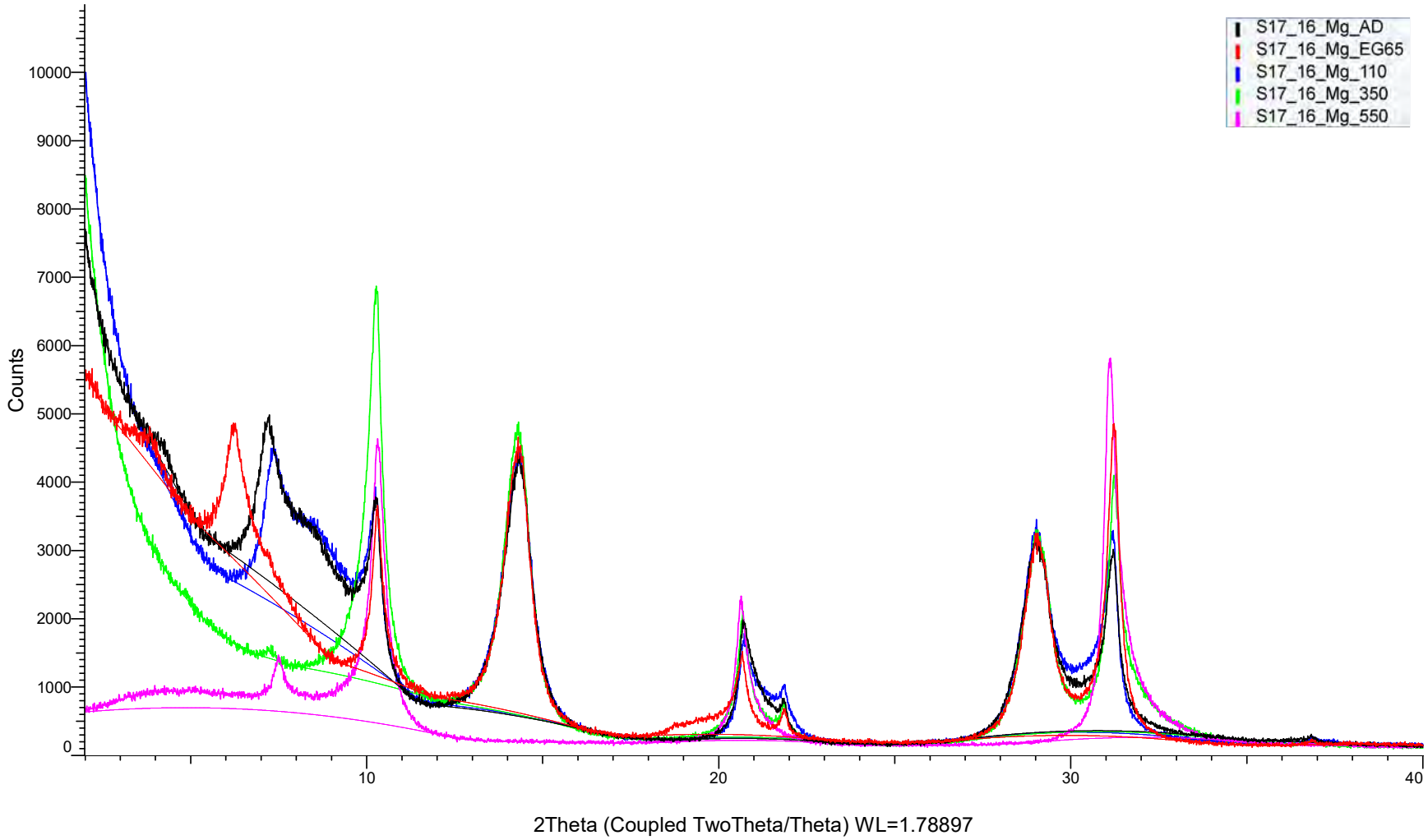

(Coupled TwoTheta/Theta)

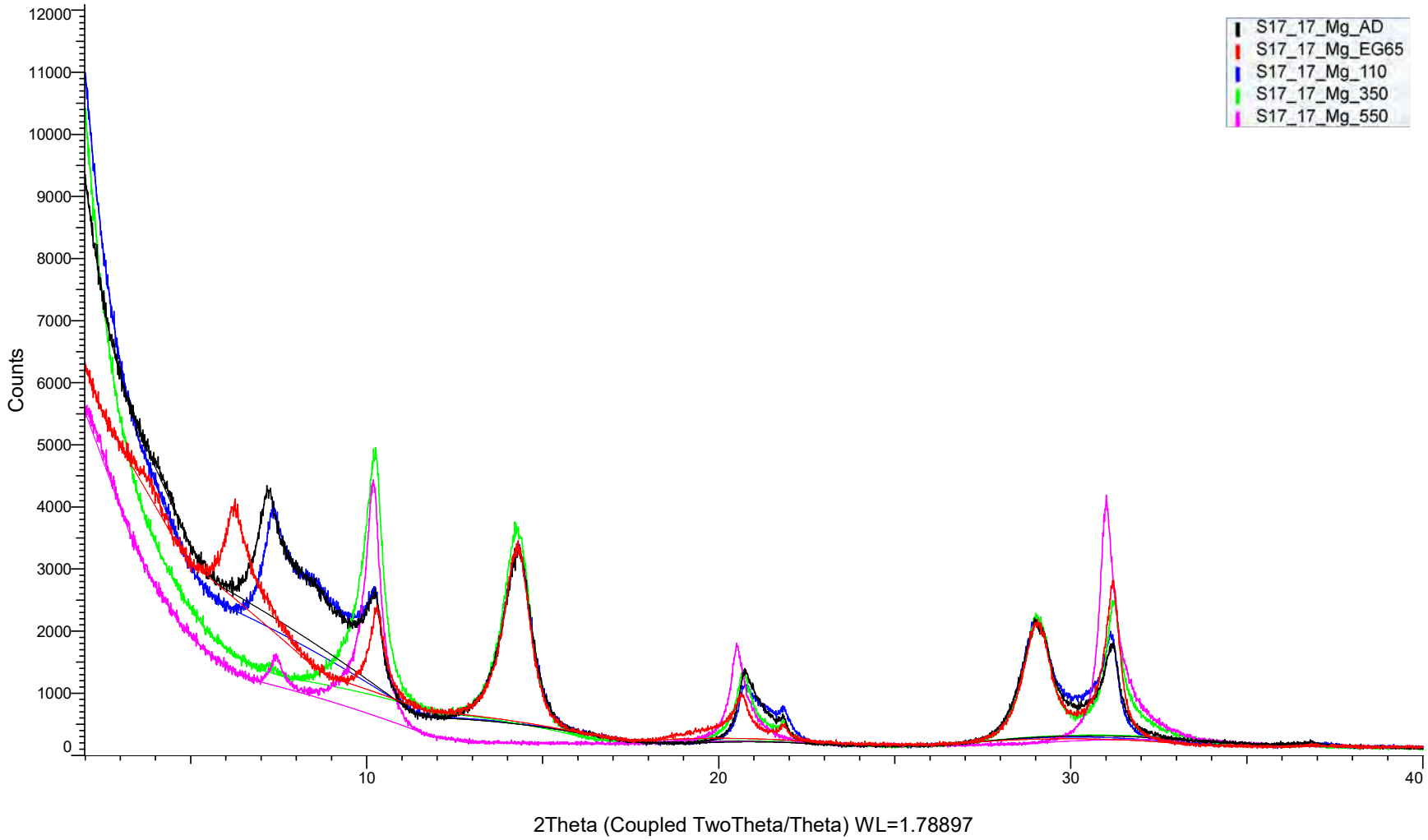

(Coupled TwoTheta/Theta)

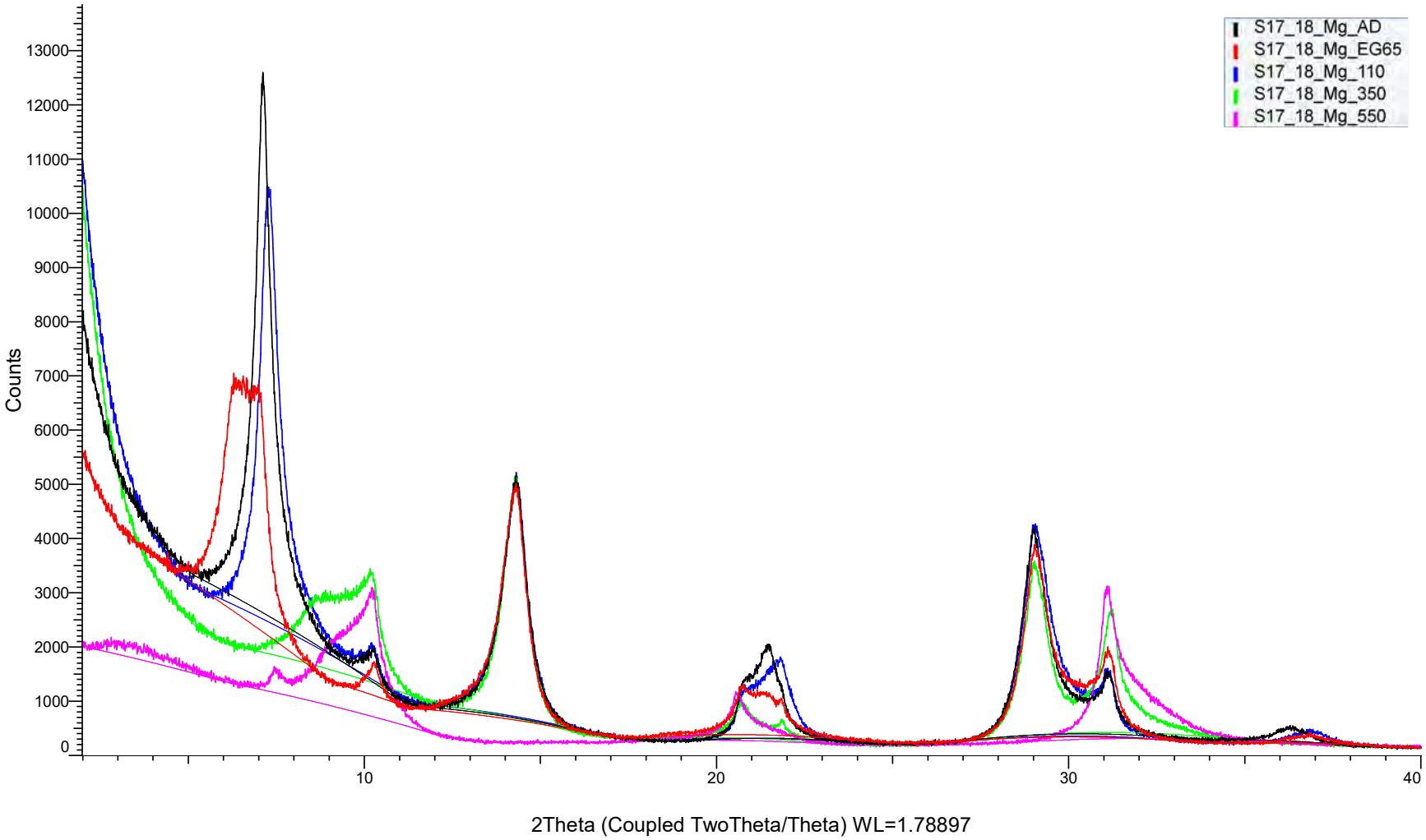

(Coupled TwoTheta/Theta)

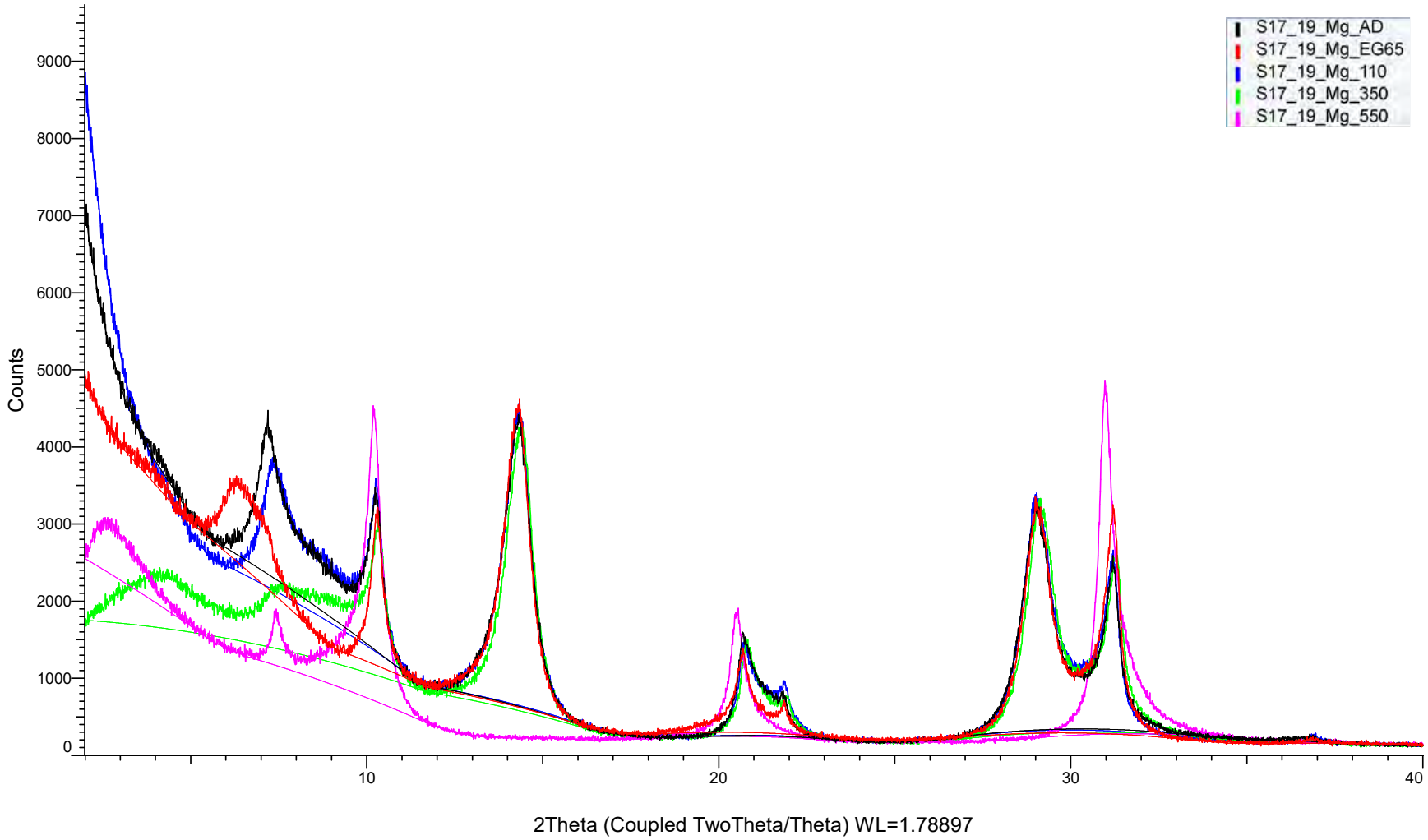

(Coupled TwoTheta/Theta)

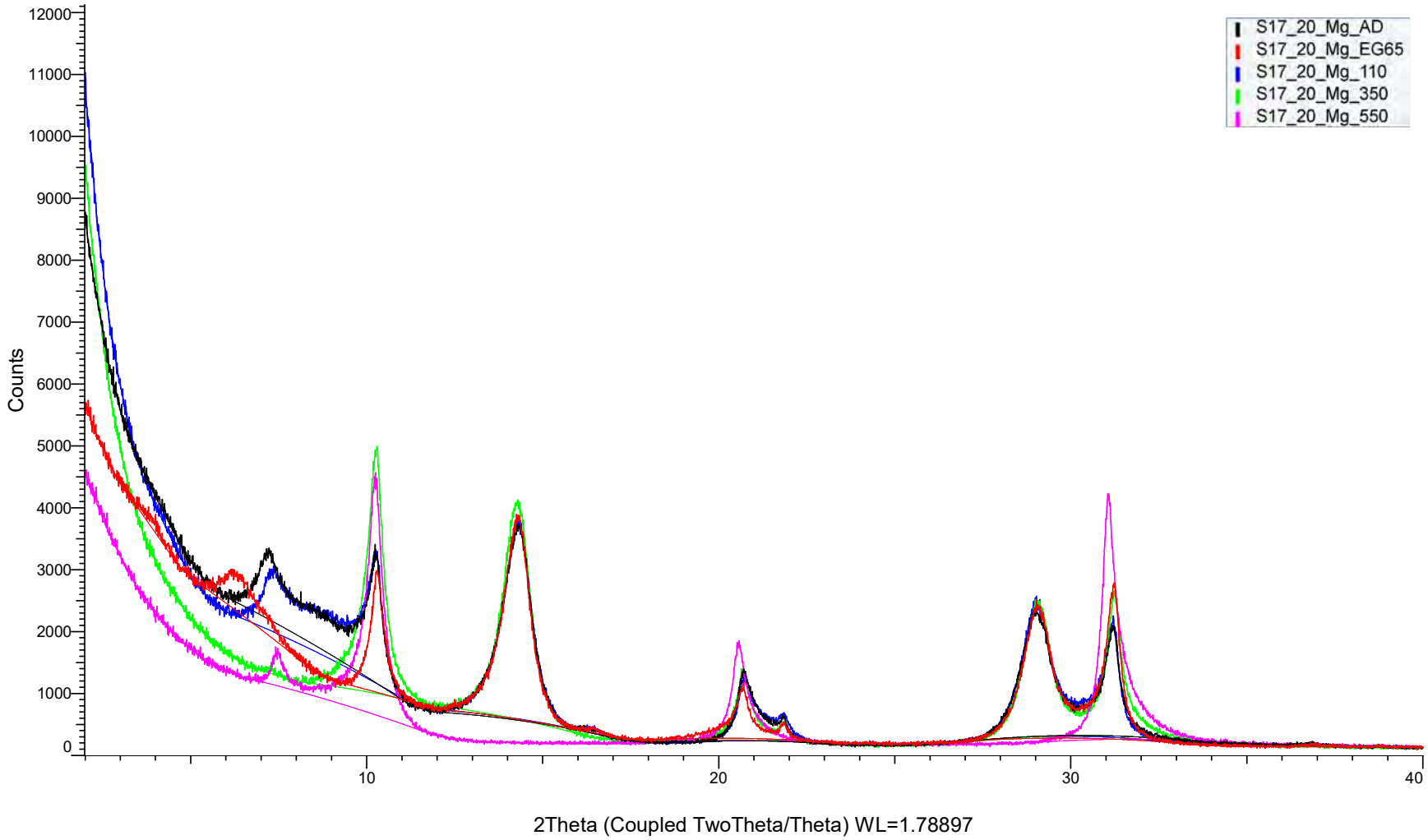

(Coupled TwoTheta/Theta)

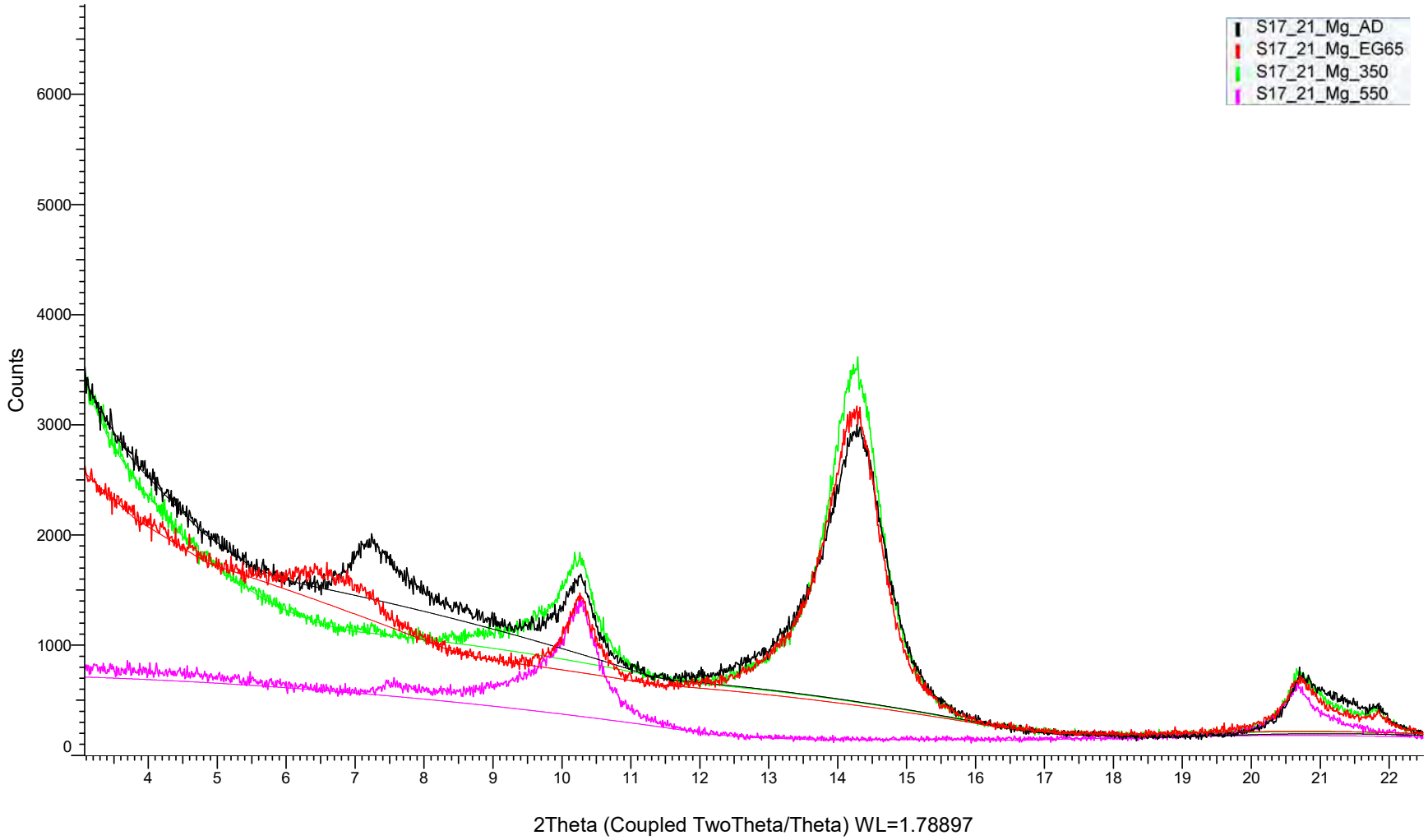

(Coupled TwoTheta/Theta)

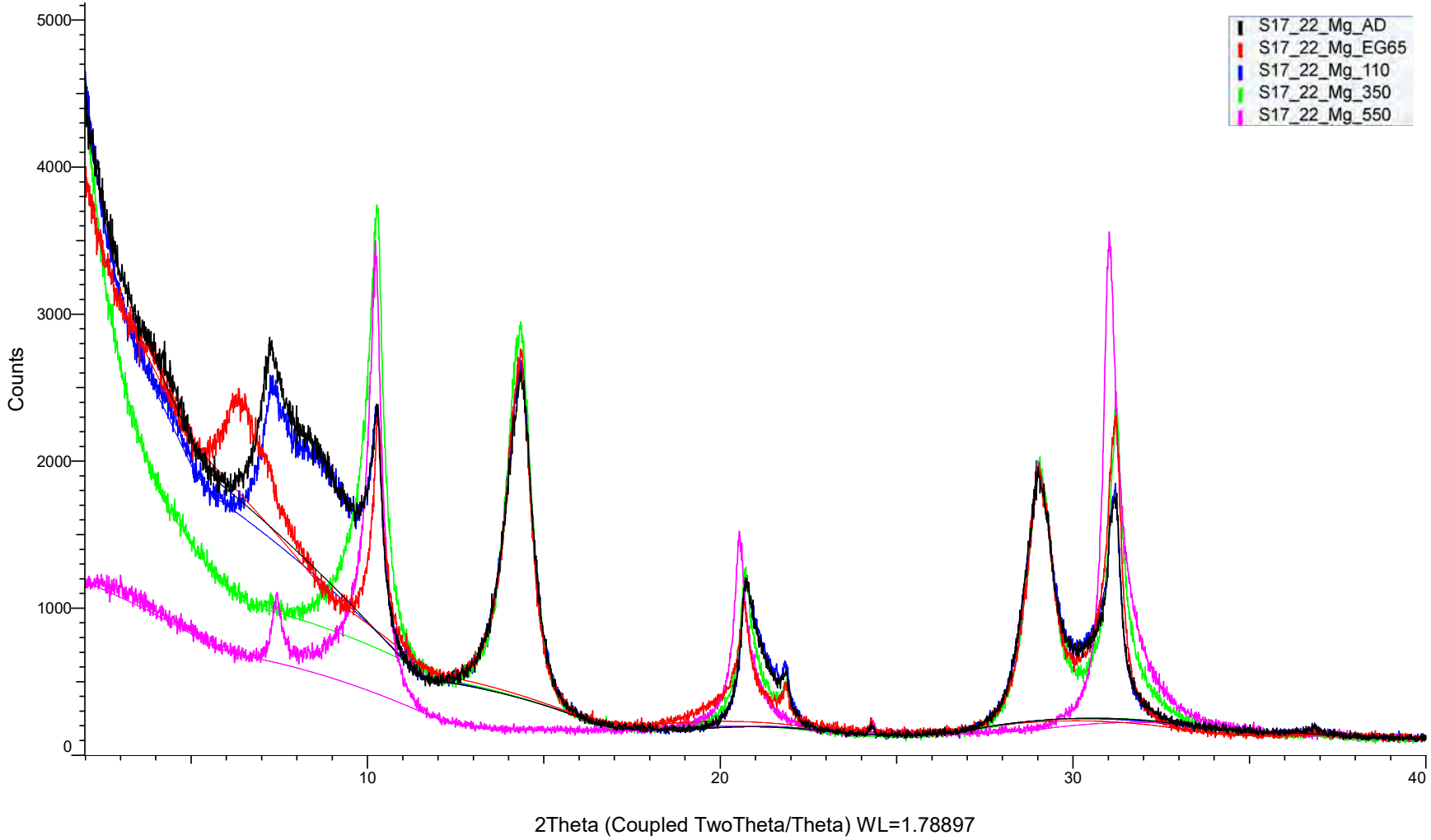

(Coupled TwoTheta/Theta)

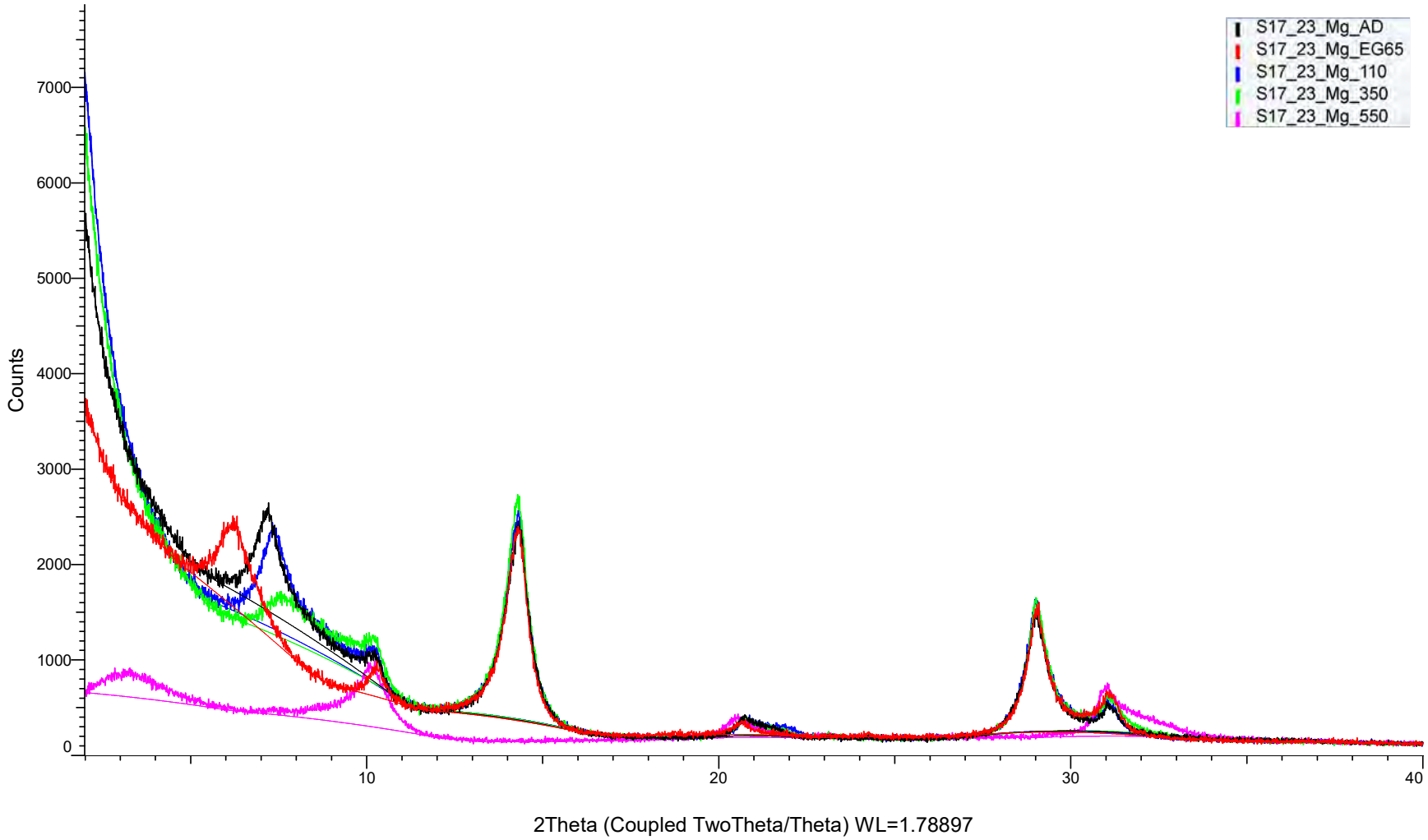

(Coupled TwoTheta/Theta)

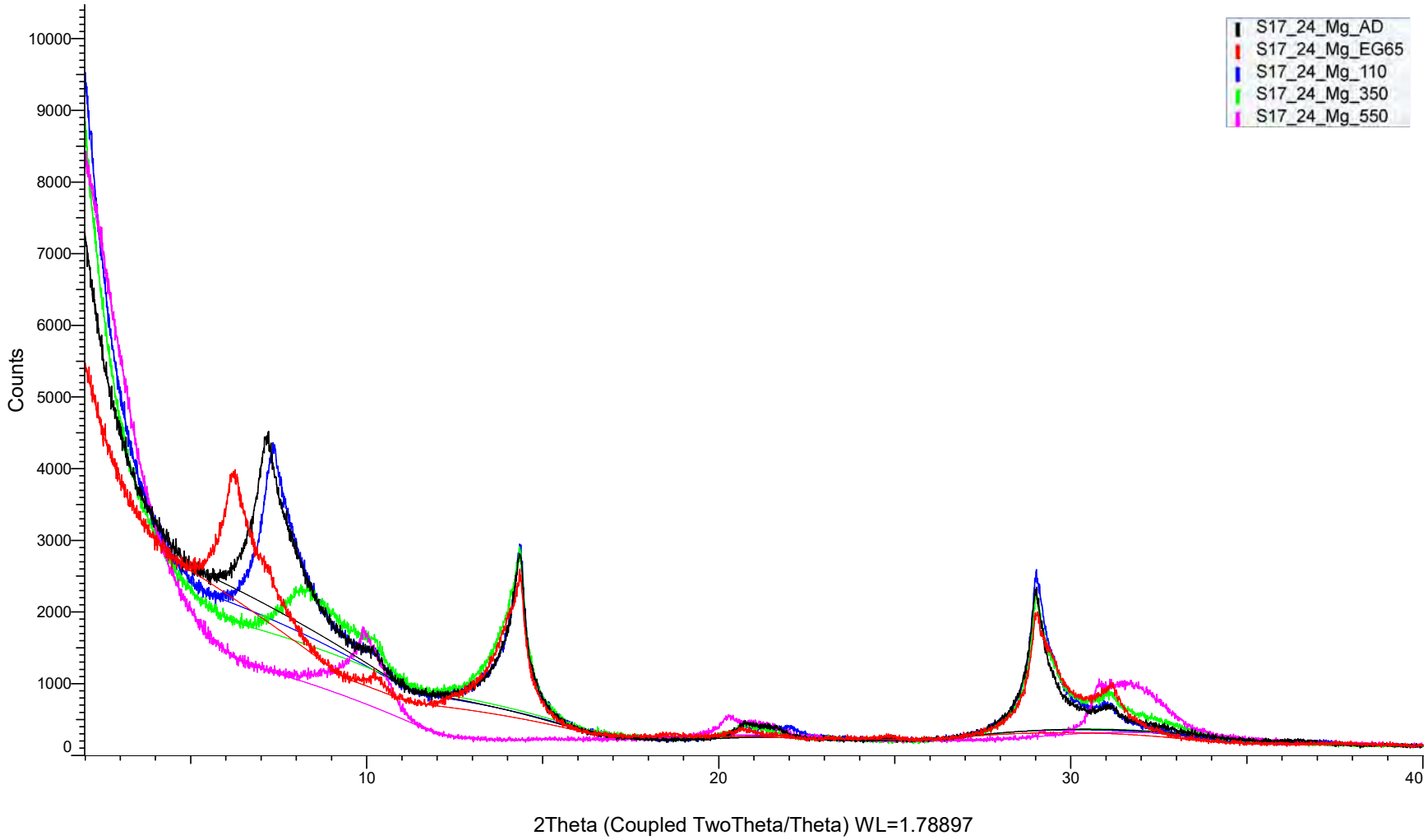

(Coupled TwoTheta/Theta)

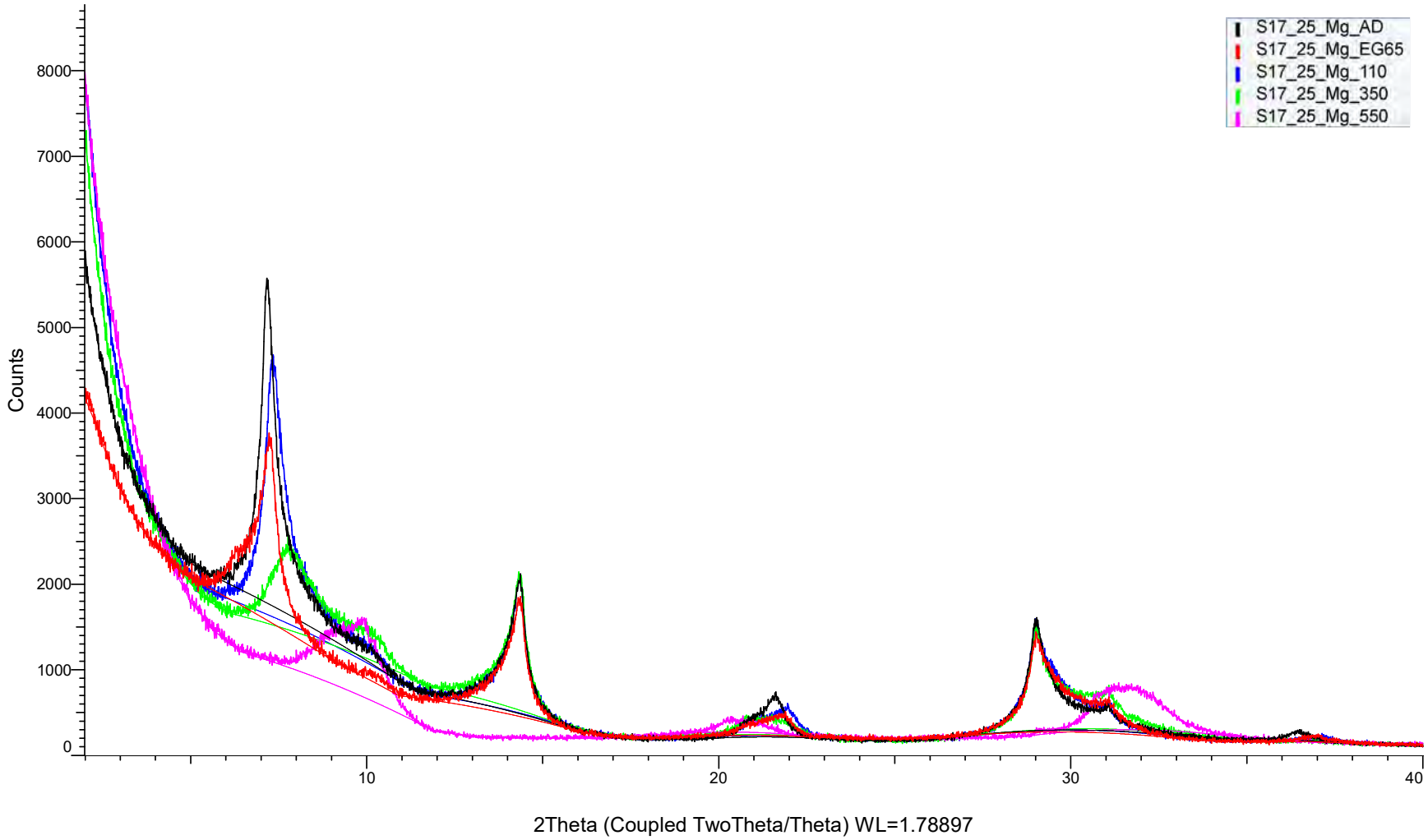

(Coupled TwoTheta/Theta)

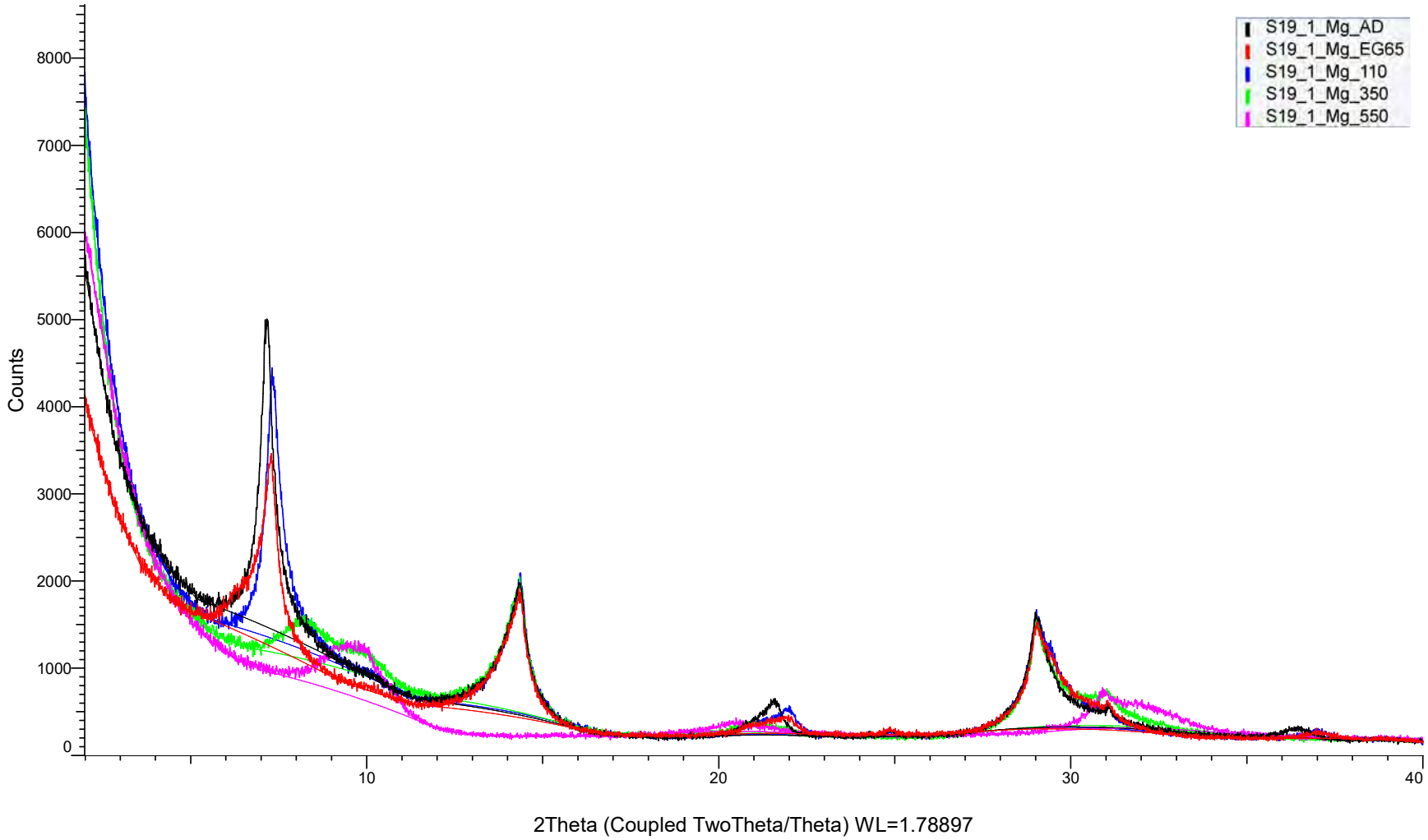

(Coupled TwoTheta/Theta)

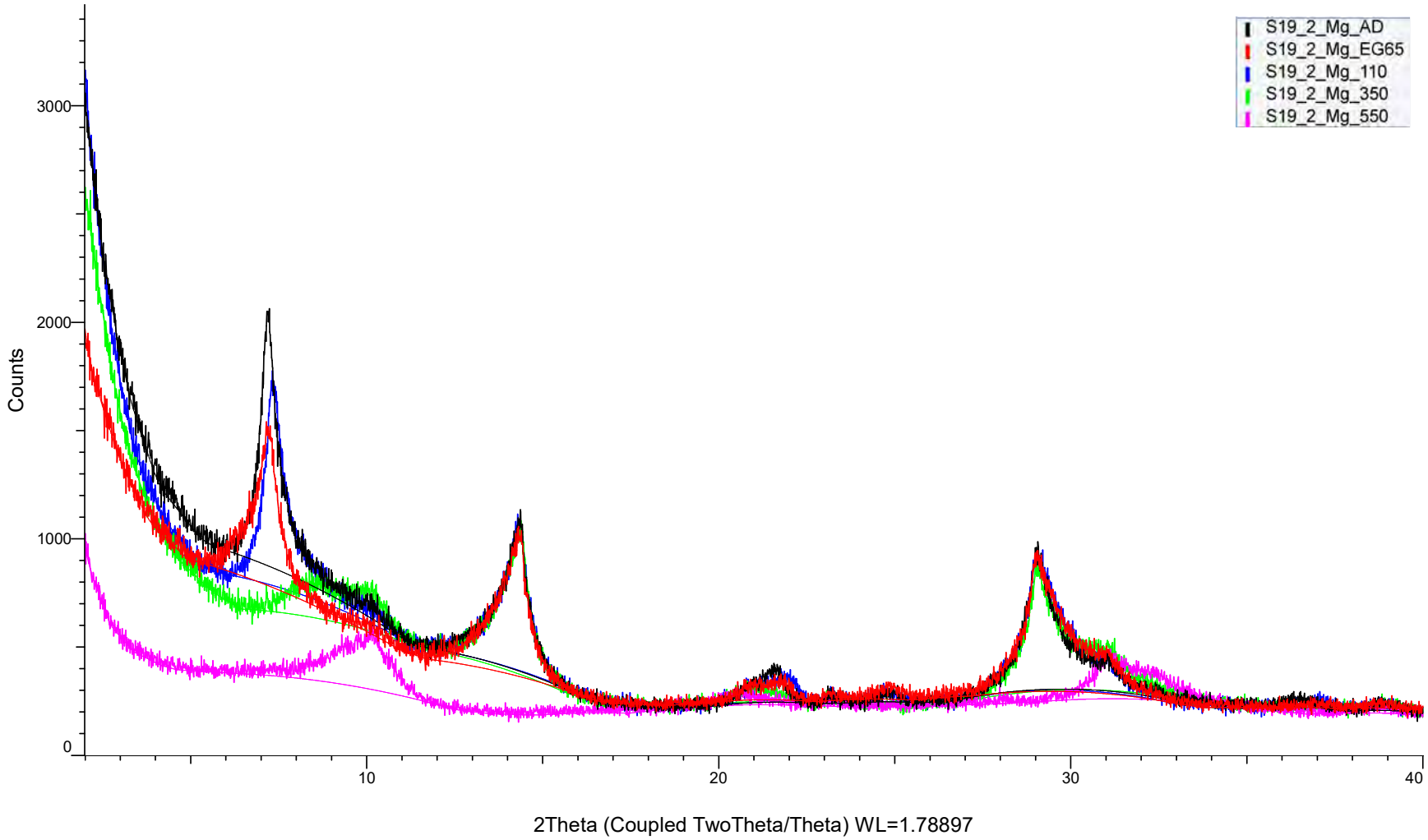

(Coupled TwoTheta/Theta)

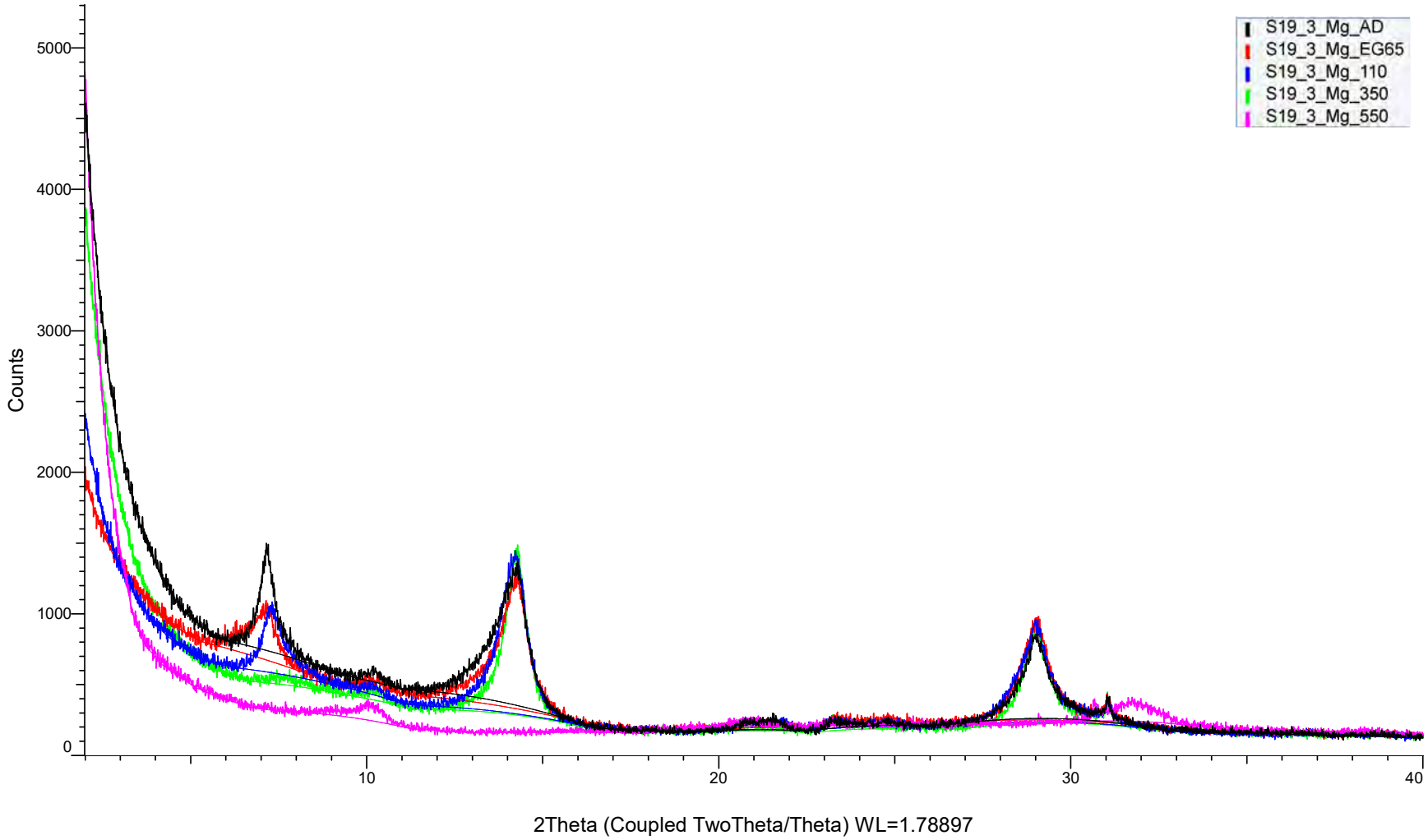

(Coupled TwoTheta/Theta)

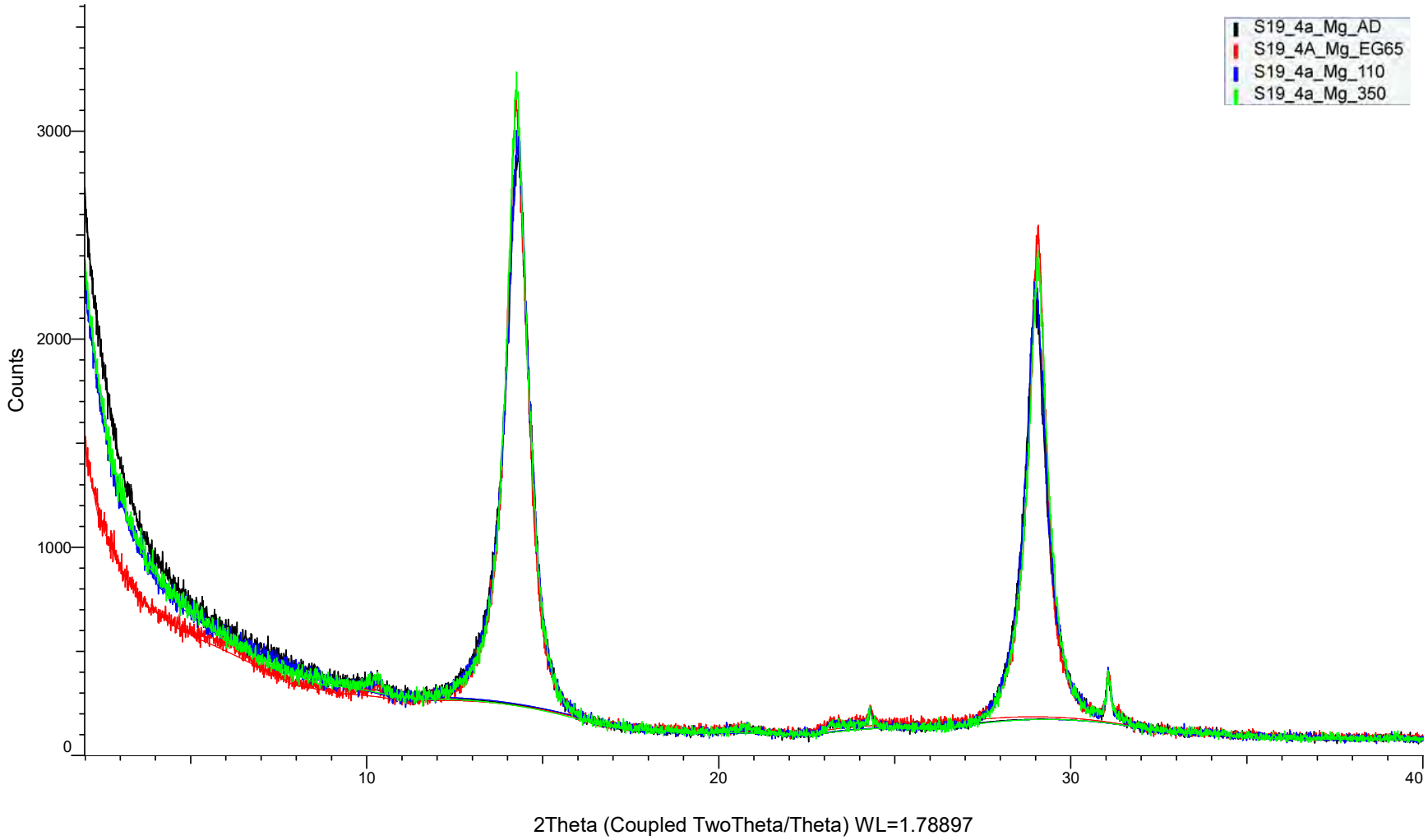

(Coupled TwoTheta/Theta)

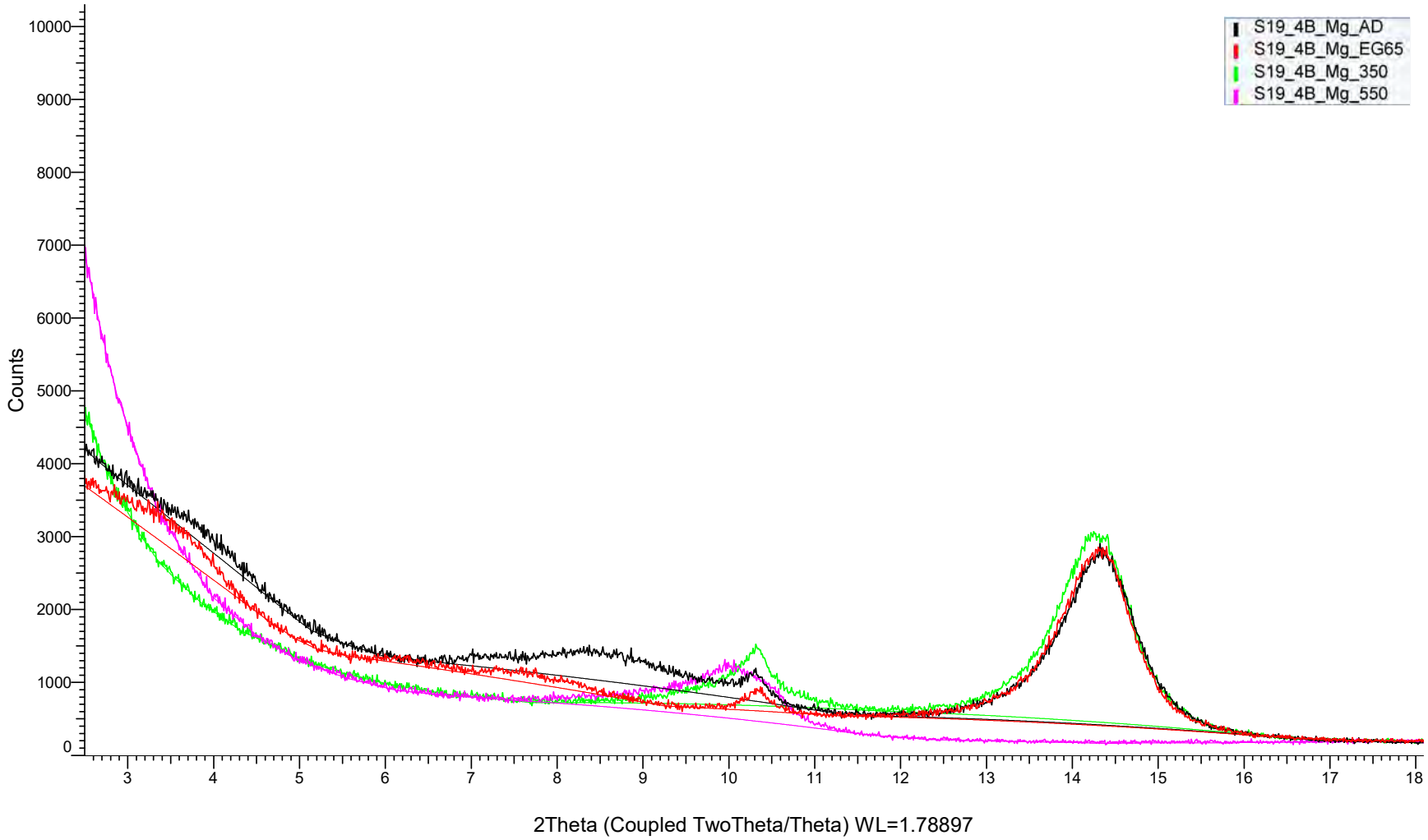

(Coupled TwoTheta/Theta)

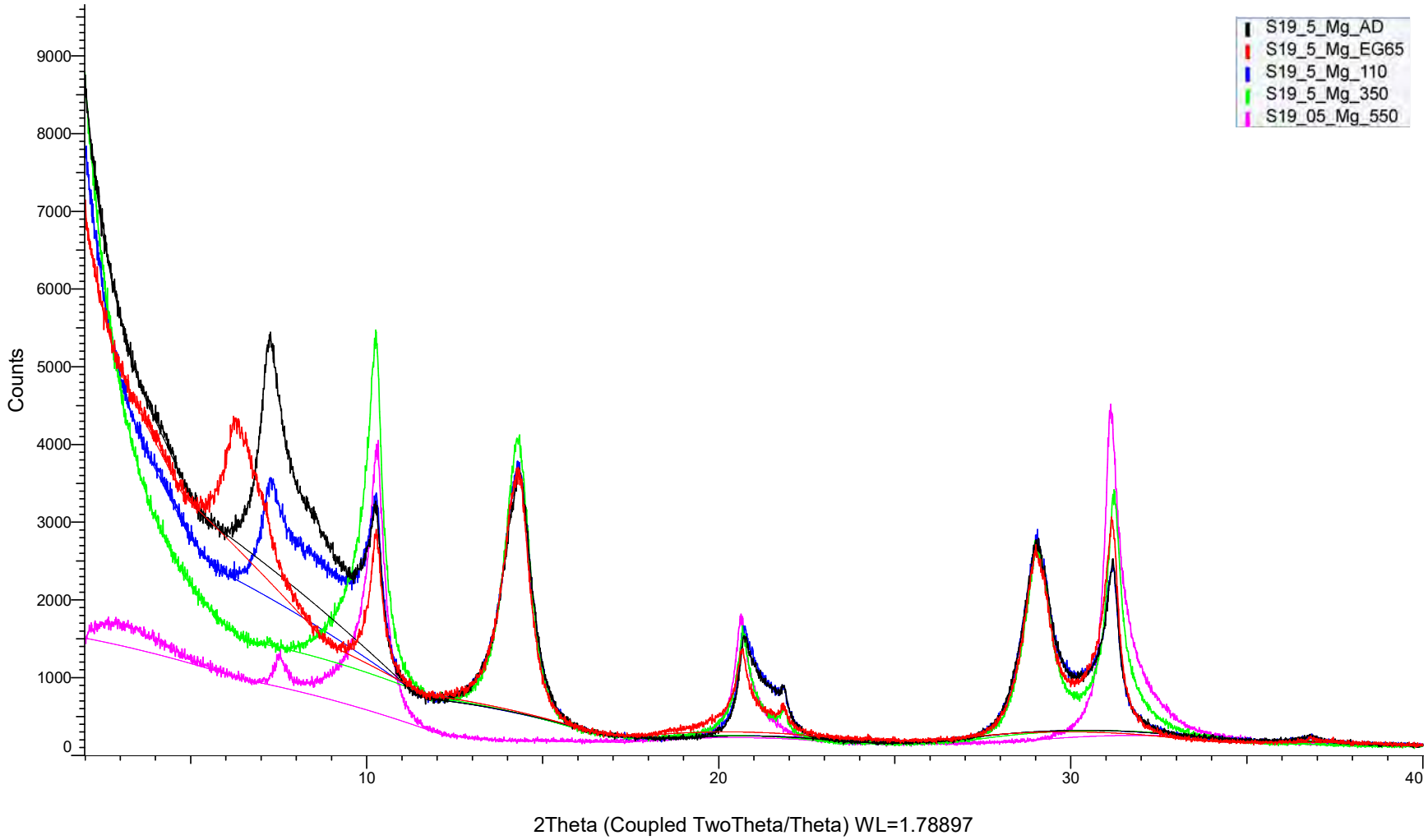

(Coupled TwoTheta/Theta)

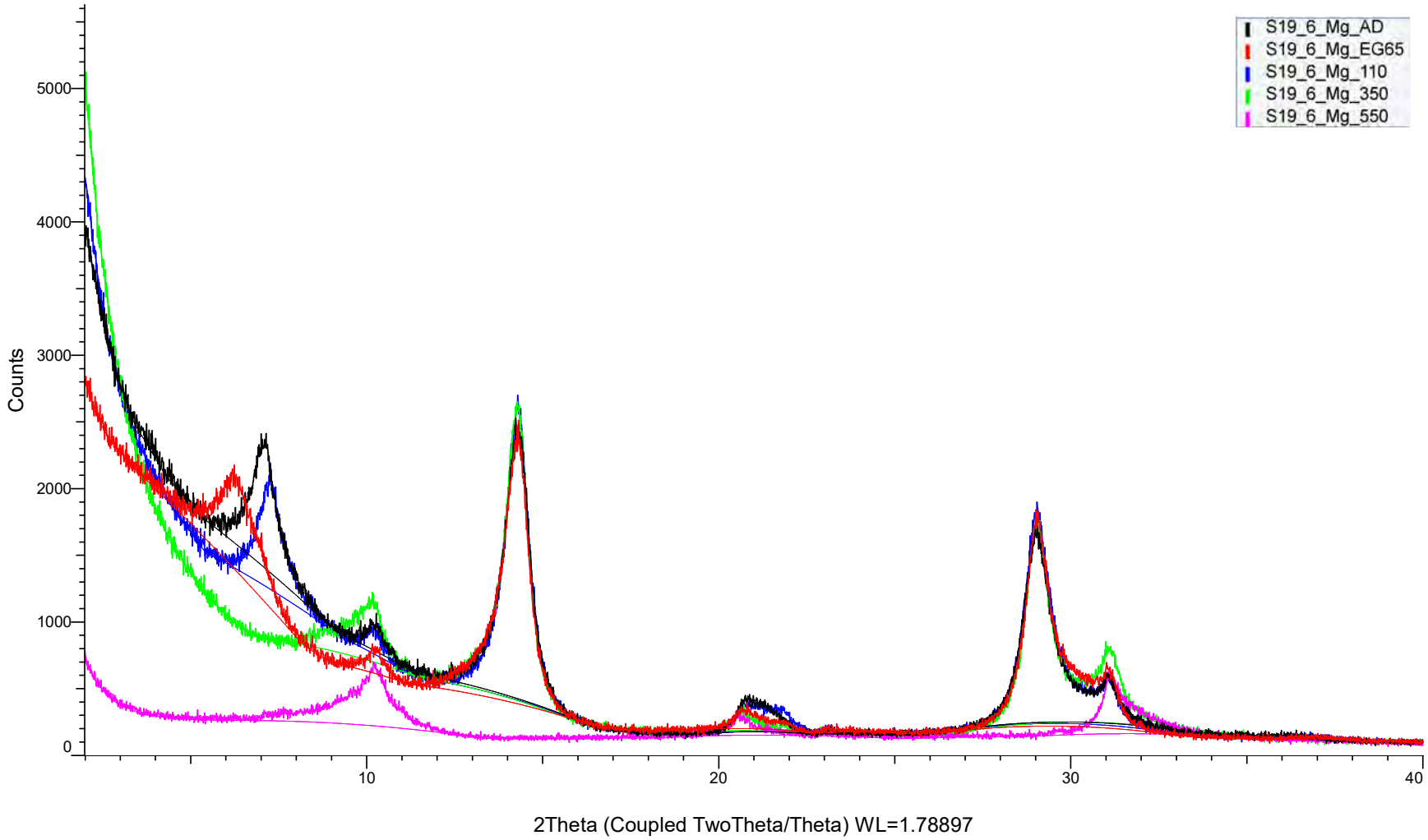

(Coupled TwoTheta/Theta)

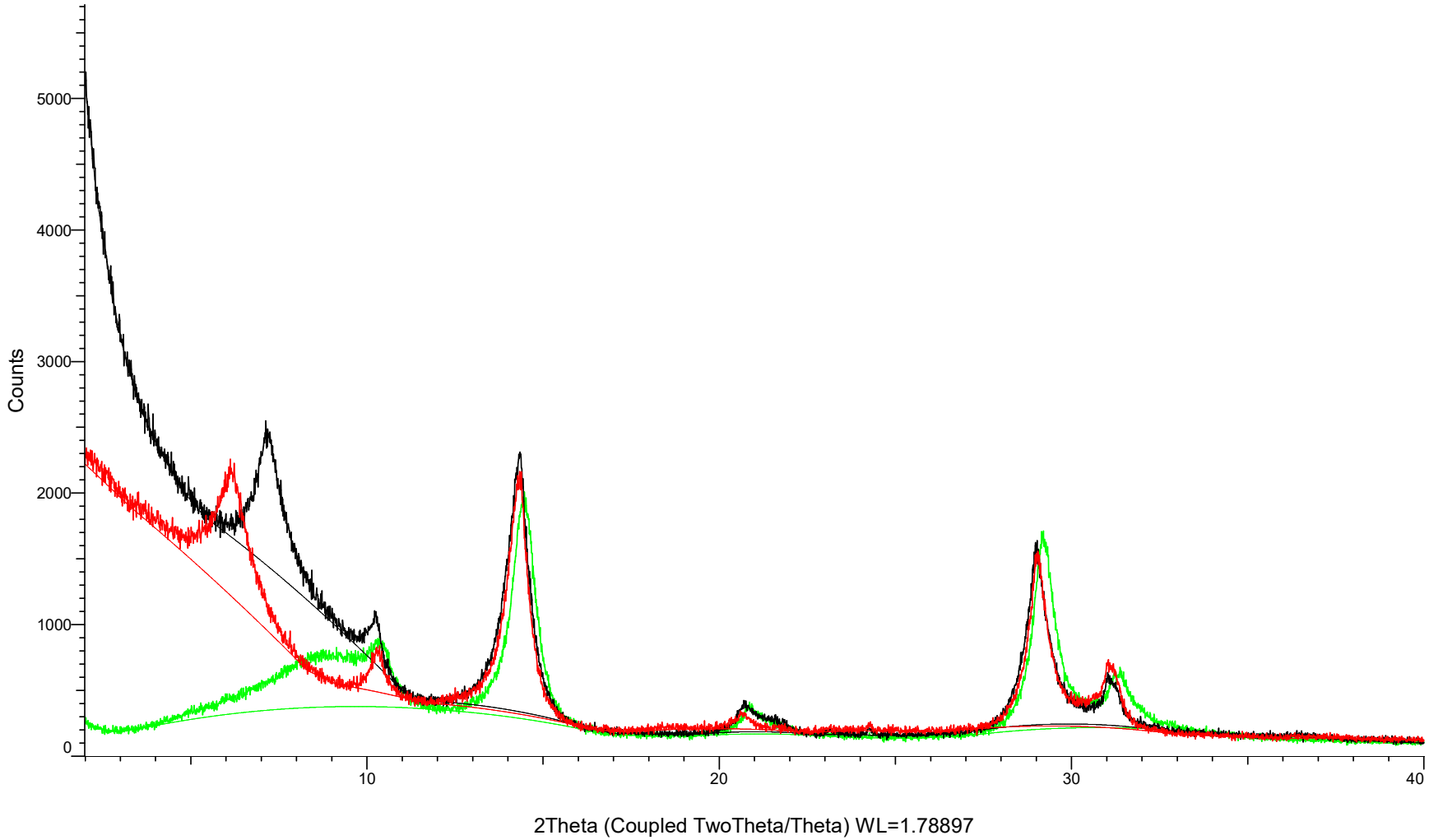

(Coupled TwoTheta/Theta)

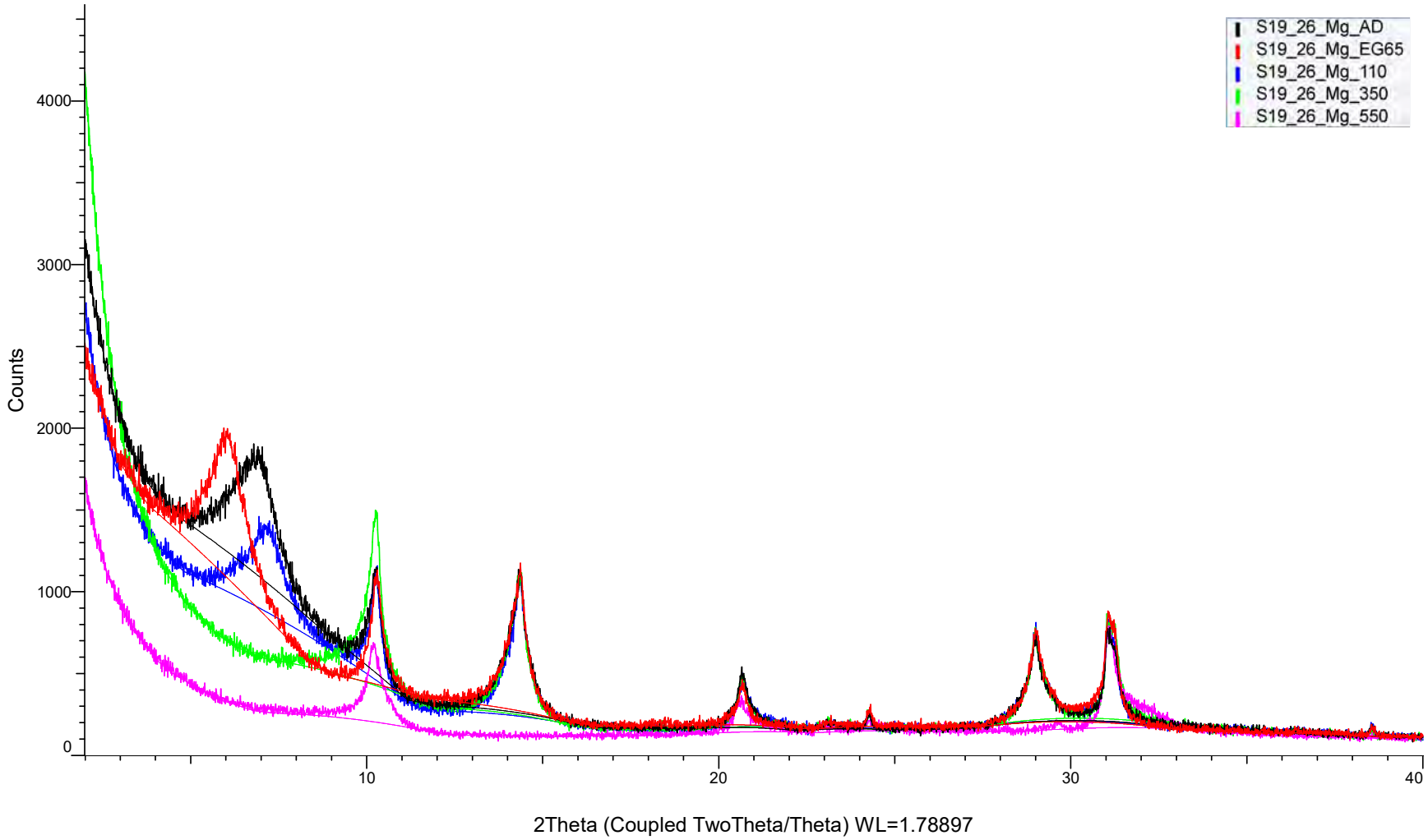

(Coupled TwoTheta/Theta)

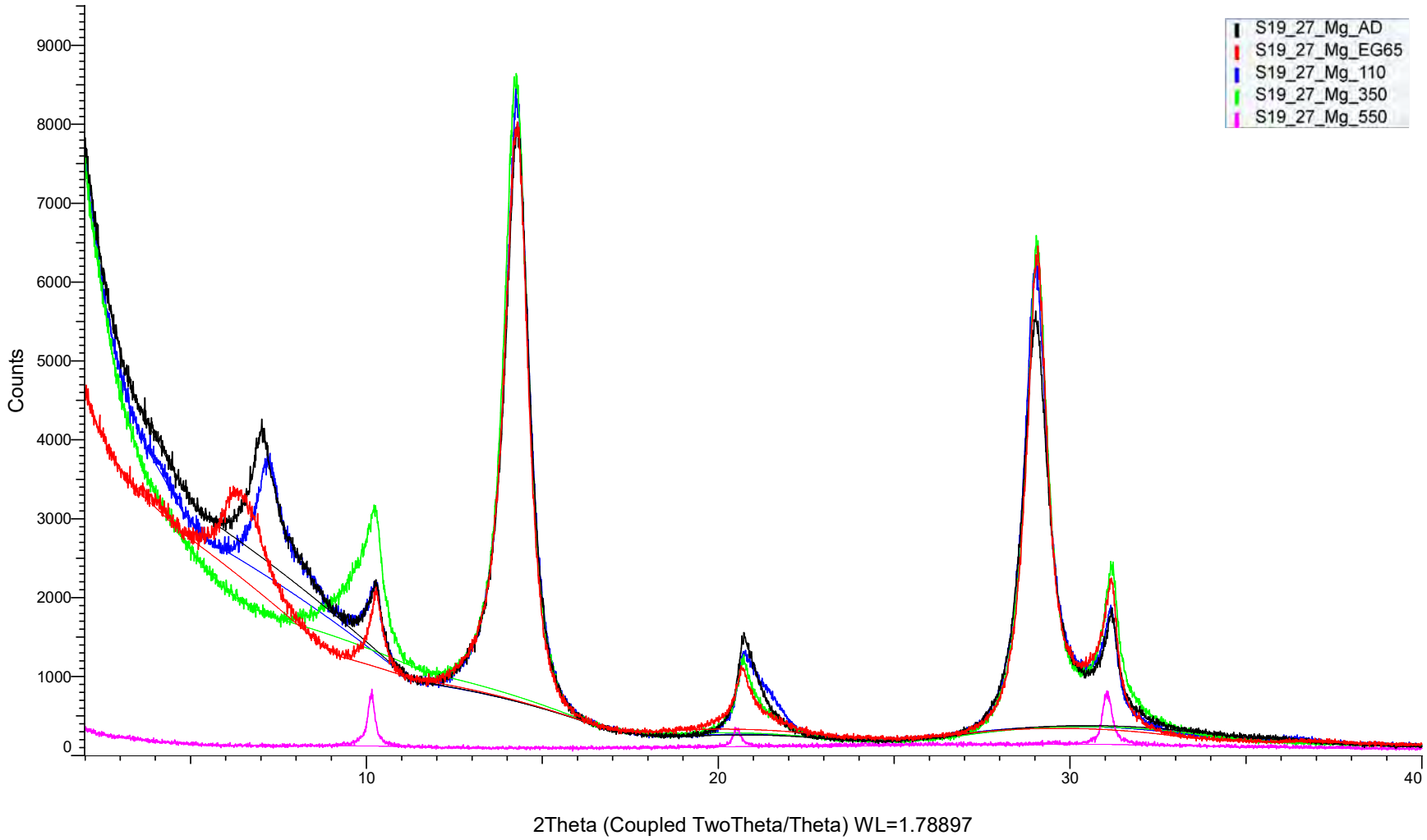

(Coupled TwoTheta/Theta)

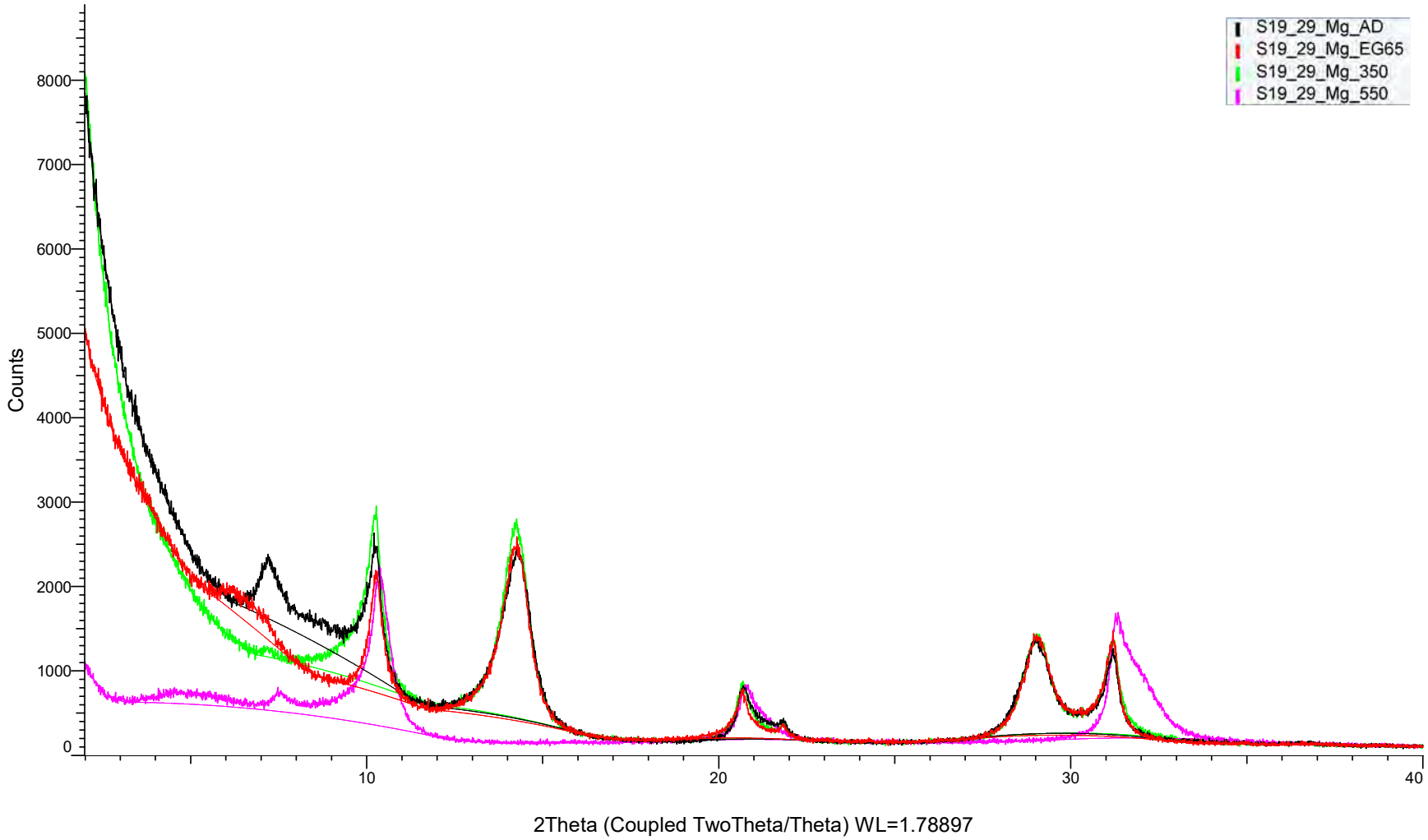

(Coupled TwoTheta/Theta)

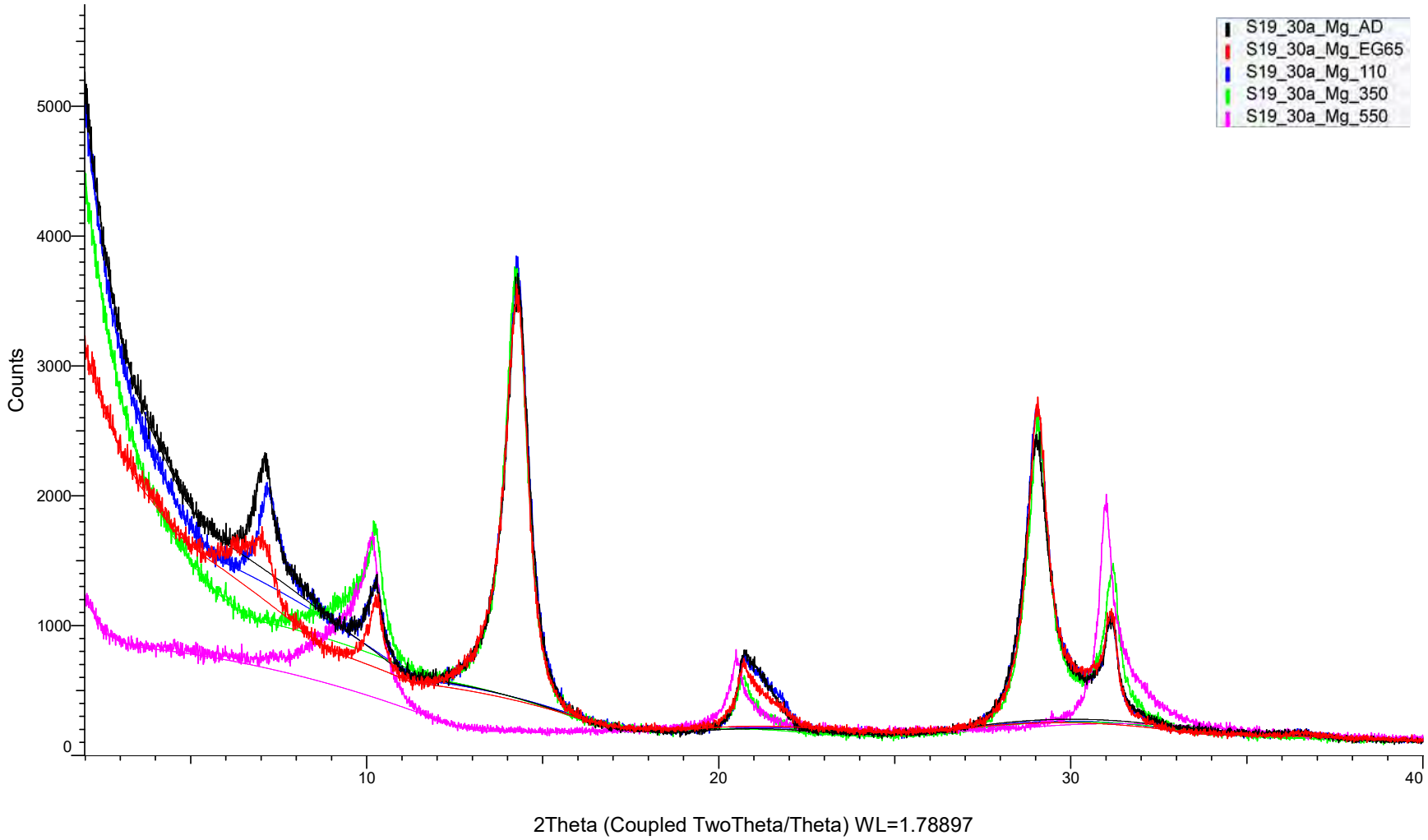

(Coupled TwoTheta/Theta)

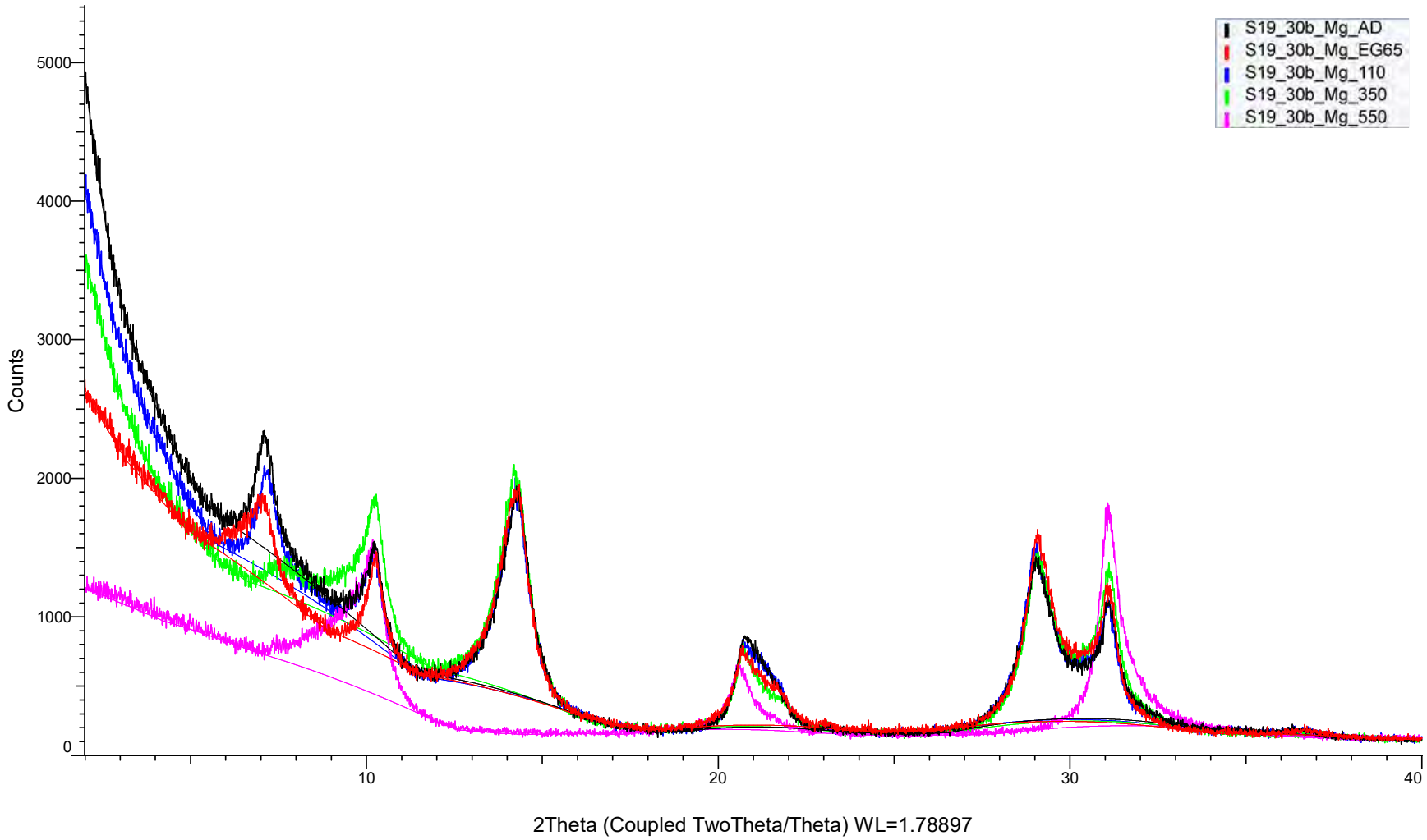

(Coupled TwoTheta/Theta)

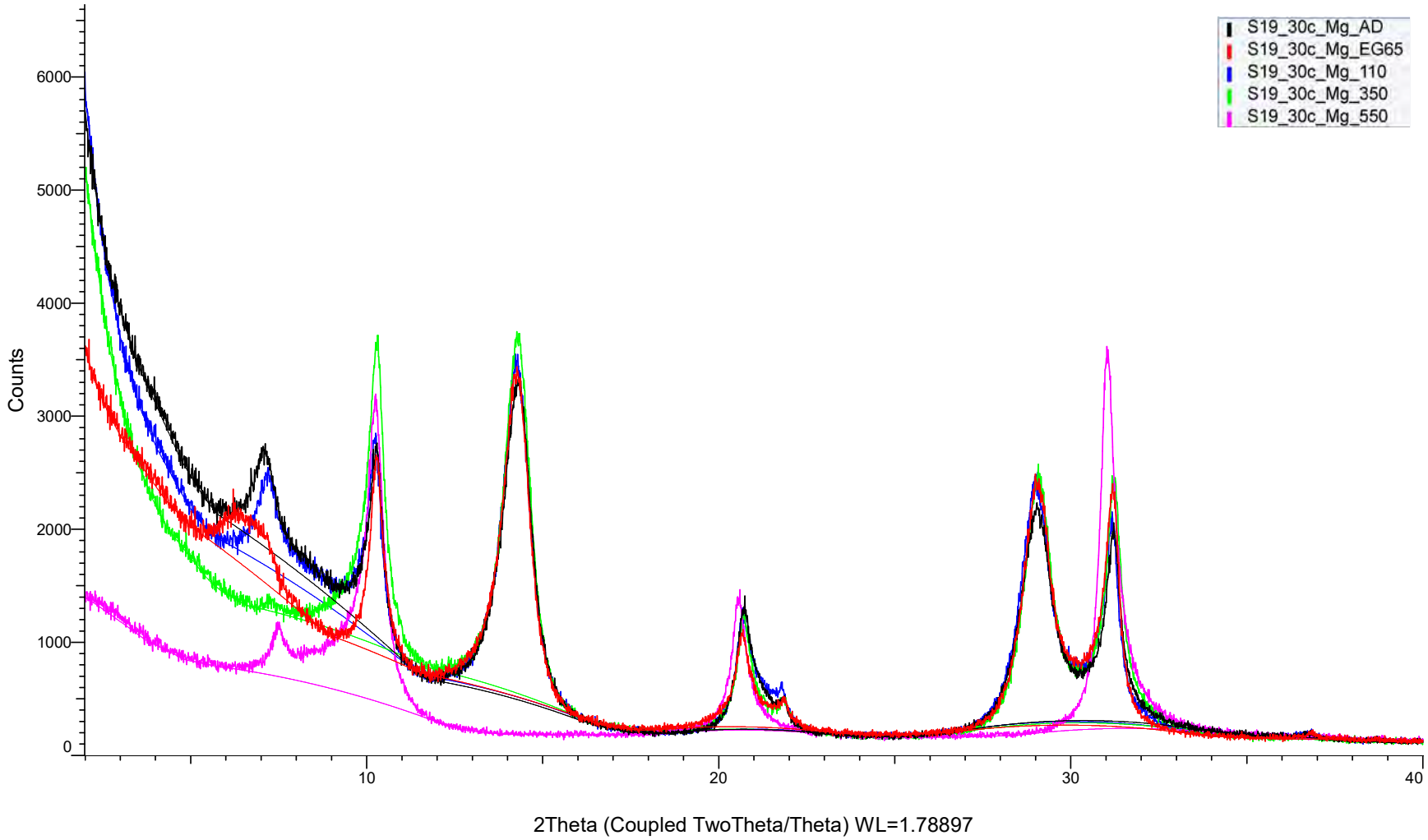

(Coupled TwoTheta/Theta)

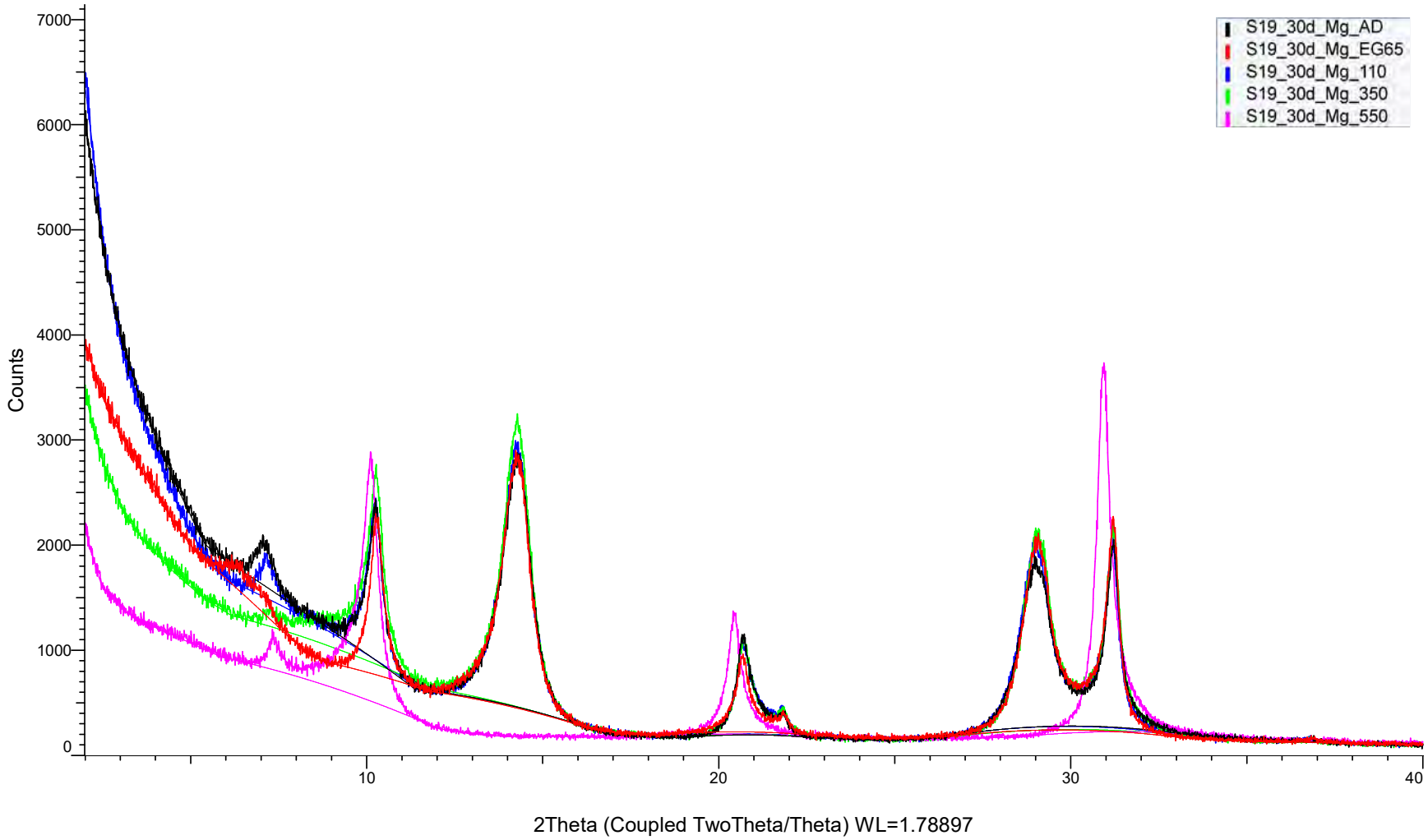

(Coupled TwoTheta/Theta)

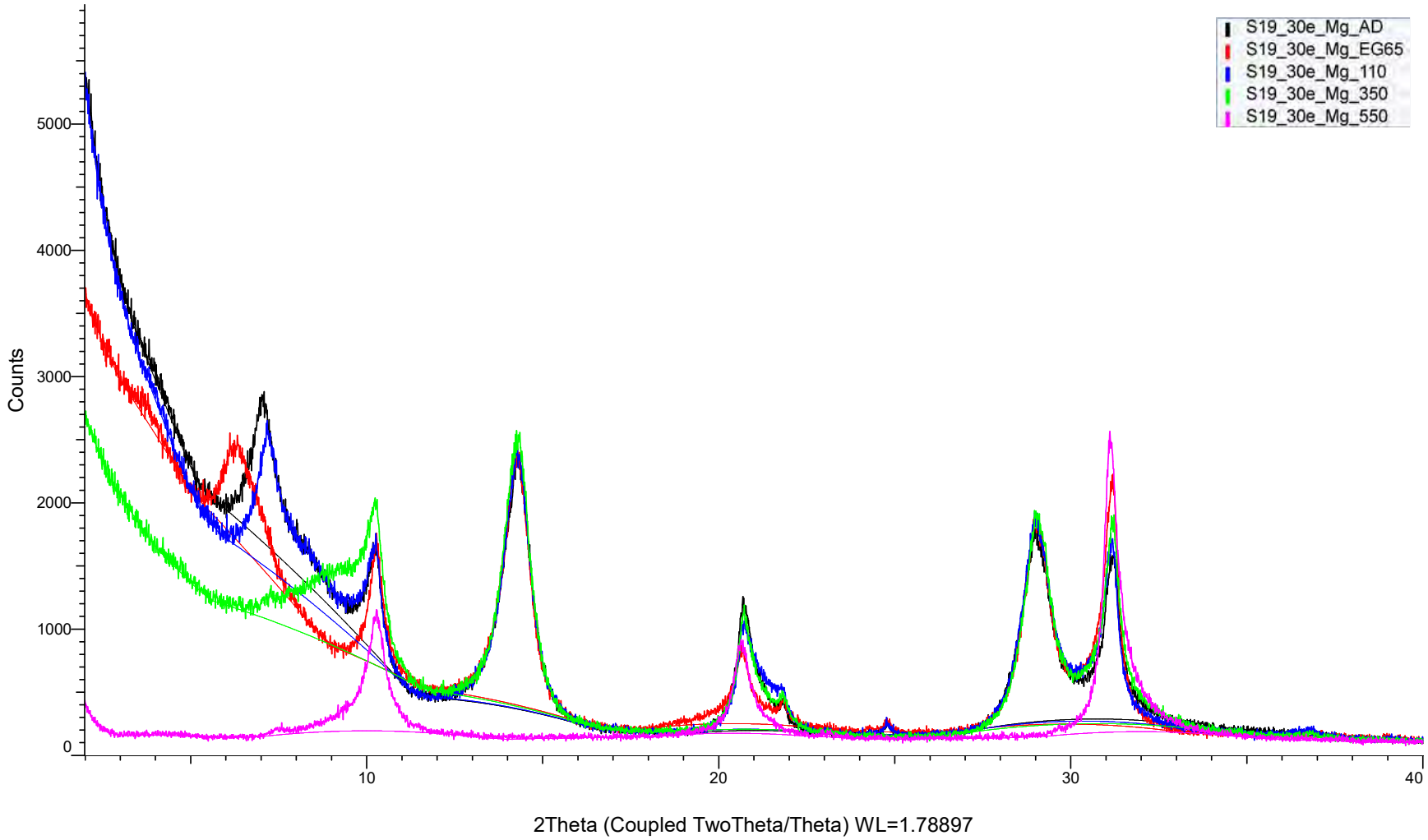

(Coupled TwoTheta/Theta)

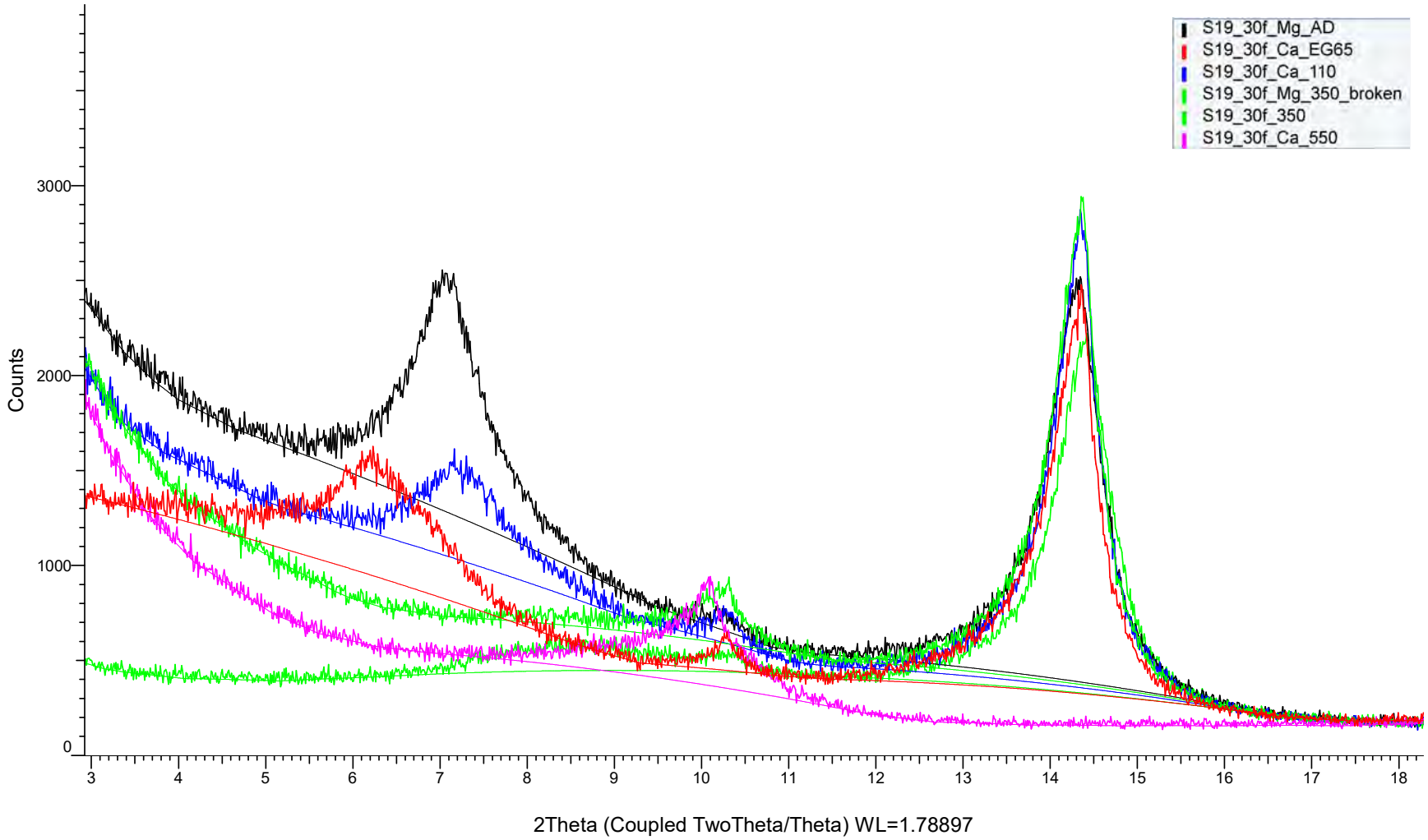

(Coupled TwoTheta/Theta)

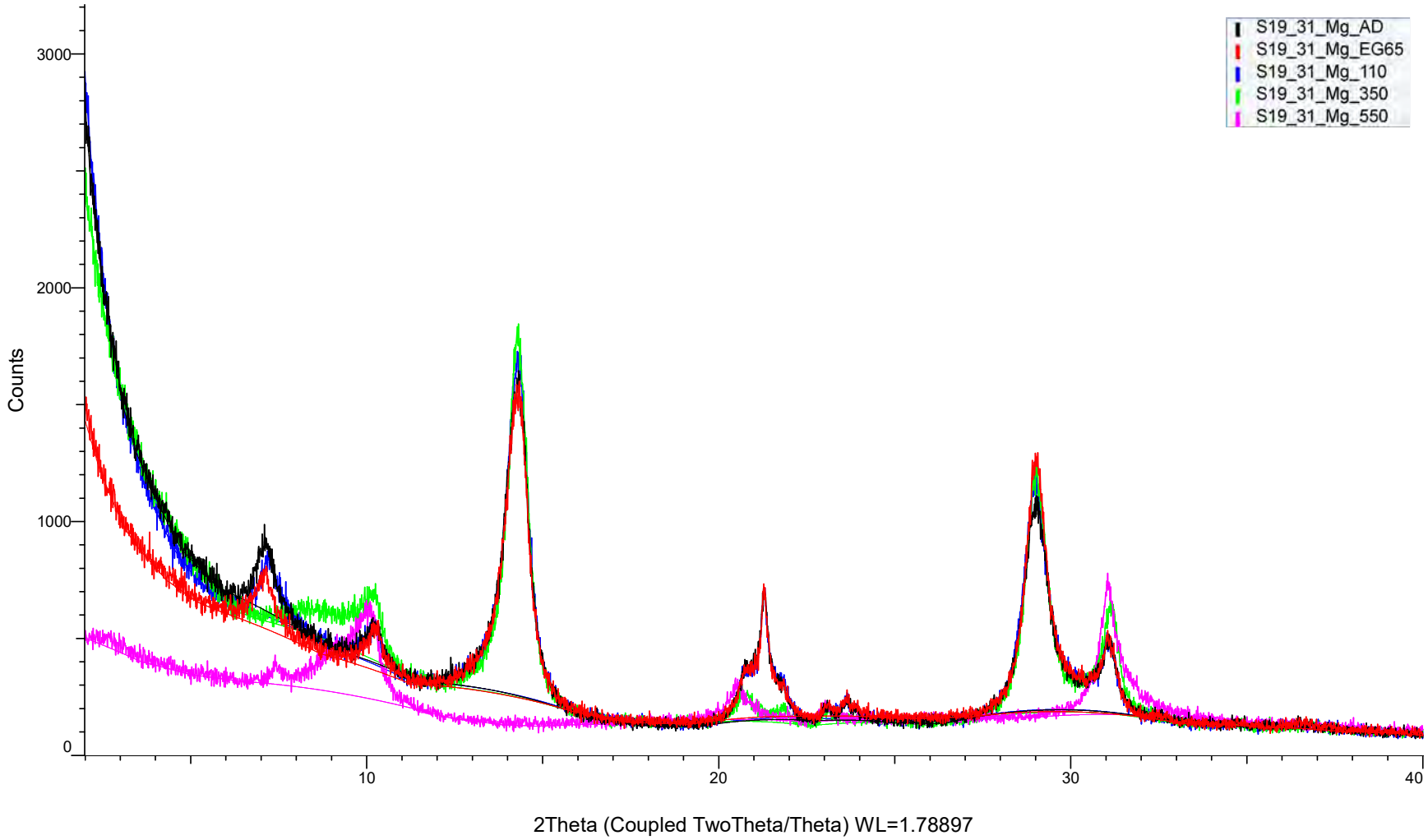

(Coupled TwoTheta/Theta)

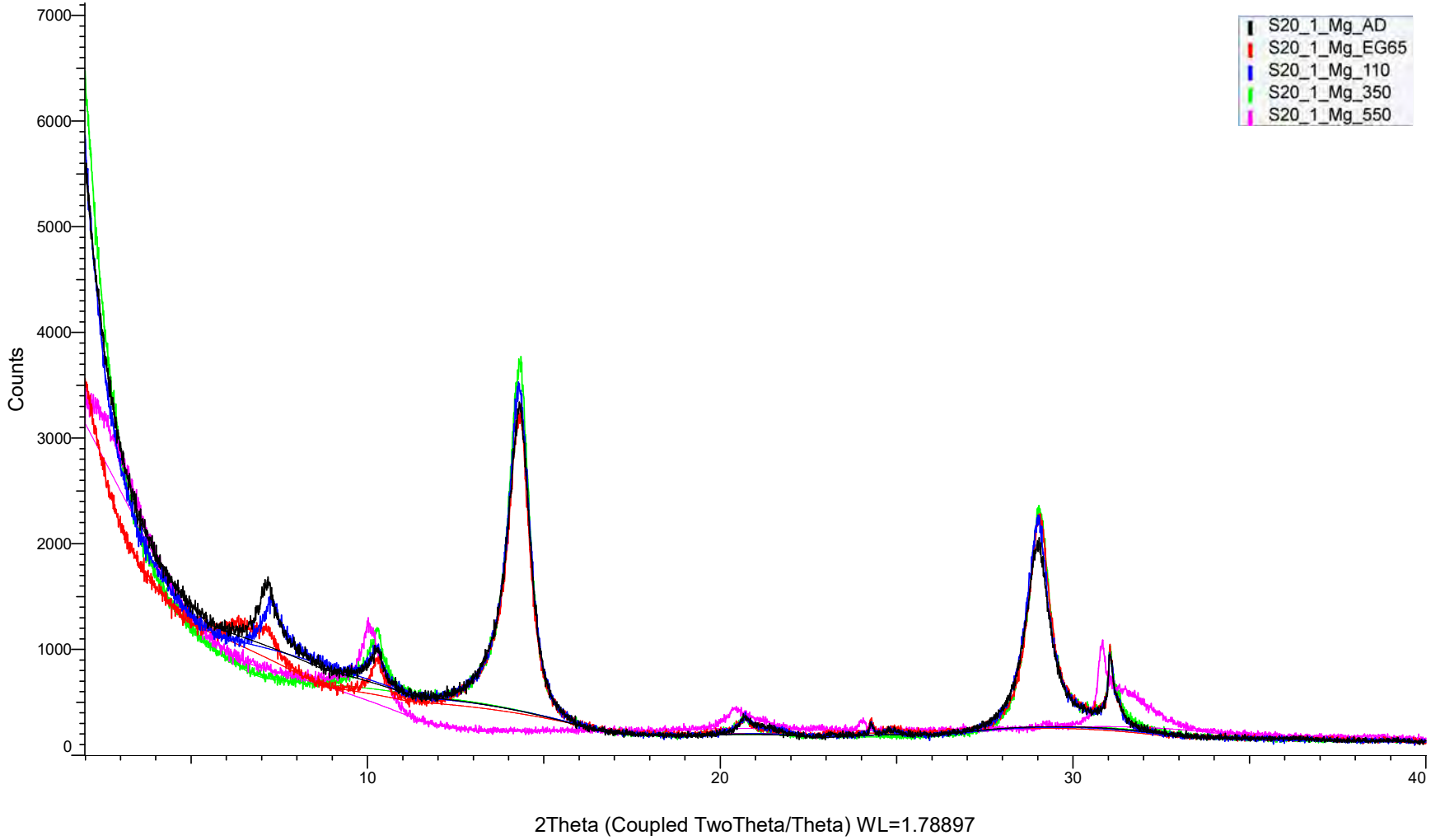

(Coupled TwoTheta/Theta)

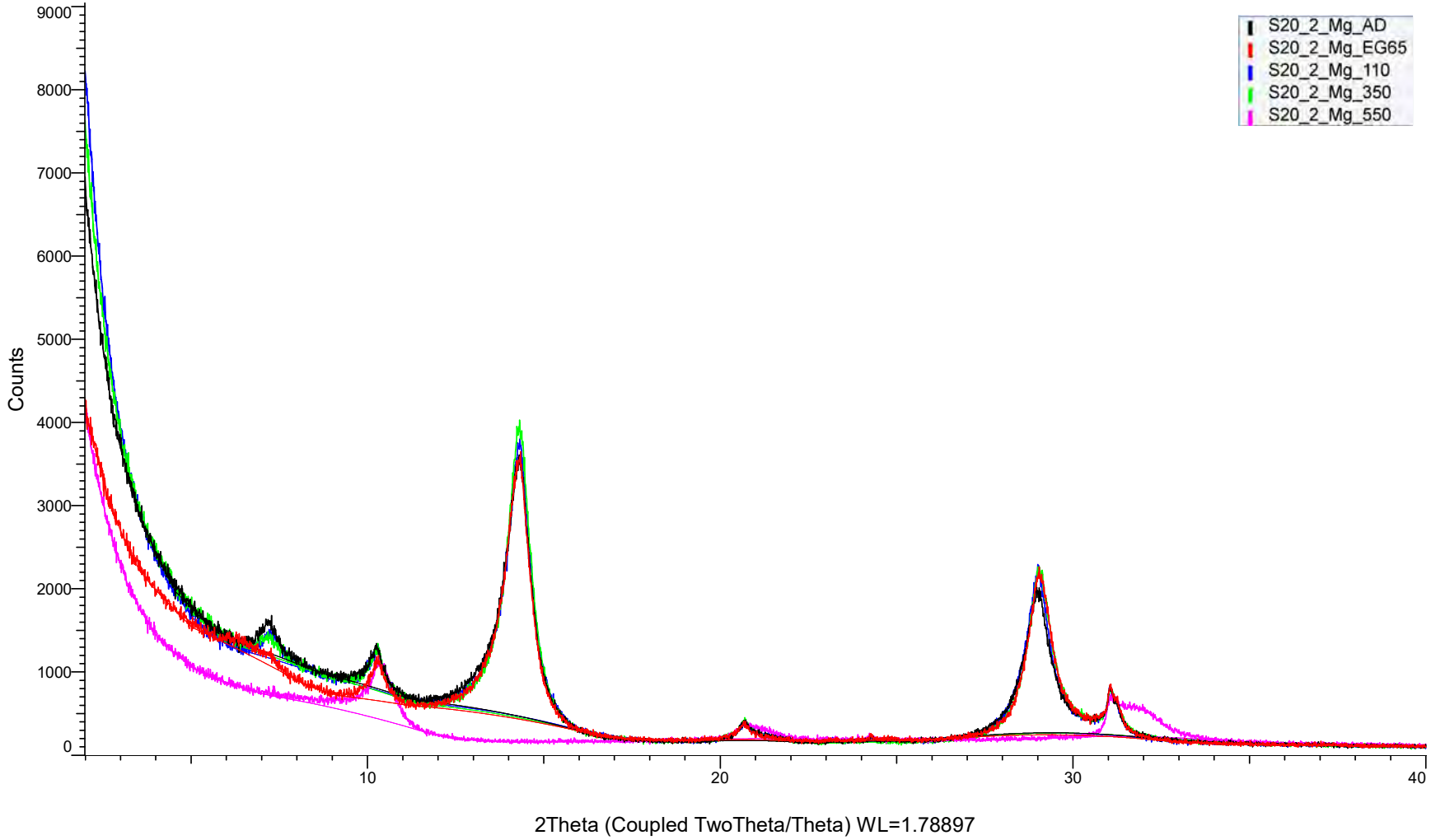

(Coupled TwoTheta/Theta)

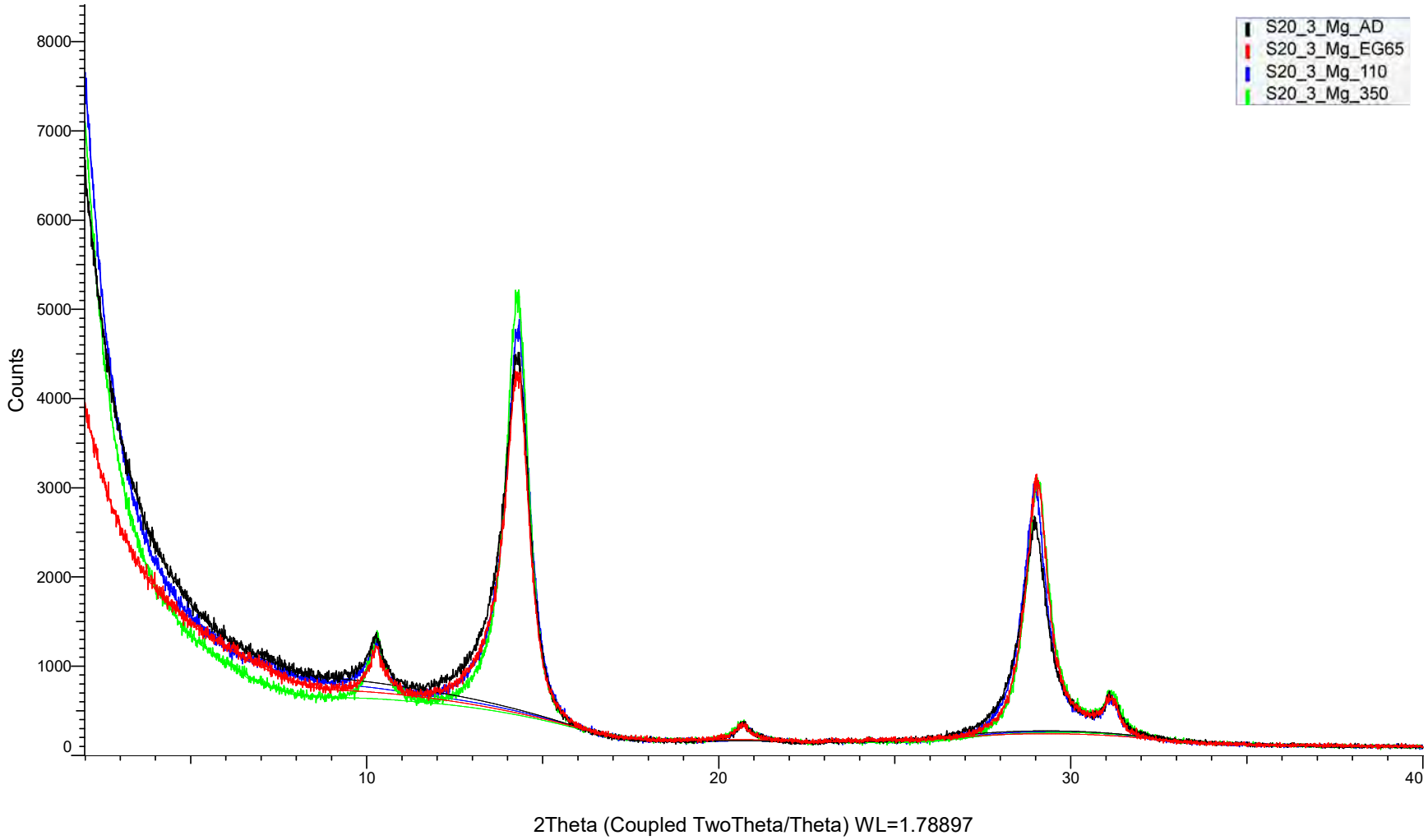

(Coupled TwoTheta/Theta)

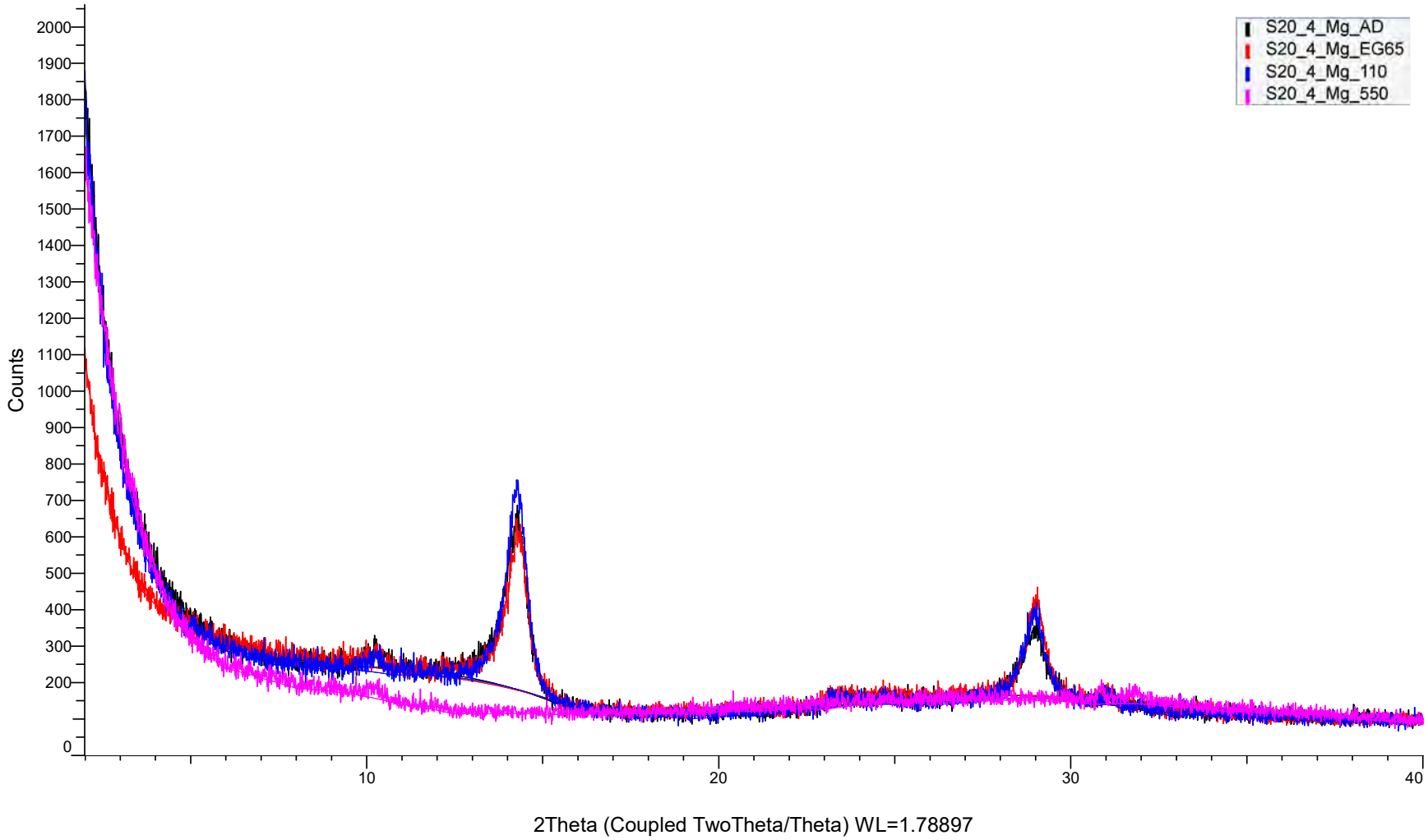

(Coupled TwoTheta/Theta)

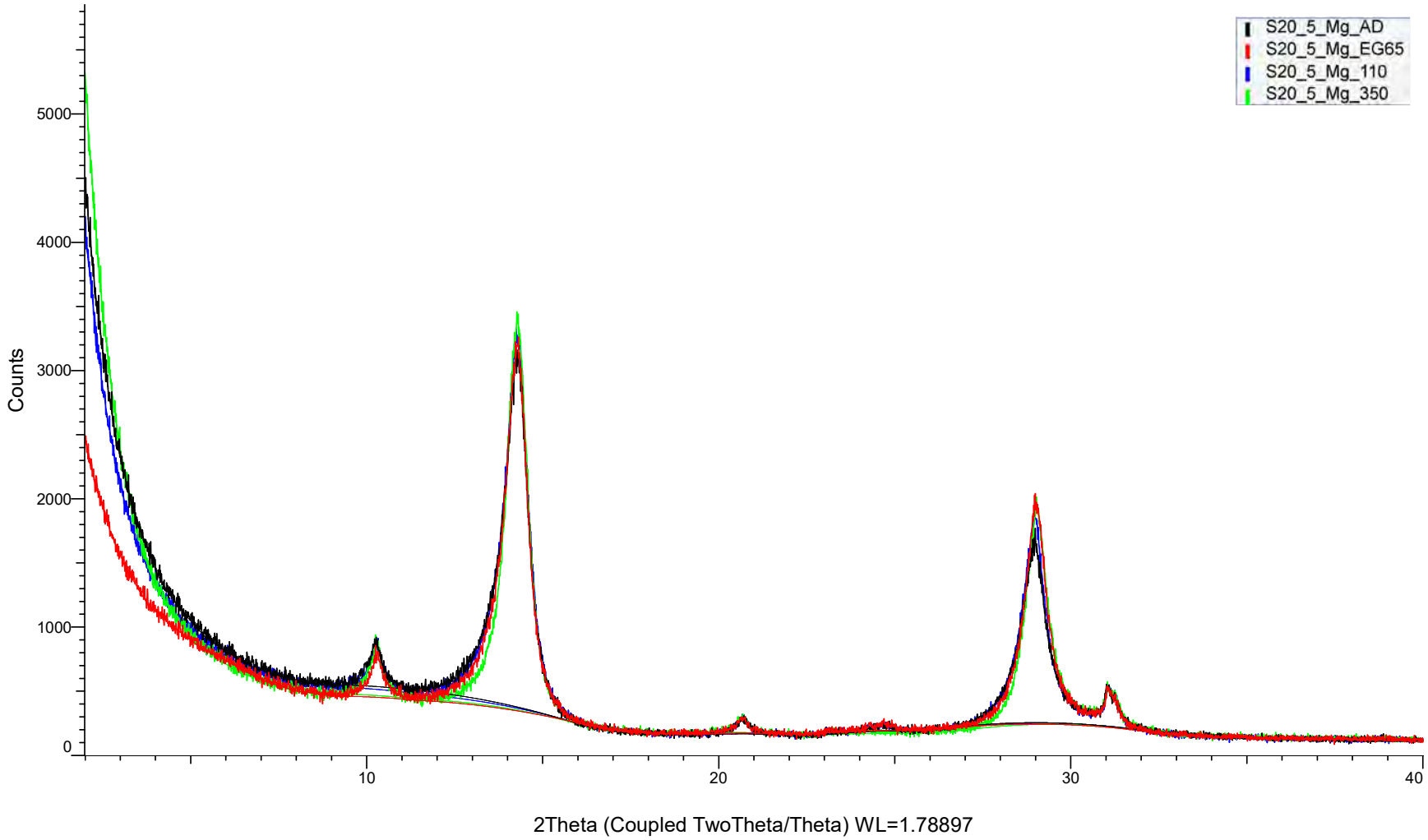

(Coupled TwoTheta/Theta)

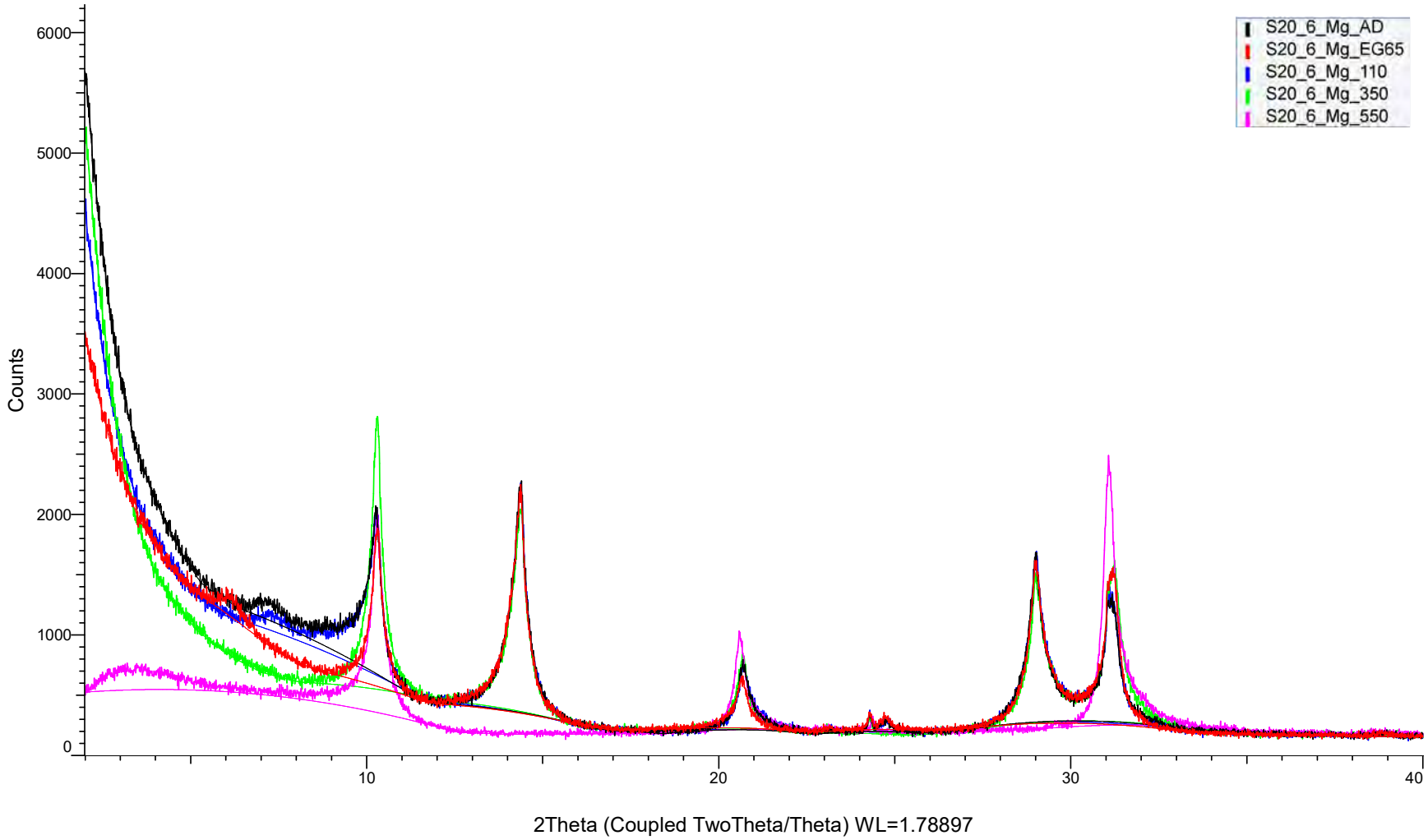

(Coupled TwoTheta/Theta)

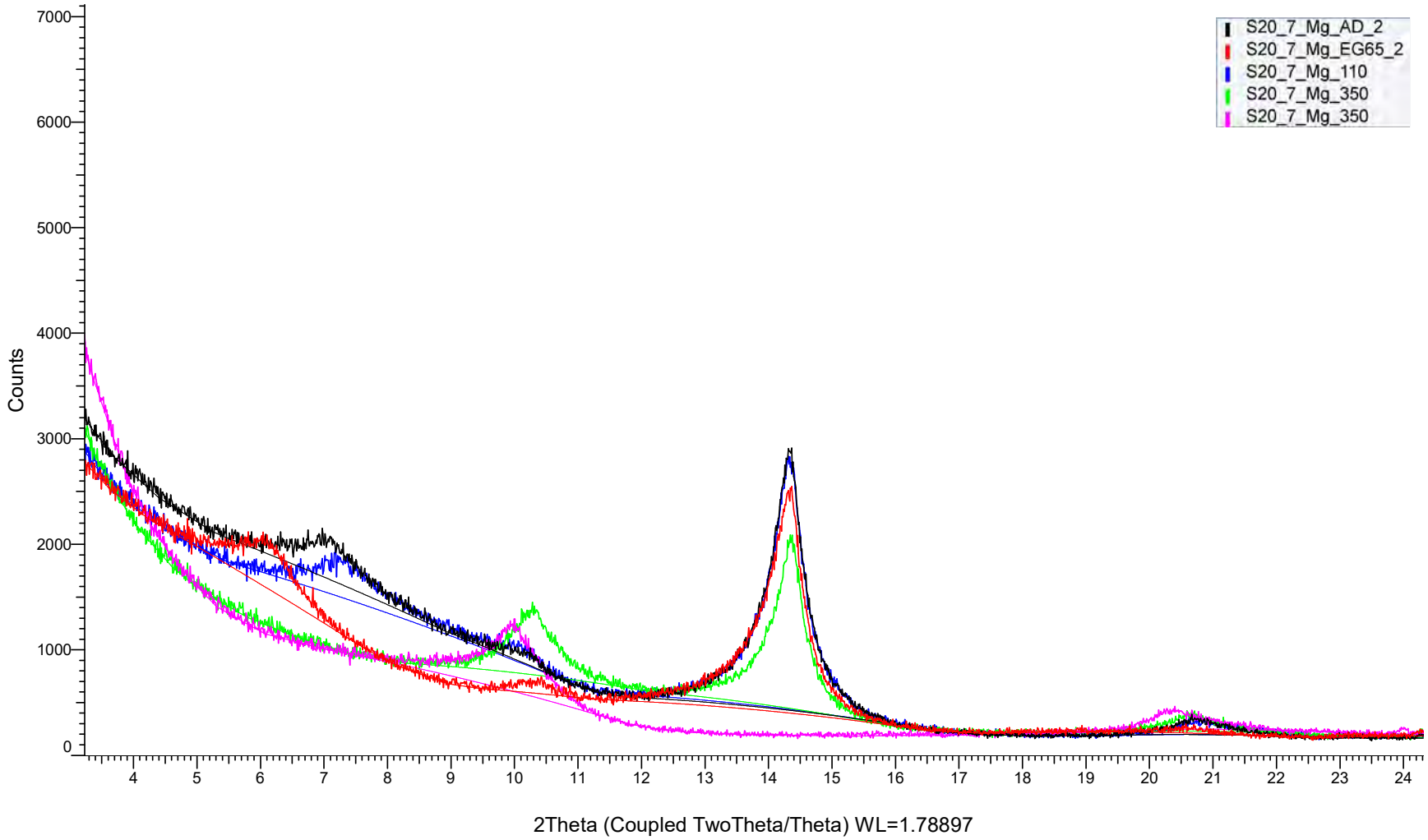

(Coupled TwoTheta/Theta)

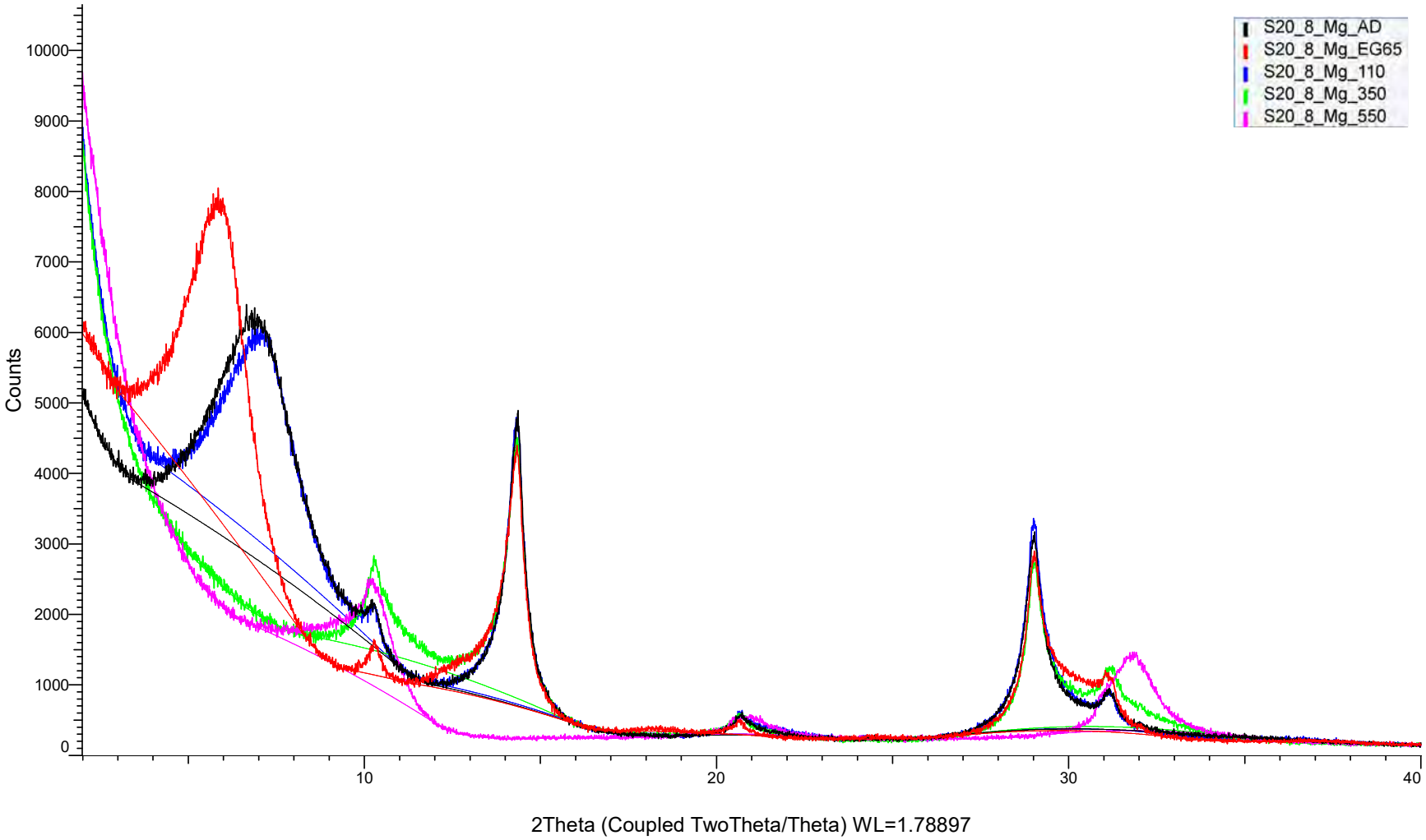

(Coupled TwoTheta/Theta)

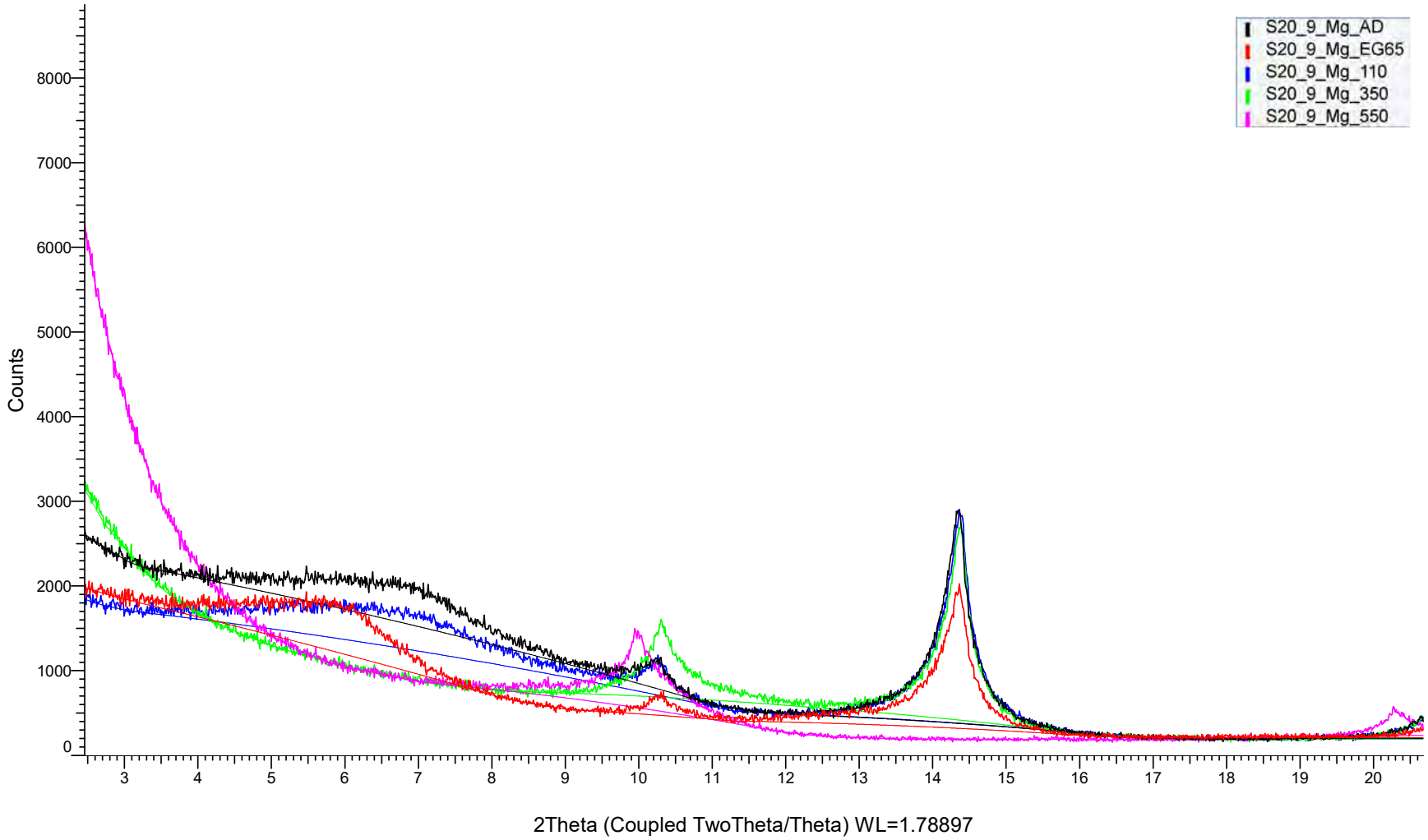

(Coupled TwoTheta/Theta)

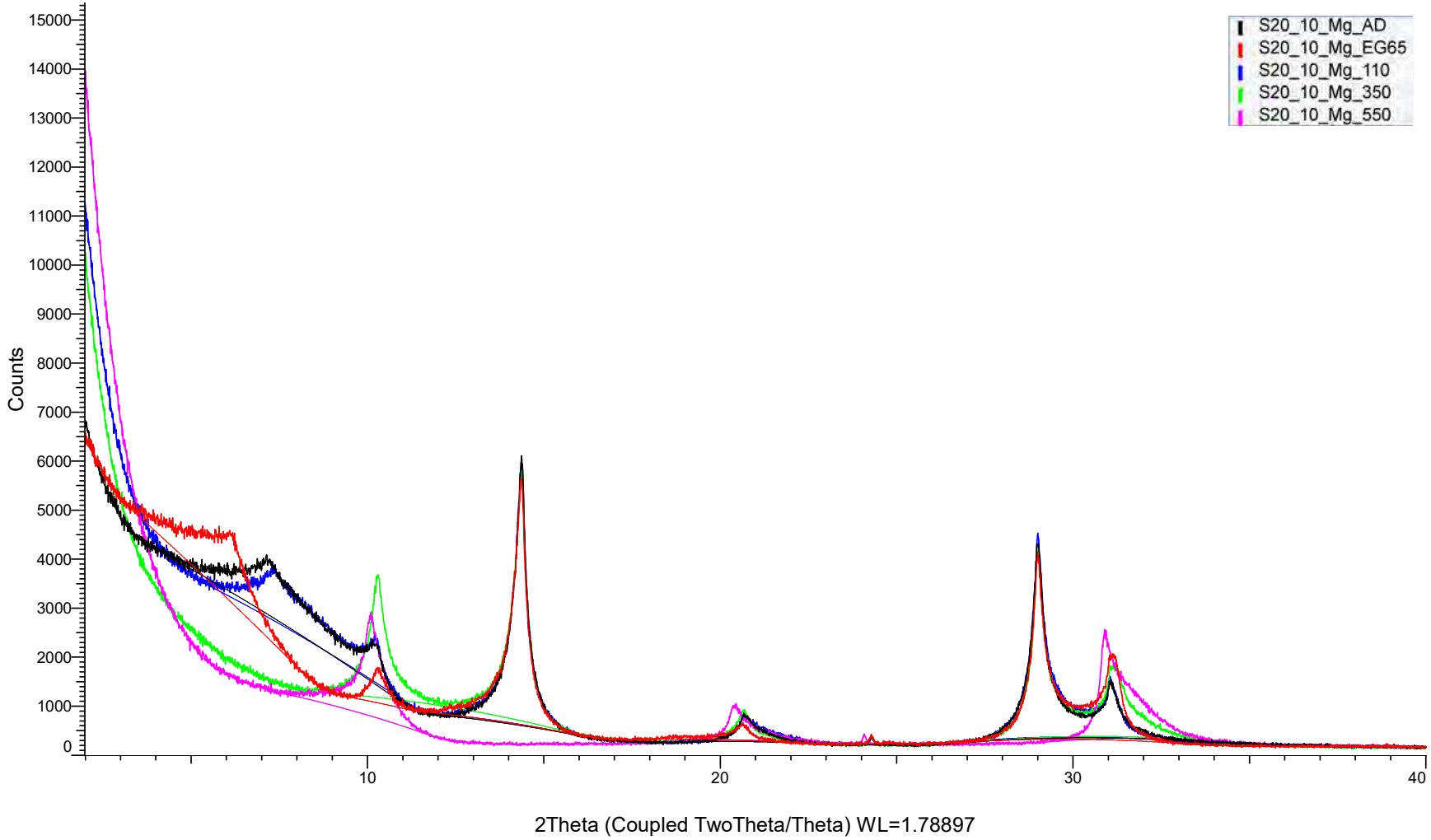

(Coupled TwoTheta/Theta)

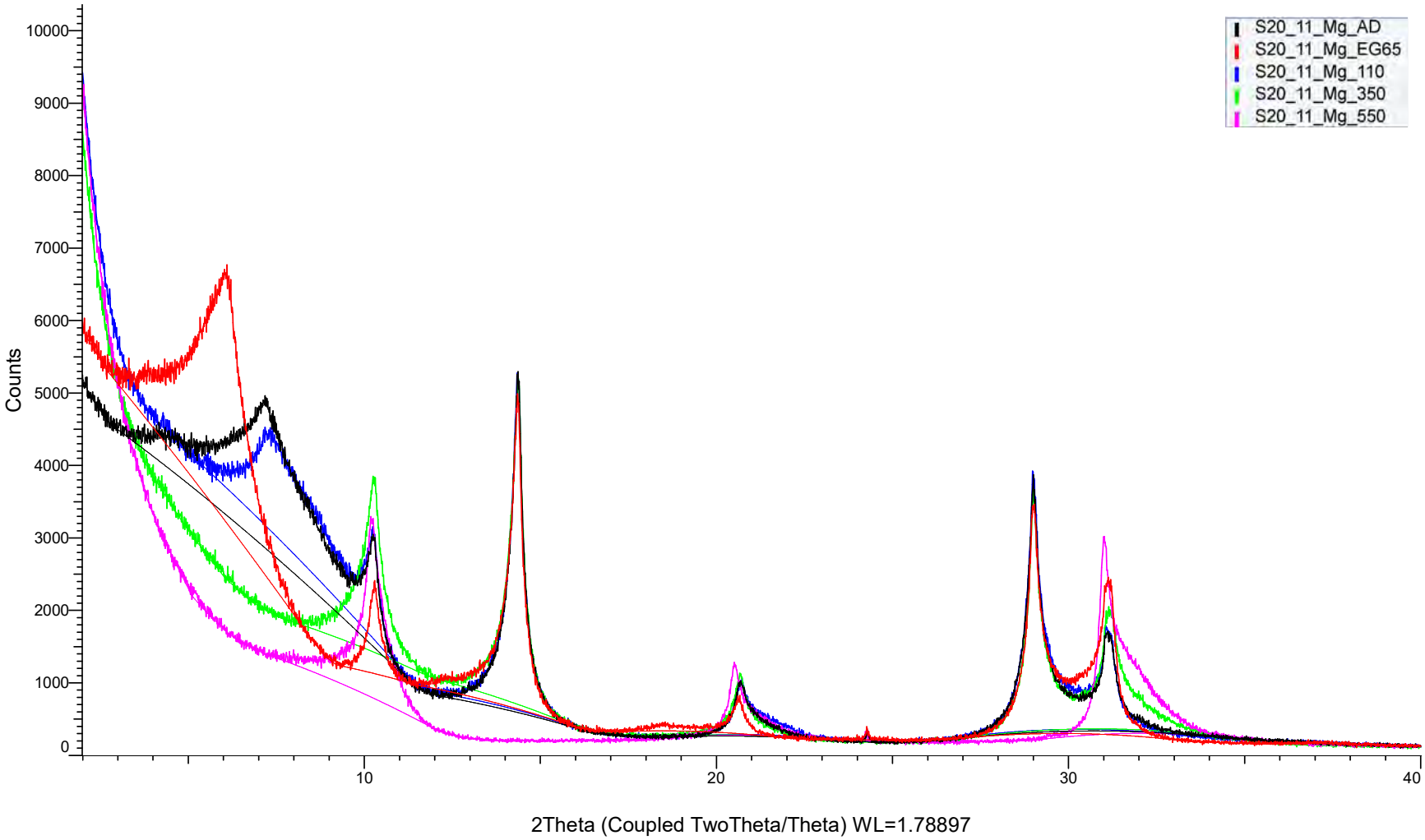

(Coupled TwoTheta/Theta)

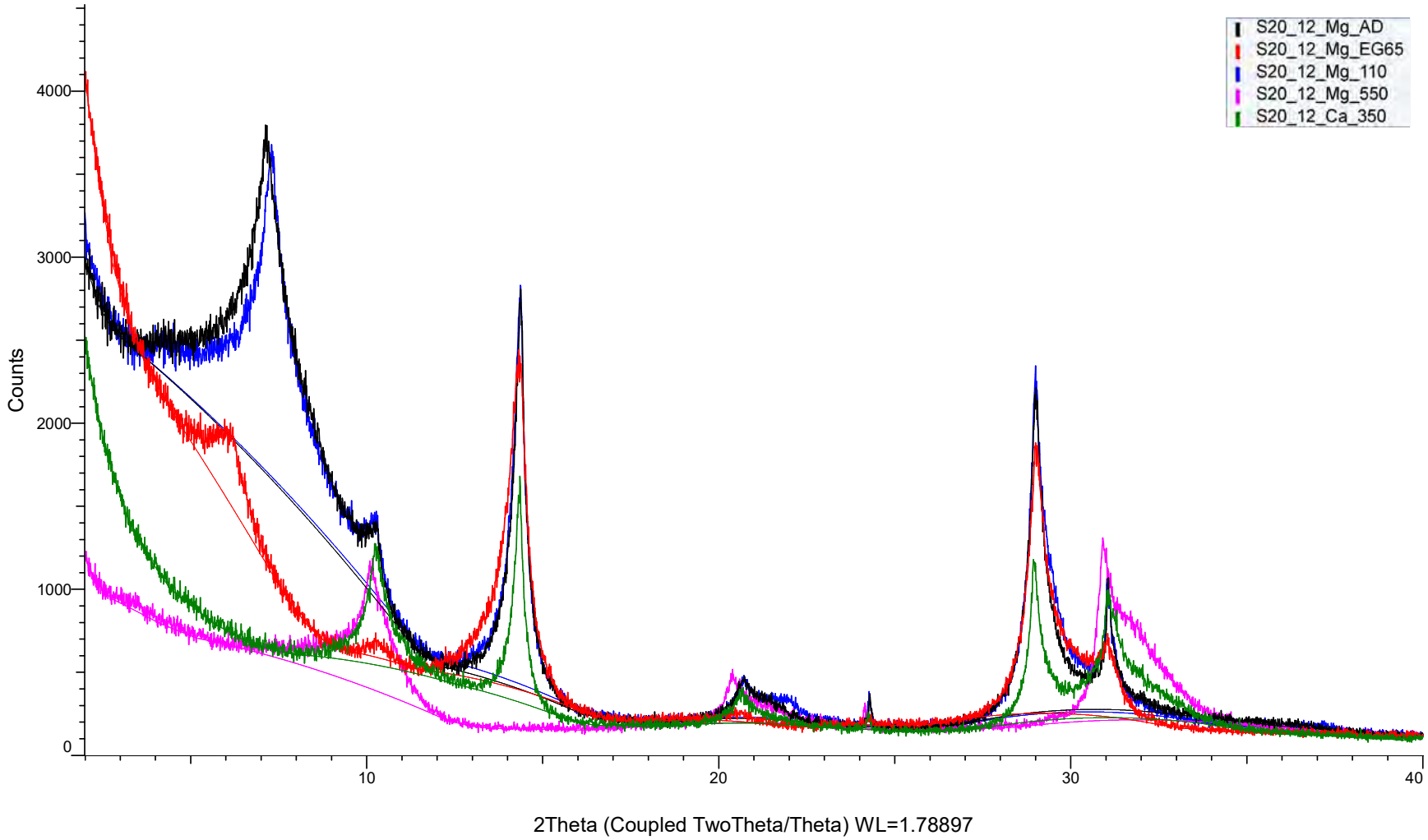

(Coupled TwoTheta/Theta)

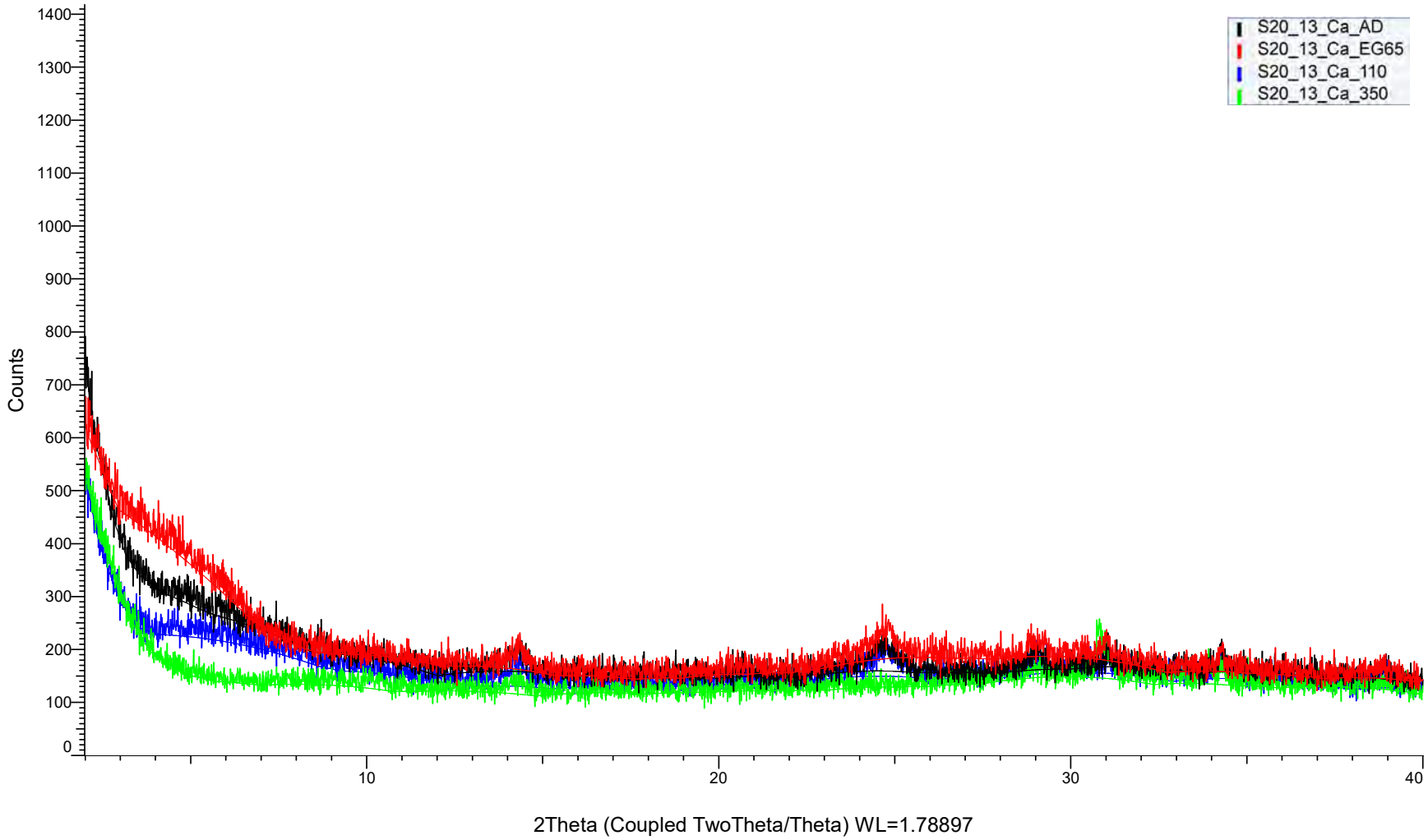

(Coupled TwoTheta/Theta)

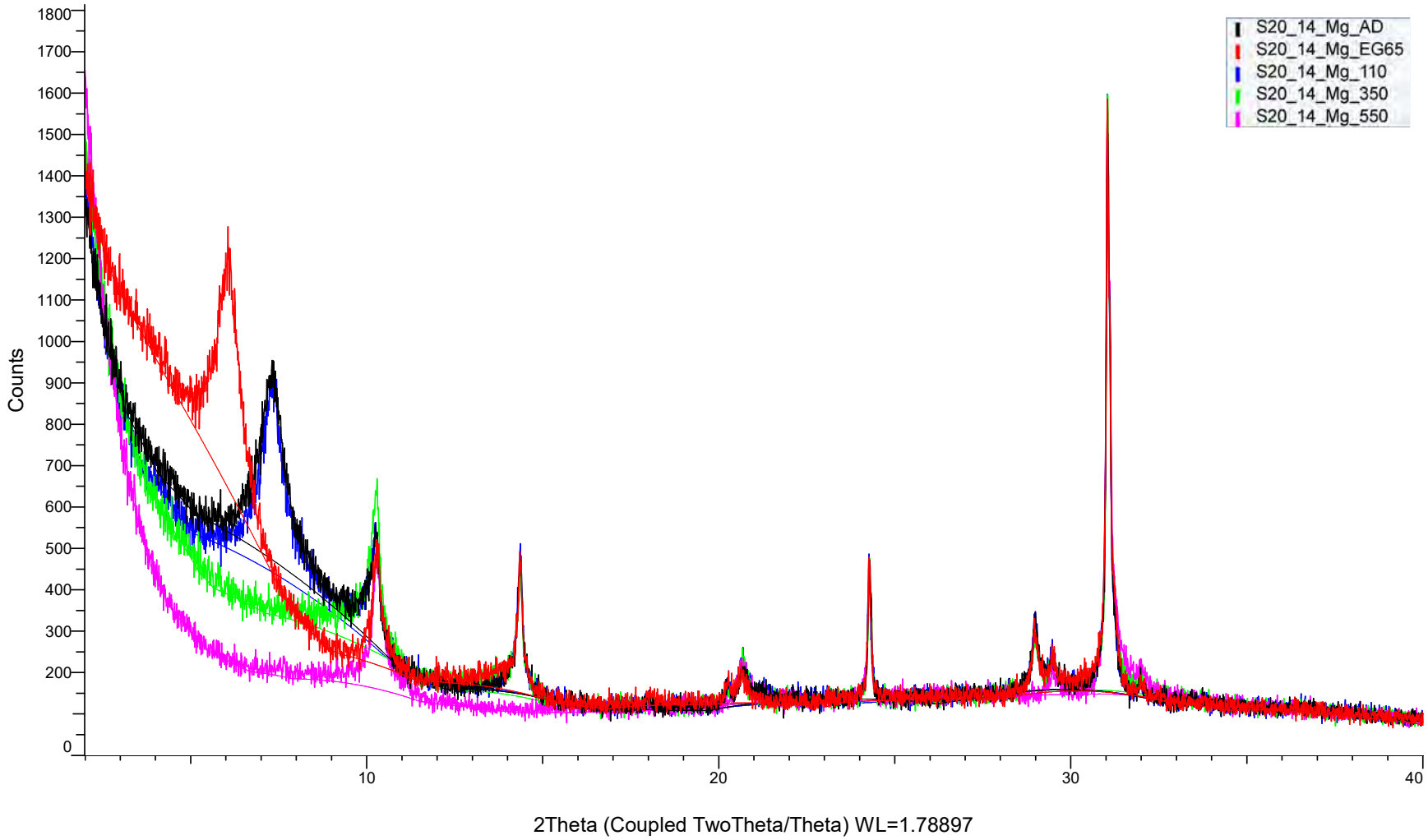

(Coupled TwoTheta/Theta)

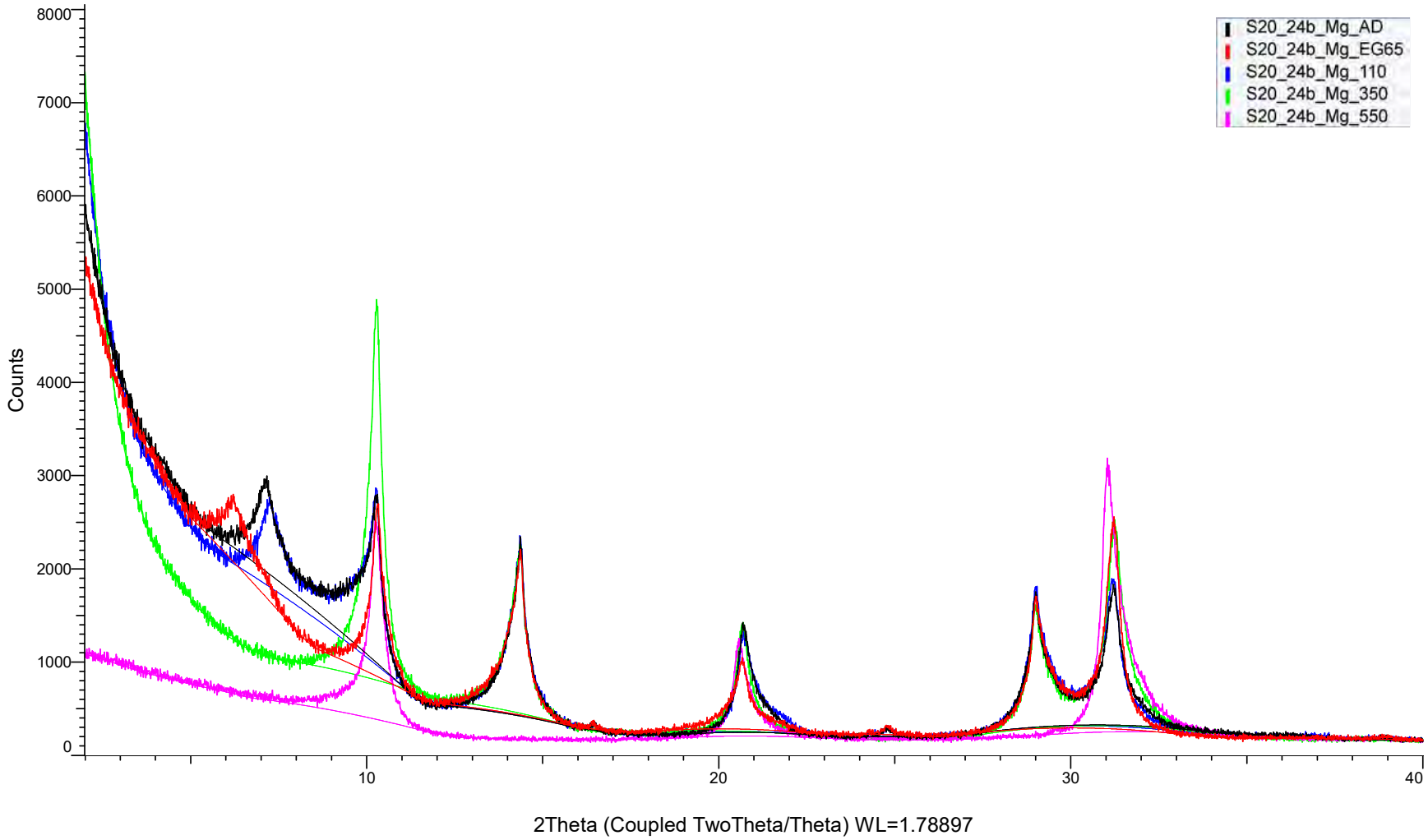

(Coupled TwoTheta/Theta)

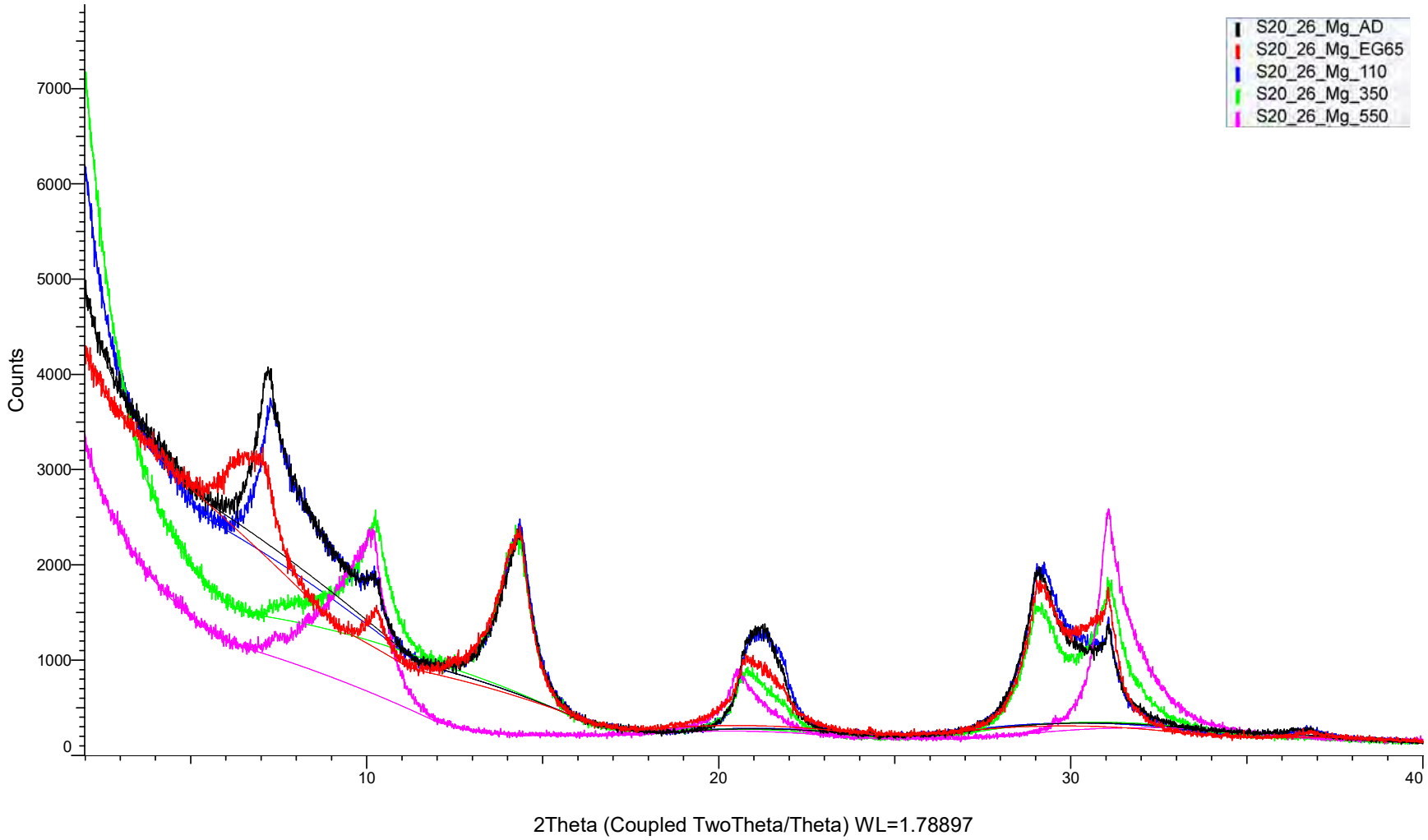

(Coupled TwoTheta/Theta)

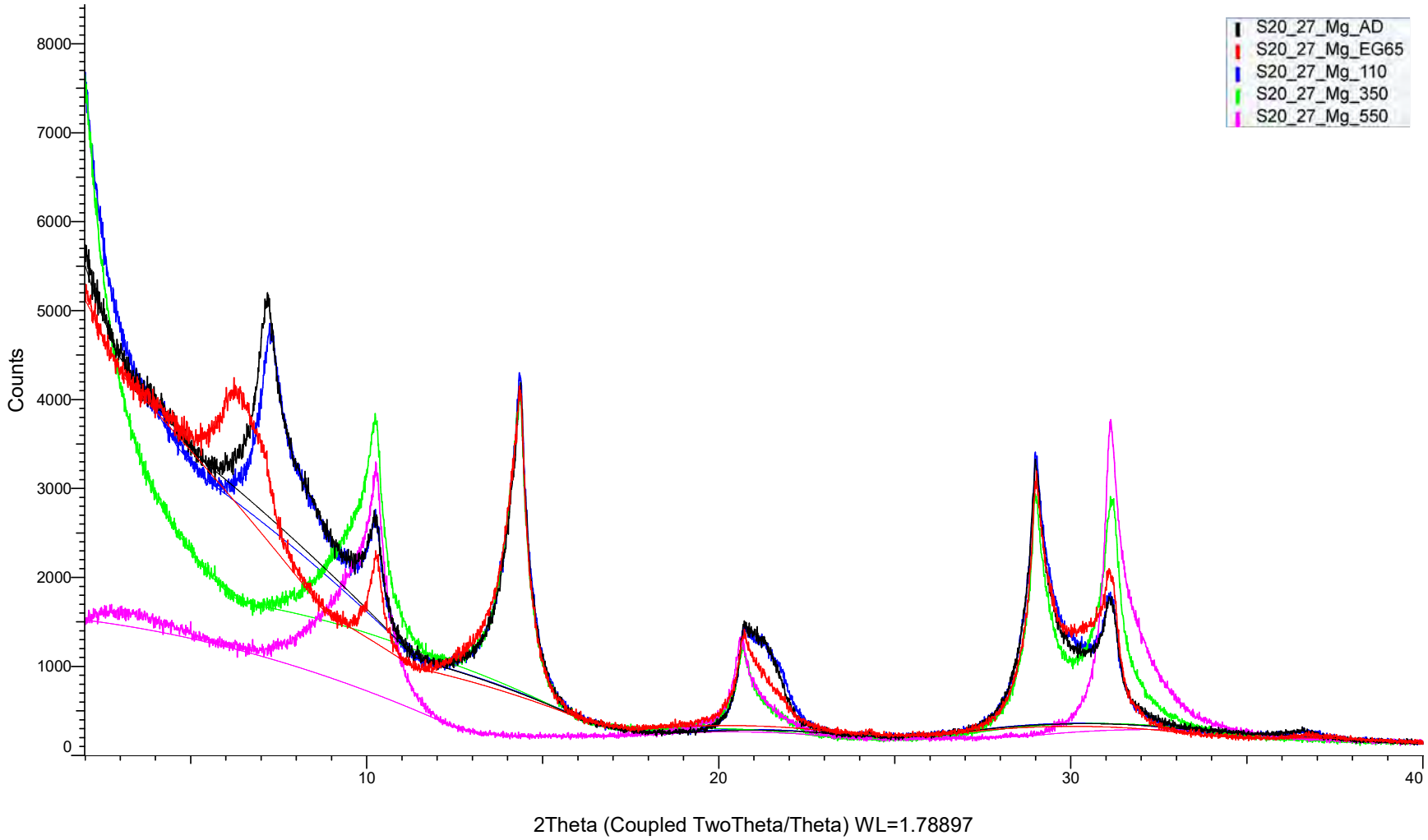

(Coupled TwoTheta/Theta)

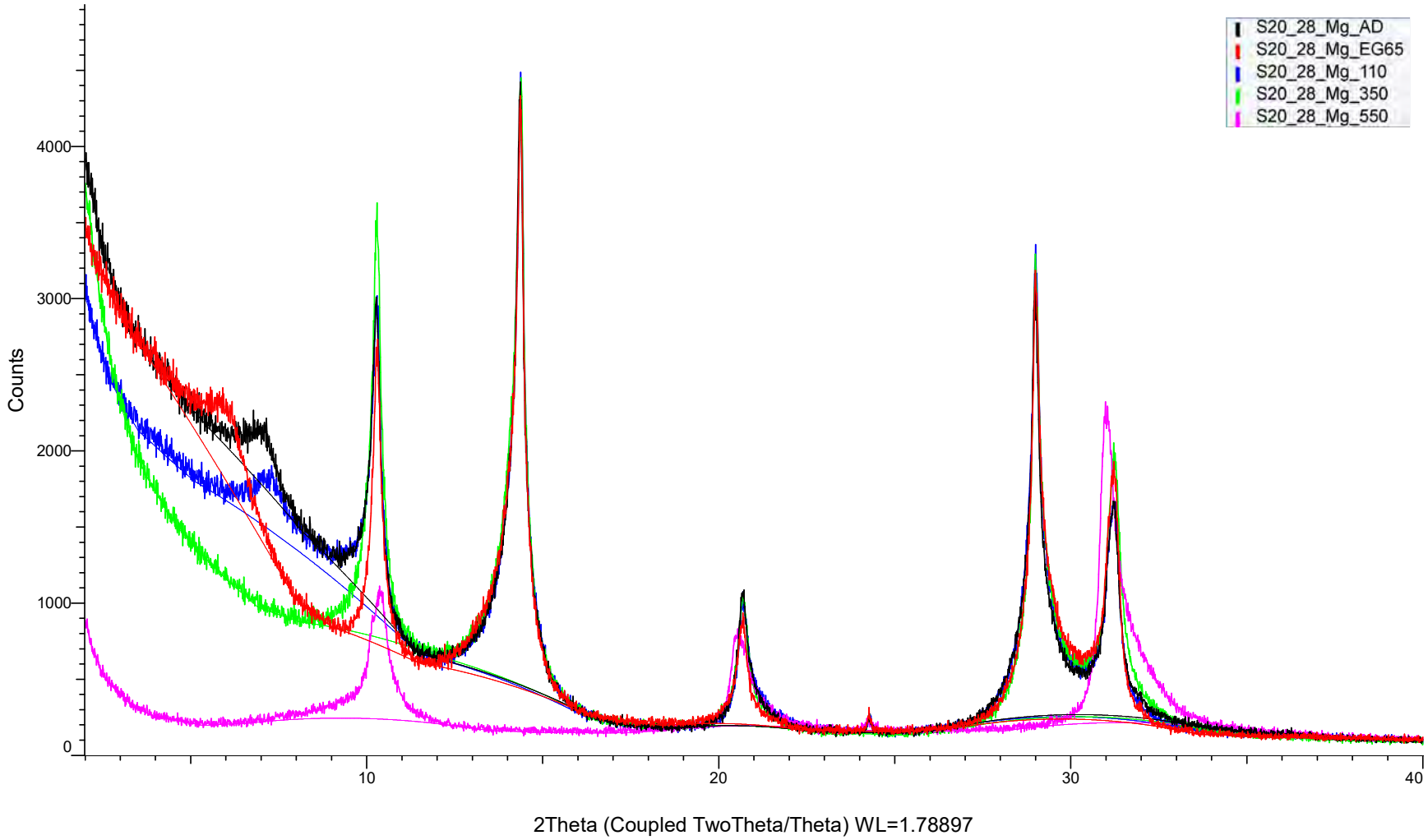

(Coupled TwoTheta/Theta)

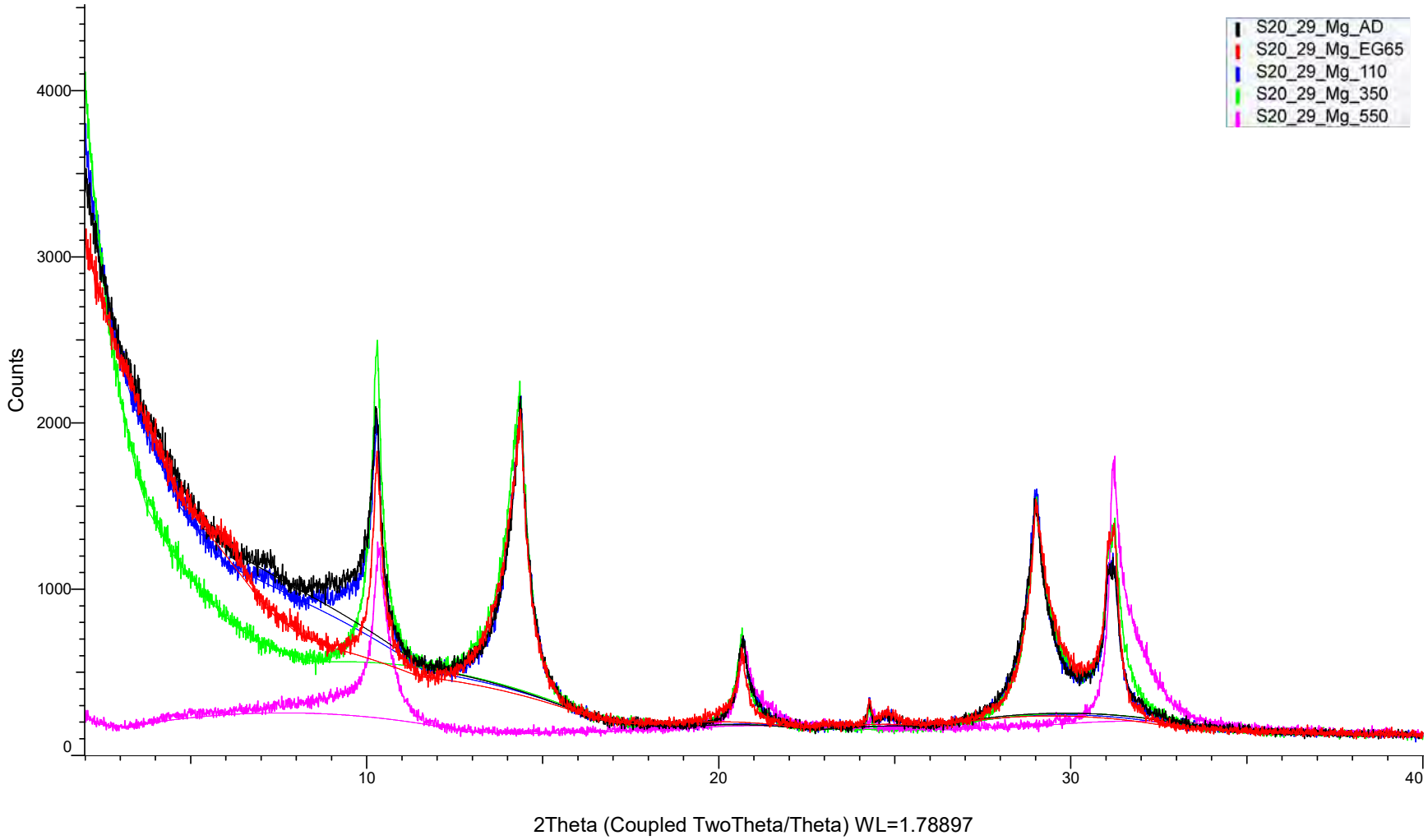

(Coupled TwoTheta/Theta)

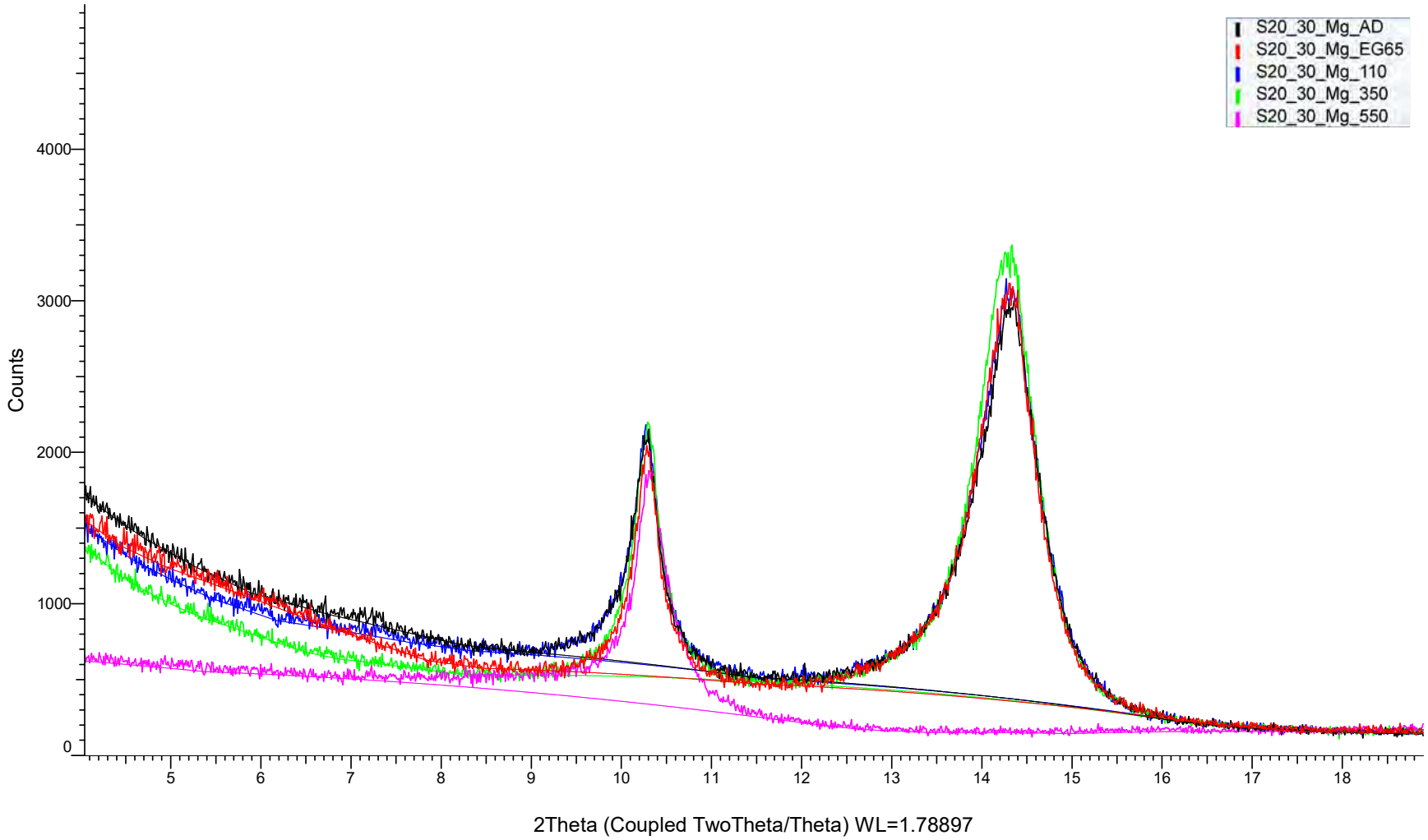

(Coupled TwoTheta/Theta)

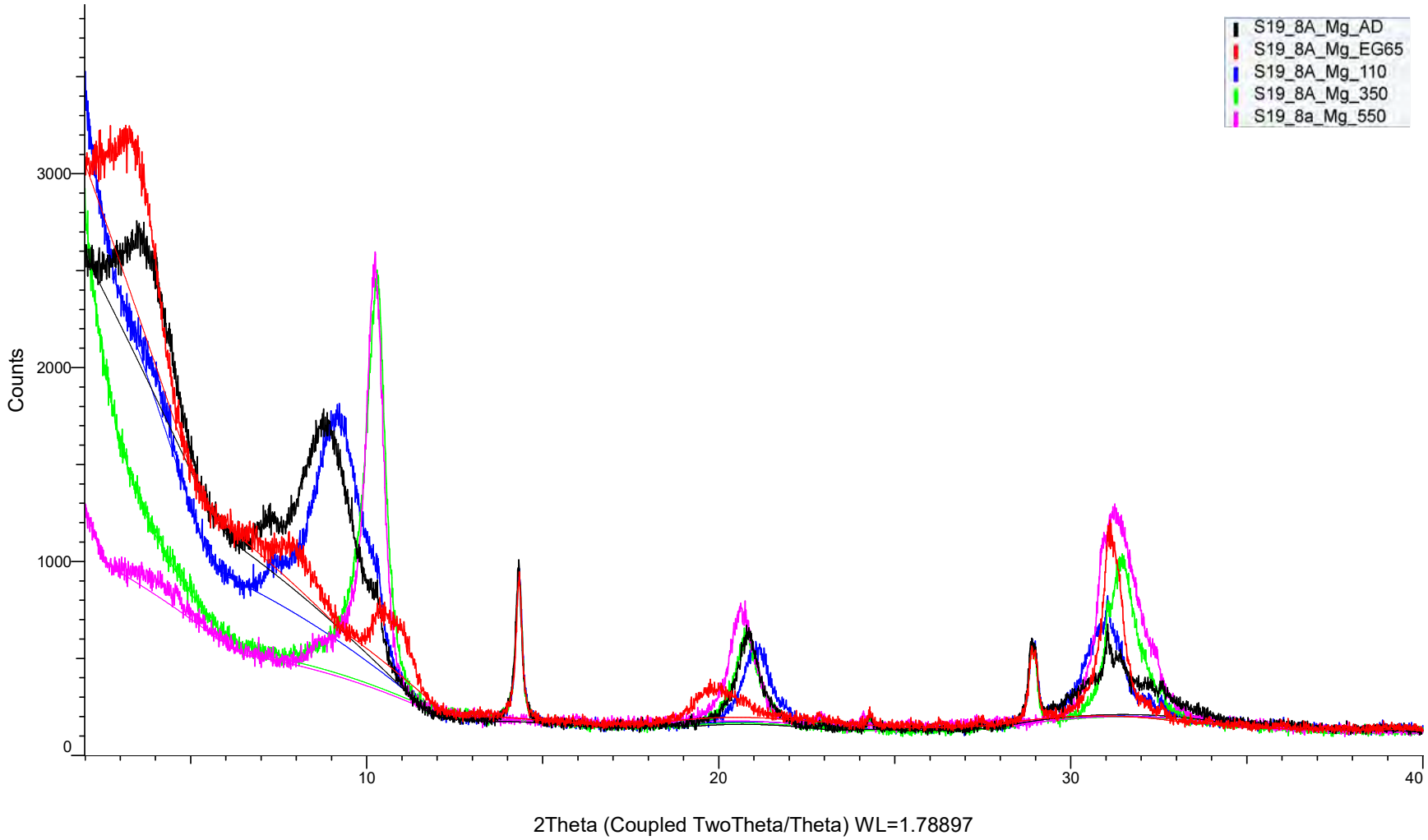

(Coupled TwoTheta/Theta)

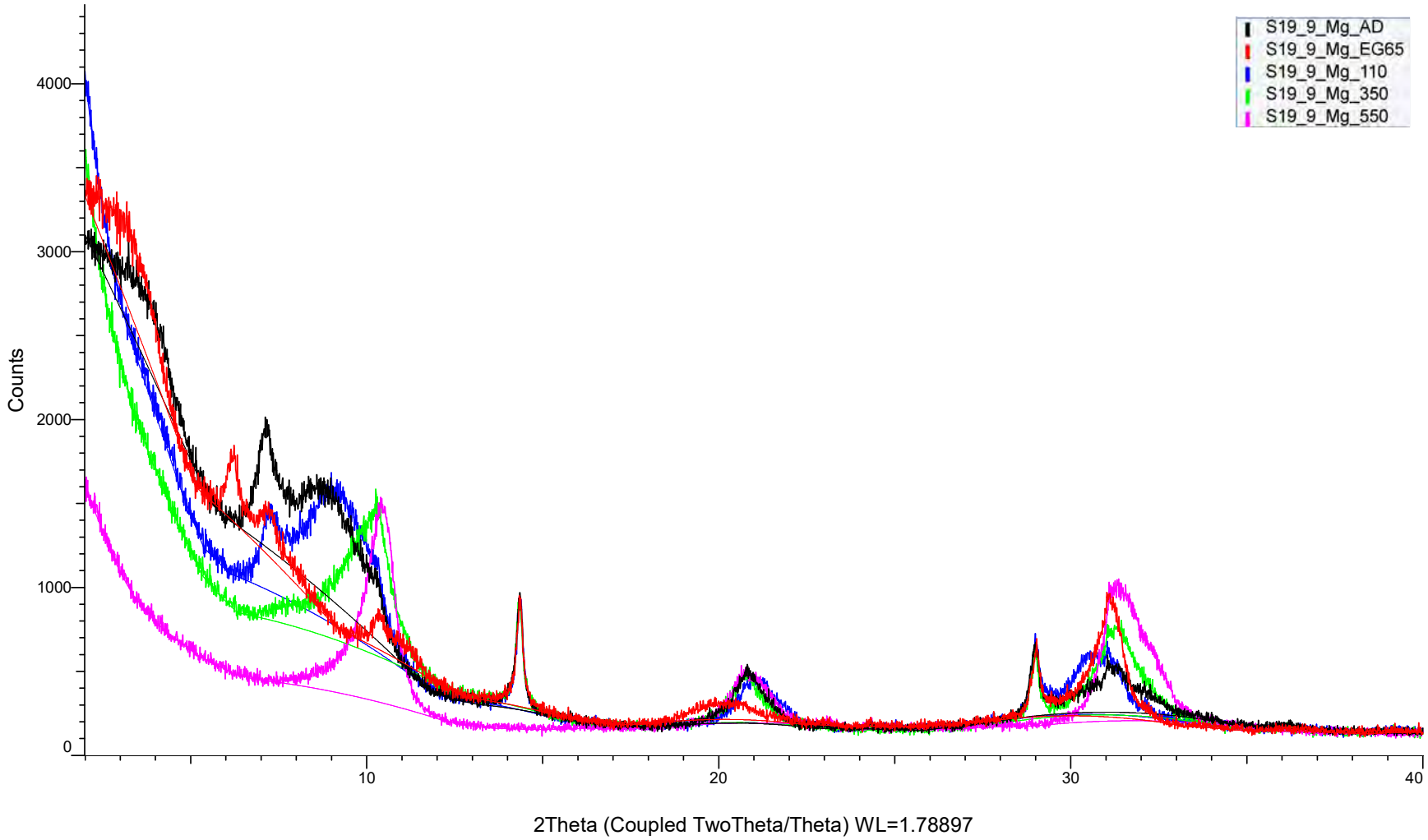

(Coupled TwoTheta/Theta)

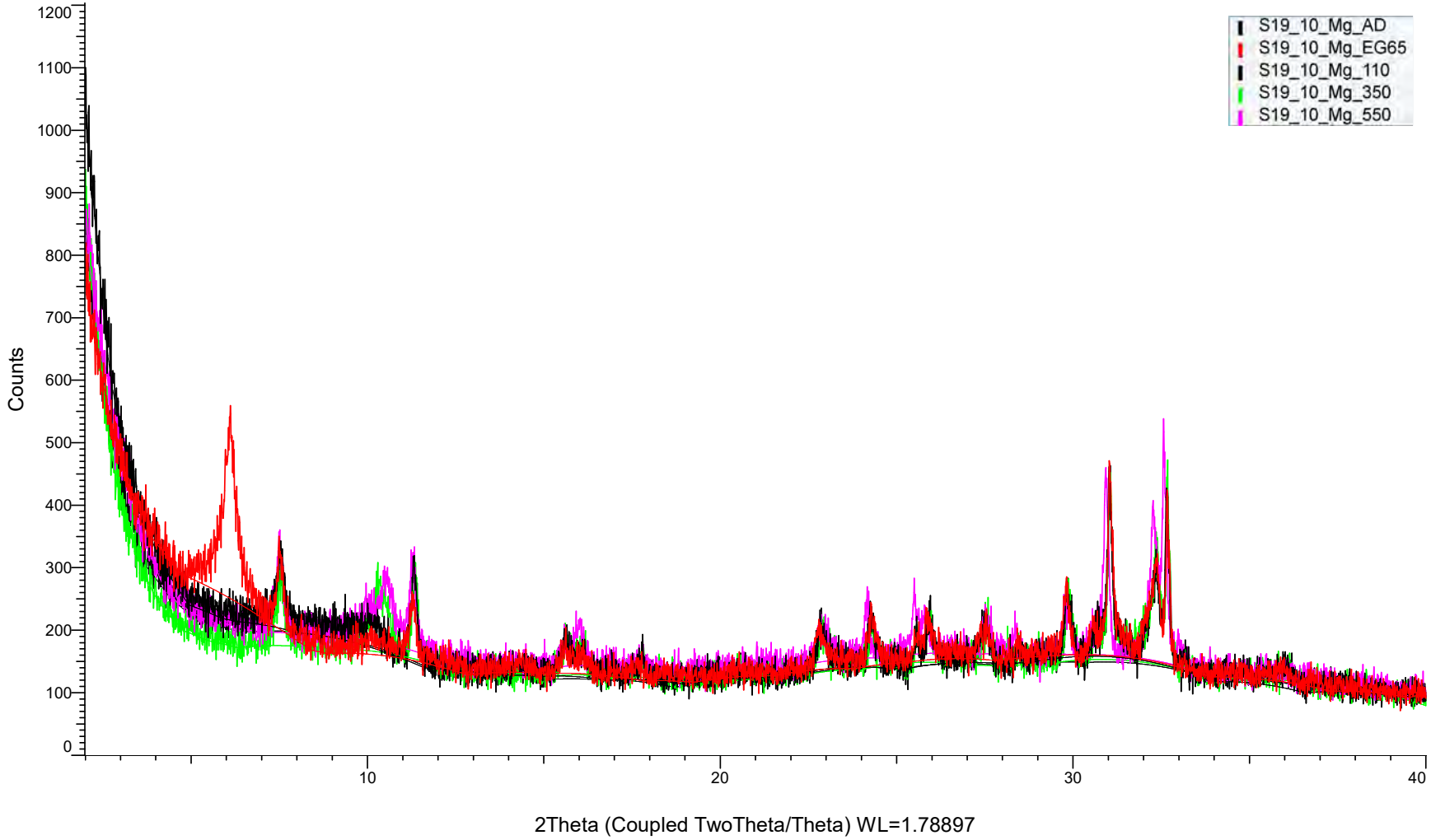

(Coupled TwoTheta/Theta)

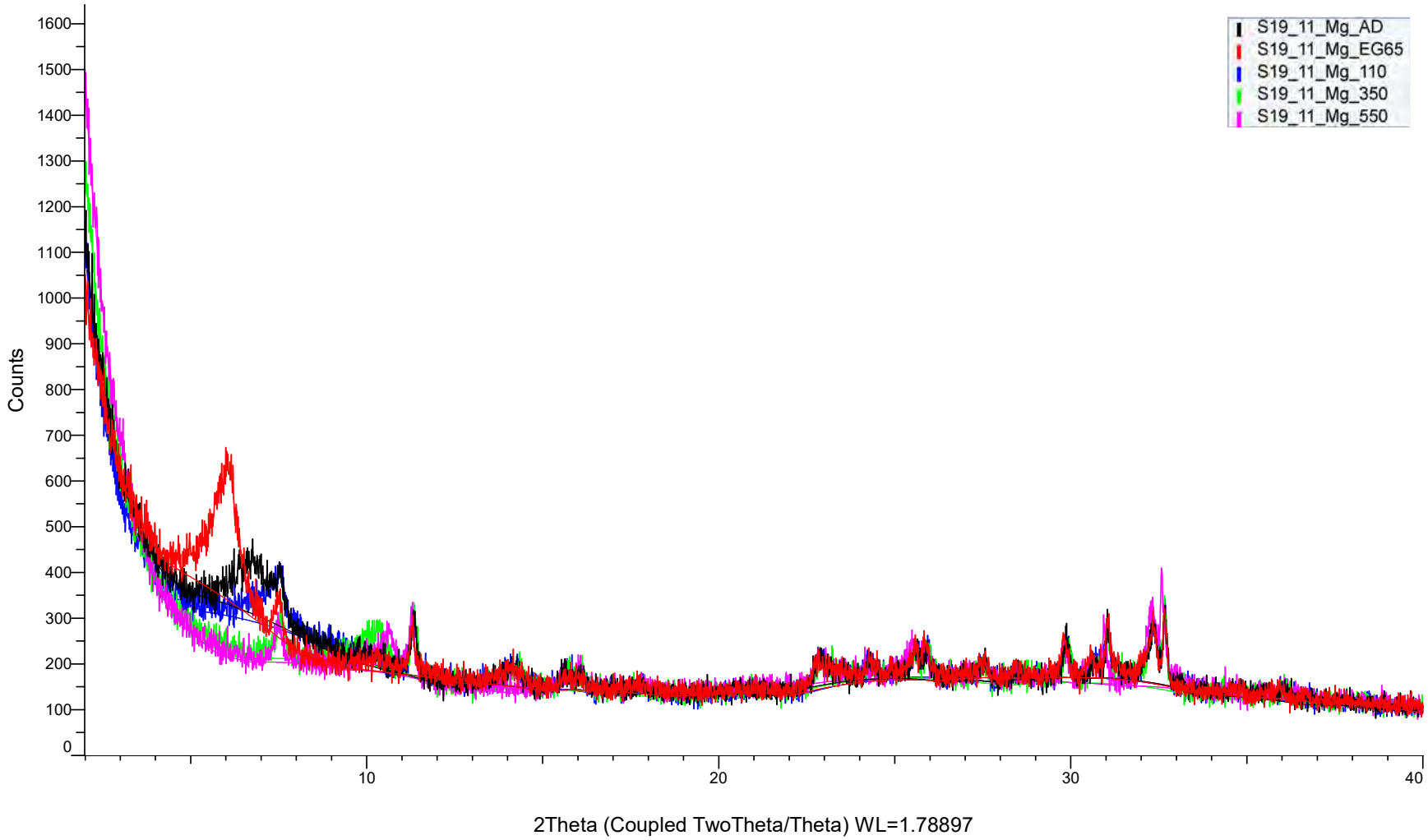

(Coupled TwoTheta/Theta)

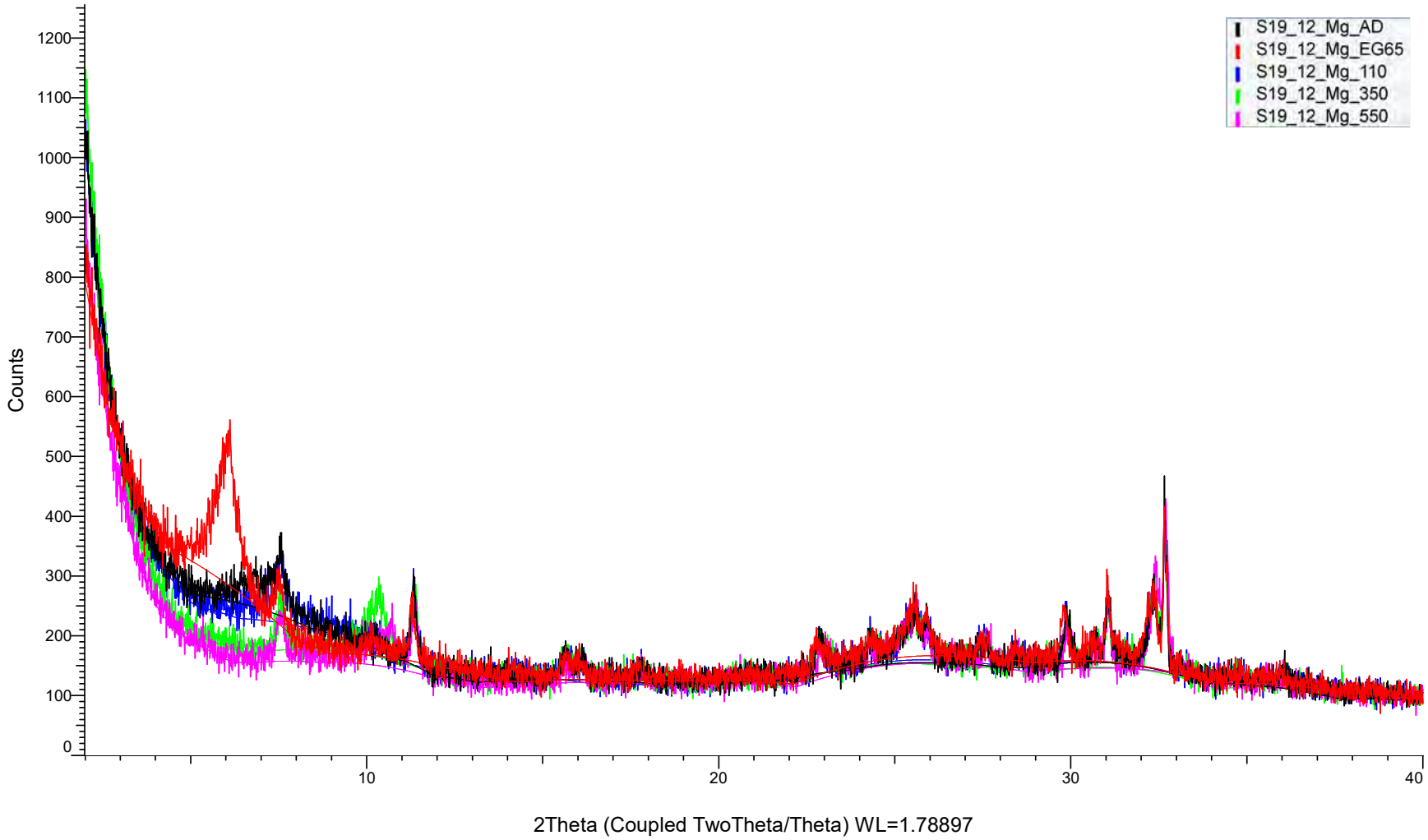

(Coupled TwoTheta/Theta)

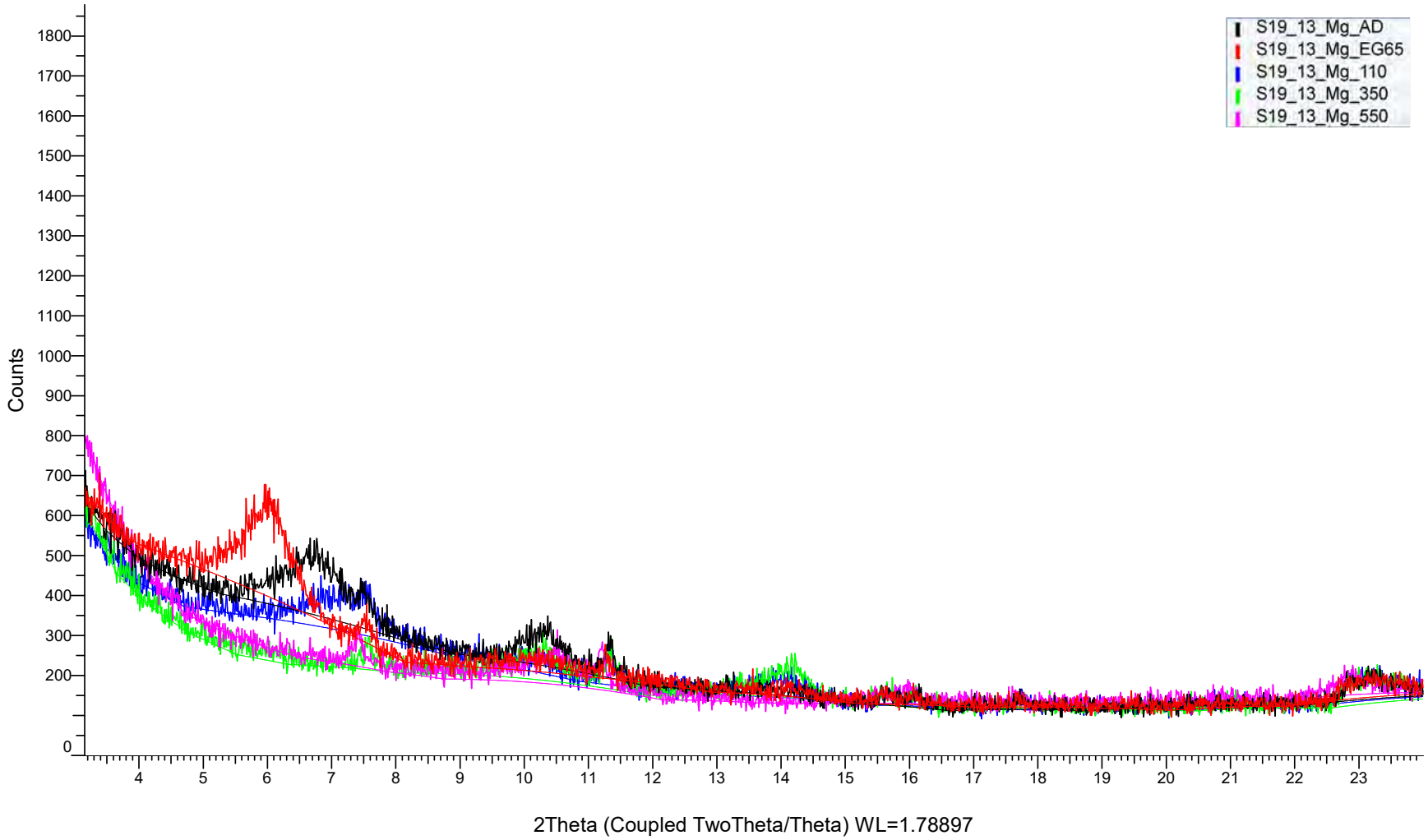

(Coupled TwoTheta/Theta)

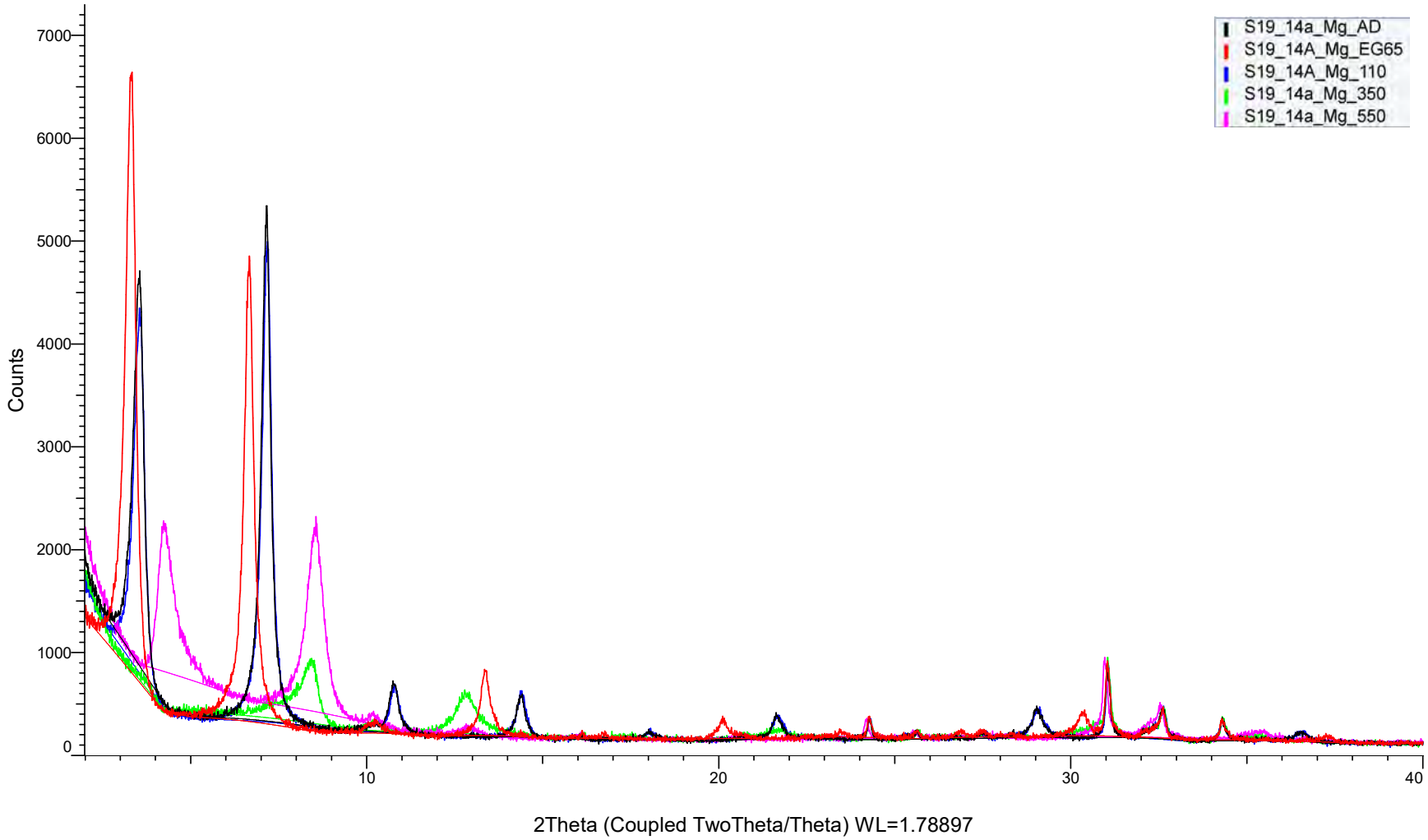

(Coupled TwoTheta/Theta)

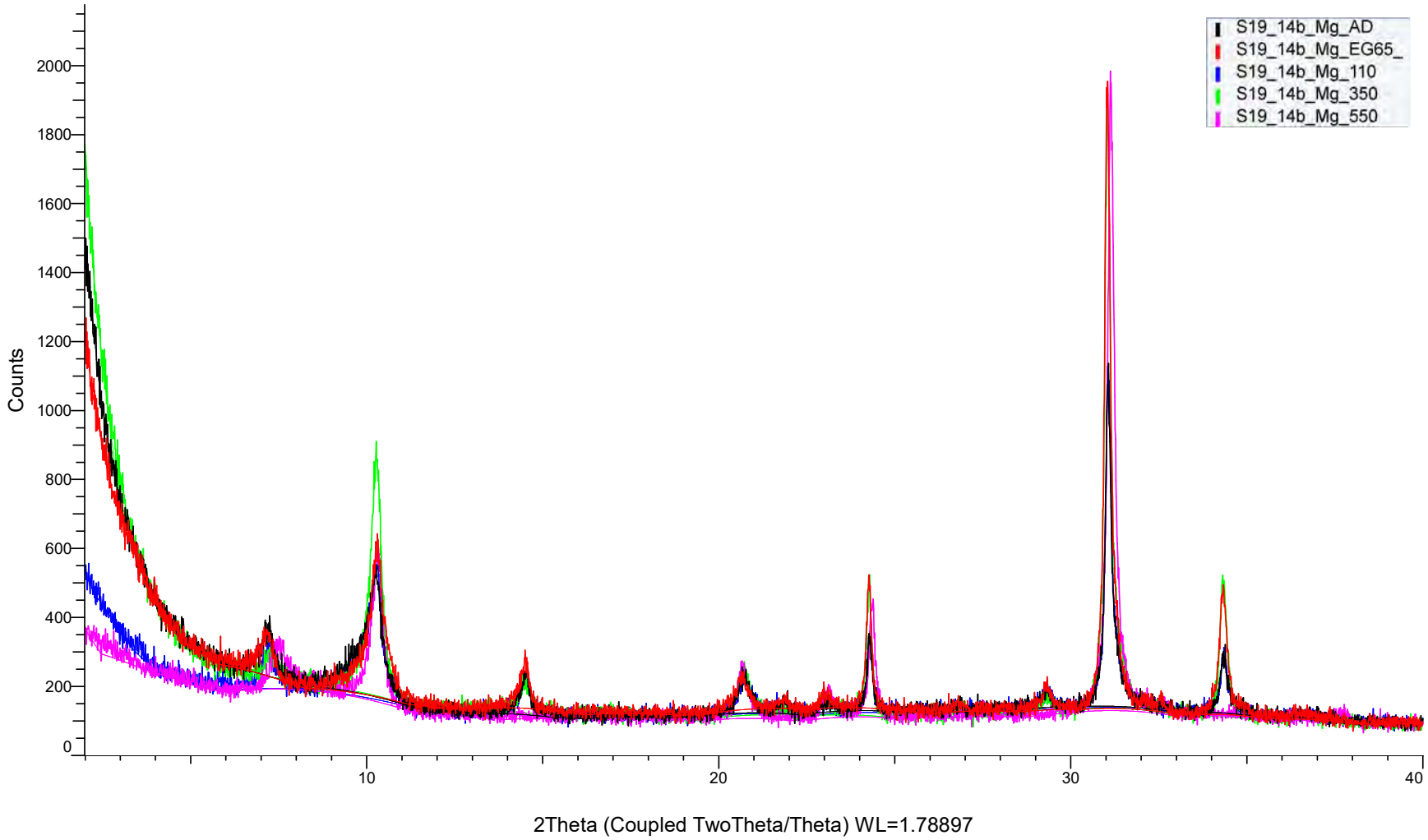

(Coupled TwoTheta/Theta)

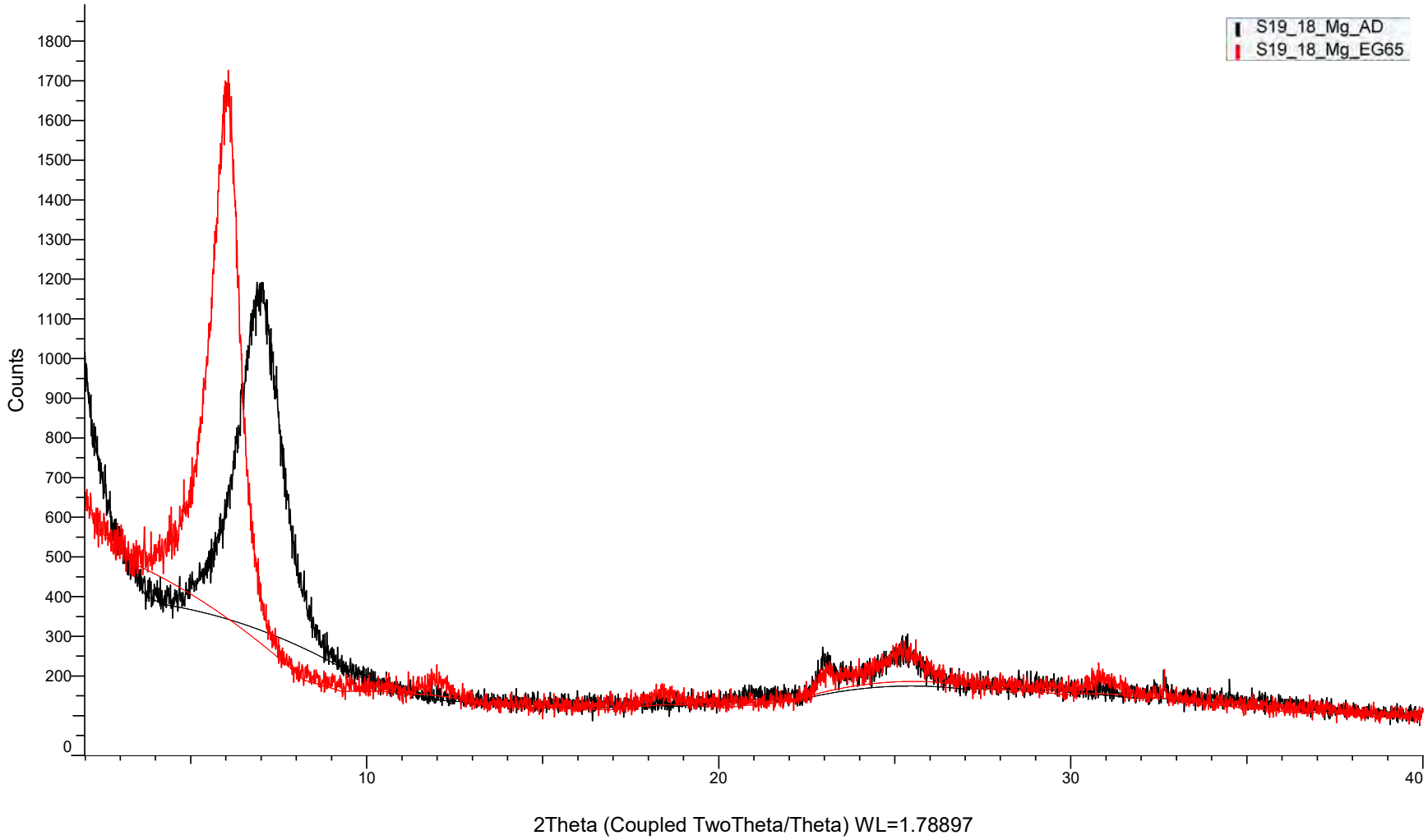

(Coupled TwoTheta/Theta)

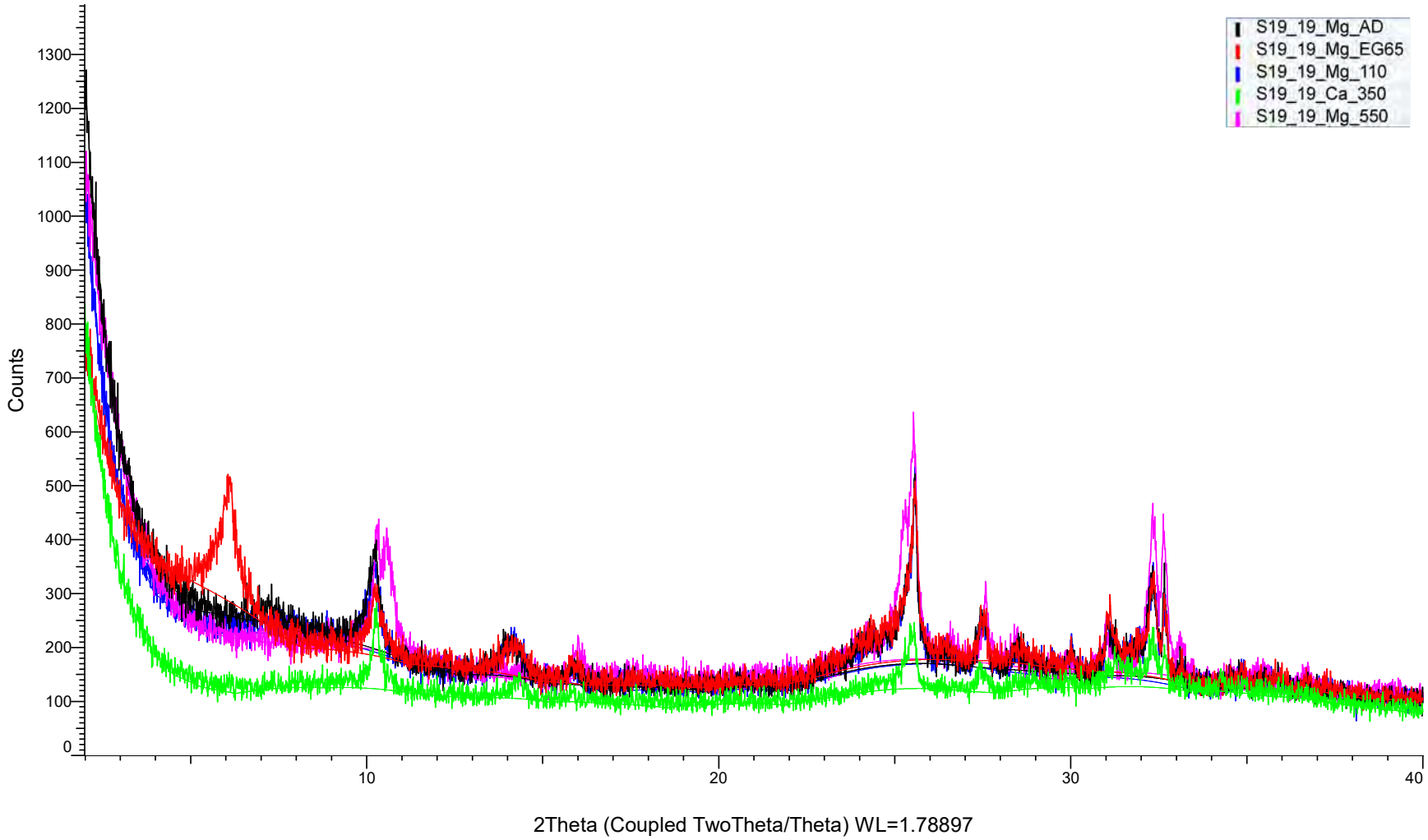

(Coupled TwoTheta/Theta)

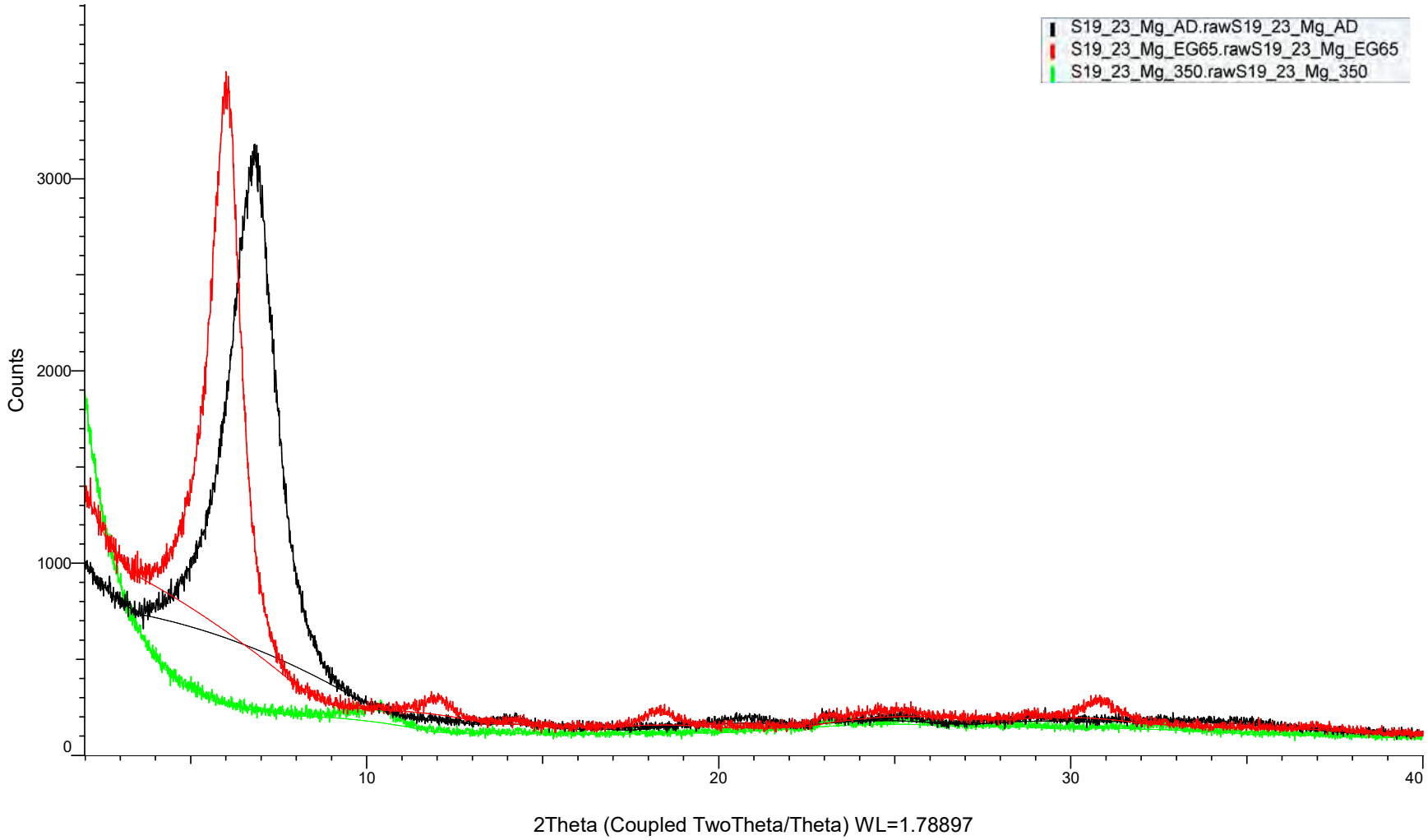

(Coupled TwoTheta/Theta)

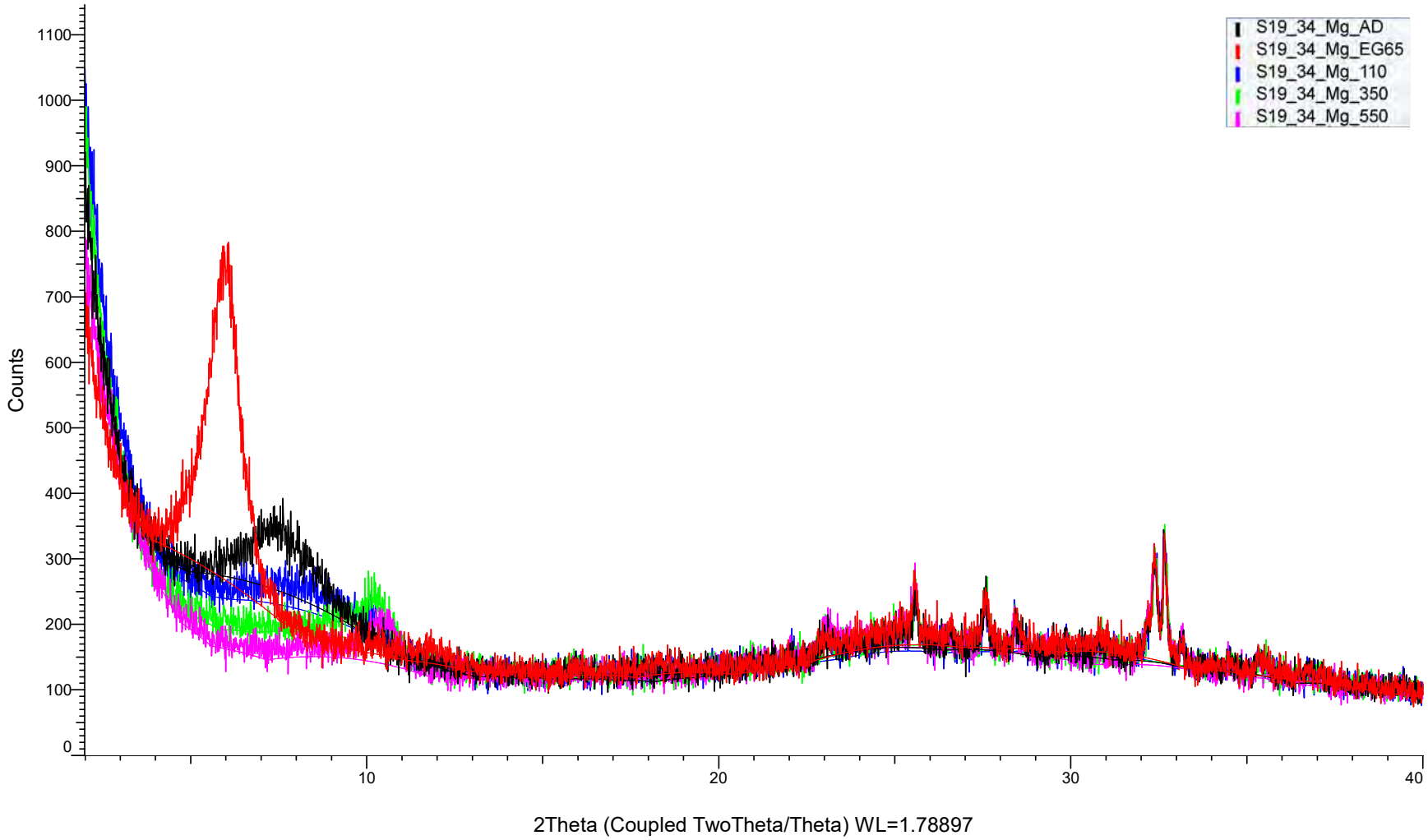

(Coupled TwoTheta/Theta)

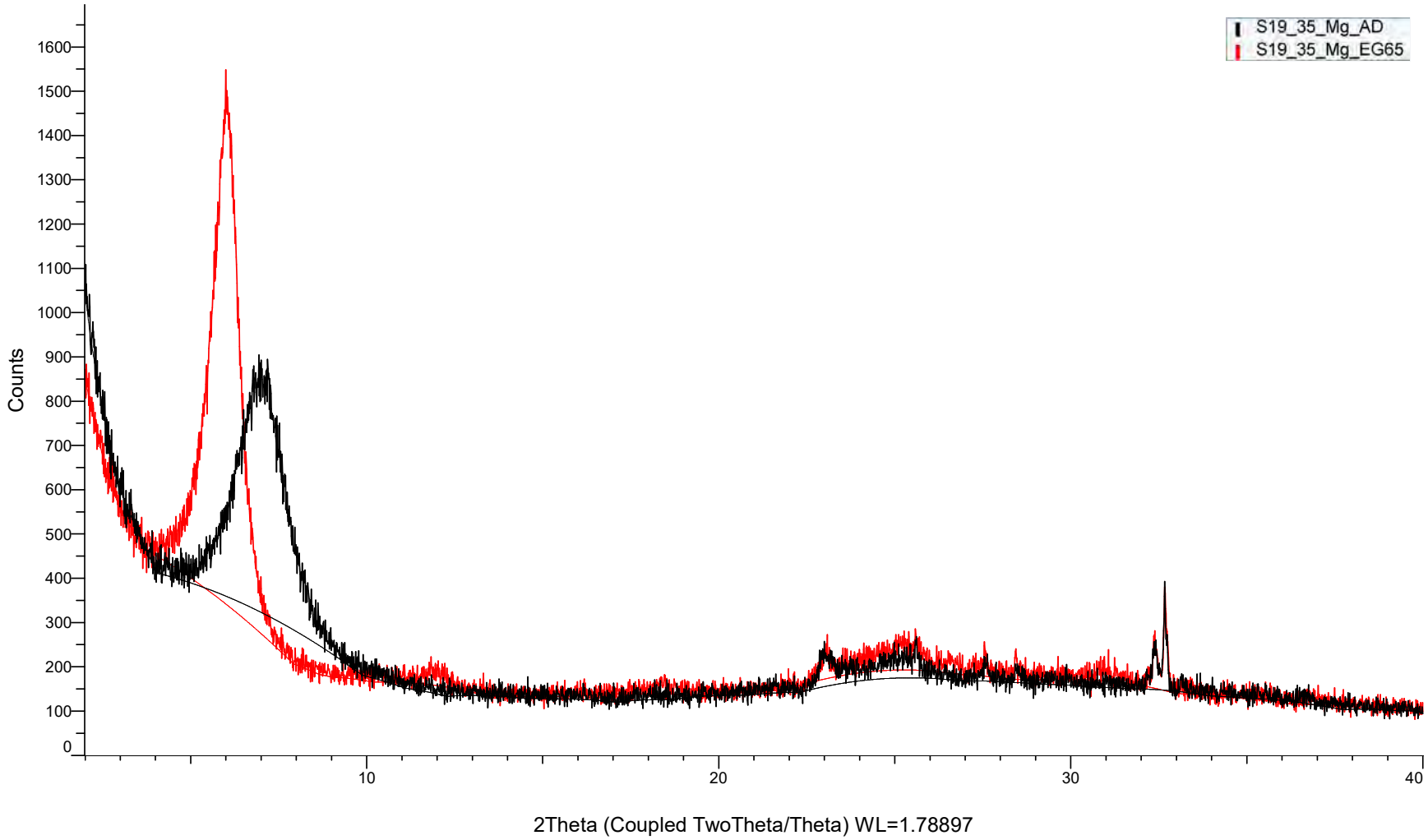

(Coupled TwoTheta/Theta)

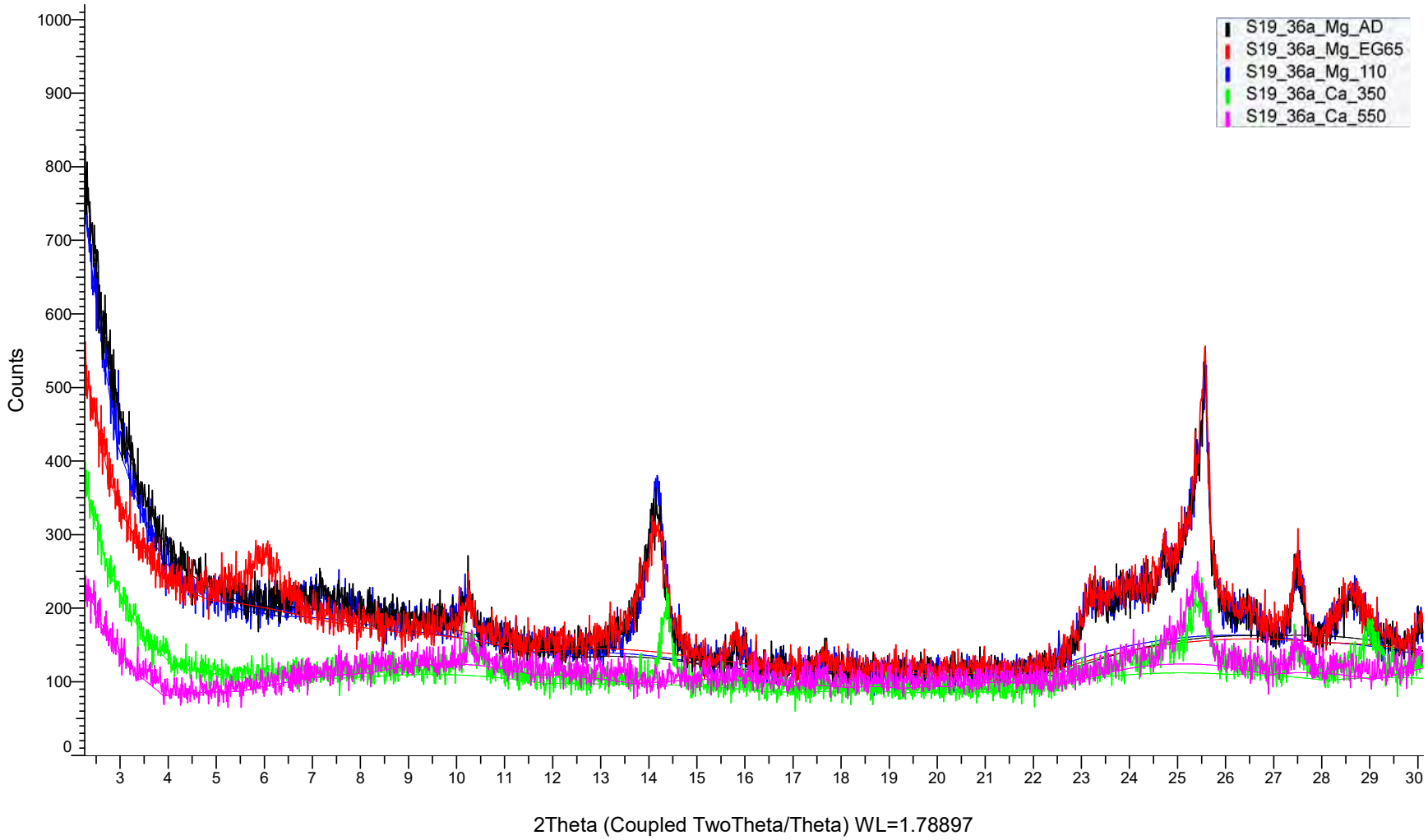

(Coupled TwoTheta/Theta)

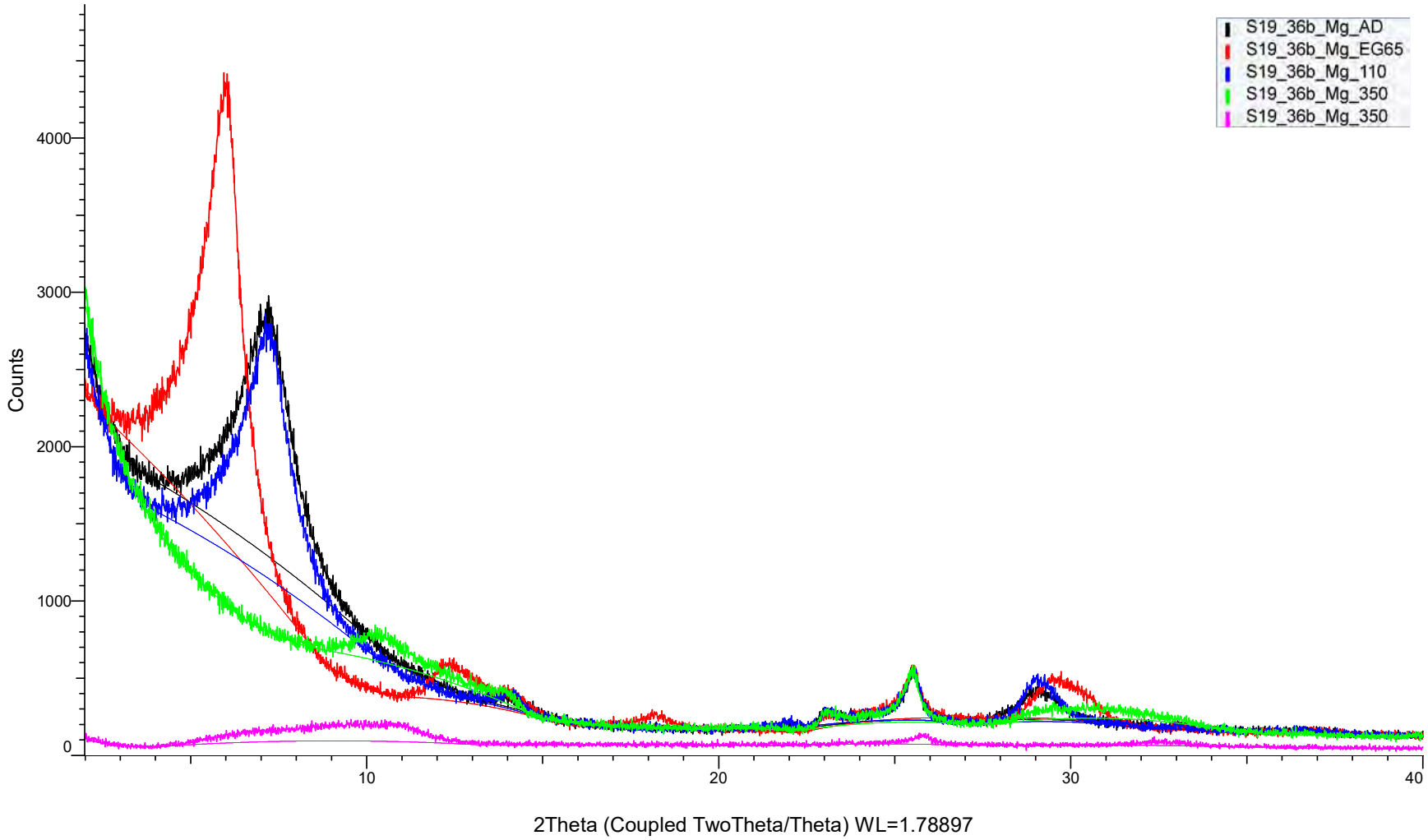

(Coupled TwoTheta/Theta)

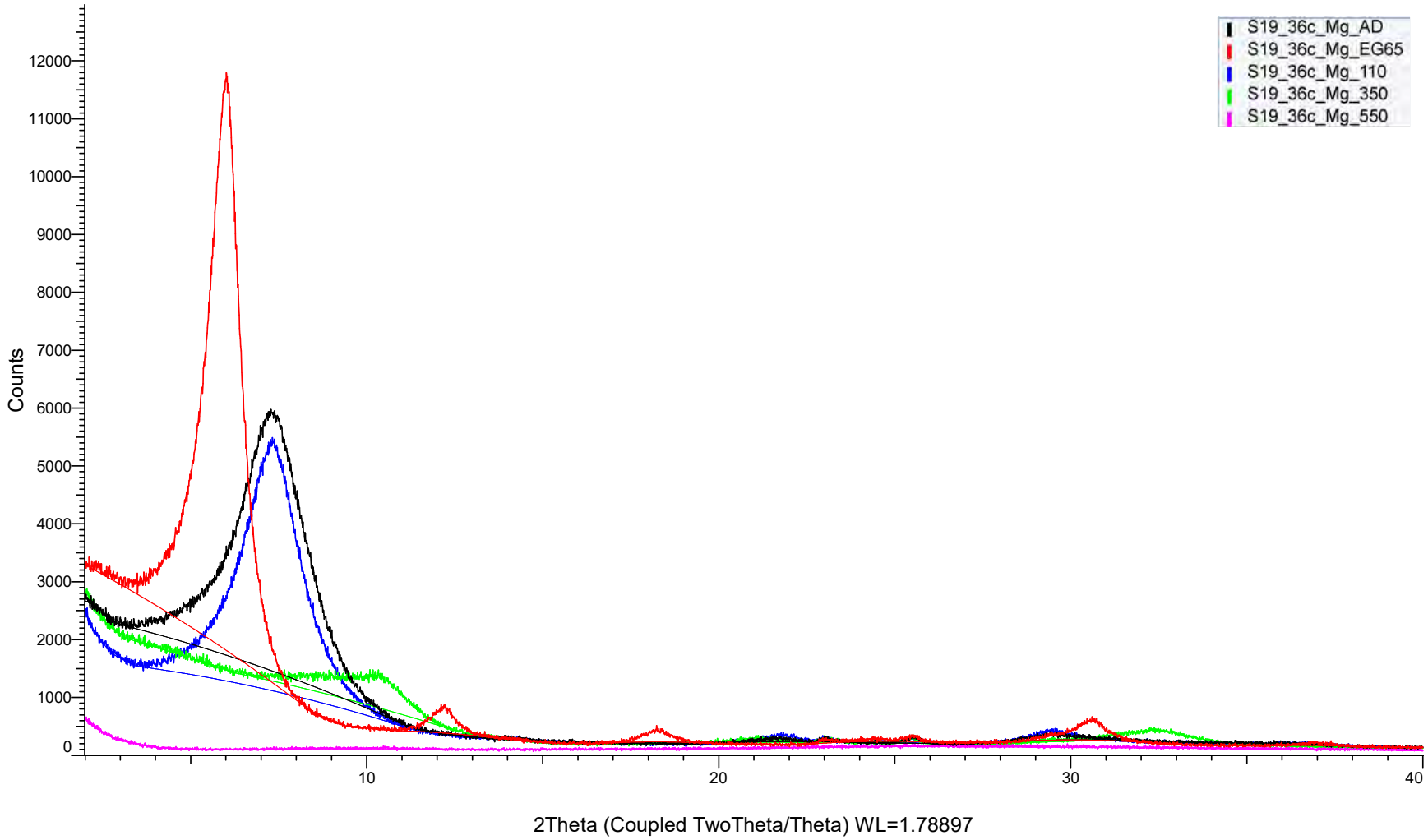

(Coupled TwoTheta/Theta)

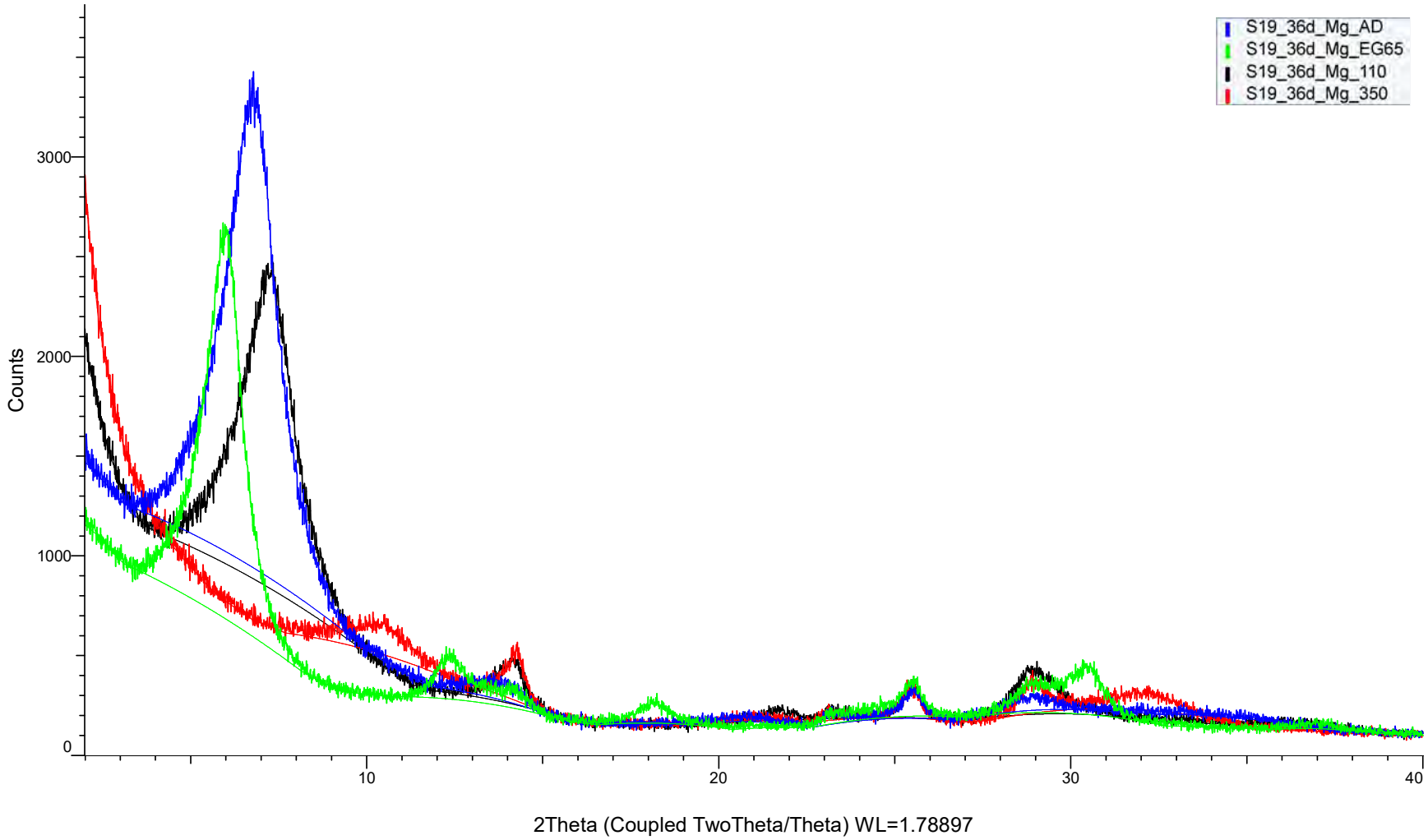

(Coupled TwoTheta/Theta)

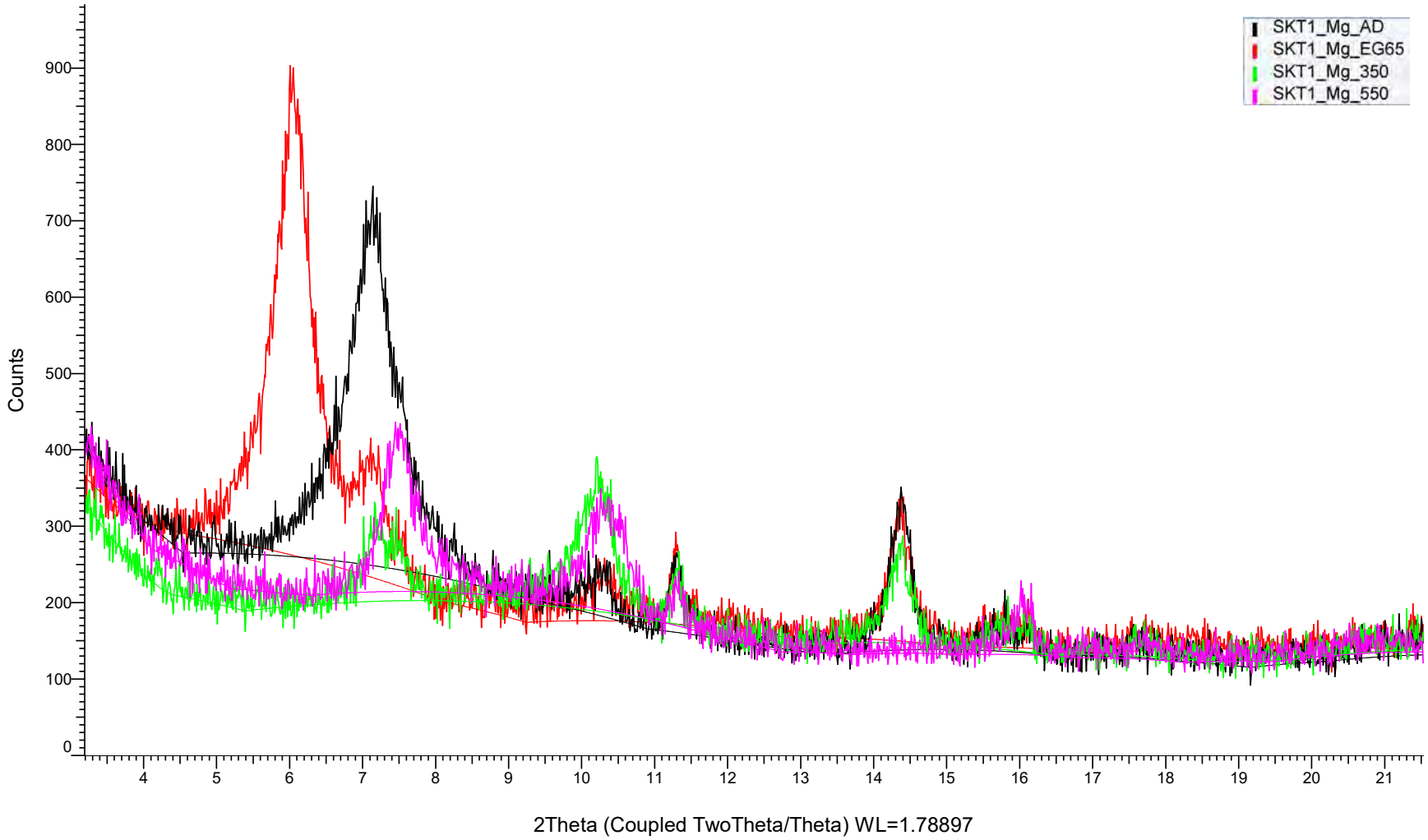

(Coupled TwoTheta/Theta)

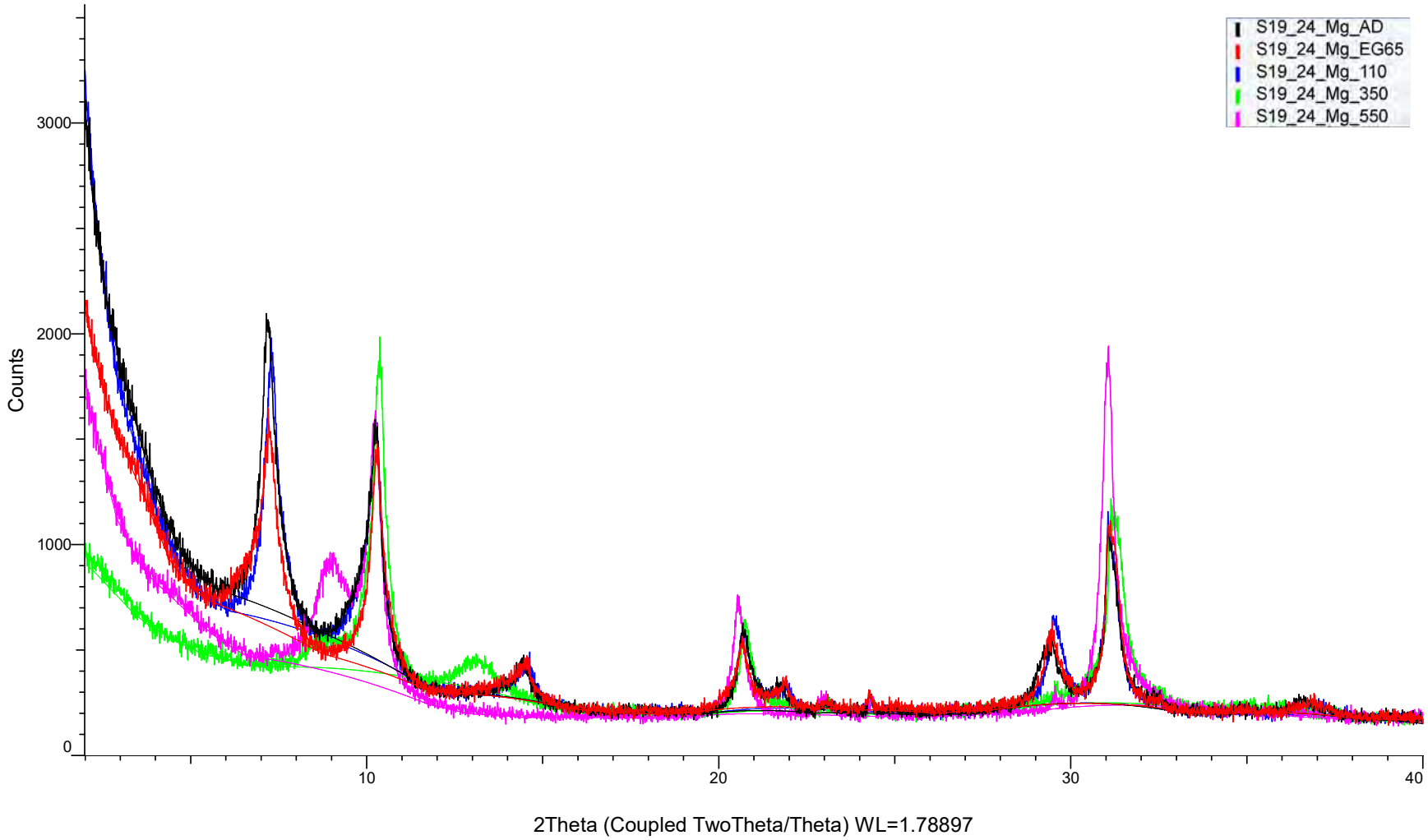

(Coupled TwoTheta/Theta)

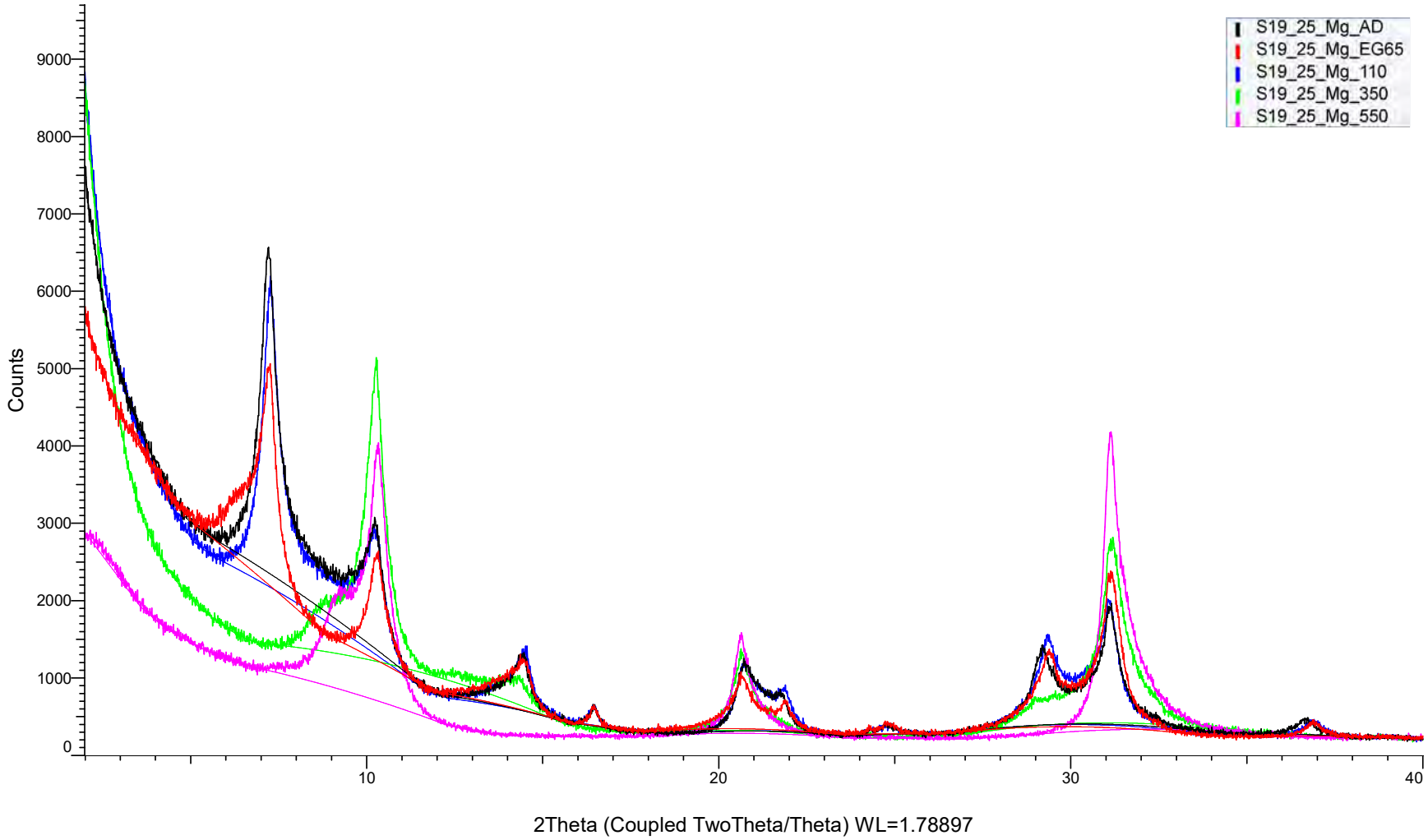

(Coupled TwoTheta/Theta)

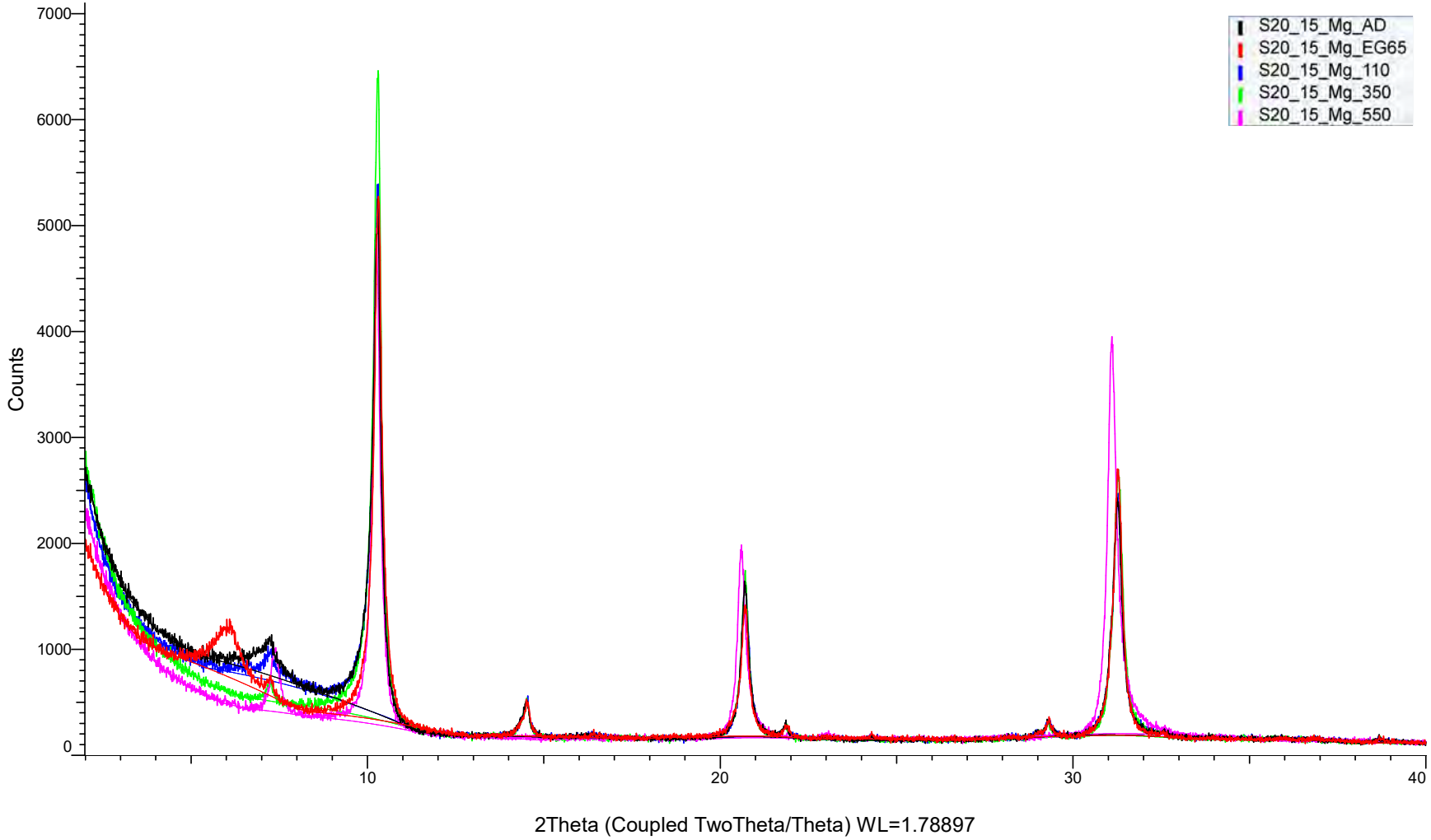

(Coupled TwoTheta/Theta)

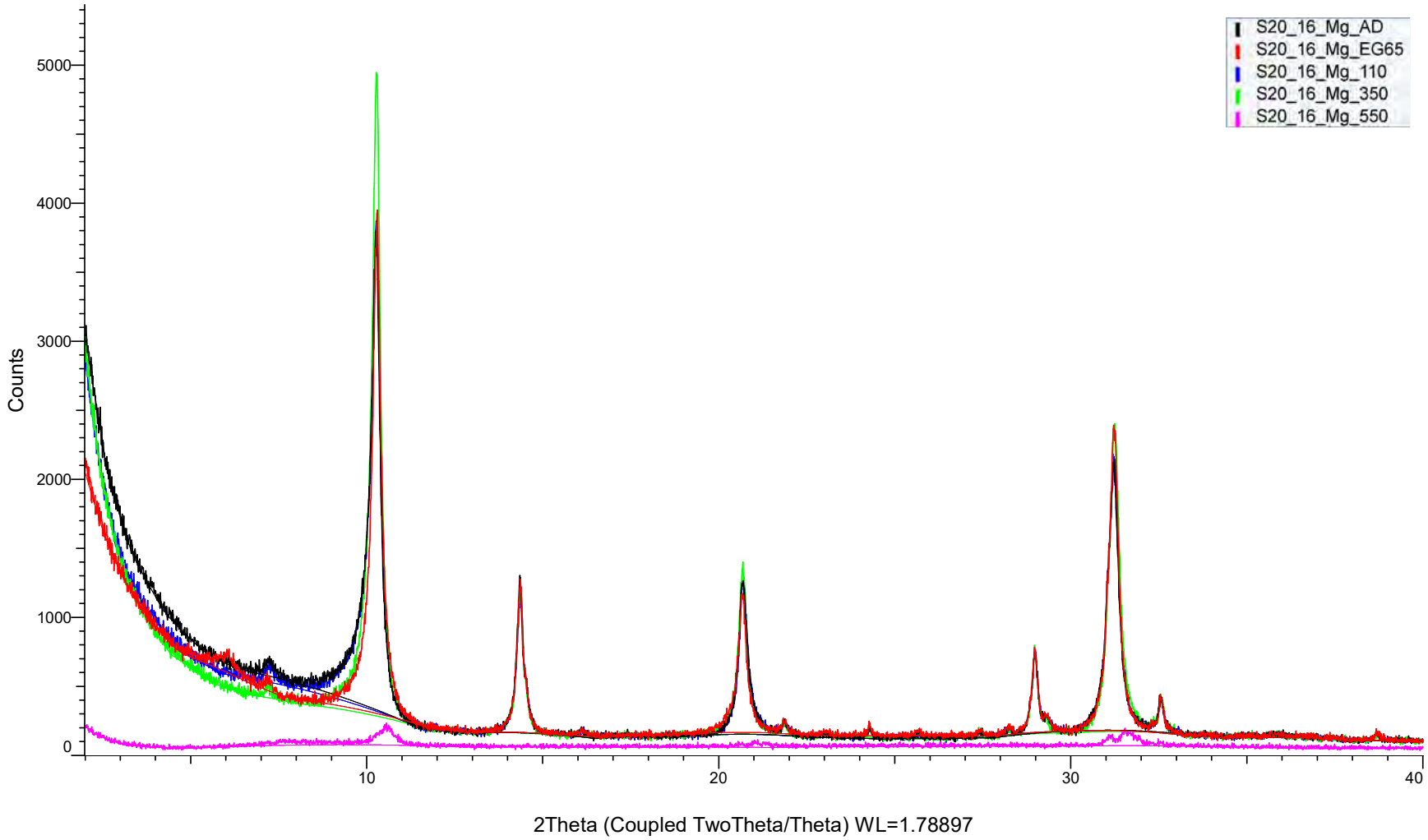

(Coupled TwoTheta/Theta)

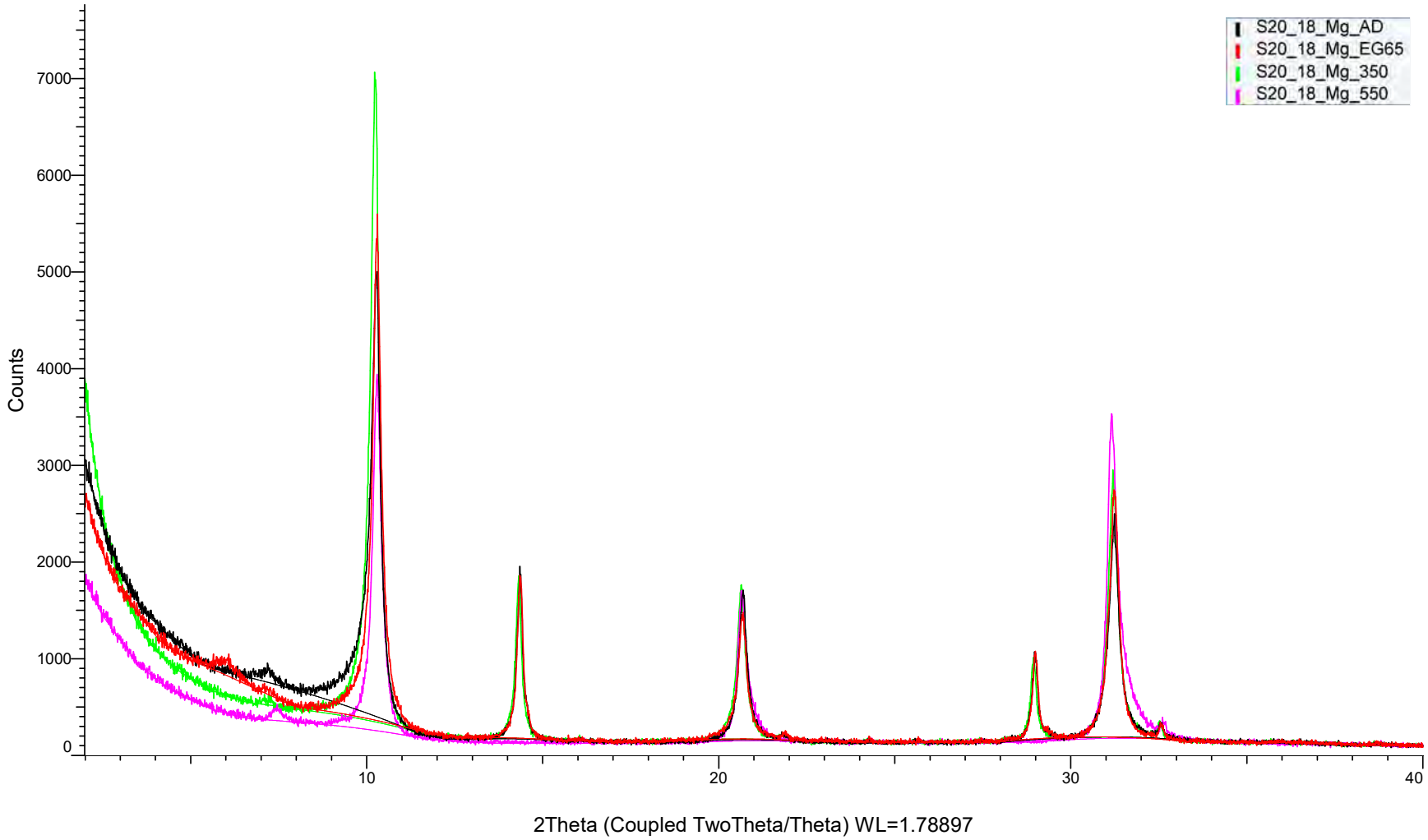

(Coupled TwoTheta/Theta)

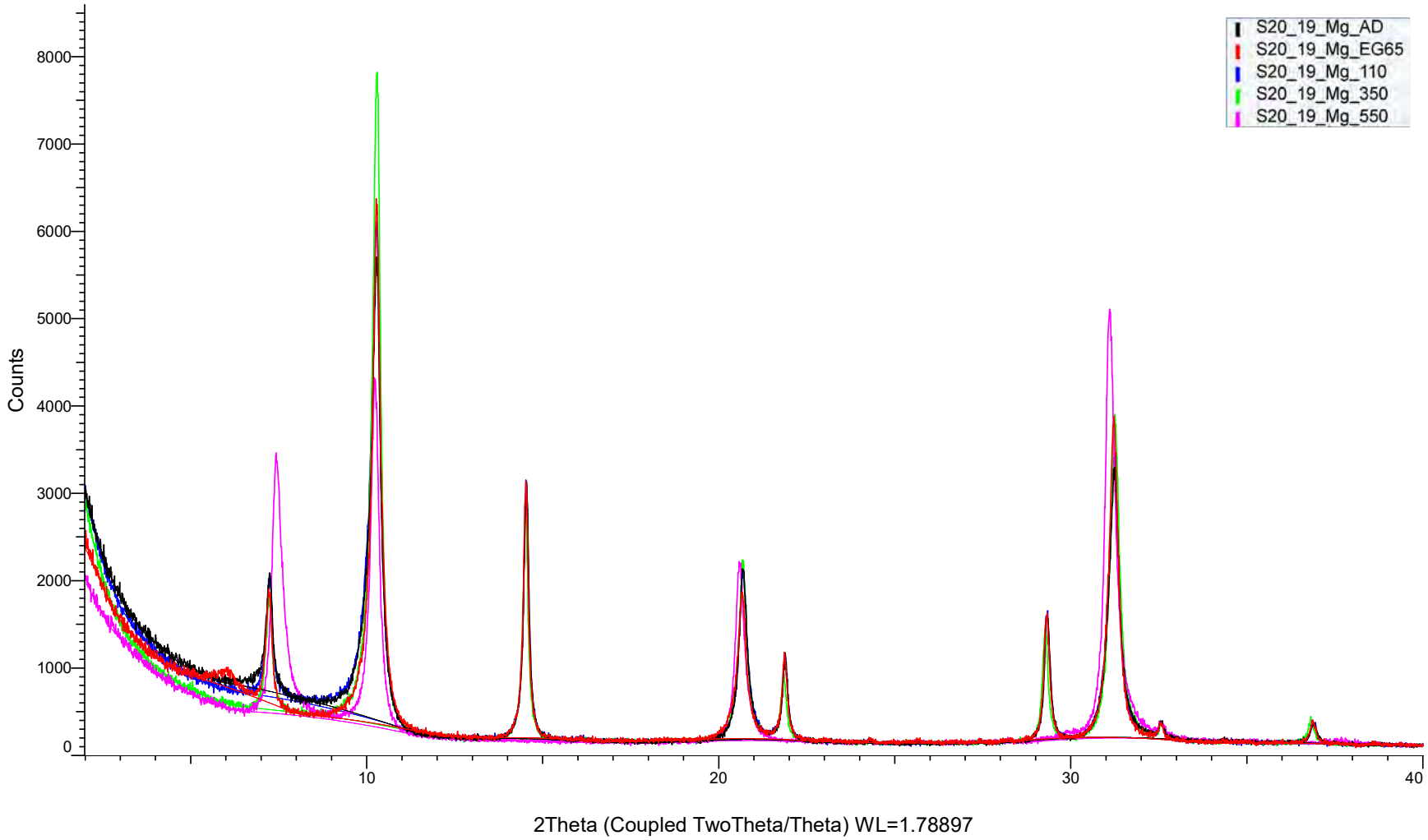

(Coupled TwoTheta/Theta)

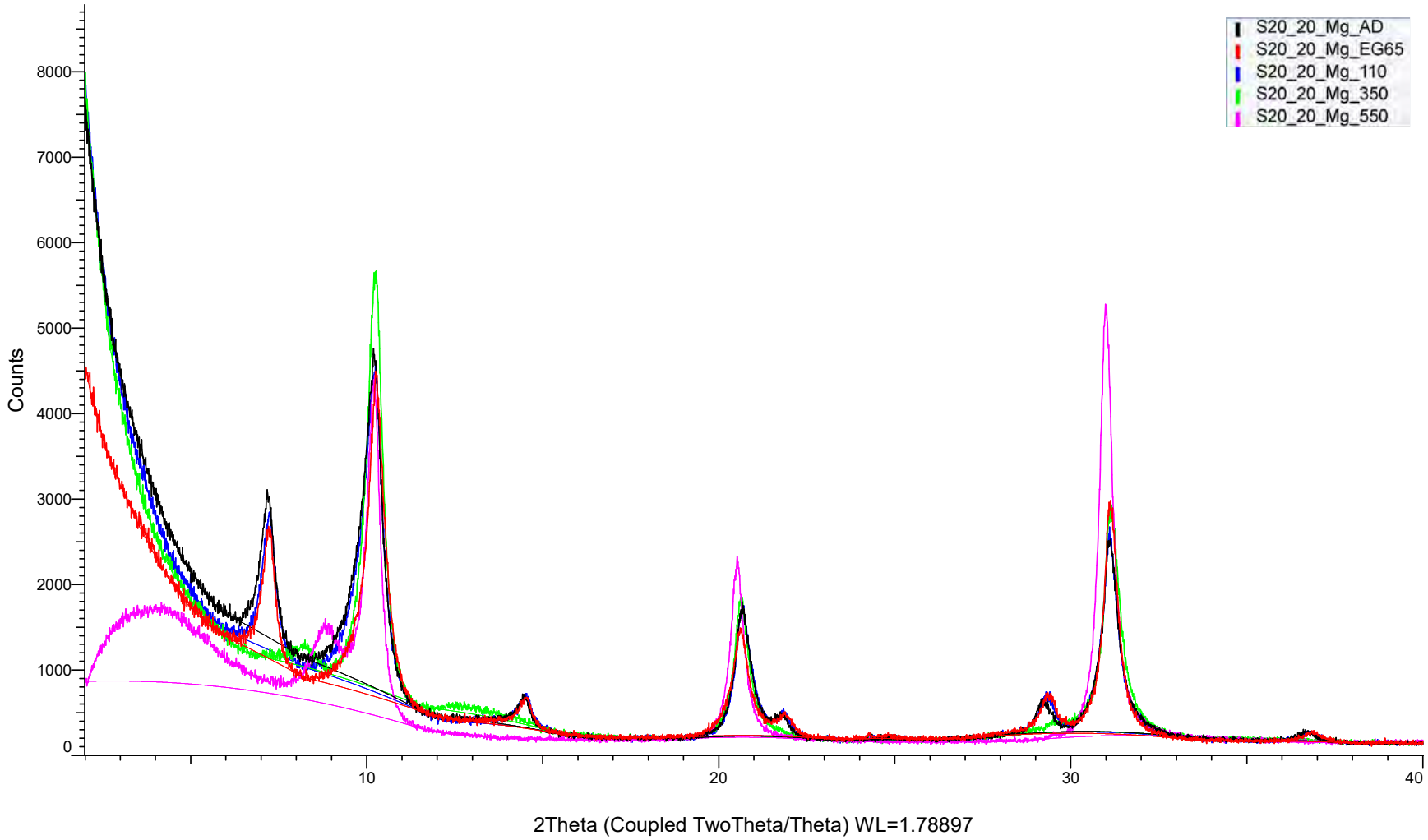

(Coupled TwoTheta/Theta)

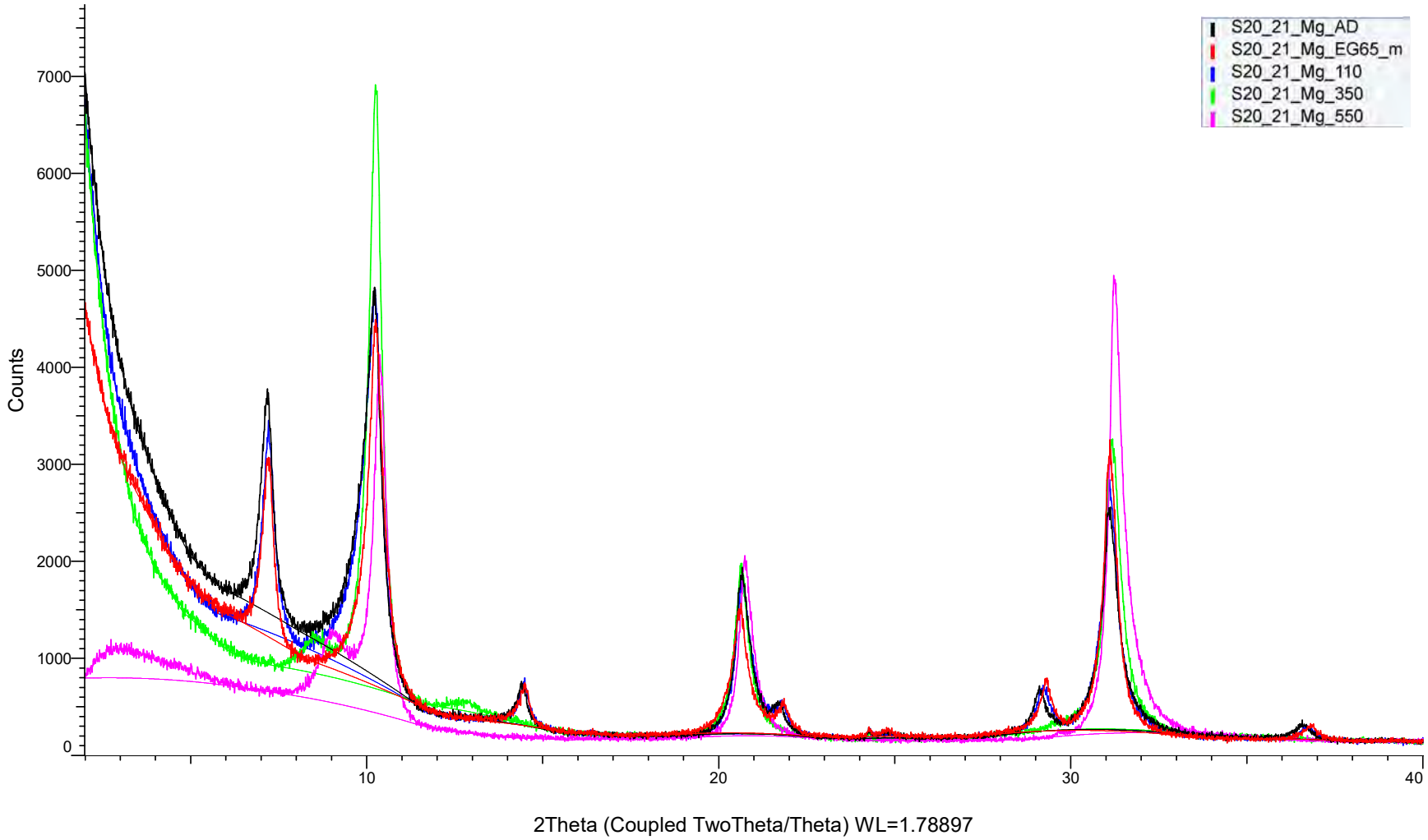

(Coupled TwoTheta/Theta)

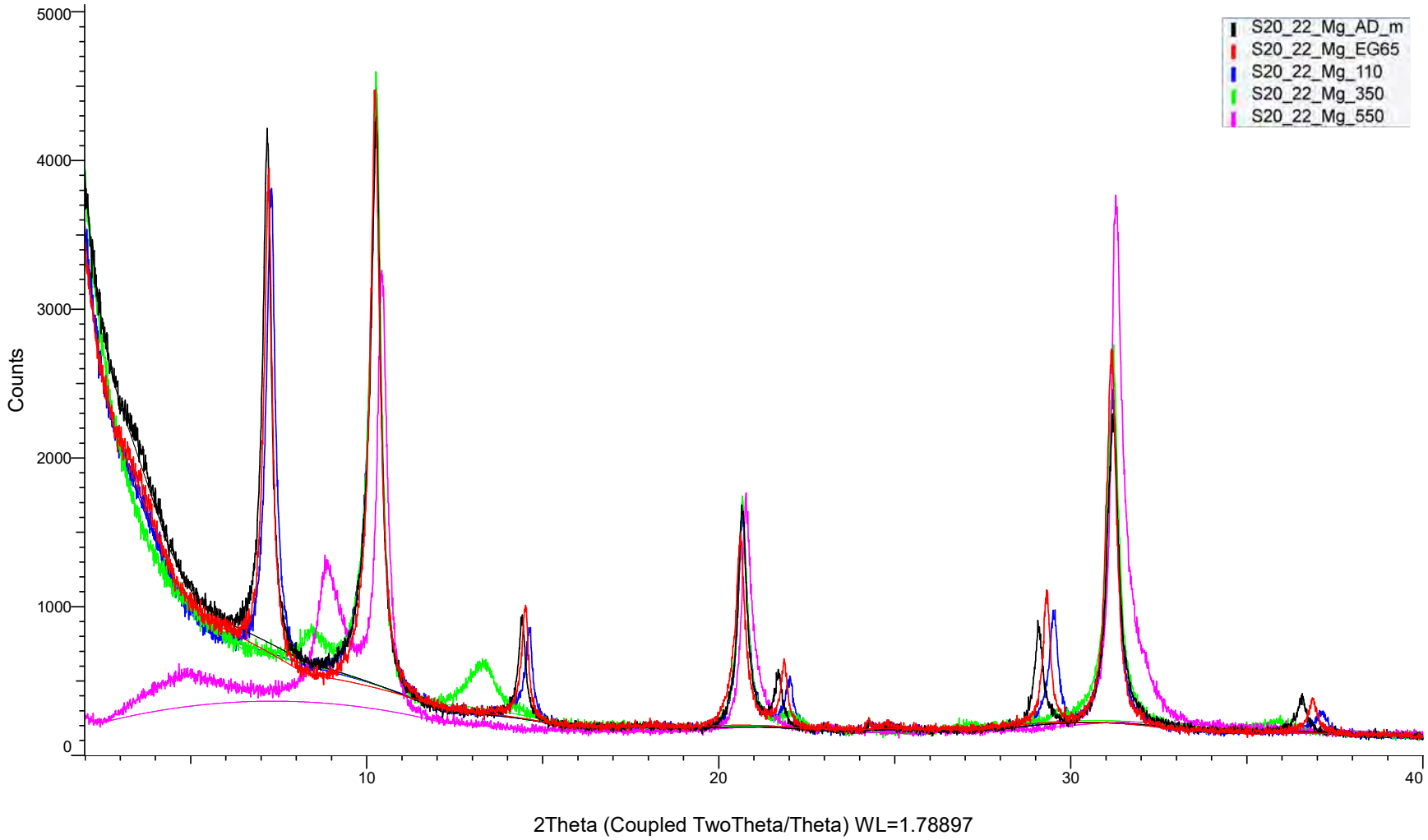

(Coupled TwoTheta/Theta)

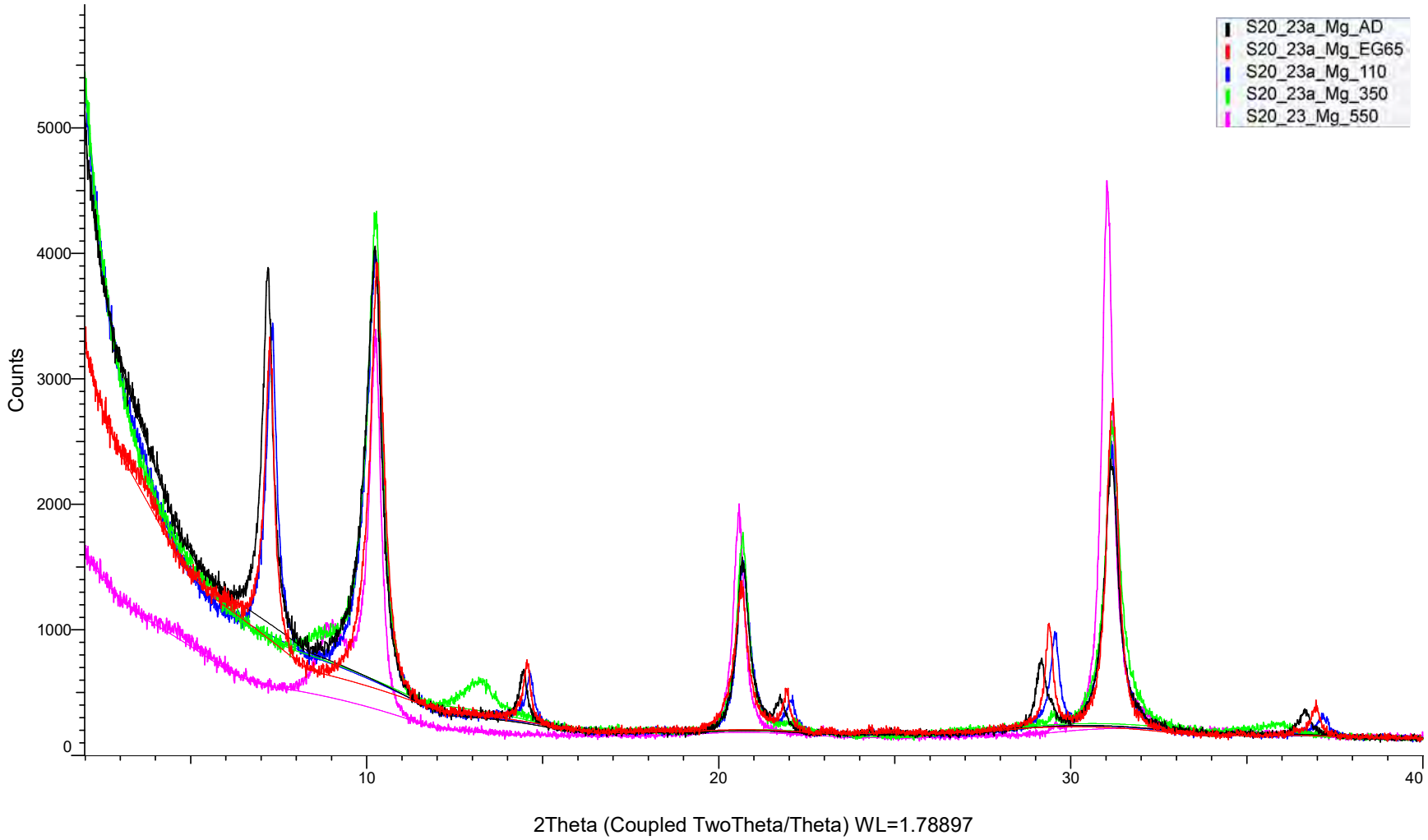

(Coupled TwoTheta/Theta)

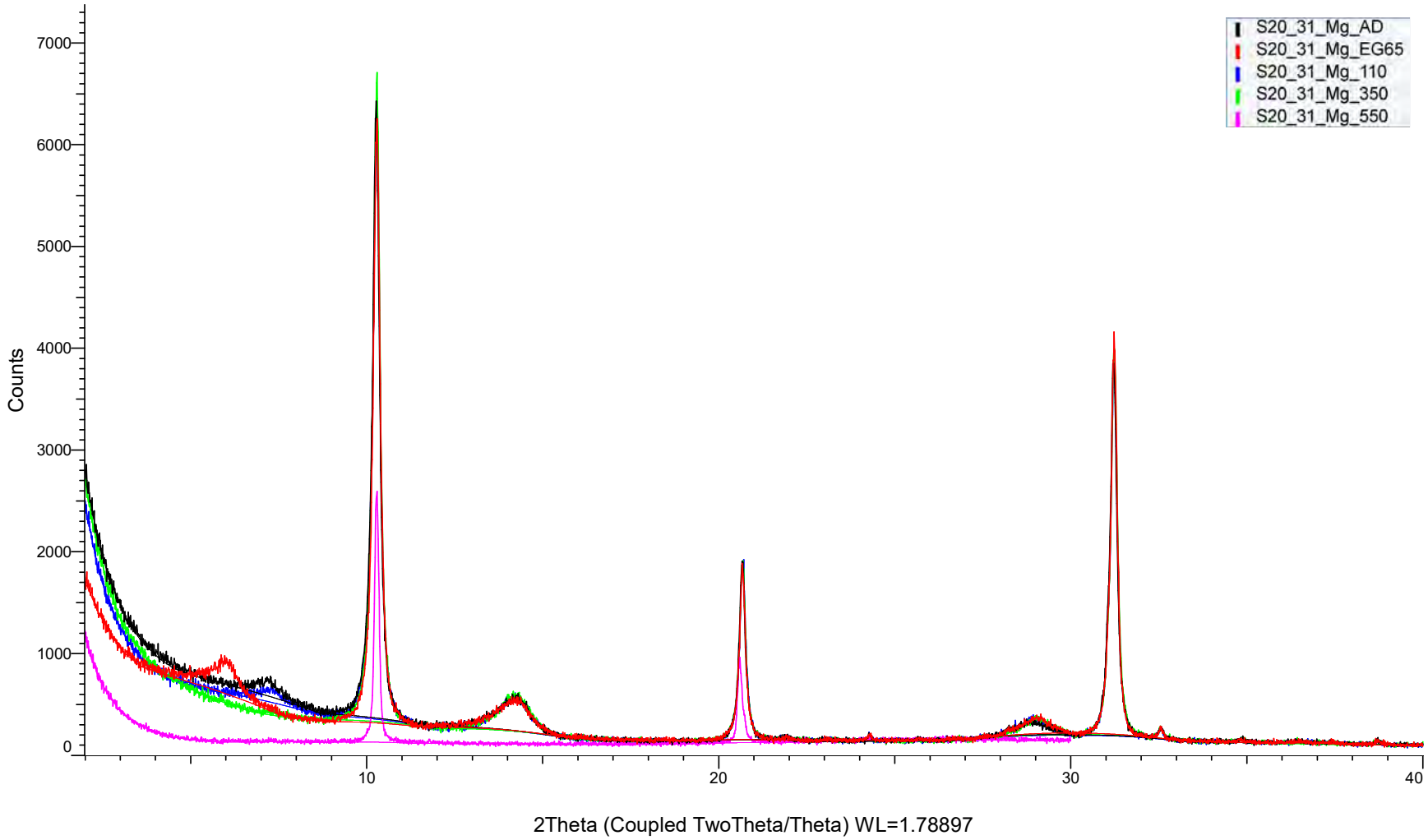

(Coupled TwoTheta/Theta)

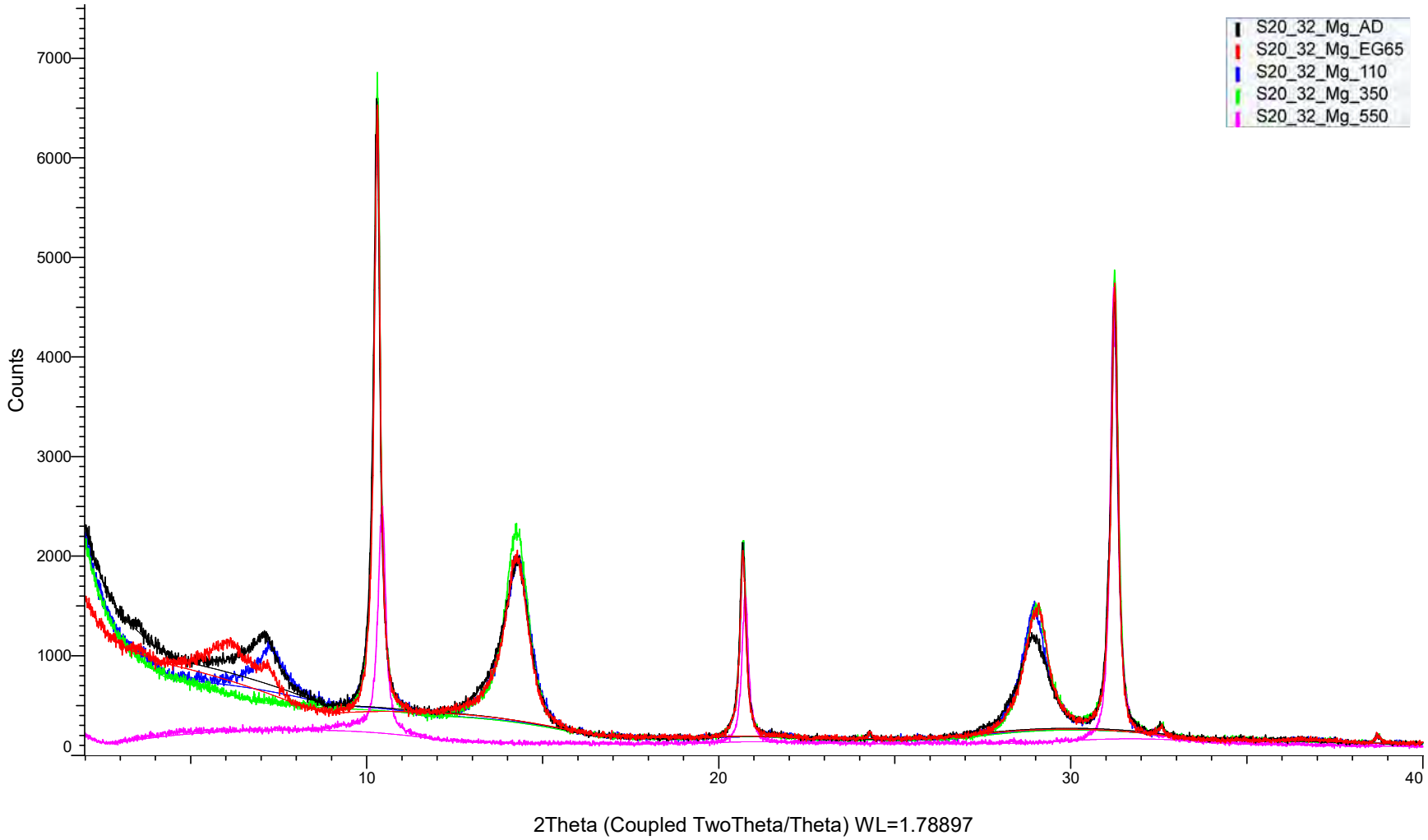

(Coupled TwoTheta/Theta)

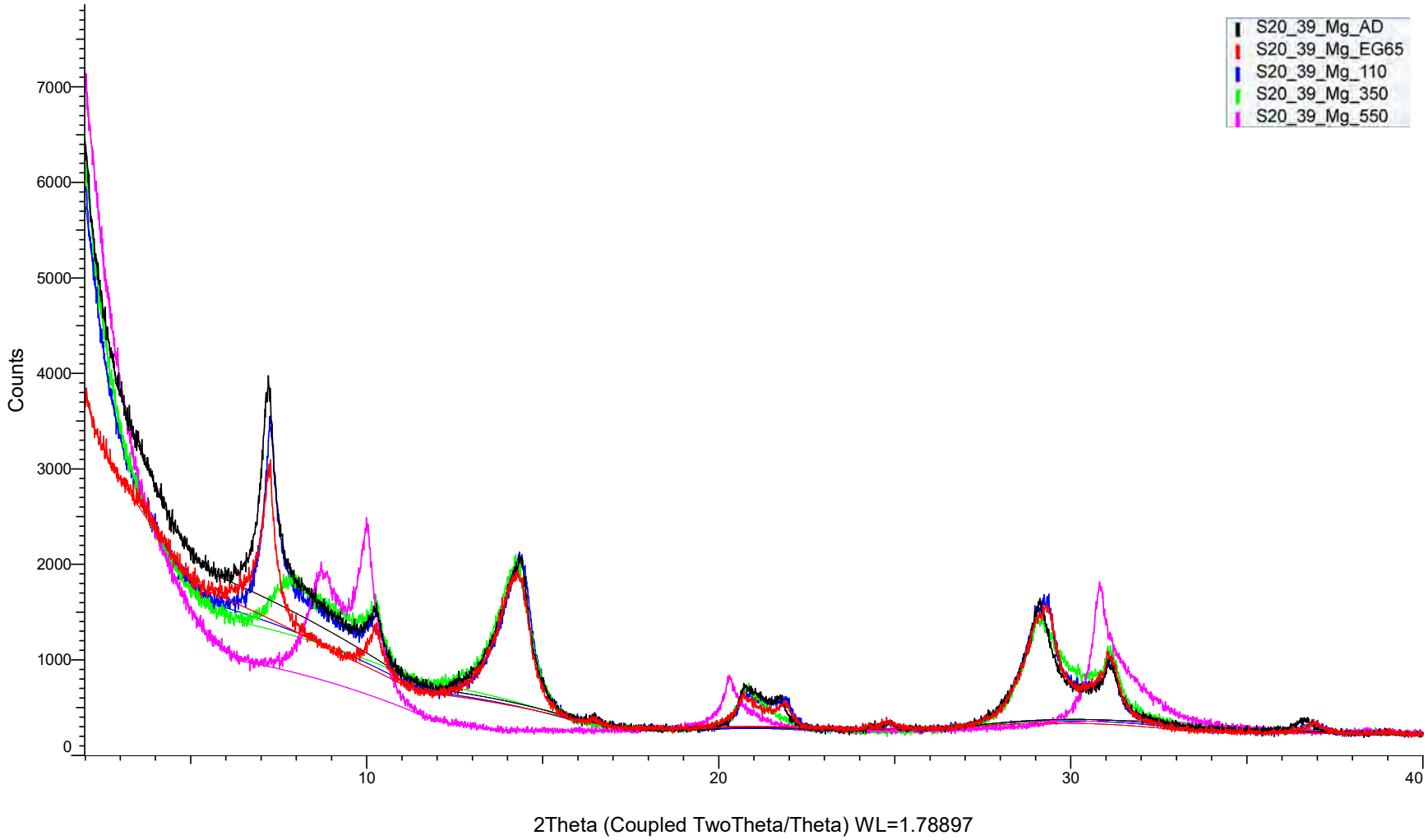

(Coupled TwoTheta/Theta)

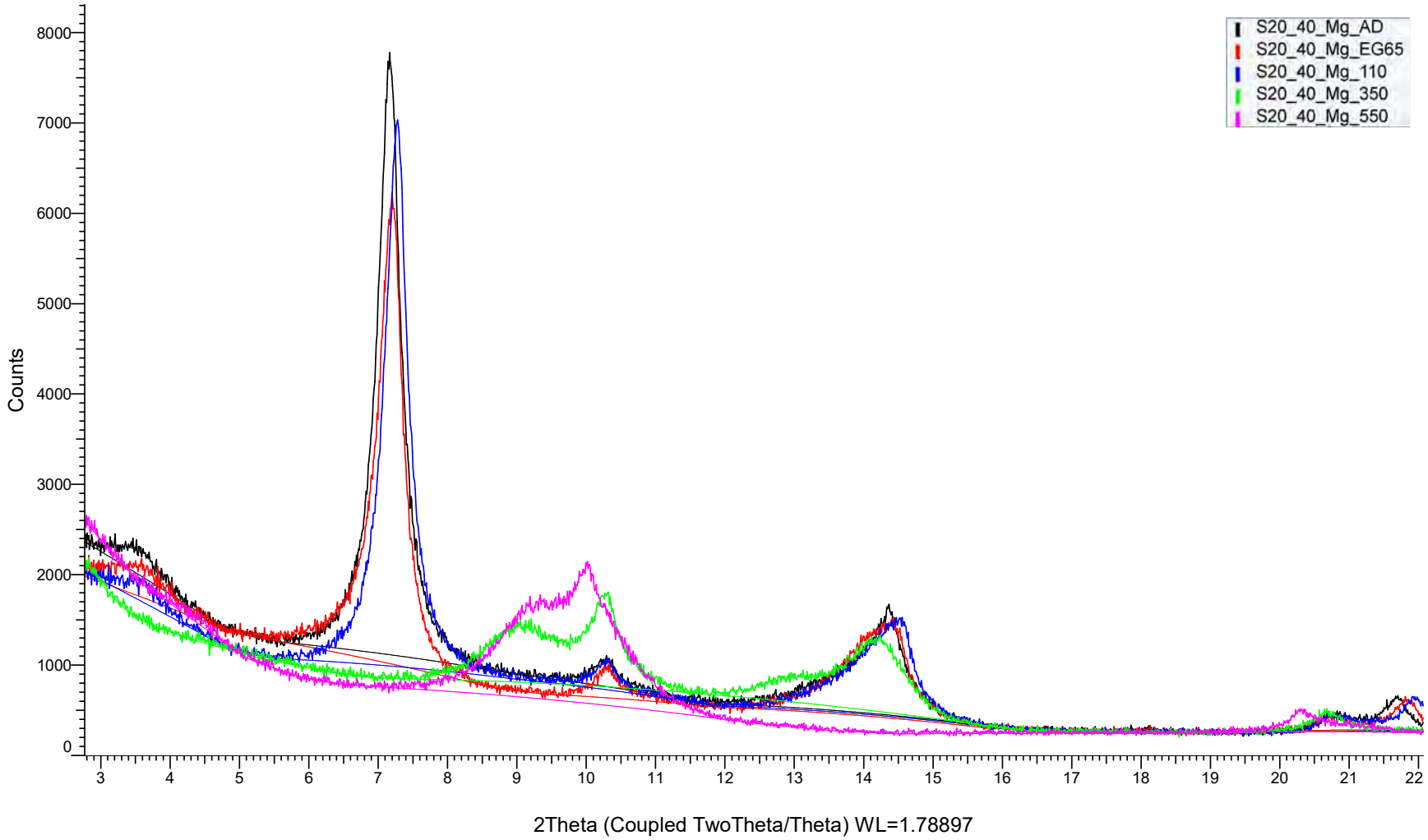

(Coupled TwoTheta/Theta)

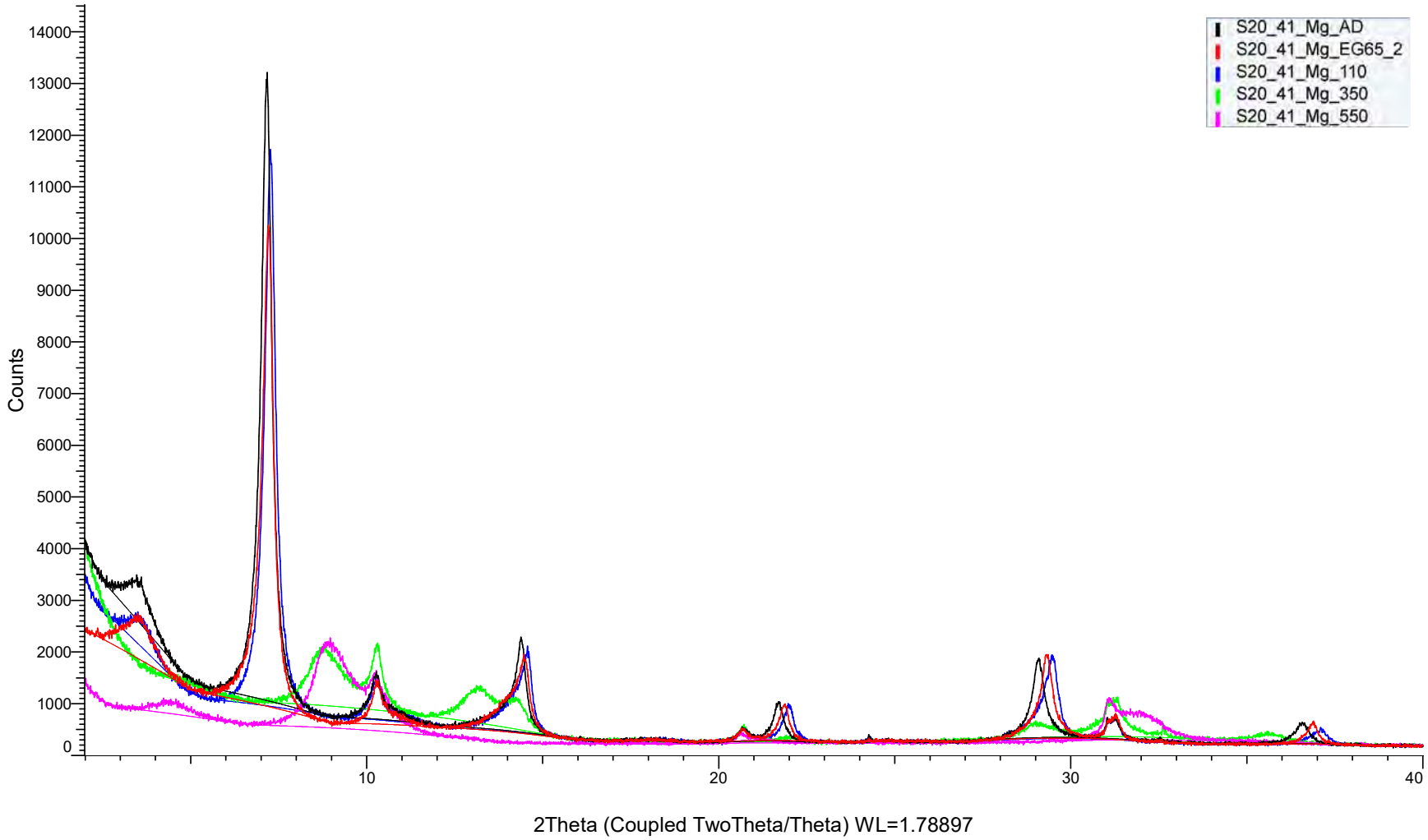

(Coupled TwoTheta/Theta)

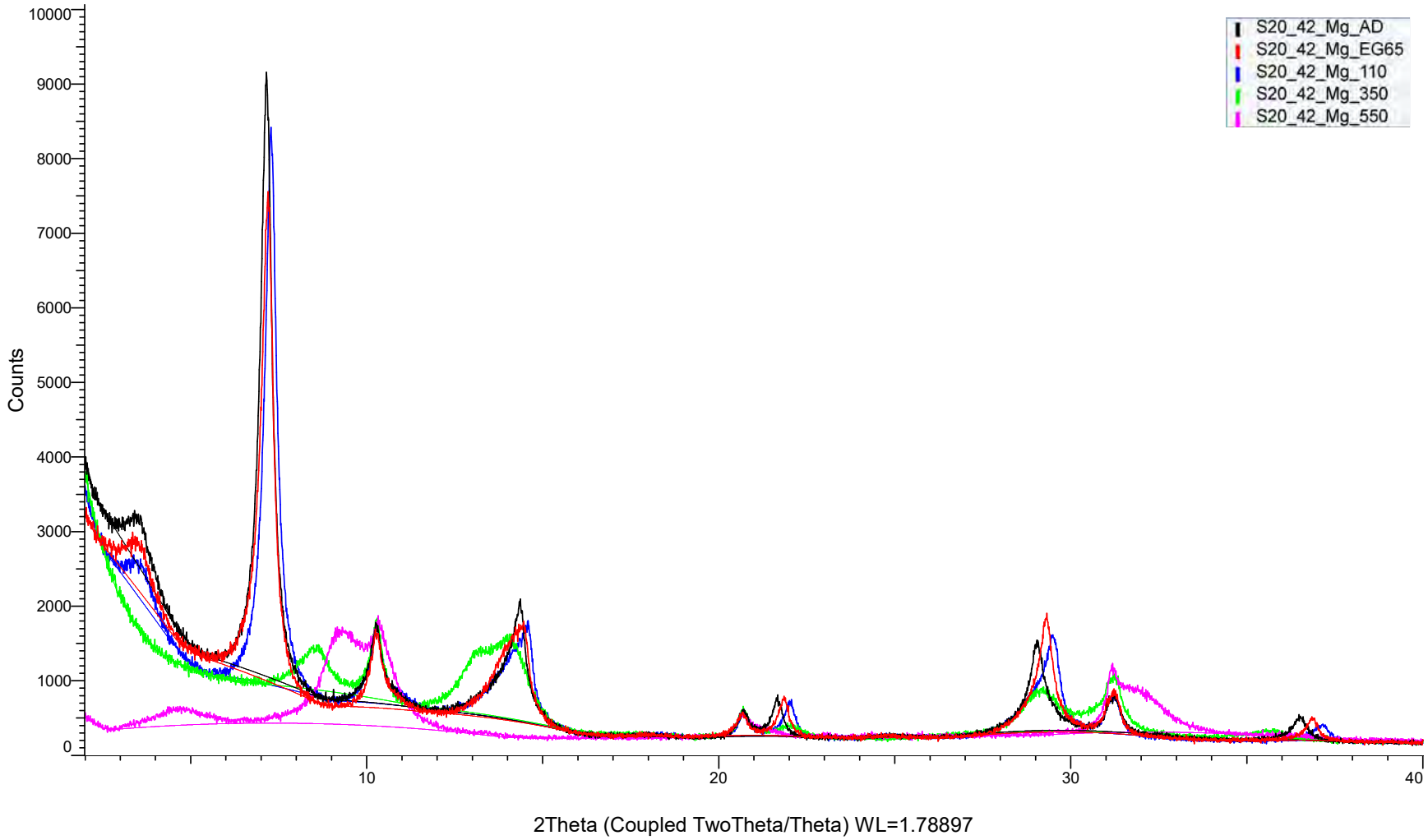

(Coupled TwoTheta/Theta)

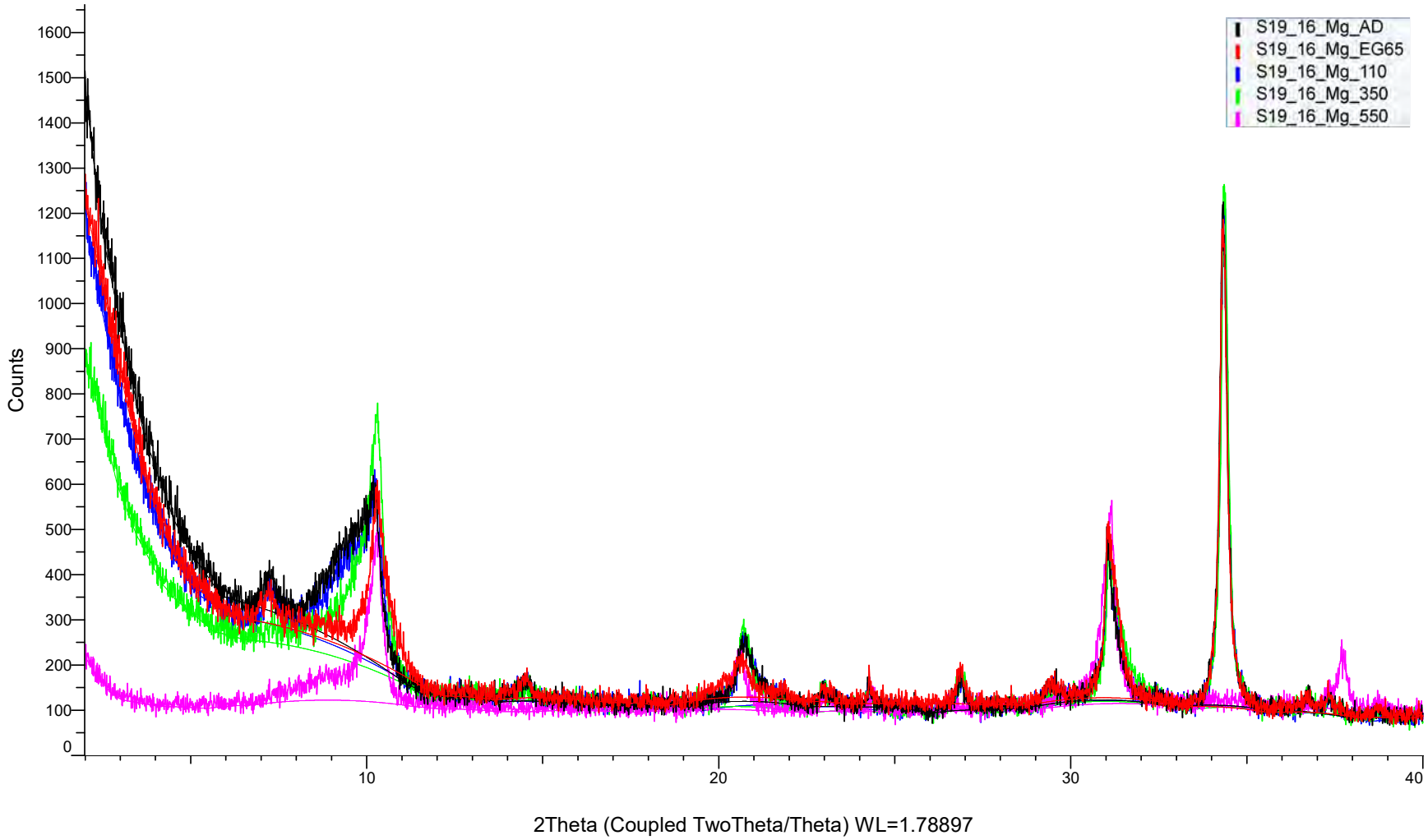

(Coupled TwoTheta/Theta)

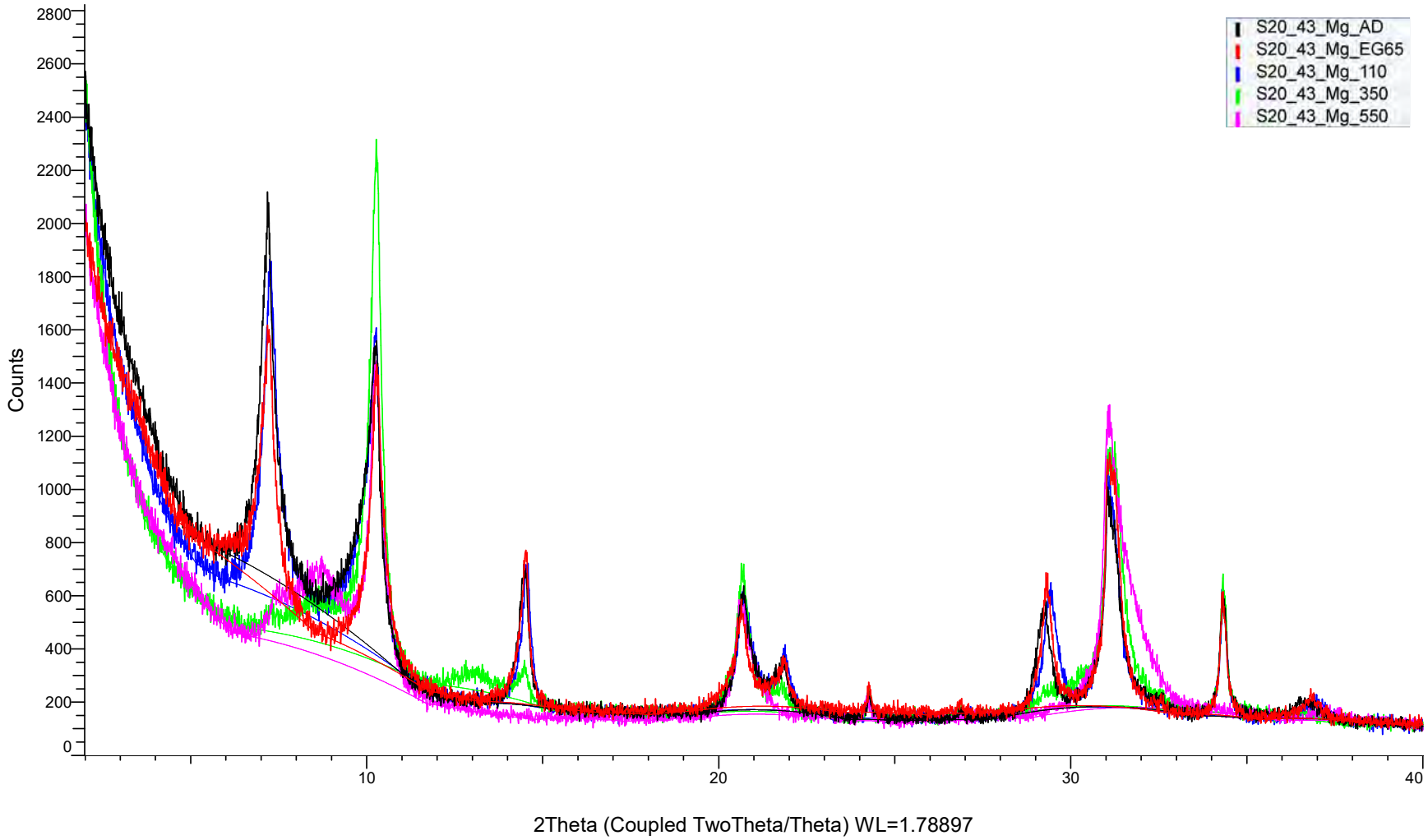

(Coupled TwoTheta/Theta)

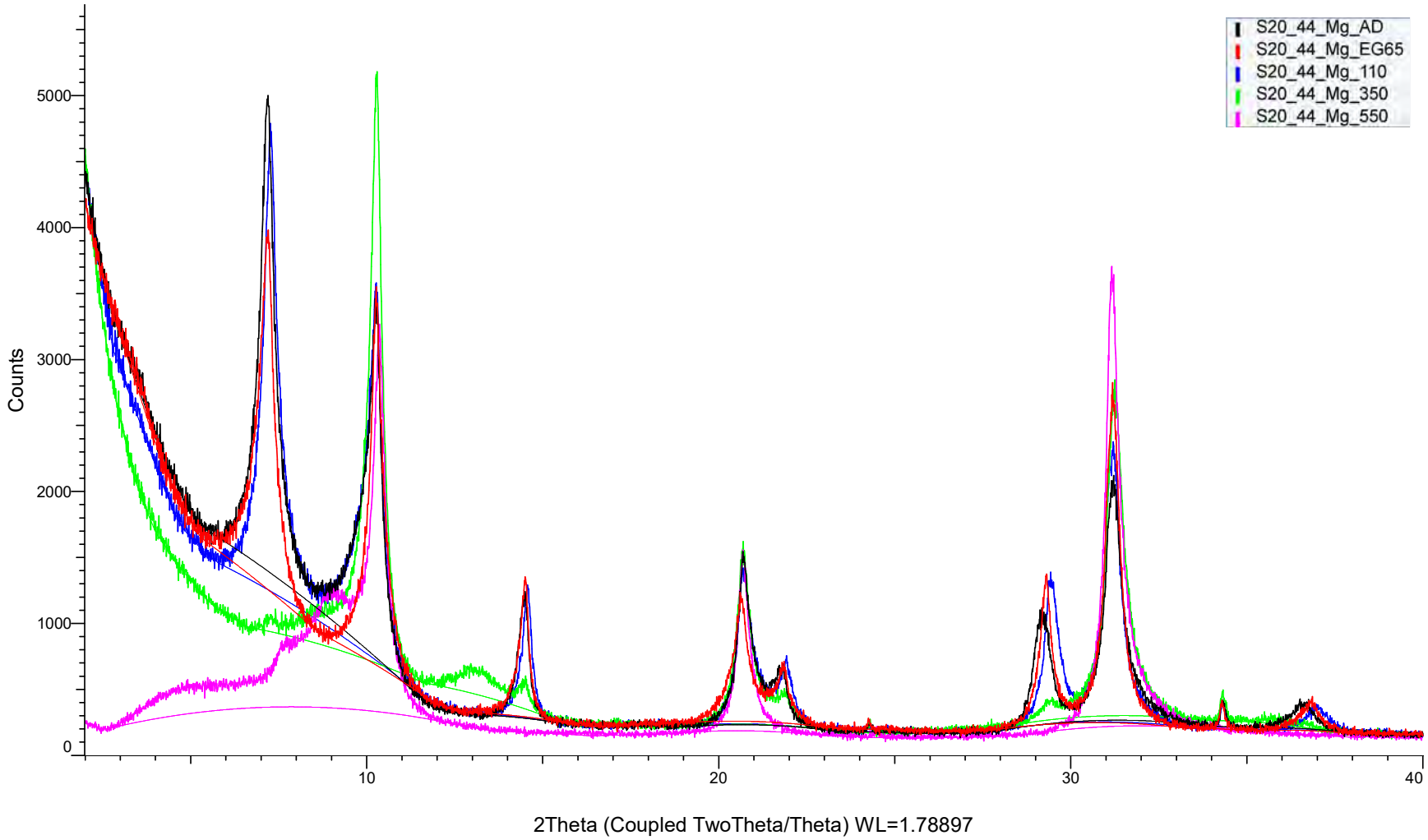

(Coupled TwoTheta/Theta)

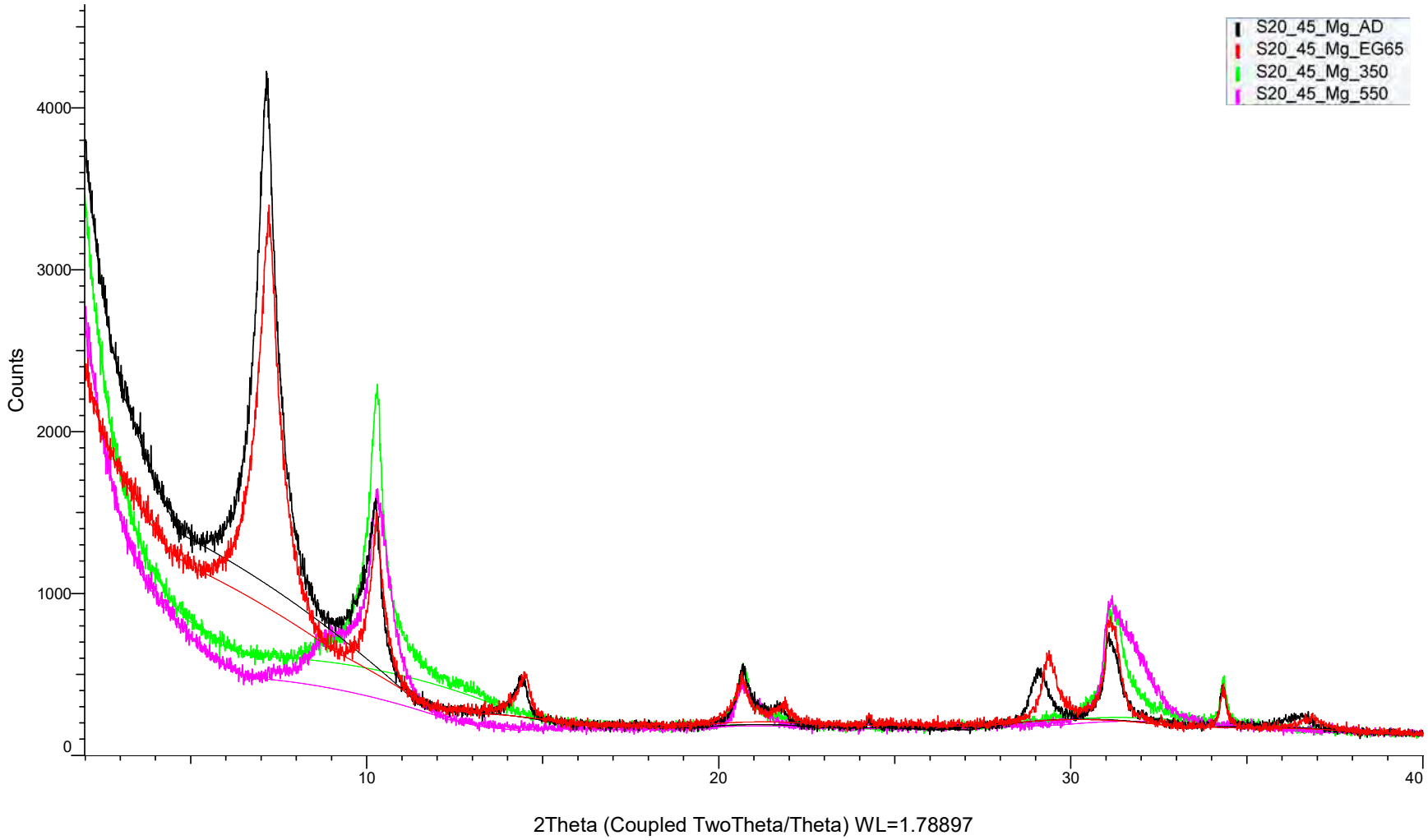

(Coupled TwoTheta/Theta)

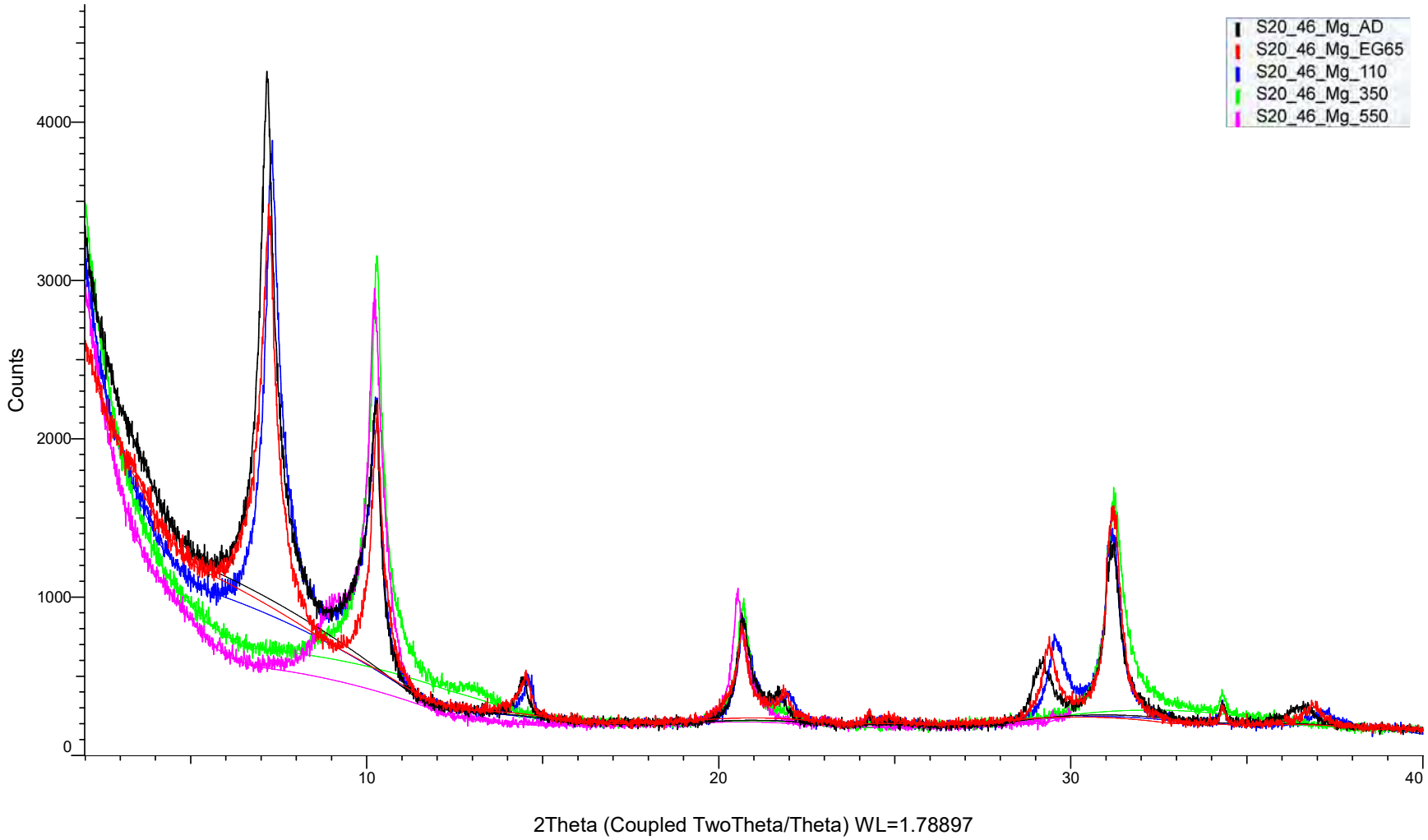

(Coupled TwoTheta/Theta)

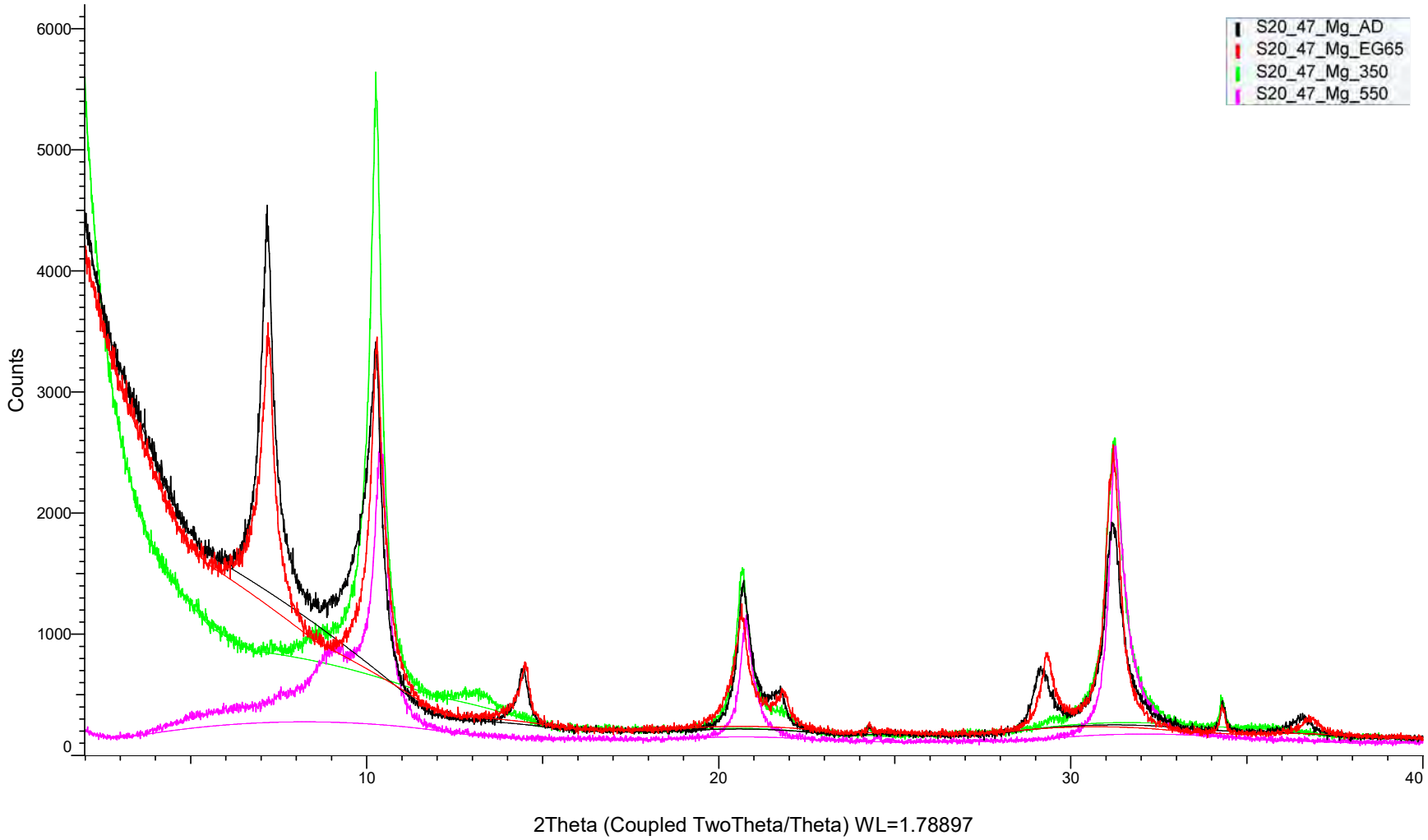

(Coupled TwoTheta/Theta)

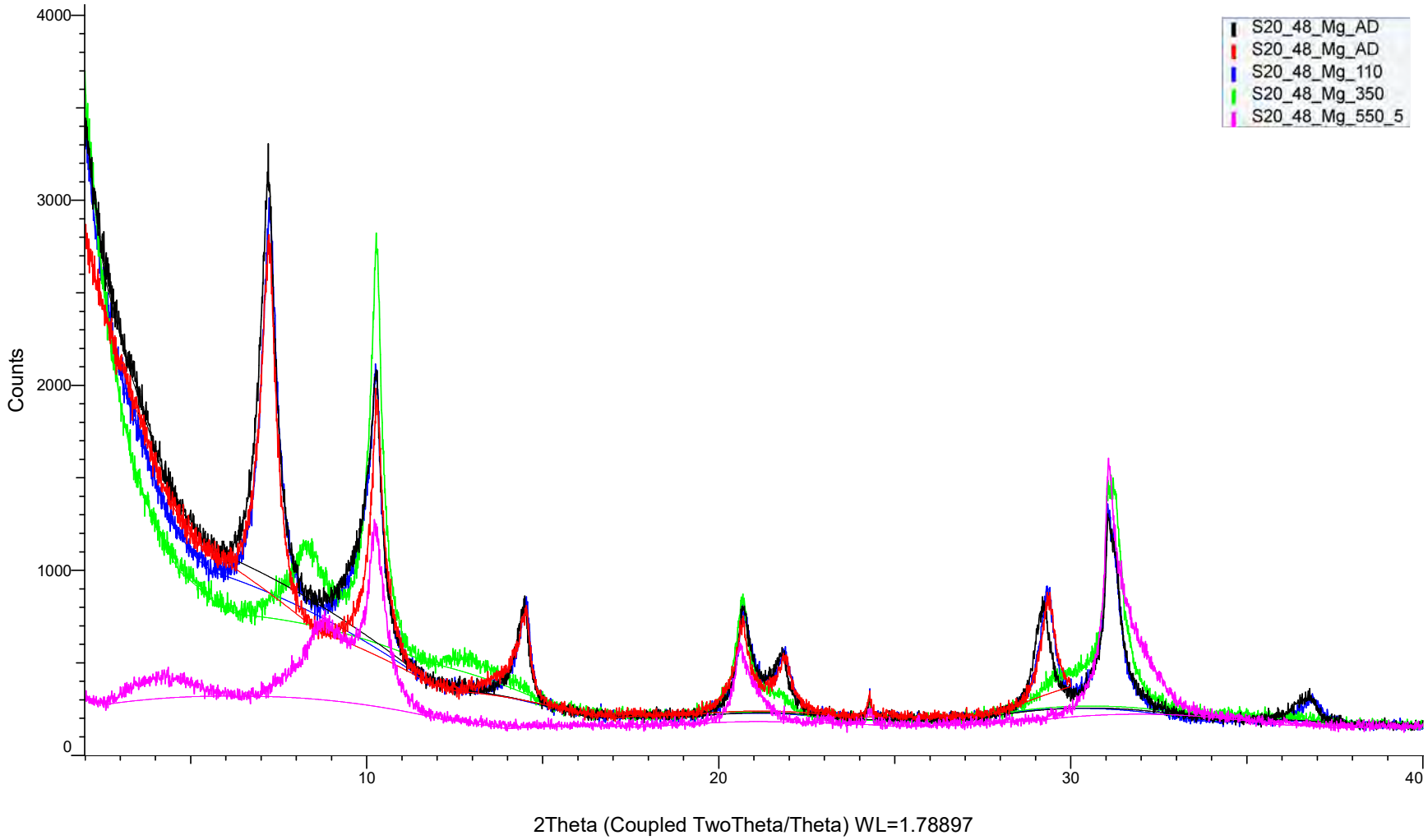

APPENDIX D

QXRD data

	quartz	illite	Kaolinite	Orthoclas	Sm/HIV/C	Siderite	Plagioclas	hematite	gibbsite
S17_1	0.53	0.20	0.19	0.00	0.05	0.02	0.02		-
S17_2	0.40	0.18	0.32	0.00	0.04	0.05	0.02	0.01	-
S17_3	0.24	0.24	0.36	0.01	0.06	0.05	0.04	-	-
S17_4	0.49	0.11	0.33	0.00	0.04	-	0.02	-	-
S17_5	0.26	0.24	0.34	0.00	0.08	0.00	0.03	-	0.05
S17_6	0.17	0.16	0.59	0.00	0.05	-	0.03	-	-
S17_7	0.25	0.16	0.51	0.00	0.05	-	0.03	-	-
S17_8	0.09	0.16	0.24	-	0.04	0.25	0.02	0.00	-
S17_9	0.18	0.15	0.54	0.00	0.05	0.06	0.02	-	-
S17_10	0.42	0.16	0.33	0.01	0.05	-	0.03	0.00	-
S17_11	0.26	0.22	0.40	0.01	0.06	0.00	0.05	-	-
S17_12	0.53	0.17	0.19	0.00	0.05	0.02	0.04	-	-
S17_13	0.32	0.15	0.33	0.03	0.04	-	0.01	-	0.10
S17_14	0.37	0.28	0.27	0.01	0.05	-	0.02	-	-
S17_15	0.43	0.20	0.27	0.01	0.05	0.00	0.03	0.00	-
S17_16	0.54	0.16	0.19	0.01	0.05	0.02	0.03	-	-
S17_17	0.43	0.25	0.18	0.00	0.06	0.02	0.06	-	-
S17_18	0.47	0.11	0.33	0.00	0.05	-	0.03	-	-
S17_19	0.34	0.21	0.34	0.00	0.06	-	0.04	-	-
S17_20	0.43	0.20	0.27	0.00	0.06	-	0.03	0.01	-
S17_21	0.38	0.14	0.40	0.00	0.05	-	0.03	-	-
S17_22	0.33	0.23	0.34	0.00	0.06	0.00	0.04	-	-
S17_23	0.24	0.12	0.54	0.00	0.05	-	0.03	-	-
S17_24	0.35	0.07	0.45	0.06	0.04	-	0.02	0.00	-
S17_25	0.47	0.08	0.34	0.05	0.04	-	0.02	0.00	-
S19_1	0.30	0.17	0.27	0.00	0.07	-	0.02	0.01	-
S19_2	0.49	0.11	0.22	0.00	0.06	-	0.02	0.00	-
S19_3	0.80	0.02	0.14	0.00	0.02	0.00	0.01	-	-
S19_5	0.33	0.28	0.31	0.00	0.05	-	0.03	-	-
S19_6	0.26	0.11	0.52	0.04	0.04	-	0.03	-	-
S19_7	0.21	0.21	0.42	0.00	0.05	-	0.02	-	-
S19_26	0.26	0.15	0.42	0.00	0.06	-	0.04	-	-
S19_27	0.31	0.26	0.35	0.00	0.04	-	0.03	-	-
S19_28	0.05	0.17	0.62	0.06	0.05	-	0.05	-	-
S19_29	0.74	0.08	0.14	0.00	0.02	-	0.01	0.00	-
S19_30a	0.66	0.09	0.19	0.00	0.04	0.00	0.01	-	-
S19_30b	0.49	0.15	0.29	0.00	0.05	-	0.03	-	-
S19_30c	0.45	0.20	0.26	0.00	0.05	-	0.03	0.00	-
S19_30d	0.63	0.13	0.17	0.00	0.05	-	0.02	-	-
S19-30e	0.38	0.20	0.32	0.00	0.06	0.00	0.04	-	-
S19_30f	0.13	0.16	0.49	0.05	0.04	-	0.02	-	0.08
S19_31	0.21	0.11	0.51	0.02	0.04	0.02	0.02	-	0.07
S19_4A									
S19_4B	0.44	0.09	0.43	0.00	0.02	-	0.02	-	-
S19_9	0.63	0.04	0.09	0.12	0.06	-	0.06	-	-
S19_8A	0.57	0.13	0.01	0.11	0.06	-	0.12	-	-

S19_8B	0.59	0.13	0.03	0.10	0.06	-	0.09	-	-
S19_8C	0.58	0.12	0.03	0.10	0.06	-	0.10	-	-
S19_10	0.34	0.03	-	0.03	0.04	-	0.45	0.01	-
S19_10a	0.43	0.09	-	0.07	0.05	-	0.23	-	-
S19_11	0.29	-	-	0.04	0.04	-	0.50	-	-
S19_12	0.21	-	-	0.03	0.05	-	0.56	-	-
S19_13	0.50	-	-	0.03	0.04	-	0.32	-	-
S19_14A	0.25	-	-	-	0.09	-	0.59	-	-
S19_14B	0.50	0.12	0.06	-	0.03	-	0.06	-	-
S19_18	-	-	-	0.07	0.11	-	0.81		-
S19_19	-	0.14	-	0.09	0.04	-	0.70	-	-
S19_23	-	-	-	0.09	0.11	-	0.80	-	-
S19_34	-	-	-	0.10	0.08	-	0.83	-	-
S19_35	-	-	-	0.12	0.07	-	0.81	-	-
S19_36a	-	0.04	-	0.16	0.09	-	0.71	-	-
S19_36b	-	-	-	0.09	0.31	-	0.60	-	-
S19_36c	-	-	-	0.18	0.32	-	0.50	-	-
S19_36d	-	-	-	0.07	0.53	-	0.40	-	-
SKT1	0.39	0.02	0.01	-	0.03	-	0.45		-
S20_43	0.50	0.15	0.02	0.00	0.05	-	0.03	-	-
S20_44	0.37	0.34	0.04	0.00	0.10	-	0.04	-	-
S20_45	0.45	0.18	0.04	0.02	0.02	-	0.03	-	-
S20_46	0.31	0.47	0.01	0.00	0.09	-	0.02	-	-
S20_47	0.40	0.39	0.03	0.00	0.08	-	0.04	-	-
S20_48	0.57	0.29	0.02	0.00	0.07	-	0.02	-	-
S20_30	0.74	0.04	0.18	0.00	0.02	-	0.02	-	-
S20_29	0.55	0.07	0.33	0.00	0.03	-	0.03	-	-
S20_28	0.29	0.07	0.51	0.06	0.03	-	0.03	-	-
S20-27	0.24	0.12	0.53	0.01	0.05	-	0.05	-	-
S20_26	0.03	0.12	0.56	0.14	0.05	-	0.01	-	-
S20_25	0.46	0.11	0.31	0.00	0.05	-	0.06	-	-
S20_24b	0.24	0.21	0.40	0.00	0.04	-	0.07	0.01	-
S20_24a	0.01	-	-	-	-	-	-	0.01	-
S20_1	0.76	0.04	0.16	0.01	0.02	-	0.01	-	-
S20_2	0.80	0.04	0.12	0.01	0.02	-	0.01	-	-
S20_3	0.60	0.04	0.32	0.00	0.02	-	0.01	-	-
S20_4	0.77	0.03	0.15	0.00	0.04	-	0.01	-	-
S20_5	0.63	0.04	0.27	0.02	0.02	-	0.02	-	-
S20_6	0.36	0.19	0.34	0.00	0.06	-	0.04	0.00	-
S20_7	0.50	0.06	0.37	0.00	0.04	-	0.02	-	-
S20_8	0.70	0.05	0.16	0.00	0.04	-	0.05	-	-
S20_9	0.50	0.09	0.33	0.00	0.05	-	0.04	-	-
S20_10	0.35	0.12	0.44	0.00	0.05	-	0.04	-	-
S20_11a	0.25	0.17	0.46	0.00	0.05	-	0.05	-	-
S20_11b	0.41	0.07	0.40	0.06	0.04	-	0.02	-	-
S20_11c	0.33	0.08	0.44	0.09	0.04	-	0.03	-	-
S20_12	0.23	0.11	0.46	0.12	0.04	-	0.04	-	-

S20_13	0.05	0.05	-	0.00	0.02	-	0.01	0.00	-
S20_14	0.99	-	-	0.00	-	-	0.00	-	-
S20_15	0.35	0.25	0.06	0.04	0.07	-	0.13	0.06	-
S20_16	0.46	0.15	0.06	0.02	0.06	-	0.21	0.03	-
S20_17	0.27	0.21	0.05	0.06	0.06	-	0.25	0.05	-
S20_18	0.43	0.15	0.05	0.00	0.02	-	0.31	0.03	-
S20_19	0.37	0.15	0.03	0.00	0.04	-	0.33	0.01	-
S20_31	0.55	0.10	0.05	0.03	0.03	-	0.19	0.03	-
S20_32	0.56	0.12	0.08	0.04	0.03	-	0.12	0.04	-
S20_20	0.49	0.35	0.01	0.00	0.09	-	0.06	-	-
S20_21	0.45	0.42	0.01	0.00	0.08	-	0.03	-	-
S20_22	0.50	0.33	0.03	0.00	0.12	-	0.02	-	-
S20_23a	0.46	0.37	-	0.00	0.15	-	0.03	-	-
S20_23b	0.21	0.12	-	-	0.03	-	0.03	-	-
S20_36	0.74	0.14	0.07	0.02	-	0.00	0.02	0.00	-
S20_37	0.68	0.16	0.11	0.00	-	0.00	0.03	0.00	-
S20_38	0.59	0.18	0.09	0.05	0.05	0.00	0.03	-	-
S20_39	0.41	0.20	0.30	0.00	0.04	-	0.05	-	-
S20_40	0.48	0.09	0.28	0.07	0.02	-	0.05	-	-
S20_41	0.55	0.14	0.17	0.06	0.02	-	0.06	-	-
S20_42	0.34	0.15	0.34	0.08	0.02	-	0.05		-

Fe-Al Oxid	Anatase	pyrite	mordenite	calcite	vermiculit	Fe-Ti oxid	dolomite
-	0.02	-	-	-	-	-	-
-	0.02	-	-	-	-	-	-
-	0.04	-	-	-	-	-	-
-	0.02	-	-	-	-	-	-
-	0.03	-	-	-	-	-	-
-	-	-	-	-	-	-	-
-	-	-	-	-	-	-	-
0.21	-	-	-	-	-	-	-
-	-	-	-	-	-	-	-
-	0.03	-	-	-	-	-	-
-	0.03	-	-	-	-	-	-
-	0.03	-	-	-	-	-	-
-	0.02	0.01	-	-	-	-	-
-	0.03	-	-	-	-	-	-
-	-	-	-	-	-	-	-
-	0.03	-	-	-	-	-	-
-	0.04	-	-	-	-	-	-
-	0.03	-	-	-	-	-	-
-	0.03	-	-	-	-	-	-
-	0.03	-	-	-	-	-	-
-	0.02	-	-	-	-	-	-
-	0.03	-	-	-	-	-	-
-	-	0.03	-	-	-	-	-
-	0.02	-	-	-	-	-	-
-	-	-	-	-	-	-	-
0.15	-	-	-	-	-	-	-
0.09	-	-	-	-	-	-	-
-	-	-	-	-	-	-	-
-	-	-	-	-	-	-	-
-	-	-	-	-	-	-	-
-	-	0.09	-	-	-	-	-
-	-	0.07	-	-	-	-	-
-	-	-	-	-	-	-	-
-	-	-	-	-	-	-	-
-	-	-	-	-	-	-	-
-	0.01	-	-	-	-	-	-
-	0.03	-	-	-	-	-	-
-	0.02	-	-	-	-	-	-
-	0.01	-	-	-	-	-	-
-	0.02	-	-	-	-	-	-
-	-	0.03	-	-	-	-	-
-	-	-	-	-	-	-	-
	-						
-	-	-	-	-	-	-	-
-	-	-	-	-	-	-	-
-	-	-	-	-	-	-	-

-	-	-	-	-	-	-	-
-	-	-	-	0.01	-	-	-
-	-	-	0.10	-	-	-	-
-	-	-	0.13	-	-	-	-
-	-	-	0.12	-	-	-	-
-	-	-	0.15	-	-	-	-
-	-	-	0.11	-	-	-	-
-	-	-	-	0.08	-	-	-
-	-	-	-	0.24	-	-	-
-	-	-	-	-	-	-	-
-	-	-	0.02	-	-	-	-
-	-	-	-	-	-	-	-
-	-	-	-	-	-	-	-
-	-	-	-	-	-	-	-
-	-	-	-	-	-	-	-
-	-	-	-	-	-	-	-
-	-	-	-	-	-	-	-
-	-	-	-	-	-	-	-
-	-	-	0.10	-	-	-	-
-	-	-	-	0.23	-	-	-
-	-	-	-	0.11	-	-	-
-	-	-	-	0.26	-	-	-
-	-	-	-	0.09	-	-	-
-	-	-	-	0.06	-	-	-
-	-	-	-	0.02	-	-	-
-	-	-	-	-	-	-	-
-	0.01	-	-	-	-	-	-
-	0.01	-	-	-	-	-	-
-	0.03	-	-	-	-	-	-
-	0.02	-	-	0.08	-	-	-
-	0.03	-	-	0.01	-	-	-
-	0.02	-	-	0.04	-	-	-
-	-	-	-	0.98	-	-	0.15
-	-	-	-	-	-	-	-
-	-	-	-	-	-	-	-
-	-	-	-	-	-	-	-
-	-	-	-	-	-	-	-
-	-	-	-	-	-	-	-
-	0.02	-	-	-	-	-	-
-	0.01	-	-	-	-	-	-
-	-	-	-	-	-	-	-
-	0.02	-	-	-	-	-	-
-	0.02	-	-	-	-	-	-
-	0.03	-	-	-	-	-	-
-	0.02	-	-	-	-	-	-
-	0.02	-	-	-	-	-	-
-	0.03	-	-	-	-	-	-

0.86	-	-	-	-	-	-	-
0.00	-	-	-	-	-	0.00	-
-	0.02	-	-	0.05	-	0.02	-
-	0.02	-	-	0.01	-	0.01	-
-	0.03	-	-	0.04	-	0.05	-
-	-	-	-	-	-	0.01	-
-	-	-	-	0.05	-	0.01	-
-	-	-	-	0.02	-	0.01	-
-	-	-	-	0.02	-	0.03	-
-	-	-	-	-	-	-	-
-	-	-	-	-	-	-	-
-	-	-	-	-	-	-	-
-	-	-	-	-	-	-	-
-	-	-	-	0.61	-	-	-
0.00	-	-	-	-	-	-	-
0.01	0.01	-	-	-	-	-	-
-	0.02	-	-	-	-	-	-
-	0.02	-	-	-	-	-	-
-	0.02	-	-	-	-	-	-
-	0.03	-	-	-	-	-	-
-	0.02	-	-	-	-	-	-

APPENDIX E

Geochemistry data

Analyte Symbol	SiO2	Al2O3	Fe2O3(T)	MnO	MgO
Unit Symbol	%	%	%	%	%
Detection Limit	0.01	0.01	0.01	0.001	0.01
Analysis Method	FUS-ICP	FUS-ICP	FUS-ICP	FUS-ICP	FUS-ICP
S20- 1	88.76	6.29	1.97	0.017	0.12
S20- 2	90.63	5.45	1.51	0.012	0.12
S20- 3	84.05	9.15	1.4	0.01	0.17
S20- 4	88.41	7.06	1.07	0.01	0.11
S20- 5	83.35	8.03	1.83	0.009	0.13
S20- 6	56.71	21.67	6.86	0.011	0.75
S20- 7	70.88	14.87	2.29	0.012	0.33
S20- 8	82.27	8.72	3.03	0.014	0.17
S20- 9	66.96	16.54	3.15	0.015	0.43
S20- 10	56.01	19.82	9.48	0.015	0.62
S20- 11 A	57.43	23.73	2.71	0.015	0.83
S20- 11 B	64.62	18.26	3.26	0.011	0.41
S20- 11 C	61.54	20.44	3.36	0.011	0.52
S20- 12	54.55	22.28	3.34	0.017	0.76
S20- 13	26.52	8.66	49.02	0.012	0.23
S20- 14	95.93	0.34	1.85	0.018	0.02
S20- 15	53.9	16.22	7.85	0.196	2.55
S20- 16	67.95	13.97	4.41	0.05	0.83
S20- 17	56.63	18.6	10	0.106	2.78
S20- 18	68.77	14.43	5.26	0.042	0.76
S20- 19	66.06	15.21	5.47	0.107	1.59
S20- 20	60.97	17.81	8.48	0.065	1.15
S20- 21	58.06	19.24	8.37	0.03	1.28
S20- 22	65.13	15.33	6.13	0.101	2.15
S20- 23 A	59.74	17.13	7.72	0.076	2.34
S20- 23 B	16.43	4.23	1.68	0.052	1.07
S20- 24 A	0.61	0.23	0.25	0.007	2.62
S20- 24 B	55.63	20.73	5.9	0.233	0.95
S20- 25	62.42	18.44	2.8	0.017	0.77
S20- 26	44.2	28.37	3.46	0.014	1.23
S20- 27	54.44	25.29	2.8	0.014	0.99

Analyte Symbol	SiO2	Al2O3	Fe2O3(T)	MnO	MgO
Unit Symbol	%	%	%	%	%
Detection Limit	0.01	0.01	0.01	0.001	0.01
Analysis Method	FUS-ICP	FUS-ICP	FUS-ICP	FUS-ICP	FUS-ICP
S20- 28	59.62	22.18	1.66	0.012	0.68
S20- 29	71.27	15.79	2.73	0.014	0.61
S20- 30	85.47	6.93	1.45	0.016	0.17
S20- 31	74.1	12.48	4.33	0.052	0.44
S20- 32	71.13	14.48	5.2	0.026	0.62
S20- 33	74.06	8.75	9.95	0.016	0.49
S20- 34	62.99	21.5	2.9	0.006	1.11
S20- 35	85.86	5.59	3.1	0.019	0.38
S20- 36	80.71	10.93	2.4	0.014	0.47
S20- 37	76.21	11.87	4.48	0.013	0.45
S20- 38	69.65	17.4	1.47	0.006	0.66
S20- 39	65.67	15.19	7.46	0.114	0.93
S20- 40	69.25	12.88	6.83	0.045	1.48
S20- 41	68.7	12.33	7.49	0.082	1.77
S20- 42	62.53	16.16	8.24	0.072	2.09
S20- 43	59.99	6.53	2.33	0.065	0.85
S20- 44	59.99	12.97	5.35	0.041	2.1
S20- 45	62.41	6.95	2.91	0.064	0.86
S20- 46	54.7	13.59	6.11	0.048	1.88
S20- 47	64.32	13.29	5.16	0.053	1.83
S20- 48	77.46	9.52	3.53	0.079	1.17
S20- 49	85.56	8.48	1.2	0.01	0.14
S19- 4 A	66.32	20.78	1.23	0.019	0.22
S19- 4 B	69.28	17.85	1.98	0.025	0.64
S19- 8 B	66.36	14.02	6.37	0.054	1.37
S19- 7	47.81	19.36	6.28	0.055	0.61
S19- 9	65.98	16.48	4.22	0.056	1.23
S19- 15	60.35	6.5	2.02	0.052	0.7
S19- 16	34	4.6	2.5	0.056	0.7
S19- 26	48.2	18.7	6.81	0.091	0.8
S19- 29	88.69	5.49	1.46	0.012	0.23

Analyte Symbol	SiO2	Al2O3	Fe2O3(T)	MnO	MgO
Unit Symbol	%	%	%	%	%
Detection Limit	0.01	0.01	0.01	0.001	0.01
Analysis Method	FUS-ICP	FUS-ICP	FUS-ICP	FUS-ICP	FUS-ICP
S19- 33 B	52.43	6.66	3.01	0.128	1.02
S17- 1	70.06	15.47	4.18	0.024	0.73
S17- 3	53.01	24.01	6.47	0.033	1.14
S17- 5	53.97	23.26	3.07	0.018	0.94
S17- 7	56.25	24.18	3.41	0.015	0.93
S17- 8	23.61	12.18	42.49	0.127	0.39
S17- 10	64.57	19.79	2.66	0.017	0.9
S17- 11	58.63	23.68	2.69	0.019	1.08
S17- 13	51.44	22.95	5.54	0.046	0.75
S17- 15	62.26	20.93	3.06	0.021	0.99
S17- 17	61.98	20.97	3.35	0.021	1.05
S17- 19	54.77	26.29	2.63	0.019	1.06
S17- 22	58.39	24.42	2.26	0.017	1.06
S17- 23	42.64	21.34	7.29	0.017	0.49
S17- 24	65.18	19.42	3.09	0.011	0.41
S19- 01	50.87	24.79	9.33	0.02	0.78
S19- 02	51.17	22.73	11.02	0.022	0.7
S19- 03	90.71	4.34	1.29	0.012	0.08
S19- 10	68.89	13.8	2.71	0.024	0.22
S19- 11	66.78	14.31	3.64	0.061	0.26
S19- 12	69.44	12.91	2.19	0.024	0.21
S19- 13	64.65	17.8	2.78	0.011	0.37
SR-19 -24	58.87	17.43	8.17	0.061	2.29
S19- -25	57.7	18.45	9.41	0.024	1.5
S19- 30a	77.44	12.12	1.9	0.019	0.42
S19- 30b	67.6	18.14	2.15	0.015	0.76
S19- 30c	65.06	19.46	2.98	0.022	0.86
S19- 30d	75.6	13.82	1.43	0.015	0.58
S19- 30e	62.46	22.18	2.22	0.016	0.96
S19- 30f	51.26	26.03	5.42	0.011	0.59
S19- 31	52.65	27.67	3.54	0.04	0.72

Analyte Symbol	SiO2	Al2O3	Fe2O3(T)	MnO	MgO
Unit Symbol	%	%	%	%	%
Detection Limit	0.01	0.01	0.01	0.001	0.01
Analysis Method	FUS-ICP	FUS-ICP	FUS-ICP	FUS-ICP	FUS-ICP
SR19- 32-1	71.69	12.33	4.14	0.063	1.6
SR19- 32-2	64.76	14.14	6.21	0.083	2.08
SR19- 33a	61.07	15.22	8.34	0.099	2.27
SR19- 36a	70.75	14.19	3.55	0.018	0.25
S19- 36b	60.27	18.51	4.75	0.043	1.25
S19- 36c	57.13	17.94	6.47	0.009	1.64
SKT-1	68.22	13.48	2.77	0.056	0.67
S19-05	60.18	23.61	2.21	0.017	0.99
S19-27	61.01	23.02	2.37	0.015	0.64

Analyte Symbol	CaO	Na2O	K2O	TiO2	P2O5
Unit Symbol	%	%	%	%	%
Detection Limit	0.01	0.01	0.01	0.001	0.01
Analysis Method	FUS-ICP	FUS-ICP	FUS-ICP	FUS-ICP	FUS-ICP
S20- 1	0.05	0.07	0.34	0.388	< 0.01
S20- 2	0.03	0.06	0.41	0.371	< 0.01
S20- 3	0.03	0.06	0.58	0.431	0.01
S20- 4	0.03	0.06	0.48	0.328	0.02
S20- 5	0.02	0.06	0.67	0.235	0.01
S20- 6	0.03	0.09	2.68	1.141	0.05
S20- 7	0.09	0.06	0.83	1.213	0.03
S20- 8	0.08	0.08	1.52	0.252	0.04
S20- 9	0.17	0.09	1.33	1.15	0.04
S20- 10	0.22	0.08	1.53	1.239	0.09
S20- 11 A	0.3	0.09	2.1	1.043	0.04
S20- 11 B	0.12	0.1	0.73	1.051	0.05
S20- 11 C	0.16	0.1	0.94	1.064	0.05
S20- 12	0.31	0.09	1.43	0.988	0.03
S20- 13	0.1	0.06	0.48	0.282	0.31
S20- 14	0.03	0.04	0.06	0.292	< 0.01
S20- 15	4.34	0.83	4.97	1.255	0.19
S20- 16	1.3	2.99	2.35	0.682	0.17
S20- 17	0.47	1.75	4.75	1.53	0.19
S20- 18	1.12	3.01	2.41	0.806	0.19
S20- 19	1.7	3.32	2.36	0.753	0.16
S20- 20	0.09	0.17	3.88	0.95	0.15
S20- 21	0.14	0.18	4.08	0.96	0.11
S20- 22	1.05	0.68	3.39	0.739	0.52
S20- 23 A	0.41	0.61	3.5	1.292	0.14
S20- 23 B	40.38	0.24	0.95	0.214	0.09
S20- 24 A	51.74	0.03	0.06	0.008	0.02
S20- 24 B	2.04	0.1	3.32	0.899	0.13
S20- 25	1.18	0.12	1.78	1.345	0.04
S20- 26	3.34	0.17	2.42	0.664	0.08
S20- 27	0.58	0.1	2.55	1.03	0.07

Analyte Symbol	CaO	Na2O	K2O	TiO2	P2O5
Unit Symbol	%	%	%	%	%
Detection Limit	0.01	0.01	0.01	0.001	0.01
Analysis Method	FUS-ICP	FUS-ICP	FUS-ICP	FUS-ICP	FUS-ICP
S20- 28	0.3	0.1	2.72	1.042	0.05
S20- 29	0.13	0.17	2.08	1.075	0.04
S20- 30	0.04	0.08	1.76	0.413	0.02
S20- 31	0.11	1.92	2.68	0.518	0.02
S20- 32	0.14	1.52	2.84	0.586	0.01
S20- 33	0.1	0.06	2.29	0.551	0.04
S20- 34	0.04	0.09	4.68	0.956	0.05
S20- 35	0.09	0.06	1.55	0.406	0.2
S20- 36	0.05	0.1	2.41	0.744	0.03
S20- 37	0.05	0.14	2.52	0.888	0.04
S20- 38	0.08	0.11	2.87	1.144	0.04
S20- 39	0.11	0.9	1.22	0.968	0.15
S20- 40	0.14	1.03	0.99	0.924	0.09
S20- 41	0.2	2.05	1.12	0.914	0.16
S20- 42	0.27	1.38	1.43	0.899	0.13
S20- 43	14.67	0.74	1.57	0.257	0.12
S20- 44	6.34	0.52	2.77	0.646	0.16
S20- 45	12.2	0.67	1.94	0.261	0.09
S20- 46	8.09	0.38	3.17	0.666	0.41
S20- 47	3.44	0.67	3.05	0.707	0.15
S20- 48	0.27	0.43	2.21	0.394	0.05
S20- 49	0.06	0.07	0.74	0.393	< 0.01
S19- 4 A	0.1	0.05	0.26	0.771	0.02
S19- 4 B	0.22	0.07	1.34	0.631	0.01
S19- 8 B	0.36	0.87	2.87	0.462	0.11
S19- 7	0.17	0.08	1.42	0.791	0.05
S19- 9	0.13	0.28	3.09	0.532	0.03
S19- 15	14.91	0.95	1.61	0.248	0.09
S19- 16	30.85	0.22	1.13	0.242	0.28
S19- 26	0.15	0.1	2.42	0.767	0.04
S19- 29	0.09	0.06	0.85	0.271	< 0.01

Analyte Symbol	CaO	Na2O	K2O	TiO2	P2O5
Unit Symbol	%	%	%	%	%
Detection Limit	0.01	0.01	0.01	0.001	0.01
Analysis Method	FUS-ICP	FUS-ICP	FUS-ICP	FUS-ICP	FUS-ICP
S19- 33 B	18.16	0.79	1.74	0.304	0.11
S17- 1	0.2	0.11	2.31	1.15	0.03
S17- 3	0.32	0.13	3.47	0.946	0.04
S17- 5	0.26	0.15	2.66	0.968	0.06
S17- 7	0.29	0.13	2.27	0.823	0.07
S17- 8	0.39	0.08	0.98	0.367	0.09
S17- 10	0.18	0.14	2.56	1.303	0.03
S17- 11	0.17	0.14	3.55	1.178	0.03
S17- 13	0.16	0.12	2.01	0.898	0.12
S17- 15	0.19	0.12	3.14	1.307	0.06
S17- 17	0.22	0.13	3.28	1.347	0.03
S17- 19	0.25	0.13	3.16	1.064	0.05
S17- 22	0.17	0.13	3.48	1.101	0.04
S17- 23	0.14	0.08	1.01	0.601	0.03
S17- 24	0.03	0.09	0.63	1.26	0.02
S19- 01	0.07	0.13	0.99	0.855	0.04
S19- 02	0.46	0.14	0.93	0.789	0.05
S19- 03	0.03	0.05	0.14	0.366	0.01
S19- 10	3.19	2.58	2.26	0.441	0.09
S19- 11	2.45	2.22	2.1	0.468	0.05
S19- 12	2.76	2.31	2.52	0.409	0.07
S19- 13	1.84	1.84	2.39	0.596	0.06
SR-19 -24	0.49	1.41	3	1.151	0.14
S19- -25	0.13	0.46	2.88	1.23	0.07
S19- 30a	0.14	0.1	1.39	1.112	0.03
S19- 30b	0.18	0.14	2.18	1.333	0.04
S19- 30c	0.14	0.11	2.84	1.48	0.03
S19- 30d	0.1	0.09	2.03	1.138	0.02
S19- 30e	0.14	0.12	3.13	1.306	0.03
S19- 30f	0.16	0.09	1.08	0.755	0.04
S19- 31	0.25	0.11	1.83	0.978	0.2

Analyte Symbol	CaO	Na2O	K2O	TiO2	P2O5
Unit Symbol	%	%	%	%	%
Detection Limit	0.01	0.01	0.01	0.001	0.01
Analysis Method	FUS-ICP	FUS-ICP	FUS-ICP	FUS-ICP	FUS-ICP
SR19- 32-1	0.17	0.51	3.1	0.588	0.06
SR19- 32-2	0.24	1.04	2.76	0.601	0.11
SR19- 33a	0.23	0.56	3.1	0.772	0.13
SR19- 36a	2.43	2.68	3.06	0.65	0.15
S19- 36b	0.74	0.17	0.27	0.789	0.03
S19- 36c	0.62	0.09	0.65	0.773	0.01
SKT-1	2.16	2.75	4.34	0.488	0.11
S19-05	0.18	0.13	3.3	1.247	0.03
S19-27	0.18	0.12	2.5	1.221	0.03

Analyte Symbol	LOI	Total	Sc	Be	V
Unit Symbol	%	%	ppm	ppm	ppm
Detection Limit		0.01	1	1	5
Analysis Method	GRAV	FUS-ICP	FUS-ICP	FUS-ICP	FUS-ICP
S20- 1	2.78	100.8	4	< 1	27
S20- 2	2.1	100.7	4	< 1	22
S20- 3	3.93	99.83	5	< 1	28
S20- 4	2.76	100.3	3	< 1	19
S20- 5	4.18	98.53	4	< 1	26
S20- 6	10.69	100.7	20	2	140
S20- 7	8.12	98.73	10	1	89
S20- 8	4.58	100.8	6	< 1	45
S20- 9	10.47	100.3	14	2	100
S20- 10	11.47	100.6	16	3	153
S20- 11 A	12.32	100.6	18	3	144
S20- 11 B	11.69	100.3	12	1	116
S20- 11 C	12.29	100.5	15	1	104
S20- 12	16.93	100.7	17	3	134
S20- 13	14.75	100.4	7	8	1019
S20- 14	-0.01	98.56	1	< 1	8
S20- 15	8.41	100.7	18	3	108
S20- 16	3.76	98.48	11	2	80
S20- 17	3.96	100.8	24	3	171
S20- 18	3.38	100.2	12	2	95
S20- 19	3.52	100.3	12	2	91
S20- 20	6.87	100.6	21	4	141
S20- 21	7.88	100.3	22	4	154
S20- 22	5.63	100.8	18	3	110
S20- 23 A	6.98	99.93	18	4	147
S20- 23 B	33.8	99.12	6	< 1	24
S20- 24 A	43.68	99.24	< 1	< 1	< 5
S20- 24 B	10.56	100.5	16	8	157
S20- 25	11.47	100.4	15	3	138
S20- 26	16.3	100.2	24	4	187
S20- 27	12.31	100.2	21	5	140

Analyte Symbol	LOI	Total	Sc	Be	V
Unit Symbol	%	%	ppm	ppm	ppm
Detection Limit		0.01	1	1	5
Analysis Method	GRAV	FUS-ICP	FUS-ICP	FUS-ICP	FUS-ICP
S20- 28	11.96	100.3	18	4	115
S20- 29	6.82	100.7	13	3	102
S20- 30	2.21	98.54	4	1	30
S20- 31	2.11	98.76	9	2	69
S20- 32	3.53	100.1	11	2	79
S20- 33	3.6	99.92	13	2	71
S20- 34	6.18	100.5	22	3	73
S20- 35	2	99.26	10	1	37
S20- 36	3.02	100.9	9	2	64
S20- 37	3.53	100.2	12	2	87
S20- 38	6.73	100.2	16	2	137
S20- 39	7.82	100.5	19	3	149
S20- 40	6.82	100.5	16	2	120
S20- 41	5.39	100.2	14	1	109
S20- 42	7.53	100.7	18	2	135
S20- 43	13.19	100.3	5	1	40
S20- 44	9.81	100.7	13	2	117
S20- 45	11.67	100	6	1	48
S20- 46	11.72	100.8	13	3	126
S20- 47	7.44	100.1	12	2	109
S20- 48	3.77	98.87	8	2	68
S20- 49	3.52	100.2	5	< 1	36
S19- 4 A	9.81	99.6	19	1	66
S19- 4 B	8.56	100.6	15	1	49
S19- 8 B	6.77	99.62	11	3	54
S19- 7	21.97	98.59	18	2	117
S19- 9	8.48	100.5	14	1	59
S19- 15	12.94	100.3	5	< 1	44
S19- 16	25.37	99.95	4	< 1	46
S19- 26	21.56	99.64	16	2	139
S19- 29	2.02	99.17	5	1	37

Analyte Symbol	LOI	Total	Sc	Be	V
Unit Symbol	%	%	ppm	ppm	ppm
Detection Limit		0.01	1	1	5
Analysis Method	GRAV	FUS-ICP	FUS-ICP	FUS-ICP	FUS-ICP
S19- 33 B	16.27	100.6	7	1	62
S17- 1	6.24	100.5	15	2	102
S17- 3	10.47	100	21	2	121
S17- 5	14.68	100.1	23	2	113
S17- 7	11.21	99.58	23	3	153
S17- 8	18.09	98.79	13	2	149
S17- 10	8.09	100.2	17	2	112
S17- 11	8.79	99.96	19	2	123
S17- 13	16.69	100.7	17	3	91
S17- 15	7.98	100.1	20	3	122
S17- 17	8.38	100.7	20	2	127
S17- 19	11.03	100.4	20	4	119
S17- 22	9.52	100.6	19	2	125
S17- 23	26.67	100.3	13	2	100
S17- 24	10.61	100.8	15	< 1	144
S19- 01	12.79	100.7	21	2	215
S19- 02	12.29	100.3	21	2	196
S19- 03	1.97	99	3	< 1	38
S19- 10	6	100.2	9	2	35
S19- 11	7.24	99.59	15	2	58
S19- 12	5.91	98.76	9	2	40
S19- 13	6.75	99.08	12	3	44
SR-19 -24	6.36	99.38	21	2	171
S19- -25	8.28	100.1	22	3	204
S19- 30a	4.42	99.09	13	2	85
S19- 30b	6.54	99.08	18	3	131
S19- 30c	6.4	99.39	18	4	124
S19- 30d	4.47	99.29	12	3	92
S19- 30e	7.59	100.2	18	2	110
S19- 30f	13.98	99.42	17	1	128
S19- 31	12.03	100	17	3	98

Analyte Symbol	LOI	Total	Sc	Be	V
Unit Symbol	%	%	ppm	ppm	ppm
Detection Limit		0.01	1	1	5
Analysis Method	GRAV	FUS-ICP	FUS-ICP	FUS-ICP	FUS-ICP
SR19- 32-1	4.46	98.7	11	2	112
SR19- 32-2	6.47	98.5	15	2	127
SR19- 33a	7.21	99	18	3	163
SR19- 36a	2.3	100	15	2	124
S19- 36b	12.05	98.87	20	4	138
S19- 36c	13.54	98.87	18	2	135
SKT-1	3.66	98.71	11	2	54
S19-05	7.76	99.64	19	2	119
S19-27	7.99	99.11	21	3	150

Analyte Symbol	Ba	Sr	Y	Zr	Cr
Unit Symbol	ppm	ppm	ppm	ppm	ppm
Detection Limit	2	2	1	2	20
Analysis Method	FUS-ICP	FUS-ICP	FUS-ICP	FUS-ICP	FUS-MS
S20- 1	118	15	7	132	120
S20- 2	111	9	6	122	120
S20- 3	131	11	6	156	130
S20- 4	113	10	5	73	70
S20- 5	154	14	4	54	40
S20- 6	377	48	22	240	130
S20- 7	191	42	24	327	90
S20- 8	218	19	13	111	40
S20- 9	238	48	29	235	80
S20- 10	251	55	35	206	110
S20- 11 A	316	60	33	197	120
S20- 11 B	183	46	25	273	80
S20- 11 C	199	49	26	215	100
S20- 12	236	57	32	179	100
S20- 13	84	17	7	64	80
S20- 14	210	20	4	186	160
S20- 15	1163	51	35	279	100
S20- 16	323	42	20	142	60
S20- 17	909	26	20	288	110
S20- 18	340	43	20	172	90
S20- 19	424	65	18	164	70
S20- 20	330	65	25	216	110
S20- 21	349	64	28	211	120
S20- 22	284	58	51	163	100
S20- 23 A	336	51	60	220	120
S20- 23 B	74	631	24	55	30
S20- 24 A	5	659	2	3	< 20
S20- 24 B	396	72	38	219	90
S20- 25	212	76	20	318	120
S20- 26	350	64	25	147	130
S20- 27	431	58	49	228	100

Analyte Symbol	Ba	Sr	Y	Zr	Cr
Unit Symbol	ppm	ppm	ppm	ppm	ppm
Detection Limit	2	2	1	2	20
Analysis Method	FUS-ICP	FUS-ICP	FUS-ICP	FUS-ICP	FUS-MS
S20- 28	409	48	41	234	70
S20- 29	310	40	38	353	90
S20- 30	205	14	12	180	30
S20- 31	443	44	16	120	30
S20- 32	560	49	17	156	50
S20- 33	157	21	18	167	50
S20- 34	379	5	15	256	60
S20- 35	282	95	65	84	30
S20- 36	323	25	23	228	70
S20- 37	361	31	25	292	80
S20- 38	317	42	29	303	130
S20- 39	306	25	27	179	100
S20- 40	329	25	38	157	100
S20- 41	314	42	18	159	110
S20- 42	370	40	22	167	110
S20- 43	202	149	15	92	30
S20- 44	295	92	15	193	80
S20- 45	292	137	13	93	30
S20- 46	311	138	26	170	70
S20- 47	289	83	20	213	80
S20- 48	257	42	12	120	50
S20- 49	223	22	9	134	100
S19- 4 A	32	8	38	256	< 20
S19- 4 B	75	22	31	200	< 20
S19- 8 B	673	31	38	150	< 20
S19- 7	233	40	33	195	90
S19- 9	183	15	23	158	< 20
S19- 15	256	103	11	88	30
S19- 16	148	518	13	87	30
S19- 26	355	44	24	167	80
S19- 29	201	12	12	100	30

Analyte Symbol	Ba	Sr	Y	Zr	Cr
Unit Symbol	ppm	ppm	ppm	ppm	ppm
Detection Limit	2	2	1	2	20
Analysis Method	FUS-ICP	FUS-ICP	FUS-ICP	FUS-ICP	FUS-MS
S19- 33 B	276	209	15	91	30
S17- 1	514	32	22	311	60
S17- 3	750	49	24	250	80
S17- 5	665	47	25	228	80
S17- 7	572	92	20	207	90
S17- 8	281	35	10	102	50
S17- 10	653	37	26	288	70
S17- 11	893	37	26	258	70
S17- 13	563	42	25	211	50
S17- 15	733	38	65	279	70
S17- 17	748	37	25	253	70
S17- 19	719	49	33	325	70
S17- 22	737	42	30	231	60
S17- 23	220	34	27	160	70
S17- 24	233	28	21	517	340
S19- 01	196	39	19	214	230
S19- 02	179	35	15	177	210
S19- 03	42	10	6	243	260
S19- 10	1308	635	29	155	< 20
S19- 11	5192	978	42	158	< 20
S19- 12	4011	791	25	130	< 20
S19- 13	3061	296	47	221	< 20
SR-19 -24	468	83	27	184	120
S19- -25	397	67	37	191	130
S19- 30a	331	33	53	275	70
S19- 30b	396	67	30	278	110
S19- 30c	659	33	34	338	60
S19- 30d	434	24	37	307	60
S19- 30e	666	36	35	242	70
S19- 30f	248	43	30	182	100
S19- 31	573	51	33	212	50

Analyte Symbol	Ba	Sr	Y	Zr	Cr
Unit Symbol	ppm	ppm	ppm	ppm	ppm
Detection Limit	2	2	1	2	20
Analysis Method	FUS-ICP	FUS-ICP	FUS-ICP	FUS-ICP	FUS-MS
SR19- 32-1	337	44	20	126	60
SR19- 32-2	482	53	34	137	50
SR19- 33a	484	53	35	160	90
SR19- 36a	552	190	23	118	< 20
S19- 36b	69	53	24	153	< 20
S19- 36c	40	46	21	149	< 20
SKT-1	630	432	26	126	< 20
S19-05	719	42	35	232	70
S19-27	622	42	26	247	100

Analyte Symbol	Co	Ni	Cu	Zn	Ga
Unit Symbol	ppm	ppm	ppm	ppm	ppm
Detection Limit	1	20	10	30	1
Analysis Method	FUS-MS	FUS-MS	FUS-MS	FUS-MS	FUS-MS
S20- 1	2	30	< 10	< 30	9
S20- 2	2	< 20	< 10	< 30	6
S20- 3	3	< 20	< 10	< 30	9
S20- 4	2	< 20	< 10	< 30	7
S20- 5	2	< 20	< 10	< 30	7
S20- 6	4	40	30	60	30
S20- 7	3	30	10	40	22
S20- 8	3	< 20	< 10	< 30	11
S20- 9	6	40	20	70	20
S20- 10	9	50	20	110	26
S20- 11 A	14	60	40	160	31
S20- 11 B	3	30	50	40	23
S20- 11 C	5	30	30	70	26
S20- 12	26	80	20	120	28
S20- 13	3	< 20	< 10	80	12
S20- 14	2	< 20	< 10	< 30	1
S20- 15	22	50	140	150	21
S20- 16	6	30	< 10	30	15
S20- 17	25	90	< 10	230	29
S20- 18	6	30	10	30	16
S20- 19	17	60	20	140	18
S20- 20	14	90	50	170	25
S20- 21	15	70	50	120	25
S20- 22	19	70	30	120	22
S20- 23 A	16	80	40	180	27
S20- 23 B	1	20	10	< 30	5
S20- 24 A	< 1	< 20	20	< 30	< 1
S20- 24 B	41	130	40	230	24
S20- 25	7	50	30	210	21
S20- 26	14	70	50	110	30
S20- 27	11	60	50	210	33

Analyte Symbol	Co	Ni	Cu	Zn	Ga
Unit Symbol	ppm	ppm	ppm	ppm	ppm
Detection Limit	1	20	10	30	1
Analysis Method	FUS-MS	FUS-MS	FUS-MS	FUS-MS	FUS-MS
S20- 28	93	120	60	100	27
S20- 29	10	30	30	60	18
S20- 30	3	< 20	< 10	< 30	8
S20- 31	5	20	< 10	< 30	13
S20- 32	6	< 20	< 10	< 30	14
S20- 33	3	< 20	10	60	12
S20- 34	2	30	10	40	22
S20- 35	4	< 20	10	< 30	11
S20- 36	3	30	20	< 30	14
S20- 37	3	30	60	30	14
S20- 38	3	50	20	40	21
S20- 39	60	70	50	110	17
S20- 40	11	80	40	100	16
S20- 41	29	90	30	90	14
S20- 42	22	100	40	220	17
S20- 43	6	30	20	30	7
S20- 44	9	50	40	100	16
S20- 45	4	< 20	20	40	7
S20- 46	9	50	30	80	16
S20- 47	9	50	30	80	15
S20- 48	9	30	20	60	10
S20- 49	2	< 20	< 10	< 30	7
S19- 4 A	21	< 20	20	50	19
S19- 4 B	11	< 20	10	< 30	16
S19- 8 B	10	< 20	30	70	13
S19- 7	17	60	40	200	21
S19- 9	8	< 20	30	50	14
S19- 15	9	< 20	20	< 30	7
S19- 16	6	20	20	< 30	5
S19- 26	14	40	40	70	22
S19- 29	4	< 20	20	80	7

Analyte Symbol	Co	Ni	Cu	Zn	Ga
Unit Symbol	ppm	ppm	ppm	ppm	ppm
Detection Limit	1	20	10	30	1
Analysis Method	FUS-MS	FUS-MS	FUS-MS	FUS-MS	FUS-MS
S19- 33 B	10	20	20	40	7
S17- 1	6	30	30	60	18
S17- 3	7	40	20	70	32
S17- 5	9	40	60	80	28
S17- 7	12	60	40	130	26
S17- 8	140	350	60	240	13
S17- 10	8	50	20	120	24
S17- 11	9	40	20	100	28
S17- 13	25	50	30	160	18
S17- 15	25	50	20	160	26
S17- 17	6	30	20	140	27
S17- 19	11	40	20	110	31
S17- 22	6	30	10	50	27
S17- 23	15	50	30	30	19
S17- 24	4	40	40	< 30	34
S19- 01	9	80	50	70	31
S19- 02	8	70	50	70	28
S19- 03	2	< 20	< 10	< 30	5
S19- 10	9	< 20	30	40	12
S19- 11	12	< 20	30	40	14
S19- 12	9	< 20	30	40	12
S19- 13	11	< 20	30	40	18
SR-19 -24	21	80	50	120	22
S19- -25	13	70	50	100	24
S19- 30a	23	50	20	80	15
S19- 30b	12	50	30	110	22
S19- 30c	11	50	20	140	24
S19- 30d	10	30	20	290	18
S19- 30e	6	40	20	70	28
S19- 30f	8	60	40	50	24
S19- 31	15	40	20	110	20

Analyte Symbol	Co	Ni	Cu	Zn	Ga
Unit Symbol	ppm	ppm	ppm	ppm	ppm
Detection Limit	1	20	10	30	1
Analysis Method	FUS-MS	FUS-MS	FUS-MS	FUS-MS	FUS-MS
SR19- 32-1	15	30	30	60	16
SR19- 32-2	19	40	40	90	12
SR19- 33a	26	70	70	140	17
SR19- 36a	15	< 20	60	80	14
S19- 36b	14	< 20	60	60	17
S19- 36c	9	< 20	40	60	17
SKT-1	9	< 20	20	30	11
S19-05	8	40	20	80	29
S19-27	17	50	20	170	27

Analyte Symbol	Ge	As	Rb	Nb	Mo
Unit Symbol	ppm	ppm	ppm	ppm	ppm
Detection Limit	1	5	2	1	2
Analysis Method	FUS-MS	FUS-MS	FUS-MS	FUS-MS	FUS-MS
S20- 1	< 1	9	16	6	< 2
S20- 2	< 1	5	22	7	< 2
S20- 3	< 1	5	29	6	< 2
S20- 4	< 1	< 5	19	5	< 2
S20- 5	< 1	5	29	4	< 2
S20- 6	2	18	176	28	3
S20- 7	1	7	83	21	2
S20- 8	< 1	7	64	6	< 2
S20- 9	1	7	98	19	3
S20- 10	2	24	137	27	3
S20- 11 A	1	5	165	24	2
S20- 11 B	1	10	52	21	3
S20- 11 C	1	6	78	23	2
S20- 12	< 1	6	96	23	2
S20- 13	< 1	228	33	6	7
S20- 14	< 1	9	2	5	2
S20- 15	< 1	7	205	12	6
S20- 16	< 1	5	98	6	< 2
S20- 17	< 1	6	199	17	< 2
S20- 18	< 1	5	103	8	< 2
S20- 19	< 1	< 5	93	9	< 2
S20- 20	1	23	177	19	< 2
S20- 21	1	25	181	20	< 2
S20- 22	1	16	150	14	< 2
S20- 23 A	1	16	158	26	2
S20- 23 B	< 1	5	35	4	< 2
S20- 24 A	< 1	8	2	< 1	< 2
S20- 24 B	2	71	183	18	< 2
S20- 25	1	9	138	20	2
S20- 26	1	9	197	12	< 2
S20- 27	1	8	208	25	< 2

Analyte Symbol	Ge	As	Rb	Nb	Mo
Unit Symbol	ppm	ppm	ppm	ppm	ppm
Detection Limit	1	5	2	1	2
Analysis Method	FUS-MS	FUS-MS	FUS-MS	FUS-MS	FUS-MS
S20- 28	< 1	10	132	20	2
S20- 29	< 1	23	106	20	< 2
S20- 30	< 1	7	62	10	< 2
S20- 31	< 1	< 5	81	5	< 2
S20- 32	< 1	< 5	87	6	< 2
S20- 33	< 1	13	63	13	< 2
S20- 34	1	26	131	30	< 2
S20- 35	1	13	44	17	< 2
S20- 36	< 1	5	87	15	< 2
S20- 37	< 1	< 5	85	19	< 2
S20- 38	1	10	124	20	< 2
S20- 39	< 1	12	57	9	2
S20- 40	< 1	11	38	8	< 2
S20- 41	< 1	10	40	10	< 2
S20- 42	< 1	19	51	21	< 2
S20- 43	< 1	9	51	5	< 2
S20- 44	1	10	111	12	< 2
S20- 45	< 1	6	56	6	< 2
S20- 46	< 1	10	120	12	< 2
S20- 47	1	9	114	10	< 2
S20- 48	1	9	76	5	< 2
S20- 49	< 1	< 5	29	6	< 2
S19- 4 A	< 1	6	16	11	< 2
S19- 4 B	1	6	60	7	< 2
S19- 8 B	< 1	5	80	5	< 2
S19- 7	< 1	17	80	12	6
S19- 9	< 1	5	91	6	< 2
S19- 15	< 1	6	48	5	< 2
S19- 16	< 1	9	41	4	< 2
S19- 26	< 1	8	125	15	6
S19- 29	< 1	< 5	41	5	< 2

Analyte Symbol	Ge	As	Rb	Nb	Mo
Unit Symbol	ppm	ppm	ppm	ppm	ppm
Detection Limit	1	5	2	1	2
Analysis Method	FUS-MS	FUS-MS	FUS-MS	FUS-MS	FUS-MS
S19- 33 B	< 1	11	54	5	< 2
S17- 1	< 1	6	107	17	< 2
S17- 3	1	10	172	18	< 2
S17- 5	< 1	10	153	16	4
S17- 7	1	8	140	14	2
S17- 8	1	31	58	6	11
S17- 10	< 1	< 5	146	20	< 2
S17- 11	1	5	164	18	< 2
S17- 13	< 1	16	106	13	2
S17- 15	1	5	150	19	< 2
S17- 17	< 1	6	153	18	4
S17- 19	< 1	5	212	22	2
S17- 22	< 1	< 5	169	19	< 2
S17- 23	< 1	13	62	12	4
S17- 24	2	5	46	22	3
S19- 01	3	23	82	16	4
S19- 02	2	23	80	14	3
S19- 03	1	5	10	5	< 2
S19- 10	1	< 5	43	5	< 2
S19- 11	1	5	59	6	< 2
S19- 12	2	5	52	4	< 2
S19- 13	2	6	55	8	< 2
SR-19 -24	2	12	130	14	< 2
S19- -25	3	29	145	17	< 2
S19- 30a	1	9	66	14	< 2
S19- 30b	2	< 5	137	21	< 2
S19- 30c	2	< 5	160	24	< 2
S19- 30d	2	< 5	110	14	< 2
S19- 30e	2	< 5	183	20	< 2
S19- 30f	1	9	83	15	3
S19- 31	1	< 5	117	14	< 2

Analyte Symbol	Ge	As	Rb	Nb	Mo
Unit Symbol	ppm	ppm	ppm	ppm	ppm
Detection Limit	1	5	2	1	2
Analysis Method	FUS-MS	FUS-MS	FUS-MS	FUS-MS	FUS-MS
SR19- 32-1	2	10	131	7	< 2
SR19- 32-2	2	14	83	7	< 2
SR19- 33a	2	15	113	10	< 2
SR19- 36a	1	8	69	4	< 2
S19- 36b	1	6	20	6	< 2
S19- 36c	1	11	25	6	< 2
SKT-1	1	6	80	4	< 2
S19-05	2	< 5	191	20	< 2
S19-27	2	5	129	21	< 2

Analyte Symbol	Ag	In	Sn	Sb	Cs
Unit Symbol	ppm	ppm	ppm	ppm	ppm
Detection Limit	0.5	0.2	1	0.5	0.5
Analysis Method	FUS-MS	FUS-MS	FUS-MS	FUS-MS	FUS-MS
S20- 1	< 0.5	< 0.2	1	< 0.5	1.1
S20- 2	0.5	< 0.2	1	< 0.5	1.3
S20- 3	0.6	< 0.2	1	< 0.5	1.6
S20- 4	< 0.5	< 0.2	1	< 0.5	0.9
S20- 5	< 0.5	< 0.2	1	< 0.5	1.4
S20- 6	0.9	< 0.2	4	1.1	13.4
S20- 7	1.4	< 0.2	3	1.2	7.5
S20- 8	< 0.5	< 0.2	1	< 0.5	2.3
S20- 9	1	< 0.2	3	0.9	6.2
S20- 10	0.8	< 0.2	4	1.3	8.6
S20- 11 A	0.8	< 0.2	4	1.4	10.7
S20- 11 B	1	< 0.2	3	1.4	6
S20- 11 C	0.9	< 0.2	4	1.3	7.9
S20- 12	0.7	< 0.2	3	1.1	8.7
S20- 13	< 0.5	< 0.2	1	4.7	2.8
S20- 14	0.6	< 0.2	1	< 0.5	< 0.5
S20- 15	3	< 0.2	4	1	8
S20- 16	0.5	< 0.2	1	< 0.5	3.2
S20- 17	1	< 0.2	4	< 0.5	4.8
S20- 18	0.6	< 0.2	2	< 0.5	3.1
S20- 19	0.7	< 0.2	2	< 0.5	2.4
S20- 20	0.7	< 0.2	3	0.9	6.5
S20- 21	0.7	< 0.2	3	0.8	6.8
S20- 22	0.5	< 0.2	3	< 0.5	5.2
S20- 23 A	0.7	< 0.2	4	< 0.5	5.5
S20- 23 B	< 0.5	< 0.2	< 1	< 0.5	1
S20- 24 A	< 0.5	< 0.2	< 1	< 0.5	< 0.5
S20- 24 B	0.7	< 0.2	3	3.7	24.3
S20- 25	1	< 0.2	3	4.4	22.1
S20- 26	0.6	< 0.2	3	< 0.5	18.6
S20- 27	0.9	< 0.2	4	0.8	13.2

Analyte Symbol	Ag	In	Sn	Sb	Cs
Unit Symbol	ppm	ppm	ppm	ppm	ppm
Detection Limit	0.5	0.2	1	0.5	0.5
Analysis Method	FUS-MS	FUS-MS	FUS-MS	FUS-MS	FUS-MS
S20- 28	0.9	< 0.2	3	< 0.5	7.8
S20- 29	1.1	< 0.2	2	1.3	6.8
S20- 30	0.6	< 0.2	1	< 0.5	1.5
S20- 31	< 0.5	< 0.2	1	< 0.5	1.9
S20- 32	0.5	< 0.2	1	< 0.5	2.1
S20- 33	0.8	< 0.2	1	< 0.5	3.7
S20- 34	1	< 0.2	4	< 0.5	3.7
S20- 35	0.8	< 0.2	1	< 0.5	1.3
S20- 36	0.8	< 0.2	2	< 0.5	3.1
S20- 37	0.9	< 0.2	2	< 0.5	2.8
S20- 38	1	< 0.2	3	< 0.5	6.2
S20- 39	0.6	< 0.2	1	< 0.5	2.8
S20- 40	< 0.5	< 0.2	1	< 0.5	2
S20- 41	0.5	< 0.2	1	< 0.5	1.6
S20- 42	0.5	< 0.2	1	< 0.5	2.4
S20- 43	< 0.5	< 0.2	1	< 0.5	2.2
S20- 44	0.6	< 0.2	2	< 0.5	6.6
S20- 45	< 0.5	< 0.2	1	< 0.5	2.1
S20- 46	0.5	< 0.2	2	< 0.5	7.6
S20- 47	0.9	0.2	2	< 0.5	6.6
S20- 48	0.5	< 0.2	1	< 0.5	3.5
S20- 49	0.5	< 0.2	1	< 0.5	1.7
S19- 4 A	0.8	< 0.2	3	< 0.5	0.5
S19- 4 B	0.6	< 0.2	2	< 0.5	2.1
S19- 8 B	0.5	< 0.2	1	< 0.5	2.7
S19- 7	0.6	< 0.2	2	< 0.5	6.4
S19- 9	0.5	< 0.2	1	< 0.5	3
S19- 15	< 0.5	< 0.2	1	< 0.5	1.7
S19- 16	< 0.5	< 0.2	< 1	< 0.5	2.8
S19- 26	0.5	< 0.2	2	< 0.5	8.5
S19- 29	< 0.5	< 0.2	1	< 0.5	1.9

Analyte Symbol	Ag	In	Sn	Sb	Cs
Unit Symbol	ppm	ppm	ppm	ppm	ppm
Detection Limit	0.5	0.2	1	0.5	0.5
Analysis Method	FUS-MS	FUS-MS	FUS-MS	FUS-MS	FUS-MS
S19- 33 B	< 0.5	< 0.2	1	< 0.5	2.1
S17- 1	1	< 0.2	2	0.9	5
S17- 3	0.6	< 0.2	3	1.6	10.4
S17- 5	0.9	< 0.2	3	0.8	7.7
S17- 7	0.7	< 0.2	3	0.6	10.5
S17- 8	< 0.5	< 0.2	1	1.6	3.8
S17- 10	0.9	< 0.2	3	0.8	6.7
S17- 11	0.8	< 0.2	3	0.9	6.9
S17- 13	0.7	< 0.2	2	0.8	4.2
S17- 15	0.9	< 0.2	3	1.2	6.6
S17- 17	0.9	< 0.2	3	1	6.7
S17- 19	1.1	< 0.2	4	1.3	13.6
S17- 22	0.7	< 0.2	4	1.2	9.1
S17- 23	0.6	< 0.2	1	< 0.5	5.4
S17- 24	1.7	< 0.2	4	< 0.5	6.2
S19- 01	0.6	< 0.2	4	1.7	8
S19- 02	0.5	< 0.2	4	1.6	7.5
S19- 03	0.8	< 0.2	1	< 0.5	0.9
S19- 10	< 0.5	< 0.2	2	< 0.5	4.1
S19- 11	< 0.5	< 0.2	2	< 0.5	8.6
S19- 12	< 0.5	< 0.2	2	0.5	16.9
S19- 13	0.6	< 0.2	2	< 0.5	6.9
SR-19 -24	0.5	< 0.2	2	0.5	5.7
S19- -25	0.5	< 0.2	3	1.2	8.4
S19- 30a	0.8	< 0.2	2	0.7	3.9
S19- 30b	0.9	< 0.2	3	1.1	9.9
S19- 30c	1.1	< 0.2	3	2.3	9.3
S19- 30d	0.9	< 0.2	2	1.8	5.4
S19- 30e	0.7	< 0.2	3	1.3	8.4
S19- 30f	0.6	< 0.2	2	1	8.9
S19- 31	0.6	< 0.2	2	1.5	5.2

Analyte Symbol	Ag	In	Sn	Sb	Cs
Unit Symbol	ppm	ppm	ppm	ppm	ppm
Detection Limit	0.5	0.2	1	0.5	0.5
Analysis Method	FUS-MS	FUS-MS	FUS-MS	FUS-MS	FUS-MS
SR19- 32-1	< 0.5	< 0.2	2	0.9	8.2
SR19- 32-2	0.5	< 0.2	2	0.8	3.5
SR19- 33a	0.6	< 0.2	2	1.1	6.1
SR19- 36a	< 0.5	< 0.2	1	0.5	18.9
S19- 36b	< 0.5	< 0.2	2	< 0.5	16.3
S19- 36c	< 0.5	< 0.2	2	< 0.5	1.9
SKT-1	< 0.5	< 0.2	1	< 0.5	1.6
S19-05	0.6	< 0.2	3	1.6	8.5
S19-27	0.7	< 0.2	3	1.1	8.2

Analyte Symbol	La	Ce	Pr	Nd	Sm
Unit Symbol	ppm	ppm	ppm	ppm	ppm
Detection Limit	0.1	0.1	0.05	0.1	0.1
Analysis Method	FUS-MS	FUS-MS	FUS-MS	FUS-MS	FUS-MS
S20- 1	10.9	20.3	2.31	8.8	1.7
S20- 2	8.8	16.7	1.93	6.9	1.4
S20- 3	11.3	22.8	2.61	9.8	1.9
S20- 4	7	14.4	1.58	5.9	1.2
S20- 5	4.8	9.1	1.05	3.8	0.8
S20- 6	36.8	62.8	7.31	26.1	4.9
S20- 7	37.5	68.5	7.95	29.1	5.8
S20- 8	27.2	60.1	6.91	26.3	5.3
S20- 9	48.8	94.8	10.9	39.9	7.6
S20- 10	72.4	153	18	65.8	12.7
S20- 11 A	58.7	107	12.3	43.9	8.1
S20- 11 B	39.6	72.4	8.34	30.3	6
S20- 11 C	51.3	95.9	11.1	40.4	7.4
S20- 12	55.1	100	11.3	41.3	7.5
S20- 13	16.6	30.7	3.62	13.5	2.6
S20- 14	3.8	6.6	0.73	2.6	0.5
S20- 15	33.4	74.6	9.14	36.4	7.8
S20- 16	21.4	44.3	5.77	22.9	4.7
S20- 17	56.4	111	12.3	44.5	8.5
S20- 18	27.1	53.3	6.65	25.7	5.1
S20- 19	23.1	47.2	6.01	23.4	4.8
S20- 20	52	99.5	11.3	40.5	6.9
S20- 21	47.4	95.4	11.1	42.7	8.6
S20- 22	51.6	102	14.5	64.6	16.5
S20- 23 A	56.6	97.7	13.9	54	12.5
S20- 23 B	13.5	27.2	4.05	17.8	4.3
S20- 24 A	0.8	1.5	0.19	0.8	0.1
S20- 24 B	60.3	105	13.7	50.8	10.2
S20- 25	38.6	69.9	8.24	29	4.7
S20- 26	36.5	67.9	8.45	31.3	6.3
S20- 27	82	158	18.9	72.3	14.4

Analyte Symbol	La	Ce	Pr	Nd	Sm
Unit Symbol	ppm	ppm	ppm	ppm	ppm
Detection Limit	0.1	0.1	0.05	0.1	0.1
Analysis Method	FUS-MS	FUS-MS	FUS-MS	FUS-MS	FUS-MS
S20- 28	70.1	131	17.2	62.9	12.7
S20- 29	44.6	68	10.2	38.2	7.9
S20- 30	18.8	38.6	4.19	15.6	2.9
S20- 31	19.4	35.9	4.77	18.5	4
S20- 32	20.1	37.9	4.91	19.2	3.9
S20- 33	32.4	58.8	7.04	24.3	4.4
S20- 34	38.8	77.1	8.79	31.5	5.4
S20- 35	221	317	63.2	238	47.8
S20- 36	30.7	59.5	7.19	27.2	5.1
S20- 37	25.9	51.3	6.19	23.1	4.7
S20- 38	53.2	102	12	43.4	7.5
S20- 39	28.9	60.4	7.66	31.1	6.9
S20- 40	36.1	60.7	10.7	48.3	11.9
S20- 41	15.5	33.7	4.28	18.1	4.3
S20- 42	22.1	46.7	5.69	23	5.3
S20- 43	12.8	25.6	3.54	14.8	3.4
S20- 44	30.6	54.7	6.14	21.9	3.8
S20- 45	15.7	30.4	3.91	15.6	3.5
S20- 46	32.1	63.6	8.19	34.1	7.6
S20- 47	31.7	59.9	7.37	27.1	5.3
S20- 48	23.6	37.7	5.25	18.3	3
S20- 49	16.5	31.4	3.67	12.9	2.6
S19- 4 A	10.6	22.4	2.8	12	3.2
S19- 4 B	20.9	39.1	5.17	20.4	4.2
S19- 8 B	26.9	64.2	7.49	31.6	7.1
S19- 7	40	67.6	10	39.7	9.1
S19- 9	26.9	59.3	6.12	22.6	4.4
S19- 15	14.6	26.1	3.27	12.9	2.8
S19- 16	11.5	22.9	2.96	12.1	3
S19- 26	38	62.6	8.34	30.7	5.8
S19- 29	16.5	35.6	4.14	15.2	3.2

Analyte Symbol	La	Ce	Pr	Nd	Sm
Unit Symbol	ppm	ppm	ppm	ppm	ppm
Detection Limit	0.1	0.1	0.05	0.1	0.1
Analysis Method	FUS-MS	FUS-MS	FUS-MS	FUS-MS	FUS-MS
S19- 33 B	15.9	31.2	4.03	16.3	3.5
S17- 1	29.9	59.8	7.17	27.2	5.2
S17- 3	34.8	63.5	8.14	30.9	6.5
S17- 5	33.2	85.3	11	45.5	10.6
S17- 7	48.2	91.4	8.49	31	6.3
S17- 8	17.5	44.1	4.24	16.6	4
S17- 10	32.4	65.6	8.07	30.8	6.4
S17- 11	31.4	58	7.26	27	5.7
S17- 13	22.1	43.4	5.28	20.1	4.7
S17- 15	60.7	123	14.7	57.7	12.9
S17- 17	27.6	51.6	6.46	24.8	5.1
S17- 19	51.7	86.6	10.6	38.3	7.3
S17- 22	39.2	67.1	8.66	32.2	6.2
S17- 23	29.3	54.6	7.79	31.5	7.8
S17- 24	29.8	68.1	6.38	23.6	4.5
S19- 01	36.7	74.5	7.2	26.7	4.5
S19- 02	31	64.3	6.1	21.7	3.8
S19- 03	11.8	21.9	2.18	7	1.2
S19- 10	22.1	45.2	5.58	21.6	5
S19- 11	80.4	55.9	20.5	80.7	16.5
S19- 12	35.9	42.1	8.35	31.6	6.5
S19- 13	160	98.4	44.5	160	29.3
SR-19 -24	33.9	67.1	8.06	31.5	6.2
S19- -25	47.8	93.7	11.8	45.5	9.2
S19- 30a	47.3	98.7	10.6	43.2	9.4
S19- 30b	43.7	88.6	10	37.1	7.1
S19- 30c	49.8	95.6	10.4	38	7.2
S19- 30d	58.7	108	12.1	44.9	8.6
S19- 30e	41.9	72.6	9.33	34.2	6.8
S19- 30f	46.6	77.3	10.1	39	7.7
S19- 31	27.8	62.4	6.91	27	5.8

Analyte Symbol	La	Ce	Pr	Nd	Sm
Unit Symbol	ppm	ppm	ppm	ppm	ppm
Detection Limit	0.1	0.1	0.05	0.1	0.1
Analysis Method	FUS-MS	FUS-MS	FUS-MS	FUS-MS	FUS-MS
SR19- 32-1	27.8	52.2	6.73	26.1	5
SR19- 32-2	29.4	53	7.76	31.4	7.4
SR19- 33a	43.4	76.4	10.4	41.7	9
SR19- 36a	18.3	35.9	4.69	19.5	4.5
S19- 36b	20.8	43.7	5.32	21.7	4.8
S19- 36c	17.7	35.3	4.29	17.6	3.8
SKT-1	18.5	37.6	4.51	18.4	4.1
S19-05	45.1	80.3	10.1	37.5	7.2
S19-27	36.4	65.7	7.62	28.4	5.3

Analyte Symbol	Eu	Gd	Tb	Dy	Ho
Unit Symbol	ppm	ppm	ppm	ppm	ppm
Detection Limit	0.05	0.1	0.1	0.1	0.1
Analysis Method	FUS-MS	FUS-MS	FUS-MS	FUS-MS	FUS-MS
S20- 1	0.36	1.3	0.2	1.4	0.3
S20- 2	0.26	1.1	0.2	1.4	0.3
S20- 3	0.34	1.5	0.2	1.4	0.3
S20- 4	0.26	1	0.2	1.1	0.3
S20- 5	0.21	0.7	0.1	0.9	0.2
S20- 6	1.01	4.1	0.7	4.6	1
S20- 7	1.11	4.6	0.8	4.8	1
S20- 8	1.19	4.6	0.7	3.6	0.6
S20- 9	1.51	6.2	1	5.5	1.1
S20- 10	2.46	9.4	1.4	7.6	1.5
S20- 11 A	1.68	6.7	1.1	6.6	1.3
S20- 11 B	1.2	4.8	0.8	4.8	1
S20- 11 C	1.45	5.9	0.9	5.5	1.1
S20- 12	1.54	6.4	1	6.1	1.2
S20- 13	0.55	2.2	0.3	2	0.4
S20- 14	0.08	0.5	0.1	0.7	0.2
S20- 15	1.72	7.2	1.1	6.7	1.3
S20- 16	1.19	4.2	0.7	4	0.8
S20- 17	1.7	5.8	0.8	4	0.9
S20- 18	1.28	4.4	0.7	4.2	0.9
S20- 19	0.99	4	0.6	3.5	0.7
S20- 20	1.29	5.1	0.9	5.1	1
S20- 21	1.76	6.6	1	5.7	1
S20- 22	2.98	13.9	2	10.4	1.9
S20- 23 A	2.53	12.6	2	11.8	2.3
S20- 23 B	0.78	3.9	0.6	3.4	0.6
S20- 24 A	< 0.05	< 0.1	< 0.1	0.1	< 0.1
S20- 24 B	2.06	8.1	1.2	7	1.3
S20- 25	0.88	3.2	0.6	3.5	0.7
S20- 26	1.32	4.9	0.8	4.7	0.9
S20- 27	2.99	12.7	1.9	10.4	1.9

Analyte Symbol	Eu	Gd	Tb	Dy	Ho
Unit Symbol	ppm	ppm	ppm	ppm	ppm
Detection Limit	0.05	0.1	0.1	0.1	0.1
Analysis Method	FUS-MS	FUS-MS	FUS-MS	FUS-MS	FUS-MS
S20- 28	2.49	9.5	1.4	8.2	1.5
S20- 29	1.65	7	1.1	6.8	1.3
S20- 30	0.55	2.2	0.4	2.1	0.4
S20- 31	0.93	3.3	0.6	3.1	0.6
S20- 32	0.91	3.5	0.5	3.2	0.7
S20- 33	0.54	3	0.5	3.1	0.6
S20- 34	0.57	3.2	0.4	2.8	0.6
S20- 35	8.98	29.8	4	18.3	2.7
S20- 36	0.99	4.2	0.7	4	0.8
S20- 37	0.92	4.1	0.7	4.3	0.9
S20- 38	1.4	5.6	0.8	5.1	1
S20- 39	1.66	6	0.9	5	1
S20- 40	3.05	11.5	1.6	8.3	1.6
S20- 41	1.01	4.5	0.7	4	0.8
S20- 42	1.26	4.8	0.8	4.3	0.9
S20- 43	0.79	3.1	0.4	2.6	0.5
S20- 44	0.75	3	0.5	2.7	0.6
S20- 45	0.85	3.1	0.5	2.5	0.5
S20- 46	1.65	6.4	0.9	5	1
S20- 47	1.16	4.2	0.7	3.9	0.8
S20- 48	0.61	2.4	0.4	2.3	0.5
S20- 49	0.53	2.1	0.3	1.9	0.4
S19- 4 A	0.79	3.9	0.8	5.7	1.3
S19- 4 B	0.9	4	0.7	5.1	1.1
S19- 8 B	1.48	6.9	1	6.2	1.2
S19- 7	2.2	8.2	1.3	7.2	1.4
S19- 9	0.81	3.9	0.6	4	0.8
S19- 15	0.63	2.4	0.3	2	0.4
S19- 16	0.61	2.5	0.4	2	0.4
S19- 26	1.23	4.8	0.7	4.4	0.9
S19- 29	0.67	2.5	0.4	2.3	0.5

Analyte Symbol	Eu	Gd	Tb	Dy	Ho
Unit Symbol	ppm	ppm	ppm	ppm	ppm
Detection Limit	0.05	0.1	0.1	0.1	0.1
Analysis Method	FUS-MS	FUS-MS	FUS-MS	FUS-MS	FUS-MS
S19- 33 B	0.84	3	0.5	2.7	0.5
S17- 1	1.1	4.4	0.7	4.1	0.8
S17- 3	1.26	5.3	0.9	5.1	1.1
S17- 5	2.26	8.1	1.2	6.9	1.3
S17- 7	1.3	4.8	0.8	4.4	0.9
S17- 8	0.81	3.1	0.5	2.9	0.5
S17- 10	1.38	5.4	0.9	5.6	1
S17- 11	1.16	4.9	0.8	5	1
S17- 13	1.05	4.3	0.8	4.9	1
S17- 15	2.88	13.1	2.1	12.3	2.3
S17- 17	1.11	4.3	0.7	4.5	1
S17- 19	1.51	6.2	1	5.9	1.2
S17- 22	1.25	4.9	0.8	4.7	0.9
S17- 23	1.82	6.6	1.1	6.2	1.2
S17- 24	0.74	3.5	0.6	3.8	0.8
S19- 01	0.94	3.5	0.6	3.3	0.7
S19- 02	0.83	3	0.5	2.9	0.6
S19- 03	0.23	0.9	0.1	0.8	0.2
S19- 10	1.08	5	0.8	5.2	1
S19- 11	4	13.2	1.8	9.1	1.7
S19- 12	1.42	5.5	0.9	4.8	0.9
S19- 13	5.98	18.8	2.5	12	2
SR-19 -24	1.4	5.6	0.9	5.2	1
S19- -25	2.04	7.8	1.2	7.1	1.4
S19- 30a	2.46	11.1	1.8	10.3	2
S19- 30b	1.53	5.8	1	6.1	1.2
S19- 30c	1.57	6.3	1.1	6.2	1.3
S19- 30d	1.83	8.1	1.3	7.2	1.3
S19- 30e	1.5	6	1	6	1.2
S19- 30f	1.71	6.3	1	5.5	1
S19- 31	1.34	5.2	0.9	5.6	1.1

Analyte Symbol	Eu	Gd	Tb	Dy	Ho
Unit Symbol	ppm	ppm	ppm	ppm	ppm
Detection Limit	0.05	0.1	0.1	0.1	0.1
Analysis Method	FUS-MS	FUS-MS	FUS-MS	FUS-MS	FUS-MS
SR19- 32-1	1.12	4.2	0.6	3.7	0.7
SR19- 32-2	1.86	7.2	1.1	6.3	1.2
SR19- 33a	2.17	8.1	1.3	6.6	1.3
SR19- 36a	1.14	4.7	0.8	4.5	0.9
S19- 36b	1.02	4.2	0.7	4.2	0.8
S19- 36c	0.98	3.9	0.6	3.8	0.8
SKT-1	1.03	4	0.7	4.5	1
S19-05	1.55	6.3	1.1	6.1	1.2
S19-27	1.19	4.8	0.8	4.9	1

Analyte Symbol	Er	Tm	Yb	Lu	Hf
Unit Symbol	ppm	ppm	ppm	ppm	ppm
Detection Limit	0.1	0.05	0.1	0.01	0.2
Analysis Method	FUS-MS	FUS-MS	FUS-MS	FUS-MS	FUS-MS
S20- 1	0.9	0.16	1	0.19	3.1
S20- 2	0.9	0.15	1	0.16	3
S20- 3	1	0.15	1	0.17	3.6
S20- 4	0.8	0.13	0.8	0.13	1.8
S20- 5	0.6	0.1	0.6	0.1	1.3
S20- 6	2.9	0.47	3.2	0.54	6.3
S20- 7	3	0.52	3.5	0.58	7.9
S20- 8	1.7	0.25	1.6	0.24	2.6
S20- 9	3.2	0.47	3.2	0.5	5.3
S20- 10	4.2	0.6	4.1	0.6	5.2
S20- 11 A	3.8	0.57	3.8	0.59	5.2
S20- 11 B	3	0.44	3.2	0.48	6.1
S20- 11 C	3.2	0.49	3.3	0.53	5.3
S20- 12	3.7	0.54	3.6	0.56	4.4
S20- 13	1.1	0.16	1.1	0.18	1.4
S20- 14	0.5	0.09	0.7	0.09	4.5
S20- 15	3.8	0.57	3.8	0.6	6.5
S20- 16	2.3	0.35	2.4	0.38	3
S20- 17	2.9	0.47	3.3	0.58	6.4
S20- 18	2.6	0.39	2.7	0.46	3.8
S20- 19	2.2	0.33	2.3	0.38	3.8
S20- 20	3	0.44	3.2	0.53	5.2
S20- 21	3.2	0.47	3.2	0.51	4.9
S20- 22	5.1	0.67	4.1	0.64	4.1
S20- 23 A	6.1	0.83	5.2	0.77	5.7
S20- 23 B	1.7	0.23	1.5	0.21	1.2
S20- 24 A	< 0.1	< 0.05	< 0.1	< 0.01	< 0.2
S20- 24 B	3.8	0.56	3.7	0.56	4.9
S20- 25	2.4	0.37	2.6	0.39	6.5
S20- 26	2.8	0.42	2.8	0.42	3.4
S20- 27	5.2	0.72	4.8	0.68	5.6

Analyte Symbol	Er	Tm	Yb	Lu	Hf
Unit Symbol	ppm	ppm	ppm	ppm	ppm
Detection Limit	0.1	0.05	0.1	0.01	0.2
Analysis Method	FUS-MS	FUS-MS	FUS-MS	FUS-MS	FUS-MS
S20- 28	4.5	0.68	4.5	0.69	5.3
S20- 29	3.9	0.59	4.2	0.63	7.5
S20- 30	1.4	0.22	1.6	0.27	4
S20- 31	1.9	0.27	1.8	0.27	2.5
S20- 32	1.9	0.28	1.9	0.31	3.2
S20- 33	2	0.3	2	0.31	3.3
S20- 34	2.1	0.36	2.7	0.44	6.2
S20- 35	6.4	0.81	4.9	0.66	1.8
S20- 36	2.5	0.37	2.4	0.38	4.8
S20- 37	2.6	0.39	2.6	0.39	5.7
S20- 38	3	0.44	3	0.47	6.7
S20- 39	2.8	0.4	2.8	0.44	3.8
S20- 40	3.9	0.56	3.5	0.46	4
S20- 41	2	0.29	2	0.28	4.1
S20- 42	2.5	0.35	2.3	0.33	3.7
S20- 43	1.3	0.19	1.2	0.17	1.9
S20- 44	1.8	0.27	1.8	0.29	4.4
S20- 45	1.3	0.19	1.2	0.17	2.1
S20- 46	2.6	0.37	2.3	0.35	4
S20- 47	2.4	0.35	2.4	0.38	4.9
S20- 48	1.5	0.22	1.4	0.22	2.6
S20- 49	1.1	0.16	1.1	0.18	3
S19- 4 A	4.2	0.69	4.9	0.76	5.8
S19- 4 B	3.4	0.52	3.8	0.6	4
S19- 8 B	3.7	0.53	3.6	0.57	3.3
S19- 7	4	0.6	4	0.66	4.5
S19- 9	2.6	0.42	2.8	0.43	3.7
S19- 15	1.1	0.15	1	0.15	2.1
S19- 16	1.1	0.14	0.9	0.11	1.8
S19- 26	2.7	0.41	2.6	0.41	3.8
S19- 29	1.4	0.2	1.4	0.22	2.4

Analyte Symbol	Er	Tm	Yb	Lu	Hf
Unit Symbol	ppm	ppm	ppm	ppm	ppm
Detection Limit	0.1	0.05	0.1	0.01	0.2
Analysis Method	FUS-MS	FUS-MS	FUS-MS	FUS-MS	FUS-MS
S19- 33 B	1.4	0.21	1.3	0.2	2.1
S17- 1	2.6	0.39	2.7	0.43	7
S17- 3	3	0.5	3.3	0.49	6.6
S17- 5	3.8	0.57	3.9	0.58	5.9
S17- 7	2.6	0.4	2.7	0.41	4.9
S17- 8	1.5	0.24	1.6	0.23	2.3
S17- 10	3.1	0.47	3.3	0.49	6.8
S17- 11	3.2	0.5	3.3	0.52	6.1
S17- 13	3	0.44	3	0.43	4.7
S17- 15	6.6	0.91	5.6	0.82	7
S17- 17	2.9	0.45	3	0.53	5.9
S17- 19	3.8	0.57	4	0.64	7.5
S17- 22	2.7	0.4	2.7	0.41	4.5
S17- 23	3.4	0.54	3.7	0.56	3.7
S17- 24	2.6	0.42	3	0.47	11.3
S19- 01	2.1	0.33	2.2	0.37	5.8
S19- 02	1.9	0.3	1.9	0.32	5
S19- 03	0.6	0.09	0.7	0.12	6.7
S19- 10	3.1	0.48	3.3	0.53	4.4
S19- 11	4.5	0.64	4.4	0.71	4.3
S19- 12	2.8	0.41	2.7	0.44	3.7
S19- 13	5.5	0.77	5	0.79	6.3
SR-19 -24	3.1	0.45	3.1	0.49	5.2
S19- -25	4.1	0.59	3.9	0.64	5.4
S19- 30a	5.3	0.72	4.6	0.69	7.4
S19- 30b	3.7	0.53	3.6	0.58	7.8
S19- 30c	3.6	0.54	3.8	0.6	9.2
S19- 30d	3.9	0.58	3.7	0.54	7.9
S19- 30e	3.5	0.52	3.5	0.58	7
S19- 30f	3	0.45	3.1	0.47	5.2
S19- 31	3.4	0.51	3.3	0.52	5.8

Analyte Symbol	Er	Tm	Yb	Lu	Hf
Unit Symbol	ppm	ppm	ppm	ppm	ppm
Detection Limit	0.1	0.05	0.1	0.01	0.2
Analysis Method	FUS-MS	FUS-MS	FUS-MS	FUS-MS	FUS-MS
SR19- 32-1	2.1	0.32	2.1	0.32	3.2
SR19- 32-2	3.3	0.48	2.8	0.43	3.7
SR19- 33a	3.6	0.51	3.2	0.49	4.3
SR19- 36a	2.7	0.39	2.5	0.41	3
S19- 36b	2.5	0.37	2.6	0.43	4.2
S19- 36c	2.3	0.33	2.2	0.35	4.3
SKT-1	3	0.45	3.2	0.5	3.5
S19-05	3.6	0.52	3.6	0.57	6.7
S19-27	3	0.46	3.3	0.53	6.9

Analyte Symbol	Ta	W	Tl	Pb	Bi
Unit Symbol	ppm	ppm	ppm	ppm	ppm
Detection Limit	0.1	1	0.1	5	0.4
Analysis Method	FUS-MS	FUS-MS	FUS-MS	FUS-MS	FUS-MS
S20- 1	0.5	< 1	< 0.1	10	< 0.4
S20- 2	0.5	< 1	0.2	5	< 0.4
S20- 3	0.5	< 1	0.3	8	< 0.4
S20- 4	0.3	< 1	0.2	5	< 0.4
S20- 5	0.2	< 1	0.3	7	< 0.4
S20- 6	1.9	4	1	40	< 0.4
S20- 7	2	3	0.9	32	< 0.4
S20- 8	0.4	1	0.5	56	< 0.4
S20- 9	1.7	3	0.9	32	< 0.4
S20- 10	2	4	1	74	0.4
S20- 11 A	1.7	2	1.2	42	< 0.4
S20- 11 B	1.7	2	0.7	48	< 0.4
S20- 11 C	1.7	3	0.9	38	< 0.4
S20- 12	1.6	2	0.9	24	< 0.4
S20- 13	0.3	< 1	0.4	111	< 0.4
S20- 14	0.5	< 1	< 0.1	15	< 0.4
S20- 15	0.9	59	1.1	16	0.5
S20- 16	0.5	1	0.6	5	< 0.4
S20- 17	1.2	2	1.1	14	< 0.4
S20- 18	0.6	2	0.7	10	< 0.4
S20- 19	0.6	1	0.6	6	< 0.4
S20- 20	1.3	2	0.8	24	< 0.4
S20- 21	1.3	6	0.9	28	< 0.4
S20- 22	1	1	0.8	18	< 0.4
S20- 23 A	1.8	1	0.8	24	< 0.4
S20- 23 B	0.1	< 1	0.3	< 5	< 0.4
S20- 24 A	< 0.1	< 1	0.2	< 5	< 0.4
S20- 24 B	1.3	3	2	49	0.4
S20- 25	1.4	2	1	41	< 0.4
S20- 26	0.8	< 1	1	13	< 0.4
S20- 27	1.7	2	1.4	44	< 0.4

Analyte Symbol	Ta	W	Tl	Pb	Bi
Unit Symbol	ppm	ppm	ppm	ppm	ppm
Detection Limit	0.1	1	0.1	5	0.4
Analysis Method	FUS-MS	FUS-MS	FUS-MS	FUS-MS	FUS-MS
S20- 28	1.4	2	1.3	56	< 0.4
S20- 29	1.5	2	0.8	16	< 0.4
S20- 30	0.9	< 1	0.5	8	< 0.4
S20- 31	0.3	< 1	0.5	< 5	< 0.4
S20- 32	0.3	< 1	0.5	< 5	< 0.4
S20- 33	0.9	1	0.5	20	< 0.4
S20- 34	2.5	1	0.6	8	< 0.4
S20- 35	0.5	2	0.3	73	< 0.4
S20- 36	1.1	< 1	0.5	9	< 0.4
S20- 37	1.5	< 1	0.4	12	< 0.4
S20- 38	1.4	1	0.7	20	< 0.4
S20- 39	0.5	< 1	0.4	10	< 0.4
S20- 40	0.5	< 1	0.1	< 5	< 0.4
S20- 41	0.6	< 1	0.1	11	< 0.4
S20- 42	0.5	< 1	0.3	9	< 0.4
S20- 43	0.2	< 1	0.3	9	< 0.4
S20- 44	0.7	< 1	0.5	27	< 0.4
S20- 45	0.2	< 1	0.3	6	< 0.4
S20- 46	0.7	< 1	0.5	20	< 0.4
S20- 47	0.7	1	0.6	15	< 0.4
S20- 48	0.4	2	0.5	20	< 0.4
S20- 49	0.4	< 1	0.3	12	< 0.4
S19- 4 A	0.6	2	0.4	12	< 0.4
S19- 4 B	0.3	21	0.5	7	< 0.4
S19- 8 B	0.3	11	0.4	7	< 0.4
S19- 7	0.8	2	0.6	14	< 0.4
S19- 9	0.3	< 1	0.5	18	< 0.4
S19- 15	0.2	41	0.3	8	< 0.4
S19- 16	0.1	35	0.3	6	< 0.4
S19- 26	0.9	1	0.9	18	< 0.4
S19- 29	0.2	< 1	0.4	19	< 0.4

Analyte Symbol	Ta	W	Tl	Pb	Bi
Unit Symbol	ppm	ppm	ppm	ppm	ppm
Detection Limit	0.1	1	0.1	5	0.4
Analysis Method	FUS-MS	FUS-MS	FUS-MS	FUS-MS	FUS-MS
S19- 33 B	0.2	38	0.4	7	< 0.4
S17- 1	1	2	0.6	27	< 0.4
S17- 3	1.1	3	1.1	31	< 0.4
S17- 5	1	3	1.2	29	< 0.4
S17- 7	0.8	1	1.1	89	< 0.4
S17- 8	0.2	< 1	0.7	33	< 0.4
S17- 10	1.3	3	0.8	28	< 0.4
S17- 11	1.2	2	0.9	36	< 0.4
S17- 13	0.8	1	0.7	34	< 0.4
S17- 15	1.1	2	0.8	34	< 0.4
S17- 17	1.1	95	0.8	34	< 0.4
S17- 19	1.4	6	1.4	42	< 0.4
S17- 22	1.5	2	0.6	26	< 0.4
S17- 23	0.7	< 1	0.8	8	< 0.4
S17- 24	1.6	3	0.4	78	< 0.4
S19- 01	1.3	22	0.6	37	0.6
S19- 02	1.2	8	0.6	35	0.5
S19- 03	0.6	12	0.2	12	< 0.4
S19- 10	0.6	50	0.4	15	< 0.4
S19- 11	0.5	43	0.5	25	< 0.4
S19- 12	0.5	55	0.4	13	< 0.4
S19- 13	0.7	2	0.7	31	< 0.4
SR-19 -24	1.3	4	0.6	12	< 0.4
S19- -25	1.4	2	0.7	16	< 0.4
S19- 30a	1.6	3	0.8	19	< 0.4
S19- 30b	2	3	1	31	< 0.4
S19- 30c	2	4	1.4	52	< 0.4
S19- 30d	1.5	3	1.1	53	< 0.4
S19- 30e	1.7	3	1.5	38	< 0.4
S19- 30f	1.2	2	1.4	16	< 0.4
S19- 31	1.1	2	1	36	< 0.4

Analyte Symbol	Ta	W	Tl	Pb	Bi
Unit Symbol	ppm	ppm	ppm	ppm	ppm
Detection Limit	0.1	1	0.1	5	0.4
Analysis Method	FUS-MS	FUS-MS	FUS-MS	FUS-MS	FUS-MS
SR19- 32-1	0.9	41	1	38	< 0.4
SR19- 32-2	0.7	50	0.7	20	< 0.4
SR19- 33a	0.9	16	0.7	48	< 0.4
SR19- 36a	0.4	67	0.7	10	< 0.4
S19- 36b	0.5	2	0.3	9	< 0.4
S19- 36c	0.4	2	0.5	8	< 0.4
SKT-1	0.4	47	0.7	14	< 0.4
S19-05	1.6	4	1.4	41	< 0.4
S19-27	1.6	2	1.7	25	< 0.4

Report Number: A20-15186
Report Date: 13/1/2021

Analyte Symbol	Th	U
Unit Symbol	ppm	ppm
Detection Limit	0.1	0.1
Analysis Method	FUS-MS	FUS-MS
S20- 1	4.6	1.1
S20- 2	3.1	1.1
S20- 3	3.4	1.2
S20- 4	2.5	0.9
S20- 5	2.7	1
S20- 6	18.9	4.6
S20- 7	14.1	3.9
S20- 8	10.9	1.2
S20- 9	13	3.2
S20- 10	16.3	4.1
S20- 11 A	17	4.4
S20- 11 B	12.3	4.4
S20- 11 C	11.2	3.3
S20- 12	14.3	3.3
S20- 13	14.7	1.5
S20- 14	1.4	0.7
S20- 15	9	3.1
S20- 16	6.1	1.8
S20- 17	10.9	3.5
S20- 18	7.2	2.1
S20- 19	6.4	1.9
S20- 20	13	4
S20- 21	13	3.6
S20- 22	11.4	3.9
S20- 23 A	11.9	4.1
S20- 23 B	2.8	1.4
S20- 24 A	0.2	1.4
S20- 24 B	18.2	5.6
S20- 25	15.4	4.7
S20- 26	13.9	3.4
S20- 27	21.5	5.7

Report Number: A20-15186
Report Date: 13/1/2021

Analyte Symbol	Th	U
Unit Symbol	ppm	ppm
Detection Limit	0.1	0.1
Analysis Method	FUS-MS	FUS-MS
S20- 28	27.5	5.7
S20- 29	13.9	4
S20- 30	8.1	1.8
S20- 31	5.2	1.5
S20- 32	6.1	1.8
S20- 33	9.4	3
S20- 34	16.4	3.6
S20- 35	4.7	3
S20- 36	7.8	2.3
S20- 37	8.6	2.5
S20- 38	12.6	3.1
S20- 39	5.7	1.9
S20- 40	4.7	1.6
S20- 41	5.2	1.6
S20- 42	4.5	1.7
S20- 43	4.1	1.3
S20- 44	9.1	2.7
S20- 45	4.2	1.1
S20- 46	9.3	3
S20- 47	9.8	2.9
S20- 48	6.6	1.8
S20- 49	4.3	1.3
S19- 4 A	10.1	4.2
S19- 4 B	7.6	2.4
S19- 8 B	6.4	1.7
S19- 7	12.9	3.9
S19- 9	7.3	1.7
S19- 15	4.1	1.1
S19- 16	3.1	1.4
S19- 26	11.4	3.3
S19- 29	6.5	2.7

Report Number: A20-15186
Report Date: 13/1/2021

Analyte Symbol	Th	U
Unit Symbol	ppm	ppm
Detection Limit	0.1	0.1
Analysis Method	FUS-MS	FUS-MS
S19- 33 B	4.5	1.3
S17- 1	11.7	5.2
S17- 3	17.2	4.7
S17- 5	15.6	10.2
S17- 7	13.9	6.2
S17- 8	6.7	6.7
S17- 10	12.6	2.9
S17- 11	10.7	3
S17- 13	8.4	2.8
S17- 15	11.2	3.3
S17- 17	11	4.1
S17- 19	30.8	9.6
S17- 22	8.5	3
S17- 23	10.9	3.5
S17- 24	12.2	3.6
S19- 01	22.2	4.5
S19- 02	21.4	4.3
S19- 03	4.8	1.2
S19- 10	7.7	2.3
S19- 11	8.1	2.3
S19- 12	7.1	2.1
S19- 13	10.8	3.5
SR-19 -24	8.2	2.5
S19- -25	9.7	3
S19- 30a	9.9	3.9
S19- 30b	16.4	4
S19- 30c	25.7	8.9
S19- 30d	17.4	12.3
S19- 30e	11.6	2.8
S19- 30f	17.8	4.5
S19- 31	12.4	4.2

Report Number: A20-15186
Report Date: 13/1/2021

Analyte Symbol	Th	U
Unit Symbol	ppm	ppm
Detection Limit	0.1	0.1
Analysis Method	FUS-MS	FUS-MS
SR19- 32-1	8.9	2.4
SR19- 32-2	7.7	2.4
SR19- 33a	9.3	3
SR19- 36a	5.7	1.6
S19- 36b	6.9	1.8
S19- 36c	5.3	1.2
SKT-1	6.6	2
S19-05	11.4	3.8
S19-27	13.2	7.6

APPENDIX F

Crystal properties

	illite ratio	FWHM_illite	FWHM_kao	d(060)	
				~1.54 Å	~1.50 Å
S17_1	1.178848177	0.4	0.868	+	+
S17_2	1.208117583	0.409	0.953		
S17_3	1.248559092	0.418	0.829	+	+
S17_4	1.293214407	0.45	1.012		
S17_5	1.098649777	0.495	0.954		
S17_6	1.184016824	0.569	0.804		
S17_7	1.255808736	0.509	0.788	+	+
S17_8	1.137908471	0.485	0.872	+	+
S17_9	1.291569892	0.574	0.811		
S17_10	1.262816598	0.5	0.906		
S17_11	1.336123917	0.447	0.87		
S17_12	1.232235951	0.495	0.888		
S17_13	1.039758096	0.536	0.8		
S17_14	1.158244008	0.434	0.881	+	+
S17_15	1.320214065	0.392	0.849	+	+
S17_16	1.680263801	0.384	0.847		
S17_17	1.720716207	0.597	0.875		
S17_18	1.466736152	0.617	0.837		
S17_19	1.343100147	0.411	0.832		
S17_20	1.481877136	0.451	0.871	+	+
S17-21	1.361129357	0.5	0.94	+	+
S17-22	1.364155977	0.375	0.817	+	+
S17_23	1.380973879	0.493	0.742	+	+
S17_24			0.919	+	
S17_25			0.691	+	+
S19_1			0.906	+	+
S19_2			1.253		
S19_3			0.89	+	
S19_5	1.373278149	0.446	0.866	+	+
S19_6	1.375972842	0.507	0.838		
S19_7	1.521866404	0.423	0.749		
S19_26	1.165731761	0.408	0.586		
S19_27	1.244066072	0.441	0.802		
S19_29	1.322659833	0.454	0.886	+	+
S19_30a	1.179668113	0.493	0.794	+	+
S19_30b	1.134321533	0.5	0.95	+	+
S19_30c	1.219109573	0.466	0.874	+	+
S19_30d	1.170290041	0.459	0.882	+	+
S19_30e	1.364684573	0.479	0.851	+	+
S19_30f			0.829	+	+
S19_31	1.034222607	0.776	0.756	+	+
avg	1.254191938	0.4798	0.8577561		

	illite ratio	FWHM_illite	FWHM_kao	d(060)	
				~1.54 Å	~1.50 Å

S20_1	1.361153006	0.409	0.751	+	+
S20_2	1.166065018	0.444	0.847		
S20_3	1.055304428	0.522	0.848	+	+
S20_4			0.722		
S20_5	1.097396348	0.411	0.792	+	
S20_6	1.297086619	0.35	0.411	+	+
S20_7			0.716		
S20_8	1.657836151	0.397	0.724	+	+
S20_9	1.626802972	0.348	0.465		
S20_10	1.708568014	0.59	0.493	+	+
S20_11	1.805247091	0.451	0.487	+	+
S20_12	2.010951027	0.335	0.355	+	+
S20_14			0.178		
avg	1.478641067	0.43577778	0.5991538		

	illite ratio	FWHM_illite	FWHM_kao	d(060) ~1.54 Å	~1.50 Å
S20_24b	1.764291267	0.386	0.712		+
S20_25	2.020508362	0.584	0.991	+	+
S20_26	1.565640419	0.562	1.022	+	+
S20-27	1.387104124	0.611	0.784		
S20_28	1.285658188	0.304	0.366	+	+
S20_29	1.353924454	0.308	0.779		
S20_30	1.090333442	0.322	0.823	+	
avg	1.495351465	0.43957143	0.7824286		